# Modelling Geochemical and Geobiological Consequences of Low-Temperature Continental Serpentinization

by

James Andrew Monton Leong

A Dissertation Presented in Partial Fulfillment
of the Requirements for the Degree
Doctor of Philosophy

Approved June 2020 by the
Graduate Supervisory Committee:

Everett Shock, Chair
Ariel Anbar
Hilairy Hartnett
Thomas Sharp
Christy Till

ARIZONA STATE UNIVERSITY

August 2020

# ABSTRACT

The hydrous alteration of ultramafic rocks, known as serpentinization, produces some of the most reduced ($H_2$ >1 *m*molal) and alkaline (pH >11) fluids on Earth. Serpentinization can proceed even at the low-temperature conditions (<50°C) characteristic of most of Earth's continental aquifers, raising questions on the limits of life deep in the subsurface and the magnitude in the flux of reduced volatiles to the surface. In this work, I explored the compositions and consequences of fluids and volatiles found in three low-temperature serpentinizing environments: (1) active hyperalkaline springs in ophiolites, (2) modern shallow and deep peridotite aquifers, and (3) komatiitic aquifers during the Archean.

Around 140 fluids were sampled from the Oman ophiolite and analyzed for their compositions. Fluid compositions can be accounted for by thermodynamic simulations of reactions accompanying incipient to advanced stages of serpentinization, as well as by simulations of mass transport processes such as fluid mixing and mineral leaching. Thermodynamic calculations were also used to predict compositions of end-member fluids representative of the shallow and deep peridotite aquifers that were ultimately used to quantify energy available to various subsurface chemolithotrophs. Calculations showed that sufficient energy and power supply can be available to support deep-seated methanogens. An additional and a more diverse energy supply can be available when surfacing deep-seated fluids mix with shallow groundwater in discharge zones of the subsurface fluid pathway. Finally, the consequence of the evolving continental composition during the Archean for the global supply of $H_2$ generated through komatiite serpentinization was quantified. Results show that the flux of serpentinization-generated

$H_2$ could have been a significant sink for $O_2$ during most of the Archean. This $O_2$ sink diminished greatly towards the end of the Archean as komatiites became less common and helped set the stage for the Great Oxidation Event. Overall, this study provides a framework for exploring the origins of fluid and volatile compositions, including their redox state, that can result from various low-temperature serpentinizing environments in the present and past Earth and in other rocky bodies in the solar system.

# DEDICATION

I dedicate this dissertation to my parents, Jesse and Connie and siblings (Joven, Hannah, and Nicole) for their unwavering support.

# ACKNOWLEDGEMENTS

This work and a rewarding PhD journey would not be possible without contributions from numerous people. Early on, my interest in scientific research started when I joined Dr. Caloy Arcilla's research group as an undergraduate student at the University of the Philippines. Doc Caloy and graduate students in the lab taught me the basics of mineral analysis and stimulated my interest in the chemistry of Earth's materials. Of course, life in the lab and as a geology major would not be exciting without my friends, teachers, and colleagues at the National Institute of Geological Sciences. Special thanks to Paolo and Emman who are fantastic friends since college and terrific travel buddies while we are finishing our PhDs here in the US.

The School of Earth and Space Exploration (SESE) at Arizona State University (ASU) has been an excellent workplace. I am thankful to the members of my dissertation committee: Hilairy Hartnett, Tom Sharp, Christy Till, and Ariel Anbar. Hilairy has been an incredible mentor for my geochemistry classes as well as for my secondary project. Hilairy and members of the CA&NDy (Carbon and Nitrogen DYnamics) lab taught me a lot of analytical skills as well as contributed to sparking my interest in biogeochemical processes early in my graduate school experience. Tom has been an excellent mentor in mineralogy. I am in gratitude to Tom for giving me the opportunity to be a teaching assistant in his undergraduate mineralogy class. It has been a fulfilling TA experience as well as a great training for teaching. Ariel, Christy, and Hilairy had been leading weekly meetings concerning the Great Oxidation Event for many years since I started graduate school. These meetings have been helpful in the formulation of Chapter 5 of this dissertation.

This work will not be possible without help from my advisor, Everett Shock. Everett encouraged me to explore numerous avenues to tackle my interest in water and rock interactions. He also brought me to Oman and Yellowstone that allowed me to literally witness the geochemical and biological consequences of water and rock interactions. Everett's support also allowed me to further explore and witness other examples of water-rock systems through participation in the ocean and continental drilling programs. Overall, under Everett's guidance, I grew to be a better researcher and someone who can recognize and appreciate various water-rock systems and their connections to the biosphere.

Everett's research group, the Group Exploring Organic Processes In Geochemistry (GEOPIG) has been my academic home for the past years. I am glad for the help and company of fellow GEOPIG members: Alta, Kirt, Tucker, Vincent, Kris, Grayson, Steven, Apar, Kristin, Melissa, Vince, Alysia, Panjai, Brian, Charlene, Peter, and many others. They had been instrumental in teaching me analytical and computational skills that are the foundation of this work. In particular, many (along with Natasha, Steve, Gwen, and Roy at the Keck and Goldwater environmental labs) contributed to the fluid compositional data presented in this work – through help sampling in the field, operation of instruments, and interpretation of data. Most of all, the weekly group meetings – oftentimes involving two or more each week for its diverse members and research topics – have been a source of new information, an avenue for helpful discussions, and critical in helping me develop a multidisciplinary mindset.

Colleagues and friends from ASU's Schools of Earth and Space Exploration, Molecular Sciences, and Life Sciences, particularly those with the NSF FESD (Frontiers

in Earth System Dynamics) Earth Oxygenation and NASA NExSS (Nexus for Exoplanetary System Science) Exoplanetary Ecosystems groups, as well as my office mates at PSF 209, have been a source of many helpful discussions. I am also thankful to colleagues aboard the *Joides Resolution* and *Chikyu* for training me in detailed rock description as well as for the insightful daily conversations. Muriel Andreani, Isabelle Daniel, and Steve Peuble, who were my hosts at the Universite de Lyon while I was Chateaubriand Fellow in France, are instrumental in developing my keen interest in serpentinization and mineral analysis. I am also thankful to discussions with and ideas shared by Peter Kelemen and members of the Oman Drilling and the NASA NAI (National Astrobiology Institute) Rock-Powered Life projects. Finally, support from NASA and NSF is also acknowledged.

# TABLE OF CONTENTS

Page

LIST OF TABLES .......... xi

LIST OF FIGURES .......... xii

CHAPTER

1 INTRODUCTION .......... 1

2 THERMODYNAMIC CONSTRAINTS ON THE GEOCHEMISTRY OF LOW-TEMPERATURE, CONTINENTAL, SERPENTINIZATION-GENERATED FLUIDS .......... 9

- 2.1. Introduction .......... 9
- 2.2. Overview of Low-Temperature Continental Serpentinization .......... 13
- 2.3. Computational Model .......... 14
- 2.4. Thermodynamic Constraints .......... 20
  - 2.4.1. Stages in the Reaction Progress .......... 21
  - 2.4.2. Variations in Temperature .......... 33
  - 2.4.3. Variations in Fluid Salinity .......... 38
  - 2.4.4. Precipitation of Ca-bearing phases .......... 40
  - 2.4.5. Variations in Contributions from Primary Minerals .......... 47
  - 2.4.6. Effect of Incorporating Mineral Solid Solutions .......... 61
- 2.5. Bioenergetic Landscapes .......... 69
- 2.6. Conclusions .......... 79
- 2.7. Acknowledgements .......... 81

CHAPTER Page

3 THERMODYNAMIC PREDICTIONS VS ENVIRONMENTAL OBSERVATIONS OF SERPENTINIZATION-GENERATED FLUIDS: LESSONS FROM THE SAMAIL OPHIOLITE IN OMAN ......................... 82

3.1. Introduction ........................................................................... 82

3.2. Methods ................................................................................ 86

3.2.1. Computational Model ...................................................... 86

3.2.2. Field and Analytical Methods .......................................... 86

3.3. Results ................................................................................. 92

3.3.1. Model Results ................................................................ 92

3.3.2. Analytical Results .......................................................... 93

3.4. Reconciling Predictions with Reality ....................................... 98

3.4.1. pH and Dissolved Si, Mg, Ca, and Inorganic Carbon ......... 98

3.4.2. Dissolved Na and Cl ..................................................... 117

3.5. Timescale of Reactions ......................................................... 123

3.6. Conclusions ......................................................................... 127

3.7. Acknowledgements .............................................................. 129

4 PREDICTION OF ENERGY AND POWER SUPPLIES FOR SUBSURFACE MICROORGANISMS IN LOW-TEMPERATURE CONTINENTAL SERPENTINIZATION ENVIRONMENTS ............................................... 137

4.1. Introduction ......................................................................... 137

4.2. Methods .............................................................................. 140

4.2.1. Quantification of Energy Supplies ................................. 140

4.2.2. Aqueous Geochemistry ........ 146

4.3. Compositions and Redox state of Oman Ophiolite Fluids ........ 147

4.3.1. Dissolved Oxygen and Hydrogen ........ 148

4.3.2. Dissolved Inorganic Carbon, Carbon Monoxide and Methane ........ 153

4.3.3. Dissolved Ferrous Iron ........ 156

4.3.4. Dissolved Sulfate and Sulfide ........ 159

4.3.5. Dissolved Nitrate, Nitrite, and Ammonia ........ 162

4.4. Energy Supplies Available in Surficial Hyperalkaline Spring Seeps ........ 163

4.5. Prediction of Subsurface Energy Supplies ........ 168

4.5.1. Estimated Composition of Subsurface Fluids ........ 169

4.5.2. Energy Supplies in the Serpentinizing Subsurface ........ 173

4.5.3. Power Supplies for Methanogens and Microbial Biomass ........ 178

4.6. Conclusions ........ 183

4.7. Acknowledgements ........ 185

5 DECREASING EXTENTS OF KOMATIITE SERPENTINIZATION TOWARDS THE END OF THE ARCHEAN CONTRIBUTED TO THE RISE OF AN OXYGENIC ATMOSPHERE ........ 186

5.1. Introduction: Serpentinization as a Sink for $O_2$ ........ 186

5.2. Methods: Estimating Global $H_2$ Production and Associated $O_2$ Sink ........ 189

5.3. Results and Discussions ........ 194

5.3.1. Serpentinization is the Key to Significant $H_2$ Production ........ 194

5.3.2. Estimating Modern $H_2$ Flux from Peridotite Serpentinization ........ 199

CHAPTER Page

5.3.3. Predicting Past $O_2$ sink via Komatiite Serpentinization.................... 202

5.4. Conclusions ........................................................................... 211

5.5. Acknowledgements.................................................................. 213

6 FUTURE DIRECTIONS ........................................................................ 214

REFERENCES ........................................................................................ 217

APPENDIX

A SUPPLEMETARY FILES TO CHAPTER 2................................................. 252

B SUPPLEMETARY FILES TO CHAPTER 3................................................. 255

C SUPPLEMETARY FILES TO CHAPTER 4.................................................. 279

D SUPPLEMETARY FILES TO CHAPTER 5................................................. 320

LIST OF TABLES

Table Page

2.1. List of Continental Locations with Documented Fluid and Gas Compositions Attributed to Serpentinization............................................................12

2.2. Compositions of Reacting Rocks Used in This Study and Figures Where Results of Each Model Appear. ............................................................................17

2.3. List of Minerals Included in this Study.........................................................19

3.1. Field and Laboratory Measurements For Samples Collected in This Study...131

4.1. List of Chemolithotrophic Reactions used in This Work ..............................142

A1. Composition of Fluids Used in Reaction Path and Mixing Calculations .......253

A2. Summary of Experimental and Estimated Thermodynamic Data for End-member Fe-bearing Serpentinization-relevant Minerals Used in this Study .......254

B1. Saturation States of Various Relevant Minerals ..........................................270

B2. Composition of Fluids Used in Mixing Calculations...................................273

C1. Fluid and Gas Compositions of Samples Used in Bioenergetic Calculations.294

C2. Calculated Eh, pe, and log f$O_2$ Values Using Dissolved $O_2$ and $H_2$ Concentrations of Investigated Fluids......................................................................300

C3. Calculated Affinities ($A_r$, kcal/mole $e^-$ transferred).....................................302

C4. Calculated Energy Yield ($E_r$, log calories/kg fluid). ....................................308

C5. Composition of End-member Fluids Used in Mixing Calculations ...............314

D1. Composition of Rocks Used in Alteration Simulations ................................328

D2. Ranges and Percentiles in Predicted $H_2$ Production and Flux During Alteration Various Reacting Rocks...................................................................337

# LIST OF FIGURES

Figure Page

2.1. Schematic of a Fluid-centered Flow-through Model ....................................16

2.2. Schematic of the Six Stages of Serpentinization ..........................................21

2.3. Evolution of Aqueous Compositions and Secondary Precipitation During Serpentinization....................................................................................22

2.4. Trends of pH and Total Dissolved Solute Concentrations at Temperatures Ranging from 0°C to 100°C ...............................................................................34

2.5. Trends of pH and Total Dissolved Solute Concentrations as Functions of Increasing Fluid Salinity .....................................................................39

2.6. Effect of Various Precipitating Ca-bearing Phases.......................................41

2.7. Results of Simulations at 25°C and 1 bar for Host Rocks of the MgO-FeO-$SiO_2$-$H_2O$ System..........................................................................49

2.8. Trends in the Dissolved Solute Concentration During Reactions with Variable Harzburgitic Compositions in the CaO-MgO-FeO-$SiO_2$-$H_2O$ System....53

2.9. CaO-MgO-$SiO_2$-$H_2O$ Activity Diagram for 25°C and 1 bar Depicting Various Reaction Pathways...............................................................................57

2.10. Reaction Path Differences in Models Where Precipitation of Secondary Phases in Solid Solutions Were and Were Not Considered. .................................63

2.11. Predicted Amount of $H_2$ Generated per kg of Rock....................................66

2.12. Fluid and Mineralogical Trends from The Alteration of Ultramafic Rocks with Variable Contributions from Olivine and Orthopyroxene .....................57

Figure Page

2.13. Predicted Energy (calories/kg fluid) Available for Hydrogenotrophic Methanogenesis....73

2.14. Predicted Energy Yields for $H_2$ Oxidation and Methanogenesis During Mixing Between Subsurface Fluids....77

3.1. Locations of Sample Sites....87

3.2. Hyperalkaline Pools Covered in White Calcite Films....88

3.3. Measured Dissolved Solutes....95

3.4. $\delta^{18}O$ vs $\delta^{2}H$ Crossplot....97

3.5. Comparison Between Predictied and Measured Dissolved Si, Mg, Ca, and DIC Concentrations....100

3.6. Calculated pH in Equilibrium with the Ctl-Brc-Di and Ctl-Brc-Cal Mineral Assemblages vs Measured pH....106

3.7. Key Serpentinization Reactions and Resulting Fluid Types Summarized in a Plot of Si concentration vs pH....115

3.8. Comparison Between Predicted and Measured Na and Cl Values....120

3.9. Trends in the Na/K and Na/Cl Ratios of Sampled Fluids....122

3.10. Timescales Required to Attain the Various pH and Stages of Serpentinization and Saturation with Relevant Minerals....125

4.1. Eh, pe and Dissolved $O_2$, $H_2$, $CH_4$, CO, and Inorganic Carbon Concentrations of Oman Fluids....151

4.2. Concentrations of Dissolved Iron and Sulfur Species Measured from Fluids from the Oman Ophiolite....158

Figure Page

4.3. Concentrations of Dissolved Nitrogen Species Measured from Fluids from the Oman Ophiolite ....................................................................162

4.4. Summary and Ranking of Calculated Energy Supplies in Surficial Hyperalkaline Fluids ..............................................................................167

4.5. Calculated Energy Supplies via Various Reactions During Mixing Between Subsurface Fluids ..................................................................174

4.6. Power Supplies for Methanogens and Microbial Biomass in Deep Serpentinizing Aquifers ..........................................................................181

5.1. The $H_2$ Generation Potential During Hydrous Alteration of Various Rock Types with Compositions Ranging from Peridotitic to Basaltic .....................198

5.2. Calculated Flux and Global Production Rate of $H_2$ Generated Through the Serpentinization of Continental Peridotites and Komatiites .................201

5.3. Calculated Global Consumption Rate for $O_2$ via Komatiite Serpentinization For the Past 3.5 Ga ..........................................................................204

5.4. Likelihood of Countering Significant Net $O_2$ Production as Function of the Extents in the Exposures of the Continents and Continental Komatiites ...........209

B1. Comparison of Dissolved Ca and Mg Values Determined with the ICP-MS and ICP-OES, respectively, vs those determined with the IC. ....................274

B2. Speciation of Dissolved Components in Sampled Fluids. ............................275

B3. Summary of Reaction Paths Simulating Various Stages of Serpentinization .276

B4. Comparison Between Ultramafic- and Gabbroic-hosted Fluids in Oman. .....277

Figure Page

B5. Fluid Compositions Plotted in Activity Diagrams for the $CaO$-$Al_2O_3$-$SiO_2$-$H_2O$ and $CaO$-$MgO$-$SiO_2$-$H_2O$ Systems ........................................................278

C1. Comparison Between Ultramafic-hosted and Gabbroic-hosted Fluids in Oman (reduced version of Figure B4)........................................................316

C2. Speciation of Dissolved Inorganic Carbon and Ferrous Iron.........................317

C3. Calculated Energy Yield (log calories/kg fluid) for Various Aerobic Chemolithotrophic Strategies ............................................................318

C4. Calculated Energy Yield (log calories/kg fluid) for Various Anaerobic Chemolithotrophic Strategies ............................................................319

D1. Controls of the Major Element Composition of Rocks on the Calculated Amounts of $H_2$ Generated......................................................................339

D2. Calculated $H_2$ Generated During Hydrous Alteration of Komatiites at Various Degrees of Water-to-Rock Ratios.....................................................339

# CHAPTER 1

# INTRODUCTION

Most rocks on Earth originally form at high temperatures during the cooling of magma. At lower temperatures and in the presence of water, the magmatic minerals that originally composed the rocks are not stable and will subsequently alter into another mineral assemblage. Mineral alteration is a major geological process as it changes the physical properties of rocks, converts rocks into soils, facilitates the chemical exchanges between rock and water that result in the mobilization of elements and nutrients, and consequently supports all life on our planet. Different rocks on Earth alter differently, given the temperature and pressure conditions, resulting in diverse compositions of alteration minerals, fluids, and volatiles. Of all rock alteration process on Earth, perhaps one of the most profound is the *serpentinization* of ultramafic rocks as it produces some of the most reduced and alkaline fluids on the planet. These unique fluids have important consequences on the habitability of rock-hosted environments and the flux of reduced volatiles to the surface, which is discussed in this work.

The overall composition of ultramafic rocks is key to the unique chemistry of fluids generated through serpentinization. Ultramafic rocks are composed of Mg-silicate minerals, mostly olivine and some pyroxene. Olivine-rich ultramafic rocks, *i.e.* peridotites, comprise the majority of the Earth's upper mantle and through tectonic events these mantle rocks can be emplaced onto the Earth’s surface – in the seafloor and in continents. Moreover, unlike in the modern Earth where the hottest volcanism leads to the formation of mafic rocks, volcanism occurring in the hotter early Earth transported ultramafic magmas to the surface where they solidified as komatiite rocks. At surface and hydrous conditions, the original minerals that compose peridotites and komatiites readily alter into hydrous minerals, mostly into serpentine, hence the term *serpentinization*, and other minerals such as brucite and magnetite. Aside from Mg and Si, olivine and pyroxene contain significant amounts of ferrous iron (~7-10% Fe) that can be oxidized to ferric iron during alteration and eventually incorporated into the precipitating serpentine and magnetite minerals. During advanced stages of serpentinization in deep aquifers, the oxidation of ferrous iron from the original magmatic minerals into ferric iron in the precipitating alteration assemblages is coupled to the reduction of $H_2O$ into $H_2$, generating some of the most reduced fluids on Earth (McCollom and Bach, 2009; Klein et al., 2013; Humphris and Klein, 2018; Klein et al., 2020). Reduced fluids produced through serpentinization provide energy for many metabolic processes (McCollom, 2007; Amend et al., 2011; Nakamura and Takai, 2014; Canovas et al., 2017), favor the synthesis of simple organic compounds (McCollom and Seewald, 2007; Lang et al., 2010; Shock and Canovas, 2010) and could have facilitated the emergence of life on Earth (Sleep et al., 2004; 2011; Holm et al., 2006; Martin and Russel, 2007; Martin et al., 2008). In addition to Mg that comprises most of the olivine and pyroxene minerals in ultramafic rocks, some of the pyroxene minerals, specifically those that are diopsidic in composition, contain Ca. As these minerals dissolved in the presence of water, both Mg and Ca are mobilized into the fluid phase leading to increasingly alkaline fluids as the rock alteration process progresses. At alkaline conditions, some of the Mg and Ca dissolved in the fluids combine with dissolved inorganic carbon (DIC) to precipitate carbonate minerals such as magnesite and calcite. Carbonate mineralization arising from the alteration of ultramafic rocks is believed to be an important component of the global carbon cycle (Kelemen and Manning, 2015) and deep ultramafic aquifers are seen as ideal settings for the permanent storage of atmospheric $CO_2$ into minerals as an approach to curb the increasing levels of anthropogenic $CO_2$ in the atmosphere (Kelemen and Matter, 2008; Kelemen et al., 2011; National Academies, 2019).

Serpentinization processes can be pervasive and can proceed even at ambient, low-temperature conditions present in most of Earth's aquifers. Reduced and hyperalkaline (pH >11) fluids seeping at temperatures <50°C are documented in continental ultramafic bodies in ~20 countries by more than a hundred studies (see Leong and Shock, 2020). Such a common occurrence of these fluids in almost all continental settings where ultramafic rocks and water can interact illustrates that serpentinization can actively proceed even at ambient conditions. Overall, serpentinization is an attractive model for facilitating the transfer of nutrients, volatiles, and chemical energy from the lithosphere to the hydro-atmo-biosphere as it can proceed spontaneously with only two requirements, *i.e.*, liquid water and ultramafic rocks, at temperature conditions ranging from hydrothermal to ambient. Serpentinization-generated fluids enable habitable environments (*e.g.*, Schrenk et al., 2013), and this process has profound implications on the habitability and redox state of Earth's early environments, its deep subsurface, and perhaps even in rocky bodies beyond our planet where ultramafic minerals are present in contact with water (*e.g.*, Vance et al., 2007).

The consequences of serpentinization on the habitability and redox state of a given environment can be best studied through investigations of serpentinization-generated fluids and volatiles. While serpentinization-generated fluids and volatiles seeping out from outcropping rocks in continents, as well as those venting out in the seafloor (*e.g.*, Lost City, Kelley et al., 2001), are accessible and well-documented, those sampled from the deep subsurface are less well known. In addition, the compositions of serpentinization-generated fluids believed to be forming in ice covered ocean worlds in the outer solar system such as Europa and Enceladus (*e.g.*, Glein et al., 2015; Waite et al., 2017) are also largely unknown and sampling will not happen in the near term. Ultramafic rocks are also believed to have been much more widespread on the hotter Early Earth and could have dictated the redox state of the Earth's atmosphere during the Archean (Smit and Metzger, 2017). However, we have yet to fully understand compositions of low-temperature serpentinization-generated fluids occurring in the Early Earth as experiments simulating early Earth conditions are focused at hydrothermal temperatures (*e.g.*, 120°C, White et al., 2020; 300°C, Lazar et al., 2012; Shibuya et al., 2015). At present, information about the compositions and implications of serpentinization-generated fluids and volatiles in inaccessible and long-gone settings can be best supplied by thermodynamic models.

In Chapter 2, thermodynamic calculations are used to investigate various reactions that facilitate the transformation of oxic, slightly acidic rainwater into reduced, hyperalkaline fluids during low-temperature serpentinization in the continents. These simulations explore a suite of factors (variabilities in temperature, host-rock compositions, fluid salinity, and the buffering capacity of various serpentinization-relevant minerals) that offer broad insights into the chemical environments formed through low-temperature serpentinization. Results of calculations show that alteration of olivine-rich lithologies will lead to fluids constrained by the serpentine-brucite-diopside equilibrium assemblage, close in pH to those measured from the most alkaline fluids hosted in ultramafic rocks. Variabilities in the compositions of fluids hosted by continental serpentinizing systems can be attributed to the shift from being in equilibrium with diopside to calcite, among other reactions. Models also account for Fe incorporation into solid solutions of serpentine and brucite and show that the global $H_2$ flux from continental serpentinization could be considerably lower than estimates based on iron oxidation to magnetite only.

Observations from natural systems can deviate from thermodynamic predictions, especially those occurring at low temperatures where the approach to equilibrium can be sluggish. To test thermodynamic predictions described in Chapter 2 with environmental observations, more than 100 low-temperature (<40°C) fluids from the Oman ophiolite were sampled and analyzed, as described in Chapter 3. Additional simulations (*e.g.*, fluid mixing, mineral leaching) were also conducted to account for deviations from equilibrium predictions. Coupled calculations and fluid analyses identify the reactions and fluid transport processes that lead to the contrasting compositions and redox potentials of end-member fluid types generated during incipient to advanced stages of serpentinization, as well as during the mixing of these end-member fluid types in discharge zones of the subsurface fluid pathway. Overall, this work demonstrates that predicted and measured compositions of low-temperature, serpentinization-derived fluids can be successfully reconciled using a combination of equilibrium and fluid-transport simulations. By demonstrating that simulations of low-temperature serpentinization can be successfully applied to analogous processes on the modern Earth, this work substantiates these calculations as useful tools in exploring serpentinization reactions in the Earth’s past as well as those occurring beyond our own planet.

Thermodynamic models outlined in Chapter 2 and aqueous geochemical trends from environmental samples described in Chapter 3 were both used to predict compositions of end-member fluids representative of the shallow and deep peridotite aquifers, as discussed in Chapter 4. Using these predicted compositions, the potential habitability of subsurface peridotite aquifers was assessed by quantifying energy supplies from 17 chemolithotrophic reactions. Calculations reveal hotspots where certain microbial communities may bloom – one in the deeply serpentinizing subsurface and the other in discharge zones of fluid pathways where reduced deep-seated fluids encounter oxidized shallow-aquifer fluids. In the deep subsurface, available energy can be exploited by methanogens, permitting the possibility of deep communities in serpentinizing aquifers. Dissolved inorganic carbon available to methanogens can be supplied from carbonate minerals and by incorporating constraints from existing laboratory experiments simulating mineral dissolution, the rate at which this energy is supplied was quantified. Despite the low solubility and slow rate of dissolution of carbonates at alkaline pH, energy is available to sustain populations of methanogens as long as carbonate minerals, particularly calcite, are sufficiently present to supply inorganic carbon. More energy is available for methanogens and other chemolithotrophs when upwelling deep-seated fluids mix with shallow groundwater. Mixing calculations show where in the mixing pathway certain chemotrophic reactions are favored more than others. Methanogenesis and other anaerobic reactions are favored in fluids characterized by no to low extents of mixing of shallow groundwater into deep-seated fluids, while the Knallgas and other aerobic reactions are favored in systems characterized by greater extent of mixing. This framework presents opportunities for exploration, and ultimately developing strategies that can target certain microbial communities in the deep serpentinizing subsurface.

In the modern Earth, serpentinization is mostly limited to a few environments such as those near slow-spreading ridges where peridotites are emplaced to the seafloor (Cannat et al., 2010) and in ophiolite complexes in continents where peridotite rocks are exposed to the atmosphere (Etiope and Whiticar, 2019; Leong and Shock, 2020). In contrast, serpentinization could have been much more widespread early in Earth's history during the Archean where the mantle was hotter, resulting in the volcanism of komatiitic magmas (Herzberg et al., 2007). In Chapter 5, thermodynamic simulations were used to quantify the consequences of the evolving continental composition during the Archean for the global supply of $H_2$ generated through the serpentinization of komatiites. Simulations of komatiite serpentinization given variabilities in the compositions of the reacting rocks and fluids, rates and extents of rock alteration, and the abundance of komatiites in the continents during the past 3.5 Ga allow robust estimates of past global $H_2$ flux. Moreover, the likelihood of estimated past $H_2$ flux that can offset the net $O_2$ produced through photosynthesis was quantified. Results of calculations show that the flux of serpentinization-generated $H_2$ could have been a significant sink for $O_2$ during most of the Archean. This $O_2$ sink diminished greatly towards the end of the Archean as komatiite volcanism became less pervasive and helped set the stage for the Great Oxidation Event.

In summary, thermodynamic models predictive of low-temperature serpentinization environments were generated. These models were successfully tested, along with simulations of mass transport processes, with a comprehensive number of fluids sampled from peridotite bodies in the Oman ophiolite. Thermodynamic models were also applied to predict geochemical energy available to subsurface microorganisms living in peridotite aquifers, as well as to assess the consequences of the decreasing extents of komatiite volcanism towards the end of the Archean in facilitating the first oxygenation of the Earth's atmosphere. While focused on continental systems, this study ultimately provides a framework for exploring the origins, compositions, and redox states of fluids and volatiles that can result from various low-temperature serpentinizing environments in the present and past Earth and in other rocky bodies beyond our own planet.

# CHAPTER 2

# THERMODYNAMIC CONSTRAINTS ON THE GEOCHEMISTRY OF LOW-TEMPERATURE, CONTINENTAL, SERPENTINIZATION-GENERATED FLUIDS

This chapter is published as: Leong, J. A. M., & Shock, E. L. (2020). Thermodynamic constraints on the geochemistry of low-temperature, continental, serpentinization-generated fluids. *American Journal of Science, 320*(3), 185–235. https://doi.org/10.2475/03.2020.01

## 2.1 Introduction

Environments where water meets ultramafic rocks enable serpentinization, one of the most profound geochemical processes on Earth. During serpentinization, minerals that compose ultramafic rocks (olivine and pyroxene), are replaced mainly by serpentine upon interaction with water. Serpentinization drives the transformation of near-neutral and oxic surface fluids like rain or seawater into alkaline, reduced fluids rich in $H_2$ and $CH_4$. These reduced fluids provide energy and nutrients for chemosynthetic communities (see review by Schrenk et al., 2013), abiotically synthesize organic compounds (see review by McCollom and Seewald, 2007), and potentially facilitate the emergence of life on Earth (Sleep et al., 2004, 2011; Holm et al., 2006; Martin and Russel, 2007; Martin et al., 2008; 2014; Russel et al., 2010; Lane and Martin, 2012). Serpentinization extends beyond Earth, as ultramafic rocks are present in a number of terrestrial bodies in the Solar System (Schulte et al., 2006; Vance et al., 2007; Ehlmann et al., 2010; Holm et al., 2015, Glein et al., 2015), raising possibilities of life powered by water-rock interactions beyond our own planet.

On Earth, serpentinization occurs wherever ultramafic rocks meet water, which is inevitable at the seafloor. Chimneys venting $H_2$- and $CH_4$-rich fluids at temperatures exceeding 100°C, including those at the Rainbow (Charlou et al., 2002; Douville et al., 2002), Logatchev (Schmidt et al., 2007), Kairei (Gallant and Von Damm, 2006; Kumagai et al., 2008), Von Damm (McDermott et al., 2015), and Lost City (Kelley et al., 2001, 2005; Lang et al., 2010; Seyfried et al., 2015) vent fields, are well known consequences of hydrothermal interactions between ultramafic rocks and seawater. Less dramatic but likely more widespread outcomes of serpentinization are low-temperature (<100°C) $H_2$- and $CH_4$-rich hyperalkaline fluids seeping diffusely from ultramafic rocks exposed near spreading ridges (Früh-Green et al., 2003; 2018), serpentinite mud volcanoes near subduction zones (Mottl et al., 2003, 2004; Wheat et al., 2008; Mottl, 2009), and exposed ultramafic outcrops in continents such as in ophiolites, ultramafic massifs, metamorphic belts and kimberlite deposits (see Table 2.1).

Serpentinizing systems hosted on the continents provide accessible opportunities to sample deep-seated fluids. These low-temperature systems also provide examples to test predictions about the consequences of water and rock interactions without the added complexity of magmatic input like those in seafloor hydrothermal systems. Recent undertakings to drill into and sample deep aquifers, and subsequently establish a borehole observatory on the Samail Ophiolite in Oman (Kelemen et al., 2013; https://www.omandrilling.ac.uk/) will advance knowledge of the subsurface reactions driving fluid transformation during the serpentinization process. In preparation, insights into these subsurface reactions can be provided by thermodynamic predictions.

Several theoretical investigations have focused on seawater-ultramafic interactions at hydrothermal conditions (Janecky and Seyfried, 1986; Wetzel and Shock, 2000; Alt and Shanks, 2003; Allen and Seyfried, 2004; Palandri and Reed, 2004; Frost and Beard, 2007; Seyfried et al., 2007; 2015; Foustoukos et al., 2008; McCollom and Bach, 2009; Klein et al., 2009; 2013; Evans et al., 2013; Bach et al., 2013). The existing theoretical studies for low-temperature continental serpentinizing settings (Pfeifer, 1977; Bruni et al., 2002; Palandri and Reed, 2004; Cipolli et al., 2004; Boschetti and Toscani, 2008; Marques et al., 2008; Okland et al., 2012; Paukert et al., 2012) tend to focus on the consequence of altering a specific composition of ultramafic rock under conditions for a given study site. Here we examine low-temperature continental serpentinization independent of conditions dictated by a specific locality. Our initial focus is on generalized reactions that drive the serpentinization process. We examine the consequences brought about by variabilities in temperatures (0-100°C), fluid salinity, and host rock compositions. Other factors such as varying dissolved inorganic carbon (DIC) input, and the buffering capacity of various Ca-bearing minerals are considered. Exploration of this suite of factors offers broad insights into the chemical environments formed through low-temperature serpentinization. In the latter part of this paper, we describe model outcomes for the amounts of $H_2$ generated, and offer a reevaluation of existing estimates for the global $H_2$ flux from continental serpentinization. Lastly, we present the energetic landscape available to subsurface microorganisms by focusing on two microbial process: methanogenesis and hydrogen oxidation.

Table 2.1

*List of Continental Locations with Documented Fluid and Gas Compositions Attributed to Serpentinization*

| **Location** | **Study**[1] |
|---|---|
| U.S.A. (Coast Range ophiolites, the Cedars, Del Puerto ophiolite, California and Oregon) | Barnes et al., 1967; Barnes and O'Neil, 1969; Blank et al., 2009*; Cardace et al., 2013; Crespo-Medina et al., 2014*; Morrill et al., 2013; Suzuki et al., 2013*; 2014*; 2017*, Kohl et al., 2016*; Twing et al., 2017*; Meyer-Dombard et al., 2018 |
| Switzerland (Engadine Valley) | Pfeiffer, 1977 |
| Italy (Voltri, Taro-Cenno, Elba) | Pfeiffer, 1977; Bruni et al., 2002; Cipolli et al., 2004; Boschetti and Toscani, 2008; Chavagnac et al., 2013a; 2013b; Boulart et al., 2013**; Schwarzenbach et al., 2013; Boschetti et al., 2013; Quéméneur et al., 2015*; Segadelli et al., 2017; Brazelton et al., 2017*; Sciarra et al., 2019**; Etiope and Whiticar, 2019** |
| Greece (Othrys and Argolida ophiolites) | Papastamaki, 1977; Etiope et al., 2013a**; D'Alessandro et al., 2018; Daskalopoulou et al., 2018** |
| Oman (Samail ophiolite) | Barnes et al., 1978; Neal and Stanger, 1983**; 1984; 1985; Bath et al., 1987*; Taylor et al., 1991; Sano et al., 1993**; Dewandel et al., 2005; Matter et al., 2006; Paukert Vankeuren et al., 2012; 2019; Chavagnac et al., 2013a; 2013b; Boulart et al., 2013**; Ollson et al., 2014; Miller et al., 2016*; Rempfert et al., 2017*; Canovas et al., 2017; Vacquand et al., 2018**; Zgonnik et al., 2019**; Fones et al., 2019*; Giampouras et al., 2020 |
| New Caledonia (Prony Bay) | Barnes et al., 1978; Monnin et al., 2014; Quéméneur et al., 2014*; Postec et al., 2015*; Vacquand et al., 2018** |
| Bosnia and Herzegovina (Dinaride ophiolite) | Barnes et al., 1978; Etiope et al., 2017** |
| Philippines (Zambales and Palawan ophiolites) | Abrajano et al., 1988**, 1990**; Fujii et al., 2010; Cardace et al., 2015; Woycheese et al., 2015*; Baculi et al., 2015*; Shimbashi et al., 2018; Vacquand et al., 2018**; Meyer-Dombard et al., 2018*; 2019* |
| New Zealand (Poison Bay, Dun Mountain) | Giggenbach et al., 1993**; Pawson et al., 2014** |
| Cyprus (Trodos massif) | Neal and Shand, 2002; Rizoulis et al., 2016* |
| Mexico (Socorro Island)[2] | Taran et al., 2002; 2010** |

| | |
|---|---|
| Canada (Kirkland Lake and Lake Timiskiming kimberlite fields, Canadian Shield, and Tablelands massif) | Sader et al., 2007; Sherwood-Lollar et al., 2007**; Szponar et al., 2013; Brazelton et al., 2012*; 2013*; Morrill et al., 2014*; Cumming et al., 2019 |
| Portugal (Iberian Hercynian Belt) | Tiago et al., 2004*; Marques et al., 2008; 2018; Etiope et al., 2013b**; Tiago and Veríssimo, 2013* |
| Finland (Outokumpu deep drill hole, Fennoscandian Shield)[3] | Sherwood-Lollar et al., 2007**; Itävaara et al., 2011*; Nyyssönen et al., 2014* |
| Turkey (Chimaera seep and Tekirova ophiolites) | Hosgormez et al., 2008**; Etiope et al., 2011**; Meyer-Dombard et al., 2015*; Neubeck et al., 2017* |
| Japan (Hakuba Happo springs, Hida belt) | Homma and Tsukahara, 2008; Suda et al., 2014**; 2017** |
| Norway (Leka ophiolite) | Okland et al., 2012; Daae et al., 2013* |
| Costa Rica (Santa Elena ophiolite) | Sanchez-Murillo et al., 2014; Crespo-Medina et al., 2017* |
| U.A.E. (Samail ophiolite) | Etiope et al., 2015** |
| Spain (Ronda massif) | Etiope et al., 2016**; Giampouras et al., 2019 |

[1] Those indicated by * are microbiological studies or geochemical studies that include microbiological data. Those indicated with ** are studies focused on gas compositions. All the rest are focused on the aqueous compositions and/or hydrogeology of serpentinizing systems.

[2] Acidic hotsprings that likely have input from volcanic gas.

[3] Borehole lithology is dominated by metasedimentary rocks with some ultramafic sequence.

## 2.2. Overview of Low-Temperature Continental Serpentinization

Since the reports in the 1960's by Barnes et al. (1967; 1972; 1978) and Barnes and O'Neil (1969), studies on the chemistry of continental hyperalkaline fluids have grown to encompass a number of settings in ~ 20 countries shown in Table 2.1. A number of these studies (Neal and Stanger, 1985; Bruni et al., 2002; Cipolli et al., 2004; Dewandel et al., 2005; Marques et al., 2008; Paukert et al., 2012; Okland et al., 2012) proposed models for the overall evolution of fluids that infiltrate into aquifers composed of ultramafic rocks. These models, together with observations from natural systems permit the following generalizations. Initially, rainwater infiltrates into the shallow aquifer and reacts with the rocks in a system open to atmospheric exchange. These reactions generate slightly basic (pH 7-9) fluids rich in $Mg^{+2}$ and $HCO_3^-$ that are often referred to as Type 1 fluids. It has been documented that Type 1 fluids occur in highly fractured zones of shallow ophiolite aquifers (<50 m, Dewandel et al., 2005), as well as in surface streams. Some fluids infiltrate into the deep subsurface and interact progressively with more and more ultramafic rocks in a system that is ultimately closed from atmospheric influence. The greater degrees of interactions between water and rock facilitate the transformation of meteoric and Type 1 fluids into reduced, hyperalkaline fluids that are enriched in $Ca^{+2}$ and $OH^-$, often referred to as Type 2. It is estimated that these fluids originate at depths of at least 500 m (Dewandel et al., 2005). Through deep-seated structures such as faults and lithological contacts, these fluids can eventually discharge back onto the surface as hyperalkaline seeps, and precipitate travertine deposits upon interaction with atmospheric $CO_{2(g)}$ or mixing with $HCO_3^-$-rich Type 1 fluids.

## 2.3. Computational Model

Reaction path calculations simulate processes occurring during rock alteration by quantifying changes in the aqueous and mineral compositions arising from irreversible mass transfer reactions as specified quantities of water and rock progressively react. An increase in reaction progress is akin to an increase in the rock-to-water ratio, as the reacting water encounters more rock while infiltrating into the subsurface. These equilibrium calculations, although idealized, allow us to adequately track changes in fluid chemistry during rock alteration as demonstrated by the above-mentioned studies on various sites of active serpentinization. The reaction path code EQ6 (Wolery and Jarek,

2003) was used for calculations in this study, together with a customized thermodynamic database (see below). A global average modern rainwater composition compiled by Hao et al. (2017) from Berner and Berner (2012) was used as the starting reacting fluid. We modified the pH and DIC from this compilation slightly to be in equilibrium with modern atmospheric $CO_{2(g)}$ levels. Details about the composition of this starting rainwater can be found in Table A1 (Appendix A). As illustrated in Figure 2.1, our calculations include both *open* and *closed* systems, related to those simulated by Cipolli et al. (2004) and Paukert et al. (2012). Water-rock interactions first proceed in a system *open* to atmospheric exchange, simulating conditions when fluids are in the shallow subsurface or close to the surface. At some point in the reaction progress, fluids infiltrate deeper into the subsurface where conditions are *closed* to atmospheric influence and input from atmosphere-derived volatiles such as $CO_{2(g)}$ and $O_{2(g)}$ ceases. Temperature and pressure conditions remain near ambient (25°C, 1 bar) in our initial models of low-temperature continental serpentinizing systems.

As in the case of kinetically enabled models by Paukert et al. (2012), simulations were run using a fluid-centered, flow-through system where compositions are tracked as reactive fluid moves through an aquifer. However, instead of using experimentally-derived dissolution rates, in this study inputs from primary minerals are controlled by relative dissolution rates to explore effects of variable contributions of primary minerals to changes in fluid composition. Compositions of reacting rocks used in our simulations are listed in Table 2.2. We first simulate rainwater interactions with an idealized ultramafic rock (Model A) with a composition typical of an ophiolitic harzburgite (Hanghoj et al., 2010) with 85 mol% olivine ($X_{Mg}$ = Mg/(Mg+Fe) = 0.9, Forsterite$_{90}$ or

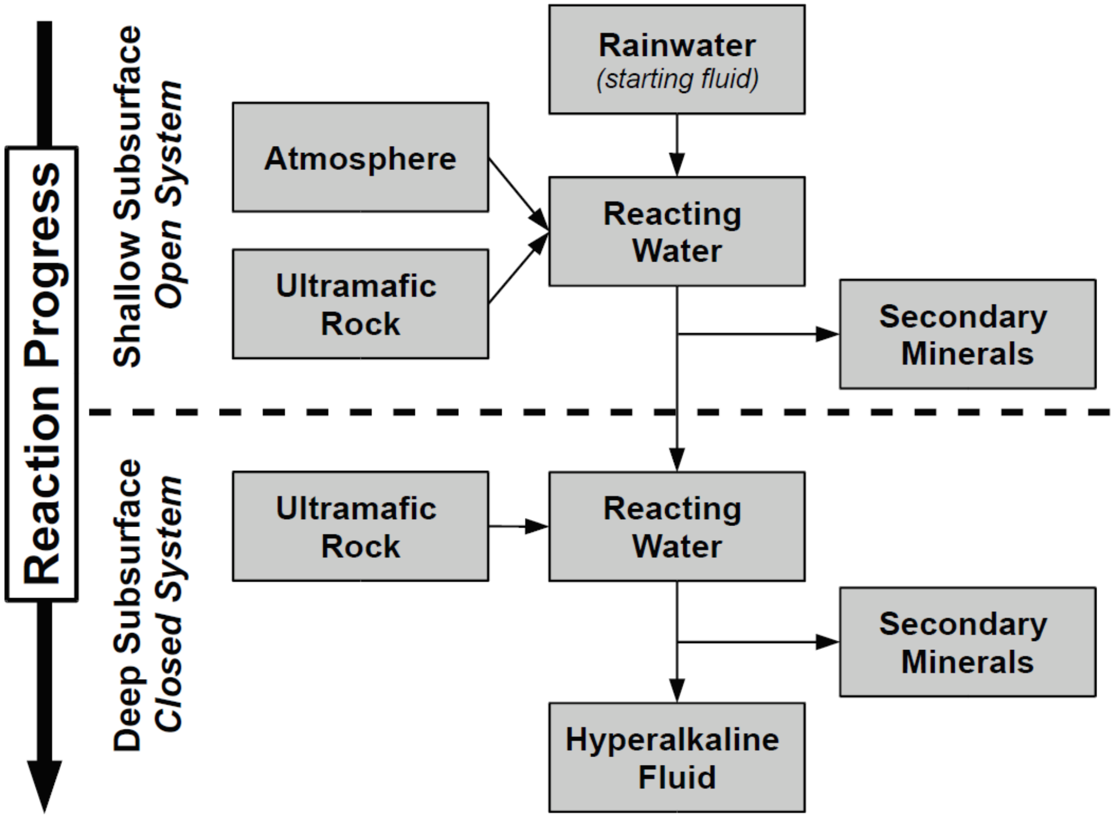

*Figure 2.1*. Schematic of a fluid-centered flow-through model, as modified from Paukert et al. (2012), showing transition from a system open to the atmosphere to one closed to atmosphere-derived volatiles as the overall serpentinization reaction progresses.

$Fo_{90}$), 14 mol% orthopyroxene ($X_{Mg}$ = 0.9, $Enstatite_{90}$ or $En_{90}$), and 1 mol% clinopyroxene ($X_{Mg}$ = 0.95, $Diopside_{95}$ or $Di_{95}$). The resulting reaction paths are divided into various stages to explore, step by step, the reactions that drive the transformation of rainwater to hyperalkaline fluids. We then explore further the consequences of reactions with rocks composed of variable amounts of primary minerals (Models B1-B5 and C1-C5) as well as with previously altered ultramafic rocks (serpentinites, Models D1-D4). To facilitate discussions in terms of idealized reactions using end-member phases, we first report results of simulations without considering the precipitation of secondary minerals as solid solutions. Later in the discussion, we report the consequences of incorporating solid solutions into our models. Effects of variable temperature and salinity were also explored, as well as the precipitation of various Ca-bearing phases, as discussed below.

Table 2.2

*Compositions of Reacting Rocks Used in This Study and Figures Where Results of Each Model Appear*

| **Model** | **Rock Name** | **Composition**[1] |
|---|---|---|
| | | *Model A: Generalized Model*<br>*(Figures 2.2-2.3, 2.7f, 2.8-2.11)* |
| A | Harzburgite | 85% Olivine-14% Orthopyroxene-1% Clinopyroxene |
| | | *Model B: Alteration of olivine- and orthopyroxene-bearing rocks*<br>*(Figures 2.7a-2.7e)* |
| B1 | Dunite | 100% Olivine |
| B2 | Harzburgite | 75% Olivine-25% Orthopyroxene |
| B3 | Harzburgite | 50% Olivine-50% Orthopyroxene |
| B4 | Orthopyroxenite | 25% Olivine-75% Orthopyroxene |
| B5 | Orthopyroxenite | 100% Orthopyroxene |
| | | *Model C: Alteration in the presence of clinopyroxene*<br>*(Figures 2.8-2.9, 2.12)* |
| C1 | Harzburgite | 85% Olivine-10% Orthopyroxene-5% Clinopyroxene |
| C2 | Harzburgite | 75% Olivine-20% Orthopyroxene-5% Clinopyroxene |
| C3 | Harzburgite | 65% Olivine-30% Orthopyroxene-5% Clinopyroxene |
| C4 | Harzburgite | 45% Olivine-50% Orthopyroxene-5% Clinopyroxene |
| C5 | Orthopyroxenite | 35% Olivine-60% Orthopyroxene-5% Clinopyroxene |
| | | *Model D: Alteration of serpentinites*<br>*(Figure 2.9b)* |
| D1 | Serpentinite | 95% Serpentine-5% Clinopyroxene |
| D2 | Serpentinite | 75% Serpentine-20% Brucite-5% Clinopyroxene |
| D3 | Serpentinite | 65% Serpentine-30% Brucite-5% Clinopyroxene |
| D4 | Serpentinite | 55% Serpentine-40% Brucite-5% Clinopyroxene |

[1] Compositions of reacting minerals are in solid solutions. $X_{Mg}$: olivine - 0.90; orthopyroxene - 0.90; clinopyroxene - 0.95, serpentine - 0.95; brucite - 0.90

Thermodynamic data used in the calculations were calculated with the SUPCRT code (Johnson et al., 1992) using standard state thermodynamic data for aqueous species taken from Shock and Helgeson (1988), Shock et al. (1989, 1992, 1997), Sverjensky et al. (1997), together with the revised Helgeson-Kirkham-Flowers equations of state (Shock et al., 1992) and data for minerals taken from Helgeson et al. (1978) and Wolery and Jove-Colon (2004). In addition, data for several minerals were added, while maintaining internal thermodynamic consistency, to explore solid solution behavior during serpentinization. New data are summarized in Table A2 in Appendix A, which also includes a discussion of data sources. In models where the precipitation of secondary phases in solid solutions are allowed, the calculations account for ideal solid solution substitution of the iron endmembers with their Mg endmember counterparts. Serpentine usually occurs as lizardite or chrysotile at low-temperature environments. Because differences in the thermodynamic properties between these two serpentine polymorphs are minor (Evans, 2004; Frost and Beard, 2007) we used chrysotile to represent the Mg-end member of serpentine. In some of our calculations, we suppressed the precipitation of certain minerals. These suppressed minerals and the reasons for suppression are explained in the discussions of model results. Primary and secondary minerals, including solid solutions modeled in this study, are listed in Table 2.3.

Table 2.3

*List of Minerals Included in this Study*

| **Mineral**[1] | **Abbreviation**[2] | **Formula** |
|---|---|---|
| | *Primary Minerals* | |
| Forsterite (*Olivine)* | Fo | $Mg_2SiO_4$ |
| Fayalite (*Olivine)* | Fa | $Fe_2SiO_4$ |
| Enstatite (*Orthopyroxene)* | En | $MgSiO_3$ |
| Ferrosilite (*Orthopyroxene)* | Fs | $FeSiO_3$ |
| Diopside (*Clinopyroxene)* | Di | $CaMgSi_2O_6$ |
| Hedenbergite (*Clinopyroxene)* | Hd | $CaFeSi_2O_6$ |
| | *Secondary Minerals* | |
| Chrysotile (*Serpentine)* | Ctl | $Mg_3Si_2O_5(OH)_4$ |
| Greenalite (*Serpentine)* | Gre | $Fe_3Si_2O_5(OH)_4$ |
| Mg-Cronstedtite (*Serpentine)* | Mg-Cro | $Mg_2Fe(FeSiO_5)(OH)_4$ |
| Hisingerite (*Serpentine)*[3] | His | $Fe_2Si_2O_5(OH)_4$ |
| Talc (*Talc)* | Tlc | $Mg_3Si_4O_{10}(OH)_2$ |
| Minnesotaite (*Talc)* | Mns | $Fe_3Si_4O_{10}(OH)_2$ |
| Brucite (*Brucite)* | Brc | $Mg(OH)_2$ |
| Ferroan Brucite (*Brucite)* | Fe-Brc | $Fe(OH)_2$ |
| Tremolite (*Amphibole)* | Tr | $Ca_2Mg_5Si_8O_{22}(OH)_2$ |
| Ferrotremolite (*Amphibole)* | Fe-Tr | $Ca_2Fe_5Si_8O_{22}(OH)_2$ |
| Goethite | Gth | $FeO(OH)$ |
| Magnetite | Mag | $Fe_3O_4$ |
| Dolomite | Dol | $CaMg(CO3)_2$ |
| Magnesite | Mgs | $MgCO_3$ |
| Calcite | Cal | $CaCO_3$ |
| Andradite | Adr | $Ca_3Fe_2Si_3O_{12}$ |
| Portlandite | Por | $Ca(OH)_2$ |

[1] If shown, minerals in italics indicate name of solid solution. All reacting primary minerals used in our models are in solid solutions. For compositions of primary phases, see Table 2.2.

[2] Mineral abbreviations follow recommendations by Whitney and Evans (2010). Minerals not included in Whitney and Evans (2010) are abbreviated using the first three letters of the minerals.

[3] The dehydrated version of hisingerite ($Fe_2Si_2O_5(OH)_4 \cdot nH_2O$, n=0) was used in this study.

## 2.4. Thermodynamic Constraints on the Evolution of Fluids during Low-Temperature Serpentinization

Results of calculations simulating the serpentinization of the model ultramafic rock introduced above (Model A, 85% olivine, 14% orthopyroxene, 1% clinopyroxene) are shown in Figures 2.2 and 2.3, and provide a framework for depicting the predicted consequences. The resulting reaction paths are divided into six stages to explore, step by step, the reactions that drive the transformation of acidic rainwater to hyperalkaline fluids. The numbers in circles in Figures 2.2 and 2.3 indicate the starting points of various stages of the overall reaction progress. Figure 2.2a depicts these six stages in a generalized schematic diagram for a subsurface flowpath in an ultramafic aquifer. Note that the transition from shallow to deep subsurface settings described in Figure 2.1 occurs in stage 3. Calculated changes in pH with reaction progress are shown in Figure 2.2b. Precipitating minerals and compositions of fluids at each stage of the overall reaction progress are summarized in Figure 2.2c and are described in detail in the following discussion. Changes in the total concentrations of Ca, Mg, Si, Fe and dissolved inorganic carbon (DIC), as well as the number of moles of secondary minerals produced or consumed are shown in Figure 2.3. Also shown in Figure 2.3 are activity diagrams that depict the stabilities of minerals relative to the activities of aqueous solutes, together with the reaction paths. Unless otherwise stated, compositions of fluids (including pH) and solid precipitates are results of calculations simulating ambient conditions (25 °C, 1 bar).

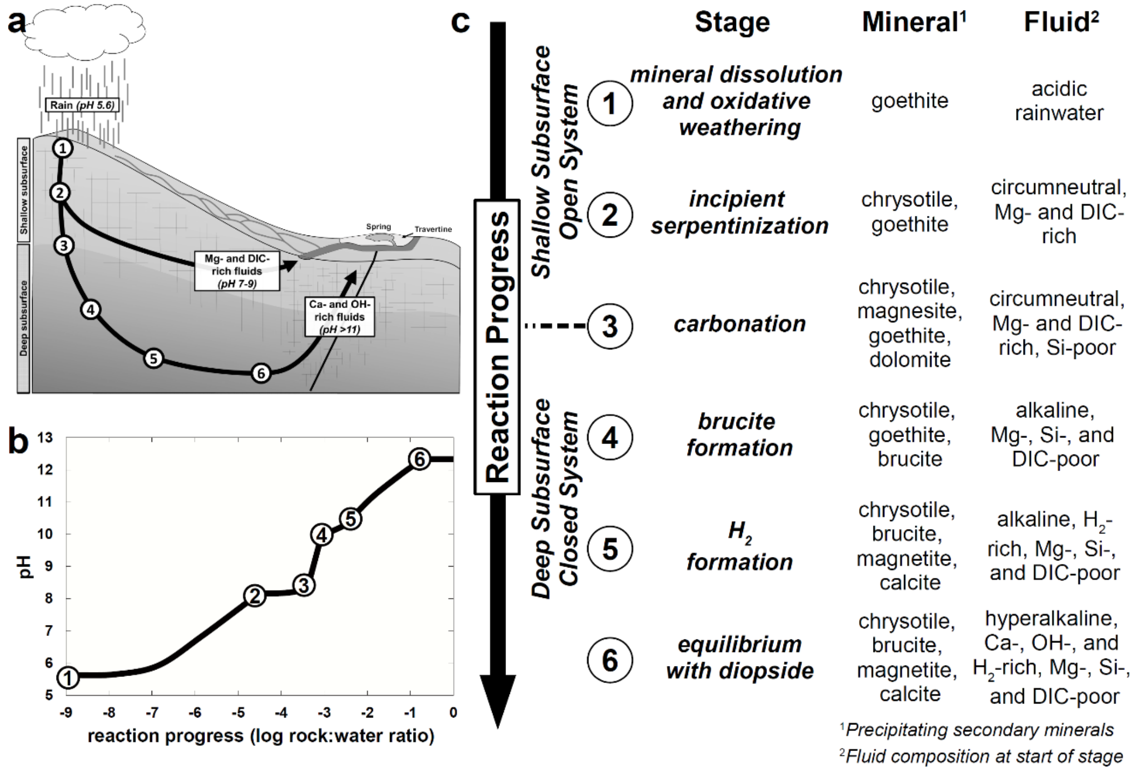

*Figure 2.2*. The progress of the overall serpentinization reaction is divided into six stages that depict conversion of meteoric water into evolved fluids (Types 1 and 2). The numbers in circles indicate the starting points of these stages. (a) depicts these stages in the generalized subsurface reaction scheme shown in Figure 2.1. (b) shows the evolution of pH during the overall reaction progress at 25°C and 1 bar. (c) summarizes precipitating minerals and fluid compositions at each stage of the overall serpentinization reaction progress. Note that stage 3 marks the transition from shallow to deep subsurface environments.

### *2.4.1. Stages in Reaction Progress*

**Stage 1, dissolution of primary minerals into rainwater.** The first stage of reaction progress begins when rainwater interacts with the rocks. At initial stages of reaction progress, the model system is *open* to the atmosphere, simulating rainwater interacting with rocks in the surface or shallow subsurface. The primary minerals that compose ultramafic rocks, formed at mantle temperatures and pressures, are unstable at the surface in the presence of rain and the atmosphere and consequently alter into

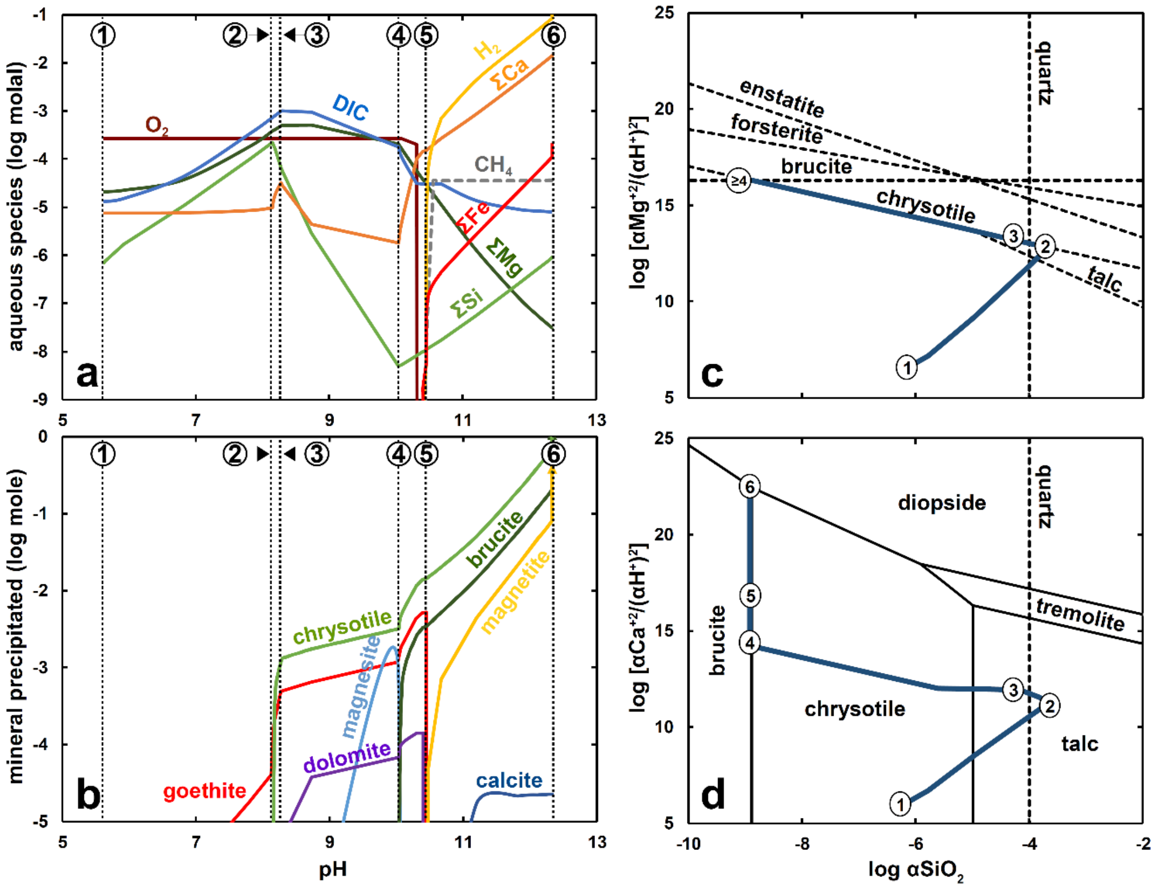

*Figure 2.3*. Evolution of (a) aqueous compositions and (b) secondary precipitation as pH increases with overall reaction progress at 25°C and 1 bar. Fluid evolution is also depicted on activity diagrams for the (c) $MgO-SiO_2-H_2O$ and (d) $CaO-MgO-SiO_2-H_2O$ systems. The numbers in circles indicate the starting points of various stages of overall reaction progress as in Figure 2.2c. Note that mineral saturation is indicated by dashed lines in (c) and (d), while solid lines in (d) represent boundaries for the stability fields of minerals.

secondary phases. Rainwater is slightly acidic (pH ~ 5.6) and contains $H^+$ derived from atmospheric $CO_{2(g)}$ via

$$CO_{2(g)} + H_2O \rightarrow HCO_3{}^- + H^+ \quad (2.1)$$

which drives the dissolution of primary minerals present in ultramafic rocks as described by the reactions

$$Mg_2SiO_{4(\mathrm{forsterite})} + 4H^+ \rightarrow 2Mg^{+2} + SiO_{2(aq)} + 2H_2O, \tag{2.2}$$

$$MgSiO_{3(\mathrm{enstatite})} + 2H^+ \rightarrow Mg^{+2} + SiO_{2(aq)} + H_2O, \text{ and} \tag{2.3}$$

$$CaMgSi_2O_{6(\mathrm{diopside})} + 4H^+ \rightarrow Ca^{+2} + Mg^{+2} + 2SiO_{2(aq)} + 2H_2O. \tag{2.4}$$

As shown in Figure 2.2b, progress of these reactions drives pH to higher values owing to the continuous consumption of $H^+$ during mineral hydrolysis. The dissolution of the primary minerals also releases solutes into the fluid, which increases their total concentrations relative to rainwater as illustrated in Figure 2.3a. At conditions open to the atmosphere, the concentration of dissolved inorganic carbon (DIC) is controlled by atmospheric $CO_{2(g)}$ levels. At a constant atmospheric fugacity, $fCO_{2(g)}$, $HCO_3^-$ and DIC must increase with pH (decrease in $H^+$) for reaction (2.1) to proceed. This increase in DIC early in the reaction progress is shown in Figure 2.3a. Ultimately, reactions (1 – 4) facilitate the transformation of dilute, acidic rainwater into a circumneutral fluid mostly enriched in Mg and DIC.

Reactions (2 – 4) refer to the Mg endmembers of natural mineral compositions that are solid solutions. The Mg endmembers provide a framework for illustrating the reactions discussed throughout this section. It should be kept in mind that dissolution of natural ultramafic minerals will also release $Fe^{+2}$, which often substitutes for $Mg^{+2}$ in minerals. As shown in Figure 2.3b, $Fe^{+2}$ released to the fluid can be oxidized by $O_2$ to form an oxyhydroxide such as goethite (FeOOH), through

$$4Fe^{+2} + O_{2(g)} + 6H_2O \rightarrow 4FeO(OH)_{(\mathrm{goethite})} + 8H^+. \tag{2.5}$$

As goethite precipitates, total Fe concentrations stay at low values that plot below the concentration range of most of Figure 2.3a. Throughout the overall reaction progress, $O_2$ consumption and oxidative weathering proceed through reaction (2.5) only. Ferric iron-bearing phases like hematite and other ferric oxyhydroxides are also known to occur in serpentinizing systems (Alt and Shanks, 2003; Mayhew et al., 2018). Precipitation of these phases would result in similarly low values of dissolved Fe as those shown in Figure 2.3a owing to their low solubilities. The fluid accumulates other major solutes (Mg, Ca, Si) from mineral dissolution, until they are concentrated enough for minerals to saturate. Increases in total dissolved concentrations of the above solutes are accompanied by increases in the activity ratios of $Mg^{+2}$ and $Ca^{+2}$ to $H^+$ [$\alpha Mg^{+2}/(\alpha H^+)^2$ and $\alpha Ca^{+2}/(\alpha H^+)^2$, respectively], as well as the activity of $SiO_{2(aq)}$ [$\alpha SiO_{2(aq)}$] as illustrated by reaction paths on activity diagrams shown in Figures 2.3c, for the $MgO$-$SiO_2$-$H_2O$ system, and 3D for the $CaO$-$MgO$-$SiO_2$-$H_2O$ system. Note that mineral saturation is indicated by dashed lines in Figures 2.3c and 2.3d, while solid lines in Figure 2.3d represent boundaries for the stability fields of minerals. At a point during Stage 1 of reaction progress, as shown by the reactions paths in Figures 2.3c and 2.3d, $\alpha SiO_{2(aq)}$ is high enough to saturate quartz and talc. These minerals, however, are rarely encountered in low-temperature serpentinites and were suppressed in the model to evaluate the maximum concentrations that Mg and Si can attain before the fluid reaches chrysotile saturation.

**Stage 2, the onset of serpentinization.** The maximum values of $\alpha SiO_{2(aq)}$ and total dissolved Si are reached at Stage 2 where the reaction path encounters the chrysotile saturation line, at which point chrysotile begins to precipitate in the model via

$$3Mg^{+2} + 2SiO_{2(aq)} + 5H_2O \rightarrow Mg_3Si_2O_5(OH)_{4(chrysotile)} + 6H^+. \qquad (2.6)$$

In response to the precipitation of chrysotile, the total dissolved Si decreases as shown in Figure 2.3a. Correspondingly, as illustrated in Figure 2.3c, when chrysotile saturation is attained, the reaction path turns and $\alpha SiO_{2(aq)}$ decreases along the chrysotile saturation line. Despite the consumption of Mg in reaction (2.6), continued dissolution of ultramafic phases means that the total dissolved Mg continues to increase in concentration. As an example, dissolution of olivine-dominated lithologies results in a surplus of Mg with respect to Si taken up during serpentinization as depicted by

$$2\mathrm{Mg_2SiO_{4(forsterite)}} + 2\mathrm{H^+} + \mathrm{H_2O} \rightarrow \mathrm{Mg_3Si_2O_5(OH)_{4(chrysotile)}} + \mathrm{Mg^{+2}}. \qquad (2.7)$$

Trends in pH result from reactions consuming and releasing $H^+$ into the fluid. In Stage 1 of reaction progress, dissolution of primary minerals consumes $H^+$ (reactions 2.2 – 2.4), and reactions that release $H^+$ include precipitation of secondary goethite (reaction 2.5), as well as the continuing dissolution of atmospheric $CO_{2(g)}$ (reaction 2.1) into the fluid. Released $H^+$, in turn, drives the dissolution of primary minerals (reactions 2.2 – 2.4) allowing reaction progress to proceed. As shown in Figures 2.2 and 2.3, the increasing trends in pH means that dissolution reactions prevail over reactions that release $H^+$. The precipitation of chrysotile (reaction 2.6) at the start of Stage 2 provides another source for $H^+$, which dampens the increasing pH trend observed since the start of Stage 1 (see Figure 2.2b). However, pH continues to increase, as production of $H^+$ through reaction (2.6) is not enough to balance its consumption through reactions (2 – 4). The overall process is exemplified by reaction (2.7), which depicts the overall process of forsterite dissolution and chrysotile precipitation (sum of reactions 2.2 and 2.6) and results in a net consumption of protons.

**Stage 3, atmosphere out, carbonates in.** As the fluid infiltrates deeper into the aquifer, it loses contact with the atmosphere as it continues to react with the rock. At the start of Stage 3, our calculations simulate a transition from an open shallow subsurface setting to a deep subsurface environment closed to atmospheric input. As shown in Figure 2.3a, DIC stops increasing without the atmosphere supplying $CO_{2(g)}$. Consequently, as illustrated in Figure 2.2b, pH increases dramatically without additional $H^+$ provided by reaction (2.1). Increasing pH and concentrations of divalent cations ($Mg^{+2}$ and $Ca^{+2}$) will saturate carbonate minerals. As shown in Figures 2.3 and 2.3, the first carbonate predicted to precipitate is dolomite via the reaction

$$\mathrm{Mg^{+2} + Ca^{+2} + 2HCO_3{}^- \rightarrow (CaMg)(CO_3)_{2(dolomite)} + 2H^+} \qquad (2.8)$$

which causes DIC and total dissolved Ca to decrease in response to dolomite precipitation. The next carbonate predicted to saturate, and in greater quantity than dolomite, is magnesite via the reaction

$$\mathrm{Mg^{+2} + HCO_3{}^- \rightarrow MgCO_{3(magnesite)} + H^+} \qquad (2.9)$$

which causes a slight decrease in the total dissolved Mg concentration.

During Stage 3, as shown in the reaction paths depicted in the activity diagrams shown in Figures 2.3c and 2.3d, the decrease in $\alpha SiO_{2(aq)}$ that started when chrysotile first precipitated at the beginning of Stage 2 continues. Despite the overall decrease in total Mg owing to dolomite, magnesite and chrysotile precipitation, the increase in pH is abrupt enough to cause the $\alpha Mg^{+2}/(\alpha H^+)^2$ to increase gently along the chrysotile saturation line (Figure 2.3c). The abrupt increase in pH also causes the $\alpha Ca^{+2}/(\alpha H^+)^2$ to increase slightly as the $\alpha SiO_{2(aq)}$ decreases (Figure 2.3d).

**Stage 4, brucite in, magnesite and dolomite out.** At Stage 4 of the overall reaction progress, pH is high enough to saturate brucite via

$$\mathrm{Mg^{+2} + 2H_2O \rightarrow Mg(OH)_{2(brucite)} + 2H^+}. \qquad (2.10)$$

Reaction (2.10) provides a new source for protons ending the dramatic increase in pH observed since the start of Stage 3 (Figure 2.2b). However, the dissolution reactions (reactions 2.2 – 2.4) that consume $H^+$ continue, allowing pH to increase more gradually than during Stage 3. As shown in Figures 2.3a and 2.3b, total dissolved Mg decreases abruptly in response to brucite precipitation. The continuous decreases in total Mg and DIC cause magnesite and eventually dolomite to become unstable and neither precipitates henceforth. Additionally, as depicted in Figure 2.3c, the trend of decreasing $\alpha SiO_{2(aq)}$ observed since the onset of serpentinization at Stage 2 stops when the reaction path attains brucite saturation at the point where the brucite and chrysotile saturation lines intersect. A major implication is that a fluid in equilibrium with both chrysotile and brucite will always remain undersaturated with respect to forsterite and enstatite, ultimately driving the total dissolution of these primary minerals. Totally serpentinized ultramafic rocks, where no relict olivine and orthopyroxene survive, are not uncommon in ultramafic settings (for example, see Oufi et al., 2002, Klein et al., 2014). Forsterite only becomes stable relative to chrysotile and brucite at temperatures > 350°C (see Klein et al., 2013).

As depicted in Figure 2.3c, the $\alpha Mg^{+2}/(\alpha H^+)^2$ becomes constant when the reaction path reaches the horizontal brucite saturation line corresponding to reaction (2.10). Moreover, the equilibrium assemblage of brucite and chrysotile will also set the $\alpha SiO_{2(aq)}$ as defined by the reaction

$$\mathrm{3Mg(OH)_{2(brucite)} + 2SiO_{2(aq)} \rightarrow Mg_3Si_2O_5(OH)_{4(chrysotile)} + H_2O}, \qquad (2.11)$$

which is the sum of reactions (2.6) and (2.10). At 25°C and 1 bar, reaction (2.11) will yield a low $\alpha SiO_{2(aq)}$ of $10^{-8.9}$. Despite the $\alpha SiO_{2(aq)}$ being fixed by reaction (2.11), the speciation of Si allows an increase in total dissolved Si, as depicted in Figure 2.3a, because the abundance of $HSiO_3^-$ increases with increasing pH via the reaction

$$\mathrm{SiO_{2(aq)} + H_2O \rightarrow \; HSiO_3{}^- + H^+.} \tag{2.12}$$

Reaction (2.12) allows total dissolved Si to increase with increasing pH while maintaining the fixed $\alpha SiO_{2(aq)}$ imposed by reaction (2.11).

Along the reaction path depicted in the activity diagram shown in Figure 2.3d, Stage 4 starts at the boundary between the brucite and chrysotile stability fields. The reaction path follows this boundary as the $\alpha Ca^{+2}/(\alpha H^+)^2$ continues to increase with reaction progress owing to increases in both pH, shown in Figure 2.2b, and total dissolved Ca concentration shown in Figure 2.3a. This point marks the transition from a *Type 1* fluid dominated by Mg and $HCO_3^-$ to a *Type* 2 fluid dominated by $Ca^{+2}$ and $OH^-$, which are the characteristic fluids found in serpentinizing systems.

**Stage 5, rise of a reduced fluid.** As fluid moves deeper into the subsurface, atmosphere-derived volatiles such as $O_{2(g)}$ and $CO_{2(g)}$ are exhausted, demarcating the start of Stage 5 of the overall reaction progress. At this point, $H_2O$ becomes the main oxidant, generating $H_2$ through the oxidation of ferrous iron in primary minerals to ferric iron in secondary minerals via

$$\mathrm{2Fe^{+2}O_{(primary\ minerals)} + H_2O \rightarrow Fe^{+3}{}_2O_{3(secondary\ minerals)} + H_{2(aq)}.} \tag{2.13}$$

Progress of reaction (2.13) causes the fluid to become more reduced with the continuous addition of $H_2$. This destabilizes goethite which is replaced by magnetite as the only Fe-bearing precipitate in this initial round of modeling because solid solution models of serpentine and brucite were not included. The consequences of allowing solid solutions to form is explored below. Moreover, as shown in Figure 2.3a, continuous addition of $H_2$ will generate a concentration of dissolved $H_2$ close to 100 millimolal by the end of Stage 5. This is 100 times as much dissolved $H_2$ as would be in equilibrium with 1 atmosphere of $H_{2(g)}$ at ambient conditions (~1 millimolal dissolved $H_2$), suggesting an overpressurized system capable of generating a free $H_{2(g)}$ phase. Further calculations incorporating constraints on confining pressures in deep subsurface aquifers can quantify the proportion of $H_2$ present as a free gas. This evaluation can provide insights into the habitability of serpentinizing subsurface as free $H_2$ is believed to promote formation of $CH_4$ (McCollom, 2016; Etiope and Whiticar, 2019).

As conditions become increasingly reduced, $CH_4$ formation is thermodynamically favorable and the concentration of DIC (represented by the species $CO_3^{-2}$ at this pH condition) will decrease if the reaction

$$\mathrm{CO_3}^{-2} + 4\mathrm{H_{2(aq)}} + 2\mathrm{H^+} \rightarrow \mathrm{CH_{4(aq)}} + 3\mathrm{H_2O} \qquad (2.14)$$

is not kinetically inhibited. Such a scenario is depicted as a downward dashed arrow from the DIC curve in Figure 2.3a. This downward trend for DIC does not occur if kinetic barriers for reaction (2.14) exist and DIC will remain in solution, albeit at low concentrations. DIC can then precipitate to yield calcite via

$$\mathrm{Ca^{+2}} + \mathrm{CO_3}^{-2} \rightarrow \mathrm{CaCO_{3(calcite)}} \qquad (2.15)$$

when pH and the total dissolved Ca are high enough, as shown in Figures 2.3a and 2.3b. A kinetic inhibition to abiotic methane generation opens the possibility for microbial methanogenesis, as discussed below.

**Stage 6, Chrysotile-Brucite-Diopside Equilibria.** Since the beginning of Stage 1 through the end of Stage 5, pH continues to increase transforming slightly acidic rainwater into an increasingly alkaline fluid. The increase in pH is driven by the consumption of $H^+$ through the dissolution of primary minerals (reactions 2.2 – 2.4). Precipitation of secondary minerals releases $H^+$, and, in turn, increases the extent of the dissolution reactions. So far, the release of $H^+$ from precipitation reactions is not enough to counter its consumption during dissolution reactions resulting in an overall net consumption of $H^+$ that drives the increasing pH trend shown in Figure 2.2b. Note that as the fluid becomes more alkaline, reactions depicted in this paper could be written using the species $OH^-$ instead of $H^+$. Nonetheless, rewriting the above reactions into those that release and consume $OH^-$ for dissolution and precipitation reactions, respectively, would still result in the same trends in the pH and concentrations of aqueous species shown in Figures 2.2 and 2.3.

In a system involving only forsterite as the dissolving primary mineral, the increase in pH stops when the overall reaction progress precipitates both chrysotile and brucite as depicted by the reaction

$$2\mathrm{Mg_2SiO_{4(forsterite)}} + 3\mathrm{H_2O} \rightarrow \mathrm{Mg_3Si_2O_5(OH)_{4(chrysotile)}} + \mathrm{Mg(OH)_{2(brucite)}}. \tag{2.16}$$

Reaction (2.16) describes the overall reaction for the dissolution of forsterite (reaction 2.2), and the precipitation of chrysotile (reaction 2.6) and brucite (reaction 2.10). As Reaction (2.16) does not result in a net consumption or production of $H^+$, pH will remain constant once chrysotile and brucite are both precipitating. The maximum pH this system can attain is that reached at the start of stage 4 (pH ~ 10) where brucite joins chrysotile in the secondary assemblage. Addition of enstatite will favor the formation of chrysotile over that of brucite, as exemplified by the reaction

$$3\mathrm{Mg_2SiO_{4(forsterite)}} + \mathrm{MgSiO_{3(enstatite)}} + 5\mathrm{H_2O} \rightarrow \qquad (2.17)$$

$$2\mathrm{Mg_3Si_2O_5(OH)_{4(chrysotile)}} + \mathrm{Mg(OH)_{2(brucite)}}.$$

However, as both chrysotile and brucite are still precipitating, the pH would still be constrained by the chrysotile-brucite equilibria and would still end up like that predicted for reaction (2.16).

It is the dissolution of diopside (reaction 2.4) that further drives the pH into hyperalkaline conditions (pH > 11). $Mg^{+2}$ and $SiO_{2(aq)}$ released through the dissolution of diopside can be consumed through the precipitation of Mg- and Si-bearing minerals such as chrysotile, dolomite, magnesite, and brucite. $Ca^{+2}$ released by the dissolution of diopside (reaction 2.4) can be potentially balanced by the precipitation of Ca-bearing phases such as dolomite (reaction 2.8) or calcite (reaction 2.15), but the minimal and continuously decreasing amount of DIC is not enough for reactions (2.8) and (2.15) to consume all of the $Ca^{+2}$ released through reaction (2.4). Unbalanced $Ca^{+2}$ will be accommodated by the consumption of $H^+$ (or, conversely, release of $OH^-$), and thus pH continues to increase.

At some point in the overall reaction progress, the increase in pH will stop. This occurs when the fluid approaches equilibrium with diopside, which means that reaction (2.4) stops going forward. As depicted in Figure 2.3d, this occurs when the reaction path reaches the invariant point defined by the equilibrium assemblage of chrysotile, brucite, and diopside (Ctl-Brc-Di), as described by the reaction

$$\mathrm{CaMgSi_2O_{6(diopside)} + 2Mg(OH)_{2(brucite)} + 2H^+ \leftrightarrow Ca^{+2} + Mg_3Si_2O_5(OH)_{4(chrysotile)} + H_2O.} \quad (2.18)$$

As this is an invariant point in the CaO-MgO-$SiO_2$-$H_2O$ system, not only the pH (Figure 2.2b) but also the total dissolved Ca, Mg, and Si (Figure 2.3a) will remain unchanged despite continuous reaction progress, until diopside is completely reacted. As fluids attain compositions dictated by this triple point, they are as close as possible to being in equilibrium with the host aquifer rocks, and defining the final stage, Stage 6, of overall reaction progress.

Fluid composition attained at Stage 6 of overall reaction progress is shown in Figure 2.3a and corresponds to reduced, Ca-OH fluid with hyperalkaline pH (pH ~12), elevated levels of total dissolved Ca (~10 millimolal), and dilute concentrations of total dissolved Si (~1 µmolal) and Mg (<1 µmolal). As an example, the pH can be derived using reaction (2.18), which, at 25°C and 1 bar, has an equilibrium constant of $10^{22.4}$. An equilibrium constant expression for reaction (2.18), assuming activities of pure solids and water at unity, is given by

$$\mathrm{K_{18}} = \frac{\alpha\mathrm{Ca^{+2}}}{(\alpha\mathrm{H^+})^2} = 10^{22.4} \quad , \quad (2.19)$$

and, incorporating an ionic balancing constraint

$$\alpha\mathrm{Ca^{+2}} = 0.5\alpha\mathrm{OH^-} = 0.5\,\frac{10^{-14}}{\alpha\mathrm{H^+}} \quad , \quad (2.20)$$

will yield a pH of ~12 at 25°C and 1 bar. Equation (2.20) is a simplified illustration compared with our calculations that account for full aqueous speciation and ionic balance. Further constraints via reaction (15, calcite precipitation) will allow the prediction of DIC concentrations. As shown in Figure 2.3a, an equilibrium assemblage of

Ctl-Brc-Di and calcite results in a predicted fluid with very low concentrations of DIC (<10 μmolal).

In summary, Stage 6 of the overall reaction progress corresponds to the final step in which the infiltrating fluid attains its maximum pH. Fluid composition imposed by the above assemblage of minerals results in an hyperalkaline fluid with elevated total concentrations of Ca, and dilute levels of total Mg, Si and DIC (see Figure 2.3a). Such equilibria also impose limits on the maximum pH that can be attained by a serpentinizing system. At ambient conditions (25°C, 1 bar) this yields a pH close to 12. This and other results discussed in this section have strong or subtle temperature dependencies as discussed next.

### *2.4.2. Variations in Temperature*

The models described above simulate water-rock interactions at ambient conditions (25°C, 1 bar). Continental serpentinizing fluids reported in the literature range in temperature up to ~50°C. Although yet to be sampled, serpentinizing fluids at higher temperatures up to ~100°C could exist deep in an ophiolite aquifer, assuming ophiolite thickness of 3-4 km and a geotherm of 30°C $km^{-1}$. To explore the chemistry of serpentinization-generated fluids that can form at various low temperatures, fluid compositions constrained by Ctl-Brc-Di plus calcite were calculated at temperatures ranging from 0°C to 100°C. Results are shown in Figure 2.4, including trends in pH, total dissolved Ca, Si, Mg, and DIC, and their speciated components over this temperature range. In the following discussion, note that the temperatures for calculated or measured pH values are indicated in subscripts.

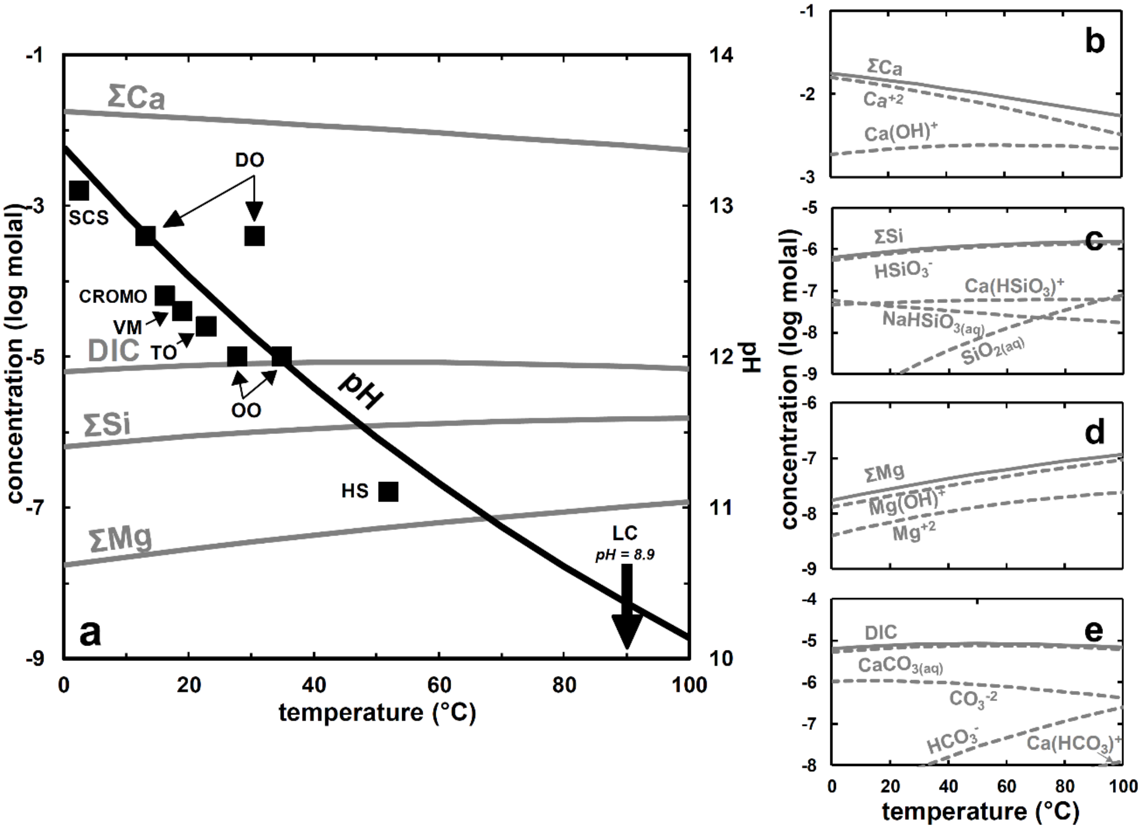

*Figure 2.4*. (a) Trends of pH and total dissolved solute concentrations, as constrained by equilibrium with Ctl-Brc-Di (reaction 2.18) and Cal (reaction 2.15) at temperatures ranging from 0°C to 100°C (see Table 2.3 for abbreviations of minerals). Also shown are the calculated speciations of (b) ΣCa, (c) ΣSi, (d) ΣMg, and (e) DIC. Plotted in (a) are some of the highest pH measured in serpentinizing systems (black squares): South Chamorro Seamount (SCS, Mottl, 2009); Coast Range Ophiolites, California (CROMO, Crespo-Medina et al., 2014); Voltri Massif, Italy (VM, Schwarzenbach et al., 2013); Oman Ophiolite (OO, Chavagnac et al., 2013b); Dinaride Ophiolite, Bosnia and Herzegovina (DO, Etiope et al., 2017); Tablelands Ophiolite, Canada (TO, Szponar et al., 2013); Hakuba Happo Springs, Japan (HS, Homma and Tsukahara, 2008); and Lost City Hydrothermal Field, Mid-Atlantic Ridge (LC, Seyfried et al., 2015). pH values for SCS and LC were measured at 25°C and were recalculated to in situ temperatures by Mottl (2009) for SCS and by this work using data from Seyfried et al. (2015) for LC.

The pH of a fluid in equilibrium with chrysotile, brucite, diopside, and calcite will decrease as temperature increases, as shown in Figure 2.4a. The calculated pH at 100°C ($pH_{100°C}$ = 10.1) is more than 3 pH units lower than that calculated at 0°C ($pH_{0°C}$ = 13.4). The latter is close to the $pH_{2.4°C}$ (13.1) calculated at *in situ* temperatures at South

Chamorro Seamount (Mottl, 2009). Mottl (2009) argued that this extremely high pH is attained through the release of $OH^-$ (or conversely, consumption of $H^+$) during the reduction of DIC to generate $CH_4$ (see reaction 2.14). Alternatively, this high pH could result from fluid-mineral equilibria as it is close to that predicted for equilibrium with Ctl-Brc-Di (Figure 2.4a). On the continents, high pH values were measured in fluids hosted in Canadian kimberlite deposits (12.46, Sader et al., 2007), the Tablelands Ophiolite in Canada (12.2, Szponar et al., 2013), Coast Range Ophiolites Microbial Observatory (CROMO) in California, USA (12.4, Crespo-Medina et al., 2014), Voltri Massif in Italy (12.3, Schwarzenbach et al., 2013), Samail Ophiolite in Oman (12, Chavagnac et al., 2013b), and the Dinaride Ophiolite in Bosnia and Herzogovina (12.8, Etiope et al., 2017). Measured pH of 12 (Oman), 12.2 (Tablelands), 12.3 (Voltri), 12.4 (CROMO) and 12.8 (Dinaride) at temperatures of 34.9°C, 21.3-24.3°C, 19°C, 16.2°C, and 13.1°C, respectively, are close to those predicted for the Ctl-Brc-Di equilibria (Figure 2.4a). A $pH_{30.5°C}$ measurement of 12.8 at Dinaride, which is 0.7 pH units above that imposed by Ctl-Brc-Di equilibria could have been produced through reduction reactions that generate $CH_4$, as Mottl (2009) postulated for the South Chamorro Seamount fluid. The $CH_4$ concentration (2706 µM) associated with this sample is the highest recorded so far in ultramafic-hosted hyperalkaline fluids (Etiope et al., 2017). Alternatively, this high pH could be a result of mineral buffering reactions other than the Ctl-Brc-Di equilibria. High pH values (~12.5) were measured from slag-filled aquifer fluids in Lake Calumet, Chicago, Illinois (Roadcap et al., 2005; 2006; Ohlsson et al., 2019) and even more basic pH values were observed in Maqarin, Jordan (Barnes et al., 1982; Khourey et al., 1985, 1992; Alexander et al., 1992; Pederson et al., 2004). These sites are not hosted in ultramafic rocks and the high pH is likely a result of mineral equilibria akin to that resulting from concrete-water interactions rather than by the Ctl-Brc-Di equilibria attained during the serpentinization of ultramafic rocks. As an example, the $\alpha Ca^{+2}/(\alpha H^{+})^{2}$ of a fluid constrained by portlandite and high Ca/Si hydrate (CSH) phases is higher than typically seen in serpentinizing fluids, owing to both higher pH and total dissolved Ca (Blanc et al., 2010). In addition to portlandite and CSH phases, fluid in equilibrium with calcite at extremely DIC-limited environments would require very high pH, as expounded upon below. These examples underscore the fact that hyperalkaline fluids are not unique to serpentinization-related environments and other fluid-rock processes that buffer pH to high values also exist.

Temperatures slightly exceeding 50°C, perhaps the highest measured in continental serpentinizing systems, were recorded by Homma and Tsukahara (2008) and Suda et al. (2014) in Hakuba Happo Hot Springs, Japan. The highest reported $pH_{52°C}$ for this area is 11.1 (Homma and Tsukahara, 2008) which is also close to that constrained by the Ctl-Brc-Di equilibrium. Taran and othes (2002, 2010) documented acidic ($pH_{25°C}$ = 2.58-2.93) hot springs (42-99°C) in Socorro Island, Mexico enriched in $H_2$ and $CH_4$ attributed to serpentinization. As it is located in an active magma-driven hydrothermal system, further work can decouple how much the compositions of these fluids were influenced by volcanic input or by serpentinization. Otherwise, temperatures higher than those recorded in Hakuba Happo for continental serpentinizing fluids have yet to be measured, but higher temperatures are observed in submarine hydrothermal fields. Calculated pH values at *in situ* temperatures (ranging from 75-116°C) for end-member fluids venting at the Lost City hydrothermal field are lower than those predicted for Ctl-

Brc-Di equilibria (Seyfried et al., 2015). For instance, at an *in situ* temperature of 90°C (Beehive Structure, Lost City hydrothermal field; Seyfried et al., 2015), the calculated $pH_{90°C}$ of 8.9 is 1.5 pH units below that predicted for a fluid in equilibrium with Ctl-Brc-Di ($pH_{90°C} = 10.4$). Seyfried et al. (2015) attributed this lower pH to the chrysotile-tremolite-diopside (Ctl-Tr-Di) equilibria, which compared to the Ctl-Brc-Di equilibria, will yield lower $\alpha Ca^{+2}/(\alpha H^{+})^{2}$ (and hence lower pH) and higher $\alpha SiO_{2(aq)}$. The shift from the Ctl-Brc-Di to the Ctl-Tr-Di equilibria results from subsurface transport in which fluids react with the intermingling peridotite and the relatively more silica-rich gabbroic bodies beneath the Lost City hydrothermal field (Seyfried et al., 2015).

Compared to pH, total dissolved Ca, Si, Mg and DIC do not vary as much with temperature (Figure 2.4a). At most, the total Mg concentration is greater by an order of magnitude at 100°C compared with 0°C, while changes in total Ca, Si, and DIC are less conspicuous. As shown in Figure 2.4b, the most abundant species contributing to the total Ca in the fluid is $Ca^{+2}$, although with an increasing contribution from $Ca(OH)^{+}$ as temperature increases. Total Si is dominantly made up of the anion $HSiO_3^{-}$, which can form aqueous complexes with cations like $Na^{+}$, $Ca^{+2}$ and $Mg^{+2}$ (Figure 2.4c). The low concentration of $Mg^{+2}$ means that the abundance of the Mg-silicate complex is predicted to be lower than the concentration range shown in Figures 2.4c and 2.4d. Total dissolved Mg is mostly made up of $Mg(OH)^{+}$ at these alkaline conditions (Figure 2.4d). Most of the dissolved inorganic carbon exists as the neutral complex, $CaCO_{3(aq)}$, in these Ca-enriched fluids followed by $CO_3^{-2}$ (Figure 2.4e).

### *2.4.3. Variations in Fluid Salinity*

Results described above are for calculations with 1 millimolal NaCl solutions. In additional models we examined the effects of varying salinity from dilute (0.1 millimolal NaCl) to that equivalent to seawater (0.5 molal NaCl). Results of calculations for conditions at 25°C and 1 bar depicted in Figure 2.5, show that pH and the concentrations of most dissolved species (DIC, total dissolved Mg and Ca) in equilibrium with the Ctl-Brc-Di plus calcite assemblage change only slightly, increasing with fluid salinity. In contrast, total dissolved Si increases by more than an order of magnitude (Figure 2.5a). This change is attributed to a shift in the dominant aqueous species that comprises the total dissolved Si pool (Figure 2.5c). In dilute highly basic solutions, most of the dissolved Si exists as the anion $HSiO_3^-$, but shifts to the sodium silicate complex, $NaHSiO_{3(aq)}$ as salinity rises. Because the activity of $SiO_{2(aq)}$ remains constant as dictated by the Ctl-Brc equilibrium (reaction 2.11), and pH increases only slightly, the concentration of $HSiO_3^-$ also remains relatively constant (see reaction 2.12) with salinity. Simultaneously, the concentration of $NaHSiO_{3(aq)}$ increases even at constant $HSiO_3^-$ as the reaction

$$\mathrm{Na^+ + HSiO_3{}^- \rightarrow\ NaHSiO_{3(aq)}} \tag{2.21}$$

proceeds with increasing salinity. The overall consequence is an increase in the total dissolved Si. This increase in dissolved Si aligns with observations of the enhanced solubility of a number of silicates with increasing salinity (see Newton and Manning, 2010) that may be attributed to changes in the speciation of dissolved silica species. However, existing stability constants for the $NaHSiO_{3(aq)}$ complex (Seward 1974;

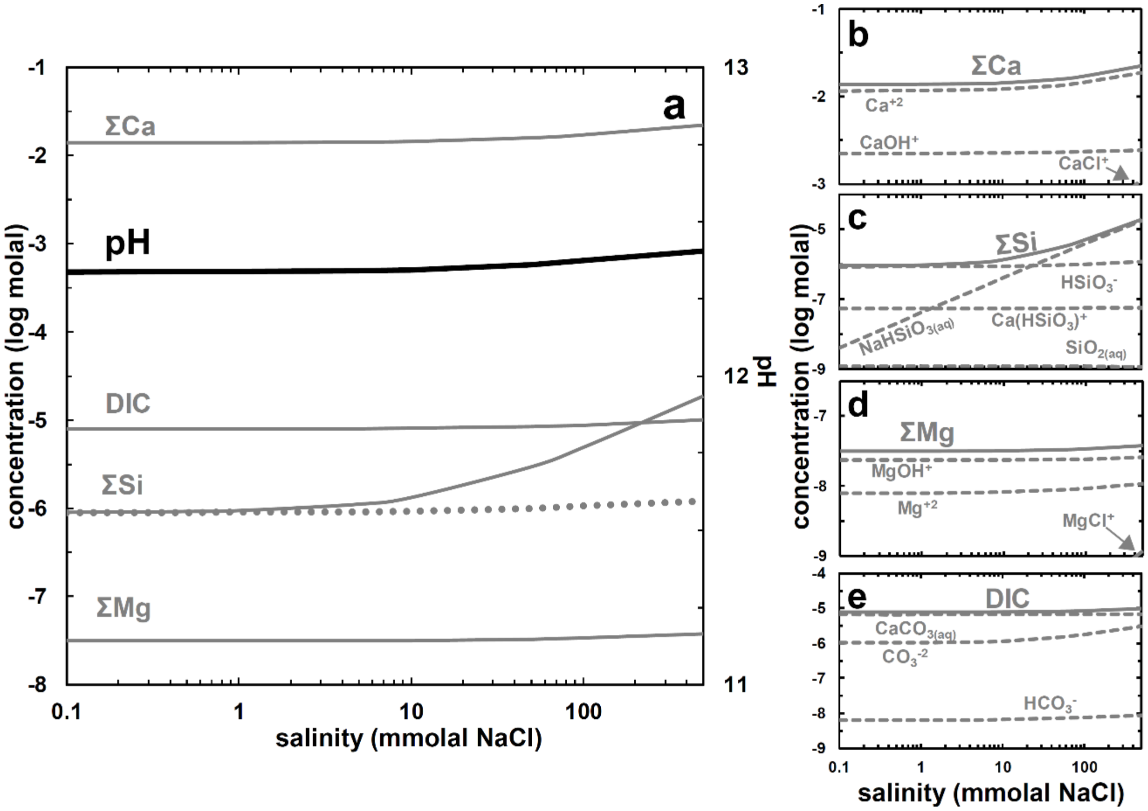

*Figure 2.5*. (a) Trends of pH and total dissolved solute concentrations constrained by Ctl-Brc-Di equilibrium (reaction 2.18) at 25°C and 1 bar, as functions of increasing fluid salinity. Also plotted are the calculated speciations of (b) ΣCa, (c) ΣSi, (d) ΣMg, and (e) DIC. Dotted line for ΣSi in (a) depicts results of simulations where the $NaHSiO_{3(aq)}$ complex is suppressed.

Sverjensky et al., 1997) used in this work are questioned by some studies (Busey and Mesmer, 1977; Tutolo and Tosca, 2018; Huang and Sverjensky, 2019). For example, the solubilities of certain silicates (amorphous silica; Marshall and Warakomski, 1980; Zarubin and Nemkina, 1990) decrease with increasing salinity indicating a much weaker drive to form this complex than depicted in our models. Suppressing this complex results in a dissolved Si trend, shown by the dotted line in Figure 2.5a, that is independent of fluid salinity. Future studies that can constrain solubilities of serpentinization-relevant minerals at highly saline environments will permit predictions of fluid compositions in other rocky bodies in our solar system where saline fluids are known to predominate (Glein et al., 2015). Nonetheless, the lowest Si concentrations measured from non-saline, continental serpentinizing fluids (1 μmolal Si, Chavagnac et al., 2013b) are consistent with our predictions. The speciation of other solutes are depicted in Figures 2.5b, 2.5d, and 2.5e for total dissolved Ca, Mg and inorganic carbon, respectively, and change minimally with variable salinity. Chloride complexes of $Ca^{+2}$ and $Mg^{+2}$ occur only in minor amounts that remain below most of the concentration range in Figure 2.5 (note how $MgCl^{+}$ appears only at the highest salinity) and would not affect the speciation of these cations as much as Na affects the total dissolved Si.

### *2.4.4. Precipitation of Ca-bearing Phases*

The dissolution of diopside and the lack of a precipitating Ca-bearing phase to counter reaction (2.4) requires the consumption of $H^{+}$ (or production of $OH^{-}$) to accommodate the otherwise unbalanced $Ca^{+2}$. During the overall serpentinization progress, this increase in pH is accommodated until the fluid attains equilibrium with diopside. As shown in Figure 2.4a, equilibria involving diopside can account for some of the highest pH values observed in serpentinizing environments. Most studies on continental serpentinizing sites report the pH of hyperalkaline fluids to be between 11-12, somewhat lower than the theoretical maxima. As an example, as shown in Figure 2.6a, most hyperalkaline fluids sampled in Oman (filled grey circles, Paukert et al., 2012; Chavagnac et al., 2013b; Canovas et al., 2017) have measured pH values lower than those set by equilibrium with diopside (solid black line in Figure 2.6a) given the measured fluid temperature. The precipitation of Ca-bearing phases can cause fluids to shift from being in equilibrium with diopside and can likely draw pH to lower values. In this section, we explore the effects of various Ca-bearing phases (portlandite, andradite, and calcite) on fluid compositions. Results of calculations are shown in the temperature *vs.* pH plot and the CaO-MgO-$SiO_2$-$H_2O$ activity diagram depicted in Figures 2.6a and 2.6b, respectively.

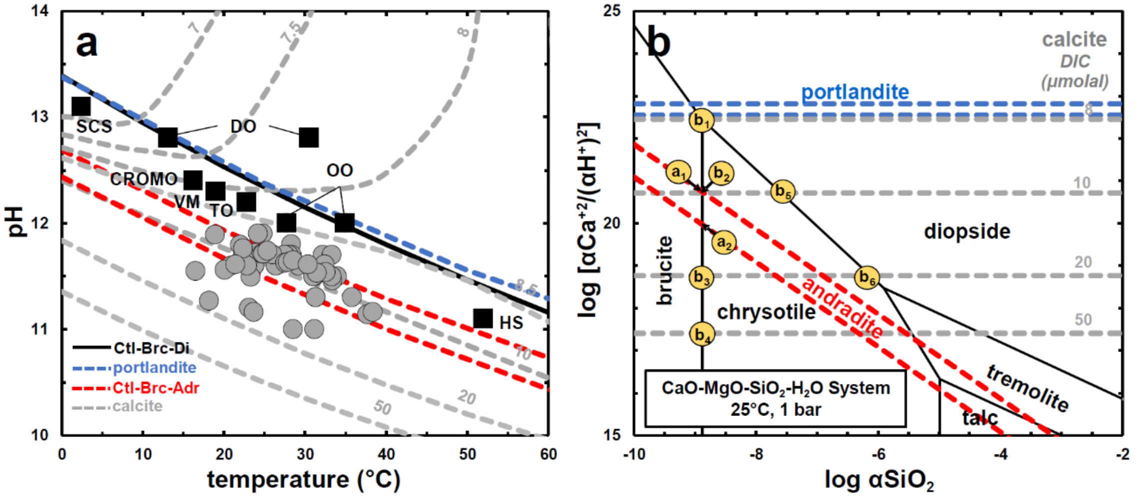

*Figure 2.6.* (a) pH and temperature of hyperalkaline fluids (pH >11) sampled from Oman (filled grey circles, data from Paukert et al., 2012, Chavagnac et al., 2013b, and Canovas et al., 2017) and other <60°C sites listed in Figure 2.4a (filled black squares). Most samples from Oman plot below the pH dictated by Ctl-Brc-Di equilibrium (solid black curve). (b) Activity diagram for the CaO-MgO-$SiO_2$-$H_2O$ system. Stability fields and saturation lines of minerals are similar to Figure 2.3d, with the addition of saturation lines for calcite (dashed grey) at variable DIC concentrations indicated above or below the line, portlandite (dashed blue), and andradite (dashed red). Upper and lower lines for portlandite represent ranges in solubility data from the literature (see text). Upper line for andradite depicts redox conditions constrained by the iron-magnetite equilibrium, lower line is constrained by the goethite-magnetite equilibrium. Points $a_1$ and $a_2$ depict equilibrium with andradite with both chrysotile and brucite (Ctl-Brc-Adr) at redox conditions mentioned above. Point $b_1$ depicts the Ctl-Brc-Di equilibrium triple point. Points $b_2$, $b_3$, and $b_4$ depict equilibrium with Ctl-Brc-Cal at DIC concentrations of 10, 20, and 50 µmolal, respectively. The lines in (a) represent pH values calculated by the equilibria noted by these points in (b) -- dashed red lines ($a_1$ and $a_2$) and dashed grey lines ($b_1$, $b_2$, $b_3$, and $b_4$) -- as well as pH values derived from the lower portlandite line (dashed blue line) and additional Ctl-Brc-Cal equilibrium points at limited DIC (<8.5 µmolal) concentrations (dashed grey lines). Equilibria without brucite are represented by points $b_5$ and $b_6$, which depict equilibrium with Ctl-Di-Cal at DIC concentrations of 10 and 20 µmolal, respectively. See Table 2.3 for abbreviations of minerals.

**Portlandite.** Albeit rarely, portlandite can occur in serpentinizing environments (Neal and Stanger, 1984; Chavagnac et al., 2013a). The $\alpha Ca^{+2}/(\alpha H^{+})^2$ needed to saturate portlandite can be derived using the equilibrium constant expression for the reaction

$$\mathrm{Ca^{+2} + 2H_2O \rightarrow Ca(OH)_{2(portlandite)} + 2H^{+}}. \tag{2.22}$$

At ambient conditions (25°C, 1 bar), $\alpha Ca^{+2}/(\alpha H^{+})^2 = 10^{22.5}$ to $10^{22.8}$ (Reardon, 1990; Wolery and Jove-Colon, 2004; Blanc et al., 2010, dashed blue lines in Figure 2.6b) where the lower value is close to that derived for Ctl-Brc-Di equilibrium ($10^{22.4}$, see point $b_1$ in Figure 2.6b). Temperature-dependent thermodynamic data for portlandite exist (Wolery and Jove-Colon, 2004) and allow us to calculate pH constrained by portlandite solubility from 0°C to 60°C. The dashed blue line plotted in Figure 2.6a depicts calculated pH values that closely align with pH values dictated by the Ctl-Brc-Di equilibrium. It follows that fluids produced through serpentinization, at the maximum pH and Ca concentration attainable through Ctl-Brc-Di- equilibrium, can potentially precipitate portlandite. However, it is only at this specific stage of the overall serpentinization progress that portlandite saturation can be attained, which is consistent with its rare occurrence in hyperalkaline pools and serpentinite outcrops.

**Andradite.** Anhydrous and hydrous andraditic garnets are known to occur in a number of serpentinites (Beard and Hopkinson, 2000; Menez et al., 2012, 2018; Plümper et al., 2014), where they are found to be intimately associated with organic matter (Menez et al., 2012, 2018). The uptake of $Ca^{+2}$ into garnet as shown by the reaction

$$\begin{aligned} &\mathrm{3Ca^{+2} + 2Fe^{+3} + 3SiO_{2(aq)} + 6H_2O} \\ &\rightarrow \mathrm{Ca_3Fe_2Si_3O_{12(andradite)} + 12H^{+}} \end{aligned} \tag{2.23}$$

can draw pH away from equilibrium with diopside. The $\alpha Ca^{+2}/(\alpha H^{+})^{2}$ of fluids in equilibrium with andradite was calculated using reaction (2.23) over ranges of $\alpha SiO_{2(aq)}$ from $10^{-10}$ to $10^{-2}$, and $\alpha Fe^{+3}/(\alpha H^{+})^{3}$ constrained by redox states buffered by either goethite-magnetite or magnetite-iron equilibria. Results of calculations are plotted as dashed red lines in Figure 2.6b and show that equilibrium with andradite requires that the fluid has lower values of $\alpha Ca^{+2}/(\alpha H^{+})^{2}$ than set by equilibrium with diopside. A more reduced environment constrained by the magnetite-iron equilibrium (top dashed red line in Figure 2.6b) results in slightly higher $\alpha Ca^{+2}/(\alpha H^{+})^{2}$ values than those set by the goethite-magnetite (lower dashed red line in Figure 2.6b). We calculated pH constrained by an equilibrium assemblage of chrysotile, brucite, and andradite (Ctl-Brc-Adr, points $a_1$ and $a_2$ in Figure 2.6b) at temperatures ranging from 0°C to 60°C and results of calculations are overlain in Figure 2.6a as dashed red lines. pH constrained by the above equilibrium at the range of temperature depicted in Figure 2.6a can account for many but not all environmental observations offset from Ctl-Brc-Di equilibria. In the calculation above, we substituted thermodynamic data for andradite in place of missing data for hydrous andraditic garnets. Further calculations incorporating thermodynamic data on hydrous andraditic garnets, and field studies documenting their occurrence in ophiolitic aquifers, would allow assessments on the role of garnets during low-temperature serpentinization. Like magnetite, andraditic garnets can potentially host ferric iron among secondary precipitates during serpentinization, which can further the potential to generate $H_2$ via reaction (2.13). For example, Plümper et al. (2014) estimated massive amounts of $H_2$ generated through andradite formation that would be enough to stabilize Fe-Ni alloys based on observations of garnet-bearing serpentinites in the Feragen ultramafic body in Norway.

**Calcite.** As discussed above, results shown in Figure 2.3a demonstrate that limits on the amount of DIC late in the overall serpentinization progress mean that calcite precipitation (reaction 2.15) will not be able to balance $Ca^{+2}$ released through diopside dissolution (reaction 2.4). However, if there is a supply of DIC from another source it may be possible for fluids to be in equilibrium with calcite instead of diopside. This may occur where deep-seated fluids devoid of atmospheric input discharge back to the surface where infiltration of $CO_{2(g)}$, interaction with near-surface carbonate veins, or mixing with DIC-rich shallow groundwater can supply DIC. The consequences are illustrated by the dashed grey lines in Figure 2.6b, which show calculated values of $\alpha Ca^{+2}/(\alpha H^{+})^2$ in equilibrium with calcite at the indicated concentrations of DIC. At DIC concentration of ~8 µmolal, a 25°C, 1 bar fluid can be in equilibrium with both diopside and calcite (point $b_1$ in Figure 2.6b). At higher DIC concentrations, the presence of calcite can draw $\alpha Ca^{+2}/(\alpha H^{+})^2$ to values lower than those constrained by diopside. If calcite precipitation is faster than diopside dissolution, fluid composition can shift from that dictated by Ctl-Brc-Di equilibrium to that constrained by chrysotile-brucite-calcite (Ctl-Brc-Cal) equilibrium such as those depicted by points $b_2$, $b_3$, and $b_4$ in Figure 2.6b for DIC concentrations of 10, 20, and 50 μmolal, respectively. The consequences for pH of this shift in controlling mineral assemblages at temperatures ranging from 0°C to 60°C are shown as dashed grey lines in Figure 2.6a, and show that equilibrium with calcite in extremely DIC limited environments (< 8 μmolal) may require pH higher that can be attained through equilibrium with diopside. This could account for the extremely high pH recorded by

Etiope et al. (2017) at one site in the Dinaride Ophiolite discussed above. Otherwise, at DIC concentrations > 8 µmolal, calcite will draw pH to lower values than equilibrium with diopside. With increasing DIC concentration the equilibrium pH constrained by Ctl-Brc-Cal will be lower. As shown in Figure 2.6a, a shift from equilibrium with diopside to calcite can account for most environmental pH observations. As an example, most hyperalkaline fluids sampled in Oman have pH values that lie between ranges possible for calcite at low DIC concentrations (8-20 µmolal) and andradite at variable redox conditions (goethite-magnetite to magnetite-iron equilibria). So far, no study has surveyed the abundance of andradite or hydrogarnets in ophiolitic aquifers. Calcite, on the other hand, is common as near-surface veins and surface travertine deposits (Kelemen and Matter, 2008; Mervine et al., 2014). It is likely that this shift to calcite equilibria occurs in the near subsurface or at the surface where deep-seated fluids encounter DIC-rich shallow groundwater or the atmosphere. It can also be seen in Figure 2.6a that a few Oman samples plot at pH values higher than that set by calcite equilibrium at 10 µmolal DIC and are close to equilibrium with diopside or with calcite at extremely DIC-limited conditions (<10 µmolal). This suggests that these fluids were less influenced by surficial or shallow subsurficial processes and remain close to equilibrium with the altered host rocks (Ctl-Brc-Di equilibrium).

Higher concentration of DIC will draw the fluid to lower pH as shown in Figure 2.6a. Pfeiffer (1977) and Bruni et al. (2002) argued that the high pH of serpentinizing springs is mainly attributed to extremely low DIC characteristic of systems closed to atmospheric influence. Our calculations agree with this statement, as very low DIC concentrations are needed for pH to remain > 11 as shown by the calcite trends in Figure

2.6a. However, reaction path calculations underscore that the path to hyperalkaline pH is facilitated by primary mineral dissolution reactions, especially diopside, and a low DIC concentration is only needed to preserve hyperalkaline conditions generated by water-rock reactions. Nevertheless, the calculations shown above underline that variabilities in pH recorded in serpentinizing systems may be attributed to variations in DIC input in addition to variations in temperature and buffering reactions involving other minerals.

In the discussions above, brucite is assumed to be present in the equilibrium mineral assemblage. Fluid pathways may encounter environments where brucite is unstable such as in the shallow subsurface where the aquifer can be composed of brucite-free serpentinites (Miller et al., 2016). Interaction with these rocks will draw fluids away from the brucite stability field depicted in Figure 2.6b and toward assemblages stable at higher $\alpha SiO_{2(aq)}$. As an example, fluids in equilibrium with chrysotile, diopside, and calcite at DIC concentrations of 10 μmolal and 20 μmolal, respectively depicted by points $b_5$ and $b_6$ in Figure 2.6b, will result in fluids with lower $\alpha Ca^{+2}/(\alpha H^{+})^2$ and higher $\alpha SiO_{2(aq)}$ and will ultimately generate fluids with lower pH and higher Si concentrations than values constrained by the Ctl-Brc-Di equilibrium. Note that points $b_5$ and $b_6$ (Ctl-Di-Cal), respectively, share similar $\alpha Ca^{+2}/(\alpha H^{+})^2$ with points $b_2$ and $b_3$ (Ctl-Brc-Cal equilibrium) and would result in fluids with similar pH with the former distinguished from the latter only by their higher dissolved Si concentrations. As such, most of the environmental pH values shown in Figure 2.6a can also be accommodated by this shift to the Ctl-Di-Cal equilibrium. In addition to the consequences of a brucite-free serpentinite aquifer, mixing with Si-rich shallow groundwater can also draw fluids to higher $\alpha SiO_{2(aq)}$. Assessment of the silica concentrations of serpentinization-generated hyperalkaline fluids is one of the most powerful ways to discriminate among various fluid pathways possible in ultramafic aquifers, as well as the consequence of fluid mixing at and below the surface.

### *2.4.5. Variations in Contributions from Primary Minerals*

The preceding discussion refers to a model of rainwater reacting with a single generalized composition of ultramafic rock (85% $Fo_{90}$-olivine, 14% $En_{90}$-orthopyroxene, and 1% $Di_{95}$-clinopyroxene). This composition is characteristic of harzburgites that are common in ophiolites.  However, modal compositions of primary minerals that compose harzburgites vary in ophiolites and in exhumed ultramafic rocks in the seafloor (see: Warren (2016) for a compilation of seafloor ultramafic rock mineralogy and geochemistry). Consequently, fluids will likely encounter rocks with variable composition during subsurface transport. Moreover, primary minerals can dissolve at differing rates resulting in variable contributions of aqueous solutes from primary minerals that may differ from the modal composition of the host rock. Therefore, in this section we discuss the consequence of variable contributions of primary minerals on the compositions of aqueous fluids. Details on the composition of the reacting rocks used in our simulations can be found in Table 2.2. This work focuses on alteration at ambient conditions and is complementary to results by Klein et al. (2013) on the variabilities in secondary mineralization and fluid and gas chemistry resulting from the alteration of ultramafic rocks of variable modal compositions at temperatures up to 400°C. In addition, this work expands the compositional variabilities explored by seminal calculations on low-temperature serpentinization by Pfeifer (1977) and Palandri and Reed (2004).

Results for 25°C and 1 bar are shown in Figures 2.7 to 2.9. We start with rainwater interactions with rocks composed only of olivine (Forsterite$_{90}$) and orthopyroxene (Enstatite$_{90}$) (Models B1-B5, MgO-FeO-$SiO_2$-$H_2O$ system), and then discuss the effects of involving clinopyroxene (Diopside$_{95}$) (Models C1-C5, CaO-MgO-FeO-$SiO_2$-$H_2O$ system) on the resulting fluid compositions. Lastly, instead of a fresh ultramafic rock, we model fluids reacting with a serpentinite (Models D1-D4). This model shares features with those conducted by Cipolli et al. (2004) and Bruni et al. (2002) who simulated rainwater-serpentinite interactions to account for the origins of hyperalkaline fluids seeping out from metaophiolitic lithologies in the Voltri Group of the Ligurian Ophiolite in Italy. However, instead of bulk serpentinite chemistry, here we use variable molal contributions of serpentine and brucite to investigate the effects of variable serpentinite compositions on the evolution of fluids. In these serpentinite models, the source of Ca is minor relict clinopyroxene.

**Olivine and Orthopyroxene alteration (MgO-FeO-$SiO_2$-$H_2O$ system).** As shown in Figure 2.7a, at late stages of reaction progress almost equal amounts of chrysotile and brucite (in moles) will precipitate if the only dissolving mineral is olivine (Model B1). This is exemplified by reaction (2.16), which depicts the sum of the reactions involving the dissolution of forsterite (reaction 2.2), and the precipitation of chrysotile (reaction 2.6) and brucite (reaction 2.10). The reason that there is slightly less brucite forming relative to chrysotile in Figure 2.7a is that iron released from olivine precipitates as goethite and magnetite during alteration. If the reacting mineral is pure forsterite, equal amounts of chrysotile and brucite (in moles) will precipitate as depicted by reaction (2.16). Note that reaction (2.16) results in neither a net consumption or

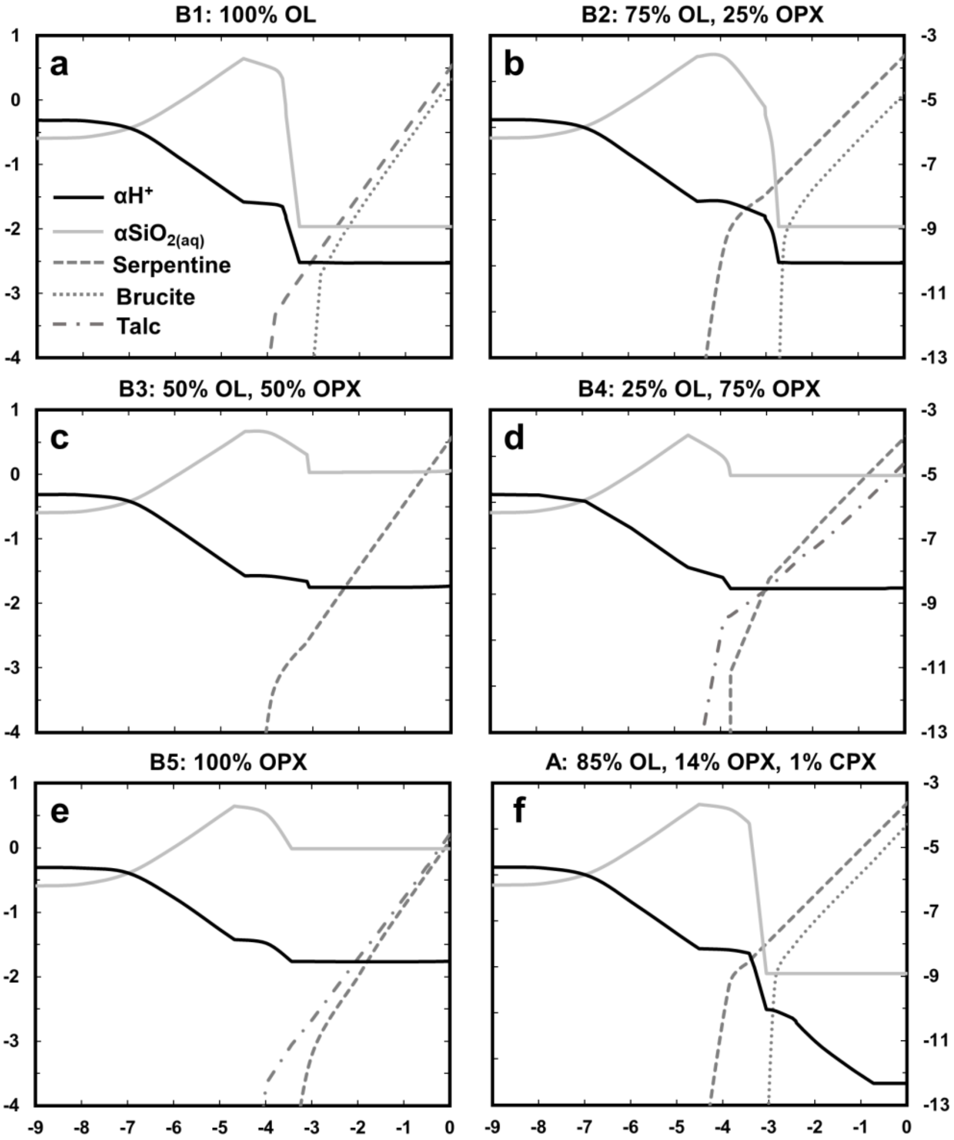

*Figure 2.7*. (a-e) Results of simulations at 25°C and 1 bar for host rocks of the MgO-FeO-$SiO_2$-$H_2O$ system (Models B1-B5) where reacting rocks contain olivine (OL) or orthopyroxene (OPX) or combinations of both. (f) Results of simulation illustrated in Figure 2.3 (Model A) for comparison. Contributions from the primary phases are indicated above each plot.

production of $H^+$ and pH will remain constant once chrysotile and brucite are both precipitating. The activity of $SiO_{2(aq)}$ will be set by Ctl-Brc equilibrium defined by reaction (2.11). The consequences of reactions (2.11) and (2.16) are shown in Figure

2.7a, including the constant pH (-log $\alpha H^+$) and $\alpha SiO_{2(aq)}$ trends once brucite joins chrysotile in the secondary assemblage. The predicted pH arising from these equilibria is near 10 which is close to the maximum pH of 9.5 measured by Okland et al. (2012) in groundwaters seeping from olivine-rich (dunite) outcrops of the Leka Ophiolite.

In contrast to dunites which are mostly composed of olivine, harzburgites have considerable abundances of orthopyroxene in addition to olivine. The involvement of orthopyroxene during alteration will decrease the amount of brucite precipitated in favor of chrysotile as shown in Figure 2.7b, which illustrates a model where rainwater interacts with a hypothetical rock composed of 75 mole % olivine and 25 mole % orthopyroxene (see reaction 2.17, Model B2). As in Figure 2.7a, both chrysotile and brucite are present, which means that fluid compositions will be controlled by the same Ctl-Brc equilibrium (reaction 2.11). As a consequence, this scenario will yield similar pH and total dissolved Si values to the results shown in Figure 2.7a for olivine-only dissolution. This pattern continues until we consider equal mole % contributions of olivine and orthopyroxene (Model B3), as depicted in Figure 2.7c, which will only produce serpentine via

$$\mathrm{Mg_2SiO_{4(forsterite)}} + \mathrm{MgSiO_{3(enstatite)}} + 2\mathrm{H_2O} \rightarrow \mathrm{Mg_3Si_2O_5(OH)_{4(chrysotile)}}. \tag{2.24}$$

In cases where the abundance of orthopyroxene exceeds that of olivine, talc is favored instead of brucite, as shown in Figure 2.7d (Model B4). In these models for orthopyroxene-rich systems, the precipitation of talc is allowed. As the abundance of primary orthopyroxene increases, talc will precipitate at the expense of chrysotile. This pattern continues for alteration of rocks composed of increasing abundances of orthopyroxene, and culminates in the results shown in Figure 2.7e for orthopyroxene-only dissolution (Model B5), which results in equal moles of precipitating chrysotile and talc, corresponding to the reaction

$$6\mathrm{MgSiO}_{3(\mathrm{enstatite})} + 3\mathrm{H_2O} \rightarrow \mathrm{Mg_3Si_2O_5(OH)}_{4(\mathrm{chrysotile})} + \mathrm{Mg_3Si_4O_{10}(OH)}_{2(\mathrm{talc})}. \quad (2.25)$$

Note that most of the plots in Figure 2.7 reveal that extensive reaction progress results in constant pH values as $H^+$ is neither consumed and produced, consistent with reactions (2.16), (2.17), (2.24) and (2.25) depending on the rock composition. In the model depicted in Figure 2.7c, pH approaches 8.5 once chrysotile starts to precipitate. In the orthopyroxene-dominated models shown in Figures 2.7d and 2.7e, constant pH is maintained once talc and chrysotile are both precipitating. At these conditions, the $\alpha SiO_{2(aq)}$ will be set by the chrysotile-talc (Ctl-Tlc) equilibria as defined by

$$\mathrm{Mg_3Si_2O_5(OH)}_{4(\mathrm{chrysotile})} + 2\mathrm{SiO}_{2(\mathrm{aq})} \rightarrow \mathrm{Mg_3Si_4O_{10}(OH)}_{2(\mathrm{talc})} + \mathrm{H_2O}\ , \quad (2.26)$$

and is higher than values set by Clt-Brc equilibrium (reaction 2.11), which is revealed by comparing Figures 2.7e and 2.7e with Figures 2.7a and 2.7b.

**Alteration in the presence of clinopyroxene (CaO-MgO-FeO-$SiO_2$-$H_2O$ system)**. As shown in Figures 2.7a to 2.7e, hyperalkaline pH (>11) can not be attained from the dissolution of any combination of olivine and orthopyroxene alone. It is the presence of diopside that drives pH to increase further with reaction progress. The precipitation of dolomite (reaction 2.8) calcite (reaction 2.15) will not be enough to counterbalance the

pH increase driven by the overall reaction among diopside, chrysotile and brucite (reaction 2.18) owing to DIC limitation at late stages of reaction progress. Thus, pH will continue to increase and the fluid will accumulate Ca until it maximizes as the fluid attains equilibrium with diopside. Results from the initial model described above (85% olivine, 14% orthopyroxene, 1% clinopyroxene) are shown again in Figure 2.7f for comparison with the other scenarios that do not involve the dissolution of diopside. It can be seen that including diopside in the model will yield pH values >12, which are higher than those attained in scenarios without it (pH ≤ 10).

The dramatic effect on pH of the single example of a diopside-bearing alteration model in Figure 2.7 raises questions about the consequences for other ultramafic assemblages. Results of simulations depicting effects of modal variations in the $CaO-MgO-FeO-SiO_2-H_2O$ system, summarized in Table 2.2, are shown in Figures 2.8 and 2.9. In both figures, reaction path A (Model A) reflects results discussed above as depicted in Figures 2.3 and 2.7f for 85% Ol-14% Opx-1% Cpx. Simulations that generally encompass variabilities in harzburgite compositions, having five times as much clinopyroxene and variable contributions from olivine and orthopyroxene, are depicted by reaction paths C1, C2, and C3, which refer to 85% Ol-10% Opx-5% Cpx, 75% Ol-20% Opx-5% Cpx, and 65% Ol-30% Opx-5% Cpx scenarios, respectively. As shown in Figure 2.8a trends in total dissolved Ca are similar among the four models tested. Note however that models with 5% clinopyroxene can attain higher Ca concentrations in fluids at pH~9 and can precipitate calcite at lower extents of reaction progress than the model with 1% clinopyroxene (reaction path A).

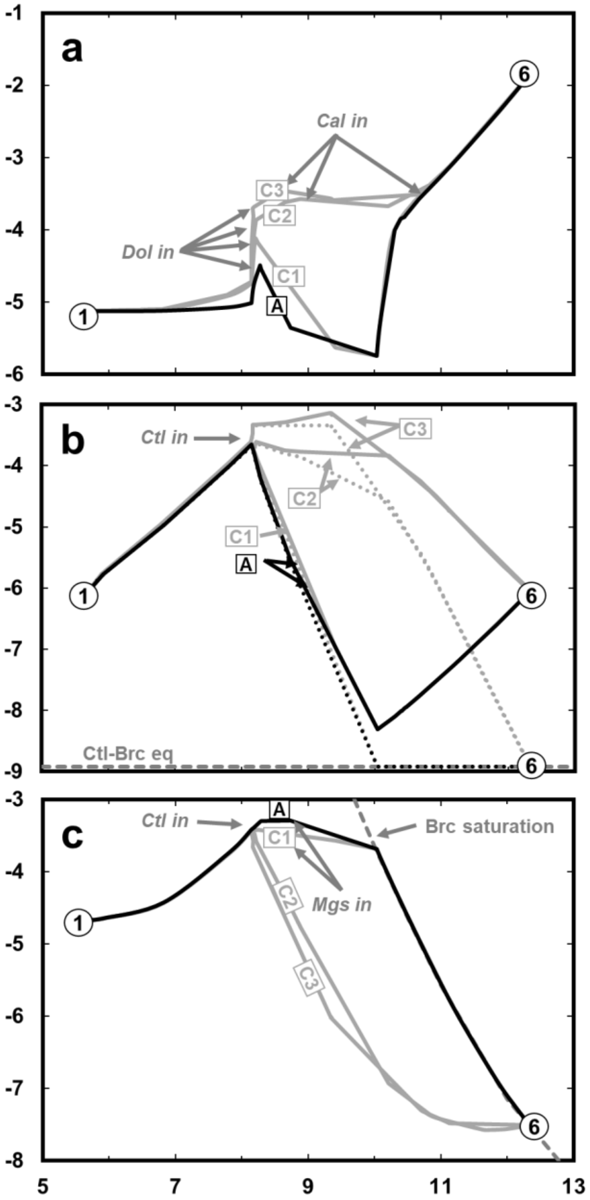

*Figure 2.8*. Trends in (a) $\Sigma$Ca, (b) $\Sigma$Si and $\alpha SiO_{2(aq)}$, and (c) $\Sigma$Mg during reactions with variable harzburgitic compositions in the CaO-MgO-FeO-$SiO_2$-$H_2O$ system at 25°C and 1 bar. Black and grey lines refer to results of simulations using Model A and C rock compositions, respectively. Note that 1 and 6 refer to the beginning and end of the reaction path depicted in Figures 2.2 and 2.3. Letters indicate reaction paths summarized in Table 2.2. Abbreviations of minerals are listed in Table 2.3. The word "in" (for example, Mgs in) refers to the point in the reaction progress where a given mineral starts to precipitate. Note that $SiO_{2(aq)}$ in (b) is one of the various species that compose $\Sigma$Si shown in Figure 2.4c.

Trends in total dissolved Si concentration (solid lines), as well as trends in the $SiO_{2(aq)}$ activity (dotted lines) are shown in Figure 2.8b. Reaction paths A and C1 follow similar patterns, characterized by dramatic decreases in the total Si concentration and $SiO_{2(aq)}$ activity once chrysotile joins the secondary assemblage (see Stage 2 of the overall reaction progress). Likewise, these reaction paths also attain $\alpha SiO_{2(aq)}$ values constrained by Ctl-Brc equilibria starting at pH~10, yet have increasing total Si concentrations until the maximum pH values are attained. In contrast, the models with greater contribution from orthopyroxene (Reaction paths C2 and C3) yield different pathways with no abrupt drop in total Si concentration once chrysotile starts precipitating. The reaction of enstatite into chrysotile involves a release in $SiO_{2(aq)}$ as depicted by the reaction

$$3\mathrm{MgSiO}_{3(\mathrm{enstatite})} + 2\mathrm{H_2O} \rightarrow \mathrm{Mg_3Si_2O_5(OH)}_{4(\mathrm{chrysotile})} + \mathrm{SiO}_{2(\mathrm{aq})}, \qquad (2.27)$$

which is in contrast to alteration of relatively more forsterite-rich systems (reaction paths A and C1) that involve release of $Mg^{+2}$ during chrysotile precipitation (see reaction 2.7). $SiO_{2(aq)}$ released through reaction (2.27) can react with forsterite to form additional chrysotile via

$$3\mathrm{Mg_2SiO}_{4(\mathrm{forsterite})} + \mathrm{SiO}_{2(\mathrm{aq})} + 4\mathrm{H_2O} \rightarrow 2\mathrm{Mg_3Si_2O_5(OH)}_{4(\mathrm{chrysotile})}. \qquad (2.28)$$

Consequently, as forsterite is reacting with excess silica from orthopyroxene to form chrysotile, the precipitation of brucite occurs much further in reaction progress in the orthopyroxene-rich model. These differences are depicted in Figure 2.8c, which illustrates trends in the total dissolved Mg concentration of the four reaction paths. Also depicted in Figure 2.8c is the saturation curve for brucite (dashed grey line), showing that brucite precipitates when the reaction paths intersect the saturation line. Reaction paths

C2 and C3 attain brucite saturation much further along the alteration process than do the other reaction paths. Moreover, and in contrast to reaction paths A and C1, magnesite precipitation does not occur along Reaction paths C2 and C3, due to interactions with rocks that are relatively less Mg-rich and more Si-rich.

These various pathways are depicted on an activity diagram for the CaO-MgO-$SiO_2$-$H_2O$ system in Figure 2.9a. Note that reaction paths C2 and C3 first attain equilibrium with both chrysotile and diopside and only attain brucite saturation at the end of the reaction path at the Ctl-Brc-Di equilibrium point. This is in contrast with models depicting interactions with more Mg-rich or forsterite-rich rocks where chrysotile and brucite equilibrium is attained first before reaching the Ctl-Brc-Di equilibrium point, as shown by reaction paths A and C1. In addition to the four reaction paths shown in Figure 2.8, results of additional calculations modelling orthopyroxene-dominated systems, 45% Ol-50% Opx-5% Cpx (reaction path C4) and 35% Ol-60% Opx-5% Cpx (reaction path C5), are also shown in Figure 2.9a. When contributions from orthopyroxene exceed those of olivine, reaction paths will not attain silica activities lower than that constrained by equilibrium with tremolite. Reaction path C4, which models system with still significant contribution from olivine but not greater than pyroxene minerals, will ultimately end at the chrysotile-tremolite-diopside (Ctl-Tr-Di) invariant point shown in Figure 2.9a. Reaction path C5 exemplifies systems with even greater orthopyroxene contributions and will end at the chrysotile-talc-tremolite (Ctl-Tlc-Tr) equilibrium triple point without proceeding to compositions with lower $\alpha SiO_{2(aq)}$. Equilibria with Ctl-Tr-Di or Ctl-Tlc-Tr results in lower $\alpha Ca^{+2}/(\alpha H^{+})^2$ and higher $\alpha SiO_{2(aq)}$ than those in equilibrium with Ctl-Brc-Di. As a consequence, water-rock interactions hosted in orthopyroxene-dominated lithologies will result in fluids with lower pH and dissolved Ca values but higher Si concentration. Further discussion of the consequences for fluid compositions arising from variabilities in primary minerals follows discussion of model results below that allow iron incorporation into solid solutions of precipitating phases.

**Alteration of serpentinites.** In addition to alteration of fresh ultramafic rocks, groundwater can interact with partially or completely serpentinized rocks. Results of four reaction paths that model alteration of serpentinites (composed mostly of serpentine and brucite) are shown in Figure 2.9b where they can be compared to the alteration of fresh ultramafic rocks discussed above (see Table 2.2). In these calculations, the source for Ca is relict clinopyroxene (5 mole % $Di_{95}$). Reaction path D1 (dashed blue line) shows the changing calculated composition of a fluid interacting with a rock whose secondary assemblage is completely composed of serpentine and relict clinopyroxene, and reaction paths D2 (dashed yellow), D3 (dashed red) and D4 (dashed orange) follow fluid compositions where the aquifer rock is composed of different proportions of serpentine and brucite with 5% clinopyroxene (see Table 2.2). Overall, these reaction paths are similar to others shown in Figures 2.8 to 2.9A, but contributions from the dissolving rock are described by the reverse of reactions (2.6) and (2.10) for chrysotile and brucite dissolution, respectively. Alteration of a serpentinite without relict clinopyroxene leads to results similar to those shown in Figure 2.7c for reaction of 50 mole % olivine and orthopyroxene. After all, a mole of serpentine (chrysotile) is the hydrated equivalent of one mole each of olivine (forsterite) and orthopyroxene (enstatite) as indicated by reaction (2.24).

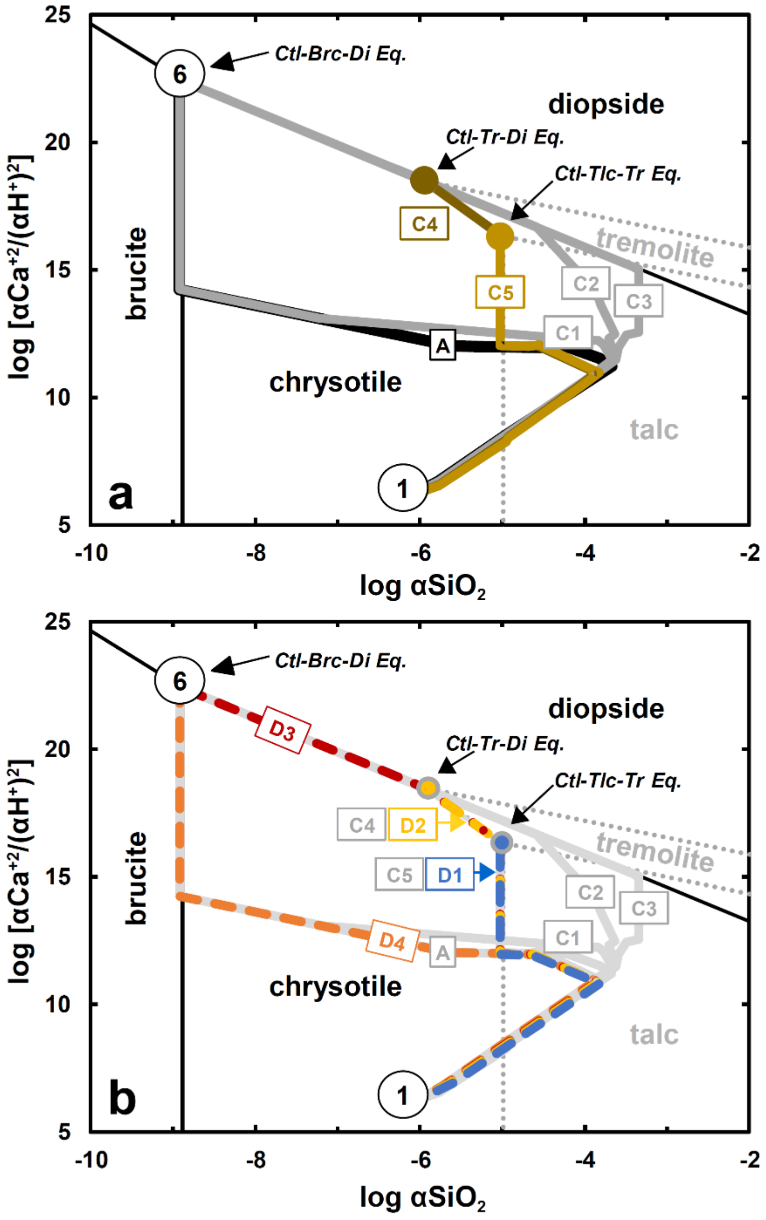

*Figure 2.9*. CaO-MgO-$SiO_2$-$H_2O$ activity diagram for 25°C and 1 bar depicting various reaction pathways summarized in table 2: (A) models A and C1-C5, (B) models D1-D4. Reaction paths A and C1-C5 depict interaction of water with fresh ultramafic rocks with variable primary mineral compositions, while reaction paths D1-D4 depict water interacting with serpentinites of variable compositions (see table 2). Stability fields bounded by dotted lines in grey are for minerals (talc and tremolite) suppressed in some calculations. Note that reaction paths D1-D4 overlap with most of reaction paths A and C1-C5, and that 1 and 6 refer to the beginning and end of the reaction path depicted in figures 2 and 3.

Reaction path D1 generates a fluid with $\alpha SiO_{2(aq)}$ controlled by Ctl-Tlc equilibrium as a fully serpentinized ultramafic rock is too silica-rich to attain the Ctl-Brc equilibria. Additionally, as depicted by the $CaO$-$MgO$-$SiO_2$-$H_2O$ activity diagram shown in Figure 2.9b, path D1 ends up at the Ctl-Tlc-Tr equilibrium triple point similar to that of reaction path C5 described above. Compared with the Ctl-Brc-Di and the Ctl-Tr-Di equilibrium triple points, fluids constrained by Ctl-Tlc-Tr equilibrium have lower $\alpha Ca^{+2}/(\alpha H^{+})^2$ and higher $\alpha SiO_{2(aq)}$. The pH of the fluid controlled by these equilibria can be derived and results of calculations yield pH (~10 at 25°C, 1 bar) lower than that attained by a fluid controlled by the Ctl-Brc-Di (pH ~ 12) or the Ctl-Tr-Di (pH ~ 11) equilibria. If the host serpentinite contains some amount of brucite, fluids can attain equilibrium with the Ctl-Tr-Di or the Ctl-Brc-Di assemblage. Models depicting serpentinites composed of 75 mol% serpentine, 20 mol% brucite, and 5 mol% clinopyroxene, represented by reaction path D2 in Figure 2.9b, ultimately result in fluids in equilibrium with Ctl-Tr-Di similar to systems modelled by reaction path C4. A greater contribution from brucite will result in reaction paths that end up at the Ctl-Brc-Di equilibrium triple point. This is shown by reaction path D3 in Figure 2.9b, which depicts results for a model fluid reacting with host rocks composed of 65 mol% serpentine, 30 mol% brucite, and 5 mol% clinopyroxene. This model follows a path that is similar to that of reaction paths C2 and C3 described above, and would even follow a similar path at earlier stages of the reaction progress if talc precipitation was suppressed. The trace of reaction path D4 in Figure 2.9b depicts interactions with rocks containing even more brucite (40 mol%) and follows a path similar to those from alteration of olivine-rich rocks (reaction paths A and C1). Specifically, if talc is suppressed in a model related to that depicted by reaction path D4, the results will follow a path close to that shown by reaction path C1.

**Further discussion on the consequences of lithological variations.** Many reaction paths for low-temperature alteration of olivine-rich rocks are similar to the overall serpentinization of a rock with the generalized composition shown in Figures 2.2 and 3 and summarized as reaction path A in Figures 2.7, 2.8, and 2.9. Examination of these figures shows that this pathway closely resembles those resulting from simulations of other olivine-rich rocks (reaction path C1) and consequently, despite these lithological variations, a useful starting assumption is that low-temperature alteration of olivine-rich rocks would follow similar stages in the overall reaction progress as that of reaction path A. It is only in models that include greater contributions from orthopyroxene (for example, reaction paths C2 and C3 starting with 25 mol% orthopyroxene) that the overall reaction progress takes a different pathway. Nevertheless, these models still attain equilibrium with chrysotile, brucite, and diopside (Stage 6) but along a different path than that followed by more olivine-rich systems. Specifically, this pathway attains equilibrium with brucite only at the last stage of the overall reaction progress. Results of further simulations involving greater orthopyroxene contributions (>50 mol%) yield pathways resulting in fluids in equilibrium with Ctl-Tr-Di or Ctl-Tlc-Tr.

The system CaO-MgO-$SiO_2$-$H_2O$, as represented by the activity diagrams shown in Figures 2.6b and 2.9, has three equilibrium triple points: (1) Ctl-Brc-Di, (2) Ctl-Tr-Di, and (3) Ctl-Tlc-Tr. It follows that fluid-rock interactions involving ultramafic rocks will ultimately lead to fluids with three distinct composition as dictated by these assemblages, despite variabilities in the compositions of the reacting rocks. Variabilities in the dissolved inorganic carbon levels, however, draw fluids away from these equilibrium triple points to equilibrate with calcite and greatly diversify the compositions of fluids approaching equilibrium with the host aquifer rocks. As shown in Figure 2.6b, greater amounts of DIC, however, would be needed to draw fluids away from being in equilibrium with Ctl-Tr-Di or Ctl-Tlc-Tr than that if the fluid composition is dictated by the Ctl-Brc-Di equilibrium.

Results of calculations involving secondary minerals (serpentine and brucite, with relict clinopyroxene) as the dissolving phases, will yield a range of fluid compositions similar to those generated when primary minerals are dissolving, as depicted in the CaO-MgO-$SiO_2$-$H_2O$ activity diagram shown in Figure 2.9b. *It follows that it would be difficult to distinguish fluids reacting with either fresh or altered ultramafic rocks based solely on their pH, and total Ca, Mg and Si content*. Perhaps this explains why when Chavagnac et al. (2013b) sampled fluids from both the Voltri group of the Ligurian Ophiolite in Italy and the Samail Ophiolite in Oman, where aquifer rocks are variably serpentinized, they found that fluids from both localities have overlapping pH and total Ca, Mg, and Si content. Rather than major solutes, other species should be considered to further evaluate how the degree of alteration of the aquifer host rock affects the resulting fluid chemistry. Serpentine and carbonate minerals can sequester certain trace elements (for example, B, U, Sr, Cl; Kodolanyi et al., 2012) during serpentinization and it follows that remobilization of these elements during further alteration of serpentinites could result in fluids with trace element compositions different from those where the host aquifer rocks are less altered. In addition to trace elements, data on timescales of reactions could be diagnostic as serpentinites would be less reactive than fresh harzburgites. Experiments show that olivine usually dissolves at a much faster rate than various polymorphs of serpentine (for example, see Pokrovsky and Schott (2000) and Oelkers (2001) for olivine, and Bales and Morgan (1985), Thom et al. (2013), and Daval et al., (2013) for serpentine). Attaining hyperalkaline conditions would likely take a greater length of time when serpentinizing serpentinites rather than fresh ultramafic rocks.

### *2.4.6. Effects of Incorporating Mineral Solid Solutions*

In the reaction paths discussed above we allow the dissolving primary minerals to be in solid solutions, but so far have discussed results of models where the precipitation of secondary minerals only as endmember compositions were considered. Studies of natural serpentines, however, show that both serpentine and brucite can incorporate Fe into their structures (O'Hanley and Dyar, 1993; 1998; Evans, 2008; Evans et al., 2012). In brucite the iron is present as $Fe^{+2}$, but in serpentine minerals iron can be both $Fe^{+2}$ and $Fe^{+3}$. Therefore, additional calculations were conducted to compare results incorporating solid solutions in product phases, as shown in Figure 2.10, with results shown in Figure 2.3 where alteration product solid-solutions were not considered. These calculations share features with those of McCollom and Shock (1998), McCollom and Bach (2009) and Klein et al. (2009, 2013) where ideal site mixing was assumed for most solid solutions. The serpentine structure incorporates $Fe^{+3}$ either through ferri-Tschermack's substitution in octahedral and tetrahedral sites (towards the Mg-cronstedtite ($(Mg_2Fe^{+3})(Fe^{+3}Si)O_5(OH)_4$) endmember) or through an octahedral vacancy model (towards the hisingerite ($([]Fe^{+3})_2Si_2O_5(OH)_4$) endmember) as shown by O'Hanley and Dyar (1993, 1998), Evans (2008), Andreani et al. (2013), and Tutolo et al. (2019). To accommodate $Fe^{+3}$ incorporation in both octahedral and tetrahedral sites in serpentine, a four member (chrysotile, greenalite, Mg-cronstedtite, hisingerite) ideal mixing model was used in our calculations.

Trends are plotted against overall reaction progress showing the number of moles of precipitated Mg-, Fe-, and Si-bearing minerals in Figure 2.10a, and concentrations of aqueous $H_2$, and total dissolved Si, Mg, and Fe in Figure 2.10b. Total dissolved Ca, DIC, and other minerals that do not differ meaningfully from results in Figure 2.3 are not included. Earlier stages (1 – 3) of reaction progress are also not shown as the models give nearly identical results.

**Overall mineralogical trends.** If solid solutions are not considered, the only secondary minerals that can host Fe throughout the overall serpentinization progress are goethite and magnetite, as depicted as the solid black curves in Figure 2.10a. If solid solutions are allowed, at later stages of the reaction progress most of the Fe will be incorporated into brucite and serpentine instead of magnetite, as shown by the dashed grey lines in Figure 2.10a. This is consistent with observations showing brucite and serpentine as the major iron-hosting precipitates in low-temperature serpentinites rather than magnetite, which forms more readily during high-temperature (>250°C) serpentinization (Klein et al., 2014). In all other cases iron released during alteration goes into either serpentine or brucite. As they first form, serpentine and brucite are Mg-rich, and increasingly incorporate Fe as reactions progress toward higher rock:water ratios. Despite incorporating some Fe, serpentine remains Mg-rich ($X_{Mg}$ = Mg/(Mg+Fe) = 0.94) at latter stages of reaction progress, and a significant amount of the iron is incorporated into brucite ($X_{Mg}$ = 0.83). These predictions are consistent with observations from serpentine ($X_{Mg}$ = 0.92-0.94) and brucite ($X_{Mg}$ = 0.82-0.84) veins cutting olivine in

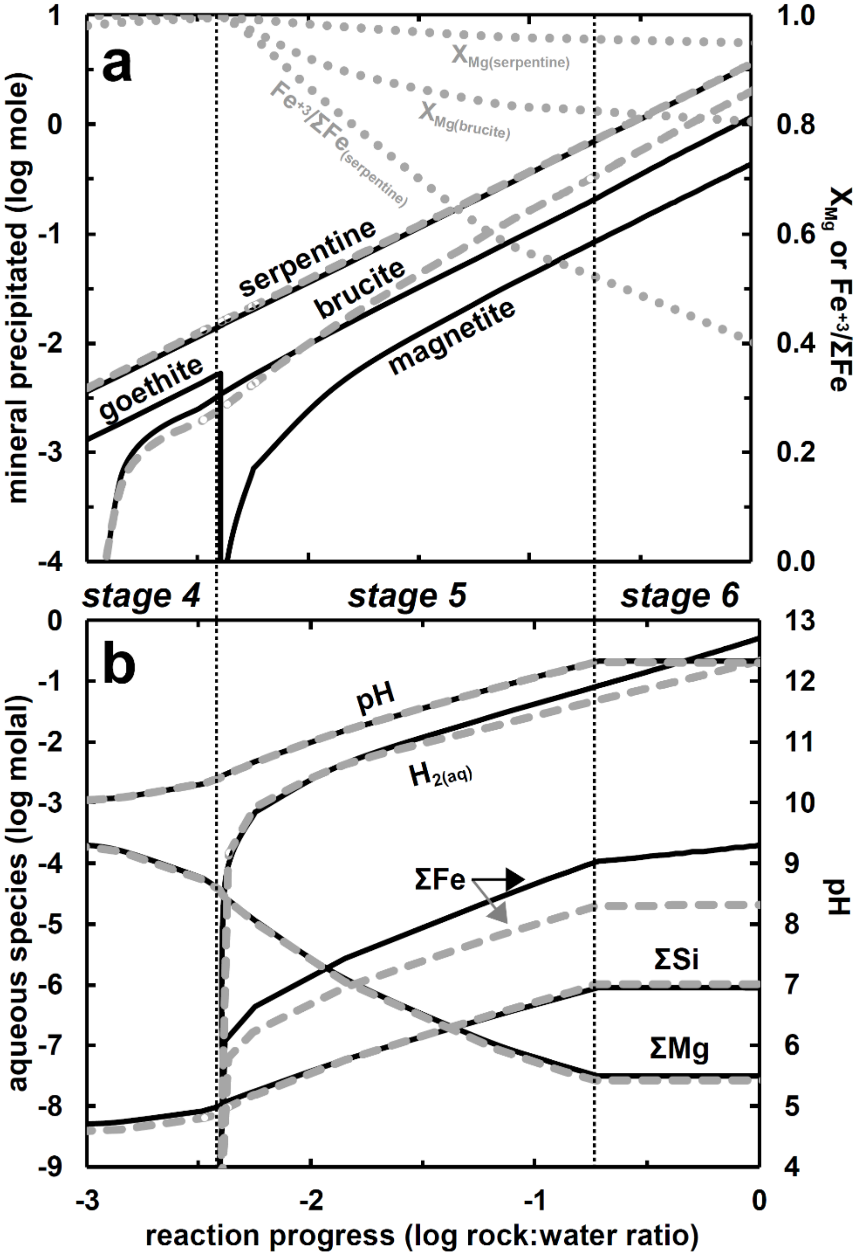

*Figure 2.10*. Reaction path differences at 25°C and 1 bar in models where precipitation of secondary phases in solid solutions were (dashed grey) and were not (solid black) considered. Trends in secondary precipitation (moles precipitated) and aqueous concentration (pH and molal concentration) are depicted in (a) and (b), respectively. Also plotted in (a) as dotted grey lines (values on right y-axis) are the mole fraction of Mg ($X_{Mg}$ = Mg/(Mg + Fe)) in precipitating serpentine and brucite, and the $Fe^{+3}/\Sigma Fe$ of precipitating serpentine in models allowing solid solutions. The vertical black dashed lines indicate the start and end of stages 4-6 of the serpentinization process summarized in figure 2C.

partially serpentinized dunites from New Caledonia (Frost et al., 2013). At low rock:water ratios $Fe^{+3}/\Sigma Fe$ in precipitating serpentine is elevated, and decreases as the system becomes more rock dominated and reduced. This is consistent with low $Fe^{+3}/\Sigma Fe$ (<0.50) of serpentine determined by Mayhew et al. (2018) and Andreani et al. (2013) in the least serpentinized samples, and high values (>0.70) in highly altered samples that formed in fluid-dominated environments. As shown in Figure 2.10a, serpentine with $Fe^{+3}/\Sigma Fe > 0.70$ would only occur in fluid-dominated systems characterized by relatively low rock:water ratios $< 10^{-1.5}$ and relatively oxidized fluids.

The $\alpha SiO_{2(aq)}$ of a fluid in equilibrium with the $Fe^{+2}$ endmembers of serpentine and brucite, as depicted by the reaction

$$3\mathrm{Fe(OH)}_{2(\mathrm{Fe-brucite})} + 2\mathrm{SiO}_{2(\mathrm{aq})} \rightarrow \mathrm{Fe_3Si_2O_5(OH)}_{4(\mathrm{greenalite})} + \mathrm{H_2O}, \quad (2.29)$$

is slightly higher at 25°C and 1 bar ($10^{-7.9}$) than that constrained by the $Mg^{+2}$-end members ($10^{-8.9}$, see reaction 2.11). The incorporation of Fe into both serpentine and brucite shifts the $\alpha SiO_{2(aq)}$ to slightly higher values and the $\alpha Mg^{+2}/(H^{+})^{2}$ to lower values, consistent with the minor differences in pH, and total Mg and Si concentrations between the two models (Figure 2.10b). In contrast, a major difference between the two models is the resulting total dissolved Fe concentration depicted in Figure 2.10b. In the model where Fe incorporation into serpentine and brucite is prohibited, the total dissolved Fe will be controlled by magnetite solubility. If solid solutions are allowed, the resulting total dissolved Fe will be a response to the precipitation of both Fe-bearing serpentine and brucite, yielding lower concentrations of total dissolved Fe.

**Implications for $H_2$ generation.** In addition to differences in dissolved Fe, models that do or do not include serpentine and brucite solid solutions result in differing amounts of $H_2$ generated, which is tied to the amount of ferrous iron from the primary minerals that was oxidized and hosted as ferric iron in the secondary phases (see reaction 2.13). Bach (2016) demonstrated differing trends of $H_2$ generation applied to low-temperature serpentinization of the seafloor depending on the model used. In this work, we discuss implications of using models with and without solid solutions for continental serpentinization. As shown in Figure 2.10b, the model allowing only magnetite formation will generate more than ~2 times as much $H_2$ as the model that allows Fe incorporation into serpentine and brucite. These differences, weighted per kg of reacting rock, are depicted in Figure 2.11 as functions of rock:water ratio. Before Stage 5 of overall reaction progress, neither model produces $H_2$ as $O_2$ from the atmosphere is still present and available to oxidize iron. Once $O_2$ is consumed, $H_2O$ will start to oxidize Fe and will, in turn, be reduced to $H_2$. Allowing the formation of ferric iron-hosting serpentine ($Fe^{+3}/\Sigma Fe < 0.67$ for most of Stages 5 and 6, Figure 2.10a) will generate $H_2$, but not as much as models in which magnetite ($Fe^{+3}/\Sigma Fe = 0.67$) is the only Fe-bearing phase allowed to precipitate. Both models predict similar potentials to generate $H_2$ only over a small interval of reaction progress right after the beginning of stage 5, as shown in Figures 2.10 and 11, when the $Fe^{+3}/\Sigma Fe$ of serpentine remained > 0.67. As shown in Figure 2.11, at rock:water ratio = 1, the amount of $H_2$ generated through serpentine formation (0.18 mole $H_2$ (kg harzburgite)$^{-1}$) is less than half as much as can be generated when magnetite is assumed to be the only Fe-bearing alteration product (0.43 mole $H_2$ (kg harzburgite)$^{-1}$).

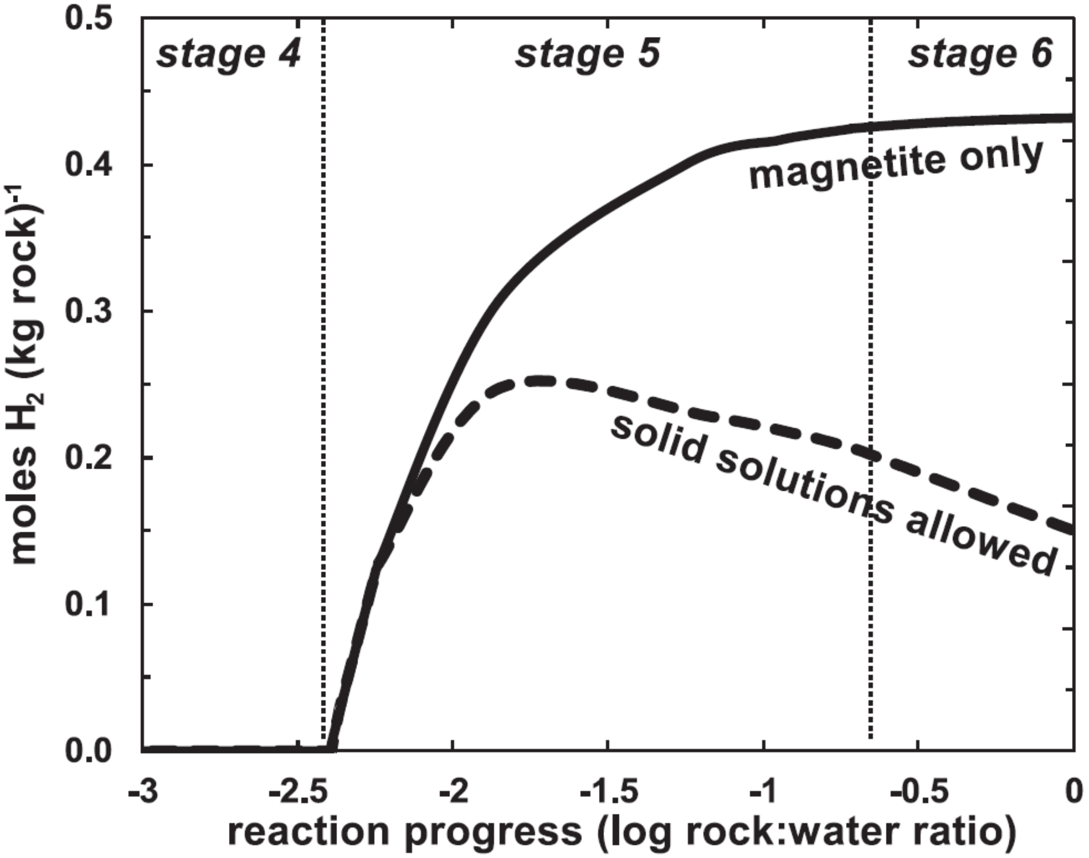

*Figure 2.11*. Predicted amount of $H_2$ generated per kg of rock at rock:water ratios ranging from $10^{-3}$ to $10^{0}$ in models assuming only magnetite as the Fe-hosting phase (solid black) and those where Fe is allowed to be incorporated into serpentine and brucite (dashed black).

It can be anticipated that variations in the composition of the reacting rock will affect the amount of $H_2$ generated. Results as functions of the ratio of primary olivine to orthopyroxene, all with minor clinopyroxene, are depicted in Figure 2.12. The pH, secondary assemblages (dashed grey lines), and $X_{Mg}$ of the secondary phases (dotted grey lines) are shown in Figure 2.12a for a rock:water ratio of 1. As discussed above, alteration of olivine-rich lithologies (left side of Figure 2.12a) results in assemblages comprised of serpentine + brucite and the high pH (>12) of the fluid will be dictated by

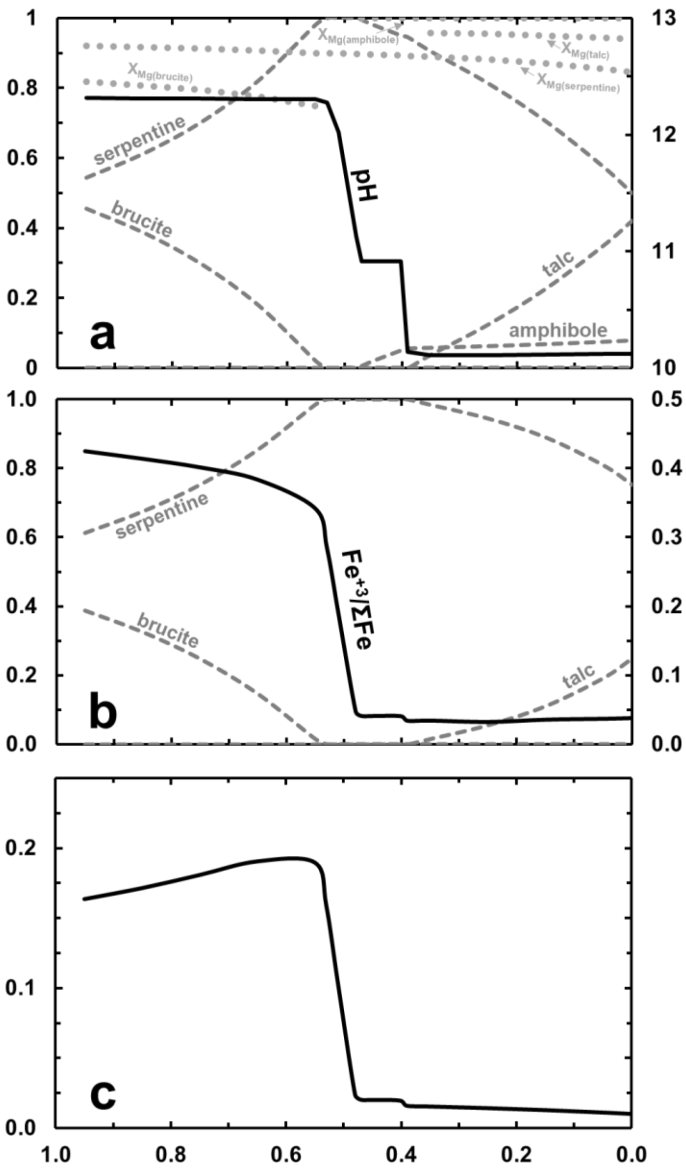

*Figure 2.12*. (a) Trends in secondary assemblages and pH values of fluids resulting from the alteration of ultramafic rocks with variable contributions from olivine and orthopyroxene (clinopyroxene constant at 5 mol% contribution). Dashed grey curves depict the mole fraction of the mineral indicated in the total secondary assemblage. Dotted grey curves show the $X_{Mg}$ of each mineral. (b) shows how iron is hosted in the secondary assemblages. Solid black curve in (b) indicates the $Fe^{+3}/\Sigma Fe$ of the precipitating serpentine. (c) indicates the predicted amount of $H_2$ generated per kg of rock. Values shown in this figure are from results of simulations of alteration of rock with composition depicted by Model A at rock:water = 1, 25°C, and 1 bar.

Ctl-Brc-Di equilibrium. Compositions of fluids shift from that constrained by the Ctl-Brc-Di equilibrium to that of Ctl-Tr-Di (pH ~11) as the primary mineral assemblage being altered shifts to one dominated by orthopyroxene. Alteration of systems containing even more orthopyroxene (right side of Figure 2.12a) yields serpentine + talc assemblages and lower pH (~10) set by the Ctl-Tlc-Tr equilibrium.

How iron is hosted in the secondary assemblage is shown in Figure 2.12b. Most of the iron is incorporated into serpentine despite variabilities in rock compositions. Some amount of iron is hosted in brucite in olivine-dominated systems but shifts to talc as orthopyroxene becomes more dominant. Changes in the $Fe^{+3}/\Sigma Fe$ ratio of the precipitating serpentine are also shown in Figure 2.12b. The ratio remains relatively constant in either olivine- and orthopyroxene-dominated lithologies, but at starkly contrasting values. As shown in Figure 2.12b, a shift to orthopyroxene-dominated lithologies will cause an abrupt drop (~6×) in the $Fe^{+3}/\Sigma Fe$ ratio of the precipitating serpentine. This shift can be represented by the reaction

$$3\mathrm{Fe^{+2}}_2\mathrm{Fe^{+3}}_2\mathrm{SiO_5(OH)}_{4(\mathrm{cronstedtite})} + 5\mathrm{SiO}_{2(\mathrm{aq})} + 3\mathrm{H_2} \rightarrow \qquad (2.30)$$

$$4\mathrm{Fe^{+2}}_3\mathrm{Si_2O_5(OH)}_{4(\mathrm{greenalite})} + \mathrm{H_2O}\,,$$

which favors the more Si-rich ferrous-iron bearing serpentine component (greenalite) relative to the dominant ferric-iron bearing serpentine component (cronstedtite) as the bulk composition shifts toward the more Si-rich orthopyroxene-dominated lithologies. Reaction (2.30) is a simplified illustration compared with our calculations that account for ideal solid solution mixing among end-member components (chrysotile, greenalite, Mg-cronstedtite, and hisingerite) of serpentine.

The distribution of iron into alteration phases causes variations in the amount of $H_2$ generated per kg of reacting rock as shown in Figure 2.12c. As the reacting rocks become less olivine-rich the calculated abundance of $H_2$ increases owing to the increased proportion of iron being incorporated into serpentine, which hosts both ferrous and ferric iron, relative to that going to form brucite, which only hosts ferrous iron. The shift from cronstedtite to greenalite in the alteration assemblage means that the amount of $H_2$ generated during the alteration of orthopyroxene-dominated lithologies is less than that from alteration of olivine-dominated systems. The results summarized in Figure 2.12 have similarities to those of Klein et al. (2013), who showed that the amount of $H_2$ generated through seawater-ultramafic interaction depends on the composition of the reacting rocks. The maximum $H_2$ generated (0.2 moles $H_2$ $kg^{-1}$ rock) shown in Figure 2.12c is two times less than that attained by only allowing iron incorporation into magnetite. Sherwood-Lollar et al. (2014) estimated the global flux of $H_2$ ($0.2\text{-}1.8 \times 10^{11}$ mole $H_2$ $year^{-1}$) from continental serpentinization using reactions to magnetite. If considering Fe incorporation into serpentine and brucite during low-temperature serpentinization, reevaluation of this flux would amount to $0.1\text{-}0.9 \times 10^{11}$ mole $H_2$ $year^{-1}$.

## 2.5. Bioenergetic Landscapes

Results of numerical models by McCollom (2007), Amend et al. (2011), and Nakamura and Takai (2014) show that deep-sea ultramafic-hosted hydrothermal systems can supply more energy to chemolithotrophs than analogous hydrothermal systems generated through basalt-seawater interactions. Moreover, these calculations show that the predominant sources of energy are from reactions that involve $H_2$ and $CH_4$. Similar findings were observed for analogous serpentinization-generated fluids in continental settings (Cardace et al., 2015; Canovas et al., 2017; Crespo-Medina et al., 2017). Though Canovas et al. (2017) inferred the likelihood of several metabolic reactions in the subsurface, available energy supplies for subsurface microorganisms in serpentinizing environments have yet to be quantified. The framework presented above allows us to calculate energy supplies available in the deep subsurface using predicted compositions of fluids close to equilibrium with the host rock, as well as the energy available as these reduced rock-equilibrated fluids mix with oxic groundwater. Details on calculations of instantaneous energetic returns for a metabolic reaction can be found in McCollom and Shock (1997), McCollom (2007), Shock et al. (2010), Amend et al. (2011) and Canovas et al. (2017).

Here, we focus on two microbial metabolisms: hydrogen oxidation, and methanogenesis as described, respectively, by

$$\mathrm{2H_{2(aq)} + O_{2(aq)} \rightarrow 2H_2O}, \tag{2.31}$$

and

$$\mathrm{CO_{2(aq)} + 4H_{2(g)} \rightarrow CH_{4(aq)} + 2H_2O}. \tag{2.32}$$

Methanogens may also use $CO_3^{-2}$ and $HCO_3^-$ as inorganic carbon sources especially at hyperalkaline conditions typical of serpentinizing environments. Methanogenesis from $CO_3^{-2}$ is depicted in reaction (2.14) while that for $HCO_3^-$ can be described by

$$\mathrm{HCO_3{}^- + 4H_{2(aq)} + H^+ \rightarrow CH_{4(aq)} + 3H_2O}. \tag{2.33}$$

As shown in Figure 2.4e, most of the dissolved inorganic carbon in Ca-rich, hyperalkaline fluids generated through serpentinization exist as the neutral complex $CaCO_{3(aq)}$ and would comprise the major dissolved source of inorganic carbon available for methanogens via

$$CaCO_{3(aq)} + 4H_{2(aq)} + 2H^+ \rightarrow Ca^{+2} + CH_{4(aq)} + 3H_2O. \qquad (2.34)$$

We chose hydrogen oxidation and methanogenesis because they are known metabolisms from serpentinizing environments, and because the subsurface concentration of the various aqueous species involved in the reactions can be constrained through mineral-fluid equilibria. Hydrogen oxidizers growing with calcite as their carbon source and belonging to the proposed genera *Serpentinomonas* were isolated by Suzuki et al. (2014) from hyperalkaline springs in the Cedars, Coast Range, California. Experiments using isotopically labeled carbon ($^{13}C$) by Brazelton et al. (2011) and Kohl et al. (2016) at Lost City and the Cedars, respectively, show evidence for microbial methane generation from various inorganic and organic substrates. Lipid biomarker analysis also provides evidence for microbial methanogenesis at Lost City on the mid-Atlantic ridge (Bradley et al., 2009a; 2009b). Further evidence for microbial $H_2$ oxidation and methanogenesis in both submarine and continental serpentinizing sites is provided by metagenomic, 16S rRNA, and 16S rDNA analyses by Schrenk et al. (2004), Brazelton et al. (2006, 2012, 2013, 2017), Blank et al. (2009), Tiago and Veríssimo (2013), Suzuki et al. (2013), Sánchez-Murillo et al. (2014), Quéméneur et al. (2014, 2015), Crespo-Medina et al. (2014; 2017); Postec et al. (2015), Woycheese et al. (2015), Baculi et al. (2015), Miller et al. (2016), Twing et al. (2017), Rempfert et al. (2017), and Fones et al. (2019).

We calculated the energetic returns for microbial $H_2$ oxidation (reaction 2.31) and microbial methanogenesis (reactions 2.14, 2.32, 2.33 and 2.34) in fluids close to equilibrium with ultramafic rocks as constrained through fluid-mineral equilibria calculations discussed above. Dissolved $H_2$ concentrations of deep-seated reduced fluids were assumed to be in equilibrium with one bar of $H_{2(g)}$, which can be considered as a minimum for a deeply serpentinizing aquifer. Discussion of Figure 2.3a above shows that an $H_2$ overpressurized system can occur at advanced stages of reaction progress. Higher dissolved $H_2$ would potentially increase energetic returns for both microbial methanogenesis and $H_2$ oxidation. There will be no energy available from reactions (2.14), (2.32), (2.33) and (2.34) if abiotic $CH_4$ generation is allowed to proceed and equilibrate. However, if abiotic $CH_4$ generation is kinetically inhibited during low-temperature serpentinization, conditions favorable for microbial methanogenesis will develop. As discussed above (see Stage 5), sluggish abiotic methane generation can result in DIC remaining in solution late in the overall serpentinization reaction progress and that DIC will be out of equilibrium with high concentrations of dissolved $H_2$. At the pH dictated by the Ctl-Brc-Di equilibria (pH = 12.3; at 25°C and 1 bar), the calculated DIC concentration is ~8 µmolal if it is in equilibrium with calcite. Assuming minimal background methane (<$10^{-12}$ molal) and $H_2$ concentrations implied above (in equilibrium with 1 bar of $H_{2(g)}$), calculations of energetic returns for microbial methanogenesis with inorganic carbon (reactions 2.14, 2.32, 2.33, and 2.34) will yield ~ 0.2 calories $kg^{-1}$ (0.9 joules $kg^{-1}$) of fluid. An increase in DIC concentration would draw fluids away from being in equilibrium with diopside (Ctl-Brc-Di) to calcite (Ctl-Brc-Cal) and shift the fluid composition to lower pH. The resulting change in the energy available for methanogens as DIC concentrations increase is shown in Figure 2.13. An increase in DIC and a decrease in pH will drive reactions (2.14), (2.32), (2.33), and (2.34) forward, ultimately increasing the energy that can be available for methanogens to exploit. As an example, a fluid in equilibrium with calcite at higher DIC (50 µmole $kg^{-1}$) and lower pH (~10.5) will yield energy amounting to 1.7 calories $kg^{-1}$ (7 joules $kg^{-1}$) of fluid, which is close to 10

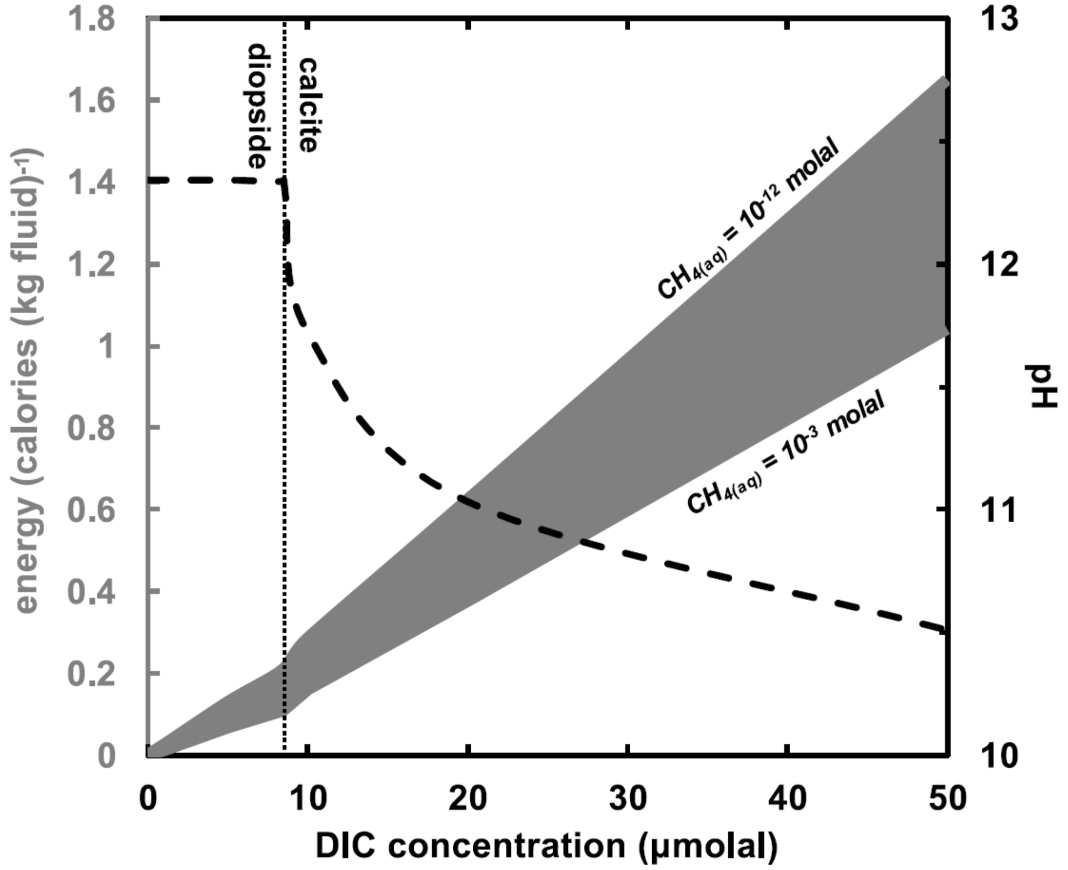

*Figure 2.13*. Predicted energy (calories/kg fluid) available for hydrogenotrophic methanogenesis in deep-seated fluids close to equilibrium with the rocks at 25°C and 1 bar. Fluid compositions were derived from Figure 2.6b, which shows that deep-seated fluids are likely close to Ctl-Brc-Di (pH ~12 at 25°C). At higher DIC concentrations, fluid can saturate with calcite and pH will be dictated by the Ctl-Brc-Cal equilibrium with higher DIC concentrations resulting in lower pH (dashed line). The solid grey area indicates ranges in the energy yield assuming variable background methane concentrations ranging from $10^{-12}$ to $10^{-3}$ molal.

times higher than that calculated above for a fluid in equilibrium with diopside. Calculations at higher background methane ($10^{-3}$ mole kg$^{-1}$) yield less energy as there is a lower drive for reactions (2.14), (2.32), (2.33), and (2.34) to proceed. However, despite the 9 orders of magnitude change in abundance of dissolved $CH_4$ this will reduce the energy yield at most by half. We allow up to 50 μmolal of DIC despite predicted DIC concentrations of deep-seated hyperalkaline of < 20 μmolal (Figure 2.6a) to accommodate minor input from infiltrating atmosphere-derived volatiles during fluid discharge. Another process that can bring additional inorganic carbon sources to deep-seated fluids is mixing with DIC-rich shallow groundwater. Consequences of mixing are discussed below.

There is no energy available for $H_2$ oxidation at deep subsurface environments owing to the predicted absence of $O_{2(aq)}$ at advanced stages of serpentinization. However, hydrogen oxidizing bacteria in the genus *Hydrogenophaga* were detected from high pH subsurface fluids in Oman (Miller et al., 2016; Rempfert et al., 2017) implying that $O_2$ could have been available in the subsurface through atmospheric infiltration or mixing with oxic groundwater. Subsurface methanogens were also detected in the same studies. We demonstrate above that energy can be available for microbial methanogenesis, but not for $H_2$ oxidation, for a deep-seated fluid without atmospheric and shallow groundwater input. Delivery of additional DIC through atmospheric and shallow groundwater mixing, however, can potentially increase energetic returns. These processes may occur in discharge zones where surfacing deep-seated hyperalkaline fluids can encounter shallow groundwater.

In our mixing calculations we used predicted compositions of deep-seated rock-equilibrated fluids and oxic shallow groundwaters in equilibrium with the atmosphere and altered rocks (serpentinites, carbonates) common in the shallow subsurface, and chose 25°C and 1 bar for both types of fluid. For the shallow groundwater, we set the pH = 8 based on measurements from well samples (7 < pH < 9, Paukert et al., 2012; 2019;

Rempfert et al., 2017). This choice of pH is also supported by mineral saturation calculations by Paukert et al. (2012) on groundwater fluids from the Oman Ophiolite showing that equilibrium with serpentine, magnesite, and calcite at pH = 8 will yield a Mg-$HCO_3$ type fluid close in composition to that observed in the field. For the deep-seated, rock-equilibrated fluid we used four different compositions to represent end-member possibilities, all at 25 °C and 1 bar including a fluid in equilibrium with Ctl-Brc-Di plus calcite, and fluids in equilibrium with Ctl-Brc-Cal at DIC concentrations of 10, 20, and 50 µmolal. We assumed minimal background methane ($10^{-12}$ molal) to quantify maximum energy yields for methanogenesis. Further compositional details of end-member fluids used in our mixing calculations can be found in Table A1 (Appendix A). The calculated energies available for hydrogen oxidation and methanogenesis during the subsurface mixing process are shown in Figure 2.14. Trends in pH during the mixing process are shown in Figure 2.14a. Note that the deep-seated fluid in equilibrium with diopside (pH = 12.3) and that in equilibrium with calcite at 10 µmolal DIC (pH = 11.7) are strong bases. As a consequence, it would take more than 80% or 50% mixing with shallow groundwater, respectively, for the pH of the mixed fluid to be <11. Energetic returns for hydrogen oxidation and methanogenesis are shown in Figure 2.14b. The curve for methanogenesis (thick grey curve in Figure 2.14b) represents mixing trends for the four deep-seated endmember fluids. These fluids have different starting pH and DIC concentrations contributing to differences in energetic yields (see Figure 2.13). The thickness of the curve represents this variation. In contrast, the energy yield for $H_2$ oxidation does not vary among these four endmember fluids resulting in the thin curve shown. As discussed above, energy is available for methanogens even without mixing with shallow groundwater. Fluids that started with more DIC, such as those in equilibrium with calcite, yield more energy throughout the mixing process than those starting with less DIC in equilibrium with diopside. The difference, however, becomes less apparent (thinner grey curve) as the mixed fluid is increasingly dominated by shallow groundwater. Maximum energy availabilities for methanogenesis (6 calories kg$^{-1}$ or 25 joules kg$^{-1}$ of fluid) are attained at mixing extents of < 30% and the amounts of energy available decrease with increasing progress of mixing. In contrast, no energy is available for $H_2$ oxidation before mixing occurs, but becomes available at the first instance of mixing. Compared to methanogenesis, energetic returns for $H_2$ oxidation maximize at greater extents of mixing (~60%) yielding energy of 17 calories kg$^{-1}$ (72 joules kg$^{-1}$) of fluid. Changes in the direction of the energetic trends for both methanogenesis and hydrogen oxidation indicate a transition depending on which of the reactants is limiting (DIC or $H_2$ for methanogenesis, $O_2$ or $H_2$ for hydrogen oxidation). Trends shown in Figure 2.14b hint that methanogens could be favored in fluids characterized by no to low extents of mixing, while $H_2$ oxidizers would prefer systems characterized by higher extents of mixing.

Energetic returns inferred for the continental serpentinizing subsurface are far less than what has been calculated for analogous mixing process accompanying fluid venting in deep sea hydrothermal environments. As an example, McCollom (2007) calculated maximums of ~100 and ~900 calories kg$^{-1}$ for methanogenesis and hydrogen oxidation, respectively, during vent fluid-seawater mixing. Nevertheless, despite being limited, available subsurface energy that can be exploited by microorganisms permits the possibility of deep communities in serpentinizing aquifers. Moreover, the above calculations also highlight discharge zones of fluid pathways as hotspots where subsurface life may bloom as reduced deep-seated fluids encounter oxidized shallow-aquifer fluids.

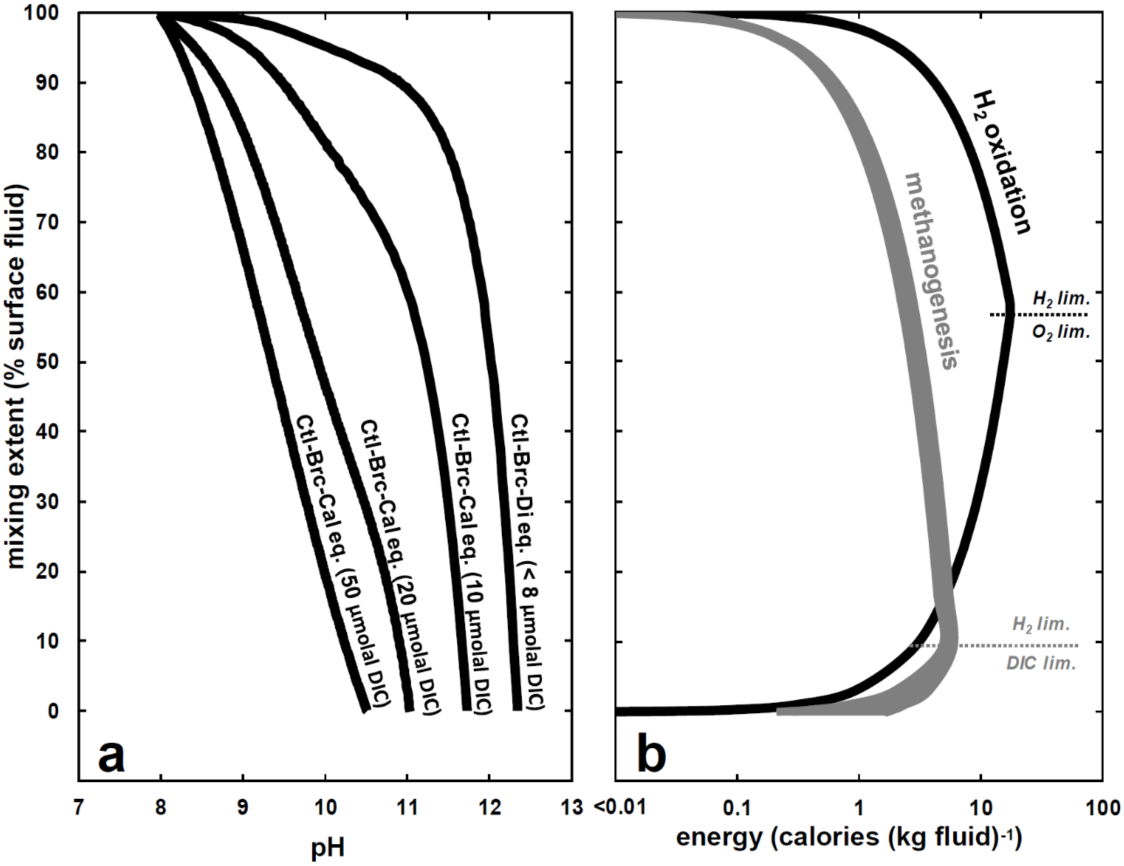

*Figure 2.14*. (a) pH and (b) energy yields for $H_2$ oxidation and methanogenesis during mixing between fluids that equilibrated with deep-seated rocks (Ctl-Brc-Di and Ctl-Brc-Cal, bottom of (b)) and those that equilibrated with the highly altered shallow aquifer host rocks (top of (b)) at 25°C and 1 bar. The four curves in (a) depict trends for pH during mixing for four deep-seated end-member fluids with variable starting DIC following Figure 2.6b: fluid in equilibrium with Ctl-Brc-Di and fluids in equilibrium with Ctl-Brc-Cal at DIC concentrations of 10, 20, and 50 µmolal. These four starting end-member fluids result in little differences in energy yield for methanogenesis as the mixing process progresses and are therefore depicted as one thick grey curve in (b). The thickness of the curve represents variations in energy bounded by that yielded by a fluid in equilibrium with Ctl-Brc-Di as the minimum and a fluid in equilibrium with Ctl-Brc-Cal at DIC concentrations of 50 µmolal as the maximum. Trends for $H_2$ oxidation are similar for these different starting fluids and are shown as one black curve in (b). Thin dashed lines in (b) indicate transition points for the limiting reactant.

Communities observed in serpentinizing systems are not limited to $H_2$ oxidation and methanogenesis (Schrenk et al., 2013; Canovas et al., 2017). A more comprehensive theoretical evaluation of subsurface energy available for various metabolic process is possible once concentrations of relevant aqueous and gaseous species are constrained. In addition, constraints on organic compounds, such as formate and acetate, can provide insights into the likelihood of deep subsurface methanogens using substrates other than inorganic carbon. As shown in Figure 2.13, simulations starting with various background concentrations of dissolved $CH_4$ do not dramatically change the calculated energy yields for methanogenesis. These yields would, however, influence the energy available for aerobic and anaerobic methanotrophs. Constraints on deep subsurface $CH_4$ concentrations will help assess the likelihood of subsurface methanotrophy, as well as refine the energetic returns for methanogens calculated above. Calculations of fluid-mineral equilibria constraining the dissolved sulfide and sulfate concentrations of deep-seated fluids will help quantify energy available for various sulfur-based metabolic processes. Similarly, constraints on dissolved nitrogen species such as ammonia, nitrite and nitrate will allow predictions of energy available for nitrogen-based metabolic reactions. We have inferred the dissolved ferrous iron concentrations of the deep subsurface through fluid-mineral equilibria with magnetite and iron-bearing brucite and serpentine, which can be used to assess energy available for iron oxidizers once more is known about iron oxidizing metabolisms in hyperalkaline systems. Constraints on the available ferric-iron hosting phases (magnetite, $Fe^{+3}$-bearing serpentine) can also help in quantifying energy available for iron reducing microbes.

## 2.6. Conclusions

Our goals in conducting this evaluation of environments generated by low-temperature serpentinization of ultramafic rocks in continental settings are to explore various reactions that drive the serpentinization process and their consequences for the concentrations of various aqueous species. By accounting for variable temperatures, salinities, host-rock compositions, and degree of alteration (fresh ultramafic rock *vs* serpentinites) we demonstrate that equilibrium thermodynamic calculations account for the highly alkaline fluids recorded in serpentinizing environments. In light of the sluggish approach to equilibrium at low temperatures, these calculations provide robust tools for exploring the consequence of mass-transfer processes at ambient conditions. An example is the apparent mismatch between measured pH values of serpentinized fluids and calculations that assume equilibrium with idealized mineral assemblages. As described above, pH and composition will shift as a fluid moves from being in equilibrium with diopside to being in equilibrium with calcite as it encounters more DIC through transport processes like fluid mixing and atmospheric input. We have shown that these processes can account for most pH values measured in hyperalkaline fluids in Oman. Nevertheless, variabilities in the chemistry of serpentinization-generated fluids can also be consequences of reactive-transport processes where reactions are kinetically controlled (Tutolo et al., 2018). Calling upon kinetic constraints is warranted after exhausting equilibrium arguments.

Our calculations also extend the findings of previous work by Klein et al. (2009; 2013; 2014) who showed that Fe is favorably incorporated into serpentine and brucite, instead of magnetite, during low-temperature serpentinization. When Fe transport occurs without oxidation there is a diminished potential for $H_2$ generation. Results of our work show that the modern $H_2$ flux could be two times lower ($0.1\text{-}0.9 \times 10^{11}$ mole $H_2$ year$^{-1}$) than recent estimates (Sherwood-Lollar et al., 2014) that assume iron oxidation to magnetite. Thermodynamic properties of Mg-cronstedtite and hisingerite components of serpentine were estimated and incorporated in our model to account for observations in serpentinites (O'Hanley and Dyar, 1993; 1998; Tutolo et al., 2019). Refinement of the thermodynamic properties of Fe end-members and solid solution models of serpentinization-relevant secondary phases such as serpentine and brucite can help improve our models, especially for calculations on the amount of $H_2$ generated during low-temperature serpentinization. In addition, by evaluating energy supplies we show how potentials for microbial methanogenesis and hydrogen oxidation can be predicted in the deep serpentinizing subsurface. Energy is available for methanogens in the deep subsurface so long as DIC can be provided through calcite dissolution. Mixing of reduced, deep-seated, rock-equilibrated hyperalkaline fluids with shallow groundwater permits hydrogen oxidation, and can provide additional sources of energy that can be exploited by microbes. Further constraints on the chemistry of subsurface fluids, which will soon be available through the Oman Drilling Project will allow a comprehensive evaluation on the habitability of the deep serpentinizing subsurface. Finally, the predictions set forth in this study provide a rigorous framework for testing ideas that can explain the compositions and microbial communities of fluids sampled at the surface in hyperalkaline spring and seeps.

## 2.7. Acknowledgements

Thanks to Alta Howells, Kirt Robinson, Peter Canovas, Tucker Ely, Grayson Boyer, Vincent Milesi, and Alysia Cox for many helpful discussions over the course of this study. We would like to thank Benjamin Tutolo and an anonymous reviewer for helpful and insightful reviews. Our work has also benefitted from ideas and data shared by Peter Kelemen, Isabelle Daniel, Muriel Andreani, Juerg Matter, and the NASA Astrobiology Institute Rock Powered Life team. We recognize support from NSF grant EAR 1515513, and the NASA Astrobiology Institute Rock-Powered Life project.

# CHAPTER 3

# THERMODYNAMIC PREDICTIONS VS ENVIRONMENTAL OBSERVATIONS OF SERPENTINIZATION-GENERATED FLUIDS: LESSONS FROM THE SAMAIL OPHIOLITE IN OMAN

This chapter is close to submission to a journal and is based on a recent draft primarily made by the author with contributions from Alta H. Howells, Kirtland J. Robinson, Alysia Cox, Randall Vincent Debes II, Kristopher Fecteau, Panjai Prapaipong, and Everett L. Shock.

## 3.1. Introduction

When surface water meets ultramafic rocks, reactions occur that ultimately generate some of the most alkaline and reduced fluids on Earth. This process, known as *serpentinization*, involves the hydrous mineral serpentine mainly replacing the anhydrous minerals olivine and pyroxene that originally composed ultramafic rocks. During serpentinization, fluids become $H_2$-rich through the coupled oxidation of ferrous iron to ferric iron in minerals and reduction of water to hydrogen. Ultimately, the enormous redox disequilibria generated when these reduced fluids mix with oxic surface fluids provide energy to drive many metabolic reactions (McCollom, 2007; Amend et al., 2011; Schrenk et al., 2013; Canovas et al., 2017) and the synthesis of organic compounds (Shock and Canovas, 2010; Lang et al., 2010). Geochemical energy supplies for microbial life make serpentinizing systems attractive model ecosystems for assessing the link between the geosphere and the biosphere, including those occurring in the Earth's subsurface ( Schrenk et al., 2013; Klein et al., 2015; Rempfert et al., 2017; Fones et al., 2019) and possibly, in other rocky bodies in our solar system (Schulte et al., 2006; Vance et al., 2007; Holms et al., 2015; Glein et al., 2015). The alkaline and reduced environments resulting from serpentinization are also proposed to have facilitated the emergence of life on Earth (Sleep et al., 2004; 2011; Holm et al., 2006; Martin and Russel, 2007; Martin et al., 2008).

Submarine vents releasing >100°C fluids to the ocean such as those in the Lost City (~120°C, Seyfried et al., 2015) and Rainbow vent fields (~360°C, Charlou et al., 2002) are famous examples of serpentinizing environments, known for their towering chimneys and vigorous vents surrounded by diverse deep-sea biological communities. Less conspicuous, but likely far more widespread, are fluids seeping diffusively from ultramafic rocks at temperatures <100°C, such as those found near spreading ridges (Früh-Green et al., 2018), serpentine mud volcanoes near subduction zones (Mottl et al., 2003, 2004; Wheat et al., 2008; 2020; Mottl, 2009), and ultramafic bodies in continents. In continents, serpentinization-generated fluids are documented in ophiolites, ultramafic massifs, metamorphic belts, and kimberlite fields in ~20 countries by >100 studies (for a list of these studies, see Etiope and Whiticar (2019) and Leong and Shock (2020)). The common occurrence of serpentinized fluids in almost all continental settings where ultramafic rocks and water can interact illustrates that serpentinization can actively proceed even at ambient conditions (25°C, 1 bar).

Mass-transfer calculations based on thermodynamic equilibrium provide insights into reactions that can drive the transformation of surface fluids such as rain and seawater into reduced, high-pH fluids. When applied, past studies (Pfeifer, 1977; Bruni et al., 2002; Palandri and Reed, 2004; Cipolli et al., 2004; Sader et al., 2007; Boschetti and Toscani, 2008; Marques et al., 2008; Okland et al., 2012; Paukert et al., 2012) show that mass-transfer calculations can account for the overall compositional trends of ultramafic-hosted fluids even at low-temperature conditions. However, at low temperatures where equilibrium is slow to be reached, deviations from predictions can occur. Fluid compositions that deviate from equilibrium expectations have not been a focus of previous theoretical studies but can inform us of the various fluid transport processes that may be important in assessing the habitability of the serpentinizing subsurface. Serpentinization is not unique to Earth and can occur in other rocky bodies in the solar system such as Mars (Schulte et al., 2006; Ehlmann et al., 2010) and ice-covered ocean worlds in the outer solar system like Europa and Enceladus (Vance et al., 2007; Glein et al., 2015; Waite et al., 2017). With limited existing data and in preparation for future sampling, expectations on the compositional variabilities of fluids and microbial communities possible in these less accessible environments can be informed by thermodynamic simulations. It is thus imperative that we test thermodynamic simulations in accessible and analogous low-temperature serpentinizing systems here on Earth to assess their utility in predicting consequences of serpentinization in other planetary bodies. In this study, we test predictions on fluid compositions by recent calculations described in Chapter 2 of this work (Leong and Shock, 2020) with fluids sampled from the Samail ophiolite in the Sultanate of Oman.

The Samail ophiolite hosts some of the largest and best preserved continental exposures of ultramafic rocks (Nicolas et al., 2000) as well as several low-temperature (< 40°C), hyperalkaline fluids that were documented by numerous studies in the past (Barnes et al., 1978; Neal and Stanger, 1983; 1984; 1985; Bath et al., 1987; Taylor et al., 1991; Sano et al., 1993; Dewandel et al., 2005; Matter et al., 2006; Paukert et al., 2012;

2019; Chavagnac et al., 2013a; 2013b; Boulart et al., 2013; Ollson et al., 2014; Miller et al., 2016; Rempfert et al., 2017; Canovas et al., 2017; Vacquand et al., 2018; Zgonnik et al., 2019; Fones et al., 2019; Giampouras et al., 2020; Boyd et al., 2020). To test thermodynamic predictions, we sampled and analyzed 140 compositionally diverse fluids from 17 locations in the ophiolite with pH values ranging from near-neutral to hyperalkaline.

We investigated reactions that account for fluids with end-member compositions: (1) near-neutral and (2) hyperalkaline pH. The former have pH values ranging from 7 to 9, are enriched in $Mg^{+2}$ and $HCO_3^-$, and typically occur in shallow aquifers and surface streams. In contrast, the latter are highly alkaline (pH >11) and enriched in $Ca^{+2}$, $OH^-$ and gases such as $H_2$ and/or $CH_4$. Hyperalkaline fluids occur mainly in deeper aquifers (>500 m) and manifest at the surface when deep-seated fluids discharge as springs (Dewandel et al., 2005). We also examined fluids with intermediate pH (9 to 11), which have been less of a focus in previous studies, to assess if they are consequences of the serpentinization pathway where meteoric water is transformed into hyperalkaline fluids, or if they result from mixing between the end-member fluids. A field-based method to identify these fluid types is also proposed that can help inform decisions involving exploration, sampling, and experiments while in the field. Ultimately, through the aid of predictions, we can quantify the contributions of various stages of serpentinization to observed fluid compositions. Eventually, these calculations, tested with analogous processes here on Earth, can provide constraints for the exploration of low-temperature serpentinizing environments such as those construed for the deep and early Earth, as well as in other rocky bodies in our Solar System.

## 3.2. Methods

### *3.2.1. Computational Model*

Thermodynamic reaction-path calculations simulate reactions of minerals with a fluid and determine the compositions of coexisting solid phases and fluid constituents attained at equilibrium at various extents of the overall reaction progress. Details on the model setup are described in Leong and Shock (2020) and are summarized in Appendix B. In addition to reaction-path calculations, dissolved concentrations of solutes as constrained by mineral solubilities were also predicted, as described in detail in Appendix B.

### *3.2.2. Field and Analytical Methods*

**Field Sites.** A total of 140 fluid samples were taken from nine surface (springs) and eight subsurface (wells) sites in the Samail ophiolite in 2009, 2010, 2012, and 2014. Locations of these sampling sites in the Samail ophiolite are shown in Figure 3.1. All sites are hosted in ultramafic rocks except for WDA-16 and Masibt which are located within a gabbroic body. The occurrence of hyperalkaline fluids at most sites can be associated with geologic structures (basal thrust and lithological boundaries) that can promote flow of deep-seated fluids to the surface through fractures. Three sites (Al Hilayw, Falaij, and Al Bana) are in outcrops close to the base of the ophiolite (basal thrust) corresponding to where the ophiolite is thrust over the Arabian Peninsula. The other sites are located within the ophiolite and many are hosted in ultramafic rocks near the ultramafic-gabbro transition. The 16 sites are distributed across several of the massifs that comprise the Samail ophiolite. Sites at Dima, Qafifah, and Falaij, together with the wells NSHQ-04 and NSHQ-14, are in the Wadi Tayin Massif. Masibt and wells SJA-03,

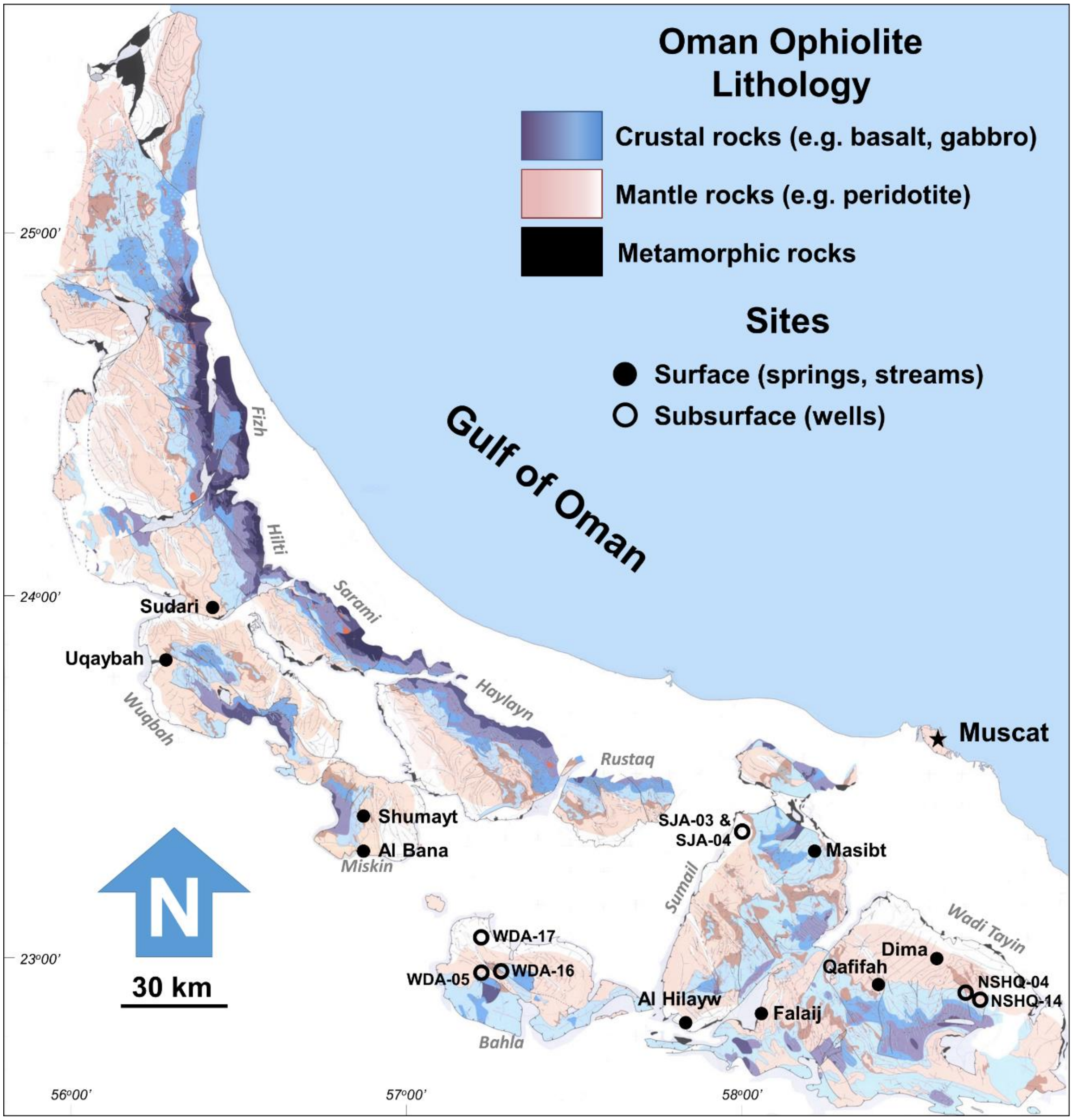

*Figure 3.1*. Locations of sample sites overlain on a lithological map of the Oman ophiolite modified from Nicolas et al. (2001). Filled black circles represent sites where fluids were sampled from the surface (springs, streams) while open circles represent sites where fluids were sampled from wells. Names of the various massifs that comprise the ophiolite are indicated in grey.

SJA-04A, and SJA-04B are in the northern part of the Samail Massif, while Al Hilayw is further south in the same massif. All of the above locations are in the southern portion of the Samail ophiolite, while wells WDA-05, WDA-16, and WDA-17 (Bahla Massif), sites

Shumayt and Al Bana (Miskin Massif), Uqaybah (Wuqbah Massif), and Sudari (Hilti Massif) are in the central part of the Samail ophiolite. Hyperalkaline springs in Masibt, Dima, Qafifah, Uqaybah, Sudari, and Shumayt are seeping at or close to stream beds (Figure 3.2), while those located near the basal thrust seep from the flanks of ultramafic outcrops with no apparent associated surface stream flows in the vicinity. Where possible, at each surface site and well, three fluid types were sampled: (1) circumneutral to slightly alkaline fluids (pH 7-9), (2) hyperalkaline fluids (pH >11), and (3) fluids with intermediate pH (pH 9-11).

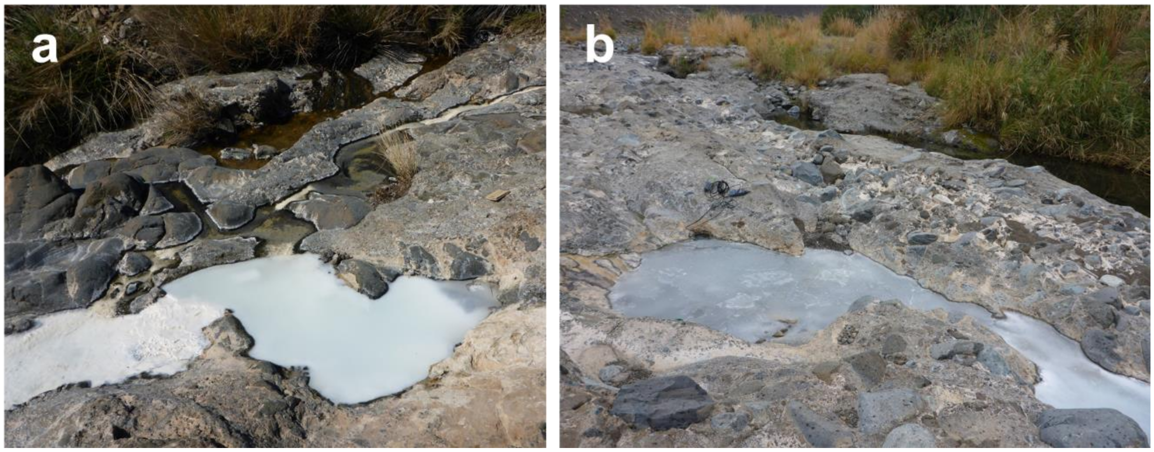

*Figure 3.2*. Hyperalkaline pools covered in white calcite films flowing into surface streams at (a) Qafifah and (b) Dima.

**Field and Analytical Methods.** Portable electrodes and meters were used for *in situ* measurements of pH, temperature, and conductivity. pH electrodes (WTW$^{TM}$ SenTix$^{TM}$ gel electrode) attached to meters (WTW$^{TM}$ 3300*i* and 3110) were calibrated daily using 7.0, 10.01 and 12.46 pH buffers. Temperature and conductivity were measured using a YSI 30 handheld meter. Measurements of redox-sensitive species (dissolved ferrous iron, $O_2$, and sulfide) were performed on-site using field spectrophotometers (Hach$^{®}$ 2400 and 2800). Dissolved ferrous iron concentrations were measured in filtered water samples using the 1,10 phenanthroline method. Dissolved $O_2$ or DO values were determined using Hach® AcuVac Ampuls® with the indigo carmine method while dissolved sulfide values were measured using the methylene blue method. Samples were filtered in the field (Pall Acrodisc® 32 mm PF syringe filter with 1.2 and 0.8/0.2 μm Supor® membrane) and stored in containers for further laboratory analyses.

For samples taken in 2014, concentrations of major anions ($F^-$, $Cl^-$, $SO_4^{-2}$, $NO_3^-$, $NO_2^-$) and major cations ($Li^+$, $Na^+$, $K^+$, $Ca^{+2}$, $Mg^{+2}$, $NH_4^+$) were determined on separate Dionex DX-600 ion chromatography (IC) systems using suppressed conductivity detection and operated by Chromeleon software (version 6.8). The anion system employed a potassium hydroxide eluent generator, a carbonate removal device, and AS11-HC/AG11-HC columns. Samples for cations were acidified with 6 N MSA in the field to approximately 19 mM final concentration to suppress carbonate precipitation and ammonia degassing. The cation system was equipped with CS-16 and CG-16 columns and cations were eluted isocratically with 19 mM methanesulfonic acid (MSA) at 0.5 mL/minute. Both systems were plumbed with an external source of deionized water for suppressor regeneration to improve the signal-to-noise ratio of the analyses. Further details on the above method can be found in Fecteau (2016) and Robinson (2018). For 2012 samples, anions and cations was measured using similar methods described in Lindsay et al. (2018). For fluids sampled in 2009 and 2010, anion and cation concentrations were determined using methods described in Canovas et al. (2017). On average, analytical precision for cation and anion analysis was better than 2% and 5% relative standard deviation (RSD), respectively.

An inductively coupled plasma-mass spectrometer (ICP-MS, Thermo Finnigan Element 2™ High Resolution ICP-MS) was used to determine dissolved Al concentrations and for samples taken in 2014, dissolved Si values, both at precision mostly within 5% RSD. For samples taken in 2009, 2010, and 2012, dissolved Ca values were determined using both the IC and the ICP-MS (precision mostly within 5% RSD). Generally, both instruments yield similar values (see Figure B1a) except for a few samples where the IC returns lower concentrations than the ICP-MS. These discrepancies are mostly attributed to fluids sampled during the 2009, 2010, and 2012 fieldwork where cation samples were not acidified. Hence, Ca values for all fluids sampled before 2014 are reported using the ICP-MS results. For fluids sampled in 2009, 2010, and 2012, dissolved Si and Mg concentrations were measured using an inductively coupled plasma-optical emission spectrometer (ICP-OES, Thermo iCAP™ 6300). Analytical precision for analysis of Si and Mg was better than 3% and 1% RSD at 1σ, respectively. The Mg concentrations of a subset of samples from 2012 and 2014 were determined using both the IC and the ICP-OES. Both instruments yield consistent results (see Figure B1b). Reported Mg values for the 2014 samples came from the IC while the rest came from the ICP-OES. For both the ICP-MS and ICP-OES, samples were acidified to pH <2 with trace metal grade $HNO_3$ in the field. Samples were measured either undiluted or diluted with the ICP-MS and ICP-OES. For calibration, a multi-element standard (HPS 68 component standard) was used for the ICP-MS while single element standards for Mg and Si was used for the ICP-OES.

Measurements of dissolved inorganic carbon (DIC) concentrations were performed using a wet oxidation total carbon analyzer (OI Analytical 1010 TOC

Analyzer). Samples were stored in VWR CS24 amber glass vials with butyl rubber septa, which has low permeability to gases. The sample was heated followed by acidification with $H_3PO_4$ o drive off the DIC as $CO_2$ to the analyzer. Further details of the method can be found in Gilles St-Jean (2003) and Robinson (2018). Stable isotope ($\delta^2$H and $\delta^{18}$O) values were determined using an Off Axis - Integrated Cavity Output Spectrometer (OA-ICOS, LGR DLT-100) using methods similar to that reported in Meyer-Dombard et al. (2015). Accounting for instrument drift and normalization from the Vienna Standard Mean Ocean Water (VSMOW) was done following van Geldern and Barth (2012). Precision was usually within ±0.5‰ and ±0.1‰ for $\delta^2$H and $\delta^{18}$O, respectively. Water isotope analysis was conducted at the Sabo Laboratory at ASU School of Life Sciences. IC and ICP-MS analyses were conducted at the ASU GEOPIG Laboratory while ICP-OES and total carbon analyses where performed at Metals, Environmental and Terrestrial Analytical Laboratory (METAL) at ASU (formerly, ASU Goldwater Environmental Laboratory and ASU W. M. Keck Foundation Laboratory for Environmental Biogeochemistry). Results of field and laboratory measurements are compiled in Table 3.1.

Results from instrumental analysis were further processed to calculate charge balance, ionic strength, mineral saturation indices, and aqueous speciation with the EQ3/6 program using the thermodynamic dataset described in Appendix B. Charge balance and ionic strength of fluids are documented in Table 3.1, while saturation indices for some minerals are reported in Table B1 (Appendix B). Results of calculations of aqueous speciation are depicted in Figure B2 (Appendix B). Analytical results for circumneutral to slightly alkaline fluids are mostly within 5% of electroneutrality. Results for a few pH

<11 well samples have high positive charge imbalance due to unmeasured DIC or, if measured, have unusually low values for this pH range. Unexpectedly low DIC values could be attributed to carbonate precipitation during well sampling or sample storage. Analytical results for hyperalkaline fluids are mostly within 5% of electroneutrality, with some near 20%. At extremes in pH, poor charge balance can be attributed to small uncertainties in pH measurements as $OH^-$ and $H^+$ are major components of basic and acidic solutions, respectively (*e.g.*, see Nordstrom et al., 2009 for charge imbalance in acidic examples). Shifting field-measured pH values by about 0.1 to 0.2 units, which is within the range of observed fluctuations in the field, results in close to complete charge balance.

Analytical data, except for isotopic and dissolved Mg and Si values, of most of samples from 2010 were previously reported in the work of Canovas et al. (2017) that focus on quantifying energy supplies available to chemotrophic microorganisms in serpentinizing fluids. Some fluids from the 2009, 2010, and 2012 fieldwork were also concomitantly sampled by collaborators (Paukert et al., 2012; 2019). DIC and dissolved Al values determined above are reported in Paukert et al. (2012; 2019) while concentrations of all other solutes were determined independently. This work expands analytical data previously reported by the above studies by supplying additional data from 80 fluid samples.

## 3.3. Results

### *3.3.1. Model Results*

Model results are described in Chapter 3 of this work (Leong and Shock, 2020) and a worked example is provided in Appendix B and illustrated in Figure B3.

Specifically, reaction paths depicting various stages of the serpentinization process – primary mineral dissolution (Stage 1), incipient serpentinization (Stage 2), mineral carbonation (Stage 3), brucite formation (Stage 4), $H_2$ formation (Stage 5), and equilibrium with diopside (Stage 6) – are summarized in Appendix B.

### *3.3.2. Analytical Results*

Results of field and laboratory analyses are summarized in Figure 3.3 where samples are classified based on their pH: circumneutral (pH 7 – 9), intermediate (pH 9 – 11), and hyperalkaline (pH >11). Fluids sampled from wells are indicated by the solid black squares regardless of their pH. Samples from Masibt, WDA-16, as well as fluids from previous studies associated with gabbroic rocks, were not included in Figure 3.3 as simulations on gabbro-water interactions were not conducted in this study. Data from gabbro-hosted fluids are plotted in Figures B4 and B5 and preliminary discussions on their similarities and differences with ultramafic-hosted fluids can be found in Appendix B.

Ultramafic-hosted fluids sampled during this study have pH values ranging from 7.2 to 11.9 and conductivities from 450 to 4050 μS/cm. Circumneutral to slightly alkaline fluids are enriched in dissolved $O_2$ and DIC (Figures 3.3a and 3.3b). The DO concentration measured from surface and mixed fluids is constrained by the solubility of atmospheric $O_{2(g)}$, which at ambient conditions (25°C) is close to 275 µmolal (dashed grey line in Figure 3.3a). On the other hand, dissolved $O_2$ concentrations of hyperalkaline fluids vary from low concentrations (~10 µmolal) to values close to those measured from circumneutral fluids. This suggests that some of the deep-seated hyperalkaline fluids interact with the atmosphere either during ascent or upon sampling. Hyperalkaline fluids are generally more conductive (Figure 3.3c) due to elevated total concentrations of Na, Cl, K, and Ca (Figures 3.3d – 3.3g). Aside from these species, $OH^-$ also contributes to the high conductivities measured in basic solutions. On the other hand, these high-pH fluids are strongly depleted in total dissolved Mg (Figure 3.3h) and Si (Figure 3.3i) by approximately 2-3 orders of magnitude relative to circumneutral fluids. Speciation of dissolved solutes are depicted in Figure B2. As shown in Figure B2a, the most common solutes in circumneutral fluids are $Mg^{+2}$ and $HCO_3^-$. Hyperalkaline fluids are mostly composed of $Na^+$ and $Cl^-$, followed by $OH^-$ and $Ca^{+2}$. As depicted in Figure B2b, most of the dissolved Si in circumneutral fluids exist as $SiO_{2(aq)}$ while the anion $HSiO_3^-$ tends to dominate in hyperalkaline solutions followed by the neutral complex, $NaHSiO_{3(aq)}$. The dominant Mg and Ca species at all pH range of investigated fluids are $Mg^{+2}$ (Figure B2c) and $Ca^{+2}$ (Figure B2d), respectively. Following $Mg^{+2}$, the $MgOH^+$ complex can comprise a third of the total dissolved Mg in hyperalkaline solutions. The dominant DIC component in circumneutral solutions is $HCO_3^-$ while both $CO_3^{-2}$ and the neutral complex $CaCO_{3(aq)}$ are predominant in hyperalkaline fluids (Figure B2e).

Hyperalkaline fluids sampled from sites close the basal thrust of the ophiolite (Falaij, Al Banah, Al Hilayw) have higher concentrations, by at most a factor of two, of total dissolved Na, K, and Cl than fluids sampled from other sites. We offer possible origins for these elevated concentrations in the discussion below. On the other hand, pH and total dissolved Mg, Si, Ca, and inorganic carbon are similar among samples retrieved from all ultramafic-hosted sites despite their variable geological settings (basal thrust, near or far from the ultramafic-gabbro contact). This suggests similar underlying reactions that constrain these concentrations. We expound further on these reactions in the following section.

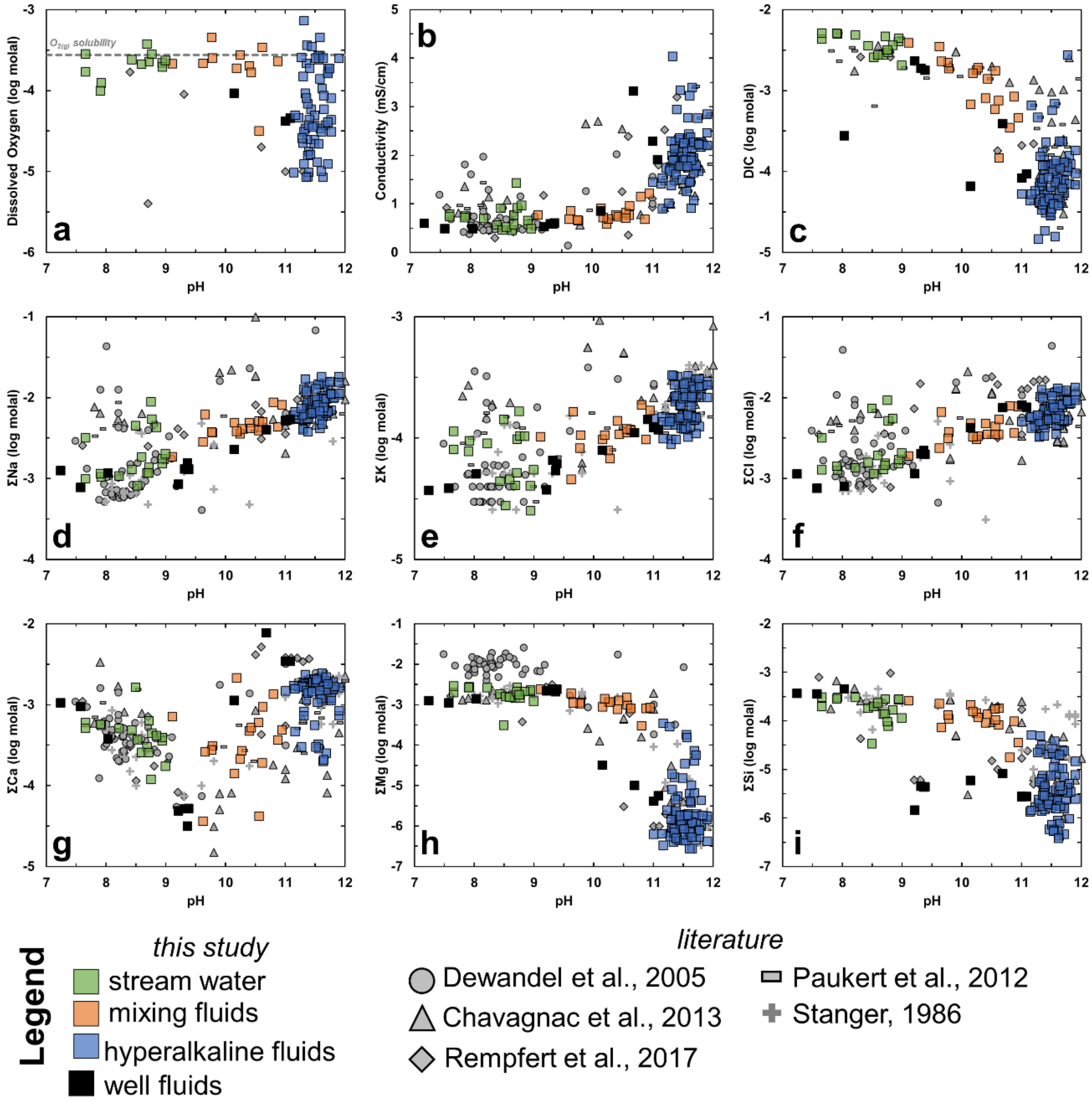

*Figure 3.3*. Measured dissolved $O_2$ (a) and conductivity (b), as well as concentrations of total dissolved inorganic carbon or DIC (c), Na (d), K (e), Cl (f), Ca (g), Mg (h), and Si (i) plotted against pH. Green and blue squares indicate stream and hyperalkaline spring fluids, respectively. Orange squares indicate where fluids resulting from significant mixing between these end-member fluids was physically observed. Black squares show fluids sampled from wells regardless of their pH. Various symbols in grey are values reported in the literature. Dashed grey line in (a) depicts the solubility of $O_2$ at current atmospheric compositions.

Stable isotopic data, $\delta^{18}O$ vs $\delta^{2}H$, of $H_2O$ for fluids sampled in this study are shown in Figure 3.4, together with relevant local meteoric water lines determined by Weyhenmeyer et al. (2002) for moisture sources coming from the north (Mediterranean, LMWL-N) and the south (Indian Ocean, LMWL-S). Note that fluids hosted in the Samail ophiolite plot between the two meteoric water lines. The Mediterranean Sea is the dominant source of precipitation in modern Oman while the southern moisture source is much rarer and comprised of cyclones and depressions generated in the Indian Ocean that only occasionally reach the northern parts of Oman where the ophiolite is located (Weyhenmeyer et al., 2002). However, Paukert et al. (2019) showed that fluids sampled from the Samail ophiolite are too enriched in $^{18}O$ and/or depleted in $^{2}H$ relative to calculated Raleigh distillation curves that model evaporation from the northern Mediterranean source. Our dataset extends that shown by Paukert et al. (2019) and further supports conclusions by previous investigators that fluids hosted in the Samail ophiolite are likely recharged by a combination of northern and southern sources (Weyhenmeyer et al., 2002; Matter et al., 2006; Paukert et al., 2019). Through noble gas geothermometry, Paukert et al. (2019) also showed that some hyperalkaline fluids in Oman were derived from fluids recharged at low temperatures during the last glacial age where the dominant moisture source was likely coming from the south.

Isotopic data from circumneutral to slightly alkaline fluids and hyperalkaline fluids overlap, though some of the latter samples are more depleted in $^{18}O$ and $^{2}H$. In addition, the $^{18}O$ and $^{2}H$ compositions of hyperalkaline fluids seem to exhibit geographical trends, that is, fluids from the Miskin Massif (Shumayt and Al Banah) located in the central part of the Samail ophiolite are more depleted in both $^{2}H$ and $^{18}O$

relative to those sampled at the Bahla (Wells WDA-05, 16 and 17) and Wadi Tayin (Falaij, Dima, and Qafifah) Massifs, which is further south. Fluids from the northern massifs Wuqbah (Uqaybah) and Hilti (Sudari) and fluids sampled from the northern portions of the Samail Massif (Masibt, Al Khoud, and wells SJA-03 and 04) are depleted in $^{2}$H relative to the other samples. Fluids sampled from Al Hilayw, located in the southern portion of the Samail Massif, have isotopic values that plot closely with those from a nearby site from the Wadi Tayin Massif (Falaij). Future isotopic and hydrologic investigations can further inform us on the processes behind these geographic distinctions.

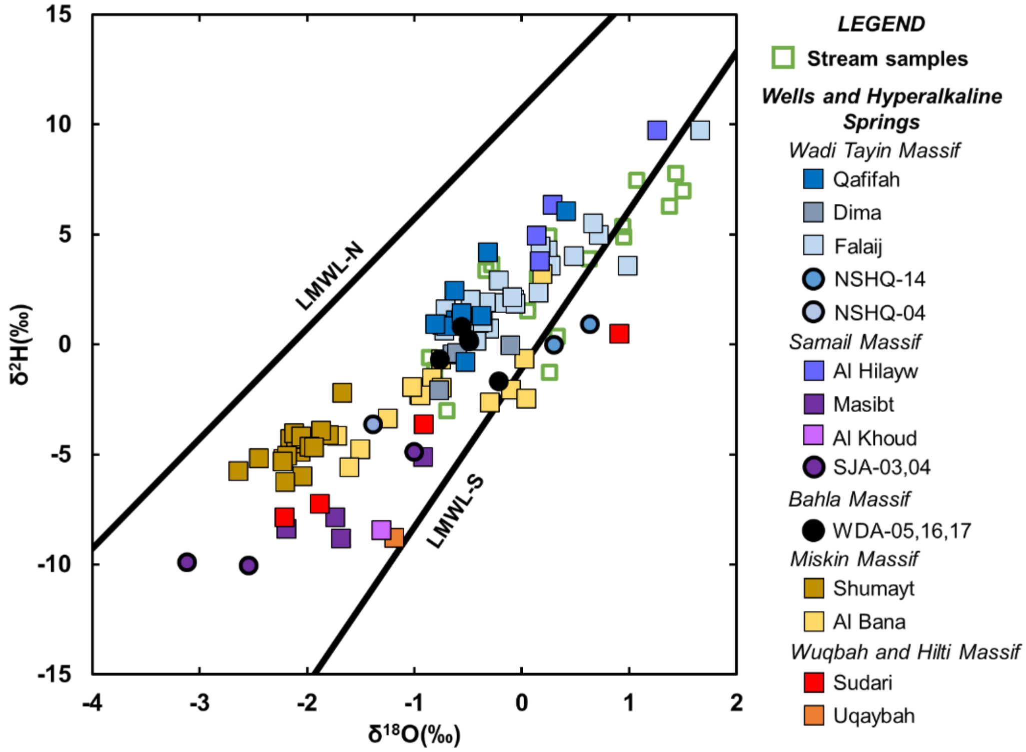

*Figure 3.4*. $\delta^{18}$O vs $\delta^{2}$H crossplot. Filled circles and squares represent well fluids and hyperalkaline spring fluids, respectively. Colors indicate sample sites of hyperalkaline and well sites (sites in legend are arranged from southeast to northwest in location). Samples in open green squares represents stream samples regardless of location. Local meteoric water lines are plotted based on the southern (LMWL-S) and northern (LMWL-N) moisture sources for Oman (Weyhenmeyer et al., 2002).

## 3.4. Reconciling Predictions with Reality

In the following section, compositions measured from environmental samples are compared with those predicted from equilibrium calculations as discussed above. Deviations from predictions may occur and are likely to be consequences of slower approaches to equilibrium due to kinetic inhibition at low temperatures. Furthermore, several transport processes such as leaching from minerals, the input of infiltrating atmospheric $CO_{2(g)}$, and shallow groundwater mixing with surfacing deep-seated fluids can shift compositions away from those predicted by equilibrium models. We simulate these transport processes, investigate their effect on fluid compositions, and test if these processes can account for natural observations that deviate from equilibrium predictions. We first discuss trends involving pH and dissolved Si, Mg, Ca, and inorganic carbon and then proceed to discuss those for dissolved Na and Cl.

### *3.4.1. pH and Dissolved Si, Mg, Ca, and Inorganic Carbon*

Thermodynamic simulations, depicted in Figure B3, predict trends in the dissolved concentrations of Si, Mg, Ca, and inorganic carbon as an outcome in the progress of the subsurface serpentinization reactions. Comparison of predictions with analytical measurements for Si, Mg, Ca, and DIC are shown in pH *vs.* concentration plots in Figures 3.5a – 3.5d and on activity diagrams representing the $MgO-SiO_2-H_2O$ (Figure 3.5e) and $MgO-CaO-SiO_2-H_2O$ (Figure 3.5f) systems. Overall, compositions of fluids measured from environmental samples are generally inconsistent with model results, as most fluid samples do not coincide with predicted reaction paths (solid dark blue curves in Figure 3.5). Trends from natural samples show that fluids evolve from relatively dilute rainwater into fluids more concentrated in Si, Mg, and DIC (mainly speciated as $HCO_3^-$) at pH 7 to 9. Compositions of fluids then evolve into hyperalkaline fluids (pH >11) with low concentrations of Si (Figure 3.5a) and Mg (Figure 3.5b). At these highly basic pH values, sampled fluids have high Ca (Figure 3.5c) and low DIC (Figure 3.5d) concentrations. The reaction paths generally follow similar trajectories but at different solute concentrations than those measured from the natural samples. A few natural samples are consistent with equilibrium predictions. As an example, measured compositions of hyperalkaline fluids seem to be bounded by equilibrium constraints as shown by the end of reaction paths depicted in Figure 3.5. Specifically, the most depleted Si (Figure 3.5a) and Mg (Figure 3.5b) values measured from end-member hyperalkaline fluids in Oman seem to be constrained by equilibrium fluid-mineral reactions (end of the dark blue curves in Figures 3.5a and 3.5b), as we will discuss below. Except for these few cases, most natural samples cannot be accounted for by equilibrium calculations alone. Hence, we discuss fluid mixing (dashed yellow lines) as a process to account for variations in samples. Compositions of end-member fluids used in our mixing calculations can be found in Table B2 and details of the calculations are expounded below. In addition, we also discuss dissolution of other minerals (*e.g.*, brucite, carbonates) aside from those modeled above (olivine and pyroxene) that can account for some compositional trends observed in natural samples. In the following discussions we first examine pH 7 to 9 fluids enriched in Mg and DIC (green squares) and then proceed to discuss fluids with hyperalkaline (pH >11, blue squares) and intermediate (pH 9 to 11, orange squares) pH. Ultimately, these discussions lead to a classification scheme for these fluid types guided by a combination of constraints from fluid-mineral equilibria and relevant transport processes.

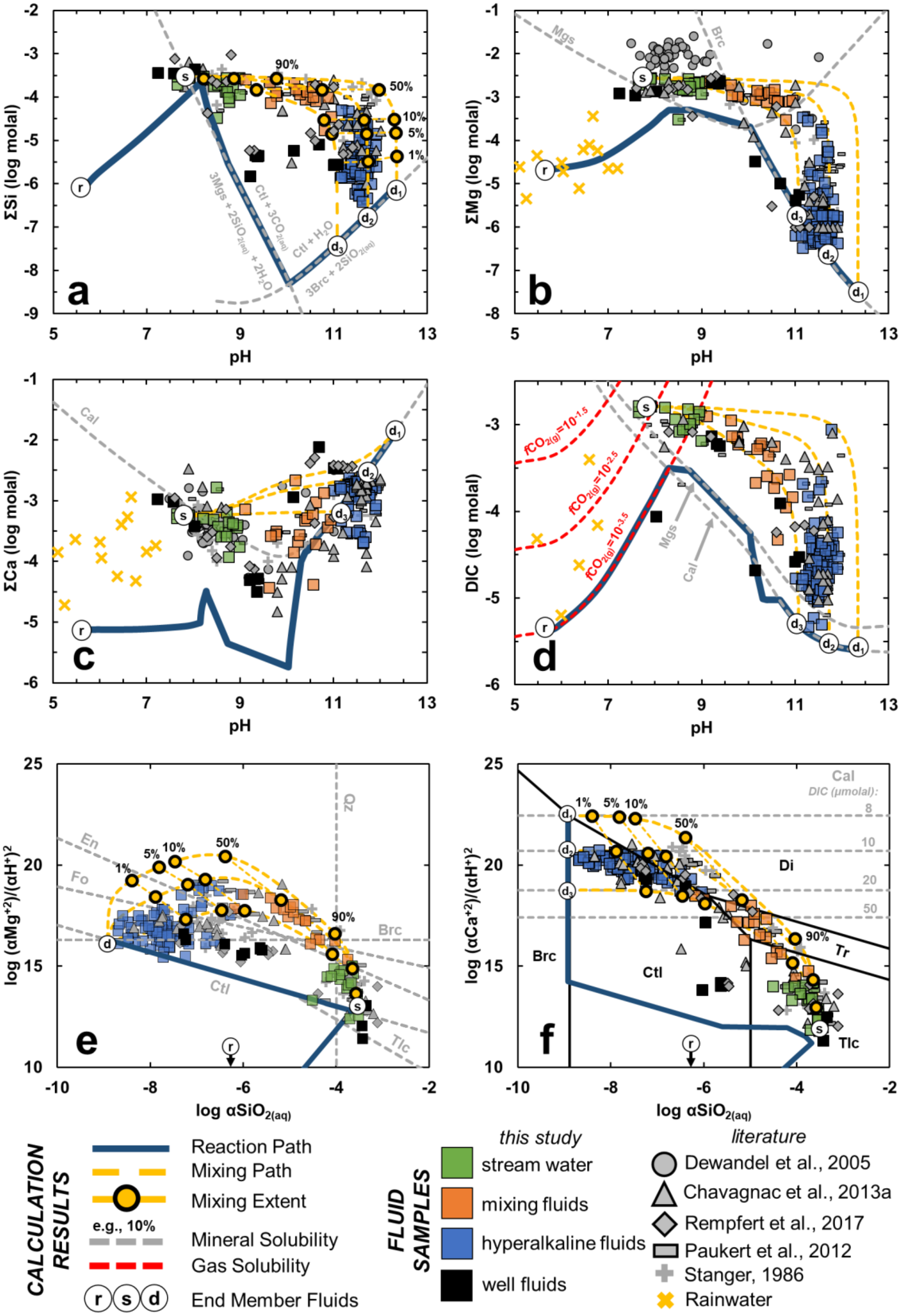

*Figure 3.5*. Comparison of results from reaction path and mineral solubility calculations with total dissolved concentrations of Si (a), Mg (b), Ca (c), and inorganic carbon or DIC (d) of samples as well as calculated activities from environmental measurements plotted in activity diagrams for the $MgO$-$SiO_2$-$H_2O$ (e) and $CaO$-$MgO$-$SiO_2$-$H_2O$ (f) systems at ambient conditions (25°C, 1 bar). Symbols for environmental samples are similar to those in Figure 3, with the addition of rainwater data from Oman and surrounding areas (yellow cross symbols, Ahmed et al., 2000; Matter et al., 2006). Solid dark blue curves represent reaction paths. Dashed grey lines in (a) to (f) show calculated saturation conditions for indicated minerals or mineral assemblages while the solid black lines in (f) depict phase boundaries between minerals. Dashed red lines in (d) depict calculated DIC at indicated $CO_{2(g)}$ fugacity values. Dashed grey line lines in (f) represent calcite saturation at indicated DIC concentrations. Circles with text represent fluids used in the calculations: rainwater (r), representative surface circumneutral fluid (s), representative deep-seated fluids in equilibrium with Ctl-Brc-Di ($d_1$), Ctl-Brc-Cal at 10 μmolal DIC ($d_2$), and 20 μmolal DIC ($d_3$). The latter four compositions (s, $d_1$, $d_2$, and $d_3$) were used as end-member fluids in mixing calculations. Dashed yellow lines represent three mixing paths between these end-member fluids (s and three deep endmembers: $d_1$, $d_2$, and $d_3$) while filled yellow circles along these mixing lines in (a), (e), and (f) represent various mixing extents in %. Upper, middle, and lower dashed yellow curves in (e) indicate mixing between fluid s and fluids $d_1$, $d_2$, and $d_3$, respectively. All three calculated deep-seated fluids ($d_1$, $d_2$, and $d_3$) are coincident in the $MgO$-$SiO_2$-$H_2O$ activity diagram and are hence just labelled as d in (e). Acronyms for minerals are based on the recommendations of Whitney and Evans (2010): Fo- forsterite, En- enstatite, Ctl- chrysotile, Brc- brucite, Tlc- talc, Qz- quartz, Di- diopside, Cal- calcite.

**pH 7-9, $Mg^{+2}$-$HCO_3^-$ Type 1 Fluids.** Fluids of this type, referred to as Type 1, mainly occur in streams (green squares in Figure 3.5) and shallow groundwater (some black squares in Figure 3.5). These fluids are characterized by neutral to slightly alkaline pH (pH 7-9) and elevated concentrations of DIC, Mg, and Si relative to rainwater and hyperalkaline fluids. As shown in Figure B2a, these the most common solutes in these fluids are $Mg^{+2}$ and $HCO_3^-$, and hence are also referred as $Mg^{+2}$-$HCO_3^-$ type fluid. In the model, Type 1 compositions are attained at early stages of the overall reaction progress where solutes accumulate in the fluid through initial dissolution of primary minerals but before Si, Mg, and DIC are consumed to form serpentine, carbonates, and brucite. Concentrations of Si in these fluids are consistent with the maximum Si concentrations

(Figure 3.5a) and $a\mathrm{SiO_2}$ (Figure 3.5e) predicted by the reaction path calculations (black solid curves) when fluids attain equilibrium with serpentine during the start of Stage 2 (see Figure B3d) of the overall reaction progress. As depicted in Figure 3.5e, environmental samples rarely plot below the chrysotile saturation line, implying constraints on the Si concentrations of ultramafic-hosted fluids by serpentine precipitation. Most of the samples, however, are oversaturated with respect to chrysotile (see Table B1), which implies a kinetic inhibition to serpentine precipitation. Furthermore, most circumneutral to slightly alkaline fluids plot above quartz and talc saturation (see Figure 3.5e), which suggests kinetic inhibition may apply to most silicates.

While there is close agreement between the equilibrium predictions and the measured Si of Type 1fluids, the agreement does not hold true for Mg, Ca and DIC. The modeled concentrations, while showing an increase in these constituents (solid dark blue curves in Figures 3.5b to 3.5d), do not increase enough to meet measured concentrations of Mg, Ca and DIC. Cipolli et al. (2004) showed that these elevated concentrations can be attained during reactions at higher $f\mathrm{CO_2}$, up to two orders of magnitude higher ($f\mathrm{CO_2}$ up to $10^{-1.5}$) than that imposed by the present atmosphere. Results constrained by elevated $f\mathrm{CO_{2(g)}}$ levels are indicated by the reaction paths depicted in Figure 3.5d as dashed red curves that depicts more dissolved $\mathrm{CO_2}$ at higher $f\mathrm{CO_{2(g)}}$ values at a given pH. Alternatively, instead of being the result of elevated $f\mathrm{CO_{2(g)}}$, high concentrations of Ca, Mg, and DIC observed in natural samples in this pH range can also be attained through interactions with minerals that are abundant in serpentinites or highly altered ultramafic rocks that comprise the shallow aquifer. As shown by the dashed grey curves in Figures

3.5b and 3.5d, respectively, the lower bounds in the Mg and DIC concentrations of natural fluids with pH values between 7 and 9 are close to those dictated by the solubility of magnesite. In addition, Mg concentrations of Type 1 fluids are between values predicted for fluids in equilibrium with magnesite or brucite (Figure 3.5b), while the trend Ca concentrations of the natural samples follows the V-shape trend of fluids in equilibrium with calcite (Figure 3.5c). Overall, it can be seen that the compositions of these circumneutral to slightly alkaline fluids are more consistent with the dissolution and precipitation of minerals (serpentine, brucite, magnesite, and calcite) common in the highly altered rocks that compose the shallow aquifer than they are with initial stages of the dissolution of primary minerals in aquifers composed of fresh or relatively less altered ultramafic rocks. This observation is consistent with Neal and Stanger (1986) and Marques et al. (2008), who argued that Mg- and $HCO_3^-$-rich (Type 1) fluids could have been generated in shallow aquifers consisting of highly altered ultramafic rocks. Fluids that plot between the brucite and magnesite solubility curves in Figure 3.5b can be described by a process involving the dissolution of brucite and subsequent precipitation of magnesite given by,

$$\mathrm{Mg(OH)_{2(brucite)}} + \mathrm{Mg^{+2}} + 2\mathrm{HCO_3}^- \rightarrow 2\mathrm{MgCO_{3(magnesite)}} + 2\mathrm{H_2O}. \qquad (3.1)$$

It is possible for reaction (3.1) to proceed readily at shallow aquifer settings, as brucite is highly soluble at circumneutral pH (see dashed grey curve for brucite in Figure 3.5b) and is experimentally known to dissolve rapidly at these pH conditions (Prokovsky and Schott, 2004). Dissolution of brucite likely accounts for the depleted Mg/Si ratios observed from highly altered ultramafic rocks relative to those that are more unaltered (Malvoism, 2015; de Obeso and Kelemen, 2018; 2020), though these observations can likewise be accounted for by enrichment in silica (de Obeso and Kelemen, 2018). It is of note that natural brucite commonly exists in solid solutions of $Mg^{+2}$ and $Fe^{+2}$, and the dissolution, mobilization, and eventual oxidation of $Fe^{+2}$-bearing brucite could supply $H_2$ independent of the $H_2$ generated during the serpentinization of fresher ultramafic rocks (Frost et al., 2013; Miller et al., 2016; Mayhew et al., 2018; Templeton and Ellison, 2020). However, the production of $H_2$ from the alteration of brucite-bearing serpentinites can only proceed at $O_2$-free regions in the aquifer, as $Fe^{+2}$ released from brucite dissolution will be otherwise oxidized by $O_2$ to form ferric oxyhydroxides.

**Hyperalkaline (pH >11) Ca+2-OH- Type 2 Fluids.** Hyperalkaline fluids were sampled from discharging springs (blue squares in Figure 3.5) and one well (NSHQ-14). These are classified as Type 2 fluids and are characterized by their hyperalkaline pH, elevated Ca concentrations, and extremely low Si and Mg concentrations. As shown in Figure B2a, the most common solutes in these fluids, after $Na^+$ and $Cl^-$, are $Ca^{+2}$ and $OH^-$, and hence are also referred as $Ca^{+2}$-$OH^-$ fluids. Despite $Na^+$ and $Cl^-$ comprising most of the total dissolved solutes, these fluids are far less saline than seawater and hence are not often classified as $Na^+$-$Cl^-$ fluids. Compositions of Type 2 fluids are characteristic of fluids constrained by the Ctl-Brc-Di assemblage (see end of reaction path in Figure B3e or reaction B7) predicted by equilibrium calculations. However, upon closer examination, Clt-Brc-Di equilibrium (point $d_1$ in Figure 3.5) yields lower Si (Figure 3.5a) and Mg (Figure 3.5b) and higher Ca (Figure 3.5c) concentrations than those measured from environmental samples. Analogous comparisons can be made with the activity diagrams shown in Figures 3.5e and 3.5f, where the $a\mathrm{SiO}_{2(aq)}$ values of hyperalkaline samples approach that dictated by Ctl-Brc equilibrium but plot below the Ctl-Brc-Di equilibrium value. We have yet to sample fluids with Si concentrations or $a\mathrm{SiO}_{2(aq)}$ lower than values dictated by Ctl-Brc equilibrium, implying constraints by this mineral assemblage on the silica content of serpentinization-generated fluids. Despite being close to or approaching predicted compositions, the variabilities in pH and concentrations of dissolved Si and Mg observed for hyperalkaline fluids cannot be fully accounted for by equilibrium predictions. Specifically, pH values of hyperalkaline fluids range from 11 to 12, and at these pH values, Si and Mg concentrations can vary by up to three orders of magnitude. Trends resulting from variabilities in host rock compositions shown by Leong and Shock (2020) cannot account for such wide variations within this small range of pH. Accounting for mineral solid solutions predicts slightly higher Si concentrations (Leong and Shock, 2020) but does not fully reconcile models with actual measurements.

Reaction paths and solubility curves depicted in Figures B3 and 3.5 simulate rainwater-ultramafic rock interactions at 25°C. However, temperatures of fluids during sampling varied from 15° to 40°C. We calculated the pH constrained by the Ctl-Brc-Di equilibrium at temperatures ranging from 0-60°C and results are plotted in Figure 3.6 (solid black curve). Most environmental samples from Oman, however, have pH values below those predicted by the Ctl-Brc-Di equilibrium. Only a few samples from Oman (grey triangles and x-marks from Chavagnac et al., 2013b and Giampouras et al., 2020, respectively) and a few from other low-temperature serpentinizing environments on Earth (filled black circles in Figure 3.6) plot near this predicted trend. However, it is of note that pH values higher than those predicted by Ctl-Brc-Di equilibrium are rare, implying that upper limits on the pH of serpentinization-generated fluids are constrained by diopside dissolution. Extremely high pH values (12.5 to >13) were observed in a few

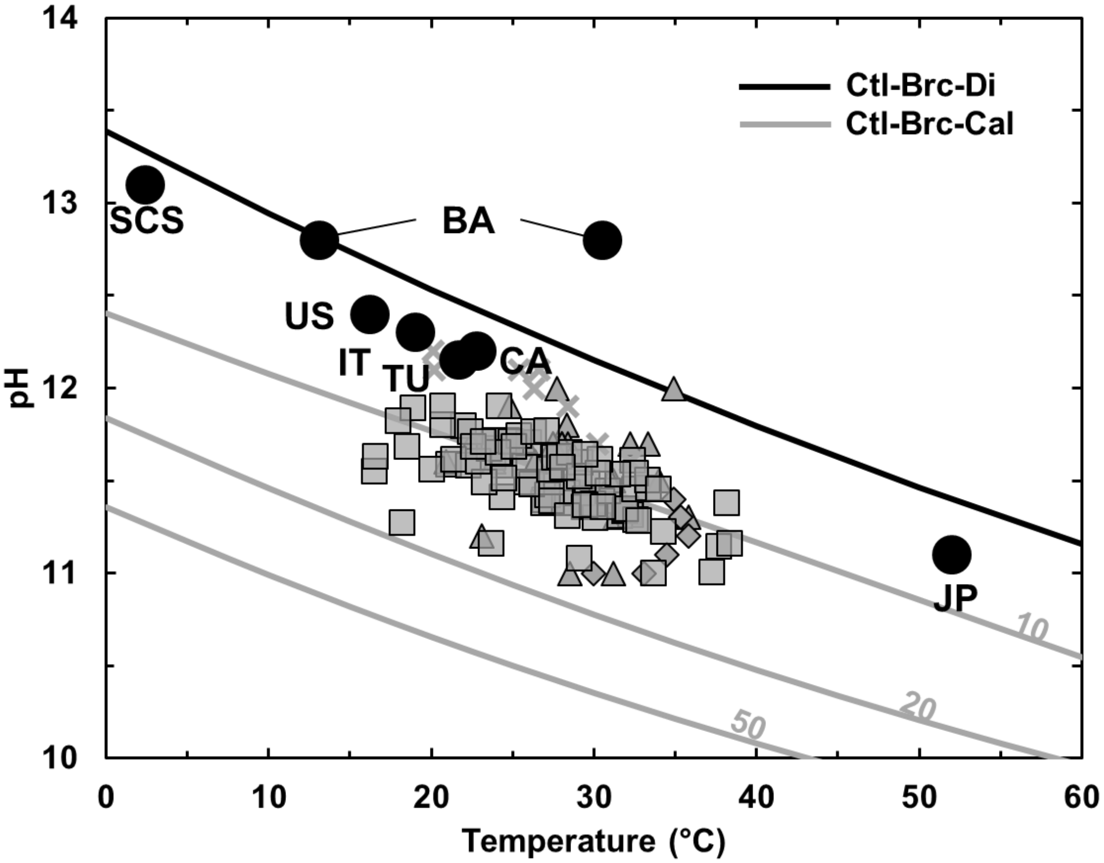

*Figure 3.6*. Calculated pH in equilibrium with the Ctl-Brc-Di (solid black curve, reaction 7) and Ctl-Brc-Cal (solid grey curves, reactions 4 and 9) mineral assemblages at temperatures ranging from 0-60°C. For the Ctl-Brc-Cal equilibrium assemblages, the DIC concentrations in μmolal are indicated above the solid grey curves. Black circles represent the highest pH values measured in low-temperature serpentinizing systems: SCS- South Chamorro Seamount in the Izu-Bonin-Mariana arc (Mottl, 2009); BA- Dinaride ophiolite in Bosnia and Herzegovina (Etiope et al., 2017); US – Coast Range ophiolites microbial observatory or CROMO, California, USA (Crespo-Medina et al., 2014); CA – Tableland ophiolite, Canada (Szponar et al., 2013); IT – Voltri Massif, Italy (Schwarzenbach et al., 2013); TU – Amik Basin, Turkey (Yuce et al., 2014); and JP – Hakuba Happo spring, Japan (Homma and Tsukahara, 2008; Suda et al., 2014). The pH of these fluids trend closely with and rarely exceed the pH predicted by the Ctl-Brc-Di equilibrium, suggesting that upper limits on the pH of serpentinizing fluids are constrained by diopside dissolution. In contrast, most hyperalkaline (pH > 11) fluids from Oman, represented by the various grey symbols, plot below these theoretical maxima but above those predicted for by Ctl-Brc-Cal equilibrium with DIC concentrations of 20 μmolal. Grey square symbols depict data resulting from this work, while those in triangles, diamonds, and crosses represent data reported in Chavagnac et al. (2013b), Rempfert et al. (2017), and Giampouras et al. (2020), respectively.

continental sites such as in Maqarin, Jordan (Khourey et al., 1985, 1992; Alexander et al., 1992; Pederson et al., 2004) and Lake Calumet, Chicago (Roadcap et al., 2005; Ohlsson et al., 2019). These localities, however, are not hosted by ultramafic lithologies and the extremely alkaline pH values are likely results of reactions akin to that of groundwater-concrete interactions (Gaucher and Blanc, 2006).

Leong and Shock (2020) discuss various mineral-fluid reactions that can shift fluid compositions in equilibrium with Ctl-Brc-Di to lower $a\mathrm{Ca}^{+2}/(a\mathrm{H}^{+})^2$ and hence to lower pH and Ca concentrations. One such process is the introduction of DIC along the fluid pathway, such as when ascending deep-seated hyperalkaline fluids are modified by infiltrating atmospheric $\mathrm{CO}_{2(g)}$, mix with DIC-rich shallow groundwaters, and/or come in contact with carbonate veins in the shallow subsurface. Magnesite and dolomite are highly and slightly undersaturated, respectively, in these Mg-poor fluids (see Table B1) and will dissolve upon interaction with surfacing deep-seated fluids. With these additional DIC inputs, Ca-rich hyperalkaline fluids can precipitate calcite, driving fluid compositions away from Ctl-Brc-Di equilibrium to conditions set by chrysotile-brucite-calcite (Ctl-Brc-Cal) equilibrium. The pH values and Ca concentrations constrained by Ctl-Brc-Cal equilibrium vary depending on the amount of DIC supplied by the transport processes mentioned above. Equilibrium with calcite, as shown through the reaction

$$\mathrm{Ca}^{+2} + \mathrm{HCO_3}^{-} \Leftrightarrow \mathrm{CaCO}_{3(\mathrm{calcite})} + \mathrm{H}^{+}, \tag{3.2}$$

dictates that a higher amount of DIC will result in lower $a\mathrm{Ca}^{+2}/(a\mathrm{H}^{+})^2$. Calculated $a\mathrm{Ca}^{+2}/(a\mathrm{H}^{+})^2$ values at variable DIC concentrations up to 50 μmolal are plotted in the activity diagram shown in Figure 3.5f. At 25°C and 1 bar, DIC concentrations exceeding 8 μmolal result in $a\mathrm{Ca}^{+2}/(a\mathrm{H}^{+})^2$ values lower than those constrained by Ctl-Brc-Di equilibrium. DIC concentrations of < 20 µmolal can account for the $a\mathrm{Ca}^{+2}/(a\mathrm{H}^{+})^{2}$ of most hyperalkaline samples. Results of calculations of pH constrained by the Ctl-Brc-Cal equilibrium accounting for both variable temperatures (0-60°C) and DIC concentrations (10-50 µmolal) are plotted in Figure 3.6 (solid grey curves). Most hyperalkaline fluids in Oman have pH values close to those predicted by equilibrium with calcite at DIC concentrations close to 10 µmolal and not more than 20 µmolal, suggesting a DIC-limited environment in the deep subsurface. Minor DIC input from the atmosphere or through mixing with DIC-rich shallow groundwater can easily saturate calcite and consequently shift the pH of surfacing deep-seated hyperalkaline fluids. Calcite and dolomite were observed to comprise near-surface veins in Oman (Kelemen and Matter, 2008) and are evidence that this shift could be actively occurring in the shallow subsurface. Moreover, the extremely low DIC (< 20 µmolal) predicted for the subsurface can inform biogeochemical studies on the amount of inorganic carbon available for subsurface microbes. In these carbon-limited environments, dissolution of carbonates can be a robust inorganic carbon source for deep-seated microbes (Miller et al., 2018), and investigations into the subsurface occurrence of these minerals provide insights into how deep the biosphere extends into ultramafic aquifers.

**Mixed Fluids.** The Si and Mg concentrations of hyperalkaline fluids vary by nearly three orders of magnitude and cannot be fully accounted for by a shift toward Ctl-Brc-Cal equilibrium or by variabilities in temperature. At temperatures between 0 – 100 °C, total dissolved Si only varies by an order of magnitude and Mg varies even less (Leong and Shock, 2020). Leong and Shock (2020) showed that reaction with more orthopyroxene-rich or more serpentinized ultramafic rocks can lead to higher Si concentrations. However, the same models also predict lower trends in Mg concentrations. Instead, variabilities observed in almost all sampled fluids can be accounted for by mixing (dashed yellow lines in Figure 3.5) between deep-seated fluids close to equilibrium with the rock as represented by Ctl-Brc-Di ($d_1$) or Ctl-Brc-Cal ($d_2$ and $d_3$) equilibria and a representative surface fluid (s, Sample 140116B). Further details on the composition of end-member fluids used in our mixing calculations can be found in Table B2. Deep-seated hyperalkaline springs often discharge where neutral to slightly alkaline shallow aquifer fluids discharge as well. Thus, mixing between these two fluid types at discharge zones is likely to occur. As surficial and shallow subsurficial fluids have Si and Mg concentrations that are several orders of magnitude elevated relative to deep-seated hyperalkaline fluids, even minor amounts of mixing can lead to large variabilities in the Si and Mg concentrations. Mixing calculations reveal that a majority of the deep-seated hyperalkaline fluids samples were modified slightly by an input of < 10% of surficial and/or shallow surficial fluids (see Figure 3.5a). Some samples have less influence (< 1%) and can be interpreted as the most pristine representatives of the deep subsurface. We use Si concentrations to quantify mixing extents (Figure 3.5a) because we have constraints on the Si concentration of at least one of the end-member fluids, and it allows us to take advantage of the highly contrasting Si concentrations of end-member fluid types and the generally conservative nature of Si during mixing. In studies involving submarine hydrothermal fluids, the extent of seawater input to venting fluids can be quantified using Na, Cl, and Mg owing to known constraints on end-member concentrations. However, unlike seawater where Na and Cl concentrations are known, end-member Na and Cl concentrations are more variable in continental serpentinizing environments. In the Samail ophiolite, end-member hyperalkaline fluids have Na and Cl concentrations that vary among sample sites, with elevated concentrations observed at sites closest to the basal thrust of the ophiolite. Si behaves more conservatively than Mg, as Mg-bearing minerals such as brucite and layered doubled hydroxides are commonly observed in hyperalkaline pools (Neal and Stanger, 1984; Paukert et al., 2012; Chavagnac et al., 2013a; Giampouras et al., 2020) and in shallow aquifers (Taylor et al., 1991). Most Type 2 hyperalkaline fluids have $a\mathrm{Mg}^{+2}/(a\mathrm{H}^{+})^{2}$ values that lie above the brucite solubility line, and few cross below it toward the chrysotile saturation line, as shown in Figure 3.5e. Despite thermodynamic drive to precipitate, most fluids remain oversaturated with respect to chrysotile. Tutolo et al. (2018) postulated kinetic inhibition for serpentine precipitation (see reaction B2) or the brucite silicification reaction (see reaction B4), resulting in Si concentrations that are persistently above those dictated by chrysotile solubility (dashed grey lines in Figures 5a-5e). Mixing can transport Si into a Si-poor deep-seated fluid, and the sluggish rate of serpentine formation makes Si a reliable mixing indicator in comparison to other aqueous species. Though rare, secondary silicate minerals such as suolunite ($Ca_2Si_2O_5(OH)_2$:$H_2O$) are known to precipitate in outcrops (Stanger and Neal, 1984) and hyperalkaline pools (Chavagnac et al., 2013b) in Oman, and determining the rate of Si incorporation into solids at low-temperature conditions will help improve its use as a tracer for mixing in serpentinizing systems. Another advantage of using Si is the ease of measurement of even dilute concentrations (< 1 ppm $SiO_{2(aq)}$) in the field using a colorimetric spectrometer. Field measurements can quantify mixing extents during sampling and exploration. Mixing calculations and field measurements of Si concentrations provide a rapid and robust method to quantify how much the deep-seated signature of serpentinization-generated fluids is affected by shallow subsurface processes.

As a result of mixing, most fluids with pH values greater than 9 have DIC concentrations that imply supersaturation with respect to magnesite and calcite (Figure 3.5d) and precipitation of these minerals can be favorable. However, at pH >11 calculated DIC levels in equilibrium with magnesite (dashed grey line in Figure 3.5d) would require Mg values (dashed grey line in Figure 3.5b) that exceed those measured in our samples, resulting in conditions that are not favorable for precipitation of magnesite (see Table B1). Thus, only calcite (or aragonite, see Table B1) is favored to precipitate in hyperalkaline environments, consistent with studies on travertine and other precipitates associated with hyperalkaline seeps (*e.g.*, Kelemen and Matter, 2008; Chavagnac et al., 2013a; Mervine et al., 2014; Giampouras et al., 2020). At pH values between 9 and 11, Mg (Figure 3.5b) and DIC (Figure 3.5d) concentrations of sampled fluids plot above those dictated by magnesite solubility, indicating the fluids are supersaturated with respect to magnesite and suggesting that there are kinetic inhibitions to precipitate magnesite in surficial mixing environments. This kinetic inhibition could lead to the precipitation of hydrated magnesium carbonates (*e.g.*, hydromagnesite, dypingite, nesquehonite) that are known to occur in hyperalkaline and mixed fluids in Oman (Giampouras et al., 2020) instead of magnesite. Our mixing calculations also highlight the strong buffering capacity of hyperalkaline fluids resulting from mineral-fluid reactions that generate Ca-OH solutions (Ctl-Brc-Di equilibrium, or Ctl-Brc-Cal equilibrium at low DIC concentrations of <20 µmolal). A significant amount of mixing is required to lower the pH below 11, amounting to 40% surface/shallow water input if pH is constrained by Ctl-Brc-Cal equilibrium at 10 µmolal DIC or up to 80% if constrained to higher pH by Ctl-Brc-Di equilibrium.

In addition to fluid mixing, the elevated Si and Mg concentrations relative to those predicted by equilibrium calculations could also result from olivine and pyroxene dissolving faster than serpentine precipitates, as argued by Nesbitt and Bricker (1978). As shown in Figure 3.5e, most hyperalkaline fluids are undersaturated with respect to forsterite and plot between the forsterite and brucite saturation lines. Observations from environmental samples likely reflect complementary primary mineral dissolution and secondary mineral precipitation processes. Quantifying how much the elevated Si and Mg concentrations of hyperalkaline fluids can be attributed to either or both dissolution and mixing processes remains to be solved. Using tritium isotopes, Paukert et al. (2019) suggested that hyperalkaline spring fluids in Oman are influenced by up to 6% modern groundwater. This is consistent with our calculated mixing extents for most hyperalkaline fluids (< 10%, see Figure 3.5a) and implies that subsurface mixing is occurring.

**pH 9-11, low Si fluids.** Most samples with pH ranging from 9 to 11 can be attributed to mixing of end-member fluids with the exception of a few samples with dilute Si concentrations (< 10 µmolal) that are comparable to those measured in hyperalkaline fluids. These unusually low concentrations of Si at these intermediate pH ranges can be attributed to various processes discuss below.

As depicted in Figure 3.5a, fluids with pH values from 9.0 to 9.5 plot close to the predicted reaction path controlled by equilibria with both chrysotile and magnesite, which signifies fluid compositions indicative of incipient serpentinization (Stage 2) and mineral carbonation (Stage 3) stages of the overall alteration progress. Most fluids of this type were sampled in wells, depicted in Figure 3.5a as solid black squares (this study) and grey diamonds (Rempfert et al., 2017), suggesting that these fluids could be representative of intermediate stages of the overall serpentinization progress where shallow aquifer fluids are infiltrating into the deep subsurface in the recharge zone. Actual Si concentrations of sampled well fluids could be lower and plot closer to values predicted by equilibrium calculations if upper aquifer fluids, which are Si-rich, contaminate deep-seated samples during sampling of wells.

Alternatively, these fluid compositions could indicate an alteration process involving gabbroic rocks, as many of these fluids were sampled in wells located close to the ultramafic-gabbro contact in the Samail ophiolite. Models simulating water interacting with gabbro or a mixture of gabbroic and ultramafic rocks at low temperatures could assess if these fluids correspond closely with predictions. However, many of the hyperalkaline spring fluids depicted in Figure 3.5a are also located close to the ultramafic-gabbro transition and do not exhibit any compositional differences from fluids located far from this transition. Like the springs, the composition of these well fluids may be more strongly influenced by fluid-mineral processes associated with ultramafic rocks than with gabbroic rocks.

**Classification of ultramafic-hosted fluids.** The discussions above provide a framework for classifying low-temperature, ultramafic-hosted fluids as constrained by predictions of the serpentinization reaction path, the solubility of serpentinization-relevant minerals, and the subsequent mixing process that occurs as fluids are discharged back to the surface. Specifically, by drawing on trends in pH and total dissolved Si, as shown in Figure 3.7, we can classify these fluids into four types:

*Type 1* $Mg^{+2}$-$HCO_3^-$ – As first proposed by Barnes and O'Neill (1969), these fluids have compositions that are enriched in Mg and bicarbonate, and could be products of the first stage of the alteration progress that leads to enrichment of solutes in fluids through the dissolution of primary minerals in systems open to atmospheric influences (Leong and Shock, 2020). However, as discussed above, these fluids are likely to result from interactions of rain with serpentinites or highly altered ultramafic rocks that are common in the shallow aquifer. Equilibria with serpentine, brucite, and magnesite in the presence of the atmosphere results in fluids with pH values between 7 and 9 that are enriched in Si (~100-500 μmolal, mostly speciated as $SiO_{2(aq)}$), as depicted in Figure 3.7. Furthermore, as shown in Figures 5b and 5d, these fluids are enriched in Mg (~1000-10,000 μmolal, mostly speciated as $Mg^{+2}$) and DIC (2,000-5,000 μmolal, almost entirely speciated as $HCO_3^-$), respectively, relative to other fluid types.

*Type 2* $Ca^{+2}$-$OH^-$ – This fluid type, also first proposed by Barnes and O'Neill (1969), is hyperalkaline and otherwise known as $Ca^{+2}$-$OH^-$-type fluids. Type 2 fluids are characterized by their high pH (>11), elevated concentrations of Ca (>1,000 μmolal, mostly speciated as $Ca^{+2}$), and very low concentrations of Mg and Si (< 1 μmolal), which are consequences of equilibria with Ctl-Brc-Di or with Ctl-Brc-Cal at limited DIC concentrations (< 20 μmolal) during advanced stages of serpentinization (*Stages 4 to 6*). As shown in Figure 3.7, a few hyperalkaline samples have Si concentrations that are < 1 μmolal (< 60 ppb $SiO_2$) and can be interpreted to be close to end-member Type 2 compositions. Most hyperalkaline fluids, however, have higher Si concentrations and can be accounted for by fluid mixing.

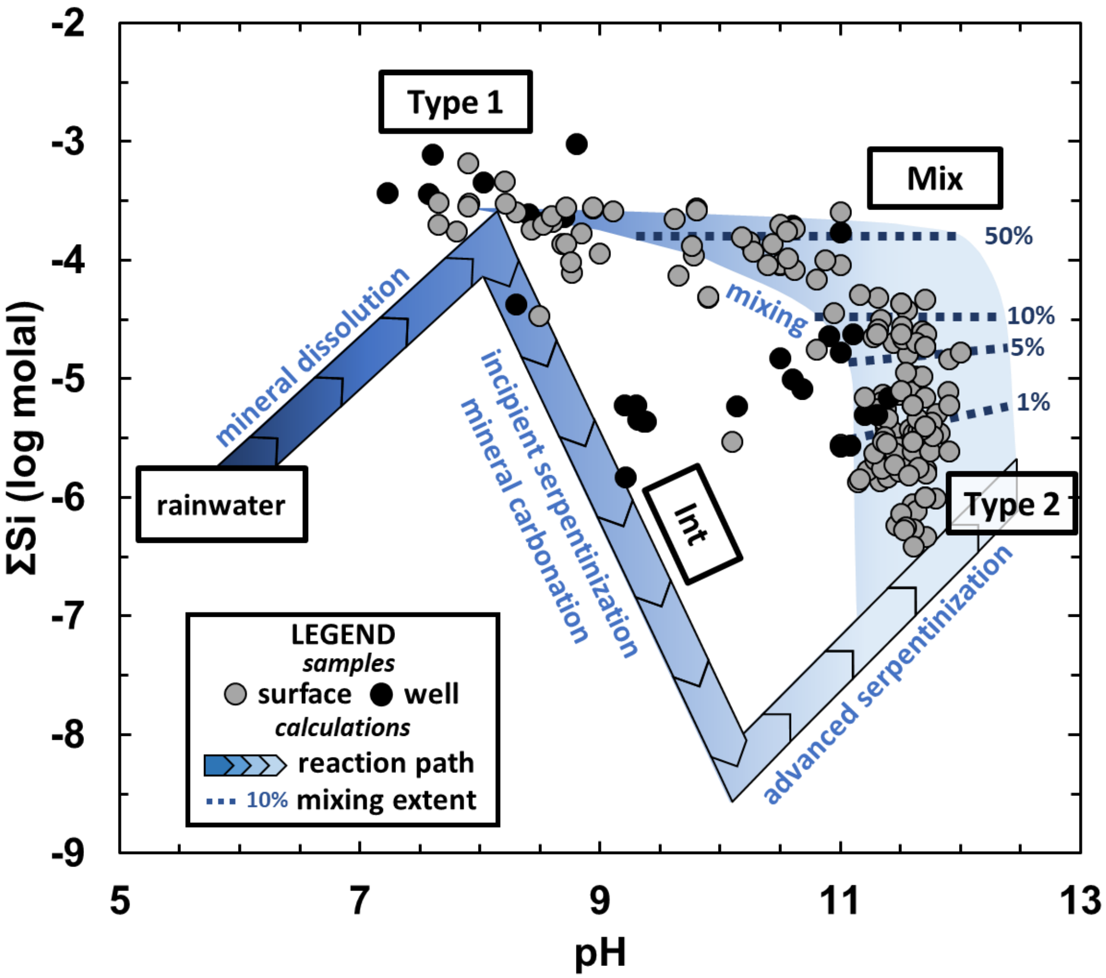

*Figure 3.7*. Key serpentinization reactions and resulting fluid types summarized in a plot of Si concentration vs pH. Fluid samples from the Oman ophiolite are plotted relative to the reaction and mixing paths. Grey circles show surface samples (streams and springs) while filled black circles indicate subsurface samples (wells). Fluid compositional data were taken from the analytical results of this work and other past studies in Oman shown in Figure 3. Overall, fluids can be accounted for by four processes: (1) mineral dissolution into rain which leads to Type 1 fluids (see Stage 1), (2) incipient serpentinization and mineral carbonation (see Stages 2-3) which leads to intermediate (Int) fluid types, (3) advanced stages of serpentinization (see Stages 4-6) which lead to Type 2 fluids, and (4) mixing (Mix) between deep-seated Type 2 and surficial or near-surficial Type 1 fluids.

*Mixed Fluids* – In this classification scheme, this fluid type encompasses fluids with pH >9 that are too alkaline to be in equilibrium with serpentine, brucite, and carbonates in the presence of the atmosphere. Note that fluids with pH < 9 can also be influenced by mixing, as most fluids sampled in this study plot along the mixing trend shown in Figure 3.7. At higher pH, this fluid type also includes hyperalkaline fluids that are Si-enriched compared with serpentine + brucite equilibrium. Mixing between circumneutral stream fluids and hyperalkaline springs is commonly observed at the surface, as they often occur together. On the other hand, it is likely that subsurface mixing between end-member Type 1 and 2 fluids in discharge zones accounts for the large variabilities in Si concentration observed in hyperalkaline fluids.

*Intermediate Fluids* – These fluids, also with pH values ranging from 9 to 11, share similar characteristics with mixed fluids. However, unlike mixed fluids, these fluids have low Si concentrations (< 10 μmolal) that are comparable to most hyperalkaline fluids. As discussed above, fluids of this composition may indicate incipient serpentinization (*Stage 2*) and mineral carbonation (*Stage 3*) during intermediate stages of the alteration progress.

Note that trends shown in Figure 3.7 can allow immediate and robust classification of fluids while in the field using a pH meter and a portable spectrometer for colorimetric measurements of dissolved $SiO_{2(aq)}$. These data provide real-time information on the extent of the serpentinization and mixing progress and can concurrently feed into decisions involving exploration, sampling, and experiments while in the field.

### ***3.4.2. Dissolved Na and Cl***

Petrological studies of serpentinized ultramafic rocks reveal that fluid-mobile elements can be sequestered during serpentinization in submarine and subduction environments (*e.g.*, Deschamps et al., 2013). The behavior of these elements during serpentinization in continents, where water-rock interactions are facilitated by meteoric fluids instead of seawater, is less well known. Trends in the Na and Cl concentrations of fluids from Oman were investigated to provide insights into their behavior during continental serpentinization.

Hyperalkaline fluids are at least twice as enriched in Na (Figure 3.8a) and Cl (Figure 3.8b) relative to circumneutral to slightly alkaline fluids and are orders of magnitude enriched relative to rainwater. Similar trends can be observed for K (Figure 3.3e). The relative enrichment in the Na, K, and Cl content of hyperalkaline fluids can result from two processes: (1) enrichment due to loss of $H_2O$ during the hydration of ultramafic rocks, and/or (2) leaching from host rocks during water-rock interactions. Both can occur concomitantly, as hyperalkaline fluids are products of large extents of water-rock interactions that lead to both water loss and possibly substantial inputs from the reacting rocks. Moreover, the fluids most enriched in Na, K, and Cl are hyperalkaline fluids sampled close to the basal thrust of the Samail ophiolite. These sample locations are typically located at topographic lows which implies longer fluid pathways that lead to more hydration and leaching. Simulations of $H_2O$ loss and leaching were performed to evaluate the influence of hydration and leaching processes in accounting for natural concentrations. The amount of $H_2O$ lost during the overall reaction progress is shown in Figure 3.8c. At log rock-to-water ratio ~0 (*i.e.*, reaction of 1 kg of rock in 1 kg of water), usually inferred as the maximum extent of reactions from deep-sea hydrothermal vent fluids (Taylor, 1974; Edmond et al., 1979; Foustoukos et al., 2008), the loss of $H_2O$ due to hydration is ~15%. Mineral hydration cannot solely account for the enrichment of Na and Cl observed in sampled fluids. Accounting for an enrichment of at least a factor of two observed from hyperalkaline fluids relative to lower-pH samples requires $H_2O$ loss of >50%, which can only be attained at extremely high rock-to-water ratios (log rock-to-water ratio of >0.5, or reaction of >3 kg of rock in 1 kg of water). Similarly high extents of water-rock interactions are needed regardless of compositional variabilities of the reacting rock (grey curves in Figure 3.8c). Serpentinization of olivine-rich rocks tend to consume more $H_2O$ as it precipitates more brucite, which contains ~30 wt.% $H_2O$ as hydroxide in its structure. Increased contributions from orthopyroxene favors the formation of serpentine (~13 wt.% $H_2O$) and talc (~5 wt.% $H_2O$) which are less hydrous than brucite and would require higher degrees of interaction to result in similar amounts of $H_2O$ loss.

In addition to increases in concentrations due to $H_2O$ loss, Na, K, and Cl can be leached from host rocks during water-rock interactions. Using chemical data from Hanghoj et al. (2010) on the Na content of partially serpentinized Oman harzburgites (~0.03 mole $Na^+$/kg rock or 0.1 wt.% $Na_2O$; Cl was calculated to balance $Na^+$ by charge), we can simulate leaching of Na and Cl during serpentinization. Results of this simulation, depicted as solid dark blue curves in Figures 3.8a and 3.8b, show that if Na and Cl were leached from the host rocks during water-rock interactions, it would entail rock-to-water ratios of between 0.2 and 0.5 (*i.e.*, reaction of 0.2 to 0.5 kg of rock in 1 kg of water) to account for environmental measurements. The above range in rock-to-water ratios depicts lower and more plausible extents of water-rock reactions than that required if Na and Cl enrichment is accounted for by mineral hydration only. Neal and Stanger (1985) also postulated in favor of a leaching origin of chloride in hyperalkaline fluids in Oman, as large amounts of $H_2O$ incorporated into serpentine and brucite would result in fluids that are extremely $^{2}H$-rich and $^{18}O$-depleted. In contrast, as shown in Figure 3.4, about half of the hyperalkaline fluid analyses (all filled colored symbols in Figure 3.4), which are indicative of large extents of water-rock interactions, are $^{2}H$-depleted relative to circumneutral fluids (open green squares in Figure 3.4). As for the source of these solutes, Neal and Stanger (1985) indicated that chloride could be leached from mineral surfaces and secondary precipitates such as salts and metal hydroxychlorides. Boschetti and Toscani (2008) also discussed leaching from saline fluid inclusions to account for the elevated concentrations of Na and Cl in hyperalkaline fluids seeping from serpentinite outcrops in Northern Italy. All the above suggests that the host rocks in these continental aquifers interacted previously with saline fluids, likely during seawater-driven serpentinization before the ophiolite was emplaced onto the continent.

Sodium and chloride concentrations of circumneutral (Type 1) fluids, on the other hand, cannot be accounted for by leaching from rocks with concentrations typical of those from unaltered or partially serpentinized Oman harzburgite, as shown by the solid dark blue curves in Figures 3.8a and 3.8b. Since many circumneutral fluids were sampled in surface stream runoffs, evaporation could contribute to enrichment of Na and Cl. However, extreme evaporation of >50% water loss to account for enrichment from typical rainwater concentrations would result in fluids highly enriched in $^{2}H$ and $^{18}O$, which was not observed. Additional input of Na and Cl could have come from interactions with rocks that are more enriched in these elements than typical partially altered ultramafic rocks. The shallow aquifers where these fluids occur are composed of highly altered rocks, which may be more enriched in Na and Cl. We simulated leaching

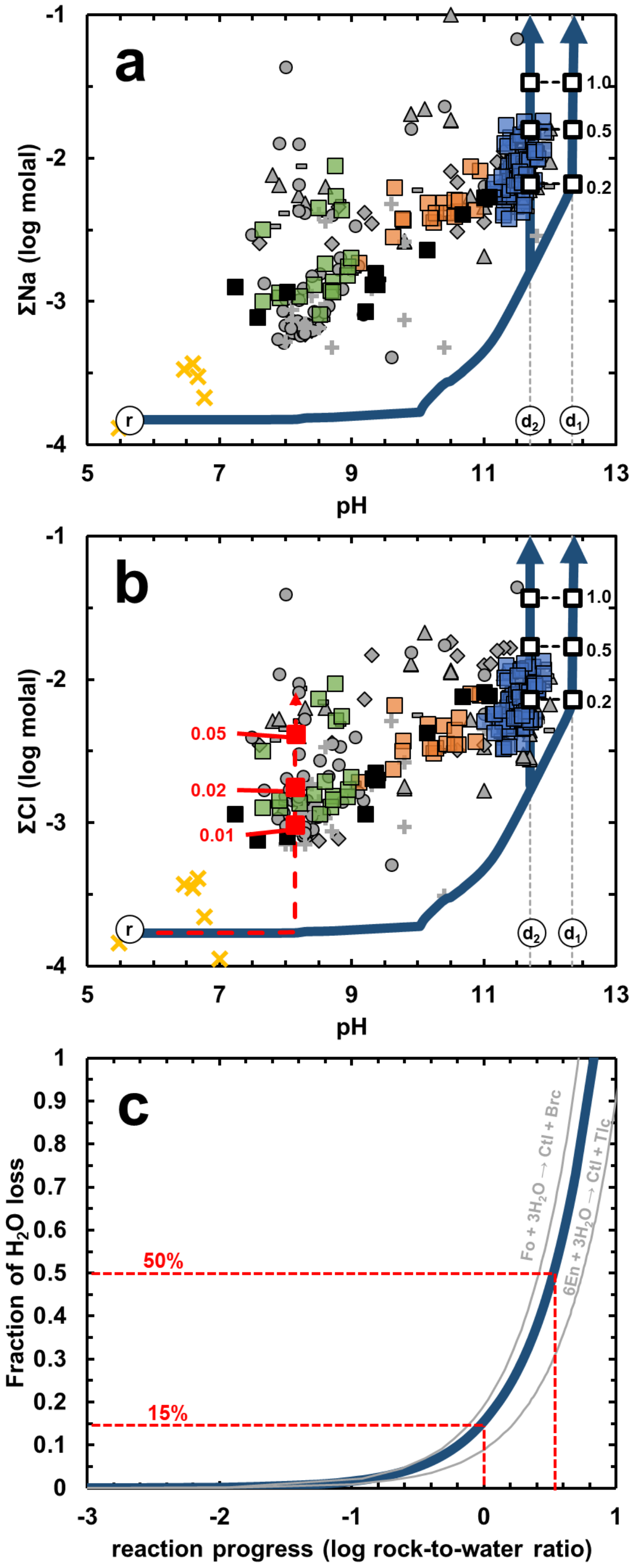
a
ΣNa (log molal)
pH
1.0
0.5
0.2
r
$d_2$
$d_1$
b
ΣCl (log molal)
0.05
0.02
0.01
c
Fraction of $H_2O$ loss
reaction progress (log rock-to-water ratio)
50%
15%
Fo + $3H_2O$ → Ctl + Brc
6En + $3H_2O$ → Ctl + Tlc

*Figure 3.8*. Reaction paths (dark blue curves) depicting predicted trends in the concentration of dissolved Na (a) and Cl (b) due to mineral leaching and amount of $H_2O$ loss (c) as serpentinization progresses. Measured dissolved Na (a) and Cl (b) from environmental samples are plotted for comparison. Symbols in (a) and (b) are the same as those in Figure 5. Reaction paths start from rainwater (r) and ends at fluids in equilibrium with either the Ctl-Brc-Di eq ($d_1$), or the Ctl-Brc-Cal at 10 μmolal DIC ($d_2$) assemblages. Solid white squares (with bold black outline) indicate extents of water-rock interactions with values of rock-to-water ratios given at the right. The dashed red curve in (b) depicts results of simulations with a serpentinite (100% chrysotile or serpentine). Solid red squares in (b) indicate extents of reactions with values of rock-to-water ratios given at the left. Dark blue curve in (c) represent reaction path for model ultramafic rock with composition 85% olivine-14% orthopyroxene-1% clinopyroxene. Grey curves in (c) represent trends for olivine-only or orthopyroxene-only scenarios. Dashed red lines in (c) show extent of reactions required to remove 15% and 50% of the starting reacting fluid.

of Cl from serpentinites using the average Cl content (~3000 ppm Cl or 80 millimole Cl/kg rock) of serpentinites or completely serpentinized ultramafic rocks compiled by Deschamp et al. (2013). Results of these calculations, depicted in Figure 3.8b as the reaction path in dashed red lines, show that only ~7 to 20 grams of serpentinite would need to react with a kilogram of water (log water-to-rock ratio ~-2 to -1.5) to account for the Cl content (0.8-2 millimolal) of most Type 1 fluids. Note that the reaction path shown in Figure 3.8b depicts reaction of rainwater with a serpentinite and hence the maximum pH at ~8.2 is attained when the rainwater approaches equilibrium with serpentine.

Further evidence that supports leaching during the evolution of rainwater into Type 1 circumneutral fluids and eventually into Type 2 hyperalkaline fluids is shown in Figure 3.9a. There is a general increase in the Na/K ratio of fluids as pH increases. The Na/K ratios of all fluid types would remain constant if hydration and evaporation were the only processes accounting for the increasing Na, K, and Cl content. The increasing Na/K ratio with pH could be attributed to leaching from precipitates that formed during previous seawater-rock interactions, as seawater is enriched in Na relative to K.

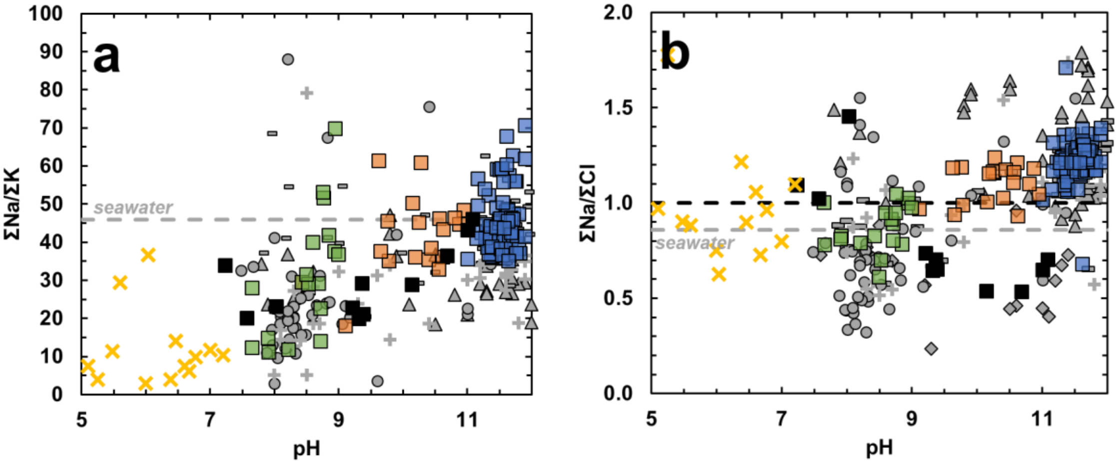

*Figure 3.9*. Trends in the total (a) Na/K and (b) Na/Cl ratios of fluids sampled from Oman. Symbols are the same as those in Figure 5. The increasing Na/K ratio in (a) suggests leaching from host rocks that were altered by seawater-rock interaction. Modern seawater has an average Na/K ratio of ~46 (dashed grey line, Millero et al., 2008). The increasing Na/Cl ratio in (b) suggests additional sources of Na or sinks for Cl. Type 2 fluids have Na/Cl ratios that are above unity (dashed black line) and that typical of seawater (0.86: dashed grey line, Millero et al., 2008).

As shown in Figure 3.9b, the trend in the Na/Cl ratio, like the trend in the Na/K ratio, is not constant with pH. Type 1 fluids (pH < 9) are depleted in Na relative to Cl, while Type 2 fluids (pH >11) have Na/Cl ratios above unity or those typical of seawater (0.8). The relative enrichment of Na with reaction progress could be due to the release of sodium from Na-bearing minerals such as plagioclase and alkali-bearing phyllosilicates (Boschetti and Toscani, 2008; Chavagnac et al., 2013a). Another source could be Na-bearing clinopyroxene, though Chavagnac et al. (2013a) argued that this contribution is likely minor, as these minerals are typically not abundant in harzburgites from Oman. Conversely, another process that could account for the trends shown in Figure 3.9b is the removal of Cl through incorporation into minerals where structural substitutions for hydroxide are possible, such as in apatite and some phyllosilicates. Layered doubled hydroxides (LDHs) can also attract anions into their positively charged interlayers and are known to occur in hyperalkaline pools and in mixing zones between Type 1 and Type 2 fluids (Paukert et al., 2012; Chavagnac et al., 2013b), as well as in ultramafic-hosted aquifers in Oman (Taylor et al., 1991). Taylor et al. (1991) characterized pyroaurite [$Mg_6Fe^{+3}{}_2(CO_3)(OH)_{16}:4H_2O$], the ferric iron end-member of hydrotalcite, from aquifer rocks in Oman that mainly hosts $CO_3^{-2}$ but also contains minor amounts of $Cl^-$ and $SO_4^{-2}$. These authors proposed that the pyroaurite was generated when $Fe^{+2}$ mobilized during silicate dissolution was partially oxidized during mixing with oxic, shallow fluid sources. Alternatively, Fe-bearing brucite in altered ultramafic rocks could be partially oxidized to form a LDH, as exemplified by the reaction

$$\begin{gathered}8\mathrm{Mg}_{0.75}\mathrm{Fe(II)}_{0.25}(\mathrm{OH})_{2(\mathrm{brucite})} + 0.5\mathrm{O}_{2(\mathrm{aq})} + 2\mathrm{Cl}^- + 3\mathrm{H}_2\mathrm{O} + 2\mathrm{H}^+ \\ \rightarrow \mathrm{Mg}_6\mathrm{Fe(III)}_2\mathrm{Cl}_2(\mathrm{OH})_{16}\text{: }4\mathrm{H}_2\mathrm{O}_{(\mathrm{iowaite})}\end{gathered} \tag{3.3}$$

for iowaite, the $Cl^-$ end-member of pyroaurite. Analogous reactions can also be written for other LDHs such as green rust or fougerite, the former of which has numerous properties that are invoked as ideal for the emergence of life on Earth (Russell, 2018). Note that most water samples retrieved from wells remain chloride-rich (black squares in Figure 3.9b), implying that alteration processes involving LDHs may be limited to deep-seated fluids surfacing as hyperalkaline seeps.

## 3.5. Timescales of Reactions

In the preceding discussions, the extents of water-rock reactions are depicted in terms of rock-to-water ratios that are independent of time. To gain insights into the timescales required to reach the various stages of serpentinization, we conducted reaction path calculations that incorporate dissolution rates of primary minerals at ambient conditions (~25 °C). Rates for forsterite, enstatite, and diopside dissolution are based on experiments of Pokrovsky and Schott (2000), Oelkers and Schott (2001), and Golubev et al. (2005), respectively, which include the pH-dependence of the dissolution rates of the reacting minerals. Calculations were done assuming constant surface area (1 $m^2$) of fresh ultramafic rock interacting with 1 kg of fluid. Results are shown in Figure 3.10a, which depicts both the timescales and the degree of water-rock interactions required to attain the various stages of the overall serpentinization process. Fluids with circumneutral pH (7 to 9) are attained with minimal reaction progress at timescales from a few months to at most a decade. Attaining serpentine saturation (pH ~8, Stage 2) is quick (a few months) while attaining carbonate saturation (Stage 3) entails a few years. However, as discussed above, these circumneutral Type 1 fluids are likely to result from fluid interacting with the highly altered host rocks of shallow aquifers composed mostly of serpentine, brucite, and carbonates. Calculations simulating the dissolution of these secondary phases at ambient conditions were conducted using data from Thom et al. (2013), Pokrovsky and Schott (2004), and Pokrovsky and Schott (1999) for chrysotile, brucite, and magnesite, respectively. The pH-dependences of the dissolution rates were also taken into consideration. Calculations for each of these minerals were done separately and were terminated when fluids reached saturation with the mineral involved. As with the reaction path involving unaltered ultramafic rocks, it is assumed that each kg of water reacts with 1 $m^2$ surface area of the involved mineral. Although shallow aquifer rocks could be made up of variable proportions of these secondary phases, this idealized assumption allows us to evaluate how rapidly each of these minerals can attain saturation. Results are depicted in Figure 3.10b, which shows that brucite saturation can be attained relatively quickly owing to its rapid dissolution rates (2 orders of magnitude faster than forsterite dissolution). Fluids would require a few months to attain equilibrium with magnesite. Serpentine saturation can be attained either through the dissolution of primary minerals in ultramafic rocks (Figure 3.10a, Stage 2) or serpentinites (Figure 3.10b). Both reach similar fluid chemistry (pH ~ 8) but the latter would require almost a decade, two orders of magnitude slower than the former due to the sluggish dissolution rate of chrysotile relative to those of the primary minerals.

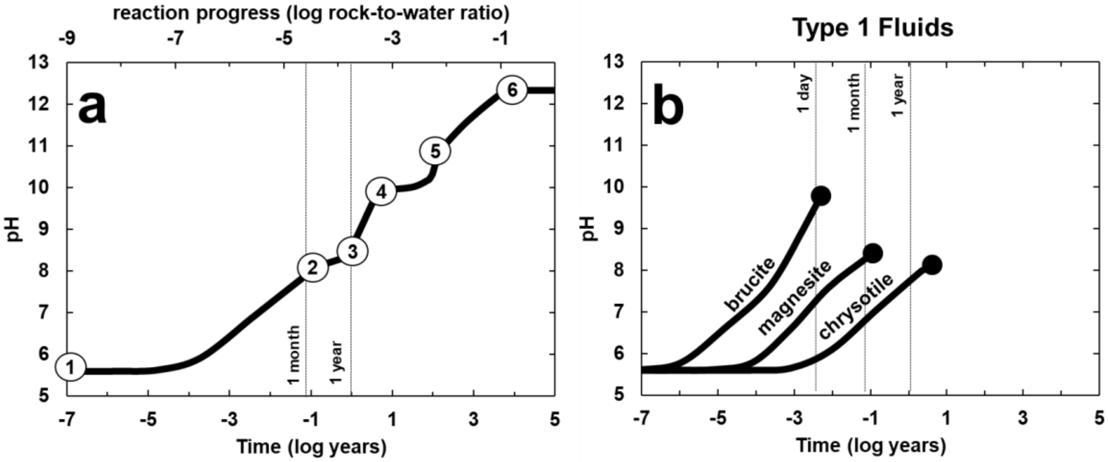

*Figure 3.10.* (a) Timescales (in log years) required to attain the various pH and stages of serpentinization. (b) Timescales (in log years) required to attain saturation of three secondary phases common in the altered ultramafic rocks in the shallow subsurface. Numbers inside circles in (a) indicate the starting points of the six stages of serpentinization. Black filled circles in (b) depict end of reaction path depicting dissolution of indicated mineral. Vertical dashed lines indicate various timepoints (1 day, month, and year) as a reference.

Compositions characteristic of Type 2 hyperalkaline fluids (Figure 3.10a) require much longer durations to attain. As shown in Figure B3, a rock-to-water ratio of at least 0.1 is needed to attain the maximum pH via Ctl-Brc-Di equilibrium (Stage 6), and this requires timescales close to 10,000 years. About 100,000 years would be needed to attain higher extents of reaction at a rock-to-water ratio of 1. Calculated timescales between

10,000-100,000 years correspond to the last glacial age, which is consistent with the hypothesis of Paukert et al. (2019) that some hyperalkaline fluids in Oman were recharged during this period. Our kinetic results also complement the experimental results of McCollom and Donaldson (2016) that show very slow rates of $H_2$ and $CH_4$ generation during low-temperature (<100 °C) serpentinization.

Inferred timescales for various stages of serpentinization, however, should be taken cautiously as discrepancies between laboratory-determined dissolution rates and those determined through field studies are well known. Field-determined rates are far slower than those measured in the laboratory, often entailing differences of several orders of magnitude (White and Brantley, 2003). For example, field-determined weathering rates of ultramafic rocks in the Amazon are at least two orders of magnitude more sluggish than laboratory-determined rates (Freyssinet and Farah, 2000). Studies of other lithological settings also report discrepancies between field and laboratory-determined rates (Velbel, 1993; White and Brantley, 2003; Maher, 2010), with the latter yielding rates at most four orders of magnitude faster than the former. These studies attribute the observed differences to numerous factors such as estimations of reacting surface areas and their evolution during the weathering process, fluid residence times, and the age of the rock. Taking the discrepancies into account, extrapolated timescales from our calculations to natural systems lead to much longer estimates, perhaps even requiring millions of years to attain hyperalkaline conditions if the deviation is at least 2 orders of magnitude. Better constraints on the natural rate at which low-temperature serpentinization occurs would provide powerful insights into the flux of reduced volatiles as well as the rate of energy transfer between the lithosphere and the biosphere in deep ultramafic aquifers here on Earth and other rock bodies in our solar system.

### 3.6. Conclusions

Overall, calculations identify the reactions that lead to the contrasting pH, fluid compositions, and redox potentials of end-member Type 1 circumneutral (pH 7 to 9) and Type 2 hyperalkaline (pH >11) fluids. The former are outcomes of mineral dissolution reactions and fluid interactions with highly altered rocks that are common in shallow ultramafic aquifers, while the latter approach equilibrium with serpentine and brucite, which actively form during advanced stages of serpentinization. The most alkaline fluids documented in low-temperature serpentinizing systems follow constraints dictated by diopside dissolution and some fluids in Oman approach this upper limit. The pH values of most hyperalkaline fluids in Oman, however, are lower than this constraint and can be attributed to a shift from diopside dissolution to calcite precipitation driven by the addition of dissolved inorganic carbon (DIC) as surfacing deep-seated hyperalkaline fluids encounter the atmosphere.

Most fluids with pH values between those of Type 1 and Type 2 can be attributed to mixing of these end-member fluids. Our calculations highlight potential imprints of *shallow* subsurficial processes on the deep-seated signatures of discharging hyperalkaline fluids through mixing. Shallow portions of the *discharge* zone could be hotspots for subsurface life that may bloom where reduced deep-seated fluids encounter oxidized shallow aquifer fluids. As systems with contrasting oxidation-reduction potentials meet, habitability is defined by the extent to which such systems fail to equilibrate abiotically, leaving opportunities for microbial communities to exploit.

In contrast, some fluids with pH values between 9 and 11 do not correspond to mixing trends between end-member fluids. Rather than forming through mixing, these fluids may be indicative of intermediate stages of serpentinization. As this stage of reaction progress corresponds to incipient serpentinization and the carbonation of ultramafic rocks, further focus on this fluid type could help inform potential studies targeting ultramafic aquifers as hosts for deep storage of sequestered atmospheric $CO_2$ (Kelemen and Matter, 2008; Matter and Kelemen, 2009; Kelemen et al., 2011; National Academies, 2019). In addition, targeting fluids with these compositions will also reveal information on reactions that facilitate the transformation of oxic surface fluids into reduced, deep-seated, hyperalkaline fluids as they infiltrate deeper into the aquifer. Conditions for habitable environments may exist through this fluid transformation and future exploration of this fluid type will provide insights into the habitability of *recharge* zones of the fluid pathway and how they differ from *discharge* zones and their surface expressions. The Oman Drilling Project (omandrilling.ac.uk, Kelemen et al., 2013) recently drilled several wells that tap into fluids indicative of various stages of serpentinization and is poised to reveal a comprehensive assessment of microbial communities powered by rock and fluid interactions in the ultramafic subsurface. Models from this work can be used to assess these samples. We also propose the practicality of measuring both pH and Si concentrations with field-portable equipment, allowing rapid assessment of fluid type and extents of mixing while in the field, which can augment exploration with real-time information.

We demonstrated that the compositions of serpentinization-generated fluids can be partly accounted for by predictions of fluid-mineral equilibria and showed how processes such as leaching and fluid mixing can account for compositions that deviate from equilibrium expectations. Both water and ultramafic rocks are believed to abound in ice-covered ocean worlds in our Solar System such as Europa and Enceladus, and serpentinization is thought to enable habitable environments in these terrestrial bodies as it does on Earth (Vance et al., 2007; Holms et al., 2015; Glein et al., 2015; Waite et al., 2017). By demonstrating that simulations of low-temperature serpentinization can be successfully applied at analogous processes here on Earth, this work substantiates these calculations as useful tools in exploring serpentinization reactions beyond our own planet.

Finally, further work on the kinetics of low-temperature serpentinization, whether determined through laboratory experiments or in the field, will ultimately provide stronger constraints on the rate of energy transfer between the lithosphere and the subsurface biosphere. Rates will also feed into reactive transport simulations that could improve upon the calculations described here and reveal how various transport processes contribute to the overall compositions of serpentinization-generated fluids.

### 3.7. Acknowledgments

Samples used in this study were gathered with the help of Peter Kelemen, Juerg Matter, Amelia Paukert Vankeuren, Lisa Streit, Peter Canovas, Jeff Havig, and Peter Marsala. We also would like to thank Natasha Zolotova and Roy Erikson for help in analysis of fluid samples at the ASU GEOPIG laboratory, W.M. Keck Foundation Laboratory for Environmental Biogeochemistry, and Goldwater Environmental Laboratory. Thanks also to Tucker Ely, Vincent Milesi, and Grayson Boyer for helpful discussions on computational tools used in this study. This work was supported by NASA

Exobiology grant NNX12AB38G, the NASA Astrobiology Institute Rock-Powered Life project, and NSF grant EAR-1515513.

Table 3.1

*Field and Laboratory Measurements For Samples Collected in This Study*

| **Sample Number** | **Site** | **pH** | **T** | **Cond** | **$\delta^{18}O$** | **$\delta^{2}H$** | **DO** | **$Fe^{+2}$** | **$S^{-2}$** | **DIC** | **$F^{-}$** | **$Cl^{-}$** | **$Br^{-}$** |
|---|---|---|---|---|---|---|---|---|---|---|---|---|---|
| | | | °C | μS/cm | (‰ VSMOW) | (‰ VSMOW) | μmolal | μmolal | μmolal | mmolal | μmolal | mmolal | μmolal |
| ***Fluids with pH between 7 to 9*** | | | | | | | | | | | | | |
| 100112AI | Al Bana | 8.5 | 29 | 467 | 3.97 | 15.35 | n.m. | n.m. | 0.33 | 2.62 | 1.05 | 1.16 | b.d.l. |
| 140110B | Dima | 8.4 | 23.5 | 568 | 1.49 | 6.99 | 244 | 0.36 | 0.34 | 3.63 | b.d.l. | 1.58 | 1.10 |
| 090118P | Dima | 8.8 | 20.2 | 973 | 2.58 | 13.43 | n.m. | n.m. | n.m. | 3.68 | 2.11 | 5.54 | 3.63 |
| 140114S | Falaij | 7.7 | 21 | 787 | -0.28 | 3.63 | 172 | 0.36 | b.d.l. | 4.39 | b.d.l. | 3.19 | 1.80 |
| 100107C | Masibt | 9.3 | 25.4 | 778 | -0.86 | -0.59 | 250 | n.m. | 6.89 | 1.93 | 1.74 | 3.71 | b.d.l. |
| 100107D | Masibt | 8.6 | 25.6 | 809 | -0.81 | -1.16 | n.m. | n.m. | n.m. | 3.08 | 3.14 | 2.98 | b.d.l. |
| 090120W | Masibt | 8.7 | 24.2 | 811 | -0.70 | -3.00 | n.m. | n.m. | n.m. | 2.83 | 3.05 | 3.41 | 1.86 |
| 140111G | Qafifah | 8.9 | 22.6 | 586 | 0.25 | 4.94 | 222 | 0.36 | 0.09 | 4.11 | b.d.l. | 1.53 | 1.04 |
| 120114O | Qafifah | 8.7 | 23 | 454.4 | 0.62 | 3.91 | 381 | n.m. | b.d.l. | 2.82 | 0.46 | 1.30 | 2.23 |
| 100109X | Qafifah | 8.9 | 23.3 | 664 | -0.34 | 3.39 | 197 | n.m. | 0.39 | 4.49 | 0.94 | 1.71 | b.d.l. |
| 090119S | Qafifah | 9.0 | 21.6 | 493.3 | 1.43 | 7.80 | 238 | n.m. | n.m. | 2.05 | b.d.l. | 2.08 | 1.30 |
| 090119T | Qafifah | 8.6 | 24.8 | 527 | 1.37 | 6.31 | 213 | n.m. | n.m. | 2.78 | b.d.l. | 1.94 | 1.25 |
| 140116B | Shumayt | 7.9 | 26.5 | 760 | 0.33 | 0.39 | 125 | 0.90 | 0.25 | 5.13 | b.d.l. | 1.28 | 0.82 |
| 140116C | Shumayt | 8.7 | 27.3 | 777 | 0.07 | 0.35 | 228 | 0.36 | 0.63 | 4.75 | b.d.l. | 1.54 | 0.93 |
| 120116Q | Shumayt | 7.7 | 25 | 744 | 1.07 | 7.47 | 288 | n.m. | 0.33 | 5.22 | 0.43 | 1.28 | 0.24 |
| 100113AP | Shumayt | 7.9 | 27 | 723 | 0.94 | 4.91 | 100 | n.m. | b.d.l. | 5.17 | 1.58 | 1.43 | b.d.l. |
| 090123E | Shumayt | 8.2 | 23.9 | 700 | 0.93 | 5.38 | n.m. | n.m. | n.m. | 4.96 | b.d.l. | 1.37 | 0.84 |
| 100114AR | Sudari | 8.8 | 21.5 | 923 | 0.14 | 3.00 | 284 | n.m. | 0.27 | 3.04 | b.d.l. | 5.19 | b.d.l. |
| 090122B | Sudari | 8.8 | 17.1 | 1440 | 0.05 | 1.54 | n.m. | n.m. | n.m. | 3.25 | b.d.l. | 9.36 | 3.43 |
| 100115AW | Uqaybah | 8.5 | 17.5 | 911 | 0.26 | -1.26 | n.m. | n.m. | n.m. | n.m. | b.d.l. | 7.36 | b.d.l. |
| ***Fluids with pH between 9 and 11*** | | | | | | | | | | | | | |
| 140110D | Dima | 10.4 | 21.8 | 778 | 0.69 | 3.73 | 203 | 0.18 | 1.31 | 0.81 | 0.31 | 4.79 | 4.70 |
| 140112L | Dima | 9.8 | 21.3 | 659 | 1.06 | 6.17 | 253 | 0.72 | 0.22 | 1.88 | 0.88 | 3.75 | 3.48 |
| 090118N | Dima | 9.7 | 17.5 | 864 | 1.15 | 8.10 | n.m. | n.m. | n.m. | 2.32 | b.d.l. | 6.63 | 4.68 |
| 100107E | Masibt | 10.1 | 26.9 | 910 | -1.75 | -4.63 | n.m. | n.m. | n.m. | 0.68 | 1.05 | 4.86 | b.d.l. |
| 090120X | Masibt | 10.6 | 27.7 | 962 | -0.98 | -4.45 | n.m. | n.m. | n.m. | 0.15 | 11.2 | 5.41 | 2.45 |
| 140111H | Qafifah | 10.2 | 20.2 | 597 | 0.20 | 4.46 | 278 | 0.18 | 1.22 | 1.80 | 2.55 | 3.08 | 1.89 |
| 140111I | Qafifah | 10.9 | 18.8 | 683 | 0.61 | 6.36 | 231 | b.d.l. | 2.03 | 0.85 | 0.17 | 3.69 | 2.36 |
| 120114N | Qafifah | 9.8 | 21.8 | 667 | -0.32 | 0.65 | 463 | n.m. | 0.64 | 2.24 | 0.36 | 3.17 | 0.89 |
| 100109T | Qafifah | 9.6 | 23.7 | 685 | -0.19 | 3.04 | 219 | n.m. | 0.54 | 3.56 | 0.50 | 2.38 | b.d.l. |
| 100109W | Qafifah | 10.3 | 20.8 | 696 | 0.24 | 5.83 | n.m. | n.m. | n.m. | 1.93 | 0.86 | 3.35 | b.d.l. |
| 090117J | Qafifah | 10.6 | 18.8 | 823 | -0.75 | 2.41 | 31.9 | n.m. | n.m. | 1.78 | 26.4 | 4.44 | 2.52 |
| 140116D | Shumayt | 9.1 | 27.1 | 777 | -0.02 | 0.40 | 216 | 0.18 | 0.66 | 3.98 | b.d.l. | 1.92 | 1.13 |
| 120116R | Shumayt | 10.6 | 25.8 | 767 | -0.72 | 1.89 | 350 | n.m. | 0.97 | 0.76 | 0.04 | 3.51 | 0.83 |
| 100113AN | Shumayt | 10.2 | 28.6 | 720 | -0.27 | 1.53 | 191 | n.m. | 1.36 | 1.66 | 0.60 | 3.32 | b.d.l. |
| 100113AO | Shumayt | 10.4 | 27.4 | 734 | -0.01 | 2.31 | 169 | n.m. | 0.76 | 1.40 | 0.46 | 3.56 | b.d.l. |
| 090123G | Shumayt | 10.6 | 27.6 | 712 | -0.45 | 1.17 | n.m. | n.m. | n.m. | 0.59 | 9.95 | 3.55 | 1.73 |
| 090122A | Sudari | 10.9 | 17.4 | 1215 | -0.72 | -2.38 | n.m. | n.m. | n.m. | 0.46 | 6.16 | 7.83 | 2.97 |
| 090122C | Sudari | 10.8 | 18.5 | 1154 | -1.10 | -3.04 | n.m. | n.m. | n.m. | 0.35 | b.d.l. | 7.97 | 3.22 |
| ***Hyperalkaline Spring Fluids (pH > 11)*** | | | | | | | | | | | | | |
| 140115X | Al Bana | 11.4 | 29.5 | 2949 | -0.95 | -2.31 | 43.8 | 13.30 | 6.97 | 0.03 | b.d.l. | 11.4 | 5.36 |
| 140115Y | Al Bana | 11.6 | 24.5 | 2778 | -0.83 | -1.55 | 141 | 20.10 | 3.59 | 0.11 | b.d.l. | 11.8 | 5.49 |
| 140115Z | Al Bana | 11.3 | 32.2 | 4050 | -0.10 | -2.08 | 34.4 | 12.40 | 6.25 | 0.03 | b.d.l. | 12.6 | 9.19 |
| 120118Y | Al Bana | 11.5 | 32.5 | 3343 | 0.04 | -2.47 | 35.4 | n.m. | 5.44 | 0.12 | b.d.l. | 6.80 | 1.27 |
| 120118Z | Al Bana | 11.4 | 30.6 | 2140 | -0.75 | -0.70 | 81.3 | n.m. | 7.56 | 0.12 | b.d.l. | 9.85 | 1.44 |
| 120129G | Al Bana | 11.0 | 37.3 | 1455 | -1.50 | -4.77 | n.m. | n.m. | n.m. | 0.05 | 0.01 | 5.11 | 1.04 |
| 120129H | Al Bana | 11.4 | 38.2 | 1616 | -1.60 | -5.61 | n.m. | n.m. | n.m. | 0.04 | 0.01 | 3.41 | 0.27 |
| 100111AA | Al Bana | 11.7 | 28.5 | 3400 | -0.94 | -2.33 | 59.4 | n.m. | 7.80 | 0.04 | b.d.l. | 12.0 | b.d.l. |

| | | | | | | | | | | | | | |
|---|---|---|---|---|---|---|---|---|---|---|---|---|---|
| 100111AB | Al Bana | 11.7 | 25.4 | 2770 | -1.02 | -1.94 | 188 | n.m. | 2.78 | 0.13 | 1.01 | 12.3 | b.d.l. |
| 100111AC | Al Bana | 11.6 | 16.5 | 1873 | 0.20 | 3.18 | 272 | n.m. | 0.24 | 0.69 | 0.75 | 11.6 | 2.52 |
| 100111AD | Al Bana | 11.6 | 32.4 | 3235 | -0.29 | -2.64 | 31.3 | n.m. | 5.41 | 0.05 | b.d.l. | 13.0 | b.d.l. |
| 100111AE | Al Bana | 11.9 | 18.9 | 2468 | 0.03 | -0.68 | 250 | n.m. | 0.24 | 0.07 | b.d.l. | 13.4 | 5.49 |
| 100111AF | Al Bana | 11.9 | 24.2 | 2850 | -0.74 | -1.98 | n.m. | n.m. | n.m. | 0.10 | b.d.l. | 11.0 | b.d.l. |
| 100112AG | Al Bana | 11.1 | 37.7 | 1421 | -1.24 | -3.38 | 9.75 | n.m. | 3.21 | 0.04 | 8.06 | 5.73 | b.d.l. |
| 100112AH | Al Bana | 11.2 | 38.4 | 1537 | -1.72 | -4.16 | 50.0 | n.m. | 3.48 | 0.05 | 1.13 | 5.77 | 1.31 |
| 090116F | Al Hilayw | 11.8 | 26.3 | 2250 | 0.14 | 4.93 | 43.8 | n.m. | n.m. | 0.11 | 24.9 | 9.37 | 3.64 |
| 090116G | Al Hilayw | 11.8 | 27.1 | 2230 | 0.17 | 3.77 | 31.3 | n.m. | n.m. | 2.80 | 14.1 | 9.11 | 3.84 |
| 090116H | Al Hilayw | 11.5 | 24.5 | 1890 | 1.26 | 9.70 | 253 | n.m. | n.m. | 0.57 | b.d.l. | 10.6 | 4.43 |
| 090116I | Al Hilayw | 11.9 | 20.7 | 2200 | 0.29 | 6.34 | n.m. | n.m. | n.m. | 0.18 | 15.5 | 9.36 | 2.79 |
| 100121BB | Al Khoud | 10.9 | 39 | 2630 | -1.30 | -8.48 | n.m. | n.m. | n.m. | n.m. | b.d.l. | 16.7 | 4.67 |
| 140110C | Dima | 11.4 | 27 | 2011 | -0.10 | -0.07 | 17.9 | 13.1 | 13.7 | 0.05 | b.d.l. | 7.45 | 7.84 |
| 140112K | Dima | 11.4 | 26.9 | 1870 | -0.77 | -2.10 | 8.63 | 12.2 | 16.7 | 0.04 | b.d.l. | 7.16 | 7.83 |
| 140112M | Dima | 11.4 | 28.2 | 2058 | -0.64 | -0.45 | 15.8 | 8.77 | 16.1 | 0.05 | b.d.l. | 7.36 | 7.91 |
| 090118O | Dima | 11.5 | 30.3 | 1905 | -0.60 | -0.42 | n.m. | n.m. | n.m. | 0.13 | 5.53 | 7.56 | 6.57 |
| 140113O | Falaij | 11.4 | 28.4 | 2329 | -0.52 | 0.83 | 59.4 | 10.6 | 5.84 | 0.06 | b.d.l. | 7.92 | 5.94 |
| 140113P | Falaij | 11.5 | 25.9 | 2224 | -0.54 | 0.98 | 50.0 | 15.6 | 1.97 | 0.05 | b.d.l. | 7.90 | 5.68 |
| 140114R | Falaij | 11.6 | 21.1 | 1844 | -0.72 | 0.62 | 34.4 | 11.3 | 1.87 | 0.04 | b.d.l. | 7.10 | 4.55 |
| 140114T | Falaij | 11.4 | 27.2 | 2061 | -0.71 | 1.58 | 16.3 | 13.1 | 17.7 | 0.04 | b.d.l. | 6.89 | 4.43 |
| 140114U | Falaij | 11.4 | 21.7 | 1479 | 0.24 | 4.27 | 219 | 0.18 | 3.41 | 0.17 | 1.17 | 4.72 | 4.58 |
| 140114V | Falaij | 11.4 | 24.4 | 1803 | -0.21 | 2.90 | 191 | 15.6 | 8.31 | 0.23 | 0.40 | 6.98 | 4.65 |
| 120111A | Falaij | 11.6 | 22.3 | 1737 | -0.07 | 2.02 | 463 | n.m. | 0.85 | 0.09 | 0.06 | 4.62 | 1.34 |
| 120111B | Falaij | 11.4 | 29.4 | 1912 | -0.41 | 1.46 | 369 | n.m. | 5.41 | 0.09 | 0.04 | 6.39 | 2.12 |
| 120111C | Falaij | 11.3 | 31.9 | 1889 | -0.45 | 0.81 | 93.8 | n.m. | 13.7 | 0.07 | 0.04 | 4.94 | 1.67 |
| 120113I | Falaij | 11.4 | 30 | 2276 | -0.30 | 0.70 | 68.8 | n.m. | 8.07 | 0.14 | 0.02 | 7.24 | 2.46 |
| 120113J | Falaij | 11.6 | 25.8 | 2343 | -0.21 | 1.87 | 275 | n.m. | 0.85 | 0.09 | 0.02 | 3.56 | 0.92 |
| 120113K | Falaij | 11.4 | 30.9 | 2364 | 0.72 | 4.97 | 356 | n.m. | 0.15 | 0.12 | 0.06 | 6.10 | 2.07 |
| 120113L | Falaij | 11.3 | 28.4 | 2297 | 1.66 | 9.71 | 744 | n.m. | b.d.l. | 0.16 | 0.08 | 10.3 | 4.14 |
| 100108J | Falaij | 11.7 | 23.9 | 2214 | -0.33 | 1.91 | 188 | n.m. | 5.65 | 0.05 | b.d.l. | 8.58 | b.d.l. |
| 100108K | Falaij | 11.7 | 24.7 | 2266 | -0.47 | 2.00 | 172 | n.m. | 5.02 | 0.07 | b.d.l. | 8.35 | b.d.l. |
| 100108L | Falaij | 11.6 | 29.2 | 2442 | 0.49 | 4.01 | 10.2 | n.m. | 5.96 | 0.07 | b.d.l. | 8.44 | b.d.l. |
| 100108M | Falaij | 11.7 | 26 | n.m. | 0.27 | 3.55 | 163 | n.m. | n.m. | 0.08 | b.d.l. | 9.99 | 2.04 |
| 100108N | Falaij | 11.6 | 27.6 | 2380 | -0.05 | 1.83 | n.m. | n.m. | n.m. | 0.04 | b.d.l. | 8.28 | b.d.l. |
| 100108O | Falaij | 11.8 | 22 | 2179 | 0.16 | 2.33 | n.m. | n.m. | n.m. | 0.07 | 0.73 | 8.70 | b.d.l. |
| 100108P | Falaij | 11.5 | 23.3 | 1507 | 0.67 | 5.48 | n.m. | n.m. | n.m. | 0.06 | 0.48 | 7.92 | b.d.l. |
| 100108Q | Falaij | 11.6 | 22.9 | 1752 | 0.18 | 4.44 | n.m. | n.m. | n.m. | 0.08 | b.d.l. | 7.59 | b.d.l. |
| 100108R | Falaij | 11.6 | 27.9 | 1967 | 0.99 | 3.57 | n.m. | n.m. | n.m. | 0.06 | b.d.l. | 7.28 | b.d.l. |
| 090115A | Falaij | 11.5 | 29.1 | 2251 | -0.42 | 0.16 | n.m. | n.m. | n.m. | 0.10 | 25.2 | 8.27 | 4.42 |
| 090115B | Falaij | 11.7 | 24.1 | 2154 | -0.40 | 0.97 | n.m. | n.m. | n.m. | 0.12 | 44.8 | 8.45 | 3.05 |
| 090115C | Falaij | 11.7 | 25.1 | 2280 | -0.73 | 0.89 | n.m. | n.m. | n.m. | 0.06 | b.d.l. | 8.21 | 4.19 |
| 090115D | Falaij | 11.8 | 20.7 | 2270 | -0.09 | 2.14 | n.m. | n.m. | n.m. | 0.16 | 9.32 | 8.45 | 4.58 |
| 090115E | Falaij | 11.8 | 18 | 2240 | -0.36 | 1.00 | n.m. | n.m. | n.m. | 0.12 | 72.9 | 8.53 | 3.83 |
| 100107A | Masibt | 11.3 | 32.4 | 1900 | -2.19 | -8.41 | 2.78 | n.m. | 117 | 0.11 | b.d.l. | 7.25 | b.d.l. |
| 100107B | Masibt | 11.3 | 30.3 | 1848 | -0.92 | -5.13 | 46.9 | n.m. | 83.3 | 0.11 | 0.56 | 7.31 | b.d.l. |
| 090120U | Masibt | 11.4 | 31.4 | 1676 | -1.74 | -7.86 | 9.38 | n.m. | n.m. | 0.11 | 9.26 | 7.10 | 3.10 |
| 090120V | Masibt | 11.4 | 30.6 | 1616 | -1.68 | -8.84 | n.m. | n.m. | n.m. | 0.05 | 24.6 | 7.13 | 2.93 |
| 140111F | Qafifah | 11.6 | 23.8 | 1470 | -0.61 | 1.07 | 8.59 | b.d.l. | 6.78 | 0.04 | 2.58 | 4.66 | 2.98 |
| 120112E | Qafifah | 11.3 | 30.1 | 1762 | -0.56 | 1.06 | 150 | n.m. | 1.69 | 0.07 | 0.02 | 3.38 | 0.93 |
| 120112F | Qafifah | 11.4 | 27.4 | 1781 | -0.70 | 0.82 | 37.8 | n.m. | 4.96 | 0.11 | 0.03 | 4.32 | 1.29 |
| 120112H | Qafifah | 11.3 | 31.9 | 1893 | -0.56 | 1.41 | n.m. | n.m. | n.m. | 0.07 | 0.25 | 4.79 | 1.69 |
| 100109S | Qafifah | 11.8 | 22.4 | 1685 | -0.37 | 1.30 | 81.3 | n.m. | 1.94 | 0.10 | 1.26 | 5.32 | b.d.l. |
| 100109U | Qafifah | 11.7 | 24.9 | 1778 | -0.80 | 0.90 | 12.5 | n.m. | 6.56 | 0.12 | b.d.l. | 5.06 | b.d.l. |
| 100109V | Qafifah | 11.2 | 23.7 | 904 | 0.41 | 6.03 | n.m. | n.m. | 3.66 | 0.66 | 0.63 | 4.25 | b.d.l. |
| 090117K | Qafifah | 11.7 | 18.5 | 1074 | -0.32 | 4.18 | n.m. | n.m. | n.m. | 0.24 | 9.74 | 5.30 | 2.49 |
| 090117M | Qafifah | 11.7 | 22.6 | 1649 | -0.62 | 2.41 | n.m. | n.m. | n.m. | n.m. | 5.63 | 5.22 | 2.68 |
| 090119Q | Qafifah | 11.7 | 23.2 | 1797 | -0.52 | -0.82 | 40.63 | n.m. | n.m. | 0.13 | 16.7 | 5.29 | 2.42 |
| 090119R | Qafifah | 11.6 | 16.6 | 911 | n.m. | n.m. | 253 | n.m. | n.m. | 0.24 | 37.1 | 5.27 | 2.78 |
| 140117F | Shumayt | 11.5 | 26.2 | 1868 | -2.04 | -6.01 | 25.0 | 12.0 | 4.72 | 0.03 | b.d.l. | 5.35 | 3.12 |
| 140117G | Shumayt | 11.4 | 30.5 | 2015 | -2.20 | -6.28 | 9.88 | 11.5 | 3.75 | 0.02 | b.d.l. | 5.33 | 3.13 |

| | | | | | | | | | | | | | |
|---|---|---|---|---|---|---|---|---|---|---|---|---|---|
| 140117H | Shumayt | 11.5 | 29.6 | 2067 | -2.06 | -4.91 | 21.9 | 13.1 | 5.47 | 0.03 | b.d.l. | 5.77 | 3.70 |
| 140117I | Shumayt | 11.3 | 32.3 | 2000 | -2.22 | -5.23 | 12.5 | 13.8 | 3.25 | 0.05 | b.d.l. | 5.32 | 3.13 |
| 140117J | Shumayt | 11.3 | 31.6 | 1387 | -1.79 | -4.14 | 31.3 | 6.98 | 2.31 | 0.07 | b.d.l. | 4.71 | 2.82 |
| 140117K | Shumayt | 11.5 | 27.4 | 1980 | -2.13 | -4.51 | 37.5 | 10.9 | 3.16 | 0.03 | b.d.l. | 5.76 | 3.77 |
| 140117L | Shumayt | 11.6 | 27.3 | 2087 | -2.15 | -4.33 | 21.9 | 8.95 | 3.59 | 0.02 | b.d.l. | 5.81 | 4.17 |
| 120116P | Shumayt | 11.2 | 34.3 | 1745 | -2.10 | -4.28 | 46.6 | n.m. | 2.81 | 0.06 | 0.02 | 4.49 | 1.06 |
| 120116S | Shumayt | 11.4 | 29.5 | 1729 | -1.87 | -3.95 | 25.0 | n.m. | 3.84 | 0.08 | 0.03 | 4.58 | 0.65 |
| 120117T | Shumayt | 11.3 | 32.6 | 1721 | -2.12 | -4.06 | 22.5 | n.m. | 2.87 | 0.04 | b.d.l. | 3.28 | 0.49 |
| 120117U | Shumayt | 11.3 | 32 | 1720 | -2.05 | -4.19 | 8.56 | n.m. | 3.51 | 0.04 | 0.01 | 5.15 | 1.41 |
| 120117V | Shumayt | 11.7 | 23.6 | 1951 | -1.67 | -2.21 | 37.5 | n.m. | 2.18 | 0.08 | 0.02 | 5.40 | 1.52 |
| 120117X | Shumayt | 11.3 | 32.8 | 1681 | -2.18 | -5.07 | 25.9 | n.m. | 2.18 | 0.01 | 0.01 | 5.10 | 1.51 |
| 100112AJ | Shumayt | 11.5 | 33.4 | 1782 | -2.22 | -5.33 | n.m. | n.m. | 3.05 | 0.05 | 0.58 | 5.58 | 1.46 |
| 100112AK | Shumayt | 11.5 | 33.3 | 1793 | -2.63 | -5.79 | n.m. | n.m. | n.m. | 0.04 | 0.80 | 5.57 | 1.78 |
| 100112AL | Shumayt | 11.5 | 32.6 | 1772 | -2.45 | -5.20 | n.m. | n.m. | n.m. | 0.04 | 1.35 | 5.54 | b.d.l. |
| 100112AM | Shumayt | 11.5 | 31.5 | 1772 | -1.97 | -4.66 | 13.1 | n.m. | 3.17 | 0.04 | 0.59 | 5.51 | 2.74 |
| 090123D | Shumayt | 11.5 | 34 | 1778 | -1.93 | -4.70 | n.m. | n.m. | n.m. | 0.09 | 7.68 | 5.35 | 2.44 |
| 090123F | Shumayt | 11.6 | 28.1 | 1770 | -1.57 | -3.96 | n.m. | n.m. | n.m. | 0.14 | 11.1 | 5.61 | 2.40 |
| 100114AS | Sudari | 11.3 | 18.2 | 1013 | 0.91 | 0.48 | 256 | n.m. | 0.91 | 0.47 | 0.28 | 6.12 | b.d.l. |
| 100114AT | Sudari | 11.6 | 30.4 | 1893 | -1.88 | -7.27 | 106 | n.m. | 2.00 | 0.04 | b.d.l. | 6.33 | b.d.l. |
| 100114AU | Sudari | 11.6 | 20.08 | 1258 | -0.91 | -3.64 | 244 | n.m. | 1.00 | 0.07 | b.d.l. | 6.24 | b.d.l. |
| 090122Z | Sudari | 11.6 | 29.5 | 1897 | -2.20 | -7.87 | 87.5 | n.m. | n.m. | 0.11 | 63.4 | 6.02 | 1725 |
| 100115AV | Uqaybah | 11.6 | 21.4 | 1442 | -1.19 | -8.79 | n.m. | n.m. | n.m. | n.m. | b.d.l. | 6.99 | b.d.l. |
| | | | | | | ***Well Fluids*** | | | | | | | |
| 120119B | NSHQ-14 | 10.1 | 24 | 855 | -0.21 | -1.71 | 93.8 | n.m. | 0.45 | 0.07 | 0.22 | 4.27 | 2.50 |
| 120119A | NSHQ-14 | 11.1 | 29.1 | 1920 | 0.64 | 0.89 | 45.8 | n.m. | b.d.l. | 0.09 | 0.13 | 7.68 | 7.61 |
| 120119C | NSHQ-14 | 11.0 | 33.7 | 2296 | 0.31 | -0.05 | 42.1 | n.m. | 1.69 | 0.08 | 0.11 | 8.12 | 8.33 |
| 120123E | NSHQ-04 | 10.7 | 28.3 | 3327 | -1.38 | -3.65 | n.m. | n.m. | n.m. | 0.39 | 0.36 | 7.58 | 4.47 |
| 120126F | WDA-16 | 8.0 | 31.8 | 492 | -0.48 | 0.11 | n.m. | n.m. | n.m. | 0.28 | 0.97 | 0.80 | 0.79 |
| 120127G | WDA-17 | 9.2 | 31 | 532 | -0.56 | 0.76 | n.m. | n.m. | n.m. | 2.35 | 0.06 | 1.16 | 0.32 |
| 120130I | WDA-05 | 9.3 | 32.7 | 595 | -0.76 | -0.72 | n.m. | n.m. | n.m. | 1.90 | 0.10 | 2.03 | 0.52 |
| 120130J | WDA-05 | 9.4 | 32.1 | 610 | -0.49 | 0.21 | n.m. | n.m. | n.m. | 1.80 | 0.07 | 2.00 | 0.49 |
| 100119AX | SJA-04B | 7.2 | 33.8 | 598 | -2.54 | -10.09 | n.m. | n.m. | n.m. | n.m. | 8.22 | 1.15 | b.d.l. |
| 100119AY | SJA-04A | 7.6 | 34 | 491 | -3.11 | -9.94 | n.m. | n.m. | n.m. | n.m. | 4.49 | 0.76 | b.d.l. |
| 100120AZ | SJA-03 | 9.4 | 34.1 | 586 | -1.00 | -4.91 | n.m. | n.m. | n.m. | n.m. | b.d.l. | 2.24 | b.d.l. |

b.d.l. - below detection limit; n.m. - not measured; IS – ionic strength (mmolal); IB – ionic imbalance (% charge)

[a] All samples were analyzed using the ICP-OES except for those with sample number starting with "14" which were analyzed using the IC.

[b] All samples were analyzed using the ICP-MS, except for these with sample number starting with "14" which were analyzed using the IC.

[c] All samples were analyzed using the ICP-OES except for those with sample number starting with "14" which were analyzed using the ICP-MS.

[d] Field and analytical data for most samples taken in 2020 were reported in Canovas et al. (2017), except for Ca, Mg, Si, and isotopic values.

[e] Also sampled by Paukert et al. (2012) during the same fieldwork but all reported field and analytical data except that for DIC and Al were determined independently by this work. Name of sample in Paukert et al. (2012) is indicated at the last column.

[f] Also sampled by Paukert et al. (2019) during the same fieldwork but all reported field and analytical data except that for Al were determined independently by this work. Name of sample in Paukert et al. (2019) is indicated at the last column.

Table 3.1. (cont'd.)

| Sample Number | $SO_4^{-2}$ | $NO_3^-$ | $NO_2^-$ | $Li^+$ | $Na^+$ | $NH_4^+$ | $K^+$ | $Mg^{+2a}$ | $Ca^{+2b}$ | $Si^{+4c}$ | $Al^{+3}$ | IS | IB | |
|---|---|---|---|---|---|---|---|---|---|---|---|---|---|---|
| | µmolal | µmolal | µmolal | µmolal | mmolal | µmolal | mmolal | µmolal | mmolal | µmolal | µmolal | | | |
| ***Fluids with pH between 7 to 9*** | | | | | | | | | | | | | | |
| 100112AI | 464 | 154 | b.d.l. | 7.64 | 0.81 | b.d.l. | 0.03 | 1602 | 0.37 | 200 | 0.07 | 7 | -2 | [e] 10_06AI |
| 140110B | 346 | 62.5 | 0.30 | 0.17 | 1.31 | b.d.l. | 0.04 | 1840 | 0.49 | 183 | 0.22 | 8 | -1 | |
| 090118P | 345 | b.d.l. | b.d.l. | 0.50 | 4.35 | b.d.l. | 0.10 | 2148 | 0.42 | 169 | 2.71 | 12 | -3 | [e] 09_W06P |
| 140114S | 443 | 116 | 0.22 | 0.56 | 3.20 | 0.31 | 0.11 | 2010 | 0.60 | 200 | 0.15 | 11 | 1 | |
| 100107C | 734 | 211 | 4.26 | 0.81 | 3.81 | b.d.l. | 0.09 | 1445 | 0.33 | 289 | 2.19 | 9 | -3 | [de] 10_01C |
| 100107D | 822 | 323 | 348 | 10.10 | 3.24 | b.d.l. | 0.07 | 1522 | 0.84 | 347 | 0.12 | 11 | -3 | [de] 10_01D |
| 090120W | 820 | 261 | n.m. | 1.09 | 3.36 | b.d.l. | 0.09 | 1691 | 0.72 | 397 | 1.67 | 11 | 0 | |
| 140111G | 326 | 49.0 | 0.31 | 0.53 | 1.53 | 0.57 | 0.04 | 2140 | 0.36 | 276 | 0.13 | 9 | -2 | |
| 120114O | 311 | 78.3 | b.d.l. | 0.65 | 1.19 | b.d.l. | 0.04 | 1451 | 0.30 | 138 | 0.42 | 7 | -3 | |
| 100109X | 381 | 79.5 | 0.40 | 7.20 | 1.76 | b.d.l. | 0.03 | 2290 | 0.40 | 283 | 0.07 | 10 | -3 | [de] 10_04X |
| 090119S | 300 | 56.3 | n.m. | 0.50 | 2.03 | b.d.l. | 0.06 | 1227 | 0.17 | 116 | 1.04 | 6 | -1 | [e] 09_W08S |
| 090119T | 343 | 161 | n.m. | 0.50 | 1.84 | b.d.l. | 0.05 | 1541 | 0.26 | 239 | 1.15 | 7 | -2 | |
| 140116B | 696 | 170 | 0.45 | 0.43 | 1.06 | 0.23 | 0.10 | 2810 | 0.56 | 303 | 0.15 | 11 | 0 | |
| 140116C | 680 | 160 | b.d.l. | 0.55 | 1.37 | 1 | 0.10 | 2680 | 0.63 | 279 | 0.12 | 11 | -1 | |
| 120116Q | 646 | 99 | 0.14 | 0.86 | 1.00 | 1 | 0.08 | 2908 | 0.51 | 309 | 0.12 | 11 | 2 | |
| 100113AP | 727 | 122 | 0.77 | 6.92 | 1.16 | b.d.l. | 0.08 | 2680 | 0.58 | 288 | 0.32 | 11 | -2 | [de] 10_08AP |
| 090123E | 748 | 247 | n.m. | 0.97 | 1.08 | b.d.l. | 0.09 | 2664 | 0.51 | 305 | 2.48 | 11 | -4 | |
| 100114AR | 519 | 14.4 | b.d.l. | 7.92 | 5.43 | b.d.l. | 0.10 | 1485 | 0.45 | 78.5 | 0.08 | 11 | 0 | [de] 10_09AR |
| 090122B | 678 | 6.52 | n.m. | 3.03 | 8.90 | b.d.l. | 0.17 | 1777 | 0.12 | 97.2 | 2.19 | 16 | -5 | [e] 09_W12B |
| 100115AW | 138 | b.d.l. | b.d.l. | 4.61 | 4.51 | b.d.l. | 0.14 | 314 | 1.65 | 33.9 | 0.15 | 10 | 6 | [e] 10_10AW |
| ***Fluids with pH between 9 and 11*** | | | | | | | | | | | | | | |
| 140110D | 180 | 27 | b.d.l. | 0.23 | 4.92 | 6.61 | 0.14 | 782 | 0.48 | 91.4 | 0.24 | 8 | 5 | |
| 140112L | 243 | 37 | b.d.l. | 0.21 | 3.72 | 3.38 | 0.11 | 1150 | 0.31 | 111 | 0.25 | 8 | -2 | |
| 090118N | 196 | b.d.l. | n.m. | 0.56 | 6.22 | b.d.l. | 0.17 | 1115 | 0.26 | 74.6 | 2.41 | 11 | -5 | [e] 09_W06N |
| 100107E | 498 | 180 | b.d.l. | 10.70 | 4.89 | b.d.l. | 0.10 | 885 | 0.14 | 214 | 6.67 | 8 | -3 | [de] 10_01E |
| 090120X | 431 | 133 | n.m. | 0.75 | 5.05 | b.d.l. | 0.12 | 810 | 0.95 | 186 | 4.04 | 10 | 8 | |
| 140111H | 182 | 13 | 0.16 | 1.29 | 3.59 | 3.80 | 0.08 | 1170 | 0.21 | 145 | 0.13 | 8 | -1 | |
| 140111I | 154 | 8 | 0.30 | 1.50 | 4.36 | 5.97 | 0.10 | 807 | 0.37 | 100 | 0.13 | 7 | 5 | |
| 120114N | 207 | 9 | 0.68 | 1.74 | 3.78 | 1.13 | 0.08 | 1082 | 0.28 | 133 | 0.09 | 8 | -1 | |
| 100109T | 334 | 52 | b.d.l. | 7.42 | 2.83 | b.d.l. | 0.05 | 1924 | 0.04 | 226 | 0.09 | 9 | -8 | [d] |
| 100109W | 208 | 24 | 0.67 | 8.15 | 4.15 | b.d.l. | 0.07 | 1192 | 0.27 | 119 | 0.07 | 8 | 0 | [e] 10_04W |
| 090117J | 207 | 8 | n.m. | 2.29 | 5.16 | b.d.l. | 0.11 | 994 | 0.04 | 104 | 1.67 | 9 | -7 | |
| 140116D | 612 | 142 | 0.07 | 0.75 | 1.86 | 2.54 | 0.10 | 2430 | 0.72 | 260 | 0.12 | 10 | 2 | |
| 120116R | 266 | 34 | 0.48 | 2.36 | 4.26 | 8.03 | 0.12 | 807 | 0.19 | 83.4 | 0.24 | 7 | 3 | |
| 100113AN | 399 | 45 | b.d.l. | 8.11 | 3.83 | b.d.l. | 0.11 | 1433 | 2.17 | 157 | 0.40 | 11 | 25 | [de] 10_08AN |
| 100113AO | 362 | 49 | b.d.l. | 8.17 | 4.18 | b.d.l. | 0.11 | 1298 | 0.52 | 138 | 0.05 | 9 | 5 | [de] 10_08AO |
| 090123G | 356 | 65 | n.m. | 1.77 | 3.94 | b.d.l. | 0.12 | 1535 | 0.60 | 176 | 4.56 | 9 | 17 | |
| 090122A | 347 | 11 | n.m. | 3.03 | 8.22 | b.d.l. | 0.17 | 860 | 0.49 | 36.3 | 5.86 | 12 | 5 | |
| 090122C | 296 | 13 | n.m. | 3.17 | 8.79 | b.d.l. | 0.19 | 305 | 1.35 | 17.8 | 4.48 | 12 | 12 | |
| ***Hyperalkaline Spring Fluids (pH > 11)*** | | | | | | | | | | | | | | |
| 140115X | 4.75 | 0.35 | b.d.l. | 2.68 | 13.9 | 58.7 | 0.32 | 0.45 | 1.89 | 2.22 | 0.92 | 18 | 7 | |
| 140115Y | 9.99 | 1.61 | 1.83 | 2.73 | 14.3 | 50.5 | 0.33 | 1.26 | 1.79 | 2.16 | 0.30 | 19 | 6 | |
| 140115Z | 2.63 | 0.12 | b.d.l. | 5.24 | 17.1 | 87.6 | 0.33 | 0.41 | 2.37 | 1.38 | 0.15 | 22 | 13 | |
| 120118Y | 2.18 | 0.39 | 0.35 | 5.60 | 9.24 | 12.2 | 0.19 | 1.02 | 1.88 | 2.36 | 0.41 | 14 | 2 | |
| 120118Z | 6.37 | 0.63 | 0.63 | 3.16 | 12.1 | 19.4 | 0.27 | 0.70 | 1.50 | 2.96 | 0.49 | 16 | 5 | |
| 120129G | 1.32 | 0.62 | 0.44 | 3.34 | 5.19 | 6.25 | 0.15 | 0.63 | 1.48 | 2.82 | 0.32 | 9 | 2 | |
| 120129H | 1.00 | 0.28 | b.d.l. | 3.61 | 3.79 | 2.72 | 0.10 | 0.51 | 1.41 | 2.89 | 0.45 | 10 | -22 | |
| 100111AA | 4.10 | b.d.l. | 2.01 | 26.4 | 15.1 | b.d.l. | 0.26 | 0.28 | 1.66 | 1.79 | 0.15 | 20 | 0 | [de] 10_05AA |

| | | | | | | | | | | | | | |
|---|---|---|---|---|---|---|---|---|---|---|---|---|---|
| 100111AB | 9.54 | b.d.l. | b.d.l. | 21.8 | 15.7 | b.d.l. | 0.28 | 0.79 | 1.61 | 2.45 | 0.52 | 20 | 0 | [de] 10_05AB |
| 100111AC | 123 | 1.95 | b.d.l. | 15.3 | 14.6 | b.d.l. | 0.29 | 181 | 0.33 | 38.1 | 0.05 | 16 | 2 | [de] 10_05AC |
| 100111AD | 2.08 | b.d.l. | b.d.l. | 34.6 | 18.1 | b.d.l. | 0.27 | 0.28 | 2.18 | 0.55 | 0.10 | 24 | 3 | [de] 10_05AD |
| 100111AE | 12.8 | 3.27 | b.d.l. | 30.1 | 18.3 | b.d.l. | 0.29 | 1.46 | 0.73 | 7.84 | 0.34 | 20 | 2 | [de] 10_05AE |
| 100111AF | 5.72 | b.d.l. | b.d.l. | 21.90 | 15.4 | b.d.l. | 0.22 | 1.74 | 1.64 | 2.49 | 0.28 | 21 | -2 | [e] 10_05AF |
| 100112AG | 1.13 | 4.28 | b.d.l. | 9.94 | 6.14 | b.d.l. | 0.15 | 0.65 | 1.73 | 1.37 | 0.07 | 11 | 0 | [de] 10_06AG |
| 100112AH | 0.93 | b.d.l. | b.d.l. | 16.6 | 6.75 | b.d.l. | 0.14 | 0.34 | 1.58 | 1.43 | 0.13 | 11 | 0 | [de] 10_06AH |
| 090116F | 40.8 | 434 | n.m. | 2.22 | 11.4 | 43.5 | 0.31 | 0.81 | 1.22 | 4.28 | 5.41 | 17 | -10 | [e] 09_W04F |
| 090116G | 28.4 | 21.4 | n.m. | 2.18 | 11.1 | b.d.l. | 0.27 | 0.79 | 1.12 | 3.35 | 5.41 | 19 | -27 | [e] 09_W04G |
| 090116H | 46.5 | 3.13 | n.m. | 2.45 | 13.0 | b.d.l. | 0.28 | 0.87 | 0.30 | 27.8 | 4.67 | 15 | -5 | |
| 090116I | 48.1 | 55.6 | n.m. | 2.31 | 11.4 | b.d.l. | 0.27 | 0.42 | 0.85 | 14.7 | 6.67 | 16 | -10 | [e] 09_W04I |
| 100121BB | 807 | b.d.l. | b.d.l. | 13.7 | 17.8 | b.d.l. | 0.14 | 0.02 | 2.22 | 23.1 | 11.5 | 24 | 3 | |
| 140110C | 10.8 | 0.47 | b.d.l. | 0.36 | 7.91 | 19.8 | 0.22 | 1.30 | 1.96 | 4.26 | 0.82 | 13 | 5 | |
| 140112K | 18.4 | 0.11 | 0.11 | 0.38 | 7.59 | 22.7 | 0.21 | 2.24 | 1.89 | 3.88 | 0.97 | 13 | 5 | |
| 140112M | 10.7 | 0.06 | b.d.l. | 0.35 | 7.89 | 21.1 | 0.22 | 0.67 | 1.98 | 5.60 | 1.33 | 13 | 5 | |
| 090118O | 8.31 | b.d.l. | n.m. | 0.95 | 8.09 | b.d.l. | 0.22 | 1.82 | 1.07 | 11.3 | 4.41 | 13 | -13 | [e] 09_W06O |
| 140113O | 3.84 | 0.18 | b.d.l. | 2.01 | 9.40 | 33.6 | 0.25 | 1.07 | 2.09 | 3.68 | 0.54 | 15 | 7 | |
| 140113P | 7.82 | 3.47 | 0.77 | 1.79 | 9.53 | 29.2 | 0.25 | 1.28 | 2.03 | 1.94 | 0.23 | 15 | 8 | |
| 140114R | 21.1 | 11.2 | 0.76 | 1.53 | 8.10 | 19.8 | 0.23 | 1.46 | 1.85 | 2.44 | 0.44 | 13 | 7 | |
| 140114T | 13.5 | 0.62 | 1.16 | 1.56 | 7.97 | 30.6 | 0.22 | 1.83 | 1.91 | 1.84 | 0.17 | 13 | 7 | |
| 140114U | 176 | 26.2 | 0.14 | 1.62 | 8.09 | 11.9 | 0.22 | 16.1 | 1.17 | 7.43 | 0.07 | 10 | 19 | |
| 140114V | 17.7 | 1.28 | 0.86 | 1.63 | 8.43 | 20.3 | 0.22 | 5.60 | 1.71 | 2.75 | 0.15 | 12 | 9 | |
| 120111A | 13.1 | 10.7 | 1.67 | 2.29 | 5.33 | 3.30 | 0.14 | 2.04 | 1.31 | 7.88 | 0.47 | 9 | -1 | |
| 120111B | 12.9 | 2.21 | 1.35 | 2.25 | 7.38 | 6.47 | 0.20 | 1.32 | 1.71 | 4.46 | 0.40 | 12 | 4 | |
| 120111C | 9.52 | 0.77 | 1.47 | 2.23 | 5.41 | 5.40 | 0.15 | 1.07 | 1.72 | 6.40 | 0.49 | 11 | -1 | |
| 120113I | 7.19 | 0.91 | 0.62 | 2.54 | 8.85 | 6.61 | 0.22 | 2.42 | 1.71 | 3.29 | 0.23 | 13 | 5 | |
| 120113J | 4.76 | 2.21 | 2.79 | 2.38 | 4.20 | 3.71 | 0.10 | 0.59 | 1.72 | 3.82 | 0.69 | 9 | -3 | |
| 120113K | 10.8 | 2.18 | 10.7 | 2.61 | 7.53 | 1.74 | 0.19 | 0.45 | 1.60 | 20.4 | 3.04 | 12 | -1 | |
| 120113L | 8.84 | 14.2 | 1.96 | 3.30 | 12.79 | 1.53 | 0.33 | 0.96 | 0.73 | 26.4 | 2.82 | 15 | 3 | |
| 100108J | 6.51 | b.d.l. | 0.14 | 31.4 | 10.4 | b.d.l. | 0.22 | 1.97 | 1.89 | 1.73 | 0.13 | 16 | 1 | [de] 10_02J |
| 100108K | 4.77 | b.d.l. | b.d.l. | 30.5 | 10.4 | b.d.l. | 0.22 | 1.78 | 1.87 | 1.60 | 0.07 | 16 | 1 | [de] 10_02K |
| 100108L | 5.05 | b.d.l. | b.d.l. | 27.9 | 10.6 | b.d.l. | 0.22 | 0.70 | 1.94 | 0.89 | 0.09 | 16 | 0 | [de] 10_02L |
| 100108M | 13.3 | 18.80 | b.d.l. | 33.7 | 12.7 | b.d.l. | 0.30 | 0.46 | 1.95 | 7.02 | 1.67 | 18 | 1 | |
| 100108N | 5.80 | b.d.l. | b.d.l. | 29.5 | 10.4 | b.d.l. | 0.21 | 0.89 | 1.75 | 0.43 | 0.12 | 16 | 0 | |
| 100108O | 7.18 | b.d.l. | b.d.l. | 31.1 | 10.8 | b.d.l. | 0.23 | 1.12 | 1.92 | 0.98 | 0.15 | 16 | 2 | |
| 100108P | 34.2 | b.d.l. | b.d.l. | 15.4 | 9.61 | b.d.l. | 0.21 | 15.3 | 0.56 | 7.48 | 0.37 | 12 | -1 | [e] 10_03P |
| 100108Q | 25.3 | b.d.l. | b.d.l. | 15.1 | 9.19 | b.d.l. | 0.20 | 6.36 | 1.19 | 2.47 | 0.10 | 13 | 1 | [e] 10_03Q |
| 100108R | 15.9 | b.d.l. | b.d.l. | 14.8 | 8.89 | b.d.l. | 0.18 | 1.27 | 1.70 | 0.78 | 0.10 | 14 | -4 | [e] 10_03R |
| 090115A | 11.9 | 16.4 | n.m. | 4.61 | 9.66 | b.d.l. | 0.25 | 34.7 | 2.07 | 21.9 | 63.4 | 16 | 1 | |
| 090115B | 3.37 | 47.6 | n.m. | 2.10 | 9.81 | b.d.l. | 0.27 | 1.23 | 1.69 | 3.68 | 5.30 | 15 | 0 | |
| 090115C | 13.6 | 134 | n.m. | 8.64 | 9.61 | b.d.l. | 0.25 | 41.0 | 2.21 | 10.6 | 36.7 | 16 | 0 | |
| 090115D | 23.7 | 6.89 | n.m. | 2.31 | 9.90 | b.d.l. | 0.26 | 4.44 | 1.55 | 5.13 | 5.63 | 15 | -2 | |
| 090115E | 19.1 | 827 | n.m. | 2.12 | 10.0 | 48.5 | 0.27 | 1.86 | 1.70 | 3.49 | 5.26 | 15 | -1 | |
| 100107A | 69.9 | b.d.l. | b.d.l. | 21.3 | 7.18 | b.d.l. | 0.12 | 0.21 | 2.06 | 37.2 | 22.6 | 13 | -1 | [de] 10_01A |
| 100107B | 63.7 | b.d.l. | b.d.l. | 21.5 | 7.16 | b.d.l. | 0.14 | 6.31 | 1.91 | 39.3 | 23.3 | 13 | 0 | [de] 10_01B |
| 090120U | 67.2 | 3.03 | n.m. | 1.77 | 6.58 | b.d.l. | 0.14 | 102 | 1.95 | 50.5 | 36.7 | 13 | -5 | |
| 090120V | 81.7 | 41.3 | n.m. | 1.35 | 6.62 | 21.1 | 0.16 | 22.3 | 1.67 | 45.0 | 23.0 | 13 | -8 | [e] 09_W10V |
| 140111F | 11.3 | 1.49 | b.d.l. | 2.05 | 5.86 | 15.5 | 0.14 | 3.82 | 1.69 | 10.5 | 0.25 | 11 | 2 | |
| 120112E | 1.87 | 0.19 | 0.45 | 3.16 | 4.20 | 1.64 | 0.10 | 0.68 | 1.74 | 5.56 | 0.54 | 9 | 8 | |
| 120112F | 4.14 | 0.31 | 0.28 | 3.07 | 5.45 | 3.09 | 0.13 | 1.93 | 1.72 | 4.62 | 0.27 | 10 | 7 | |
| 120112H | 9.52 | 0.42 | 0.22 | 2.87 | 6.33 | 1.60 | 0.14 | 0.74 | 1.80 | 31.5 | 0.79 | 11 | 6 | |
| 100109S | 3.71 | 3.60 | b.d.l. | 15.8 | 7.03 | b.d.l. | 0.13 | 0.54 | 1.59 | 3.77 | 0.63 | 12 | -2 | [de] 10_04S |
| 100109U | 4.57 | b.d.l. | b.d.l. | 15.4 | 6.90 | b.d.l. | 0.11 | 1.23 | 1.51 | 0.47 | 0.35 | 12 | -5 | [de] 10_04U |
| 100109V | 121 | 14.1 | b.d.l. | 8.37 | 5.60 | b.d.l. | 0.10 | 347 | 0.47 | 51.7 | 0.26 | 8 | 0 | [e] 10_04V |

|  |  |  |  |  |  |  |  |  |  |  |  |  |  |  |
|---|---|---|---|---|---|---|---|---|---|---|---|---|---|---|
| 090117K | 58.9 | 135 | b.d.l. | 1.87 | 6.60 | b.d.l. | 0.14 | 74.5 | 0.25 | 25.3 | 1.85 | 9 | -11 |  |
| 090117M | 3.54 | b.d.l. | b.d.l. | 2.58 | 6.41 | b.d.l. | 0.15 | 6.65 | 1.52 | 3.82 | 5.63 | 11 | 0 |  |
| 090119Q | 14.5 | 47.1 | n.m. | 2.23 | 6.76 | b.d.l. | 0.15 | 56.5 | 1.82 | 24.0 | 15.6 | 12 | 0 |  |
| 090119R | 74.0 | 132 | n.m. | 0.69 | 6.89 | b.d.l. | 0.15 | 10.5 | 0.20 | 20.2 | 2.37 | 8 | -6 |  |
| 140117F | 3.64 | 0.44 | 0.06 | 2.70 | 6.41 | 18.3 | 0.15 | 1.94 | 1.85 | 2.65 | 0.25 | 11 | 6 |  |
| 140117G | 1.38 | 0.02 | b.d.l. | 2.62 | 6.27 | 19.5 | 0.15 | 0.79 | 1.90 | 1.50 | 0.13 | 12 | 4 |  |
| 140117H | 1.58 | 0.11 | b.d.l. | 2.59 | 7.14 | 23.5 | 0.16 | 1.04 | 2.08 | 1.66 | 0.13 | 13 | 3 |  |
| 140117I | 6.46 | 0.10 | b.d.l. | 2.61 | 6.28 | 19.4 | 0.15 | 8.09 | 1.86 | 1.96 | 0.12 | 11 | 4 |  |
| 140117J | 111 | 0.08 | b.d.l. | 2.33 | 5.83 | 16.9 | 0.14 | 19.5 | 0.83 | 48.9 | 0.06 | 9 | -7 |  |
| 140117K | 1.58 | 0.09 | b.d.l. | 2.58 | 7.16 | 21.3 | 0.16 | 1.48 | 2.08 | 2.26 | 0.23 | 13 | 7 |  |
| 140117L | 1.60 | 0.10 | b.d.l. | 2.79 | 7.33 | 22.7 | 0.16 | 1.47 | 2.14 | 1.87 | 0.19 | 13 | 5 |  |
| 120116P | 1.78 | 0.87 | 0.38 | 3.28 | 5.45 | 5.31 | 0.13 | 2.49 | 1.67 | 1.70 | 0.38 | 10 | 4 |  |
| 120116S | 4.38 | 0.22 | 0.39 | 3.37 | 5.61 | 5.45 | 0.13 | 4.54 | 1.70 | 2.23 | 0.13 | 10 | 5 |  |
| 120117T | 1.13 | 0.59 | 0.67 | 3.49 | 4.01 | 3.69 | 0.09 | 1.48 | 1.65 | 2.08 | 0.43 | 9 | 2 |  |
| 120117U | 1.78 | 0.80 | 0.35 | 3.63 | 6.25 | 6.86 | 0.15 | 0.87 | 1.65 | 1.77 | 0.39 | 11 | 2 |  |
| 120117V | 2.21 | 3.76 | 0.70 | 3.26 | 6.81 | 5.64 | 0.14 | 0.68 | 1.75 | 3.63 | 0.61 | 12 | 1 |  |
| 120117X | 1.26 | 2.38 | 1.74 | 3.54 | 6.04 | 3.14 | 0.15 | 0.56 | 1.67 | 2.37 | 0.42 | 11 | 3 |  |
| 100112AJ | 1.30 | b.d.l. | b.d.l. | 15.1 | 7.13 | b.d.l. | 0.12 | 1.33 | 1.90 | 0.59 | 0.33 | 13 | -3 | [de] 10_07AJ |
| 100112AK | 0.61 | b.d.l. | b.d.l. | 16.0 | 7.06 | b.d.l. | 0.12 | 0.45 | 1.86 | 0.73 | 0.13 | 13 | -6 |  |
| 100112AL | 0.97 | b.d.l. | b.d.l. | 16.9 | 7.12 | b.d.l. | 0.12 | 0.44 | 1.82 | 0.57 | 0.07 | 13 | -7 |  |
| 100112AM | 1.04 | b.d.l. | b.d.l. | 16.7 | 7.13 | b.d.l. | 0.12 | 0.62 | 1.92 | 0.53 | 0.06 | 13 | -3 | [de] 10_08AM |
| 090123D | 2.60 | b.d.l. | n.m. | 0.97 | 6.48 | b.d.l. | 0.15 | 1.80 | 1.46 | 1.91 | 3.41 | 12 | -10 |  |
| 090123F | 4.51 | 2.77 | n.m. | 1.77 | 6.80 | b.d.l. | 0.16 | 1.86 | 1.50 | 1.55 | 5.97 | 12 | -6 | [e] 09_W13F |
| 100114AS | 221 | 12.3 | b.d.l. | 9.31 | 7.42 | b.d.l. | 0.14 | 291 | 0.30 | 22.7 | 0.04 | 9 | 0 | [de] 10_09AS |
| 100114AT | 12.10 | b.d.l. | b.d.l. | 16.4 | 8.40 | b.d.l. | 0.14 | 0.70 | 1.72 | 3.53 | 0.58 | 14 | -5 | [de] 10_09AT |
| 100114AU | 155 | 7.29 | b.d.l. | 9.70 | 7.80 | b.d.l. | 0.14 | 157 | 0.29 | 16.1 | 0.10 | 10 | -3 | [de] 10_09AU |
| 090122Z | 33.90 | b.d.l. | n.m. | 2.45 | 7.68 | 28.5 | 0.22 | 0.54 | 0.21 | 4.66 | 1.96 | 12 | -28 |  |
| 100115AV | 62.5 | 5.59 | b.d.l. | 4.55 | 4.75 | b.d.l. | 0.12 | 4.15 | 2.48 | 0.39 | 0.09 | 13 | -4 | [e] 10_10AV |
| ***Well Fluids*** |  |  |  |  |  |  |  |  |  |  |  |  |  |  |
| 120119B | 117 | 17.8 | 0.43 | 0.64 | 2.31 | 11.6 | 0.08 | 32.6 | 1.14 | 5.95 | 0.52 | 6 | 0 | [f] 12_03M |
| 120119A | 9.20 | 1.48 | 0.24 | 0.65 | 5.40 | 14.9 | 0.12 | 5.68 | 3.42 | 2.78 | 0.46 | 14 | 12 | [f] 12_03N |
| 120119C | 9.30 | 0.98 | 0.31 | 0.57 | 5.29 | 17.0 | 0.12 | 4.19 | 3.47 | 2.72 | 0.37 | 15 | 8 | [f] 12_03O |
| 120123E | 420 | 0.27 | 0.22 | 3.00 | 4.05 | 75.1 | 0.11 | 10.2 | 7.73 | 8.29 | 0.75 | 22 | 35 | [f] 12_04P |
| 120126F | 327 | 187 | 12.5 | 0.60 | 1.17 | b.d.l. | 0.05 | 1420 | 0.38 | 456 | 0.34 | 5 | 44 | [f] 12_05S |
| 120127G | 674 | 84 | b.d.l. | 1.28 | 0.85 | 1.58 | 0.04 | 2218 | 0.05 | 1.48 | 0.29 | 7 | 0 | [f] 12_06T |
| 120130I | 724 | 129 | b.d.l. | 0.88 | 1.32 | 0.51 | 0.07 | 2458 | 0.05 | 4.53 | 0.12 | 8 | 4 | [f] 12_08Z |
| 120130J | 746 | 119 | b.d.l. | 0.92 | 1.31 | 0.34 | 0.06 | 2419 | 0.05 | 4.42 | 0.10 | 8 | 4 | [f] 12_07Y |
| 100119AX | 371 | 219 | b.d.l. | 4.18 | 1.26 | b.d.l. | 0.04 | 1273 | 1.06 | 375 | 0.09 | 7 | 49 | [f] 10_11AX |
| 100119AY | 255 | 204 | 3.89 | 4.32 | 0.78 | b.d.l. | 0.04 | 1123 | 0.96 | 366 | 0.09 | 5 | 55 | [f] 10_11AY |
| 100120AZ | 994 | 107 | b.d.l. | 3.96 | 1.58 | b.d.l. | 0.05 | 2100 | 0.03 | 4.38 | 0.07 | 8 | 16 | [ef] 10_12AZ |

# CHAPTER 4

# PREDICTION OF ENERGY AND POWER SUPPLIES FOR SUBSURFACE MICROORGANISMS IN LOW-TEMPERATURE CONTINENTAL SERPENTINIZATION ENVIRONMENTS

## 4.1. Introduction

The continental subsurface hosts a significant portion of Earth's microbial biomass (Gold, 1992; Whitman et al., 1998; McMahon and Parnell, 2014; Bar-on et al., 2018; Magnabosco et al., 2018) that is estimated to be on par or even greater than those living in sub-seafloor environments (Whitman et al., 1998; Lipp et al., 2008; Kallmeyer et al., 2012; Parkes et al., 2014; Bar-on et al., 2018) and other continental environments such as those in soils (Whitman et al., 1998; Bar-on et al., 2018). The significance of microbial ecosystems hosted beneath Earth's landmasses raises questions on the limits of life deep in the subsurface where carbon and energy sources can be limited. Unlike most organisms on the surface, subsurface communities acquire their energy independently from photosynthesis through chemotrophic reactions supported by water-rock interactions (Stevens and McKinley, 1995; Kotelnikova, 2002; Moser et al., 2005; Lin et al., 2006; Osburn et al., 2014; Magnabosco et al., 2016; Lau et al., 2016). A pertinent example is when serpentinization of ultramafic rocks generates fluids rich in reduced gases, such as $H_2$ and $CH_4$, that can support subsurface lithoautotrophic microbial ecosystems (SLiMEs, *e.g.*, Nealson et al., 2005). In the process of serpentinization, ferrous iron in the rocks is oxidized to ferric iron in secondary minerals and in turn, $H_2O$ is reduced into $H_2$, generating some of the most reduced fluids on Earth (McCollom and Bach, 2009; Klein et al., 2013; Leong and Shock, 2020). Consequently, at $H_2$-rich conditions, methane is favored to form from inorganic and other organic carbon sources. Serpentinization is a pertinent process as it can proceed even at the ambient low-temperature conditions characteristic of most continental aquifers on Earth, without the added input of heat from magmatic bodies that characterize more well-known hydrothermal systems. Overall, serpentinization is an attractive process that can facilitate transfer of energy from the lithosphere to the biosphere as it can proceed spontaneously with only two requirements – liquid water and ultramafic rocks, and can enable habitable environments in the deep subsurface and perhaps even in rocky bodies beyond our planet.

While the environment generated by serpentinization is enriched in electron donors, microbial communities encounter limitations in electron acceptors and inorganic carbon sources due to the reduced and hyperalkaline nature of serpentinization-generated fluids. Infiltrating fluids from the surface or shallow aquifers in communication with the atmosphere as well as through dissolution of minerals (*e.g.*, carbonates, sulfates) can ultimately supply electron acceptors and support microbial ecosystems in the deep serpentinizing aquifers. In addition, surfacing reduced deep-seated fluids can potentially encounter oxic shallow aquifer fluids in discharge zones of fluid pathways. The enormous redox disequilibria generated when these fluids mix at these subsurface settings can support many chemotrophic strategies similar to those observed in mixing systems at the surface and seafloor like those surrounding hydrothermal vents. So far, chemotrophic energy supplies in serpentinizing environments have been quantified from a number of surface expressions of deep-seated serpentinization processes in submarine (*e.g.*, hydrothermal vents; McCollom, 2007; Amend et al., 2011; Nakamura and Takai., 2014) and continental (*e.g.*, hyperalkaline spring and well fluids, Cardace et al., 2015;

Canovas et al., 2017; Crespo-Medina et al., 2017; Sabuda et al., 2020; Boyd et al., 2020) settings. In continental settings, hyperalkaline fluids normally occur along fault zones and lithological boundaries that tap into deep aquifers and facilitate the transport of these deep-seated fluids onto the surface where they usually seep out from outcropping rocks as springs (Dewandel et al., 2005). In this work we quantified energy available to chemolithotrophs in hyperalkaline seeps in Oman and expand findings from the above previous work. In addition, we provide the first estimations of energy supplies in gabbro-hosted fluids and discuss how these energy supplies compare to those available in ultramafic-hosted fluids.

While hyperalkaline spring fluids provide a glimpse of the energetic supplies that can be available in deep serpentinizing aquifers, subsurface geochemical energies can be best quantified through analysis of deep-seated fluids. However, data on pristine deep-seated fluids obtained through wells are currently limited. Recent efforts to sample subsurface fluids through deep wells in serpentinizing environments (*e.g.*, CROMO in California and the Oman Drilling Project in Oman, Cardace et al., 2013; Crespo-Medina et al., 2014; Seyler et al., 2020; Sabuda et al., 2020; Oman, Miller et al., 2016; Rempfert et al., 2017; Fones et al., 2019) are starting to populate datasets concerning fluid and microbial compositions of the deep serpentinizing subsurface. Uncertainties in surficial or shallow surficial inputs on deep-seated signatures are also currently unknown. Analyses of several deep well samples in the Oman ophiolite by Miller et al. (2016) and Rempfert et al. (2017) reveal the presence of oxidized aqueous species (dissolved sulfate, nitrate, oxygen, inorganic carbon) that could be introduced by atmospheric and/or shallow groundwater infiltration. Meanwhile, an extensive dataset that includes both surficial and well fluids sampled from serpentinizing and surrounding environments can be used to predict compositions of end-member subsurface fluids. In this work, we used a large compositional dataset of fluids sampled from the Oman ophiolite in combination with calculations of fluid-mineral-gas equilibria to derive end-member compositions of fluids representative of the *shallow* and *deep* serpentinizing aquifers. Predicted composition of shallow-seated fluids that occur in the highly fractured shallow aquifers (<50 m, Dewandel et al., 2005) are in equilibrium with the atmosphere while estimated deep-seated fluids occurring in deeper aquifers (>500 m, Dewandel et al., 2005) result from advanced stages of the serpentinization process and are devoid of atmospheric and shallow aquifer inputs. Available energy supplies through various redox reactions are quantified using these predicted end-member compositions, as well as when these end-member fluids mix at discharge zones of the subsurface fluid pathway, permitting estimates on maximum energy available when these two fluids of extremely different redox potentials encounter each other. These models were also used to assess where certain metabolic strategies are favored over others along the mixing gradient. Lastly, we quantified the rate at which energy is supplied to autotrophic and hydrogenotrophic methanogens living in the deep subsurface and estimate the amount of biomass such power supply can support given constraints in the supply of inorganic carbon available through the dissolution of various carbonate minerals.

## 4.2. Methods

### *4.2.1. Quantification of Energy Supplies*

Chemotrophic microorganisms obtain their energy sources through chemical reactions. In conditions where the forward direction of a reaction is favored due to disequilibrium between the reactants and products, energy can be supplied to chemotrophic microorganisms such as in the case for the aerobic oxidation of hydrogen or the Knall-gas reaction,

$$2H_2 + O_2 \rightarrow H_2O. \tag{4.1}$$

$H_2$ produced through serpentinization is out of equilibrium with the amount of $O_2$ expected in the surface, driving reaction (1) forward and yielding energy that can be used by hydrogen oxidizers such as those belonging to the genus *Hydrogenophaga* that are ubiquitous in many serpentinizing environments (Schrenk et al., 2013). Serpentinization provides a pertinent case to study how chemical disequilibrium translates to microbial energy supplies as it generates some of the most reduced fluids on Earth even at the low temperature conditions that characterize most of Earth's continental aquifers. Substantial amounts of energy can be supplied to microorganisms when these reduced fluids, enriched in $H_2$ and other reduced species (methane, sulfide, ammonia), encounter oxic fluids common in the surface and shallow aquifers and are enriched in electron acceptors such as dissolved $O_2$, inorganic carbon, sulfate, and nitrate. Aside from the aerobic oxidation of hydrogen (reaction 4.1), we quantified disequilibria and resulting energy yields per mass of fluid (calories/kg fluid) via 16 other chemolithotrophic reactions (reactions 4.2 – 4.17) that are detected or inferred to be present in serpentinizing environments, as summarized in Table 4.1 and described in detail in Appendix C of this work. While these 17 reactions are not exhaustive of metabolic strategies known in serpentinizing environments (see Appendix C), available geochemical data used in this work limit evaluation of energy supplies via other strategies such as those involving organic compounds. Nevertheless, applying future constraints on these species into our models, described below, will permit a more complete understanding on the various energy sources available to microbial communities in subsurface serpentinizing environments.

Table 4.1

*List of Chemolithotrophic Reactions used in This Work and Supporting Evidence For The Presence of a Given Chemolithotrophic Process in Serpentinizing Environments.*

| **Name** | **Reaction** | | **Sites and References** |
|---|---|---|---|
| | | **Aerobic Reactions** | |
| Hydrogen Oxidation | 4.1 | $2H_2 + O_2 \rightarrow 2H_2O$ | The Cedars, CA, USA (Suzuki et al., 2013[V]; 2014[I]; 2017[IV]); Lost City, Mid-Atlantic Ridge (Brazelton et al., 2011[IV]); Tablelands ophiolite, Canada (Brazelton et al., 2012[IV]; 2013[IV,V]); CROMO, CA, USA (Twing et al., 2017[IV]); Voltri Massif, Italy (Brazelton et al., 2017[IV]); Cabeco de Vide, Portugal (Tiago and Veríssimo, 2013[V]); Leka ophiolite, Norway (Daae et al., 2013[V]); Santa Elena ophiolite, Costa Rica (Sanchez-Murillo et al., 2014[V]); Prony Bay, New Caledonia (Quéméneur et al., 2014[V]); Voltri Massif, Italy (Quéméneur et al., 2015[V]); Samail ophiolite, Oman (Miller et al., 2016[V]; Rempfert et al., 2017[V]); Zambales ophiolite, Philippines (Woycheese et al., 2015[V]); Rizoulis et al., (2016[V]); Outokumpu deep borehole, Finland (Itavaara et al., 2011[V]); Tekirova ophiolite (Neubeck et al., 2017[V]); Lake Calumet, IL, USA (Ohlsson et al., 2019[IV,V])* |
| Methane Oxidation | 4.2 | $CH_4 + 2O_2 \rightarrow CO_2 + 2H_2O$ | Voltri Massif, Italy (Brazelton et al., 2017[IV]); CROMO, CA, USA (Seyler et al., 2020[IV]); Santa Elena ophiolite, Costa Rica (Sanchez-Murillo et al., 2014[V]; Crespo-Medina et al., 2017[V]); Prony Bay, New Caledonia (Quéméneur et al., 2014[V]); Voltri Massif, Italy (Quéméneur et al., 2015[V]); Samail ophiolite, Oman (Miller et al., 2016[V]; Rempfert et al., 2017[V]); Tekirova ophiolite (Neubeck et al., 2017[V]); Zambales ophiolite (Woycheese et al., 2015[V]) |
| Carbon Monoxide Oxidation | 4.3 | $2CO + O_2 \rightarrow 2CO_2$ | Tablelands ophiolite, Canada (Brazelton et al., 2012[IV], 2013[V], Morril et al., 2014[II]); Lost City, Mid-Atlantic Ridge (Brazelton et al; 2012[IV]); CROMO, CA, USA (Twing et al., 2017[IV]); Samail ophiolite, Oman (Fones et al., 2019[II,IV]) |
| Sulfide Oxidation | 4.4 | $H_2S + 2O_2 \rightarrow SO_4^{-2} + 2H^+$ | Lost City, Mid-Atlantic Ridge (Brazelton and Baross, 2010[IV]); Cabeco de Vide, Portugal (Tiago and Veríssimo, 2013[IV]); CROMO, CA, USA (Sabuda et al., 2020[IV,V]); Prony Bay, New Caledonia (Quéméneur et al., 2014[V]) |
| Ammonia Oxidation | 4.5 | $NH_3 + 2O_2 \rightarrow NO_3^- + H^+ + H_2O$ | Lost City, Mid-Atlantic Ridge (Lincoln et al., 2013[III]); Leka ophiolite, Norway (Daae et al., 2013[V]); Prony Bay, New Caledonia (Quéméneur et al., 2014[V]); Voltri Massif, Italy (Quéméneur et al., 2015[V]); Zambales ophiolite, Philippines (Baculi et al., 2015[V]); Tekirova ophiolite (Neubeck et al., 2017[V]) |
| Nitrite Oxidation | 4.6 | $2NO_2^- + O_2 \rightarrow 2NO_3^-$ | Cabeco de Vide, Portugal (Tiago and Veríssimo, 2013[V]); Leka ophiolite, Norway (Daae et al., 2013[V]); Samail ophiolite, Oman (Rempfert et al., 2017[V]) |

|  |  |  |  |
|---|---|---|---|
| Iron Oxidation | 4.7 | $4Fe^{+2} + O_2 + 6H_2O \rightarrow 4FeOOH + 8H^+$ | Leka ophiolite, Norway (Daae et al., 2013$^{V}$); Zambales ophiolite, Philippines (Woycheese et al., 2015$^{V}$); Lake Calumet, IL, USA (Roadcap et al., 2006$^{V}$)* |
|  |  | **Anaerobic Reactions** |  |
| Hydrogenothrophic and Autotrophic Methanogenesis | 4.8 | $CO_2 + 4H_2 \rightarrow CH_4 + 2H_2O$ | Lost City, Mid-Atlantic Ridge (Brazelton et al., 2006$^{V}$; 2011$^{II}$); The Cedars, CA, USA (Kohl et al., 2016$^{II}$); Lost City, Mid-Atlantic Ridge (Bradley et al., 2009a$^{III}$; 2009b$^{III}$); Prony Bay, New Caledonia (Postec et al., 2015$^{III,IV}$; Quéméneur et al., 2014$^{IV}$); Voltri Massif, Italy (Brazelton et al., 2017$^{IV}$); Del Puerto ophiolite, CA, USA (Blank et al., 2009$^{V}$); Santa Elena ophiolite, Costa Rica (Sanchez-Murillo et al., 2014$^{V}$; Crespo-Medina et al., 2017$^{IV}$); Prony Bay, New Caledonia (Quéméneur et al., 2014$^{V}$; 2015$^{V}$); Samail ophiolite, Oman (Miller et al., 2016$^{V}$; Rempfert et al., 2017$^{V}$; Fones et al., 2019$^{II,IV}$); Zambales ophiolite, Philippines (Baculi et al., 2015$^{V}$, Woycheese et al., 2015$^{V}$); Voltri Massif, Italy (Quéméneur et al., 2015$^{V}$); Outokumpu deep borehole, Finland (Nyyssonen et al., 2014$^{V}$) |
| Sulfate Reduction | 4.9 | $SO_4^{-2} + 4H_2 + 2H^+ \rightarrow H_2S + 4H_2O$ | South Chamorro Seamount, Mariana Forearc (Mottl et al., 2003$^{III}$, Curtis et al., 2013$^{V}$); Lost City, Mid-Atlantic Ridge (Bradley et al., 2009b$^{III}$, Brazelton et al., 2006$^{V}$); Iberian Margin (fossil site, Klein et al., 2015$^{III}$); Prony Bay, New Caledonia (Quéméneur et al., 2014$^{IV,V}$; Postec et al., 2015$^{V}$); Del Puerto ophiolite, CA, USA (Blank et al., 2009$^{IV,V}$); The Cedars, CA, USA (Suzuki et al., 2017$^{IV}$); CROMO, CA, USA (Sabuda et al., 2020$^{IV,V}$); Cabeco de Vide, Portugal (Tiago and Veríssimo, 2013$^{IV,V}$); Voltri Massif, Italy (Brazelton et al., 2017$^{IV}$); Samail ophiolite, Oman (Miller et al., 2016$^{V}$; Rempfert et al., 2017$^{V}$) |
| Anaerobic Oxidation of Methane | 4.10 | $CH_4 + SO_4^{-2} + 2H^+ \rightarrow H_2S + CO_2 + 2H_2O$ | Lost City, Mid-Atlantic Ridge (Brazelton et al., 2011$^{II}$); Lost City, Mid-Atlantic Ridge (Bradley et al., 2009a$^{III}$; Lincoln et al., 2013$^{III}$); Prony Bay, New Caledonia (Quéméneur et al., 2014$^{IV}$; Postec et al., 2015$^{IV}$); Mariana Forearc (Curtis et al., 2013$^{V}$); Santa Elena Ophiolite (Crespo-Medina et al., 2017$^{V}$) Prony Bay, New Caledonia (Quéméneur et al., 2014$^{V}$; 2015$^{V}$); (?)Samail ophiolite, Oman (Miller et al., 2016$^{V}$; Rempfert et al., 2017$^{V}$); Voltri Massif, Italy (Quéméneur et al., 2015$^{V}$) |
|  | 4.11 | $5CH_4 + 8NO_3^- + 8H^+ \rightarrow 4N_2 + 5CO_2 + 14H_2O$ |  |
|  | 4.12 | $3CH_4 + 8NO_3^- + 8H^+ \rightarrow 4N_2 + 3CO_2 + 10H_2O$ |  |
| Nitrate Reduction | 4.13 | $NO_3^- + H^+ + 4H_2 \rightarrow NH_3 + 3H_2O$ | Tekirova ophiolite, Turkey (Meyer-Dombard et al., 2015$^{IV}$); The Cedars, CA, USA (Suzuki et al., 2017$^{IV}$) |
| Nitrogen Reduction | 4.14 | $N_2 + 3H_2 \rightarrow 2NH_3$ | Lost City, Mid-Atlantic Ridge (Brazelton et al., 2011$^{IV}$; Lang et al. 2013$^{G}$); Voltri Massif, Italy (Quéméneur et al., 2015$^{V}$); Zambales ophiolite, Philippines (Woycheese et al., 2015$^{V}$); Tekirova ophiolite, Turkey (Neubeck et al., 2017$^{V}$) |
| Water-Gas Shift | 4.15 | $CO + H_2O \rightarrow CO_2 + H_2$ | Samail ophiolite, Oman (Canovas et al., 2017$^{G}$) |
| Annamox | 4.16 | $NO_2^- + NH_3 + H^+ \rightarrow N_2 + 2H_2O$ | Samail ophiolite, Oman (Canovas et al., 2017$^{G}$) |
| Carbon Monoxide Reduction | 4.17 | $CO + 3H_2 \rightarrow CH_4 + H_2O$ | Samail ophiolite, Oman (Canovas et al., 2017$^{G}$) |

Note: We used classification scheme developed by Canovas et al. (2017) to distinguish evidences for a given chemolithotrophic metabolism in serpentizing environments: (I) physiological studies of isolates from natural systems; (II) experimental work probing enhanced redox rate of chemotrophic reactions relative to abiotic controls; (III) transcriptomic, proteomic, or biomarker studies that yield evidence of expression of genes attributed to a metabolic process; (IV) genomic work that identifies presence of genes attributed to a metabolic process; (V) community analysis through molecular techniques (*e.g.*, 16s rRNA) that identifies presence of microorganisms that could be capable of a given metabolic process; and (G) inferences using geochemical data (*e.g.*, affinity for a given metabolic reaction, geochemical or isotopic trends). * denotes study sites that are not produced through serpentinization but emulate the hyperalkaline nature of serpentinizing systems (also see Pedersen et al., 2004).

Chemical disequilibria yielding energy that can be harvested by catalyzing a given reaction is quantified by the chemical affinity ($A_r$) of that particular reaction. $A_r$ is defined as the change in the overall Gibbs free energy ($\Delta_r G$) over the change in the overall progress of reaction *r* ($\xi_r$),

$$A_r = -\left(\frac{\delta \Delta_r G}{\delta \xi_r}\right) \tag{4.18}$$

(de Donder, 1927; de Donder and Van Rysselberghe, 1936; Helgeson, 1979). The Gibbs free energy of reaction ($\Delta_r G$) is comprised of two components: (1) the standard state thermodynamic properties of the reactants and products in the reaction ($\Delta_r G°$), and the (2) ratio of activities of those reactants and products in a given environment ($Q_r$), yielding

$$\Delta_r G = \Delta_r G° + RTlnQ_r. \tag{4.19}$$

The standard Gibbs free energy of a reaction ($\Delta_r G°$), the first component of $\Delta_r G$, is related to the equilibrium constant, $K_r$, as expressed in the equation

$$\Delta_r G° = RTlnK_r\ . \tag{4.20}$$

In equations (4.19) and (4.20), R and T stand for the gas constant and temperature (in K), respectively. The activity ratio ($Q_r$) of the reactants and products of a reaction *r*, the second component of $\Delta_r G$, is as follows,

$$Q_r = \Pi_i (a_i)^{v_{i,r}} \tag{4.21}$$

where $a_i$ represents the activity of the *i*th compound in the reaction raised to its stoichiometric coefficient in the *r*th reaction, $v_{i,r}$, which is positive for products and negative for reactants. The activity ($a_i$) can be calculated from the molality of a given species *i* ($m_i$) and the activity coefficient ($\gamma_i$), as depicted by the equation

$$a_i = m_i \gamma_i. \tag{4.22}$$

In this work, activity coefficients were derived using the extended Debye-Hückel equation (Helgeson, 1969).

Combining equations (4.18), (4.19), and (4.20) will yield the following expression

$$A_r = RTln\left(\frac{K_r}{Q_r}\right). \tag{4.23}$$

A positive value for $A_r$ means that $K_r > Q_r$ or a negative value for $\Delta_r G$, and the forward direction of the reaction is favorable. Overall, the amount of energy that can be provided for by a reaction depends on how different the ratio of products and reactants determined from a study site (represented by $Q_r$) are from what it should be if it is in equilibrium (represented by $K_r$). The overall affinity yielded by various reactions can be normalized by the number of electrons transferred to compare different chemotrophic reactions in similar units (*i.e.*, calories per mole $e^-$, *e.g.*, see Shock et al., 2010; Canovas et al., 2017). If the limiting reactant in a given reaction is known, the amount of energy yielded per mass of fluid ($E_r$) can be derived by multiplying the concentration of the limiting reactant *l*, $m_l$ (in moles per kg of fluid), with the affinity of a reaction ($A_r$), taking into account the stoichiometry of the limiting reactant *l* in the reaction ($v_l$),

$$E_r = m_l\left(\frac{A_r}{v_l}\right), \tag{4.24}$$

as demonstrated by McCollom and Shock (1998), McCollom (1999, 2007), and Amend et al. (2011).

It would follow that deriving $A_r$ and $E_r$ available through various chemotrophic reactions for a given study site would require the following steps. (1) Firstly, we need to calculate the standard Gibbs free energy ($\Delta_r G°$) for a reaction given the temperature and pressure conditions of an investigated system. (2) Secondly, the concentration ($m_i$) of reactants and products *i* involved in the reactions need to be determined. (3) We also need to calculate the activities ($a_i$) of each reactant and product. This involves obtaining the activity coefficient ($\gamma_i$) for each reactant and product at the appropriate temperature, pressure, and ionic strength. The ionic strength can be determined if the concentration of each ion is known and thus a comprehensive measurement of solutes, not just those involved in each redox reaction, is required. Part (1) can be conducted using available calculators of standard Gibbs free energy such as SUPCRT (Johnson et al., 1992) and in the case for the present work, CHNOSZ (Dick, 2008; 2019). Both codes use standard state thermodynamic data for aqueous species taken from Shock and Helgeson (1988), Shock and others (1989, 1992, 1997), Sverjensky and others (1997), together with the revised Helgeson-Kirkham-Flowers equations of state (Shock and others, 1992) and data for minerals from Helgeson et al. (1978) and the mineral goethite (reaction 4.7) from Shock (2008). Parts (2) and (3) use analytical data from field samples as described in the next section.

### ***4.2.2. Aqueous Geochemistry***

Compositions of fluids from the Oman ophiolite used in quantification of energy supplies are taken from companion studies (Canovas et al., 2017; Howells, in prep; Chapter 3 of this document) of the present work. These studies provide a comprehensive set of chemical data needed to support calculations of energy yield for chemotrophic reactions listed in Table 4.1. This set of measurements includes pH, temperature, and concentrations of major and trace species as well as dissolved gaseous species ($O_2$, $H_2$, CO, $CH_4$). The pH, temperature, and concentrations of several redox-sensitive species (dissolved $O_2$, $Fe^{+2}$, sulfide) were measured in the field with portable meters and colorimeters. Major and trace species ($Na^+$, $K^+$, $Ca^{+2}$, $Mg^{+2}$, $Al^{+3}$, $Si^{+4}$, $NH_4^+$, $Cl^-$, $SO_4^{-2}$, $NO_3^-$, $NO_2^-$) were measured using ion chromatography (IC), inductively coupled plasma-mass spectroscopy, and inductively coupled plasma-optical emission spectroscopy (ICP-OES). Dissolved inorganic carbon (DIC) concentrations was measured using a wet oxidation total carbon analyzer. Dissolved $H_2$ and CO levels were determined through gas chromatography coupled with a reducing compound photometer (GC-RCP), while dissolved $CH_4$ concentrations were measured through a gas chromatograph with a flame ion detector (GC-FID). Results of measurements reported by the above companion studies are summarized in Table C1 in Appendix C while additional information on the study sites, sampling and analytical protocols, and instrumentation can be found in the above studies. Dissolved $N_2$ warranted for some chemotrophic reactions in Table 4.1 was not measured. Following findings of Boulart et al. (2013) where dissolved $N_2$ levels of stream and hyperalkaline fluids hosted in the Oman ophiolite are close to or above saturation with respect to atmospheric levels of $N_2$, 100% atmospheric saturation was assumed for all samples as a minimum constraint. Results from instrumental analysis were further processed, using the EQ3 speciation-solubility code (Wolery and Jarek, 2003) with the same thermodynamic data mentioned above, to derive ionic strengths, the activity of water, and the activity coefficients and activities of each of the dissolved species. All of these calculated values were used as inputs for calculations of available energy supplies via chemotrophic reactions listed in Table 4.1.

### 4.3. Compositions and Redox State of Oman Ophiolite-hosted Fluids

The pH of fluids investigated in this work and previously reported by companion works (Canovas et al., 2017; Howells, in prep; Chapter 3 of this work) ranges from 7 to

11.7 and includes a variety of fluid types hosted in either ultramafic or gabbroic rocks. Trends in the overall compositions of various fluid types – circumneutral Type 1 and hyperalkaline Type 2 fluids, as well as those with pH intermediate to these end-member fluids – are detailly discussed in Chapter 3 of this work and summarized in Appendix C, where similarities and differences in geochemical trends observed in ultramafic- and gabbro-hosted fluids sampled from the Oman ophiolite are also discussed .

While concentrations of redox-sensitive aqueous species (dissolved $O_2$, $H_2$, inorganic carbon, $CH_4$, CO, ferrous iron, sulfate, sulfide, nitrite, nitrate, ammonia) were reported in accompanying studies (Canovas et al., 2017; Howells, in prep; Chapter 3 of this document), processes that can account for their compositional trends have never been assessed. In the following discussions, we incorporate these analytical results with outcomes of calculations of fluid-mineral-gas equilibria to evaluate whether observed trends can be accounted for by processes such as fluid-mineral reactions and/or solubilities of gaseous species. Such assessments allow predictions on the compositions of end-member subsurface fluids that have not been modified by surficial processes.

### *4.3.1. Dissolved Oxygen and Hydrogen*

Trends in the pH and the dissolved $O_2$ (DO) concentrations of fluids investigated in this work are shown in Figure 4.1a. The DO concentrations of most fluids with pH values below 11 (circumneutral Type 1 and intermediate pH fluids) are close to saturation with the atmosphere (275 μmolal, dashed red line in Figure 4.1a) and are consistent with that of a fluid open to atmospheric exchange. On the other hand, dissolved oxygen concentrations of hyperalkaline Type 2 fluids vary from saturation with the atmosphere to very depleted levels. The depleted levels of DO in some hyperalkaline fluids are consistent with deep-seated sources for these fluids where conditions are closed to atmospheric influence and fluids are driven to reduced conditions through water-rock interactions. Variations in the DO levels measured from hyperalkaline fluids reflect variable atmospheric input during sampling and analysis with the field spectrophotometer. There are no clear differences in the DO levels of gabbro- and ultramafic-hosted fluids as depicted by the orange and grey symbols, respectively in Figure 4.1a.

The dissolved hydrogen ($H_2$) concentration of fluids generally increases with pH, as shown in Figure 4.1b. Serpentinization leads to $H_2$ generation where the oxidation of ferrous iron from the primary minerals to ferric iron in secondary minerals during rock alteration is accompanied by the reduction of $H_2O$ to $H_2$. However, not all hyperalkaline fluids that result from serpentinization are enriched in $H_2$. Dissolved $H_2$ concentrations of hyperalkaline Type 2 fluids vary by almost six orders of magnitude from 10 nanomolal to 3 millimolal, as shown in Figure 4.1b. These variabilities could either be a result of modifications from microbes consuming or generating $H_2$ or subsurface flowpaths where input of reduced gases is decoupled from the overall aqueous pathway. In addition, ultramafic rocks comprising the Oman ophiolite are variable from dunitic (olivine-rich) to harzburgitic (olivine-rich with significant presence of orthopyroxene) in composition (Hanghoj et al., 2010) and these variabilities can also lead to variable amounts of $H_2$ generated during the serpentinization process (Klein et al., 2013; Leong and Shock, 2020). In contrast to ultramafic-hosted fluids where many are known to contain >100 μmolal $H_2$, dissolved $H_2$ levels of hyperalkaline fluids hosted in gabbroic rocks are low (maximum at 1 μmolal), as shown in Figure 4.1b. It is likely that water-rock interactions in gabbroic bodies lead to fluids that are less reduced (less $H_2$-rich) than those generated through the hydrous alteration of ultramafic rocks. This is consistent with findings from hydrothermal systems hosted in basalts, which are chemically similar to gabbroic rocks, that are usually less $H_2$-rich than their counterparts hosted in ultramafic rocks (McCollom and Bach, 2009; Nakamura and Takai, 2014).

Both dissolved $O_2$ and $H_2$ concentrations of circumneutral Type 1 and hyperalkaline Type 2 fluids can be used to assess the redox state of the shallow and deep subsurface, respectively, and ultimately the extent of the redox contrast that can be potentially harvested by microbes when these two end-member fluids mix. To assess their redox state, we calculated the Eh, pe, and oxygen fugacity ($fO_2$) of these fluids as dictated by their dissolved $O_2$ and $H_2$ concentrations. Calculated values are compiled in Table S2 and are plotted in an Eh/pe-pH diagram shown in Figure 4.1c. Eh and pe calculated from the dissolved $O_2$ and $H_2$ values are depicted as red and blue squares, respectively, in Figure 4.1c. Eh and pe values calculated from the DO levels of fluids with pH values lower than 11 plot close to saturation with the atmosphere (upper black line in Figure 4.1c). Calculated Eh and pe values of hyperalkaline fluids are more variable with some plotting slightly lower than that dictated by atmospheric saturation. In contrast, Eh and pe values calculated using dissolved $H_2$ concentrations (blue squares in Figure 4.1c) lead to a redox state close to that dictated by the reduction of $H_2O$ to $H_2$ (at 25 °C and 1 bar $H_2$) as depicted by the lower black line in Figure 4.1c. The Eh and pe of fluids approach this equilibrium line as pH increases, suggesting upper limits in the $H_2$ concentration of deep-seated fluids close to those constrained by the $H_2O$-$H_2$ reduction process.

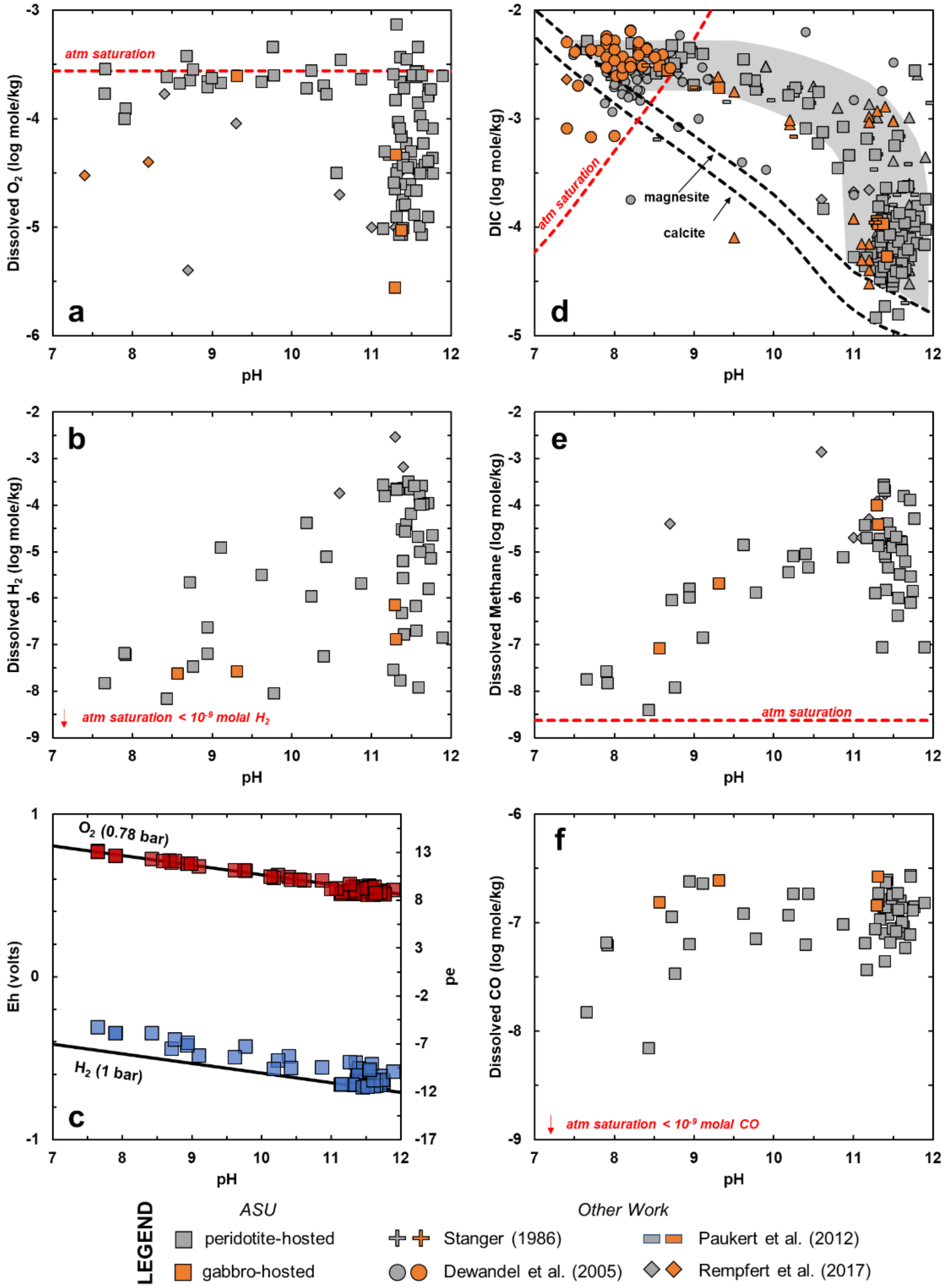

*Figure 4.1*. Dissolved $O_2$ (a) and $H_2$ (b) concentrations of Oman fluids. (c) Eh and pe of fluids calculated using the dissolved $O_2$ (red squares) and $H_2$ (blue squares) values of fluids. Upper and lower solid black lines depict Eh and pe values in equilibrium at 25°C

with the current atmosphere and with 1 bar of $H_{2(g)}$, respectively. (d – f) show concentrations of dissolved carbon species: inorganic carbon (d), methane (e), and carbon monoxide (f). Dashed red lines in (a), (d), and (e) depict dissolved concentrations at saturation with current atmospheric levels of $O_{2(g)}$, $CO_{2(g)}$, and $CH_{4(g)}$, respectively. Dissolved concentrations in equilibrium with atmospheric levels of $H_{2(g)}$ and $CO_{(g)}$ lie below the lower limits of plots shown in (b) and (f), respectively. Dashed black lines in (d) denote concentrations of DIC in equilibrium with calcite or magnesite. Grey field depicts results of mixing calculations of end-member fluids as shown in Chapter 3 of this work. Grey and orange symbols depict fluids sampled from ultramafic and gabbroic bodies, respectively. Square symbols are taken from data produced by accompanying work (Canovas et al., 2017; Howells, in prep; Chapter 3 of this work). Other symbols denote other work concerning fluids from the Oman ophiolite.

$H_{2(g)}$ levels in the atmosphere (0.6 ppmv, Glueckauf and Kitt, 1957) correspond to dissolved concentrations of 0.5 nanomolal at 100% atmospheric saturation at 25°C. $H_2$ concentrations (7-60 nanomolal) of circumneutral Type 1 fluids (pH 7 to 8) are 14-120 times oversaturated suggesting that deep-seated and serpentinization-generated $H_2$ could have dissolved into shallow groundwater or stream fluids. On the other hand, maximum $H_2$ levels measured from hyperalkaline Type 2 spring (0.3 millimolal, Canovas et al., 2017; Howells, in prep) and well (3 millimolal; Rempfert et al., 2017) fluids are oversaturated by 60,000 and 6,000,000 times, respectively, relative to that constrained by current atmospheric levels. The latter value is close to that of a fluid saturated with a 1 bar atmosphere composed entirely of $H_2$ gas. This is consistent with thermodynamic simulations (McCollom and Bach, 2009; Klein et al., 2009; 2013; Leong and Shock, 2020) that predict a transition to reduced conditions dominated by $H_2$, approaching that constrained by reduction of $H_2O$ to $H_2$, as serpentinization progresses. As fluids ascend to discharge in the surface, dissolved levels of $H_2$ will be highly oversaturated with respect to the atmosphere leading to degassing and bubble formation observed in many continental serpentinizing environments.

Figure 4.1c ultimately points to a massive redox disequilibrium in the $O_2$-$H_2$-$H_2O$ system given the dissolved $H_2$ and $O_2$ concentrations of serpentinizing fluids. This difference in redox states, one dictated by the atmosphere and another by the reduction limit of $H_2O$ to $H_2$, is perhaps one of the greatest contrasts observed in nature. This can lead to enormous disequilibrium that can be taken advantage of by aerobic hydrogen oxidizers, as quantified below. Such upper limit constraints on dissolved $H_2$ also allow quantification of the maximum energy supply available to other hydrogenotrophs, expounded upon below.

### *4.3.2. Dissolved Inorganic Carbon, Carbon Monoxide and Methane*

The concentration of dissolved inorganic carbon generally decreases with pH, as shown in Figure 4.1d. This decrease is attributed to incorporation of carbon into precipitating carbonate minerals during subsurface water-rock interactions. As fluids infiltrate into the subsurface during the initial stages of the rock alteration process, Mg-bearing minerals (olivine, pyroxene, serpentine, brucite) in aquifer host rocks dissolve and Mg is released into the fluid and combines with DIC to precipitate magnesite ($MgCO_3$). Water-rock interaction also mobilizes Ca from Ca-bearing minerals (*e.g.*, pyroxene) into the fluid that can be incorporated into dolomite ($CaMg(CO_3)_2$). These mineral carbonation reactions compounded by the transition to a system closed to atmospheric input when fluids infiltrate deeper into the aquifer, will lead to decreasing concentration of DIC while pH increases as the rock alteration process progresses. Along with an increase in pH is an increase in Ca concentration that can eventually saturate calcite ($CaCO_3$). As shown in Figure 4.1d, the lowest DIC concentrations measured in circumneutral Type 1 and hyperalkaline Type 2 fluids are consistent with those dictated by the solubilities of magnesite and calcite (dashed red lines), respectively. In contrast, trends in the DIC concentrations of fluids with pH values intermediate between Type1 and 2 fluids can be accounted for by the mixing of these end-member fluids, as shown by the grey field in Figure 4.1d from mixing calculations discussed in Chapter 3 of this work. Overall, the low concentrations of DIC in hyperalkaline fluids raises questions about the consequences of the limited amounts of inorganic carbon that can be available to microorganisms living in deep aquifers. Nevertheless, DIC can still be replenished through dissolution of carbonate minerals despite the low solubilities of carbonate minerals and their slow dissolution rates at hyperalkaline conditions. At the latter part of this work, we quantify the amount of energy and power supplied through this process and predict how much microbial biomass this energy supply can support in deep serpentinizing environments. Speciation of DIC in investigated fluids is shown in Figure C2a. Most of DIC at circumneutral pH exists as $HCO_3^-$ while those at hyperalkaline pH are mostly $CO_3^{-2}$ and the neutral complex $CaCO_{3(aq)}$.

Another process that can lead to a decrease in DIC concentration is the increasing potential to transform inorganic carbon into $CH_4$ as fluids become more reduced ($H_2$-rich). This is consistent with increasing levels of $CH_4$ with pH, as shown in Figure 4.1e. Abiotic formation of methane during serpentinization is believed to be the main source of the elevated amounts of $CH_4$ observed in hyperalkaline springs and well fluids (Etiope and Whiticar, 2019). Whether this forms actively along the present low-temperature subsurface flowpath or during previous water-rock interactions at higher temperatures remains a subject of a debate. Measurement of $CH_4$ isotopologues from both low- and high-temperature seafloor hydrothermal fluids support the high-temperature origins of methane in water-rock systems (Wang et al., 2018). $CH_4$ generated during high temperature water-rock interactions can be trapped in fluid inclusions hosted in mineral phases that are then released during modern groundwater circulation (McDermott et al., 2015; Klein et al., 2019; Grozeva et al., 2020). Dissolved $CH_4$ concentrations observed from gabbro- and ultramafic-hosted fluids are overlapping, though $CH_4$ values of gabbro-hosted fluids tend to plot closely with the most $CH_4$-rich ultramafic-hosted fluids. This contrasts with their $H_2$ trend where gabbro-hosted fluids tend to be $H_2$-poor (see Figure 4.1b). Klein et al. (2019) and Grozeva et al. (2020) observed that a mass of gabbro tends to host more $CH_4$ in fluid inclusions than an equivalent mass of ultramafic rock and this could account for the elevated amounts of dissolved $CH_4$ observed in gabbro-hosted hyperalkaline fluids relative to most of those hosted in ultramafic rocks. Overall, the above discussions suggest kinetic inhibitions to generate abiotic methane at low temperatures despite the favorable conditions (*i.e.*, high $H_2$ levels) and opens the possibility for microbial methanogenesis. In addition, $CH_4$ that is recently mobilized from mineral fluid inclusions and that is in the presence of electron acceptors ($O_2$, sulfate, nitrate, nitrite) allows potentials for methanotrophic reactions. Potentials for both methanogenic and methanotrophic reactions in surface and subsurface environments hosting serpentinizing fluids are quantified below.

Like those observed for $CH_4$, dissolved CO values measured in gabbro-hosted fluids plot close to the highest values measured from ultramafic-hosted fluids, as shown in Figure 4.1f. There is a weak pH trend in the dissolved carbon monoxide (CO) levels of fluids from the Oman ophiolite. At pH > 9, CO levels vary from 100 to 250 nanomolal. In contrast, fluids with pH < 9 usually have less than 100 nanomolal of CO. All measured

CO levels are much higher than a fluid in equilibrium with atmospheric levels of CO. Saturation at atmospheric levels of ~ 200 ppbv $CO_{(g)}$ will lead to dissolved CO concentrations of ~0.2 nanomolal. The elevated levels of dissolved CO relative to atmospheric constraints, as shown in Figure 4.1f, could arise from biological sources or input from the reducing subsurface. Nonetheless, supply of CO together with the presence of DO from surficial sources and dissolved $H_2$ from deeper sources can lead to potentials for carbon monoxide oxidation and reduction, respectively, as expounded upon below.

### *4.3.3. Dissolved Ferrous Iron*

Iron is a major component in ultramafic rocks and is mostly hosted as ferrous iron in primary phases such as olivine and pyroxene. Simulations by Leong and Shock (2020) show that early in the rock alteration progress ferrous iron released from the dissolution of primary minerals oxidizes and precipitates into goethite, buffering the total Fe concentration to very low values. As serpentinization progresses, the reacting fluid becomes increasingly reduced and Fe dissolved from primary phases is either precipitated into minerals such as magnetite, Fe-bearing brucite and/or Fe-bearing serpentine or remains dissolved as ferrous iron species in the fluid at concentrations in equilibrium with these mineral phases. Total dissolved Fe in equilibrium with these minerals is approximately 10 - 100 μmolal at hyperalkaline pH (Leong and Shock, 2020), consistent with values measured from hyperalkaline fluids in the Oman ophiolite as shown in Figure 4.2a, which compares dissolved ferrous iron measured from field samples (grey symbols) with that dictated by mineral assemblages (dashed lines: ferrous hydroxide – magnetite, magnetite – goethite, and for end-member Fe-bearing serpentine with different valence states for iron) that are common in partially and completely serpentinized ultramafic rocks (*e.g.*, Andreani et al., 2013; Mayhew et al., 2018; Mayhew and Ellison, 2020; Templeton and Ellison, 2020). Hyperalkaline fluids sampled from seeps (square symbols in Figure 4.2a) plot close or above values dictated by the ferrous-hydroxide and magnetite assemblage. Well fluids (grey diamond symbols from Rempfert et al., 2017) are more enriched in dissolved iron and plot entirely in the ferrous hydroxide field, or close to values dictated by the transition from Fe end-member serpentine bearing both $Fe^{+2}$ and $Fe^{+3}$ (cronstedtite, $Fe(II)_2Fe(III)_2SiO_5(OH)_4$) to that only bearing $Fe^{+2}$ (greenalite, $Fe(II)_3Si_2O_5(OH)_4$). Circumneutral fluids plot closer to values dictated by equilibrium with more oxidized counterparts of the above minerals such as goethite or ferric iron-bearing serpentine (hisingerite, $Fe(III)_2Si_2O_5(OH)_4$), as shown in the left portion of Figure 4.2a.

Ferrous iron concentrations measured from hyperalkaline Type 2 fluids are generally an order of magnitude more elevated than those measured from circumneutral Type 1 fluids, despite the fast rates of ferrous iron oxidation observed at alkaline pH (Stumm and Lee, 1961; Millero, 1985; Trapp and Millero, 2007; Morgan and Lahav, 2007; St. Clair et al., 2019). It has been shown that oxidation of dissolved ferrous iron becomes more rapid as more dissolved ferrous iron is associated into hydroxide complexes with increasing pH (Millero, 1985; Morgan and Lahav, 2007). As shown in Figure C2b, hydroxide complexes become the predominant dissolved ferrous iron species

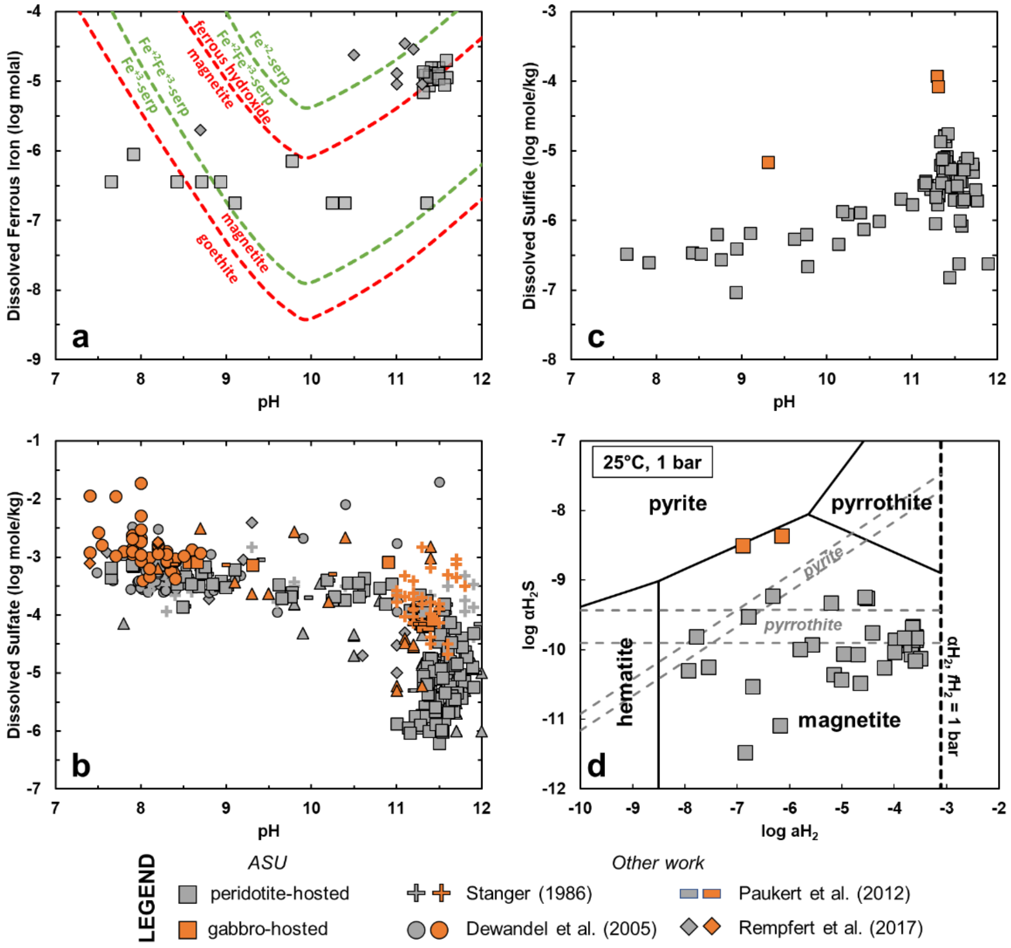

*Figure 4.2*. Concentrations of dissolved iron and sulfur species measured from fluids from the Oman ophiolite. (a) dissolved concentrations of ferrous iron. Upper and lower dashed red curves depict concentrations in equilibrium with the ferrous hydroxide-magnetite and magnetite-goethite assemblages, respectively. Upper dashed green curve represents dissolved concentrations in equilibrium with Fe end-member of serpentine bearing only $Fe^{+2}$ (greenalite) and both $Fe^{+2}$ and $Fe^{+3}$ (cronstedtite). Lower dashed green curve depicts concentrations in equilibrium with end-member serpentine bearing both $Fe^{+2}$ and $Fe^{+3}$ (cronstedtite) and only $Fe^{+3}$ (hisingerite). Concentrations of dissolved sulfate and sulfide are shown in (b) and (c), respectively. (d) activity diagram showing calculated $\alpha H_2S$ and $\alpha H_2$ of samples. Solid lines in (d) depict stability boundaries of various sulfide and oxide minerals while dashed grey lines depict solubilities of pyrrhotite and pyrite. Upper and lower solubility lines for these minerals are calculated considering the range in iron concentrations in equilibrium with these minerals. Lower (10 µmolal) and upper (30 µmolal) limits on the dissolved iron concentrations are taken from observations in hyperalkaline fluids (see Figure 4.2a) and result in the upper and lower solubility lines, respectively, for both sulfide minerals. Symbols are similar to those shown in Figure 4.1.

in investigated fluids as the pH becomes more basic. Thus, the reason for the persistence of ferrous iron at hyperalkaline pH conditions is unknown. Much of existing studies (*e.g.*, Millero, 1985; Trapp and Millero, 2007; Morgan and Lahav, 2007) examined pH conditions where the first ($FeOH^+$) and second ($Fe(OH)_{2(aq)}$) hydroxide complexes are the major dissolved ferrous iron species and none so far has investigated oxidation rates at hyperalkaline conditions (pH >11) where the third hydroxide complex ($Fe(OH)_3^-$) is dominant (see Figure C2b). The presence of this anion could likely inhibit oxidation and allow dissolved ferrous iron to remain in solution. Alternatively, instead of the speciation of dissolved ferrous iron, it is also likely that the DO-limited and $H_2$-rich nature of Type 2 fluids allows dissolved ferrous iron species to continue to exist in these reduced fluids. In addition, supply from the dissolution of $Fe^{+2}$-bearing minerals can also be faster than their oxidation. One source for dissolved ferrous iron is through the dissolution of ferroan brucite, which is common in subsurface serpentinites (Templeton and Ellison, 2020) and relatively soluble (Pokrovsky and Schott, 2004). Overall, the persistence of dissolved ferrous iron in these fluids provides opportunities for iron oxidizers that are otherwise inaccessible due to rapid rates of abiotic iron oxidation at other alkaline but less reduced environments (St. Clair et al., 2019). In order to assess this energetic yield, potentials for microbial oxidation of dissolved ferrous iron to a ferric oxyhydroxide mineral (goethite) are quantified below.

### *4.3.4. Dissolved Sulfate and Sulfide*

Trends in the dissolved sulfate levels of investigated fluids are plotted in Figure 4.2b. Typically, fluids hosted in gabbroic rocks (orange symbols in Figure 4.2b) are more enriched in dissolved sulfate than those hosted in ultramafic rocks (grey symbols).

Sources for dissolved sulfate in these fluids are currently unknown. A possible source for sulfate in fluids is through dissolution of sulfate minerals such as those inferred for sulfate-rich fluids sampled from the Troodos ophiolite in Cyprus (Neal and Shand, 2002; Rizoulis et al., 2014). Calculations for mineral saturations reveal that hyperalkaline fluids in Oman are highly undersaturated with respect to anhydrite (see Table B2 in Appendix B) and are likely soluble in the presence of these fluids. However, unlike those observed in Cyprus where dissolved sulfate levels generally increase with pH (Rizoulis et al., 2014), dissolved sulfate concentrations of fluids in Oman trend in the opposite direction, as shown in Figure 4.2c. Rather than sulfate leaching, this trend is more consistent with a fluid that is concomitantly becoming more reduced and alkaline as the rock alteration process progresses. Thus, the decreasing trend of dissolved sulfate with pH can be a result of increasing potentials to transform dissolved sulfate into sulfide as fluids become more reduced and alkaline. Conversely, oxidation of sulfide minerals in the presence of more oxic Type 1fluids can mobilized sulfate and account for the elevated sulfate concentrations in circumneutral fluids. As depicted in Figure 4.2c, all the above processes are consistent with a trend of increasing dissolved sulfide levels with pH. To further evaluate controls by various relevant minerals, results from calculations of mineral solubilities and stabilities are depicted in Figure 4.2d in an $\alpha H_2S_{(aq)}$-$\alpha H_{2(aq)}$ activity diagram calculated for the $FeO$-$Fe_2O_3$-$H_2O$-$H_2S$ system at 25°C. The activities of dissolved $H_2S$ ($\alpha H_2S$) and $H_2$ ($\alpha H_2$) of hyperalkaline fluids hosted in ultramafic rocks (grey symbols in Figure 4.2d) are calculated from environmental values and plot within the magnetite field, below the stability fields of the common sulfides, pyrite and pyrrhotite. However, without considering solid-solid phase transitions between minerals and only accounting for the solubilities of pyrite and pyrrhotite, depicted as dashed grey lines in Figure 4.2d, dissolved sulfide levels of most ultramafic-hosted hyperalkaline fluids are close to saturation with these minerals, most especially with respect to pyrrhotite. Solubilities for these sulfide minerals where calculated given dissolved $Fe^{+2}$ concentrations ranging from 10 to 30 µmolal constrained from the solubilities of Fe-bearing minerals discussed above at hyperalkaline pH (see Figure 4.2a) where the upper and lower dashed grey lines in Figure 4.2d correspond to the minimum and maximum range in dissolved $Fe^{+2}$, respectively. In contrast, dissolved sulfide concentration that are an order of magnitude elevated (>100 µmolal), and comparable to the Lost City Hydrothermal Vents (Seyfried and others, 2015), were measured from hyperalkaline fluids hosted in gabbroic rocks (orange symbols in Figure 4.2d). As shown in Figure 4.2d, dissolved sulfide and $H_2$ levels of these fluids plot close to the phase boundary between pyrite and magnetite. This suggests that the dissolved sulfide levels of gabbro-hosted fluids are dictated by a process of pyrite oxidation to magnetite, or conversely magnetite reduction to pyrite. It is also possible for these fluids to be within the stability fields of pyrite or pyrrhotite as dissolved sulfide and $H_2$ concentrations are likely higher in the deep subsurface. Similarly high dissolved sulfide concentrations (>1000 ppb or >30 µmolal) were also measured by Cardace and others (2015) from the Manleleuag site in the Zambales Ophiolite, which is likewise hosted within a gabbroic body. These observations are consistent with bulk rock measurements showing that sulfide and total sulfur are most abundant in gabbros among the various rock types that make up the Oman ophiolite (Oeser and others, 2012). Fluid interactions with gabbroic rocks can thus contribute to elevated dissolved sulfide levels of fluids compared to those interacting with ultramafic rocks. Sulfur isotopes can further trace possible sources of sulfur species and track their fates during serpentinization. Focusing on fluids associated with gabbroic bodies can reveal the processes behind some of the most sulfidic fluids occurring in low temperature environments.

### *4.3.5. Dissolved Nitrate, Nitrite, and Ammonia*

Trends in the concentrations of dissolved nitrogen species (nitrate, nitrite, and ammonia) are shown in Figure 4.3. Dissolved nitrate concentrations decrease with pH, as shown in Figure 4.3a. The trend in the concentrations of dissolved nitrite does not have a

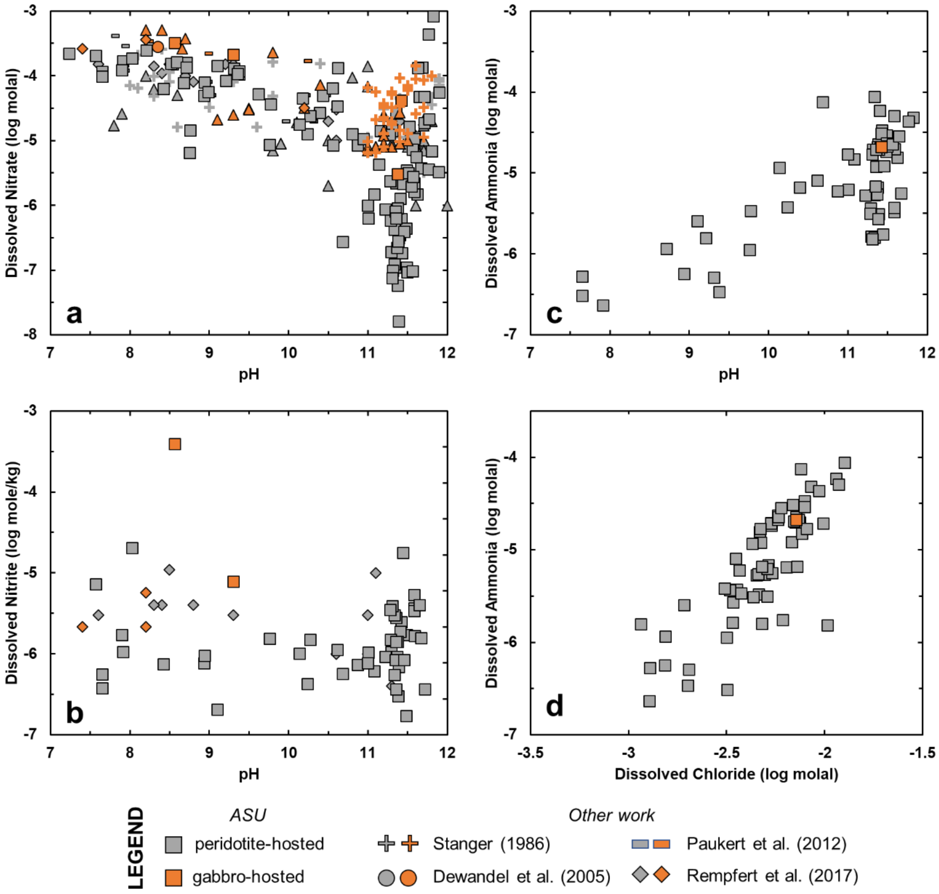

*Figure 4.3*. Trends in the concentrations of dissolved nitrogen species with pH: nitrate (a), nitrite (b), and ammonia (c). (d) trend in the dissolved ammonia concentration with the dissolved chloride concentration. Symbols are similar to those shown in Figure 4.1.

strong pH dependence, as shown in Figure 4.3b. In contrast, as depicted in Figure 4.3c, dissolved ammonia concentrations of fluids increase with pH. Ammonia values correlate with dissolved chloride levels as shown in Figure 4.3d. Chloride and other salt-forming elements (Na, K) in hyperalkaline fluids are likely to result from leaching from minerals present in aquifer host rocks, as argued by Neal and Stanger (1985) and in Chapter 3 of this work. Dissolution of ammonium-bearing salts could likewise supply ammonia to the fluid and concomitantly account for elevated concentrations in the most saline serpentinizing fluids in Oman which typically occur near the basal thrust of the ophiolite (Chavagnac et al., 2013b; see Chapter 3 of this work). A comprehensive sampling of fluids across different geological settings in Oman would reveal insights on the variable lithological sources for nitrogen in subsurface environments. In the discussions below, we quantify energy sources for reactions involving various nitrogen species ($NO_3^-$, $NO_2^-$, $N_2$, and $NH_3$).

## 4.4. Energy Supplies Available in Surficial Hyperalkaline Seeps

The co-existence of several aqueous species that are out of equilibrium with each other can lead to energy supplies that can be harvested by several chemotrophic microorganisms. To evaluate how this disequilibrium translates to geochemical energy supplies, the potentials of 17 different chemolithotrophic processes are quantified in hyperalkaline seeps, which are surficial expressions of the deep-seated serpentinization process. The affinities of 16 of these reactions in surficial fluids in Oman were previously quantified by Canovas et al. (2017). We added one more reaction (iron oxidation), and also constrain the maximum energy available per kg of fluid. Energy supplies calculated via reactions 4.1 through 4.17 using data from Oman expand upon previous calculations for other serpentinizing sites hosted in continental (Cardace et al., 2015; Crespo-Medina et al., 2017) and submarine (McCollom, 2007; Amend et al., 2011; Nakamura and Takai, 2014) settings. Energy supplies available in fluids hosted in ultramafic bodies are also compared to those available in gabbro-hosted fluids in the following discussion. A summary and ranking of the energy supply available in *hyperalkaline fluids* through these 17 chemolithotrophic reactions is depicted in Figure 4.4. The grey circles and bars depict the average and the range of the 25th and 75th percentile, respectively, of calculated energy supplies available in ultramafic-hosted fluids. The orange circles represent available energy in individual gabbro-hosted samples. Energy available in all fluids investigated in this work, including those that are non-hyperalkaline (pH<11), are discussed in Appendix C and are depicted in Figures C3 and C4.

In hyperalkaline fluids seeping from outcropping ultramafic rocks, aerobic reactions provide the highest energy yield, as shown in Figure 4.4 The aerobic oxidation of dissolved methane, ammonia, sulfide, hydrogen, and ferrous iron can supply >0.1 calories per kg of fluid to microbial communities in hyperalkaline pools. The highest amount of energy available for an anaerobic community, albeit highly variable, can be provided by nitrogen reduction or fixation followed by the anaerobic oxidation of ammonia and methane (with nitrate, nitrite and sulfate as electron acceptors). On average, the amount of energy available for methanogens is close to the other anaerobic reactions but is highly variable ranging from 0.01 to 1 calories per kg of fluid. Sulfate and nitrate reduction offer 0.01 to 0.1 calories per kg of fluid. Of all of the aerobic reactions investigated by this work, the least amount of energy can be derived from the oxidation of nitrite and carbon monoxide. Despite the low energy yield, Canovas et al. (2017) show that carbon monoxide oxidation provides the highest thermodynamic drive ($A_r$) among all studied reactions. However, low amounts of dissolved CO present in the fluid (see Figure 4.1f) leads to minimal available energy ($E_r$). Despite the limited energy supply, carbon monoxide oxidizers have been detected in various serpentinizing sites through experimental and molecular techniques (Morrill et al., 2014; Fones et al., 2019) and strategies that can efficiently tap into limited amounts of CO or alternative energy sources can likely help CO oxidizers to survive in these low-energy environments. Lastly, as shown in Figure 4.4, the least amount of energy can be supplied through the carbon monoxide reduction and water-gas shift reactions. Consistent with our calculations, microorganisms using such metabolic strategies have yet to be detected in serpentinizing environments.

In contrast to the extensive data available for ultramafic-hosted fluids (grey symbols and bars in Figure 4), only two hyperalkaline gabbro-hosted samples (orange symbols) have complete compositional datasets required to calculate energy supplies for some reactions listed in Table 4.1. Despite limited data on gabbroic-hosted fluids, we compare energy supplies predicted for these fluids to trends observed from ultramafic-hosted fluids for preliminary discussions on their metabolic potentials, which can vary significantly from those hosted in ultramafic rocks. Comparisons of the geochemical energy supplies at submarine hydrothermal systems hosted in various lithologies (ultramafic, basaltic, intermediate, and felsic rocks) have been conducted by Amend et al. (2011) and Nakamura and Takai (2014) but none so far have been conducted for continental-hosted systems. High dissolved methane and sulfide values observed in gabbro-hosted fluids (see Figures 1e and 2c, respectively) imply that these environments predominantly host a methanotrophic and sulfide-based community. However, energy supplies for the aerobic oxidation of methane and sulfide are highly variable in the two investigated gabbro-hosted fluids, as shown in Figure 4.4 This is mainly attributed to the variations in the amount of dissolved $O_2$, which in this case can be the limiting reactant. However, note that the maximum energy available for methane and sulfide oxidizers can be an order of magnitude higher in one of the gabbro-hosted sites compared to most of those hosted in ultramafic rocks. In addition, anaerobic methanotrophs using sulfate as the electron acceptor are highly favored in gabbro-hosted systems, as shown in Figure 4.4. Moreover, there is also slightly higher energy available for CO oxidizers in gabbro-hosted sites relative to most of those hosted in ultramafic rocks. In contrast, as $H_2$ is depleted in gabbro-hosted fluids relative to most of those hosted in ultramafic rocks (see Figure 4.1b), energy supplies available for hydrogenotrophs like hydrogen oxidizers, methanogens and sulfate reducers are lower in gabbro-hosted systems. Rempfert et al. (2017) characterized the microbial community compositions of circumneutral to slightly alkaline gabbro-hosted fluids in the subsurface of the Oman ophiolite and found it to be diverse but lacking the presence of microorganisms capable of these metabolic strategies, which are more common in fluids sampled from ultramafic-hosted aquifers. Work probing the compositions of fluids and microorganisms (Mason et al., 2010; Li et al., 2020) hosted in deep gabbroic rock are still scarce. Future work that will populate aqueous compositional datasets on gabbro-hosted environments, especially those with hyperalkaline pH, will allow more comprehensive insights into their bioenergetic potentials. Like ultramafic rocks, gabbroic rocks are pervasive in the seafloor (Cannat et al. 2010) and can potentially store extensive amounts of geochemical energy that can support deep subsurface life. Studies improving our datasets on gabbro-hosted environments, in parallel to our growing understanding of ultramafic-hosted systems, would better capture the potential diversity of rock alteration and fluid compositions expected in various subsurficial settings, which in turn may vary significantly in their potential to support life.

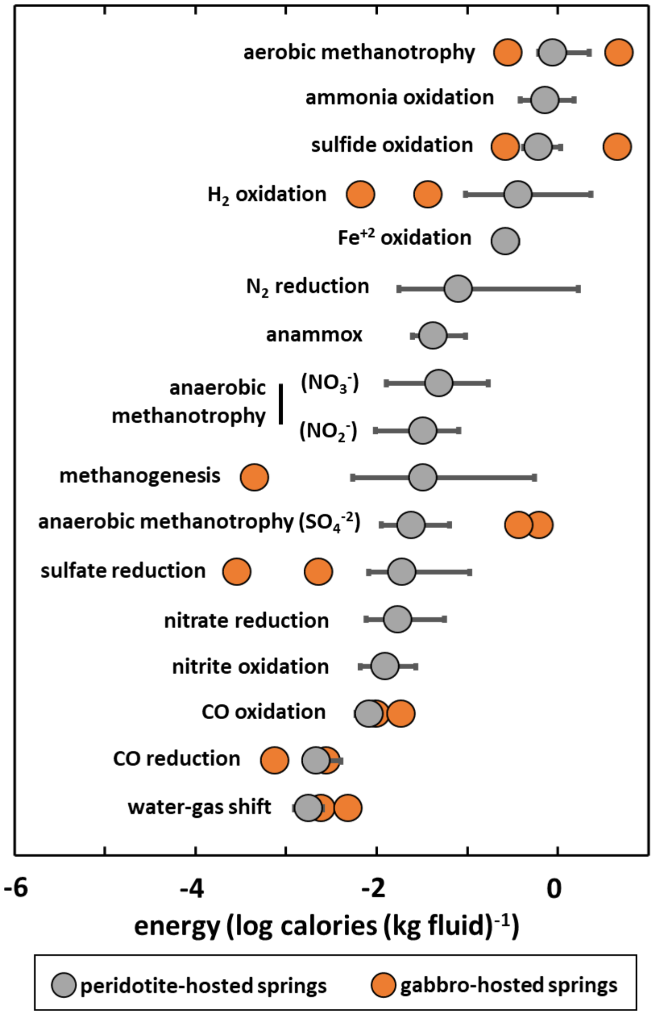

*Figure 4.4*. Summary and ranking of calculated energy supplies in hyperalkaline fluids via 17 different chemolithotrophic reactions. Energy supplies from these reactions are ranked from the most (top) to least (bottom) energy yielding. Grey circles depict average energy yield calculated from fluids hosted in ultramafic rocks. Bars denote the 25th and 75th percentile of energy yield calculated from these samples. At most, only two of the investigated gabbro-hosted fluids have complete datasets of aqueous compositions needed for calculating energy yields for some reactions and are plotted accordingly.

## 4.5. Prediction of Subsurface Energy Supplies

In the preceding discussions, we quantified energy supplies available for chemolithotrophic microorganisms by using data from natural samples collected in surficial settings (*i.e.*, springs). Hyperalkaline fluids seeping from outcropping rocks are surface manifestations of deep-seated serpentinization processes, and predictions of geochemical energy supplies for deep subsurficial environments using these samples are limited by uncertainties brought about by surficial modifications of deep-seated signatures. Prediction of energy supplies available in deep subsurface settings is best quantified using subsurface samples. Quantifications of geochemical energy supplies from the few hyperalkaline subsurface samples obtained from wells in the Oman ophiolite, using geochemical data from Rempfert et al. (2017), show elevated energy supply for methanogens in well fluids, as shown by the diamond symbols in Figure C4a, which can be attributed to elevated levels of $H_2$ observed in well fluids relative to those measured in springs (see diamond symbols Figure 4.1a). The dramatic effect of elevated levels of $H_2$ in subsurface settings on this single example of the energy supply for subsurface methanogens raises questions about the potentials for other redox reactions. In light of the limited data on subsurface samples and uncertainties in surficial inputs to these deep-seated samples, compositions of end-member subsurface fluids were estimated through calculations of fluid-mineral-gas controls on subsurface fluid compositions enhanced by an extensive dataset for fluids sampled from ultramafic environments. Specifically, compositions of end-member fluids representative of both the *deep* and *shallow* serpentinizing aquifers were derived. Deep-seated fluids are in equilibrium with minerals forming actively during advanced stages of serpentinization, and shallow-seated fluids are in equilibrium with minerals comprising the highly altered shallow aquifer host rocks. These estimated end-member fluids were then used to evaluate energy supplies available in the shallow and deep serpentinizing aquifers. In addition, mixing between the two end-member fluids, each buffered to extremely different redox potentials, can yield massive redox disequilibria that can be potentially harvested by microorganisms. Energy supplies across the mixing gradient can then be quantified to evaluate maximum energy yield along the mixing gradient. Mixing between the end-member fluids represents subsurface environments such as discharge zones where surfacing deep-seated hyperalkaline fluids encounter shallow groundwater. This zone could serve as a hotspot where subsurface life may bloom when these two end-member fluids mix. The above model was previously described in Leong and Shock (2020) to predict subsurface energy supplies for methanogens and hydrogen oxidizers in low-temperature ultramafic aquifers in continents. In this work, we extend this model to the rest of the reactions compiled in Table 4.1. Similar models can also be applied to gabbroic aquifers once more data are available to warrant predictions on subsurface fluid compositions.

### *4.5.1. Estimated Composition of Subsurface Fluids in Continental Ultramafic Aquifers*

Calculated compositions of deep-seated fluids forming at advanced stages of serpentinization are dictated by the chrysotile-brucite-diopside equilibrium, along with calcite (Leong and Shock, 2020). As calculated by Leong and Shock (2020), this assemblage of minerals yields a hyperalkaline fluid (pH ~ 12) elevated in Ca (>10 millimolal) and depleted in dissolved Si (< 1 µmolal), Mg (<0.1 µmolal), and inorganic carbon (<10 µmolal) at 25°C. This predicted composition approximates those that are observed in $Ca^{+2}$-$OH^-$ (Type 2) fluids characteristic of advance stages of serpentinization (see Chapter 3 of this work). In contrast, we fixed the pH value of the shallow end-member to 8 following observed trends in shallow wells and stream water hosted in ultramafic rocks in Oman (pH 7 – 9, *e.g.*, see Paukert et al., 2012; Chavagnac et al., 2013b; Rempfert et al., 2017; Chapter 3 of this work).

The host rocks in the shallow aquifer are mostly composed of highly serpentinized ultramafic rocks that are comprised mainly of the minerals: serpentine, carbonates (magnesite, calcite, dolomite), and iron oxides and oxyhydroxides (Miller et al., 2016). The calculated composition for a fluid in equilibrium with these minerals is akin to the $Mg^{+2}$-$HCO_3^-$ (Type 1) fluids typical in the surface and shallow aquifers in ultramafic-hosted environments. Specifically, calculations by Leong and Shock (2020) yield fluids with high dissolved Mg (>1 millimolal), inorganic carbon (>1 millimolal) and Si (>100 μmolal) and depleted Ca (<1 millimolal) concentrations relative to Type 2 fluids. We set the salinities of shallow- and deep-seated end-member fluids to 1 and 10 millimolal NaCl, respectively, following environmental trends.

Dissolved oxygen of shallow- and deep-seated end-member fluids is set to 100% (0.3 millimolal) and 0% saturation with the atmosphere, respectively. In contrast, we set the dissolved $H_2$ level of deep-seated fluids to be in equilibrium with 1 bar $H_2$ (0.75 millimolal) following limits by the $H_2O$-$H_2$ reduction reaction shown in Figure 4.1c. We set the dissolved sulfide concentration of deep-seated fluids to be in equilibrium with pyrrhotite (0.1 millimolal), following Figure 4.2d. Additionally, the dissolved ammonia of deep-seated fluids was set to 0.1 millimolal based on that shown in Figure 4.3d for the most saline sample, which could be a result of extensive water-rock reaction. In contrast, we assume the dissolved $H_2$, sulfide and ammonia concentrations of end-member shallow-seated fluids are very low following constraints on atmospheric levels of $H_{2(g)}$, $H_2S_{(g)}$, and $NH_{3(g)}$ and are set to zero in our models. We assume values of 0.5 millimolal for nitrate and 1 μmolal for nitrite in the shallow-seated end-member fluid using averages of observed values in circumneutral fluids as depicted in Figures C4a and C4b, respectively. We also assume that these oxic species are not present in end-member deep-seated fluids. For carbon monoxide, we assume a zero value for the shallow subsurface end-member following 100% atmospheric saturation. As we found no further evidence of constraints on deep-seated levels of CO, we assume a value of 0.3 μmolal following observations from hyperalkaline fluids.

Dissolved $N_2$ concentrations of both shallow and deep end-member fluids are set to atmospheric saturation (0.5 millimolal). Interestingly, unlike other gaseous species common in the atmosphere ($O_2$, $CO_2$) where dissolved components can be very low in hyperalkaline fluids, Boulart et al. (2013) found that dissolved $N_2$ levels of hyperalkaline fluids are even higher, mostly between 1 – 2 times, than that constrained by atmospheric saturation (~500 μmolal at 25°C). $N_2$ present from the starting reacting fluid could have become concentrated along the subsurface flowpath as liquid water is sequestered into minerals through mineral hydration reactions. Calculations in Chapter 3 of this work show that accounting for 50% of water loss to mineral hydration would require extreme extents of water-rock reaction involving water-to-rock ratio of <0.33 (*e.g.*, reaction of >3 kg of rock in 1 kg of water). As we lack information on the extents of subsurface water-rock reactions, as a minimum, we assume similar constraints on $N_2$ for end-member deep-seated fluids (0.5 millimolal) as that for the shallow end-member fluid set by atmospheric saturation.

Dissolved Fe levels of deep-seated fluids are assumed to be in equilibrium with the magnetite-ferrous hydroxide assemblage (0.1 millimolal) at the pH set for deep-seated fluids (pH ~12), while dissolved Fe values for shallow-seated fluids are constrained by equilibrium with a ferric oxyhydroxide (goethite, close to zero concentration) at modern atmospheric conditions.

We set methane levels of the shallow-seated end-member fluid to be close to zero, following atmospheric constraints. Assumed $CH_4$ values for the deep-seated fluids vary in our model as abiotic methane generation during water-rock interactions at low temperatures is still uncertain. Recent evidence shows that methane detected in many low-temperature serpentinizing environments is not formed actively in the subsurface but is introduced from leaching of gas-rich fluid inclusions. Methane in these inclusions was formed during previous water-rock interactions at high temperatures (>270 °C) that are eventually trapped in fluid inclusions and released during active groundwater circulation (McDermott et al., 2015; Wang et al., 2018; Klein et al., 2019). To accommodate variations in the input of methane to deep-seated sources, we used two extreme values of methane for the deep-seated end-member fluids. We first set methane concentration to a very low value (1 picomolal or close to zero) to indicate no input from fluid inclusions and then set it to high values typically observed in fluids sampled from wells (~1 millimolal, Rempfert et al., 2017; Etiope et al., 2017). The former and latter scenarios maximize potentials for methanogens and methanotrophs, respectively, and can be considered robust estimates of subsurface energy supplies involving methane. All the above constraints and assumptions on the composition of end-member shallow and deep-seated fluids are summarized in Table S5.

### *4.5.2. Energy Supplies in the Serpentinizing Subsurface*

Calculated energy supplies available for various chemolithotrophs living in end-member fluids characteristic of the shallow and deep serpentinizing aquifers and in zones where these two different fluids mix are shown in Figure 4.5. The trend in the evolution of pH during the mixing process is shown as a dashed grey curve. Curves shown in Figure 4.5a are results of calculations assuming minimal background methane levels (1 picomolal) which lead to low values of energy supplies for methanotrophic reactions that are below the range shown in the diagram. In shallow-seated fluids (100% shallow fluid in the top of Figure 4.5a), energy for all investigated chemotrophic reactions are less than 0.1 calories/kg fluid due to limitations in the supply of electron donors. For deep-seated end-member fluids (0% shallow at the bottom of Figure 4.5a), most reactions also yield less than 0.1 calories/kg fluid due to limitations in electron acceptors. Only methanogenesis (~0.2 calories/kg fluid) and nitrogen reduction (~6 calories/kg fluid) reactions yield energy supplies exceeding 0.1 calories/kg fluid.

Unlike reactions where the electron acceptor supply ($O_2$, sulfate, nitrate, nitrite) in the deep-seated end-member is close to zero, dissolved inorganic carbon can be supplied by subsurface carbonate minerals, as shown in Figure 4.1d where the lowest DIC concentrations measured in hyperalkaline fluids approach values constrained by the solubilities of carbonate minerals (calcite and magnesite). Thus, the distribution of carbonate minerals in the deep subsurface could help sustain conditions favorable for methanogens in deep aquifers by suppling the necessary electron acceptors.

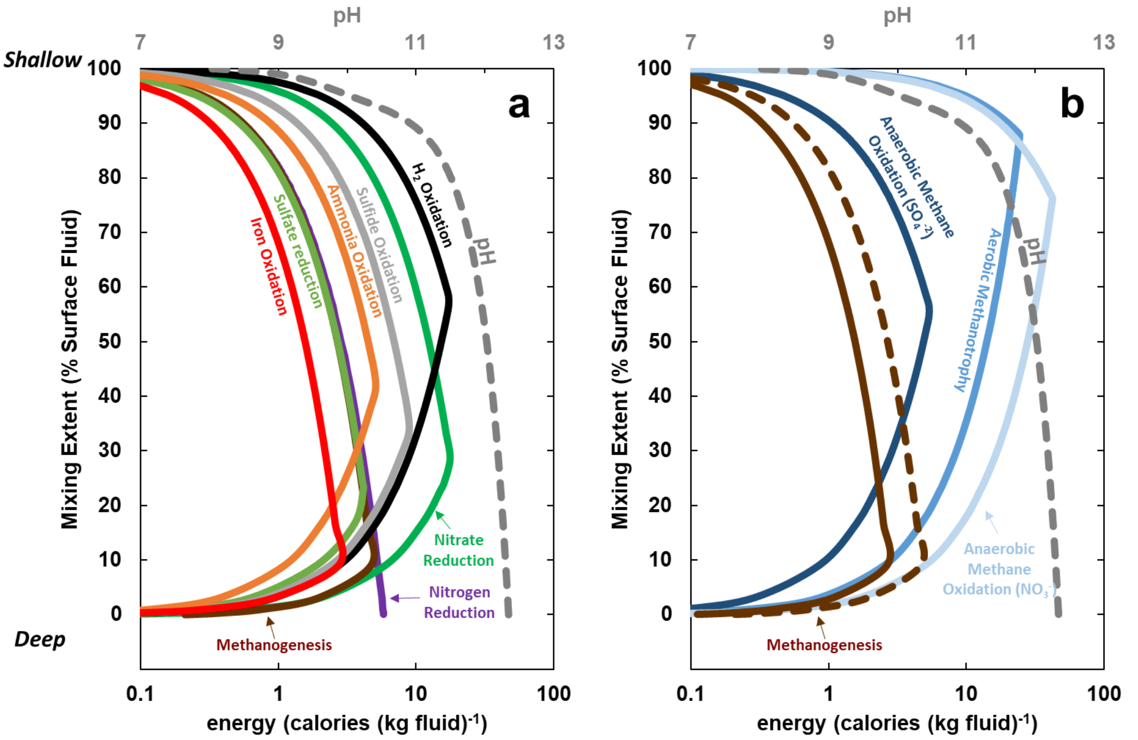

*Figure 4.5*. Calculated energy supplies via various reactions during mixing between fluids that equilibrated with deep-seated rocks (bottom of figure) and those that equilibrated with the atmosphere and highly altered rocks composing the upper aquifers (top of figure). Dashed grey curve depicts pH during mixing with values represented at the top of the chart. (a) results of mixing calculations assuming minimal background methane (1 picomolal), which maximizes energy supply for methanogens and yields no energy for methanotrophs. (b) results of models assuming elevated background methane (1 millmolal) depicting energy supplies via various methanotrophic reactions. At these high levels of methane, the drive for methanogenesis is lower and yields less energy than that depicted in (a), which is represented as the dashed brown curve in (b). Energy supplies from other reactions in this scenario are similar to those shown in (a) and are thus not plotted in (b). From bottom to top, a change in the direction in the curves depicting energy supplies in (a) and (b) marks the transition to a system limited by electron donors from that a system limited by electron acceptors. Energy via all reactions listed in Table 4.1 were calculated but some are not shown as energy yield is <0.1 calories/kg fluid.

In addition to methanogenesis, energy is also available via the nitrogen reduction or fixation reaction as $N_2$ is believed to be available in deep-seated fluids. However, unlike methanogenesis which has been detected in many serpentinizing sites, there is less evidence for the presence of nitrogen fixers capable of reducing $N_2$ in the serpentinizing subsurface despite the relatively higher available energy. Brazelton et al. (2011) identified the *nifH* genes in biofilms from the submarine Lost City vents that strongly suggests the presence of $N_2$ fixers. Whether they are active in deep-seated continental serpentinizing environments remains to be seen.

Additional energy through a more diverse variety of redox reactions can be available when the two end-member fluids mix, as shown in Figure 4.5a. Overall, nitrate reduction and hydrogen oxidation provide the most energy during the mixing process. Their high energy yield ($E_r$) can be attributed to extensive disequilibria that results in high $A_r$ values (Canovas et al., 2017, also see Table C3). This high disequilibria and/or energy yield could contribute to the dominance of $H_2$ and sulfur-oxidizing denitrifiers in deep aquifers in the Witwatersrand Basin, South Africa (Lau et al., 2016) compared with those that are capable of methanogenesis, sulfate reduction, and the anaerobic oxidation of methane that are typical of most subsurface lithoautotrophic microbial ecosystems (SLiMEs) supported by $H_2$ (Moser et al., 2005; Lever et al., 2013; Magnabosco et al., 2016; Fones et al., 2019).

The changes in the direction of the slopes of curves depicting various energy supplies in Figure 4.5a indicate a transition in the limiting reactants (*e.g.*, DIC or $H_2$ for methanogenesis, $O_2$ or $H_2$ for hydrogen oxidation, etc.) at a given mixing extent, with the oxidant usually being limiting at low degrees of mixing of shallow end-member fluid into deep-seated fluids (lower part of Figure 4.5a). The highest energy for a given reaction is attained at this point of the mixing progress. Anaerobic reactions tend to shift from being oxidant-limiting to reductant-limiting and thus maximize their energy yield at no to low extents of shallow fluid mixing into deep-seated fluids. In contrast, except for iron oxidation, energy through aerobic reactions usually maximizes at greater extents of mixing. Energy is maximized for hydrogen oxidizers late in the mixing process (~60% mixing), while those for ammonia and sulfide oxidizers occurs at 42% and 33% mixing, respectively. Energy for methanogens is maximized at minimal mixing extents (~10%) while sulfate and nitrate reducers can get the most energy at a little higher mixing extent, that is at ~25% and ~30%, respectively. Energy via nitrogen reduction decreases as the mixing process progresses. These predicted trends suggest that methanogens and other anaerobes could be favored in fluids characterized by no to low extents of mixing at deeper portions of the discharge zone of the aquifer, while aerobes would prefer systems characterized by higher extents of mixing close to the surface.

In the scenario where elevated levels of methane (~1 millimolal) are available in the deep-seated fluid end-member, such as those measured from some subsurface fluids in serpentinizing environments (Rempfert et al., 2017; Etiope and others, 2017), conditions for both aerobic and anaerobic methanotrophs become favorable. Results of energetic calculations for methanotrophic reactions along the mixing process are shown in Figure 4.5b as blue curves of different shades. Similar to trends for other aerobic reactions shown in Figure 4.5a, energy yielded by the aerobic methanotrophic reaction is maximized at high extents of mixing (~87%) while anaerobic methane oxidation reactions are maximized at lower extents of mixing. Among the various electron acceptors available to methanotrophs, high energy is available for those capable of reducing nitrate followed by those capable of reducing sulfate. Methanotrophy using nitrite as an electron acceptor yields energy <0.1 calories/kg and hence is not shown in Figure 4.5b. If the modeled methane level is less than that of 1 millimolal, energy values will shift to the left and the change in direction of the slope of the curves will occur at lower extents of mixing as lower concentrations of methane will be limiting earlier in the mixing progress. In addition, the high levels of methane assumed for the scenario depicted in Figure 4.5b would result in lower potentials for methanogenesis and hence will yield less energy. Despite the 12 orders of magnitude difference in the methane levels assumed in this scenario (1 millimolal) *vs*. that depicted in Figure 4.5a (1 picomolal), the reduction in the amount of energy supplies is reduced by only ~50% as shown by the two brown curves in Figure 4.5b with the dashed curve representing values from the methane-poor scenario depicted in Figure 4.5a.

Energetic returns inferred for the continental serpentinizing subsurface are less than those predicted for analogous mixing process accompanying fluid venting in submarine hydrothermal environments (*e.g.*, >100 calories/kg for methanogenesis alone, McCollom, 2007; Amend et al., 2011; Nakamura and Takai, 2014). Although limited, these energy supplies could still support microbial communities in the continental subsurface. Results from calculations for the mixing of end-member fluids shows that energy inferred for the subsurface, which can be >10 calories/kg for some reactions (Figure 4.5), are on par or even greater than those calculated from surficial samples (<10 calories/kg, see Figure 4). Howells (in prep) shows that chemotrophs such as methanogens and other hydrogenotrophs are present in serpentinizing fluids at the surface despite the limited energy. Therefore, similar or even higher amounts of energy predicted for the subsurface seem likely to sustain subsurface communities. Furthermore, discharge zones along fluid pathways can enhance energy availability through fluid mixing and could be hotspots for subsurface life. Mixing calculations can also predict where certain microbial communities are favored in the subsurface and can help future work that targets certain microbial strategies during subsurface sampling. Further work can also test the predictions made here through detailed sampling of the subsurface and experiments simulating the mixing processes.

### *4.5.3. Power Supplies for Methanogens and Microbial Biomass in Deep Serpentinizing Aquifers*

Energy supplies will eventually decrease as reactants are consumed. The forward direction of a redox reaction can be still be favorable and sustained if the rate at which reactants are delivered is equal to or faster than that at which they are consumed. Overall, habitable systems are attained when the rate to which energy is supplied exceeds biological demand (Shock and Holland, 2007; Hoehler, 2007). Thus, quantification of how fast can energy be supplied to a subsurface community in combination with estimates of microbial energy demand would provide powerful tools for mapping and targeting hotspots in the deep subsurface where life may proliferate.

In habitable subsurface environments, groundwater flow must be fast enough to supply reactants that favor the forward direction of chemolithotrophic reactions. While there are constraints in the magnitude of groundwater flow in the shallow aquifers in the Oman ophiolite (Dewandel et al., 2005), flow rates in the deep subsurface are not yet quantified. In the deep aquifers, supplies of electron acceptors or inorganic carbon from the surface is limited. However, alternative sources of inorganic species such as carbon and sulfate can be readily available in the deep subsurface through the dissolution of minerals. It would follow that the rate at which minerals dissolve can provide constraints on the rate to which energy can be supplied to subsurface microbial communities. As an example, we discussed above that conditions favorable for methanogens in carbon-poor systems are possible so long as inorganic carbon is supplied from the dissolution of carbonate minerals. This is likely to be the case in deep subsurface environments as the supply of inorganic carbon (electron acceptors) will be limiting instead of the supply of $H_2$ (electron donor), which is enriched in serpentinization-generated fluids. However, at the hyperalkaline conditions characteristic of serpentinization-derived fluids, carbonate minerals are highly insoluble and are very slow to dissolve. These constraints raise questions about whether the presence of deep carbonate minerals is enough to support deep-seated methanogens. To answer these questions, power supplies for methanogens were calculated using energy yields derived above for methanogenesis in combination with experimental constraints on the rate of dissolution of carbonate minerals common in the Oman subsurface: calcite, magnesite, and dolomite (Mervine et al., 2014).

The rate of calcite dissolution decreases with decreasing pH but becomes constant when pH exceeds values between 6 and 7 (Plummer et al., 1978; Chou et al., 1979). At circumneutral to basic pH (~12) and ambient temperatures (~25°C) assumed for serpentinization-generated fluids flowing in continental serpentinizing aquifers, the rate of dissolution of calcite varies from $10^{-6}$-$10^{-5}$ mole C $m^2$ $sec^{-1}$ (Plummer et al., 1978; Chou et al., 1979; Shiraki et al., 2000; Arvidsson et al., 2003). Dissolution of magnesite at 25°C and circumneutral to alkaline conditions is much slower than that shown for calcite and varies from $10^{-10}$-$10^{-9.5}$ mole C $m^2$ $sec^{-1}$ (Pokrovsky and Schott, 1999). The dissolution rate of dolomite is intermediate between those of calcite and magnesite and more variable, from $10^{-10}$-$10^{-8}$ mole C $m^2$ $sec^{-1}$, following results of experiments by Pokrovsky and Schott (2001).

At minimal background methane (1 picomolal) and at $H_2$ concentrations dictated by the $H_2O$-$H_2$ redcution process, the methanogenesis reaction will yield $A_r$ values of ~3250 calories/mole $e^-$ transferred or a total of 26,000 calories/mole C (3250 × 8 $e^-$ transferred from one mole of DIC to one mole of $CH_4$). This is equivalent to ~110,000 Joules/mole C. If background methane is high (1 millimolal) such as that depicted in Figure 4.5b, energy yield will decrease by approximately half yielding 60,000 Joules/mole C. Multiplying $A_r$ (Joules/mole C) with the dissolution rates (mole C/cm$^2$ sec) will result in a power yield per m$^2$ of carbonate (watts/cm$^2$). The total power supply per mass of fluid (watts/kg fluid) is obtained assuming variations in the specific surface area that is possible in the subsurface from a highly fluid-dominated system ($10^{-5}$ m$^2$ carbonate in contact with 1 kg of fluid) to one that is rock-dominated ($10^1$ m$^2$ carbonate per kg of fluid).

Results of calculations, depicted in Figure 4.6a, show increasing power yield with increasing specific surface area. The colored area for each carbonate mineral depicts variations in the dissolution rate and energy yield discussed above, with the upper bound representing the scenario with the fastest dissolution rate and highest energy yield (*i.e.*, at low background methane). Calcite, which has the fastest rate of dissolution among the three carbonate minerals, will yield the fastest rate at which energy can be supplied for methanogens. A lower power supply is available through dissolution of dolomite followed by dissolution of magnesite. Incorporating constraints on the energetic demands of methanogens (watt/cell) allows estimates on how much methanogenic biomass (cells/kg fluid) these power supplies (watt/kg fluid) can support in the deep subsurface. For methanogens, we used the power requirement of 1400-1600 fW/cell needed for cell

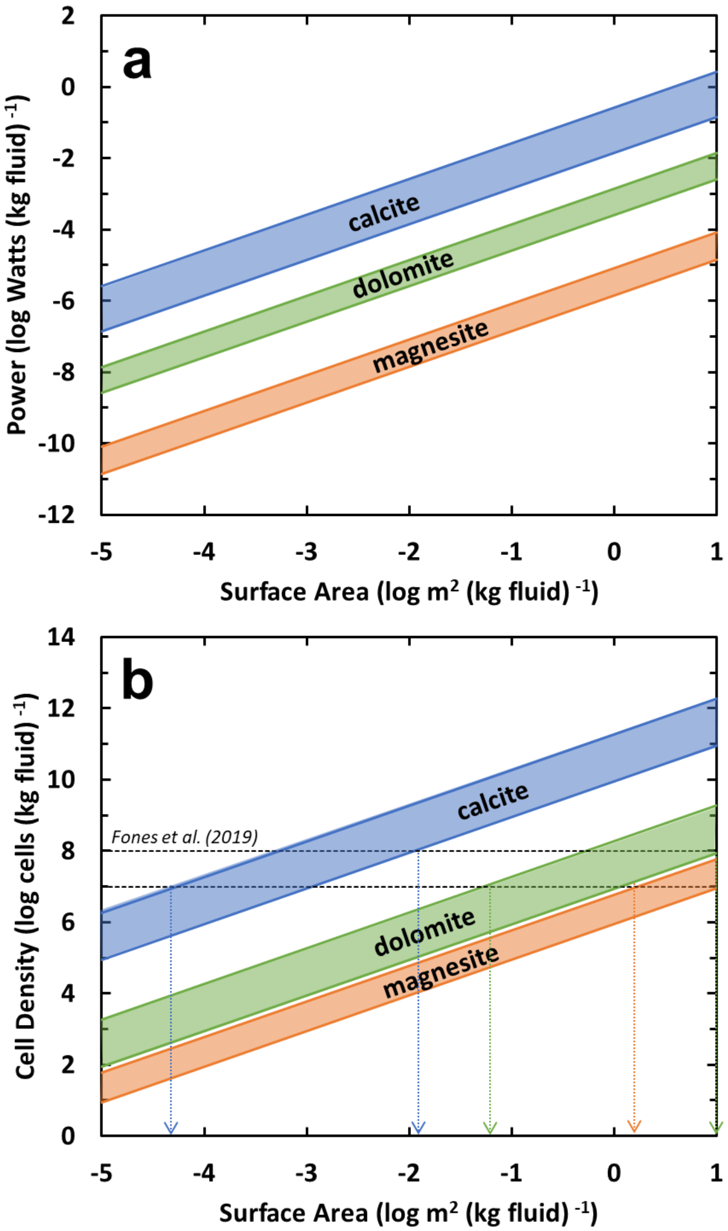

*Figure 4.6*. (a) Power supplies (log watts/kg fluid) available for deep-seated methanogens as functions of the availability of carbonate minerals (log $m^2$ calcite, dolomite, or magnesite per kg of fluid) supplying inorganic carbon. (b) Amount of methanogenic biomass that can be supported by this power supply. Lower and upper dashed horizontal lines depict 10% and 100%, respectively, of biomass (~$10^8$ cells/kg fluid) measured from hyperalkaline fluids obtained from deep wells in Oman (Fones et al., 2019). Ranges in the availability of carbonate minerals necessary to support this amount of biomass, assuming it is all methanogenic, are shown by the arrow lines.

maintenance (Tijhuis et al., 1993; Larowe and Amend, 2015). Calculated biomass as functions of the availability of carbonate minerals is depicted in Figure 4.6b. By comparison, biomass observed from hyperalkaline fluids obtained from wells in the Oman ophiolite was quantified to ~$10^8$ cells/kg fluid (Fones et al., 2019). If l00% and 10% of these cells are methanogens, respectively depicted by the upper and lower horizontal dashed line in Figure 4.6b, this would entail that ~$10^{-4.4}$ to $10^{-1.9}$ $m^2$ (<1 – ~100 $cm^2$) of calcite would be required to be in contact with a kg of fluid to support this amount of methanogens living in deep $H_2$-rich, serpentinizing aquifers. In contrast, the same amount of dolomite and magnesite can support far less biomass (<$10^6$ cells/kg fluid) and the presence of much more of these minerals is required to support the same magnitude of biomass detected by Fones et al. (2019) for the Oman serpentinizing subsurface, as depicted by the green and orange arrows in Figure 4.6b.

A survey of the extent of mineral carbonation through detailed fieldwork or investigation of recovered cores from the deep subsurface would reveal if methanogenesis from carbonates is a realistic scenario. The above calculations only simulate advection of inorganic carbon sources through mineral carbonate dissolution that can potentially be harvested by subsurface microbial communities. Alternative modes of harvesting substrates like those of autotrophs capable of directly assimilating carbon from minerals (*e.g.*, Guida et al., 2017) can overcome limitations from constraints on mineral dissolution rates. Nevertheless, the model proposed here presents opportunities to combine constraints from mineral dissolution experiments with calculations of microbial energy supply and demand to predict not only the rate to which geochemical energy is supplied to subsurface communities but also to infer how much biomass this energy supply can support. Ultimately, these calculations can provide information on where to target deep-seated communities with the aid of field observations and estimations on the distribution of minerals that can supply electron acceptors (*e.g.*, carbonates, sulfates, iron oxide/oxyhydroxides) or donors (*e.g.*, reduced iron and sulfur minerals) in the deep subsurface.

## 4.6. Conclusions

Chemical energy stored in rocks and released during water-rock reactions can potentially support a rich deep biosphere. A pertinent example is when the serpentinization of ultramafic rocks yields some of the most reduced fluids on Earth that can ultimately sustain deep subsurface microbial communities. This work presents a comprehensive quantification of geochemical energy supplies available in both the serpentinizing surface and subsurface. We evaluate energy supplies in hyperalkaline fluids seeping from both ultramafic and gabbroic outcrops and find that these fluids can have a variety of energy sources for chemotrophic reactions. In surficial samples, the highest energy available to microorganisms is supplied through aerobic reactions. Gabbro-hosted fluids generally can yield greater potentials for sulfide, methane, and CO oxidation reactions than most fluids sampled in ultramafic bodies. Specifically, methane oxidation tied to sulfate reduction is highly favorable in gabbro-hosted fluids. In contrast, energy supplies for hydrogenotrophs like hydrogen oxidizers, methanogens and sulfate reducers are lower in gabbro-hosted systems. Studies focused on low-temperature gabbro-hosted environments are lacking and improving our datasets on gabbro-hosted environments, in parallel with the more well-known basalt- and ultramafic-hosted systems, would better capture the potential diversity of fluid compositions expected in rock-hosted systems deep in the Earth's subsurface, which in turn may vary significantly in their potential to support life.

In addition, we predict energy available in subsurface environments by estimating the compositions of end-member fluids representative of shallow and deep ultramafic aquifers. The compositions of these end-member fluids were derived using constraints from fluid-mineral-gas equilibria in combination with trends observed from a comprehensive dataset of fluid compositions from surface and well fluids in Oman. Through these inferred subsurface compositions, we quantify energy that can be available through several chemotrophic reactions. Our calculations reveal hotspots where certain microbial communities may bloom – one in the deeply serpentinizing subsurface and the other in discharge zones of fluid pathways where these reduced deep-seated fluids encounter oxidized shallow-aquifer fluids. In the deep subsurface, available energy can be exploited by methanogens (~0.2 calories/kg fluid) and nitrogen reducers (~6 calories/kg fluid), permitting the possibility of deep communities in serpentinizing aquifers. Energy supplied by other chemolithotrophic processes is minor due to limited supplies of electron acceptors (*e.g.*, $O_2$, sulfate, nitrate, nitrite).

Dissolved inorganic carbon available to deep subsurface communities can be supplied from carbonate minerals. By incorporating constraints from mineral dissolution experiments, we quantified the rate to which energy is supplied, in watts/kg fluid, to subsurface methanogens through the mobilization of DIC from carbonates. Despite the low solubility and slow rate of dissolution of carbonates at alkaline pH, energy is available to methanogens as long as carbonate minerals are sufficiently present to supply inorganic carbon through mineral dissolution. A reasonable extent of calcite-fluid interactions (at most ~100 $cm^2$ calcite per kg of water) can support the amount of biomass estimated for the deep serpentinizing environments (~$10^8$ cells/kg fluid, Fones et al., 2019). Similar amounts of magnesite and dolomite can sustain far less biomass (<$10^6$ cells/kg fluid).

More energy is available for methanogens and other chemolithotrophs when upwelling deep-seated fluids mix with shallow groundwater. Mixing calculations show where in the mixing pathway certain chemotrophic reactions are favored more than others. Methanogenesis and other anaerobic reactions are favored in fluids characterized by no to low extents of mixing, while the Knallgas and other aerobic reactions are favored in systems characterized by higher extent of mixing. This framework presents opportunities for exploring and ultimately developing strategies that target microorganisms or communities in the deep serpentinizing subsurface. It is anticipated that future work can test predictions set forth by this study through detailed sampling of subsurface samples and experimental work simulating the mixing process.

## 4.7. Acknowledgements

The author would like to thank Alta Howells, Grayson Boyer, Kris Fecteau, Kirt Robinson, Tucker Ely, and Alysia Cox for discussions on fluid samples investigated in this work and calculations of energy supplies. Calculations of energy supplies in this work was conducted using a Jupyter notebook, hosted in the ENKI server and developed by Grayson Boyer, that integrates functions of the EQ3 and CHNOSZ programs. This work was supported by NASA Exobiology grant NNX12AB38G, the NASA Astrobiology Institute Rock-Powered Life project, the NASA SUBSEA project, and NSF grant EAR-1515513.

# CHAPTER 5

# DECREASING EXTENTS OF KOMATIITE SERPENTINIZATION TOWARDS THE END OF THE ARCHEAN CONTRIBUTED TO THE RISE OF AN OXYGENIC ATMOSPHERE

## 5.1. Introduction: Serpentinization as a sink for $O_2$

The Great Oxidation Event (GOE) after the end of the Archean is a remarkable period in Earth's history. This period marks the initial oxygenation of the Earth's surface through a dramatic increase in the atmospheric $O_2$ levels from minor amounts ($<10^{-5}$ of present atmospheric levels or PAL) to much higher values ($10^{-4} – 10^{-2}$ PAL, Farquhar et al., 2000; Lyons et al., 2004) around 2.5 to 2.3 billion years (Ga) ago (Bekker et al., 2014; Philippot et al., 2018). While the production of $O_2$ through oxygenic photosynthesis evolved much earlier (*e.g.*, Brocks et al., 1999) and contributed to localized accumulation of $O_2$ well before the GOE (*e.g.*, Anbar et al., 2007; Kendall et al., 2010; Crowe et al., 2013; Planavsky et al., 2014; Ostrander et al., 2019), it was only after the end of the Archean when $O_2$ began to accumulate to significant levels in the atmosphere. It is proposed that the period preceding the GOE was characterized by the dominance of geochemical and biological processes that consume $O_2$ (sink) over its production (source). Ultimately, the decreasing magnitude of $O_2$ sinks in the form of reduced chemical species as volatiles (*e.g.*, $H_2$, $CH_4$) and as solids (*e.g.*, $Fe^{+2}$-bearing minerals) permitted the accumulation of $O_2$ in the atmosphere towards the end of the Archean.

These decreases could have been brought about by the escape of $H_2$ from the atmosphere (Kasting et al., 1993; Catling et al., 2001; Catling and Claire, 2005; Claire et al., 2006) and a transition to outgassing of more oxidized volatiles from magmas (Kasting et al., 1993; Holland 2002; 2009; Kump et al., 2001; Kump and Barley, 2007; Gaillard et al., 2011). In addition, the rise of $O_2$ has been tied to secular changes in the composition of the Earth's continental crust (*e.g.*, Lee et al., 2016; Smit and Mezger, 2017). The Earth's crust has vast potentials to consume $O_2$ via the oxidation of ferrous iron in rocks into ferric iron in minerals that formed during rock alteration and weathering, as depicted by the reaction

$$4\mathrm{Fe^{+2}O}_{(\text{primary minerals})} + \mathrm{O_2} \rightarrow 2\mathrm{Fe^{+3}{}_2O}_{3(\text{secondary minerals})}. \tag{5.1}$$

The transition from a continental crust composed dominantly of Fe-rich mafic rocks to one that is composed mostly of Fe-poor felsic rocks during the Archean resulted in a decrease in the reductive efficiency of the Earth's crust that could have facilitated the initial oxygenation of Earth's surface (Lee et al., 2016).

The absence of $O_2$ does not impede the oxidation of rocks. At great extents of water-rock interactions such as those occurring in deeper aquifers when $O_2$ and other dissolved oxidants are exhausted, ferrous iron in the protolith is oxidized to ferric iron in the alteration assemblages and in turn, water is reduced into $H_2$ as depicted by the reaction

$$2\mathrm{Fe^{+2}O}_{(\text{primary minerals})} + \mathrm{H_2O} \rightarrow \mathrm{Fe^{+3}{}_2O}_{3(\text{secondary minerals})} + \mathrm{H_2}, \tag{5.2}$$

supplying an additional sink for $O_2$ through

$$\mathrm{O_2} + 2\mathrm{H_2} \rightarrow 2\mathrm{H_2O} \tag{5.3}$$

The amount of $H_2$ that can be generated through reaction (5.2) is independent of the iron content of the reacting rocks and is instead dependent on their bulk compositions

(McCollom and Bach, 2009). An extreme example is when the hydrous alteration of ultramafic rocks, known as serpentinization because serpentine replaces the original minerals, produces some of the most $H_2$-rich fluids on Earth that contribute to much of the modern supply of abiotic $H_2$ (Klein et al., 2020). However, locations where substantial amounts of abiotic $H_2$ are actively generated are limited in modern Earth settings to those found near slow-spreading ridges where ultramafic rocks are exposed in the seafloor (*e.g.*, Lost City Hydrothermal Field, Kelley et al., 2001) and in uplifted ultramafic bodies on continents (*e.g.*, ophiolites) where $H_2$-rich, hyperalkaline ($pH > 11$) fluids actively seep from outcropping ultramafic rocks (*e.g.*, Barnes et al., 1967; Etiope and Whiticar, 2019; Leong and Shock, 2020). In contrast to the modern Earth, ultramafic rocks such as komatiites were much more widespread early in Earth's history (*e.g.*, Tang et al. 2016; Greber et al., 2016; Smit and Mezger, 2017), which implies that $H_2$ production through continental serpentinization could have been more prevalent.

Several authors have proposed that the decreasing flux of serpentinization-generated volatiles via the progressive loss of ultramafic rocks exposed at the surface as the mantle cooled through the Archean could have helped facilitate the GOE (Kasting, 2005; 2013; Kasting and Canfield, 2012; Smit and Mezger, 2017). However, it is unclear if this trend is sufficient to permit significant accumulation of $O_2$ in the atmosphere as the magnitude of the decrease in the flux of serpentinization-generated volatiles has never been quantified for the period leading to the GOE. The purpose of this communication is to report results of such computations. This work combines numerous thermodynamic simulations of water-rock interaction with mass-transport calculations to estimate the flux of $H_2$ generated through the serpentinization of komatiites, which were common in the

Archean continents, and assess quantitively whether the decreasing extent of komatiite volcanism towards the end of the Archean set the stage for the Great Oxidation Event.

### 5.2. Methods: Estimating global $H_2$ production and associated $O_2$ sink

The annual global outgassing of $H_2$ (mole $H_2$ $yr^{-1}$) derived from the serpentinization of komatiites at a given point of Earth's history, $\left(\frac{\delta H_2}{\delta t}\right)_K$, can be described by the equation

$$\left(\frac{\delta H_2}{\delta t}\right)_K = a_K r_K x_K \tag{5.4}$$

where

$a_K$ = extent of komatiite distribution in the continents ($km^2$),

$r_K$ = rate of komatiite serpentinization (km $yr^{-1}$), and

$x_K$ = the $H_2$ generation potential of a given volume of komatiite (mole $H_2$ $km^{-3}$).

As shown in reaction (5.3) consuming a mole of $O_2$ would require two moles of degassed $H_2$, which means that the global $O_2$ consumption can be estimated via

$$\left(\frac{\delta O_2}{\delta t}\right)_K = 0.5\left(\frac{\delta H_2}{\delta t}\right)_K. \tag{5.5}$$

The amount of $H_2$ that can be generated through the serpentinization of a given volume of komatiite, depicted by $x_K$ in equation (5.4), can be variable and will depend on the compositions of the reacting rock and fluid, as well as the extent of the rock alteration process. Simulations of hydrous alteration of komatiites of various compositions was conducted using the reaction-path code EQ36 (Wolery and Jarek, 2003) together with a customized thermodynamic database (see below) to calculate $x_K$ values. These calculations simulate the hydrous alteration of a rock by a fluid and determine the compositions of coexisting solid phases and fluid constituents attained at thermodynamic equilibrium at each step of overall progress in rock alteration. An increase in reaction progress is analogous to a decrease in the water-to-rock ratio, as the reacting water encounters more rock while infiltrating deeper into the subsurface. Our models account for $H_2$ generated at various extents of water-rock reaction, quantified as the water-to-rock ratio.

Although idealized, these calculations allow us to adequately track changes in fluid chemistry during rock alteration as demonstrated by a number of studies on various sites of serpentinization actively occurring today (*e.g.*, Bruni et al., 2002; Paukert et al., 2012; Leong and Shock, 2020). Simulated temperature is set to 25°C to model continental aquifers at depths $\geq$ 500m where serpentinization is thought to be actively occurring (Dewandel et al., 2005). Compositions of reacting rocks were taken from Sossi et al. (2016), which includes 34 different komatiites from various locations on Earth. The hydrous alterations of other Fe-bearing igneous rock types (peridotite, picrite, and basalt) were also modelled to compare their $H_2$ generation potentials with those calculated via komatiite alteration. Compositions of picrites and basalts used in this work are from Starkey et al. (2009) and Gale et al. (2014), respectively. Compositions of peridotites used in the model were taken from the compilations of Niu (2001) and Hanhoj et al. (2010) on abyssal and ophiolitic peridotites, respectively. The latter work focuses on rocks from the Oman ophiolite, which our simulations use in a worked example for evaluating modern global $H_2$ generated through serpentinization of continental peridotites. Compositions of all rocks used in simulations are compiled in Table D1.

While the rock record can constrain compositions of reacting rocks, the composition of reacting fluids representative of the Archean Earth is highly uncertain.

Therefore, our idealized model used neutral fluids with dilute concentrations (<1 nmolal) of solutes as starting reactants. The dissolved oxygen content of reacting fluids used in the model was made to be varied, ranging from that being in equilibrium with an atmosphere with partial pressures of $O_2$ of $10^{-5}$ bars to that with $10^{-0.7}$ bars, to account for all scenarios possible for the starting redox state of reacting fluids during the past 3.5 Ga. The lower bound of this range approximates the maximum predicted levels of dissolved $O_2$ for most of the Archean while the upper bound is close to modern levels. We did not include dissolved $CO_2$ in our idealized fluids due to scarcity of information on mineral carbonation reactions in the deep past. However, note that $pCO_2$ could have been much higher in the Archean. Consequently, pH of meteoric-derived fluids infiltrating the continental subsurface could be lower (*e.g.*, Hao et al., 2016) and affect reaction rates. Moreover, while the inclusion of $CO_2$ in the reacting fluid can permit prediction on the amount of $CH_4$ generated, which is another sink for $O_2$, generation of abiotic $CH_4$ during low-temperature serpentinization has been questioned (McCollom 2016; Wang et al., 2018). Future work constraining the concentrations of dissolved $CO_2$ as well as other solutes in the reacting fluid can refine model results. Thermodynamic data used in the simulations are calculated with the SUPCRT code (Johnson et al., 1992) using standard state thermodynamic data for aqueous species taken from Shock and Helgeson (1988), Shock et al. (1989, 1992, 1997), and Sverjensky et al. (1997), together with the revised Helgeson-Kirkham-Flowers equations of state (Shock et al., 1992). Data for minerals were mostly taken from Helgeson et al. (1978) and Wolery and Jove-Colon (2004) with the addition of estimated thermodynamic data for clay minerals, consistent with these databases, from Catalano (2013).

The rate of komatiite serpentinization, $r_K$, can be informed by experimental work. However, experimental data on komatiite serpentinization are focused on hydrothermal conditions (≥300 °C, Lazar et al., 2012; Shibuya et al., 2015). Existing low-temperature experiments (Neubeck et al., 2011; Mayhew et al., 2013; Okland et al., 2014) examined serpentinization of other ultramafic rocks (*e.g.*, harzburgites) or minerals (*e.g.*, olivine). Moreover, recent experiments of McCollom and Donaldsson (2016) show that $H_2$ generation rates during low-temperature serpentinization are much slower than rates determined by the above studies to the point that $H_2$ is undetectable on the timescales of laboratory experiments. Alternatively, alteration rates can be derived from field-based investigations at the watershed scale. Using reported weathering rate data from various field-based studies (*e.g.*, Dessert et al., 2003), Navarre-Sitchler and Brantley (2007) derived weathering advance rates in basaltic terranes that ranges from $10^{-8}$ to $10^{-6.5}$ km $yr^{-1}$. Denudation rates estimated for rocks comprising the Oman ophiolite, which are mostly ultramafic, are in the order of $10^{-6.5}$ km $yr^{-1}$ (Poupeau et al., 1998) similar to the maximum values measured in basaltic environments. However, estimated denudation rates for komatiitic bodies are unknown. In addition, it is uncertain if deep subsurface processes characteristic of serpentinization occur at rates similar to those derived through surficial or shallow sub-surficial weathering processes. Nevertheless, to account for these uncertainties, rates ranging from $10^{-8}$ to $10^{-6}$ km $yr^{-1}$ for komatiite serpentinization are used in our models, following the range of rates observed in modern mafic and ultramafic terranes.

The extent to which komatiites are present in continents, $a_K$, throughout Earth's history is informed by two types of data: (1) the mass of exposed continents, and (2) how much of the continents are komatiitic in composition. Estimates on the extent of continental exposures during the Archean are highly variable ranging from that close to modern levels (Armstong, 1981) to a much-reduced presence (*e.g.*, <50% of present level, Allegre and Rousseau, 1983; Condie and Aster, 2010). Taylor and McLennan (1985) predict less exposures of continents throughout most of the early Archean followed by a rapid growth at ~3.2 Ga ago until finally attaining around ~70% of present levels by the end of the Archean. Recent reports (Belousova et al., 2010; Dhuime et al., 2012) argue for a more gradual growth throughout the Archean, attaining ~60% – 70% of present levels ~2.5 Ga ago. Our simulations account for all the above variations in the estimated mass of continents exposed during the past 3.5 Ga. In addition, recent estimates of the compositions of the continents during the past 3.5 Ga reveal that the crust evolved from being dominantly mafic in composition to one that is predominantly composed of felsic rocks sometime during the Archean (Tang et al., 2016; Lee et al., 2016; Greber et al., 2017). While Greber et al. (2017) disagrees with Tang et al. (2016) on the timing of this transition, both studies are consistent with their estimates of past komatiite distribution, and both estimate significant presence of komatiites in continents during the early Archean (10 – 20% of continents) and a greatly diminished distribution towards the end of the Archean. Although these estimates of past komatiite distribution are based on assumptions given a single bulk rock composition (Tang et al., 2016; Greber et al., 2017), natural komatiites are compositionally variable and can consequently yield varying potentials to generate $H_2$. Our calculations account for these variabilities by including komatiites of variable compositions ranging from those enriched in Mg to those that are Mg-depleted, using bulk data from Sossi et al. (2016).

Our calculations of the global $H_2$ flux during the past 3.5 Ga are focused on those derived from komatiite serpentinization and do not account for $H_2$ generation from other sources. In the modern Earth, much of the $H_2$ is sourced from water-rock interactions, particularly from the serpentinization of peridotite rocks (Klein et al., 2020). However, unlike that for komatiites where their past distribution can be constrained, past flux of $H_2$ generated through peridotite serpentinization is difficult to quantify as the distribution of peridotites during the past 3.5 Ga is largely unknown. Mafic and felsic rocks have much lower potential to be serpentinized and generate $H_2$ at low temperatures and are thus not included in this work. In addition to the quantities produced in continents, significant amounts of $H_2$ can be sourced from hydrothermal reactions in the subseafloor. However, the distribution of ultramafic rocks in the oceanic crust during the past 3.5 Ga remains unknown. Elevated temperatures for the upper mantle in the Archean could have led to the formation of more Mg-rich rocks in the upper oceanic crust. Whether the composition of these rocks permits extensive serpentinization and consequently $H_2$ generation remains to be tested in future work. Aside from water-rock interactions, other sources for abiotic $H_2$ are through degassing of magmas, radiolysis of water, and comminution of rocks (Klein et al., 2020) which are all difficult to constrain for the past 3.5 Ga.

## 5.4. Results and Discussions

### *5.4.1. Serpentinization is the key to significant $H_2$ production*

The hydrous alteration of igneous rocks with similar ferrous iron content does not always yield similar amounts of $H_2$. As an example, basaltic and ultramafic rocks have similar ferrous iron content (~10% FeO) and, seemingly, the hydrous alteration of both types of rocks should generate the same amounts of $H_2$ via reaction (5.2). However, fluids that are most enriched in $H_2$, such as those venting at the Lost City and Rainbow hydrothermal fields (Seyfried et al., 2015; Charlou et al., 2002), are commonly associated with ultramafic-hosted environments. Ultramafic-hosted fluids can attain >10 mmolal $H_2$ which is at least 10x more concentrated than those measured from most basalt-hosted hydrothermal fluids (see Humphris and Klein, 2018). This contrast is much more distinct in lower temperature environments such as those occurring in continents. Ultramafic-hosted hyperalkaline seeps can attain >1 mmolal $H_2$ (*e.g.*, Oman ophiolite, Rempfert et al., 2017) while most basalt-hosted fluids rarely exceed >0.01 mmolal $H_2$ (*e.g.*, Columbia river basalt, Stevens and McKinley, 1995). The greater potential for ultramafic rocks to generate $H_2$ during alteration is attributed to their composition (McCollom and Bach, 2009). However, only a few studies have related the starting compositions of the reacting rocks with the redox potentials of the resulting hydrothermal fluid (*e.g.*, Wetzel and Shock, 2000; Klein et al., 2013) and none has so far conducted an extensive assessment of the $H_2$-generation potentials of rocks with compositions ranging from ultramafic to mafic.

The diversity in redox conditions generated during water-rock interactions can be predicted through thermodynamic simulations. Results of simulations are depicted in Figure 5.1a which shows the calculated amount of $H_2$ generated during low-temperature (25 °C) alteration of several rock types at water-to-rock ratio of 100 (*i.e.*, alteration of 1 kg of rock in 100 kg of water). Predictions are summarized in Figures 5.1a and 5.1b for hydrous alteration of >300 igneous rocks with compositions ranging from those that are ultramafic, *i.e.* rocks that have high Mg content such as peridotites and komatiites (right side of Figures 5.1a and 5.1b), to those relatively depleted in Mg (left side of Figures 5.1a and 5.1b) such as basalts and picrites. Komatiites, picrites, and basalts solidified from melts that formed during partial melting of the mantle. Specifically, these three classes of rocks are formed from decreasing degrees of mantle melting and are respectively characterized by decreasing Mg content, as shown in Figures 5.1a and 5.1b, as well as increasing Si and Al content (Herzberg et al., 2006). Most of the peridotites exposed in the seafloor and in the continents are harzburgites and dunites, which are the residual rocks that remained after melting of the mantle and hence are characterized by high Mg content and low Si and Al values. As shown in Figure 5.1b at around 20 – 40% MgO, model results depict decreasing $H_2$ generation potentials as the reacting compositions become less magnesium-rich, corroborating natural observations that ultramafic-hosted fluids are more enriched in $H_2$ than those hosted in basalts. In addition, most peridotites and a few komatiites have higher potentials to form $H_2$ than the other investigated rocks as revealed through Figure 5.1a.

The key to the transitions in the $H_2$-generation potentials during rock alteration documented in Figures 5.1a and 5.1b is the formation of serpentine. All peridotites, most komatiites and some picrites, favor the formation of serpentine during rock alteration, as shown in Figure 5.1c, which depicts the overall abundances of secondary minerals (in mole fraction) calculated to form. Serpentine typically excludes ferrous iron from its crystal structure leading to its oxidation to ferric iron that can eventually be incorporated into later generations of serpentine, garnet, and at higher temperatures, magnetite (Klein et al., 2014). In contrast, rocks that are poorer in Mg (MgO <20%), such as some picrites and all basalts simulated in this work, do not favor serpentine formation during rock alteration. Instead, alteration of these Mg-poor but more Si- and Al-rich rocks stabilizes minerals such as chlorite, talc and clay minerals. Most of the iron mobilized from the protolith is incorporated into chlorite, talc, and clay minerals without much oxidation because these minerals tend to allow ferrous iron into their crystal structure. Consequently, less $H_2$ is generated as the iron oxidation process depicted by reaction (5.2) occurs at lower extents compared to those when serpentine is precipitating extensively. Ultimately, $H_2$ flux (moles $H_2$ $km^{-2}$ $yr^{-1}$) can be derived by incorporating rock alteration rates (km rock $yr^{-1}$) with calculated $H_2$ generation potentials (moles $H_2$ ($km^3$ rock)$^{-1}$). Calculations show that the serpentinization of peridotites will yield the highest flux rates, followed by secondary mineralization processes of komatiitic, picritic, and basaltic bodies, as shown in Figure 5.1d. Flux values were derived from $H_2$ generation potentials calculated at water-rock ratios ranging from 100 to 0.2 and assuming alteration rates of 0.3 and 1 mm $yr^{-1}$ as a minimum and maximum, respectively. Ranges and percentiles in calculated $H_2$ generation potentials and fluxes are compiled in Table D2.

Overall, results show that non-redox-sensitive components of rocks (*e.g.*, Mg, Si, Al) determine the distribution and the fate of Fe during secondary mineralization, and therefore the redox processes that generate reduced volatiles during fluid-rock interactions. Key to the production of significant levels of $H_2$ is the formation of serpentine which is favored in Mg-rich ultramafic rocks such as peridotites and komatiites. Other forms of mineralization, such as the chloritization, clay mineralization, and talcization of mafic rocks, yield considerably less $H_2$. Further discussions on how various types of mineralization, as well as how various non-redox sensitive elements, control $H_2$ production (Figure D1) can be found in Appendix D.

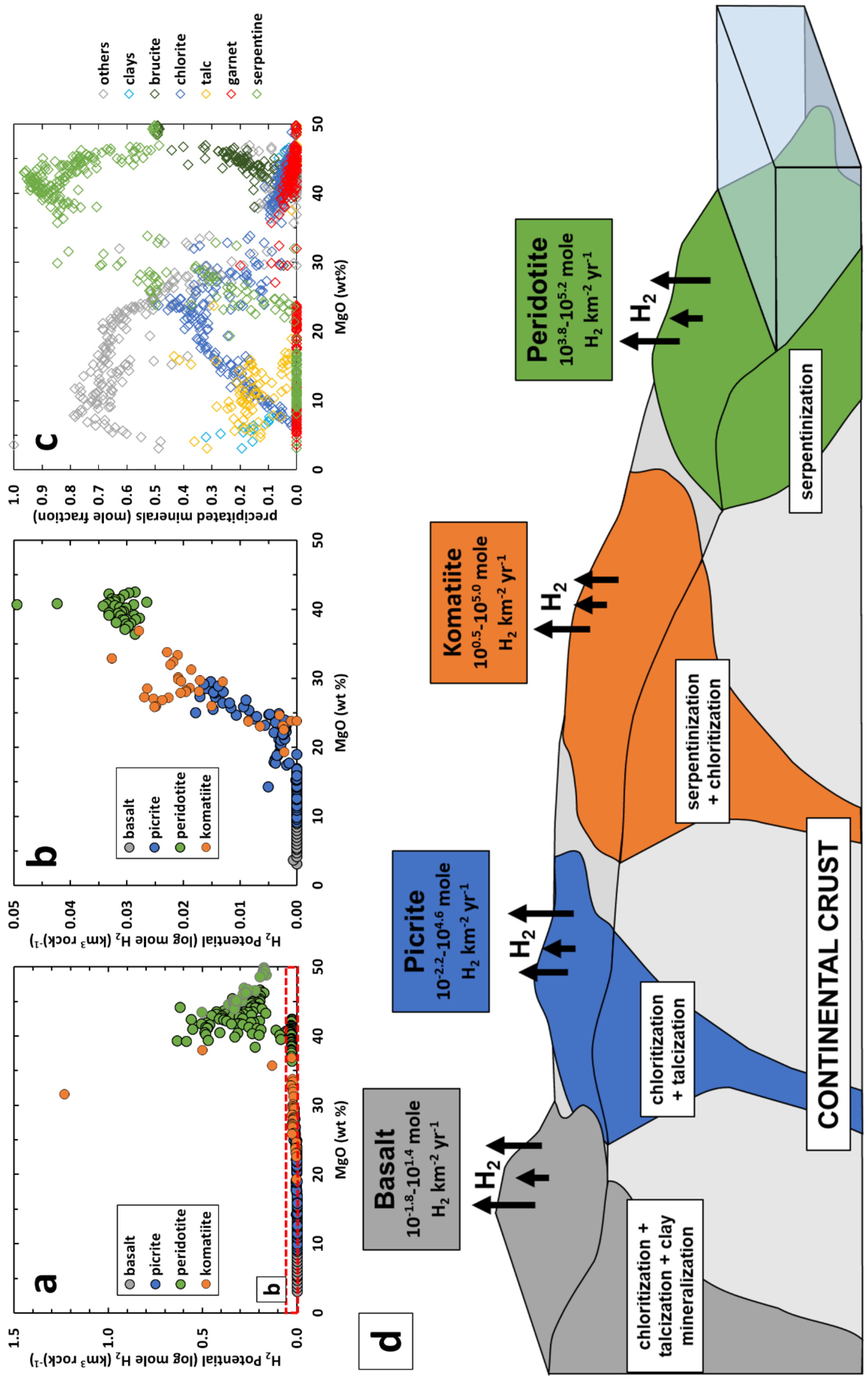
a
b
c
d
H$_2$ Potential (log mole H$_2$ (km$^3$ rock)$^{-1}$)
MgO (wt %)
MgO (wt%)
precipitated minerals (mole fraction)
basalt
picrite
peridotite
komatiite
others
clays
brucite
chlorite
talc
garnet
serpentine
Basalt
10$^{-1.8}$-10$^{1.4}$ mole H$_2$ km$^{-2}$ yr$^{-1}$
Picrite
10$^{-2.2}$-10$^{4.6}$ mole H$_2$ km$^{-2}$ yr$^{-1}$
Komatiite
10$^{0.5}$-10$^{5.0}$ mole H$_2$ km$^{-2}$ yr$^{-1}$
Peridotite
10$^{3.8}$-10$^{5.2}$ mole H$_2$ km$^{-2}$ yr$^{-1}$
H$_2$
chloritization + talcization + clay mineralization
chloritization + talcization
serpentinization + chloritization
serpentinization
CONTINENTAL CRUST

*Figure 5.1*. (a) The $H_2$ generation potential during hydrous alteration of various rock types with compositions ranging from peridotitic (right, high MgO%) to basaltic (left, low MgO%). $H_2$ generation values are from simulations depicting low-temperature (25°C) conditions at a water-to-rock ratio = 1. Green symbols surrounded by grey outline represent results for peridotites sampled from the Oman ophiolite in contrast to those sampled from the seafloor (green symbols with black outline). (b) is a close-up of the $H_2$ generation potentials of rocks within the red box in (a). (c) shows minerals (in mole fraction) that formed in simulations. (d) depicts 5th-95th percentile of $H_2$ flux derived from the $H_2$ generation potentials yielded by simulations at various water-rock ratios (100, 10, 1, and 0.2) and assuming alteration rates of 0.3 mm $yr^{-1}$. The dominant modes of secondary mineralization (*e.g.*, serpentinization, chloritization) for each reacting rock type are also indicated.

### *5.4.2. Estimating modern $H_2$ flux from the serpentinization of continental peridotites*

A significant component of the modern supply of abiotic $H_2$ is generated through the serpentinization of peridotites in the seafloor and continents, among various other geological sources (Klein et al., 2020). Following our example in Figure 5.1 of the $H_2$ generation potentials of various rocks types including peridotites ($x_P$, in moles $H_2$ ($km^3$ rock)$^{-1}$), the modern global flux from continental serpentinization can be calculated if extents of peridotite in continents ($a_P$, $km^2$) and the rate to which it can be serpentinized ($r_P$, km $yr^{-1}$) are known. The $x_P$ of continental peridotites can be calculated using bulk rock compositions of peridotites from the Oman ophiolite (data from Hanhoj et al., 2010) reacting with fluids in equilibrium with the modern atmospheric composition. Computed values of $x_P$ at various extents of water-rock reactions can be multiplied by a $r_P$ of $10^{-6.5}$ km $yr^{-1}$ (or 0.3 mm $yr^{-1}$) determined for the Oman mountains by Poppeau et al. (1998) to yield flux rates (mole $H_2$ $km^{-2}$ $yr^{-1}$). Results of such calculations are shown in Figure 5.2a as green symbols. Results show $H_2$ flux, at water-to-rock ratios ranging from 100 to 0.2, are on the order of 25,000 – 150,000 moles $H_2$ $km^{-2}$ $yr^{-1}$, which, at the very most, is two orders of magnitude lower than fluxes determined by Zgonnik et al. (2019) using $H_2$-degassing rates from hyperalkaline seeps in the Oman ophiolite (1,200,000 – 2,400,000 moles $H_2$ $km^{-2}$ $yr^{-1}$, green field in Figure 5.2a). These hyperalkaline seeps are associated with geological structures that tap into the deep aquifer through deep-seated faults and fracture zones and that channelize flow from surrounding interconnected aquifers of an unknown volume into the discharge zone. Relating field measurements by Zgonnik et al. (2019) with our calculations, we infer that subsurface fluid pathways likely focus flows to discharge zones that encompass ~1 – 10% of the total ultramafic area.

Numerous possible global outgassing rates of $H_2$ produced through continental serpentinization can be estimated by incorporating the above flux estimates with the amounts of peridotites exposed in continents (~0.3 million $km^2$ or ~0.2% of continents, Durr et al., 2005). Results are depicted in Figure 5.2b. Predicted global $H_2$ production rates from the serpentinization of various continental peridotites range from 0.005 – 0.05 Tmole $H_2$ $yr^{-1}$. Many of the predicted values are within the range, albeit closer to the lower bounds, of estimates by Sherwood Lollar et al. (2014) on the global $H_2$ generated from serpentinization of cratonic rocks (0.02 – 0.18 Tmole $H_2$ $yr^{-1}$, grey field in Figure 5.2b). Estimates of the amounts $H_2$ generated from continental serpentinization are lower than those estimated to form via subseafloor serpentinization (0.1 – 10 Tmole $H_2$ $yr^{-1}$, Canfield et al., 2006; Sleep and Bird, 2007; Cannat et al., 2010; Kasting and Canfield, 2012; Worman et al., 2016). The resulting variations in our flux estimates result from accounting for the composition of various ultramafic rocks and the extents in the rock alteration progress, as well as allowing for precipitation of various $Fe^{+3}$-bearing assemblages in the alteration phases that are mostly not considered in previous studies where estimates of $H_2$ production are based on one or a few iron oxidation reactions. Estimates on the global $H_2$ production, shown by the green symbols in Figure 5.2b, can vary even more if variable serpentinization rates and extents of ultramafic exposures in continents are considered as discussed next for estimates of global $H_2$ generation and $O_2$ consumption via komatiite serpentinization during the past 3.5 Ga.

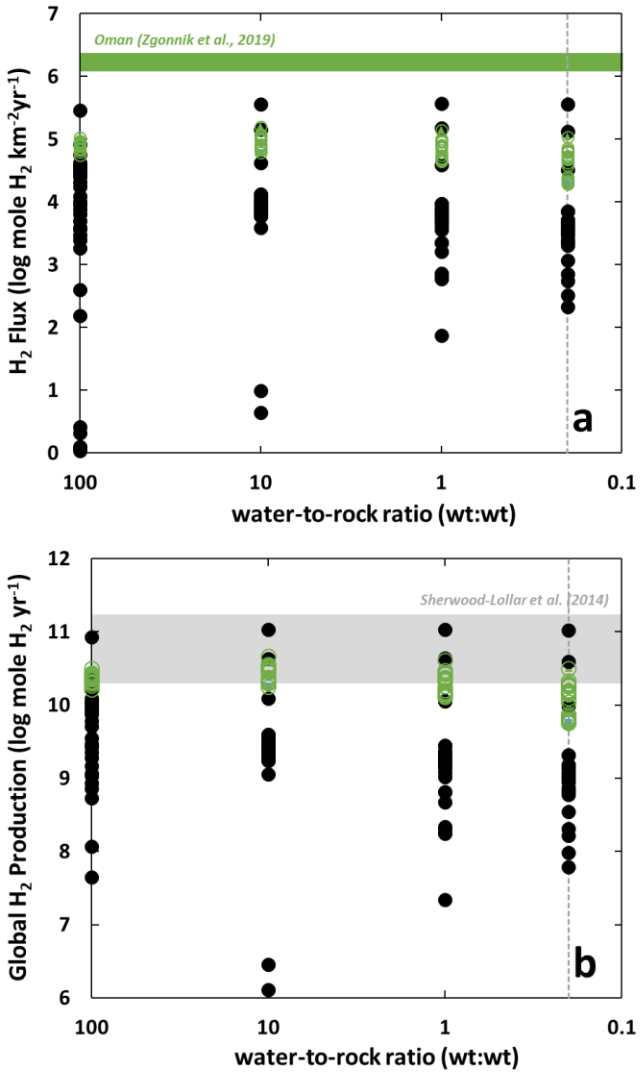

*Figure 5.2*. Calculated (a) flux and (b) global production rate of $H_2$ generated through the serpentinization of continental peridotites (green symbols) and komatiites (black symbols). Green field in (a) indicates range in $H_2$ flux determined by Zgonnik et al. (2019) from outgassing springs in Oman. Grey field in (b) depicts range in the global $H_2$ production calculated by Sherwood Lollar et al. (2014) for the serpentinization of continental cratonic rocks. Vertical dashed grey lines in (a) and (b) depict lowest water-to-rock ratio (0.2) modelled in the study. Calculations were terminated once a water-to-rock ratio = 0.2 is attained as any lower values result in simulations with no water left due to the extensive mineral hydration process.

### *5.4.3. Predicting the potentials for significant $O_2$ sink via komatiite serpentinization during the past 3.5 Ga*

As shown in Figures 5.1a and 5.1b, the serpentinization of a few Mg-rich komatiites can yield as much $H_2$ as that estimated during the serpentinization of peridotites. The example of some komatiites yielding similar potentials for $H_2$ generation observed today in peridotite bodies raises questions about the consequences of komatiite serpentinization on the global production of $H_2$ when these rocks were more common during the Archean. In the modern Earth, ultramafic rocks comprise only ~0.2% of the continental surface (Durr et al., 2005), mostly as harzburgites and other peridotitic rocks in ophiolite complexes. In the Archean, komatiites are estimated to have comprised a significant component of the continental crust (~10 – 20% during the early Archean, Tang et al., 2016; Greber et al., 2017). This elicits scenarios of substantial fluxes of serpentinization-derived $H_2$ to the atmosphere that could have consumed $O_2$ generated from photosynthesis and prevent its accumulation until the end of the Archean when the presence of komatiites in the continents significantly diminished. Like the case shown for peridotites above, the $H_2$-generation potentials of various komatiitic rocks ($x_K$) depend on various factors such as the compositions of the starting fluids and rocks, as well as the extent of the rock alteration process (quantified as the water-to-rock ratio in this work). Details in the calculations of the $H_2$ generation potentials of komatiites investigated in this work are described further in Appendix D. Calculated $x_K$ are used in predictions in the global $H_2$ production and $O_2$ consumption potentials through equations (5.4) and (5.5), respectively, throughout the past 3.5 Ga.

To evaluate how the magnitude of $H_2$ generated through komatiite serpentinization compares with those from peridotites, $H_2$ fluxes through serpentinization of komatiites were calculated using the alteration rate ($10^{-6.5}$ km $yr^{-1}$) assumed for peridotites in Oman. Calculated $H_2$ flux rates for komatiites are depicted as black symbols in Figure 5.2a and show higher variability than those calculated via peridotite serpentinization, with some komatiites yielding $H_2$ fluxes that are an order of magnitude higher while most yield lower flux values. As a result of this variable flux, estimated global outgassing rates of $H_2$ generated through komatiite serpentinization are highly variable, as shown in Figure 5.2b, assuming similar magnitudes in the continental exposures of komatiites with peridotites. However, komatiite distribution in modern continents is less well known and mappable units are often associated with complex greenstone belts that consist of other volcanic rocks such as basalts and picrites. Using the Ni/Co ratios and titanium isotopes informed from the terrigenous rock record, Greber et al. (2017) estimated that komatiites have composed <0.2 % of the continents for the past 1.0 Ga, though other ultramafic rocks could have contributed to this estimated value as well. The same study also estimated the extent of komatiite presence in continents beyond 1.0 Ga up until 3.5 Ga ago. Through equation (5.4), these constraints permit robust estimates on past $H_2$ fluxes generated through komatiite serpentinization, and through equation (5.5) their $O_2$ consumption potentials throughout the past 3.5 Ga. Specifically, the global $O_2$ consumption potentials were estimated assuming serpentinization rates ranging from $10^{-6.5}$ to $10^{-6}$ km $yr^{-1}$ (*i.e.*, 0.3 to 1.0 mm $yr^{-1}$), and average komatiite distribution and continental presence calculated by Greber et al. (2017) and Dhuime et al., (2012), respectively. Serpentinization rates lower than $10^{-6.5}$ km $yr^{-1}$

result in insignificant amounts of $O_2$ consumption and are not further described.

Additional calculations incorporating estimates of continent and komatiite exposures other than those assumed above are described below.

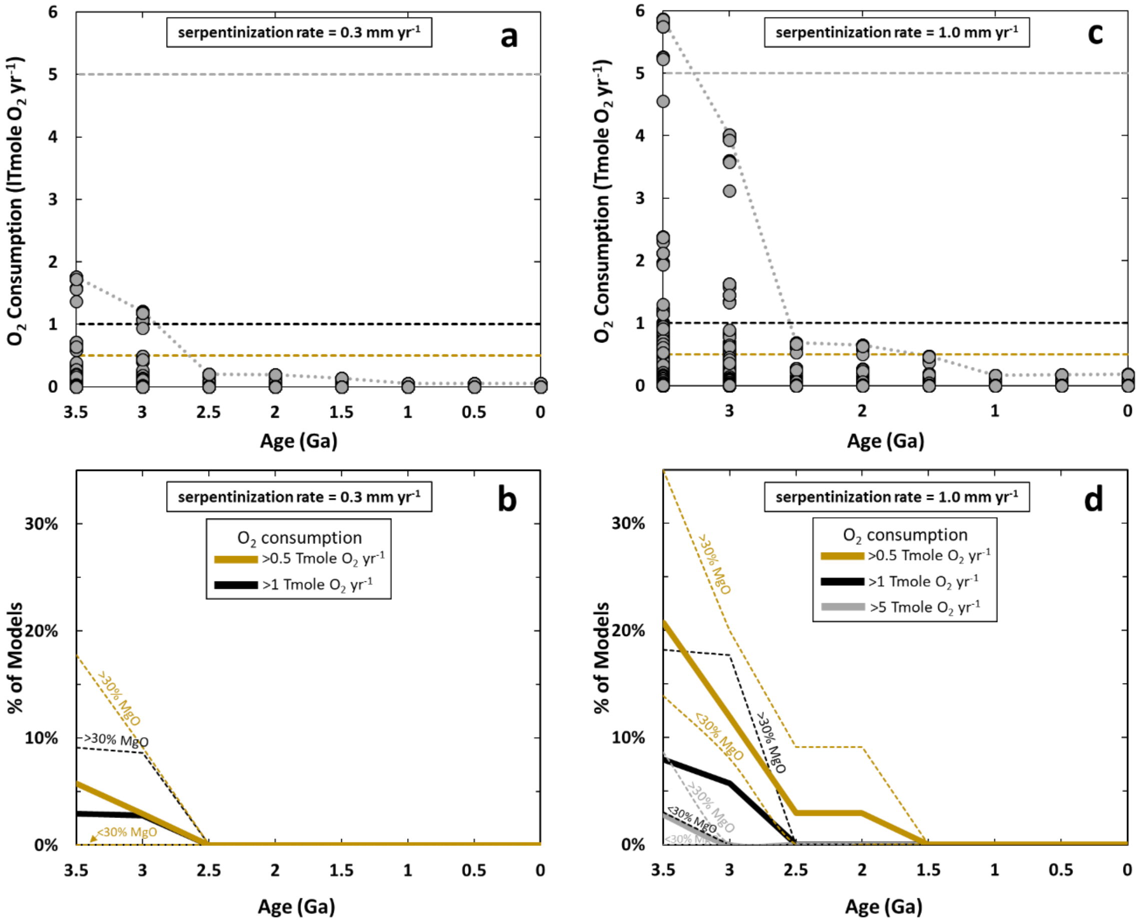

*Figure 5.3*. (a) Global consumption rate for $O_2$ calculated for the past 3.5 Ga assuming a komatiite alteration rate of 0.3 mm yr$^{-1}$ (or $10^{-6.5}$ km yr$^{-1}$). Grey symbols represent individual calculations and the dotted grey line depict upper bounds in calculated $O_2$ consumption rate. Grey, black, and brown dashed lines depict $O_2$ consumption rates of 5, 1, and 0.5 Tmole yr$^{-1}$, respectively. (b) Percentage (%) of all simulated scenarios, for a given time period, in which $O_2$ consumption rate exceeds 0.5 (solid brown curve) and 1 Tmole $O_2$ yr$^{-1}$ (solid black curve). Dashed brown and black curves depict results of simulations concerning Mg-rich komatiites (MgO >30%). The potential for consuming the same amounts of $O_2$ by Mg-poor komatiites (MgO <30%) is zero. (c) Calculated $O_2$ consumption rate assuming alteration rate of 1.0 mm yr$^{-1}$ (or $10^{-6}$ km yr$^{-1}$). (d) Percentage of all modelled scenarios shown in (c) that results in consumption of greater than 0.5 (solid brown curve), 1 (solid black curve), and 5 (solid grey curve) Tmole $O_2$ yr$^{-1}$. Dashed brown, black, and grey lines depict results of models concerning komatiites with a given range of MgO composition shown above these lines.

$O_2$ consumption potentials yielded by simulations of komatiite serpentinization at an alteration rate of $10^{-6.5}$ km $yr^{-1}$ (0.3 mm $yr^{-1}$) are shown as grey symbols in Figure 5.3a. There are 680 different grey symbols for each time period that depict results of simulations accounting for variable factors in the starting rock (34 komatiites) and fluid compositions (5 different compositions in equilibrium with $pO_2 = 10^{-5}$, $10^{-4}$, $10^{-3}$, $10^{-2}$, and $10^{-0.7}$) as well as variable extents of reaction (4 water-to-rock ratios: 100, 10, 1, and 0.2). As shown in Figure 5.3a, the global $O_2$ consumption arising from komatiite serpentinization is variable but is generally decreasing for the past 3.5 Ga, and this decrease is directly attributed to the decrease in the extent of komatiite exposures in continents. A marked decrease in komatiite distribution from ~7% to ~1% of continents from 3.0 to 2.5 Ga (Greber et al., 2017) caused a decrease in the $O_2$ consumption potentials during this time interval. Also shown in Figure 5.3a is a minor decrease in the $O_2$ consumption potentials that occurred between 1.5 and 1.0 Ga years ago when komatiite exposures in continents decreased from a maximum estimated value of at most 0.6% to at most 0.2% of continents. Note that results shown in Figure 5.3a are solely dependent on past komatiite estimates ($a_K$ component of equation 5.3) as the rate ($r_K$), and $H_2$ generation potential ($x_K$) are assumed to be constant at all given time periods for each investigated komatiite. The alteration rate ($r_K$), $H_2$ generation potentials ($x_K$), and therefore the $O_2$ consumption potentials could have larger values for the Archean due to the warmer conditions and more acidic starting fluids derived from an atmosphere with higher $pCO_2$. Thus, results of our calculation should be considered conservative and decreases in the $O_2$ consumption values during the past 3.5 Ga could be even more dramatic than those depicted in Figure 5.3a.

To evaluate if the predicted amounts of $H_2$ flux from serpentinization during the past 3.5 Ga are sufficient sinks for $O_2$ to prevent its accumulation in the atmosphere, the proportion of the 680 different $H_2$ generation rates calculated for each time period that can result in offsetting net $O_2$ production rates of 0.5, 1, and 5 Tmole $yr^{-1}$ were calculated. These assumed net $O_2$ production rates are ~2.5%, 5%, and 25%, respectively, of modern values (~20 Tmole $O_2$ $yr^{-1}$, Holland 2002) and can be representative for the Archean where smaller net production of $O_2$ is expected due to lower extents of organic sedimentation (Husson and Peters, 2017). Results of our calculations are shown in Figure 5.3b (solid brown curve), where ~6% of all simulations depicting 3.5 Ga ago result in scenarios where >0.5 Tmole of $O_2$ can be potentially consumed annually. The potential to consume >0.5 Tmole of $O_2$ decreases for the next billion years until it attains zero values at periods following the end of the Archean 2.5 Ga ago. Furthermore, ~3% of modelled scenarios between 3.5 – 3.0 Ga ago yield consumption of more than 1 Tmole $O_2$ $yr^{-1}$ (solid black curve in Figure 5.3b). This potential also decreases to zero values by the end of Archean 2.5 Ga ago. All model results depicting all time periods yield zero potentials to consume greater than 5 Tmole $O_2$ $yr^{-1}$ and hence are not shown in Figure 5.3b. The composition of the reacting komatiite can dictate the amount of $H_2$ generated through serpentinization. If only considering simulations depicting Mg-rich komatiites (*i.e.*, those with MgO >30%), there are higher potentials, close to 20% and 10%, in generating significant amounts of $H_2$ that can consume greater than 0.5 and 1 Tmole $O_2$ $yr^{-1}$, respectively, as shown by the dashed lines in Figure 5.3b. Nevertheless, like the examples above, this potential will be absent by the end of the Archean around 2.5 Ga ago. The amounts of $H_2$ generated through the serpentinization of komatiites that are relatively depleted in Mg (*i.e.*, MgO <30%) are not likely to counter net $O_2$ production of between 0.5 and 1 Tmole $yr^{-1}$ at all time periods.

Increasing the alteration rate ($r_K$) three-fold from $10^{-6.5}$ to $10^{-6}$ km $yr^{-1}$ (0.3 to 1.0 mm $yr^{-1}$) results in larger amounts of $H_2$ generated and hence $O_2$ consumed, as shown in Figure 5.3c. This high rate is not observed in modern environments but could be likely in the warmer Archean if more acidic meteoric fluids and more reactive rocks (komatiites) predominated. The higher serpentinization rate would lead to greater potentials for consuming more than 0.5 Tmole $O_2$ $yr^{-1}$, as shown by the solid brown curve in Figure 5.3d, than those shown in Figure 5.3b. The potential is also much higher if only considering serpentinization of Mg-rich komatiites (MgO >30%), as shown by the upper dashed brown curve in Figure 5.3d. There is a small potential for consuming >0.5 Tmole $O_2$ $yr^{-1}$ during the billion years following the end of Archean but it is a much lower compared to that estimated at 3.5 and 3.0 Ga. Serpentinization of less Mg-rich komatiites (MgO < 30%) results in lower potentials to consume $O_2$ where the potential for consuming >0.5 Tmole $O_2$ $yr^{-1}$ at post-Archean periods is zero. Model results in which consumption of even larger amounts of $O_2$ such as >1 Tmole $O_2$ $yr^{-1}$ (solid black curve in Figure 5.3d) are non-existent in post-Archean periods even considering only high $H_2$-yielding Mg-rich komatiites (upper dashed black curve). Overall, almost all simulations depicting time periods after the end of the Archean yield zero potentials for consuming $O_2$, assuming net $O_2$ production between 0.5 and 1 Tmole $O_2$ $yr^{-1}$, which can result in the progressive accumulation of $O_2$ in the atmosphere after 2.5 Ga ago. This is in contrast with the billion years preceding the end of the Archean where there are varying potentials for $H_2$ production from komatiite serpentinization in offsetting this range in net $O_2$

production. At a higher net $O_2$ production of 5 Tmole $O_2$ $yr^{-1}$, the amount of $H_2$ produced through serpentinization that can offset this production rate is only possible earlier than 3.0 Ga ago, as shown by the solid and dashed grey curves in Figure 5.3d. This suggests that if the net $O_2$ production is around or greater than 5 Tmole $yr^{-1}$ during the Archean, accumulation of $O_2$ in the atmosphere was likely to have begun by 3.0 Ga.

The calculations summarized above use estimates of past continental mass from Dhuime et al. (2012), which predicts that the amounts of continents throughout the Archean is intermediate to more extreme estimates in earlier studies (*e.g.*, Armstrong 1991; Allegre and Rousseau, 1984; Taylor and McLennan, 1985; Condie and Aster, 2010). To further explore consequences of these variations, we calculated the potential for consuming significant levels of $O_2$ via komatiite serpentinization given variable extents in the exposures of continents and extents of continental komatiites. Results of these calculations are shown in Figure 5.4 which depicts the proportion of simulations where >0.5 Tmole $O_2$ $yr^{-1}$ is consumed at alteration rates of 0.3 (Figure 5.4a) and 1.0 (Figure 5.4b) mm $yr^{-1}$ at various extents of continental exposures ranging from 0 to 100% of modern levels and komatiite exposures ranging from 0 to 25% of continents. Potentials for consuming >1 Tmole $O_2$ $yr^{-1}$ at rates of 0.3 and 1.0 mm $yr^{-1}$ are shown in Figures 5.4c and 5.4d, respectively. The potentials for offsetting net global $O_2$ production rates >0.5 Tmole $O_2$ $yr^{-1}$ increases when greater mass of continents and komatiites are exposed at the surface, as shown in Figures 5.4a – 5.4d. The dark grey fields shown in Figure 5.4 depict ranges in the potentials for preventing $O_2$ accumulation given the inferred amount of komatiite exposed in continents 3.5 Ga ago (15±5%, Greber et al., 2017). In contrast, the light grey and yellow fields depict range in of the potentials for preventing $O_2$

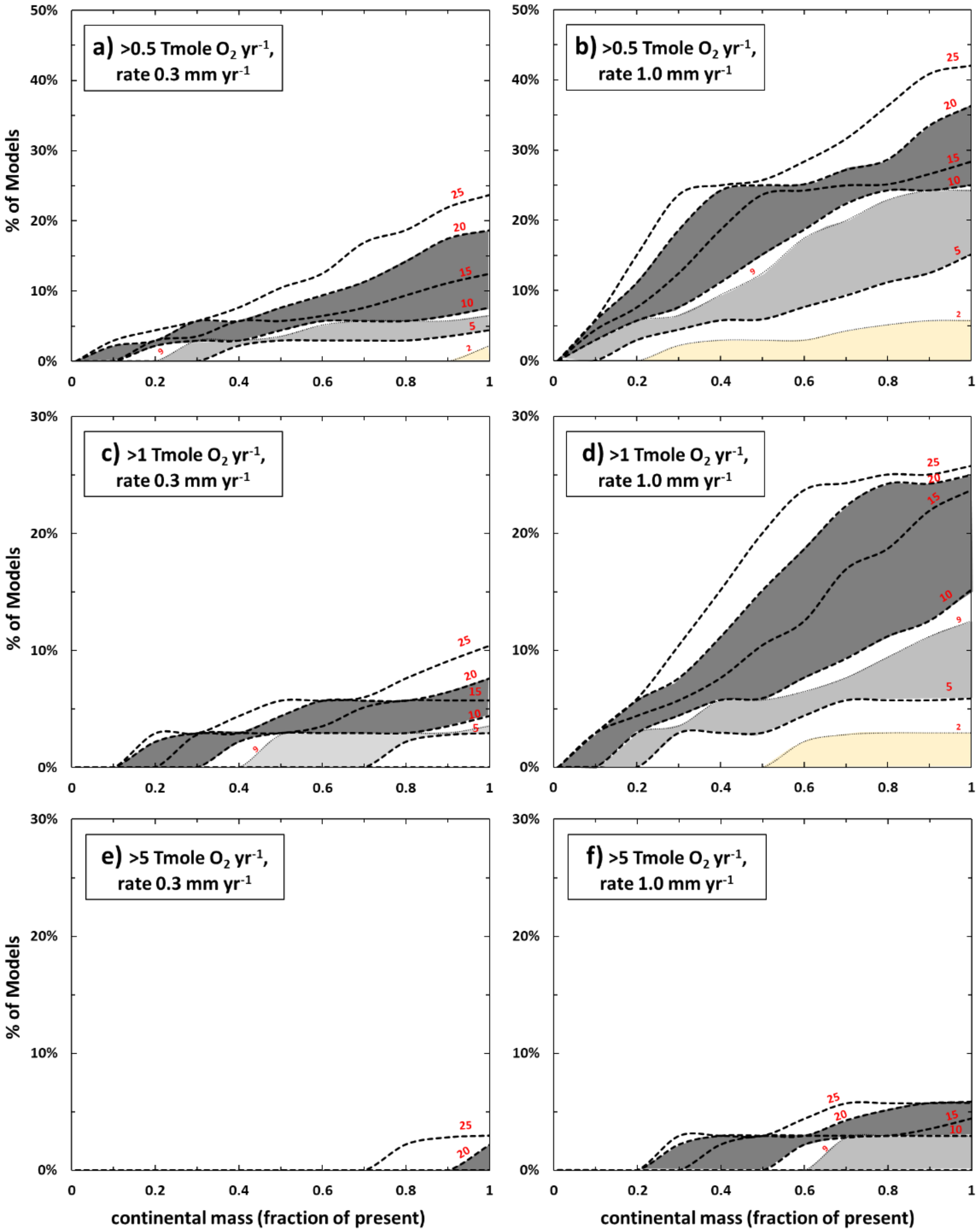

*Figure 5.4*. Potential for consuming greater than 0.5, 1, or 5 Tmole $O_2$ yr$^{-1}$ as function of the extents in the exposures of the continents (x-axis) and continental komatiites (red numbers indicating % distribution in continents). % of komatiite exposed is given at intervals of 5% unless otherwise shown (2% and 9%). (a) and (b) show potentials for consuming >0.5 Tmole $O_2$ yr$^{-1}$ at alteration rates of 0.3 and 1.0 mm yr$^{-1}$, respectively. (c) and (d) show potentials for consuming >1 Tmole $O_2$ yr$^{-1}$ at alteration rates of 0.3 and 1.0 mm yr$^{-1}$, respectively. (e) and (f) show potentials for consuming >5 Tmole $O_2$ yr$^{-1}$ at alteration rates of 0.3 and 1.0 mm yr$^{-1}$, respectively. Dark grey, light grey, and yellow fields indicate range in the potentials for consuming given amounts of $O_2$ at 3.5, 3.0, and 2.5 Ga ago, respectively, incorporating ranges in the estimated exposures of komatiites during these time periods.

accumulation following komatiite exposure inferred for 3.0 (7±2%) and 2.5 (1±1%) Ga ago, respectively, by Greber et al. (2017). Note that by the end of the Archean 2.5 Ga ago, the potentials for offsetting a net annual production of 0.5 Tmole $O_2$ is only possible at a serpentinization rate of 0.3 mm $yr^{-1}$ when the mass of continents present during that time is similar or close to modern levels, as shown by the yellow field in Figure 5.4a.

If net $O_2$ production is at most 1 Tmole $yr^{-1}$, serpentinization of komatiites inferred to be present by the end of the Archean 2.5 Ga ago is not enough to consume all $O_2$ at all simulated extents in the exposures of continents, as shown in Figure 5.4c. If the serpentinization rate is higher (1.0 mm $yr^{-1}$), there is a small potential (<5%) for $H_2$ generated through serpentinization of komatiites to counter $O_2$ production rates of 0.5 and 1 Tmole $yr^{-1}$ at the end of the Archean, as shown respectively by the yellow fields in Figures 5.4b and 5.4d. For the billion years preceding the end of the Archean, the potential for consuming 0.5 – 1 Tmole $O_2$ $yr^{-1}$ is higher and variable, as respectively depicted by the dark and light grey fields for the Paleoarchean (3.5 Ga ago) and Mesoarchean (3.0 Ga ago) eras in Figures 5.4a – 5.4d. Consumption of >5 Tmoles $O_2$ $yr^{-1}$ would require greater extents of continents exposed that are composed of substantial amounts of komatiites, as shown in Figures 5.4e and 5.4f. Given the range in the amounts of komatiite present during the Archean and serpentinization rates of 0.3 mm $yr^{-1}$, preventing $O_2$ accumulation is only possible, albeit at small chances and requiring modern levels of continental exposures, during the Paleoarchean as shown by the dark grey field in Figure 5.4e. At higher serpentinization rates of 1.0 mm $yr^{-1}$, annual consumption of >5 Tmoles of $O_2$ may have been possible during the Mesoarchean, as shown by the light grey field in Figure 5.4f, but not by the end of the Archean. Overall, results of numerous simulations of komatiite serpentinization show that the potential to consume significant amounts of $O_2$ decreases towards the end of the Archean. By 2.5 Ga ago, almost all of our simulations show that the reduced presence of komatiites in continents leads to scenarios where the $H_2$ flux through serpentinization is significantly diminished and cannot counter even a net $O_2$ production rate of 0.5 Tmole $yr^{-1}$, insuring accumulation of $O_2$ into the atmosphere and setting the stage for the Great Oxidation Event.

## 5.5. Conclusions: Decreasing extents of komatiite serpentinization as a driver for the GOE

Critical to the generation of significant fluxes of $H_2$ during hydrous alteration of ultramafic rocks is the formation of serpentine that promotes the reduction of $H_2O$ to $H_2$ via the oxidation of ferrous iron in the protoliths to ferric iron in alteration minerals that are otherwise not favored to form extensively in Mg-depleted and Si- and Al-enriched rocks such as basalts and picrites. Whereas ultramafic rocks are rare in modern continents, they were more common during the Archean when komatiite volcanism was more widespread. Consequently, the extensive distribution of komatiites and their consequential serpentinization contribute to substantial flux of $H_2$ into the atmosphere, which ultimately provided a sink for $O_2$ throughout most of the Archean. However, as consistently shown in all our simulations, this potential decreases towards the end of Archean eventually yielding close-to-zero potentials to consume significant amounts of $O_2$ at 2.5 Ga ago, permitting its accumulation and eventually setting the stage for Great Oxidation Event.

Our simulations explore a suite of factors (*e.g.*, compositions of reacting rocks and fluids, extents of water-rock interactions, alteration rate, extent of continental and komatiite distribution) and comprehensively quantify the magnitude of the $O_2$ sink arising from komatiite serpentinization during the past 3.5 Ga. The extent of this sink is notably sensitive to composition of the reacting rocks, the rate of alteration, the extent of continents and the presence of continental komatiites in the past. As an example, Mg-enriched komatiites (>30% MgO) are more likely to generate significant fluxes of $H_2$ that result in larger sinks for $O_2$. In addition, our models show that serpentinization rates exceeding 0.3 mm $yr^{-1}$ would be required to yield $H_2$ fluxes that can offset net $O_2$ production greater than 0.5 Tmole $yr^{-1}$. Higher serpentinization rates, close to 1 mm $yr^{-1}$, would be needed to counter higher net $O_2$ production rates of 5 Tmole $yr^{-1}$. Future investigations that can constrain these values applicable to periods leading to the GOE will considerably refine models shown in this work. Experiments that aim to simulate komatiite alteration at Archean conditions can also help identify reaction mechanisms and constrain rates that can inform future models. Efforts to characterize the speciation and distribution of Fe in secondary minerals in komatiites and other Fe-bearing rocks can also supply further constraints on the $H_2$ generation potential of a given composition of rock.

The serpentinization of komatiites is only one of the many sources of reductants to the Earth’s surface (*e.g.*, volatiles that are volcanically and microbially derived). Our models of komatiite serpentinization, however, yield diminished $H_2$ fluxes that can permit significant $O_2$ accumulation by the end of the Archean independent of other proposed mechanisms for the GOE. We hope that our simulations will ultimately contribute to an integrated model that incorporates evolution of various redox sources and sinks, many of which can be facilitated by the secular change in the extents and compositions of Earth's continents, and that can yield forward models predictive of surface redox environments.

### 5.6. Acknowledgements

I would like to thank the ASU Frontiers in Earth System Dynamics (FESD) team - Ariel Anbar, Hilairy Hartnett, Christy Till, Dan Shim, Mingming Li, Aleisha Johnson, Donny Glaser, Chad Ostrander, Meghan Guild, Kayla Iacovino, and many others - for the numerous weekly discussions concerning the Great Oxidation Event. Special thanks to Tom Sharp for all the help in making me proficient in mineralogy. Many years of discussions on rock alteration simulations with various members of GEOPIG especially Tucker Ely and Vincent Milesi have also been helpful. Support from the NSF FESD project on Earth System Oxygenation, NASA NExSS Exoplanetary Ecosystems project as well as the NASA NAI Rock-Powered Life project is acknowledged.

# CHAPTER 6

# FUTURE DIRECTIONS

Through thermodynamic simulations, the fluxes and compositions of fluids and volatiles generated through low-temperature serpentinization, including their bioenergetic potentials, were explored in this work. The robustness of thermodynamic models can be improved upon by refining the thermodynamic properties of solid, aqueous, and gaseous species involved in the serpentinization process. For example, refinement of the thermodynamic properties of Fe endmembers and solid solution models of serpentinization-relevant secondary minerals such as serpentine and brucite can help improve models, especially for calculations on the amount of $H_2$ generated during low-temperature serpentinization. Specifically, experiments and detailed mineral analyses that can reveal solid solution behavior of Fe into mineral structures can inform future models and improve upon the calculations presented in this work where ideal site mixing was assumed for most solid solutions. In addition, incorporation of ferric iron into chlorite, which has been observed in natural samples (Dyar et al., 1992; Munoz et al., 2006; Vidal et al., 2006), albeit at lesser extents than those measured in serpentine (*e.g.*, Andreani et al., 2013), can refine estimates on $H_2$ production during mafic rock alteration where chlorite formation can be significant.

In Chapter 3, the compositions of serpentinization-generated fluids were shown to be partly accounted for by predictions of fluid-mineral equilibria while processes such as mineral leaching and fluid mixing can account for compositions that deviate from equilibrium expectations.  Further work incorporating the kinetics of low-temperature serpentinization and the hydrogeology of ultramafic aquifers will inform reactive-transport simulations that could improve upon the calculations described here, constrain timescales of reactions leading to different fluid types, and reveal how various transport processes contribute to the overall compositions of serpentinization-generated fluids.

Energy supplies from 17 chemolithotrophic reactions were estimated for surface and subsurface peridotite-hosted fluids in Chapter 4. These 17 reactions are not exhaustive of chemotrophic processes present in serpentinzing systems. Several other chemolithotropic and chemoorganotrophic reactions are suggested to be present in serpentinizing environments but are otherwise not quantified in this work due to lack of data (*e.g.*, dissolved organic species for organotrophic strategies). Additional constraints would permit future quantification of available energy supplies through a wider array of reactions. A worked example that estimates the power supply available to methanogens, as well as the maximum biomass such a power supply can support given limitations on the dissolved inorganic carbon supply from carbonate minerals, was shown in Chapter 4. Ultimately, simulations in combination with field observations and estimations of the distribution of minerals that can supply electron acceptors (*e.g.*, carbonates, sulfates, iron oxide/oxyhydroxides) or donors (*e.g.*, reduced iron and sulfur minerals) can inform future strategies that target specific deep-seated communities in the subsurface.

Although data are limited, various chemotrophic energy supplies available in gabbro-hosted environments were quantified and compared to those calculated from more well-studied ultramafic-hosted environments. Preliminary calculations show that gabbro-hosted environments can support ecosystems that are distinct from those hosted in ultramafic rocks. Gabbroic rocks are pervasive in the seafloor and in continental ophiolites and can potentially store extensive amounts of geochemical energy that can support deep subsurface life. It is thus imperative that we start to investigate gabbro-hosted systems to complement our growing understanding on ultramafic-hosted environments. Such parallel studies would better capture the potential diversity of rock alteration and fluid compositions expected in various subsurface environments, as well as in other terrestrial bodies our solar system, which in turn may vary significantly in their potential to support life.

It would follow that a more comprehensive alteration model encompassing all types of rocks, such as gabbros, picrites, and basalts and not just peridotites and komatiites modelled in Chapter 5 of this work, will refine estimates on the overall flux of reduced volatiles produced through rock alteration. Ultimately, estimates on the global fluxes of alteration-generated volatiles that integrate all rock types in combination with models depicting volatile fluxes from other sources (*e.g.*, volcanos, biosphere) can yield forward models predictive of surface redox environments in the Earth's past, as well as in other rocky bodies in our solar system and beyond where crustal compositions can vary.

# REFERENCES

Abrajano, T. A., Sturchio, N. C., Bohlke, J. K., Lyon, G. L., Poreda, R. J., & Stevens, C. M. (1988). Methane-hydrogen gas seeps, Zambales Ophiolite, Philippines: Deep or shallow origin? *Chemical Geology*, *71*(1), 211–222. https://doi.org/10.1016/0009-2541(88)90116-7

Abrajano, T. A., Sturchio, N. C., Kennedy, B. M., Lyon, G. L., Muehlenbachs, K., & Bohlke, J. K. (1990). Geochemistry of reduced gas related to serpentinization of the Zambales ophiolite, Philippines. *Applied Geochemistry*, *5*(5), 625–630. https://doi.org/10.1016/0883-2927(90)90060-I

Ahmed, A. F. M., Singh, R. P., & Elmubarak, A. H. (1990). Chemistry of atmospheric precipitation at the Western Arabian Gulf Coast. *Atmospheric Environment. Part A. General Topics*, *24*(12), 2927–2934. https://doi.org/10.1016/0960-1686(90)90473-Z

Aissa, F., Postec, A., Erauso, G., Payri, C., Pelletier, B., Hamdi, M., Ollivier, B., & Fardeau, M.-L. (2014). Vallitalea pronyensis sp. nov., isolated from a marine alkaline hydrothermal chimney. *International Journal of Systematic and Evolutionary Microbiology*, *64*(4), 1160–1165. https://doi.org/10.1099/ijs.0.055756-0

Alexander, W. R., Dayal, R., Eagleson, K., Eikenberg, J., Hamilton, E., Linklater, C. M., McKinley, I. G., & Tweed, C. J. (1992). A natural analogue of high pH cement pore waters from the Maqarin area of northern Jordan. II: Results of predictive geochemical calculations. *Journal of Geochemical Exploration*, *46*(1), 133–146. https://doi.org/10.1016/0375-6742(92)90104-G

Allègre, C. J., & Rousseau, D. (1984). The growth of the continent through geological time studied by Nd isotope analysis of shales. *Earth and Planetary Science Letters*, *67*(1), 19–34. https://doi.org/10.1016/0012-821X(84)90035-9

Allen, D. E., & Seyfried, W. E. (2004). Serpentinization and heat generation: Constraints from Lost City and Rainbow hydrothermal systems. *Geochimica et Cosmochimica Acta*, *68*(6), 1347–1354. https://doi.org/10.1016/j.gca.2003.09.003

Alt, J. C., & Shanks, W. C. (2003). Serpentinization of abyssal peridotites from the MARK area, Mid-Atlantic Ridge: Sulfur geochemistry and reaction modeling. *Geochimica et Cosmochimica Acta*, *67*(4), 641–653. https://doi.org/10.1016/S0016-7037(02)01142-0

Amend, J. P., McCollom, T. M., Hentscher, M., & Bach, W. (2011). Catabolic and anabolic energy for chemolithoautotrophs in deep-sea hydrothermal systems hosted in different rock types. *Geochimica et Cosmochimica Acta*, *75*(19), 5736–5748. https://doi.org/10.1016/j.gca.2011.07.041

Anbar, A. D., Duan, Y., Lyons, T. W., Arnold, G. L., Kendall, B., Creaser, R. A., Kaufman, A. J., Gordon, G. W., Scott, C., Garvin, J., & Buick, R. (2007). A whiff of oxygen before the Great Oxidation Event? *Science, 317*(5846), 1903–1906. https://doi.org/10.1126/science.1140325

Andreani, M., Muñoz, M., Marcaillou, C., & Delacour, A. (2013). MXANES study of iron redox state in serpentine during oceanic serpentinization. *Lithos, 178,* 70–83. https://doi.org/10.1016/j.lithos.2013.04.008

Armstrong, R. L. (1991). The persistent myth of crustal growth. *Australian Journal of Earth Sciences, 38*(5), 613–630. https://doi.org/10.1080/08120099108727995

Arvidson, R. S., Ertan, I. E., Amonette, J. E., & Luttge, A. (2003). Variation in calcite dissolution rates: A fundamental problem? *Geochimica et Cosmochimica Acta*, *67*(9), 1623–1634. https://doi.org/10.1016/S0016-7037(02)01177-8

Bach, W. (2016). Some compositional and kinetic controls on the bioenergetic landscapes in oceanic basement. *Frontiers in Microbiology, 7,* no. 107. https://doi.org/10.3389/fmicb.2016.00107

Bach, W., Alt, J. C., Niu, Y., Humphris, S. E., Erzinger, J., & Dick, H. J. B. (2001). The geochemical consequences of late-stage low-grade alteration of lower ocean crust at the SW Indian Ridge: Results from ODP Hole 735B (Leg 176). *Geochimica et Cosmochimica Acta*, *65*(19), 3267–3287. https://doi.org/10.1016/S0016-7037(01)00677-9

Bach, W., Jöns, N., & Klein, F. (2013). Metasomatism within the ocean crust. In D. E. Harlov & H. Austrheim (Eds.), *Metasomatism and the Chemical Transformation of Rock: The Role of Fluids in Terrestrial and Extraterrestrial Processes* (pp. 253–288). Springer Berlin Heidelberg. https://doi.org/10.1007/978-3-642-28394-9_8

Baculi, R. Q., Lantican, N. B., de los Reyes, F. L., & Raymundo, A. K. (2015). Prokaryotic community analysis of a hyperalkaline spring in the Philippines using 16S rRNA gene clone library construction. *Philippine Journal of Science*, *144*(1), 1–15.

Baes, C. F., & Mesmer, R. E. (1976). *The hydrolysis of cations*. Wiley.

Bales, R. C., & Morgan, J. J. (1985). Dissolution kinetics of chrysotile at pH 7 to 10. *Geochimica et Cosmochimica Acta*, *49*(11), 2281–2288. https://doi.org/10.1016/0016-7037(85)90228-5

Barnes, I., LaMarche, V. C., & Himmelberg, G. (1967). Geochemical evidence of present-day serpentinization. *Science*, *156*(3776), 830–832. https://doi.org/10.1126/science.156.3776.830

Barnes, I., & O’Neil, J. R. (1969). The Relationship between fluids in some fresh Alpine-type ultramafics and possible modern serpentinization, Western United States. *GSA Bulletin*, *80*(10), 1947–1960. https://doi.org/10.1130/0016-7606(1969)80[1947:TRBFIS]2.0.CO;2

Barnes, I., Rapp, J. B., O’Neil, J. R., Sheppard, R. A., & Gude, A. J. (1972). Metamorphic assemblages and the direction of flow of metamorphic fluids in four instances of serpentinization. *Contributions to Mineralogy and Petrology*, *35*(3), 263–276. https://doi.org/10.1007/BF00371220

Barnes, I., O'Neil, J. R., & Trescases, J. J. (1978). Present day serpentinization in New Caledonia, Oman and Yugoslavia. *Geochimica et Cosmochimica Acta*, *42*(1), 144–145. https://doi.org/10.1016/0016-7037(78)90225-9

Barnes, I., Presser, T. S., Saines, M., Dickson, P., & Van Groos, A. F. K. (1982). Geochemistry of highly basic calcium hydroxide groundwater in Jordan. *Chemical Geology*, *35*(1), 147–154. https://doi.org/10.1016/0009-2541(82)90024-9

Bar-On, Y. M., Phillips, R., & Milo, R. (2018). The biomass distribution on Earth. *Proceedings of the National Academy of Sciences*, *115*(25), 6506–6511. https://doi.org/10.1073/pnas.1711842115

Bath, A., Christofi, N., Neal, C., Philp, J., Cave, M., McKinley, I., & Berner, U. (1987). *Trace element and microbiological studies of alkaline groundwaters in Oman, Arabian Gulf: A natural analogue for cement pore-waters*. British Geological Survey, Fluid Processes Research Group.

Beard, J. S., & Hopkinson, L. (2000). A fossil, serpentinization-related hydrothermal vent, Ocean Drilling Program Leg 173, Site 1068 (Iberia Abyssal Plain): Some aspects of mineral and fluid chemistry. *Journal of Geophysical Research: Solid Earth*, *105*(B7), 16527–16539. https://doi.org/10.1029/2000JB900073

Bekker, A., Holland, H. D., Wang, P.-L., Rumble, D., Stein, H. J., Hannah, J. L., Coetzee, L. L., & Beukes, N. J. (2004). Dating the rise of atmospheric oxygen. *Nature*, *427*(6970), 117–120. https://doi.org/10.1038/nature02260

Belousova, E. A., Kostitsyn, Y. A., Griffin, W. L., Begg, G. C., O'Reilly, S. Y., & Pearson, N. J. (2010). The growth of the continental crust: Constraints from zircon Hf-isotope data. *Lithos*, *119*(3), 457–466. https://doi.org/10.1016/j.lithos.2010.07.024

Berner, E. K., & Berner, R. A. (2012). *Global Environment: Water, air, and geochemical Cycles.* Princeton University Press. http://public.eblib.com/choice/publicfullrecord.aspx?p=873308

Blanc, Ph., Bourbon, X., Lassin, A., & Gaucher, E. C. (2010). Chemical model for cement-based materials: Thermodynamic data assessment for phases other than C–S–H. *Cement and Concrete Research*, *40*(9), 1360–1374. https://doi.org/10.1016/j.cemconres.2010.04.003

Blank, J. G., Green, S. J., Blake, D., Valley, J. W., Kita, N. T., Treiman, A., & Dobson, P. F. (2009). An alkaline spring system within the Del Puerto Ophiolite (California, USA): A Mars analog site. *Planetary and Space Science*, *57*(5), 533–540. https://doi.org/10.1016/j.pss.2008.11.018

Boschetti, T., & Toscani, L. (2008). Springs and streams of the Taro–Ceno Valleys (Northern Apennine, Italy): Reaction path modeling of waters interacting with serpentinized ultramafic rocks. *Chemical Geology*, *257*(1), 76–91. https://doi.org/10.1016/j.chemgeo.2008.08.017

Boschetti, T., Etiope, G., Pennisi, M., Romain, M., & Toscani, L. (2013). Boron, lithium and methane isotope composition of hyperalkaline waters (Northern Apennines, Italy): Terrestrial serpentinization or mixing with brine? *Applied Geochemistry*, *32*, 17–25. https://doi.org/10.1016/j.apgeochem.2012.08.018

Boulart, C., Chavagnac, V., Monnin, C., Delacour, A., Ceuleneer, G., & Hoareau, G. (2013). Differences in gas venting from ultramafic-hosted warm springs: The example of Iman and Voltri Ophiolites. *Ofioliti*, *38*(2), 142–156. https://doi.org/10.4454/ofioliti.v38i2.423

Boyd, E. S., Amenabar, M. J., Poudel, S., & Templeton, A. S. (2020). Bioenergetic constraints on the origin of autotrophic metabolism. *Philosophical Transactions of the Royal Society A: Mathematical, Physical and Engineering Sciences*, *378*(2165), 20190151. https://doi.org/10.1098/rsta.2019.0151

Bradley, A. S., Fredricks, H., Hinrichs, K.-U., & Summons, R. E. (2009a). Structural diversity of diether lipids in carbonate chimneys at the Lost City Hydrothermal Field. *Organic Geochemistry*, *40*(12), 1169–1178. https://doi.org/10.1016/j.orggeochem.2009.09.004

Bradley, A. S., Hayes, J. M., & Summons, R. E. (2009b). Extraordinary $^{13}$C enrichment of diether lipids at the Lost City Hydrothermal Field indicates a carbon-limited ecosystem. *Geochimica et Cosmochimica Acta*, *73*(1), 102–118. https://doi.org/10.1016/j.gca.2008.10.005

Brazelton, W. J., & Baross, J. A. (2010). Metagenomic comparison of two thiomicrospira lineages inhabiting contrasting deep-Sea hydrothermal environments. *PLoS ONE*, *5*(10), e13530. https://doi.org/10.1371/journal.pone.0013530

Brazelton, W. J., Schrenk, M. O., Kelley, D. S., & Baross, J. A. (2006). Methane- and sulfur-metabolizing microbial communities dominate the Lost City Hydrothermal Field ecosystem. *Applied and Environmental Microbiology*, *72*(9), 6257–6270. https://doi.org/10.1128/AEM.00574-06

Brazelton, W. J., Mehta, M. P., Kelley, D. S., & Baross, J. A. (2011). Physiological differentiation within a single-species biofilm fueled by serpentinization. *MBio*, *2*(4), e00127-11. https://doi.org/10.1128/mBio.00127-11

Brazelton, W. J., Nelson, B., & Schrenk, M. O. (2012). Metagenomic evidence for $H_2$ oxidation and $H_2$ production by serpentinite-hosted subsurface microbial communities. *Frontiers in Microbiology*, *2*, no. 268. https://doi.org/10.3389/fmicb.2011.00268

Brazelton, W. J., Morrill, P. L., Szponar, N., & Schrenk, M. O. (2013). Bacterial communities associated with subsurface geochemical processes in continental serpentinite springs. *Applied and Environmental Microbiology*, *79*(13), 3906–3916. https://doi.org/10.1128/AEM.00330-13

Brazelton, W. J., Thornton, C. N., Hyer, A., Twing, K. I., Longino, A. A., Lang, S. Q., Lilley, M. D., Früh-Green, G. L., & Schrenk, M. O. (2017). Metagenomic identification of active methanogens and methanotrophs in serpentinite springs of the Voltri Massif, Italy. *PeerJ*, *5*, e2945. https://doi.org/10.7717/peerj.2945

Brocks, J. J., Logan, G. A., Buick, R., & Summons, R. E. (1999). Archean Molecular Fossils and the Early Rise of Eukaryotes. *Science*, *285*(5430), 1033–1036. https://doi.org/10.1126/science.285.5430.1033

Bruni, J., Canepa, M., Chiodini, G., Cioni, R., Cipolli, F., Longinelli, A., Marini, L., Ottonello, G., & Vetuschi Zuccolini, M. (2002). Irreversible water–rock mass transfer accompanying the generation of the neutral, Mg–HCO3 and high-pH, Ca–OH spring waters of the Genova province, Italy. *Applied Geochemistry*, *17*(4), 455–474. https://doi.org/10.1016/S0883-2927(01)00113-5

Busey, R. H., & Mesmer, R. E. (1977). Ionization equilibriums of silicic acid and polysilicate formation in aqueous sodium chloride solutions to 300.degree.C. *Inorganic Chemistry*, *16*(10), 2444–2450. https://doi.org/10.1021/ic50176a004

Cabria, G. L. B., Argayosa, V. B., Lazaro, J. E. H., Argayosa, A. M., & Arcilla, C. A. (2014). Draft genome sequence of haloalkaliphilic Exiguobacterium sp. Strain AB2 from Manleluag Ophiolitic Spring, Philippines. *Genome Announcements*, *2*(4), e00840-1. https://doi.org/10.1128/genomeA.00840-14

Canfield, D. E., Rosing, M. T., & Bjerrum, C. (2006). Early anaerobic metabolisms. *Philosophical Transactions of the Royal Society B: Biological Sciences*, *361*(1474), 1819–1836. https://doi.org/10.1098/rstb.2006.1906

Cannat, M., Fontaine, F., & Escartín, J. (2010). Serpentinization and associated hydrogen and methane fluxes at slow spreading ridges. In P. A. Rona, C. W. Devey, J. Dyment, & B. J. Murton (Eds.), *Geophysical Monograph Series* (Vol. 188, pp. 241–264). American Geophysical Union. https://doi.org/10.1029/2008GM000760

Canovas, P. A., Hoehler, T., & Shock, E. L. (2017). Geochemical bioenergetics during low-temperature serpentinization: An example from the Samail ophiolite, Sultanate of Oman: Serpentinization Bioenergetics. *Journal of Geophysical Research: Biogeosciences*, *122*(7), 1821–1847. https://doi.org/10.1002/2017JG003825

Cardace, D., Hoehler, T., McCollom, T., Schrenk, M., Carnevale, D., Kubo, M., & Twing, K. (2013). Establishment of the Coast Range ophiolite microbial observatory (CROMO): Drilling objectives and preliminary outcomes. *Scientific Drilling*, *16*, 45–55. https://doi.org/10.5194/sd-16-45-2013

Cardace, Dawn, Meyer-Dombard, D. R., Woycheese, K. M., & Arcilla, C. A. (2015). Feasible metabolisms in high pH springs of the Philippines. *Frontiers in Microbiology*, *6*, no. 10. https://doi.org/10.3389/fmicb.2015.00010

Catalano, J. G. (2013). Thermodynamic and mass balance constraints on iron-bearing phyllosilicate formation and alteration pathways on early Mars. *Journal of*

*Geophysical Research: Planets*, *118*(10), 2124–2136. https://doi.org/10.1002/jgre.20161

Catling, D. C., & Claire, M. W. (2005). How Earth's atmosphere evolved to an oxic state: A status report. *Earth and Planetary Science Letters*, *237*(1), 1–20. https://doi.org/10.1016/j.epsl.2005.06.013

Catling, D. C., Zahnle, K. J., & McKay, C. P. (2001). Biogenic methane, hydrogen escape, and the irreversible oxidation of Early Earth. *Science*, *293*(5531), 839–843. https://doi.org/10.1126/science.1061976

Charlou, J. L., Donval, J. P., Fouquet, Y., Jean-Baptiste, P., & Holm, N. (2002). Geochemistry of high $H_2$ and $CH_4$ vent fluids issuing from ultramafic rocks at the Rainbow hydrothermal field (36°14′N, MAR). *Chemical Geology*, *191*(4), 345–359. https://doi.org/10.1016/S0009-2541(02)00134-1

Chavagnac, V., Ceuleneer, G., Monnin, C., Lansac, B., Hoareau, G., & Boulart, C. (2013a). Mineralogical assemblages forming at hyperalkaline warm springs hosted on ultramafic rocks: A case study of Oman and Ligurian ophiolites: Mineral Precipitate at Alkaline Springs. *Geochemistry, Geophysics, Geosystems*, *14*(7), 2474–2495. https://doi.org/10.1002/ggge.20146

Chavagnac, V., Monnin, C., Ceuleneer, G., Boulart, C., & Hoareau, G. (2013b). Characterization of hyperalkaline fluids produced by low-temperature serpentinization of mantle peridotites in the Oman and Ligurian ophiolites: Hyperalkaline Waters in Oman and Liguria. *Geochemistry, Geophysics, Geosystems*, *14*(7), 2496–2522. https://doi.org/10.1002/ggge.20147

Chou, L., Garrels, R. M., & Wollast, R. (1989). Comparative study of the kinetics and mechanisms of dissolution of carbonate minerals. *Chemical Geology*, *78*(3), 269–282. https://doi.org/10.1016/0009-2541(89)90063-6

Cipolli, F., Gambardella, B., Marini, L., Ottonello, G., & Vetuschi Zuccolini, M. (2004). Geochemistry of high-pH waters from serpentinites of the Gruppo di Voltri (Genova, Italy) and reaction path modeling of $CO_2$ sequestration in serpentinite aquifers. *Applied Geochemistry*, *19*(5), 787–802. https://doi.org/10.1016/j.apgeochem.2003.10.007

Claire, M. W., Catling, D. C., & Zahnle, K. J. (2006). Biogeochemical modelling of the rise in atmospheric oxygen. *Geobiology*, *4*(4), 239–269. https://doi.org/10.1111/j.1472-4669.2006.00084.x

Cohen, M. F., Hu, P., Nguyen, M. V., Kamennaya, N., Brown, N., Woyke, T., Kyrpides, N., Holman, H.-Y., & Torok, T. (2015). Genome sequence of the alkaline-tolerant Cellulomonas sp. Strain FA1. *Genome Announcements*, *3*(3), e00646-15. https://doi.org/10.1128/genomeA.00646-15

Condie, K. C., & Aster, R. C. (2010). Episodic zircon age spectra of orogenic granitoids: The supercontinent connection and continental growth. *Precambrian Research*, *180*(3), 227–236. https://doi.org/10.1016/j.precamres.2010.03.008

Crespo-Medina, M., Twing, K. I., Kubo, M. D. Y., Hoehler, T. M., Cardace, D., McCollom, T., & Schrenk, M. O. (2014). Insights into environmental controls on microbial communities in a continental serpentinite aquifer using a microcosm-based approach. *Frontiers in Microbiology*, *5*, no. 604. https://doi.org/10.3389/fmicb.2014.00604

Crespo-Medina, M., Twing, K. I., Sánchez-Murillo, R., Brazelton, W. J., McCollom, T. M., & Schrenk, M. O. (2017). Methane dynamics in a tropical serpentinizing environment: The Santa Elena Ophiolite, Costa Rica. *Frontiers in Microbiology*, *8*, no. 916. https://doi.org/10.3389/fmicb.2017.00916

Crowe, S. A., Døssing, L. N., Beukes, N. J., Bau, M., Kruger, S. J., Frei, R., & Canfield, D. E. (2013). Atmospheric oxygenation three billion years ago. *Nature*, *501*(7468), 535–538. https://doi.org/10.1038/nature12426

Cumming, E. A., Rietze, A., Morrissey, L. S., Cook, M. C., Rhim, J. H., Ono, S., & Morrill, P. L. (2019). Potential sources of dissolved methane at the Tablelands, Gros Morne National Park, NL, CAN: A terrestrial site of serpentinization. *Chemical Geology*, *514*, 42–53. https://doi.org/10.1016/j.chemgeo.2019.03.019

Daae, F. L., Økland, I., Dahle, H., Jørgensen, S. L., Thorseth, I. H., & Pedersen, R. B. (2013). Microbial life associated with low-temperature alteration of ultramafic rocks in the Leka ophiolite complex. *Geobiology, 11*(4), 318–339. https://doi.org/10.1111/gbi.12035

D'Alessandro, W., Daskalopoulou, K., Calabrese, S., & Bellomo, S. (2018). Water chemistry and abiogenic methane content of a hyperalkaline spring related to serpentinization in the Argolida ophiolite (Ermioni, Greece). *Marine and Petroleum Geology*, *89*, 185–193. https://doi.org/10.1016/j.marpetgeo.2017.01.028

Daskalopoulou, K., Calabrese, S., Grassa, F., Kyriakopoulos, K., Parello, F., Tassi, F., & D'Alessandro, W. (2018). Origin of methane and light hydrocarbons in natural fluid emissions: A key study from Greece. *Chemical Geology*, *479*, 286–301. https://doi.org/10.1016/j.chemgeo.2018.01.027

Daval, D., Hellmann, R., Martinez, I., Gangloff, S., & Guyot, F. (2013). Lizardite serpentine dissolution kinetics as a function of pH and temperature, including effects of elevated $pCO_2$. *Chemical Geology*, *351*, 245–256. https://doi.org/10.1016/j.chemgeo.2013.05.020

De Donder, T. (1927). L'affinité. *Mémoires de La Classe Des Sciences. Académie Royale de Belgique. Collection in 8, 9*(7), 1–94.

De Donder, T., & Van Rysselberghe, P. (1936). *Thermodynamic theory of affinity* (Vol. 1). Stanford university press.

de Obeso, J. C., & Kelemen, P. B. (2018). Fluid rock interactions on residual mantle peridotites overlain by shallow oceanic limestones: Insights from Wadi Fins, Sultanate of Oman. *Chemical Geology*, *498*, 139–149. https://doi.org/10.1016/j.chemgeo.2018.09.022

de Obeso, J. C., & Kelemen, P. B. (2020). Major element mobility during serpentinization, oxidation and weathering of mantle peridotite at low temperatures. *Philosophical Transactions of the Royal Society A: Mathematical, Physical and Engineering Sciences*, *378*(2165), 20180433. https://doi.org/10.1098/rsta.2018.0433

Deschamps, F., Godard, M., Guillot, S., & Hattori, K. (2013). Geochemistry of subduction zone serpentinites: A review. *Lithos*, *178*, 96–127. https://doi.org/10.1016/j.lithos.2013.05.019

Dessert, C., Dupré, B., Gaillardet, J., François, L. M., & Allègre, C. J. (2003). Basalt weathering laws and the impact of basalt weathering on the global carbon cycle. *Chemical Geology*, *202*(3), 257–273. https://doi.org/10.1016/j.chemgeo.2002.10.001

Dewandel, B., Lachassagne, P., Boudier, F., Al-Hattali, S., Ladouche, B., Pinault, J.-L., & Al-Suleimani, Z. (2005). A conceptual hydrogeological model of ophiolite hard-rock aquifers in Oman based on a multiscale and a multidisciplinary approach. *Hydrogeology Journal*, *13*(5–6), 708–726. https://doi.org/10.1007/s10040-005-0449-2

Dhuime, B., Hawkesworth, C. J., Cawood, P. A., & Storey, C. D. (2012). A change in the geodynamics of continental growth 3 billion Years Ago. *Science*, *335*(6074), 1334–1336. https://doi.org/10.1126/science.1216066

Dick, J. M. (2008). Calculation of the relative metastabilities of proteins using the CHNOSZ software package. *Geochemical Transactions*, *9*(1), no. 10. https://doi.org/10.1186/1467-4866-9-10

Dick, J. M. (2019). CHNOSZ: Thermodynamic calculations and diagrams for geochemistry. *Frontiers in Earth Science*, *7*, no. 180. https://doi.org/10.3389/feart.2019.00180

Douville, E., Charlou, J. L., Oelkers, E. H., Bienvenu, P., Jove Colon, C. F., Donval, J. P., Fouquet, Y., Prieur, D., & Appriou, P. (2002). The Rainbow vent fluids (36°14′N, MAR): The influence of ultramafic rocks and phase separation on trace metal content in Mid-Atlantic Ridge hydrothermal fluids. *Chemical Geology*, *184*(1–2), 37–48. https://doi.org/10.1016/S0009-2541(01)00351-5

Dürr, H. H., Meybeck, M., & Dürr, S. H. (2018). Lithologic composition of the Earth's continental surfaces derived from a new digital map emphasizing riverine material transfer. *Global Biogeochemical Cycles*, *19*, GB4S10. https://doi.org/10.1029/2005GB002515@10.1002/(ISSN)1944-9224.GNEWS1

Dyar, M. D., Guidotti, C. V., Harper, G. D., McKibben, M. A., & Saccocia, P. J. (1992). Controls on ferric iron in chlorite. *Geological Society of America Abstracts*, *24:7*, Article CONF-921058-. https://www.osti.gov/biblio/5888101

Edmond, J. M., Measures, C., McDuff, R. E., Chan, L. H., Collier, R., Grant, B., Gordon, L. I., & Corliss, J. B. (1979). Ridge crest hydrothermal activity and the balances of the major and minor elements in the ocean: The Galapagos data. *Earth and*

*Planetary Science Letters*, *46*(1), 1–18. https://doi.org/10.1016/0012-821X(79)90061-X

Ehlmann, B. L., Mustard, J. F., & Murchie, S. L. (2010). Geologic setting of serpentine deposits on Mars. *Geophysical Research Letters*, *37*(6), L06201. https://doi.org/10.1029/2010GL042596

Etiope, G., & Whiticar, M. J. (2019). Abiotic methane in continental ultramafic rock systems: Towards a genetic model. *Applied Geochemistry*, *102*, 139–152. https://doi.org/10.1016/j.apgeochem.2019.01.012

Etiope, Giuseppe, Schoell, M., & Hosgörmez, H. (2011). Abiotic methane flux from the Chimaera seep and Tekirova ophiolites (Turkey): Understanding gas exhalation from low temperature serpentinization and implications for Mars. *Earth and Planetary Science Letters*, *310*(1), 96–104. https://doi.org/10.1016/j.epsl.2011.08.001

Etiope, G., Tsikouras, B., Kordella, S., Ifandi, E., Christodoulou, D., & Papatheodorou, G. (2013a). Methane flux and origin in the Othrys ophiolite hyperalkaline springs, Greece. *Chemical Geology*, *347*, 161–174. https://doi.org/10.1016/j.chemgeo.2013.04.003

Etiope, Giuseppe, Vance, S., Christensen, L. E., Marques, J. M., & Ribeiro da Costa, I. (2013b). Methane in serpentinized ultramafic rocks in mainland Portugal. *Marine and Petroleum Geology*, *45*, 12–16. https://doi.org/10.1016/j.marpetgeo.2013.04.009

Etiope, G., Judas, J., & Whiticar, M. J. (2015). Occurrence of abiotic methane in the eastern United Arab Emirates ophiolite aquifer. *Arabian Journal of Geosciences*, *8*(12), 11345–11348. https://doi.org/10.1007/s12517-015-1975-4

Etiope, G., Vadillo, I., Whiticar, M. J., Marques, J. M., Carreira, P. M., Tiago, I., Benavente, J., Jiménez, P., & Urresti, B. (2016). Abiotic methane seepage in the Ronda peridotite massif, southern Spain. *Applied Geochemistry*, *66*, 101–113. https://doi.org/10.1016/j.apgeochem.2015.12.001

Etiope, G., Samardžić, N., Grassa, F., Hrvatović, H., Miošić, N., & Skopljak, F. (2017). Methane and hydrogen in hyperalkaline groundwaters of the serpentinized Dinaride ophiolite belt, Bosnia and Herzegovina. *Applied Geochemistry*, *84*, 286–296. https://doi.org/10.1016/j.apgeochem.2017.07.006

Evans, B. W. (2004). The serpentinite multisystem revisited: Chrysotile is metastable. *International Geology Review*, *46*(6), 479–506. https://doi.org/10.2747/0020-6814.46.6.479

Evans, B. W. (2008). Control of the products of serpentinization by the $Fe^{2+}Mg_{-1}$ exchange potential of olivine and orthopyroxene. *Journal of Petrology*, *49*(10), 1873–1887. https://doi.org/10.1093/petrology/egn050

Evans, B. W., Dyar, M. D., & Kuehner, S. M. (2012). Implications of ferrous and ferric iron in antigorite. *American Mineralogist*, *97*(1), 184–196. https://doi.org/10.2138/am.2012.3926

Evans, K. A., Powell, R., & Frost, B. R. (2013). Using equilibrium thermodynamics in the study of metasomatic alteration, illustrated by an application to serpentinites. *Lithos*, *168–169*, 67–84. https://doi.org/10.1016/j.lithos.2013.01.016

Farquhar, J., Bao, H., & Thiemens, M. (2000). Atmospheric influence of Earth's earliest sulfur cycle. *Science*, *289*(5480), 756–758. https://doi.org/10.1126/science.289.5480.756

Fecteau, K. M. (2016). *Organic Carbon in Hydrothermal Systems: From Phototrophy to Aldehyde Transformations*. Arizona State University.

Fones, E. M., Colman, D. R., Kraus, E. A., Nothaft, D. B., Poudel, S., Rempfert, K. R., Spear, J. R., Templeton, A. S., & Boyd, E. S. (2019). Physiological adaptations to serpentinization in the Samail Ophiolite, Oman. *The ISME Journal*, *13*(7), 1750–1762. https://doi.org/10.1038/s41396-019-0391-2

Foustoukos, D. I., Savov, I. P., & Janecky, D. R. (2008). Chemical and isotopic constraints on water/rock interactions at the Lost City hydrothermal field, 30°N Mid-Atlantic Ridge. *Geochimica et Cosmochimica Acta*, *72*(22), 5457–5474. https://doi.org/10.1016/j.gca.2008.07.035

Freyssinet, P., & Farah, A. S. (2000). Geochemical mass balance and weathering rates of ultramafic schists in Amazonia. *Chemical Geology*, *170*(1), 133–151. https://doi.org/10.1016/S0009-2541(99)00245-4

Frost, B. R., & Beard, J. S. (2007). On silica activity and serpentinization. *Journal of Petrology*, *48*(7), 1351–1368. https://doi.org/10.1093/petrology/egm021

Frost, B. R., Evans, K. A., Swapp, S. M., Beard, J. S., & Mothersole, F. E. (2013). The process of serpentinization in dunite from New Caledonia. *Lithos*, *178*, 24–39. https://doi.org/10.1016/j.lithos.2013.02.002

Früh-Green, G. L., Kelley, D. S., Bernasconi, S. M., Karson, J. A., Ludwig, K. A., Butterfield, D. A., Boschi, C., & Proskurowski, G. (2003). 30,000 years of hydrothermal activity at the Lost City Vent Field. *Science*, *301*(5632), 495–498. https://doi.org/10.1126/science.1085582

Früh-Green, G. L., Orcutt, B. N., Rouméjon, S., Lilley, M. D., Morono, Y., Cotterill, C., Green, S., Escartin, J., John, B. E., McCaig, A. M., Cannat, M., Ménez, B., Schwarzenbach, E. M., Williams, M. J., Morgan, S., Lang, S. Q., Schrenk, M. O., Brazelton, W. J., Akizawa, N., Boschi, C., Dunkel, K. G., Quéméneur, M., Whattam, S. A., Mayhew, L., Harris, M., Bayrakci, G., Behrmann, J.-H., Herrero-Bervera, E. Hesse, K., Liu, H.-Q., Ratnayake, A. S., Twing, K., Weis, D., Zhao, R., & Bilenker, L. (2018). Magmatism, serpentinization and life: Insights through drilling the Atlantis Massif (IODP Expedition 357). *Lithos*, *323*, 137–155. https://doi.org/10.1016/j.lithos.2018.09.012

Fujii, N., Arcilla, C. A., Yamakawa, M., Pascua, C., Namiki, K., Sato, T., Shikazono, N., & Alexander, W. R. (2010). *Natural analogue studies of bentonite reaction under hyperalkaline conditions: Overview of ongoing work at the Zambales Ophiolite, Philippines*. 41–50. https://doi.org/10.1115/ICEM2010-40022

Gaillard, F., Scaillet, B., & Arndt, N. T. (2011). Atmospheric oxygenation caused by a change in volcanic degassing pressure. *Nature, 478*(7368), 229–232. https://doi.org/10.1038/nature10460

Gale, A., Dalton, C. A., Langmuir, C. H., Su, Y., & Schilling, J.-G. (2013). The mean composition of ocean ridge basalts. *Geochemistry, Geophysics, Geosystems*, *14*(3), 489–518. https://doi.org/10.1029/2012GC004334

Gallant, R. M., & Damm, K. L. V. (2006). Geochemical controls on hydrothermal fluids from the Kairei and Edmond Vent Fields, 23°–25°S, Central Indian Ridge. *Geochemistry, Geophysics, Geosystems*, *7*(6), Q06018. https://doi.org/10.1029/2005GC001067

Gamo, T., Chiba, H., Yamanaka, T., Okudaira, T., Hashimoto, J., Tsuchida, S., Ishibashi, J., Kataoka, S., Tsunogai, U., Okamura, K., Sano, Y., & Shinjo, R. (2001). Chemical characteristics of newly discovered black smoker fluids and associated hydrothermal plumes at the Rodriguez Triple Junction, Central Indian Ridge. *Earth and Planetary Science Letters*, *193*(3), 371–379. https://doi.org/10.1016/S0012-821X(01)00511-8

Gaucher, E. C., & Blanc, P. (2006). Cement/clay interactions – A review: Experiments, natural analogues, and modeling. *Waste Management*, *26*(7), 776–788. https://doi.org/10.1016/j.wasman.2006.01.027

Geldern, R. van, & Barth, J. A. C. (2012). Optimization of instrument setup and post-run corrections for oxygen and hydrogen stable isotope measurements of water by isotope ratio infrared spectroscopy (IRIS). *Limnology and Oceanography: Methods*, *10*(12), 1024–1036. https://doi.org/10.4319/lom.2012.10.1024

Giampouras, M., Garrido, C. J., Zwicker, J., Vadillo, I., Smrzka, D., Bach, W., Peckmann, J., Jiménez, P., Benavente, J., & García-Ruiz, J. M. (2019). Geochemistry and mineralogy of serpentinization-driven hyperalkaline springs in the Ronda peridotites. *Lithos*, *350–351*, no. 105215. https://doi.org/10.1016/j.lithos.2019.105215

Giampouras, M., Garrido, C. J., Bach, W., Los, C., Fussmann, D., Monien, P., & García-Ruiz, J. M. (2020). On the controls of mineral assemblages and textures in alkaline springs, Samail Ophiolite, Oman. *Chemical Geology*, *533*, no. 119435. https://doi.org/10.1016/j.chemgeo.2019.119435

Giggenbach, W. F., Sano, Y., & Wakita, H. (1993). Isotopic composition of helium, and $CO_2$ and $CH_4$ contents in gases produced along the New Zealand part of a convergent plate boundary. *Geochimica et Cosmochimica Acta*, *57*(14), 3427–3455. https://doi.org/10.1016/0016-7037(93)90549-C

Glein, C. R., Baross, J. A., & Waite, J. H. (2015). The pH of Enceladus' ocean. *Geochimica et Cosmochimica Acta*, *162*, 202–219. https://doi.org/10.1016/j.gca.2015.04.017

Glein, C. R., & Zolotov, M. Y. (2020). Hydrogen, hydrocarbons, and habitability across the solar system. *Elements*, *16*(1), 47–52. https://doi.org/10.2138/gselements.16.1.47

Glueckauf, E., & Kitt, G. P. (1957). The hydrogen content of atmospheric air at ground level. *Quarterly Journal of the Royal Meteorological Society*, *83*(358), 522–528. https://doi.org/10.1002/qj.49708335808

Gold, T. (1992). The deep, hot biosphere. *Proceedings of the National Academy of Sciences*, *89*(13), 6045–6049. https://doi.org/10.1073/pnas.89.13.6045

Golubev, S. V., Pokrovsky, O. S., & Schott, J. (2005). Experimental determination of the effect of dissolved $CO_2$ on the dissolution kinetics of Mg and Ca silicates at 25 °C. *Chemical Geology*, *217*(3), 227–238. https://doi.org/10.1016/j.chemgeo.2004.12.011

Greber, N. D., Dauphas, N., Bekker, A., Ptáček, M. P., Bindeman, I. N., & Hofmann, A. (2017). Titanium isotopic evidence for felsic crust and plate tectonics 3.5 billion years ago. *Science*, *357*(6357), 1271–1274. https://doi.org/10.1126/science.aan8086

Grozeva, N. G., Klein, F., Seewald, J. S., & Sylva, S. P. (2020). Chemical and isotopic analyses of hydrocarbon-bearing fluid inclusions in olivine-rich rocks. *Philosophical Transactions of the Royal Society A: Mathematical, Physical and Engineering Sciences*, *378*(2165), 20180431. https://doi.org/10.1098/rsta.2018.0431

Guida, B. S., Bose, M., & Garcia-Pichel, F. (2017). Carbon fixation from mineral carbonates. *Nature Communications*, *8*(1), no. 1025. https://doi.org/10.1038/s41467-017-00703-4

Hanghøj, K., Kelemen, P. B., Hassler, D., & Godard, M. (2010). Composition and genesis of depleted mantle peridotites from the Wadi Tayin Massif, Oman Ophiolite; Major and trace element geochemistry, and Os isotope and PGE systematics. *Journal of Petrology*, *51*(1–2), 201–227. https://doi.org/10.1093/petrology/egp077

Hao, J., Sverjensky, D. A., & Hazen, R. M. (2017). A model for late Archean chemical weathering and world average river water. *Earth and Planetary Science Letters*, *457*, 191–203. https://doi.org/10.1016/j.epsl.2016.10.021

Hao, J., Sverjensky, D. A., & Hazen, R. M. (2019). Redox states of Archean surficial environments: The importance of $H_{2,g}$ instead of $O_{2,g}$ for weathering reactions. *Chemical Geology*, *521*, 49–58. https://doi.org/10.1016/j.chemgeo.2019.05.022

Helgeson, H. C. (1969). Thermodynamics of hydrothermal systems at elevated temperatures and pressures. *American Journal of Science*, *267*(7), 729–804. https://doi.org/10.2475/ajs.267.7.729

Helgeson, H. C. (1979). Mass transfer among minerals and hydrothermal solutions. In H. L. Barnes (Ed.), *Geochemistry of hydrothermal ore deposits* (2d ed, pp. 568–610). Wiley.

Helgeson, H. C., Delaney, J. M., Nesbitt, H. W., & Bird, D. K. (1978). Summary and critique of the thermodynamic properties of rock-forming minerals. *American Journal of Science*, *278*, 1–229.

Herzberg, C., Asimow, P. D., Arndt, N., Niu, Y., Lesher, C. M., Fitton, J. G., Cheadle, M. J., & Saunders, A. D. (2007). Temperatures in ambient mantle and plumes: Constraints from basalts, picrites, and komatiites. *Geochemistry, Geophysics, Geosystems*, *8*(2), Q02006. https://doi.org/10.1029/2006GC001390

Hoehler, T. M. (2007). An energy balance concept for habitability. *Astrobiology*, *7*(6), 824–838. https://doi.org/10.1089/ast.2006.0095

Holland, H. D. (2002). Volcanic gases, black smokers, and the great oxidation event. *Geochimica et Cosmochimica Acta*, *66*(21), 3811–3826. https://doi.org/10.1016/S0016-7037(02)00950-X

Holland, H. D. (2009). Why the atmosphere became oxygenated: A proposal. *Geochimica et Cosmochimica Acta*, *73*(18), 5241–5255. https://doi.org/10.1016/j.gca.2009.05.070

Holm, N. G., Dumont, M., Ivarsson, M., & Konn, C. (2006). Alkaline fluid circulation in ultramafic rocks and formation of nucleotide constituents: A hypothesis. *Geochemical Transactions*, *7*(1), no. 7. https://doi.org/10.1186/1467-4866-7-7

Holm, N. G., Oze, C., Mousis, O., Waite, J. h., & Guilbert-Lepoutre, A. (2015). Serpentinization and the formation of $H_2$ and $CH_4$ on celestial bodies (planets, moons, comets). *Astrobiology*, *15*(7), 587–600. https://doi.org/10.1089/ast.2014.1188

Homma, A., & Tsukahara, H. (2008). Chemical characteristics of hot spring water and geological environment in the northernmost area of the Itoigawa Shizuoka tectonic line. *Bull Earthw Res Inst Univ Tokyo*, *83*, 217–225.

Hosgormez, H., Etiope, G., & Yalçin, M. N. (2008). New evidence for a mixed inorganic and organic origin of the Olympic Chimaera fire (Turkey): A large onshore seepage of abiogenic gas. *Geofluids*, *8*(4), 263–273. https://doi.org/10.1111/j.1468-8123.2008.00226.x

Howells, A. E. G., Leong, J. A. M., Ely, T., Santana, M., Robinson, K., Esquivel Eliszondo, S., Cox, A., Poret-Peterson, A., Krajmalnik-Brown, R., & Shock, E. L. (*in prep*). Energetically informed niche models of hydrogenotrophs detected in serpentinized fluids of the Samail ophiolite of Oman, a combined geochemical and microbiome approach.

Huang, F., & Sverjensky, D. A. (2019). Extended Deep Earth Water Model for predicting major element mantle metasomatism. *Geochimica et Cosmochimica Acta*, *254*, 192–230. https://doi.org/10.1016/j.gca.2019.03.027

Humphris, S. E., & Klein, F. (2018). Progress in deciphering the controls on the geochemistry of fluids in seafloor hydrothermal systems. *Annual Review of Marine Science*, *10*(1), 315–343. https://doi.org/10.1146/annurev-marine-121916-063233

Husson, J. M., & Peters, S. E. (2017). Atmospheric oxygenation driven by unsteady growth of the continental sedimentary reservoir. *Earth and Planetary Science Letters*, *460*, 68–75. https://doi.org/10.1016/j.epsl.2016.12.012

Itävaara, M., Nyyssönen, M., Kapanen, A., Nousiainen, A., Ahonen, L., & Kukkonen, I. (2011). Characterization of bacterial diversity to a depth of 1500 m in the Outokumpu deep borehole, Fennoscandian Shield. *FEMS Microbiology Ecology*, *77*(2), 295–309. https://doi.org/10.1111/j.1574-6941.2011.01111.x

Janecky, D. R., & Seyfried, W. E. (1986). Hydrothermal serpentinization of peridotite within the oceanic crust: Experimental investigations of mineralogy and major element chemistry. *Geochimica et Cosmochimica Acta*, *50*(7), 1357–1378. https://doi.org/10.1016/0016-7037(86)90311-X

Johnson, J. W., Oelkers, E. H., & Helgeson, H. C. (1992). SUPCRT92: A software package for calculating the standard molal thermodynamic properties of minerals, gases, aqueous species, and reactions from 1 to 5000 bar and 0 to 1000°C. *Computers & Geosciences*, *18*(7), 899–947. https://doi.org/10.1016/0098-3004(92)90029-Q

Kallmeyer, J., Pockalny, R., Adhikari, R. R., Smith, D. C., & D'Hondt, S. (2012). Global distribution of microbial abundance and biomass in subseafloor sediment. *Proceedings of the National Academy of Sciences*, *109*(40), 16213–16216. https://doi.org/10.1073/pnas.1203849109

Kasting, J. F. (2005). Methane and climate during the Precambrian era. *Precambrian Research*, *137*(3), 119–129. https://doi.org/10.1016/j.precamres.2005.03.002

Kasting, J. F. (2013). What caused the rise of atmospheric $O_2$? *Chemical Geology*, *362*, 13–25. https://doi.org/10.1016/j.chemgeo.2013.05.039

Kasting, J. F., & Canfield, D. E. (2012). The global oxygen cycle. In *Fundamentals of Geobiology* (pp. 93–104). John Wiley & Sons, Ltd. https://doi.org/10.1002/9781118280874.ch7

Kasting, J. F., Eggler, D. H., & Raeburn, S. P. (1993). Mantle redox evolution and the oxidation state of the archean atmosphere. *The Journal of Geology*, *101*(2), 245–257. https://doi.org/10.1086/648219

Kelemen, P., Al Rajhi, A., Godard, M., Ildefonse, B., Köpke, J., MacLeod, C., Manning, C., Michibayashi, K., Nasir, S., Shock, E., Takazawa, E., & Teagle, D. (2013). Scientific drilling and related research in the Samail Ophiolite, Sultanate of Oman. *Scientific Drilling*, *15*, 64–71. https://doi.org/10.5194/sd-15-64-2013

Kelemen, P. B., & Manning, C. E. (2015). Reevaluating carbon fluxes in subduction zones, what goes down, mostly comes up. *Proceedings of the National Academy of Sciences*, *112*(30), E3997–E4006. https://doi.org/10.1073/pnas.1507889112

Kelemen, P. B., & Matter, J. (2008). In situ carbonation of peridotite for $CO_2$ storage. *Proceedings of the National Academy of Sciences*, *105*(45), 17295–17300. https://doi.org/10.1073/pnas.0805794105

Kelemen, P. B., Matter, J., Streit, E. E., Rudge, J. F., Curry, W. B., & Blusztajn, J. (2011). Rates and mechanisms of mineral carbonation in peridotite: Natural processes and recipes for enhanced, in situ $CO_2$ capture and storage. *Annual Review of Earth and Planetary Sciences*, *39*(1), 545–576. https://doi.org/10.1146/annurev-earth-092010-152509

Kelley, D. S., Karson, J. A., Blackman, D. K., Früh-Green, G. L., Butterfield, D. A., Lilley, M. D., Olson, E. J., Schrenk, M. O., Roe, K. K., Lebon, G. T., Rivizzigno, P., & the AT3-60 Shipboard Party. (2001). An off-axis hydrothermal vent field near the Mid-Atlantic Ridge at 30° N. *Nature*, *412*(6843), 145–149. https://doi.org/10.1038/35084000

Kelley, D. S., Karson, J. A., Früh-Green, G. L., Yoerger, D. R., Shank, T. M., Butterfield, D. A., Hayes, J. M., Schrenk, M. O., Olson, E. J., Proskurowski, G., Jakuba, M., Bradley, A., Larson, B., Ludwig, K., Glickson, D., Buckman, K., Bradley, A. S., Brazelton, W. J., Roe, K., Elend, M. J., Delacour, A., Bernasconi, S. M., Lilley, M. D., Baross, J. A., Summons, R. E., & Sylva, S. P. (2005). A serpentinite-hosted ecosystem: The Lost City Hydrothermal Field. *Science*, *307*(5714), 1428–1434. https://doi.org/10.1126/science.1102556

Kendall, B., Reinhard, C. T., Lyons, T. W., Kaufman, A. J., Poulton, S. W., & Anbar, A. D. (2010). Pervasive oxygenation along late Archaean ocean margins. *Nature Geoscience*, *3*(9), 647–652. https://doi.org/10.1038/ngeo942

Khoury, Hani N., Salameh, E., & Abdul-Jaber, Q. (1985). Characteristics of an unusual highly alkaline water from the Maqarin area, northern Jordan. *Journal of Hydrology*, *81*(1), 79–91. https://doi.org/10.1016/0022-1694(85)90168-4

Khoury, H. N., Salameh, E., Clark, I. D., Fritz, P., Bajjali, W., Milodowski, A. E., Cave, M. R., & Alexander, W. R. (1992). A natural analogue of high pH cement pore waters from the Maqarin area of northern Jordan. I: Introduction to the site. *Journal of Geochemical Exploration*, *46*(1), 117–132. https://doi.org/10.1016/0375-6742(92)90103-F

Klein, F., Bach, W., Humphris, S. E., Kahl, W.-A., Jöns, N., Moskowitz, B., & Berquó, T. S. (2014). Magnetite in seafloor serpentinite—Some like it hot. *Geology*, *42*(2), 135–138. https://doi.org/10.1130/G35068.1

Klein, F., Bach, W., Jöns, N., McCollom, T., Moskowitz, B., & Berquó, T. (2009). Iron partitioning and hydrogen generation during serpentinization of abyssal peridotites from 15°N on the Mid-Atlantic Ridge. *Geochimica et Cosmochimica Acta*, *73*(22), 6868–6893. https://doi.org/10.1016/j.gca.2009.08.021

Klein, F., Bach, W., & McCollom, T. M. (2013). Compositional controls on hydrogen generation during serpentinization of ultramafic rocks. *Lithos*, *178*, 55–69. https://doi.org/10.1016/j.lithos.2013.03.008

Klein, F., Humphris, S. E., Guo, W., Schubotz, F., Schwarzenbach, E. M., & Orsi, W. D. (2015). Fluid mixing and the deep biosphere of a fossil Lost City-type hydrothermal system at the Iberia Margin. *Proceedings of the National Academy of Sciences*, *112*(39), 12036–12041. https://doi.org/10.1073/pnas.1504674112

Klein, F., Grozeva, N. G., & Seewald, J. S. (2019). Abiotic methane synthesis and serpentinization in olivine-hosted fluid inclusions. *Proceedings of the National Academy of Sciences*, *116*(36), 17666–17672. https://doi.org/10.1073/pnas.1907871116

Klein, F., Tarnas, J. D., & Bach, W. (2020). Abiotic sources of molecular hydrogen on Earth. *Elements*, *16*(1), 19–24. https://doi.org/10.2138/gselements.16.1.19

Kodolányi, J., Pettke, T., Spandler, C., Kamber, B. S., & Gméling, K. (2012). Geochemistry of ocean floor and fore-arc serpentinites: Constraints on the ultramafic input to subduction zones. *Journal of Petrology*, *53*(2), 235–270. https://doi.org/10.1093/petrology/egr058

Kohl, L., Cumming, E., Cox, A., Rietze, A., Morrissey, L., Lang, S. Q., Richter, A., Suzuki, S., Nealson, K. H., & Morrill, P. L. (2016). Exploring the metabolic potential of microbial communities in ultra-basic, reducing springs at The Cedars, CA, USA: Experimental evidence of microbial methanogenesis and heterotrophic acetogenesis. *Journal of Geophysical Research: Biogeosciences*, *121*(4), 1203–1220. https://doi.org/10.1002/2015JG003233

Kotelnikova, S. (2002). Microbial production and oxidation of methane in deep subsurface. *Earth-Science Reviews*, *58*(3), 367–395. https://doi.org/10.1016/S0012-8252(01)00082-4

Kumagai, H., Nakamura, K., Toki, T., Morishita, T., Okino, K., Ishibashi, J., Tsunogai, U., Kawagucci, S., Gamo, T., Shibuya, T., Sawaguchi, T., Neo, N., Joshima, M., Sato, T., & Takai, K. (2008). Geological background of the Kairei and Edmond hydrothermal fields along the Central Indian Ridge: Implications of their vent fluids' distinct chemistry. *Geofluids*, *8*(4), 239–251. https://doi.org/10.1111/j.1468-8123.2008.00223.x

Kump, L. R., & Barley, M. E. (2007). Increased subaerial volcanism and the rise of atmospheric oxygen 2.5 billion years ago. *Nature*, *448*(7157), 1033–1036. https://doi.org/10.1038/nature06058

Kump, L. R., Kasting, J. F., & Barley, M. E. (2001). Rise of atmospheric oxygen and the "upside-down" Archean mantle. *Geochemistry, Geophysics, Geosystems*, *2*(1), 2000GC000114. https://doi.org/10.1029/2000GC000114

Lane, N., & Martin, W. F. (2012). The origin of membrane bioenergetics. *Cell*, *151*(7), 1406–1416. https://doi.org/10.1016/j.cell.2012.11.050

Lang, S. Q., Früh-Green, G. L., Bernasconi, S. M., & Butterfield, D. A. (2013). Sources of organic nitrogen at the serpentinite-hosted Lost City hydrothermal field. *Geobiology*, *11*(2), 154–169. https://doi.org/10.1111/gbi.12026

Lang, S. Q., Butterfield, D. A., Schulte, M., Kelley, D. S., & Lilley, M. D. (2010). Elevated concentrations of formate, acetate and dissolved organic carbon found at the Lost City hydrothermal field. *Geochimica et Cosmochimica Acta*, *74*(3), 941–952. https://doi.org/10.1016/j.gca.2009.10.045

LaRowe, D. E., & Amend, J. P. (2015). Catabolic rates, population sizes and doubling/replacement times of microorganisms in natural settings. *American Journal of Science*, *315*(3), 167–203. https://doi.org/10.2475/03.2015.01

Lau, M. C. Y., Kieft, T. L., Kuloyo, O., Linage-Alvarez, B., van Heerden, E., Lindsay, M. R., Magnabosco, C., Wang, W., Wiggins, J. B., Guo, L., Perlman, D. H., Kyin, S., Shwe, H. H., Harris, R. L., Oh, Y., Yi, M. J., Purtschert, R., Slater, G. F., Ono, S., Wei, S., Li, L., Sherwood-Lollar, B., & Onstott, T. C. (2016). An oligotrophic deep-subsurface community dependent on syntrophy is dominated by sulfur-driven autotrophic denitrifiers. *Proceedings of the National Academy of Sciences*, *113*(49), E7927–E7936. https://doi.org/10.1073/pnas.1612244113

Lazar, C., McCollom, T. M., & Manning, C. E. (2012). Abiogenic methanogenesis during experimental komatiite serpentinization: Implications for the evolution of the early Precambrian atmosphere. *Chemical Geology*, *326–327*, 102–112. https://doi.org/10.1016/j.chemgeo.2012.07.019

Lee, C.-T. A., Yeung, L. Y., McKenzie, N. R., Yokoyama, Y., Ozaki, K., & Lenardic, A. (2016). Two-step rise of atmospheric oxygen linked to the growth of continents. *Nature Geoscience*, *9*(6), 417–424. https://doi.org/10.1038/ngeo2707

Leong, J. A. M., & Shock, E. L. (2020). Thermodynamic constraints on the geochemistry of low-temperature, continental, serpentinization-generated fluids. *American Journal of Science*, *320*(3), 185–235. https://doi.org/10.2475/03.2020.01

Lever, M. A., Rouxel, O., Alt, J. C., Shimizu, N., Ono, S., Coggon, R. M., Shanks, W. C., Lapham, L., Elvert, M., Prieto-Mollar, X., Hinrichs, K.-U., Inagaki, F., & Teske, A. (2013). Evidence for microbial carbon and sulfur cycling in deeply buried ridge flank Basalt. *Science*, *339*(6125), 1305–1308. https://doi.org/10.1126/science.1229240

Li, J., Mara, P., Schubotz, F., Sylvan, J. B., Burgaud, G., Klein, F., Beaudoin, D., Wee, S. Y., Dick, H. J. B., Lott, S., Cox, R., Meyer, L. A. E., Quémener, M., Blackman, D. K., & Edgcomb, V. P. (2020). Recycling and metabolic flexibility dictate life in the lower oceanic crust. *Nature*, *579*(7798), 250–255. https://doi.org/10.1038/s41586-020-2075-5

Lin, L.-H., Hall, J., Onstott, T. C., Gihring, T., Lollar, B. S., Boice, E., Pratt, L., Lippmann-Pipke, J., & Bellamy, R. E. S. (2006). Planktonic microbial communities associated with fracture-derived groundwater in a deep gold mine of South Africa. *Geomicrobiology Journal*, *23*(6), 475–497. https://doi.org/10.1080/01490450600875829

Lincoln, S. A., Bradley, A. S., Newman, S. A., & Summons, R. E. (2013). Archaeal and bacterial glycerol dialkyl glycerol tetraether lipids in chimneys of the Lost City Hydrothermal Field. *Organic Geochemistry*, *60*, 45–53. https://doi.org/10.1016/j.orggeochem.2013.04.010

Lindsay, M. R., Amenabar, M. J., Fecteau, K. M., Debes, R. V., Martins, M. C. F., Fristad, K. E., Xu, H., Hoehler, T. M., Shock, E. L., & Boyd, E. S. (2018). Subsurface processes influence oxidant availability and chemoautotrophic hydrogen metabolism in Yellowstone hot springs. *Geobiology, 16*(6), 674–692. https://doi.org/10.1111/gbi.12308

Lipp, J. S., Morono, Y., Inagaki, F., & Hinrichs, K.-U. (2008). Significant contribution of Archaea to extant biomass in marine subsurface sediments. *Nature*, *454*(7207), 991–994. https://doi.org/10.1038/nature07174

Lyons, T. W., Reinhard, C. T., & Planavsky, N. J. (2014). The rise of oxygen in Earth's early ocean and atmosphere. *Nature, 506*(7488), 307–315. https://doi.org/10.1038/nature13068

Magnabosco, C., Lin, L.-H., Dong, H., Bomberg, M., Ghiorse, W., Stan-Lotter, H., Pedersen, K., Kieft, T. L., van Heerden, E., & Onstott, T. C. (2018). The biomass and biodiversity of the continental subsurface. *Nature Geoscience*, *11*(10), 707–717. https://doi.org/10.1038/s41561-018-0221-6

Magnabosco, Cara, Ryan, K., Lau, M. C. Y., Kuloyo, O., Sherwood Lollar, B., Kieft, T. L., van Heerden, E., & Onstott, T. C. (2016). A metagenomic window into carbon metabolism at 3 km depth in Precambrian continental crust. *The ISME Journal*, *10*(3), 730–741. https://doi.org/10.1038/ismej.2015.150

Maher, K. (2010). The dependence of chemical weathering rates on fluid residence time. *Earth and Planetary Science Letters*, *294*(1), 101–110. https://doi.org/10.1016/j.epsl.2010.03.010

Marques, J. M., Carreira, P. M., Carvalho, M. R., Matias, M. J., Goff, F. E., Basto, M. J., Graça, R. C., Aires-Barros, L., & Rocha, L. (2008). Origins of high pH mineral waters from ultramafic rocks, Central Portugal. *Applied Geochemistry*, *23*(12), 3278–3289. https://doi.org/10.1016/j.apgeochem.2008.06.029

Marques, J. M., Etiope, G., Neves, M. O., Carreira, P. M., Rocha, C., Vance, S. D., Christensen, L., Miller, A. Z., & Suzuki, S. (2018). Linking serpentinization, hyperalkaline mineral waters and abiotic methane production in continental peridotites: An integrated hydrogeological-bio-geochemical model from the Cabeço de Vide $CH_4$-rich aquifer (Portugal). *Applied Geochemistry*, *96*, 287–301. https://doi.org/10.1016/j.apgeochem.2018.07.011

Marshall, W. L., & Warakomski, J. M. (1980). Amorphous silica solubilities—II. Effect of aqueous salt solutions at 25°C. *Geochimica et Cosmochimica Acta*, *44*(7), 915–924. https://doi.org/10.1016/0016-7037(80)90281-1

Martin, W., & Russell, M. J. (2007). On the origin of biochemistry at an alkaline hydrothermal vent. *Philosophical Transactions of the Royal Society B: Biological Sciences*, *362*(1486), 1887–1926. https://doi.org/10.1098/rstb.2006.1881

Martin, W., Baross, J., Kelley, D., & Russell, M. J. (2008). Hydrothermal vents and the origin of life. *Nature Reviews Microbiology*, *6*(11), 805–814. https://doi.org/10.1038/nrmicro1991

Martin, W. F., Sousa, F. L., & Lane, N. (2014). Energy at life's origin. *Science, 344*(6188), 1092–1093. https://doi.org/10.1126/science.1251653

Mason, O. U., Nakagawa, T., Rosner, M., Van Nostrand, J. D., Zhou, J., Maruyama, A., Fisk, M. R., & Giovannoni, S. J. (2010). First investigation of the microbiology of the deepest layer of ocean crust. *PLoS ONE*, *5*(11), e15399. https://doi.org/10.1371/journal.pone.0015399

Matter, J. M., & Kelemen, P. B. (2009). Permanent storage of carbon dioxide in geological reservoirs by mineral carbonation. *Nature Geoscience*, *2*(12), 837–841. https://doi.org/10.1038/ngeo683

Matter, J. M., Waber, H. N., Loew, S., & Matter, A. (2006). Recharge areas and geochemical evolution of groundwater in an alluvial aquifer system in the Sultanate of Oman. *Hydrogeology Journal*, *14*(1), 203–224. https://doi.org/10.1007/s10040-004-0425-2

Mayhew, L. E., & Ellison, E. T. (2020). A synthesis and meta-analysis of the Fe chemistry of serpentinites and serpentine minerals. *Philosophical Transactions of the Royal Society A: Mathematical, Physical and Engineering Sciences*, *378*(2165), 20180420. https://doi.org/10.1098/rsta.2018.0420

Mayhew, L. E., Ellison, E. T., McCollom, T. M., Trainor, T. P., & Templeton, A. S. (2013). Hydrogen generation from low-temperature water–rock reactions. *Nature Geoscience*, *6*(6), 478–484. https://doi.org/10.1038/ngeo1825

Mayhew, L. E., Ellison, E. T., Miller, H. M., Kelemen, P. B., & Templeton, A. S. (2018). Iron transformations during low temperature alteration of variably serpentinized rocks from the Samail ophiolite, Oman. *Geochimica et Cosmochimica Acta*, *222*, 704–728. https://doi.org/10.1016/j.gca.2017.11.023

McCollom, T. M. (1999). Methanogenesis as a potential source of chemical energy for primary biomass production by autotrophic organisms in hydrothermal systems on Europa. *Journal of Geophysical Research: Planets*, *104*(E12), 30729–30742. https://doi.org/10.1029/1999JE001126

McCollom, T. M. (2007). Geochemical constraints on sources of metabolic energy for chemolithoautotrophy in ultramafic-hosted deep-sea hydrothermal systems. *Astrobiology*, *7*(6), 933–950. https://doi.org/10.1089/ast.2006.0119

McCollom, T. M. (2016). Abiotic methane formation during experimental serpentinization of olivine. *Proceedings of the National Academy of Sciences*, *113*(49), 13965–13970. https://doi.org/10.1073/pnas.1611843113

McCollom, T. M., & Bach, W. (2009). Thermodynamic constraints on hydrogen generation during serpentinization of ultramafic rocks. *Geochimica et Cosmochimica Acta*, *73*(3), 856–875. https://doi.org/10.1016/j.gca.2008.10.032

McCollom, T. M., & Donaldson, C. (2016). Generation of hydrogen and methane during experimental low-temperature reaction of ultramafic rocks with water. *Astrobiology*, *16*(6), 389–406. https://doi.org/10.1089/ast.2015.1382

McCollom, T. M., & Seewald, J. S. (2007). Abiotic synthesis of organic compounds in deep-sea hydrothermal environments. *Chemical Reviews*, *107*(2), 382–401. https://doi.org/10.1021/cr0503660

McCollom, T. M., & Shock, E. L. (1997). Geochemical constraints on chemolithoautotrophic metabolism by microorganisms in seafloor hydrothermal systems. *Geochimica et Cosmochimica Acta*, *61*(20), 4375–4391. https://doi.org/10.1016/S0016-7037(97)00241-X

McCollom, T. M., & Shock, E. L. (1998). Fluid-rock interactions in the lower oceanic crust: Thermodynamic models of hydrothermal alteration. *Journal of Geophysical Research: Solid Earth*, *103*(B1), 547–575. https://doi.org/10.1029/97JB02603

McDermott, J. M., Seewald, J. S., German, C. R., & Sylva, S. P. (2015). Pathways for abiotic organic synthesis at submarine hydrothermal fields. *Proceedings of the National Academy of Sciences*, *112*(25), 7668–7672. https://doi.org/10.1073/pnas.1506295112

McMahon, S., & Parnell, J. (2014). Weighing the deep continental biosphere. *FEMS Microbiology Ecology*, *87*(1), 113–120. https://doi.org/10.1111/1574-6941.12196

Mellini, M. (1982). The crystal structure of lizardite 1T: Hydrogen bonds and polytypism. *American Mineralogist*, *67*(5–6), 587–598. https://pubs.geoscienceworld.org/msa/ammin/article/67/5-6/587/41395/The-crystal-structure-of-lizardite-1T-hydrogen

Mellini, M., & Zanazzi, P. F. (1987). Crystal structures of lizardite-1T and lizardite-2H1 from Coli, Italy. *American Mineralogist*, *72*(9–10), 943–948. https://pubs.geoscienceworld.org/msa/ammin/article/72/9-10/943/42011/Crystal-structures-of-lizardite-1T-and-lizardite

Ménez, B., Pasini, V., & Brunelli, D. (2012). Life in the hydrated suboceanic mantle. *Nature Geoscience*, *5*(2), 133–137. https://doi.org/10.1038/ngeo1359

Ménez, B., Pasini, V., Guyot, F., Benzerara, K., Bernard, S., & Brunelli, D. (2018). Mineralizations and transition metal mobility driven by organic carbon during low-temperature serpentinization. *Lithos*, *323*, 262–276. https://doi.org/10.1016/j.lithos.2018.07.022

Mervine, E. M., Humphris, S. E., Sims, K. W. W., Kelemen, P. B., & Jenkins, W. J. (2014). Carbonation rates of peridotite in the Samail Ophiolite, Sultanate of Oman, constrained through 14C dating and stable isotopes. *Geochimica et Cosmochimica Acta*, *126*, 371–397. https://doi.org/10.1016/j.gca.2013.11.007

Meyer-Dombard, D'Arcy R., Woycheese, K. M., Yargıçoğlu, E. N., Cardace, D., Shock, E. L., Güleçal-Pektas, Y., & Temel, M. (2015). High pH microbial ecosystems in a newly discovered, ephemeral, serpentinizing fluid seep at Yanartaş (Chimera), Turkey. *Frontiers in Microbiology*, *5*, no. 723. https://doi.org/10.3389/fmicb.2014.00723

Meyer-Dombard, D'Arcy R., Casar, C. P., Simon, A. G., Cardace, D., Schrenk, M. O., & Arcilla, C. A. (2018). Biofilm formation and potential for iron cycling in serpentinization-influenced groundwater of the Zambales and Coast Range ophiolites. *Extremophiles*, *22*(3), 407–431. https://doi.org/10.1007/s00792-018-1005-z

Meyer-Dombard, D'Arcy R., Osburn, M. R., Cardace, D., & Arcilla, C. A. (2019). The effect of a tropical climate on available nutrient resources to springs in ophiolite-hosted, deep biosphere ecosystems in the Philippines. *Frontiers in Microbiology*, *10*, no. 761. https://doi.org/10.3389/fmicb.2019.00761

Miller, H. M., Matter, J. M., Kelemen, P., Ellison, E. T., Conrad, M. E., Fierer, N., Ruchala, T., Tominaga, M., & Templeton, A. S. (2016). Modern water/rock reactions in Oman hyperalkaline peridotite aquifers and implications for microbial habitability. *Geochimica et Cosmochimica Acta*, *179*, 217–241. https://doi.org/10.1016/j.gca.2016.01.033

Miller, H. M., Chaudhry, N., Conrad, M. E., Bill, M., Kopf, S. H., & Templeton, A. S. (2018). Large carbon isotope variability during methanogenesis under alkaline conditions. *Geochimica et Cosmochimica Acta*, *237*, 18–31. https://doi.org/10.1016/j.gca.2018.06.007

Millero, F. J. (1985). The effect of ionic interactions on the oxidation of metals in natural waters. *Geochimica et Cosmochimica Acta*, *49*(2), 547–553. https://doi.org/10.1016/0016-7037(85)90046-8

Monnin, C., Chavagnac, V., Boulart, C., Ménez, B., Gérard, M., Gérard, E., Pisapia, C., Quéméneur, M., Erauso, G., Postec, A., Guentas-Dombrowski, L., Payri, C., & Pelletier, B. (2014). Fluid chemistry of the low temperature hyperalkaline hydrothermal system of Prony Bay (New Caledonia). *Biogeosciences*, *11*(20), 5687–5706. https://doi.org/10.5194/bg-11-5687-2014

Morgan, B., & Lahav, O. (2007). The effect of pH on the kinetics of spontaneous Fe(II) oxidation by $O_2$ in aqueous solution – basic principles and a simple heuristic description. *Chemosphere*, *68*(11), 2080–2084. https://doi.org/10.1016/j.chemosphere.2007.02.015

Morrill, P. L., Kuenen, J. G., Johnson, O. J., Suzuki, S., Rietze, A., Sessions, A. L., Fogel, M. L., & Nealson, K. H. (2013). Geochemistry and geobiology of a present-day serpentinization site in California: The Cedars. *Geochimica et Cosmochimica Acta*, *109*, 222–240. https://doi.org/10.1016/j.gca.2013.01.043

Morrill, P. L., Brazelton, W. J., Kohl, L., Rietze, A., Miles, S. M., Kavanagh, H., Schrenk, M. O., Ziegler, S. E., & Lang, S. Q. (2014). Investigations of potential microbial methanogenic and carbon monoxide utilization pathways in ultra-basic reducing springs associated with present-day continental serpentinization: The Tablelands, NL, CAN. *Frontiers in Microbiology*, *5*, no. 613. https://doi.org/10.3389/fmicb.2014.00613

Moser, D. P., Gihring, T. M., Brockman, F. J., Fredrickson, J. K., Balkwill, D. L., Dollhopf, M. E., Lollar, B. S., Pratt, L. M., Boice, E., Southam, G., Wanger, G., Baker, B. J., Pfiffner, S. M., Lin, L.-H., & Onstott, T. C. (2005). Desulfotomaculum and Methanobacterium spp. Dominate a 4- to 5-Kilometer-Deep Fault. *Applied and Environmental Microbiology*, *71*(12), 8773–8783. https://doi.org/10.1128/AEM.71.12.8773-8783.2005

Mottl, M. J. (2009). Highest pH. *Geochemical News*.

Mottl, M. J., Komor, S. C., Fryer, P., & Moyer, C. L. (2003). Deep-slab fluids fuel extremophilic Archaea on a Mariana forearc serpentinite mud volcano: Ocean Drilling Program Leg 195. *Geochemistry, Geophysics, Geosystems*, *4*(11), no. 9009. https://doi.org/10.1029/2003GC000588

Mottl, M. J., Wheat, C. G., Fryer, P., Gharib, J., & Martin, J. B. (2004). Chemistry of springs across the Mariana forearc shows progressive devolatilization of the subducting plate. *Geochimica et Cosmochimica Acta*, *68*(23), 4915–4933. https://doi.org/10.1016/j.gca.2004.05.037

Muñoz, M., Andrade, V. D., Vidal, O., Lewin, E., Pascarelli, S., & Susini, J. (2006). Redox and speciation micromapping using dispersive X-ray absorption spectroscopy: Application to iron in chlorite mineral of a metamorphic rock thin section. *Geochemistry, Geophysics, Geosystems*, *7*(11), Q11020. https://doi.org/10.1029/2006GC001381

Nakamura, K., & Takai, K. (2014). Theoretical constraints of physical and chemical properties of hydrothermal fluids on variations in chemolithotrophic microbial communities in seafloor hydrothermal systems. *Progress in Earth and Planetary Science*, *1*(1), no. 5. https://doi.org/10.1186/2197-4284-1-5

National Academies of Sciences, Engineering, and Medicine. (2019). Chapter 6: Carbon Mineralization of $CO_2$. In *Negative Emissions Technologies and Reliable Sequestration: A Research Agenda* (pp. 247–318). National Academies Press. https://doi.org/10.17226/25259

Navarre-Sitchler, A., & Brantley, S. (2007). Basalt weathering across scales. *Earth and Planetary Science Letters*, *261*(1), 321–334. https://doi.org/10.1016/j.epsl.2007.07.010

Neal, C., & Shand, P. (2002). Spring and surface water quality of the Cyprus ophiolites. *Hydrology and Earth System Sciences*, *6*(5), 797–817. https://doi.org/10.5194/hess-6-797-2002

Neal, C., & Stanger, G. (1983). Hydrogen generation from mantle source rocks in Oman. *Earth and Planetary Science Letters*, *66*, 315–320. https://doi.org/10.1016/0012-821X(83)90144-9

Neal, C., & Stanger, G. (1984). Calcium and magnesium hydroxide precipitation from alkaline groundwaters in Oman, and their significance to the process of serpentinization. *Mineralogical Magazine*, *48*(347), 237–241. https://doi.org/10.1180/minmag.1984.048.347.07

Neal, C., & Stanger, G. (1985). Past and present serpentinisation of ultramafic rocks; an example from the Semail Ophiolite Nappe of Northern Oman. In *The Chemistry of Weathering* (pp. 249–275). Springer.

Nealson, K. H., Inagaki, F., & Takai, K. (2005). Hydrogen-driven subsurface lithoautotrophic microbial ecosystems (SLiMEs): Do they exist and why should we care? *Trends in Microbiology*, *13*(9), 405–410. https://doi.org/10.1016/j.tim.2005.07.010

Nesbitt, H. W., & Bricker, O. P. (1978). Low temperature alteration processes affecting ultramafic bodies. *Geochimica et Cosmochimica Acta*, *42*(4), 403–409. https://doi.org/10.1016/0016-7037(78)90271-5

Neubeck, A., Duc, N. T., Bastviken, D., Crill, P., & Holm, N. G. (2011). Formation of $H_2$ and $CH_4$ by weathering of olivine at temperatures between 30 and 70°C. *Geochemical Transactions*, *12*(1), no. 6. https://doi.org/10.1186/1467-4866-12-6

Neubeck, A., Sun, L., Müller, B., Ivarsson, M., Hosgörmez, H., Özcan, D., Broman, C., & Schnürer, A. (2017). Microbial community structure in a serpentine-hosted abiotic gas seepage at the Chimaera Ophiolite, Turkey. *Applied and Environmental Microbiology*, *83*(12), e03430-16. https://doi.org/10.1128/AEM.03430-16

Newton, R. C., & Manning, C. E. (2010). Role of saline fluids in deep-crustal and upper-mantle metasomatism: Insights from experimental studies. *Geofluids*, 58–72. https://doi.org/10.1111/j.1468-8123.2009.00275.x

Nicolas, A., Boudier, F., Ildefonse, B., & Ball, E. (2000). Accretion of Oman and United Arab Emirates ophiolite – Discussion of a new structural map. *Marine Geophysical Researches*, *21*(3), 147–180. https://doi.org/10.1023/A:1026769727917

Niu, Y. (2004). Bulk-rock major and trace element compositions of abyssal peridotites: Implications for mantle melting, melt extraction and post-melting processes beneath mid-ocean ridges. *Journal of Petrology*, *45*(12), 2423–2458. https://doi.org/10.1093/petrology/egh068

Nordstrom, K. D., McCleskey, B. R., & Ball, J. W. (2009). Sulfur geochemistry of hydrothermal waters in Yellowstone National Park: IV Acid–sulfate waters. *Applied Geochemistry*, *24*(2), 191–207. https://doi.org/10.1016/j.apgeochem.2008.11.019

Nyyssönen, M., Hultman, J., Ahonen, L., Kukkonen, I., Paulin, L., Laine, P., Itävaara, M., & Auvinen, P. (2014). Taxonomically and functionally diverse microbial communities in deep crystalline rocks of the Fennoscandian shield. *The ISME Journal*, *8*(1), 126–138. https://doi.org/10.1038/ismej.2013.125

Oelkers, E. H. (2001). An experimental study of forsterite dissolution rates as a function of temperature and aqueous Mg and Si concentrations. *Chemical Geology*, *175*(3–4), 485–494. https://doi.org/10.1016/S0009-2541(00)00352-1

Oelkers, E. H., & Schott, J. (2001). An experimental study of enstatite dissolution rates as a function of pH, temperature, and aqueous Mg and Si concentration, and the mechanism of pyroxene/pyroxenoid dissolution. *Geochimica et Cosmochimica Acta*, *65*(8), 1219–1231. https://doi.org/10.1016/S0016-7037(00)00564-0

Oeser, M., Strauss, H., Wolff, P. E., Koepke, J., Peters, M., Garbe-Schönberg, D., & Dietrich, M. (2012). A profile of multiple sulfur isotopes through the Oman ophiolite. *Chemical Geology*, *312–313*, 27–46. https://doi.org/10.1016/j.chemgeo.2012.04.008

O'Hanley, D. S., & Dyar, M. D. (1993). The composition of lizardite 1T and the formation of magnetite in serpentinites. *American Mineralogist*, *78*(3–4), 391–404.

O'Hanley, D. S., & Dyar, M. D. (1998). The composition of chrysotile and its relationship with lizardite. *The Canadian Mineralogist*, *36*(3), 727–739.

Ohlsson, J. I., Osvatic, J. T., Becraft, E. D., & Swingley, W. D. (2019). Microbial community in hyperalkaline steel slag-fill emulates serpentinizing springs. *Diversity*, *11*(7), 103. https://doi.org/10.3390/d11070103

Okland, I., Huang, S., Dahle, H., Thorseth, I. H., & Pedersen, R. B. (2012). Low temperature alteration of serpentinized ultramafic rock and implications for microbial life. *Chemical Geology*, *318–319*, 75–87. https://doi.org/10.1016/j.chemgeo.2012.05.015

Okland, I., Huang, S., Thorseth, I. H., & Pedersen, R. B. (2014). Formation of $H_2$, $CH_4$ and N-species during low-temperature experimental alteration of ultramafic rocks. *Chemical Geology*, *387*, 22–34. https://doi.org/10.1016/j.chemgeo.2014.08.003

Olsson, J., Stipp, S. L. S., & Gislason, S. R. (2015). Element scavenging by recently formed travertine deposits in the alkaline springs from the Oman Semail Ophiolite. *Mineralogical Magazine*, *78*(6), 1479–1490. https://doi.org/10.1180/minmag.2014.078.6.15

Osburn, M. R., LaRowe, D. E., Momper, L. M., & Amend, J. P. (2014). Chemolithotrophy in the continental deep subsurface: Sanford Underground Research Facility (SURF), USA. *Frontiers in Microbiology*, *5*, no. 610. https://doi.org/10.3389/fmicb.2014.00610

Ostrander, C. M., Nielsen, S. G., Owens, J. D., Kendall, B., Gordon, G. W., Romaniello, S. J., & Anbar, A. D. (2019). Fully oxygenated water columns over continental shelves before the Great Oxidation Event. *Nature Geoscience*, *12*(3), 186–191. https://doi.org/10.1038/s41561-019-0309-7

Oufi, O., Cannat, M., & Horen, H. (2002). Magnetic properties of variably serpentinized abyssal peridotites. *Journal of Geophysical Research: Solid Earth*, *107*(B5), no. 2095.

Palandri, J. L., & Reed, M. H. (2004). Geochemical models of metasomatism in ultramafic systems: Serpentinization, rodingitization, and sea floor carbonate chimney precipitation. *Geochimica et Cosmochimica Acta*, *68*(5), 1115–1133. https://doi.org/10.1016/j.gca.2003.08.006

Papastamataki, A. (1977). The alkalinity and the chemical composition of springs issuing from peridotites. *Ann. Geol. Pays. Hell.*, *28*, 551–566.

Parkes, R. J., Cragg, B., Roussel, E., Webster, G., Weightman, A., & Sass, H. (2014). A review of prokaryotic populations and processes in sub-seafloor sediments, including biosphere-geosphere interactions. *Marine Geology*, *352*, 409–425. https://doi.org/10.1016/j.margeo.2014.02.009

Paukert, A. N., Matter, J. M., Kelemen, P. B., Shock, E. L., & Havig, J. R. (2012). Reaction path modeling of enhanced in situ $CO_2$ mineralization for carbon sequestration in the peridotite of the Samail Ophiolite, Sultanate of Oman. *Chemical Geology*, *330–331*, 86–100. https://doi.org/10.1016/j.chemgeo.2012.08.013

Paukert Vankeuren, A. N., Matter, J. M., Stute, M., & Kelemen, P. B. (2019). Multitracer determination of apparent groundwater ages in peridotite aquifers within the Samail ophiolite, Sultanate of Oman. *Earth and Planetary Science Letters*, *516*, 37–48. https://doi.org/10.1016/j.epsl.2019.03.007

Pawson, J. F., Oze, C., Etiope, G., & Horton, T. W. (2014). Discovery of new methane-bearing hyperalkaline springs in the serpentinized Dun Mountain Ophiolite, New Zealand. *AGU Fall Meeting Abstracts*, *53*, V53A-4824. http://adsabs.harvard.edu/abs/2014AGUFM.V53A4824P

Pedersen, K., Nilsson, E., Arlinger, J., Hallbeck, L., & O’Neill, A. (2004). Distribution, diversity and activity of microorganisms in the hyper-alkaline spring waters of Maqarin in Jordan. *Extremophiles*, *8*(2), 151–164. https://doi.org/10.1007/s00792-004-0374-7

Pfeifer, H.-R. (1977). A model for fluids in metamorphosed ultramafic rocks: Observations at surface and subsurface conditions (high pH spring waters). *Schweizerische Mineralogische Und Petrographische Mitteilungen*, *57*(3), 361–396. https://doi.org/10.5169/seals-44441

Philippot, P., Ávila, J. N., Killingsworth, B. A., Tessalina, S., Baton, F., Caquineau, T., Muller, E., Pecoits, E., Cartigny, P., Lalonde, S. V., Ireland, T. R., Thomazo, C., van Kranendonk, M. J., & Busigny, V. (2018). Globally asynchronous sulphur isotope signals require re-definition of the Great Oxidation Event. *Nature Communications*, *9*(1), no. 2245. https://doi.org/10.1038/s41467-018-04621-x

Planavsky, N. J., Asael, D., Hofmann, A., Reinhard, C. T., Lalonde, S. V., Knudsen, A., Wang, X., Ossa Ossa, F., Pecoits, E., Smith, A. J. B., Beukes, N. J., Bekker, A., Johnson, T. M., Konhauser, K. O., Lyons, T. W., & Rouxel, O. J. (2014). Evidence for oxygenic photosynthesis half a billion years before the Great Oxidation Event. *Nature Geoscience*, *7*(4), 283–286. https://doi.org/10.1038/ngeo2122

Plummer, L. N., Wigley, T. M. L., & Parkhurst, D. L. (1978). The kinetics of calcite dissolution in $CO_2$-water systems at 5 degrees to 60 degrees C and 0.0 to 1.0 atm CO 2. *American Journal of Science*, *278*(2), 179–216. https://doi.org/10.2475/ajs.278.2.179

Plümper, O., Beinlich, A., Bach, W., Janots, E., & Austrheim, H. (2014). Garnets within geode-like serpentinite veins: Implications for element transport, hydrogen production and life-supporting environment formation. *Geochimica et Cosmochimica Acta*, *141*, 454–471. https://doi.org/10.1016/j.gca.2014.07.002

Pokrovsky, O. S., & Schott, J. (1999). Processes at the magnesium-bearing carbonates/solution interface. II. Kinetics and mechanism of magnesite dissolution. *Geochimica et Cosmochimica Acta*, *63*(6), 881–897. https://doi.org/10.1016/S0016-7037(99)00013-7

Pokrovsky, O. S., & Schott, J. (2000). Kinetics and mechanism of forsterite dissolution at 25°C and pH from 1 to 12. *Geochimica et Cosmochimica Acta*, *64*(19), 3313–3325. https://doi.org/10.1016/S0016-7037(00)00434-8

Pokrovsky, O. S., & Schott, J. (2001). Kinetics and mechanism of dolomite dissolution in neutral to alkaline solutions revisited. *American Journal of Science*, *301*(7), 597–626. https://doi.org/10.2475/ajs.301.7.597

Pokrovsky, O. S., & Schott, J. (2004). Experimental study of brucite dissolution and precipitation in aqueous solutions: Surface speciation and chemical affinity control. *Geochimica et Cosmochimica Acta*, *68*(1), 31–45. https://doi.org/10.1016/S0016-7037(03)00238-2

Postec, A., Quéméneur, M., Bes, M., Mei, N., Benaïssa, F., Payri, C., Monnin, C., Pelletier, B., Guentas, L., Ollivier, B., Gérard, E., Pisapia, C., Gérard, M., Ménez, B., & Erauso, G. (2015). Microbial diversity in a submarine carbonate edifice from the serpentinizing hydrothermal system of the Prony Bay (New Caledonia) over a 6-year period. *Frontiers in Microbiology*, *6*, no. 857. https://doi.org/10.3389/fmicb.2015.00857

Poupeau, G., Saddiqi, O., Michard, A., Goffé, B., & Oberhänsli, R. (1998). Late thermal evolution of the Oman Mountains subophiolitic windows: Apatite fission-track thermochronology. *Geology*, *26*(12), 1139–1142. https://doi.org/10.1130/0091-7613(1998)026<1139:LTEOTO>2.3.CO;2

Quéméneur, M., Bes, M., Postec, A., Mei, N., Hamelin, J., Monnin, C., Chavagnac, V., Payri, C., Pelletier, B., Guentas-Dombrowsky, L., Gérard, M., Pisapia, C., Gérard, E., Ménez, B., Ollivier, B., & Erauso, G. (2014). Spatial distribution of microbial communities in the shallow submarine alkaline hydrothermal field of the Prony Bay, New Caledonia. *Environmental Microbiology Reports*, *6*(6), 665–674. https://doi.org/10.1111/1758-2229.12184

Quéméneur, M., Palvadeau, A., Postec, A., Monnin, C., Chavagnac, V., Ollivier, B., & Erauso, G. (2015). Endolithic microbial communities in carbonate precipitates from serpentinite-hosted hyperalkaline springs of the Voltri Massif (Ligurian Alps, Northern Italy). *Environmental Science and Pollution Research*, *22*(18), 13613–13624. https://doi.org/10.1007/s11356-015-4113-7

Reardon, E. J. (1990). An ion interaction model for the determination of chemical equilibria in cement/water systems. *Cement and Concrete Research*, *20*(2), 175–192. https://doi.org/10.1016/0008-8846(90)90070-E

Rempfert, K. R., Miller, H. M., Bompard, N., Nothaft, D., Matter, J. M., Kelemen, P., Fierer, N., & Templeton, A. S. (2017). Geological and geochemical controls on subsurface microbial life in the Samail Ophiolite, Oman. *Frontiers in Microbiology*, *8*, no. 56. https://doi.org/10.3389/fmicb.2017.00056

Rizoulis, A., Milodowski, A. E., Morris, K., & Lloyd, J. R. (2016). Bacterial diversity in the hyperalkaline Allas Springs (Cyprus), a natural analogue for cementitious radioactive waste repository. *Geomicrobiology Journal*, *33*(2), 73–84. https://doi.org/10.1080/01490451.2014.961107

Roadcap, G. S., Kelly, W. R., & Bethke, C. M. (2005). Geochemistry of extremely alkaline (pH > 12) ground water in slag-fill aquifers. *Groundwater*, *43*(6), 806–816. https://doi.org/10.1111/j.1745-6584.2005.00060.x

Roadcap, G. S., Sanford, R. A., Jin, Q., Pardinas, J. R., & Bethke, C. M. (2006). Extremely alkaline (pH > 12) ground water hosts diverse microbial community. *Groundwater*, *44*(4), 511–517. https://doi.org/10.1111/j.1745-6584.2006.00199.x

Robinson, K. J. (2017). *Modeling Aqueous Organic Chemistry in Experimental and Natural Systems*. Arizona State University.

Russell, M. J. (2018). Green Rust: The simple organizing ‘Seed’ of all life? *Life*, *8*(3), no. 35. https://doi.org/10.3390/life8030035

Russell, M. J., Hall, A. J., & Martin, W. (2010). Serpentinization as a source of energy at the origin of life. *Geobiology*, *8*(5), 355–371. https://doi.org/10.1111/j.1472-4669.2010.00249.x

Sader, J. A., Leybourne, M. I., McClenaghan, M. B., & Hamilton, S. M. (2007). Low-temperature serpentinization processes and kimberlite groundwater signatures in the Kirkland Lake and Lake Timiskiming kimberlite fields, Ontario, Canada: Implications for diamond exploration. *Geochemistry: Exploration, Environment, Analysis*, *7*(1), 3–21. https://doi.org/10.1144/1467-7873/06-900

Sánchez-Murillo, R., Gazel, E., Schwarzenbach, E. M., Crespo-Medina, M., Schrenk, M. O., Boll, J., & Gill, B. C. (2014). Geochemical evidence for active tropical serpentinization in the Santa Elena Ophiolite, Costa Rica: An analog of a humid early Earth? *Geochemistry, Geophysics, Geosystems*, *15*(5), 1783–1800. https://doi.org/10.1002/2013GC005213

Sano, Y., Urabe, A., Wakita, H., & Wushiki, H. (1993). Origin of hydrogen-nitrogen gas seeps, Oman. *Applied Geochemistry*, *8*(1), 1–8. https://doi.org/10.1016/0883-2927(93)90053-J

Schmidt, K., Koschinsky, A., Garbe-Schönberg, D., de Carvalho, L. M., & Seifert, R. (2007). Geochemistry of hydrothermal fluids from the ultramafic-hosted Logatchev hydrothermal field, 15°N on the Mid-Atlantic Ridge: Temporal and spatial investigation. *Chemical Geology*, *242*(1), 1–21. https://doi.org/10.1016/j.chemgeo.2007.01.023

Schrenk, M. O., Kelley, D. S., Bolton, S. A., & Baross, J. A. (2004). Low archaeal diversity linked to subseafloor geochemical processes at the Lost City Hydrothermal Field, Mid-Atlantic Ridge. *Environmental Microbiology*, *6*(10), 1086–1095. https://doi.org/10.1111/j.1462-2920.2004.00650.x

Schrenk, M. O., Brazelton, W. J., & Lang, S. Q. (2013). Serpentinization, carbon, and deep life. *Reviews in Mineralogy and Geochemistry*, *75*(1), 575–606. https://doi.org/10.2138/rmg.2013.75.18

Schulte, M., Blake, D., Hoehler, T., & McCollom, T. (2006). Serpentinization and its Implications for life on the Early Earth and Mars. *Astrobiology*, *6*(2), 364–376. https://doi.org/10.1089/ast.2006.6.364

Schwarzenbach, E. M., Lang, S. Q., Früh-Green, G. L., Lilley, M. D., Bernasconi, S. M., & Méhay, S. (2013). Sources and cycling of carbon in continental, serpentinite-hosted alkaline springs in the Voltri Massif, Italy. *Lithos*, *177*, 226–244. https://doi.org/10.1016/j.lithos.2013.07.009

Sciarra, A., Saroni, A., Etiope, G., Coltorti, M., Mazzarini, F., Lott, C., Grassa, F., & Italiano, F. (2019). Shallow submarine seep of abiotic methane from serpentinized peridotite off the Island of Elba, Italy. *Applied Geochemistry*, *100*, 1–7. https://doi.org/10.1016/j.apgeochem.2018.10.025

Segadelli, S., Vescovi, P., Ogata, K., Chelli, A., Zanini, A., Boschetti, T., Petrella, E., Toscani, L., Gargini, A., & Celico, F. (2017). A conceptual hydrogeological model of ophiolitic aquifers (serpentinised peridotite): The test example of Mt. Prinzera (Northern Italy). *Hydrological Processes*, *31*(5), 1058–1073. https://doi.org/10.1002/hyp.11090

Seward, T. M. (1974). Determination of the first ionization constant of silicic acid from quartz solubility in borate buffer solutions to 350°C. *Geochimica et Cosmochimica Acta*, *38*(11), 1651–1664. https://doi.org/10.1016/0016-7037(74)90183-5

Seyfried, W. E., Ding, K., & Berndt, M. E. (1991). Phase equilibria constraints on the chemistry of hot spring fluids at mid-ocean ridges. *Geochimica et Cosmochimica Acta*, *55*(12), 3559–3580. https://doi.org/10.1016/0016-7037(91)90056-B

Seyfried, W. E., Foustoukos, D. I., & Allen, D. E. (2004). Ultramafic-hosted hydrothermal systems at mid-ocean ridges: Chemical and physical controls on pH, redox and carbon reduction reactions. In *Geophysical Monograph Series* (pp. 267–284). American Geophysical Union. https://doi.org/10.1029/148GM11

Seyfried, W. E., Foustoukos, D. I., & Fu, Q. (2007). Redox evolution and mass transfer during serpentinization: An experimental and theoretical study at 200°C, 500bar with implications for ultramafic-hosted hydrothermal systems at Mid-Ocean Ridges. *Geochimica et Cosmochimica Acta*, *71*(15), 3872–3886. https://doi.org/10.1016/j.gca.2007.05.015

Seyfried, W. E., Pester, N. J., Tutolo, B. M., & Ding, K. (2015). The Lost City hydrothermal system: Constraints imposed by vent fluid chemistry and reaction path models on subseafloor heat and mass transfer processes. *Geochimica et Cosmochimica Acta*, *163*, 59–79. https://doi.org/10.1016/j.gca.2015.04.040

Sherwood Lollar, B., Voglesonger, K., Lin, L.-H., Lacrampe-Couloume, G., Telling, J., Abrajano, T. a., Onstott, T. c., & Pratt, L. m. (2007). Hydrogeologic controls on episodic $H_2$ release from Precambrian fractured rocks—Energy for deep subsurface life on Earth and Mars. *Astrobiology, 7*(6), 971–986. https://doi.org/10.1089/ast.2006.0096

Sherwood Lollar, B., Onstott, T. C., Lacrampe-Couloume, G., & Ballentine, C. J. (2014). The contribution of the Precambrian continental lithosphere to global H 2 production. *Nature*, *516*(7531), 379–382. https://doi.org/10.1038/nature14017

Shibuya, T., Yoshizaki, M., Sato, M., Shimizu, K., Nakamura, K., Omori, S., Suzuki, K., Takai, K., Tsunakawa, H., & Maruyama, S. (2015). Hydrogen-rich hydrothermal environments in the Hadean ocean inferred from serpentinization of komatiites at 300 °C and 500 bar. *Progress in Earth and Planetary Science*, *2*(1), no. 46. https://doi.org/10.1186/s40645-015-0076-z

Shimbashi, M., Sato, T., Yamakawa, M., Fujii, N., & Otake, T. (2018). Formation of Fe- and Mg-Rich smectite under hyperalkaline conditions at Narra in Palawan, the Philippines. *Minerals, 8*(4), no. 155. https://doi.org/10.3390/min8040155

Shiraki, R., Rock, P. A., & Casey, W. H. (2000). Dissolution kinetics of calcite in 0.1 M NaCl solution at room temperature: An Atomic Force Microscopic (AFM) study. *Aquatic Geochemistry*, *6*(1), 87–108. https://doi.org/10.1023/A:1009656318574

Shock, E. L. (1992). Chemical environments of submarine hydrothermal systems. In N. G. Holm (Ed.), *Marine Hydrothermal Systems and the Origin of Life: Report of SCOR Working Group 91* (pp. 67–107). Springer Netherlands. https://doi.org/10.1007/978-94-011-2741-7_5

Shock, E. L. (2009). Minerals as energy sources for microorganisms. *Economic Geology*, *104*(8), 1235–1248. https://doi.org/10.2113/gsecongeo.104.8.1235

Shock, E. L., & Canovas, P. (2010). The potential for abiotic organic synthesis and biosynthesis at seafloor hydrothermal systems. *Geofluids*, *10*(1–2), 161–192. https://doi.org/10.1111/j.1468-8123.2010.00277.x

Shock, E. L., & Helgeson, H. C. (1988). Calculation of the thermodynamic and transport properties of aqueous species at high pressures and temperatures: Correlation algorithms for ionic species and equation of state predictions to 5 kb and 1000°C. *Geochimica et Cosmochimica Acta*, *52*(8), 2009–2036. https://doi.org/10.1016/0016-7037(88)90181-0

Shock, E. L., & Holland, M. E. (2007). Quantitative habitability. *Astrobiology*, *7*(6), 839–851. https://doi.org/10.1089/ast.2007.0137

Shock, E. L., Helgeson, H. C., & Sverjensky, D. A. (1989). Calculation of the thermodynamic and transport properties of aqueous species at high pressures and temperatures: Standard partial molal properties of inorganic neutral species. *Geochimica et Cosmochimica Acta*, *53*(9), 2157–2183. https://doi.org/10.1016/0016-7037(89)90341-4

Shock, E. L., Holland, M., Meyer-Dombard, D., Amend, J. P., Osburn, G. R., & Fischer, T. P. (2010). Quantifying inorganic sources of geochemical energy in hydrothermal ecosystems, Yellowstone National Park, USA. *Geochimica et*

*Cosmochimica Acta*, *74*(14), 4005–4043. https://doi.org/10.1016/j.gca.2009.08.036

Shock, E. L., Oelkers, E. H., Johnson, J. W., Sverjensky, D. A., & Helgeson, H. C. (1992). Calculation of the thermodynamic properties of aqueous species at high pressures and temperatures. Effective electrostatic radii, dissociation constants and standard partial molal properties to 1000°C and 5 kbar. *Journal of the Chemical Society, Faraday Transactions*, *88*(6), 803–826. https://doi.org/10.1039/FT9928800803

Shock, E. L., Sassani, D. C., Willis, M., & Sverjensky, D. A. (1997). Inorganic species in geologic fluids: Correlations among standard molal thermodynamic properties of aqueous ions and hydroxide complexes. *Geochimica et Cosmochimica Acta*, *61*(5), 907–950. https://doi.org/10.1016/S0016-7037(96)00339-0

Sleep, N. H., & Bird, D. K. (2007). Niches of the pre-photosynthetic biosphere and geologic preservation of Earth's earliest ecology. *Geobiology*, *5*(2), 101–117. https://doi.org/10.1111/j.1472-4669.2007.00105.x

Sleep, N. H., Meibom, A., Fridriksson, T., Coleman, R. G., & Bird, D. K. (2004). $H_2$-rich fluids from serpentinization: Geochemical and biotic implications. *Proceedings of the National Academy of Sciences*, *101*(35), 12818–12823. https://doi.org/10.1073/pnas.0405289101

Sleep, N. H., Bird, D. K., & Pope, E. C. (2011). Serpentinite and the dawn of life. *Philosophical Transactions of the Royal Society B: Biological Sciences*, *366*(1580), 2857–2869. https://doi.org/10.1098/rstb.2011.0129

Smit, M. A., & Mezger, K. (2017). Earth's early $O_2$ cycle suppressed by primitive continents. *Nature Geoscience*, *10*(10), 788–792. https://doi.org/10.1038/ngeo3030

Smyth, J. R., Dyar, M. D., May, H. M., Bricker, O. P., & Acker, J. G. (1997). Crystal structure refinement and Mössbauer spectroscopy of an ordered, triclinic clinochlore. *Clays and Clay Minerals*, *45*(4), 544–550. https://doi.org/10.1346/CCMN.1997.0450406

Sossi, P. A., Eggins, S. M., Nesbitt, R. W., Nebel, O., Hergt, J. M., Campbell, I. H., O'Neill, H. S. C., Van Kranendonk, M., & Davies, D. R. (2016). Petrogenesis and geochemistry of archean komatiites. *Journal of Petrology*, *57*(1), 147–184. https://doi.org/10.1093/petrology/egw004

St Clair, B., Pottenger, J., Debes, R., Hanselmann, K., & Shock, E. (2019). Distinguishing biotic and abiotic iron oxidation at low temperatures. *ACS Earth and Space Chemistry*, *3*(6), 905–921. https://doi.org/10.1021/acsearthspacechem.9b00016

Starkey, N. A., Stuart, F. M., Ellam, R. M., Fitton, J. G., Basu, S., & Larsen, L. M. (2009). Helium isotopes in early Iceland plume picrites: Constraints on the composition of high 3He/4He mantle. *Earth and Planetary Science Letters*, *277*(1), 91–100. https://doi.org/10.1016/j.epsl.2008.10.007

Stevens, T. O., & McKinley, J. P. (1995). Lithoautotrophic microbial ecosystems in deep basalt aquifers. *Science*, *270*(5235), 450–455. https://doi.org/10.1126/science.270.5235.450

St-Jean, G. (2003). Automated quantitative and isotopic ($^{13}$C) analysis of dissolved inorganic carbon and dissolved organic carbon in continuous-flow using a total organic carbon analyser. *Rapid Communications in Mass Spectrometry*, *17*(5), 419–428. https://doi.org/10.1002/rcm.926

Stumm, W., & Lee, G. F. (1961). Oxygenation of ferrous iron. *Industrial & Engineering Chemistry*, *53*(2), 143–146. https://doi.org/10.1021/ie50614a030

Suda, K., Ueno, Y., Yoshizaki, M., Nakamura, H., Kurokawa, K., Nishiyama, E., Yoshino, K., Hongoh, Y., Kawachi, K., Omori, S., Yamada, K., Yoshida, N., & Maruyama, S. (2014). Origin of methane in serpentinite-hosted hydrothermal systems: The $CH_4$–$H_2$–$H_2O$ hydrogen isotope systematics of the Hakuba Happo hot spring. *Earth and Planetary Science Letters*, *386*, 112–125. https://doi.org/10.1016/j.epsl.2013.11.001

Suda, K., Gilbert, A., Yamada, K., Yoshida, N., & Ueno, Y. (2017). Compound– and position–specific carbon isotopic signatures of abiogenic hydrocarbons from on–land serpentinite–hosted Hakuba Happo hot spring in Japan. *Geochimica et Cosmochimica Acta*, *206*, 201–215. https://doi.org/10.1016/j.gca.2017.03.008

Suzuki, S., Ishii, S., Wu, A., Cheung, A., Tenney, A., Wanger, G., Kuenen, J. G., & Nealson, K. H. (2013). Microbial diversity in The Cedars, an ultrabasic, ultrareducing, and low salinity serpentinizing ecosystem. *Proceedings of the National Academy of Sciences*, *110*(38), 15336–15341. https://doi.org/10.1073/pnas.1302426110

Suzuki, S., Kuenen, J. G., Schipper, K., van der Velde, S., Ishii, S., Wu, A., Sorokin, D. Y., Tenney, A., Meng, X., Morrill, P. L., Kamagata, Y., Muyzer, G., & Nealson, K. H. (2014). Physiological and genomic features of highly alkaliphilic hydrogen-utilizing *Betaproteobacteria* from a continental serpentinizing site. *Nature Communications*, *5*, no. 3900. https://doi.org/10.1038/ncomms4900

Suzuki, S., Ishii, S., Hoshino, T., Rietze, A., Tenney, A., Morrill, P. L., Inagaki, F., Kuenen, J. G., & Nealson, K. H. (2017). Unusual metabolic diversity of hyperalkaliphilic microbial communities associated with subterranean serpentinization at The Cedars. *The ISME Journal*, *11*(11), 2584–2598. https://doi.org/10.1038/ismej.2017.111

Sverjensky, D. A. (1985). The distribution of divalent trace elements between sulfides, oxides, silicates and hydrothermal solutions: I. Thermodynamic basis. *Geochimica et Cosmochimica Acta*, *49*(3), 853–864. https://doi.org/10.1016/0016-7037(85)90177-2

Sverjensky, D. A., & Molling, P. A. (1992). A linear free energy relationship for crystalline solids and aqueous ions. *Nature*, *356*(6366), 231–234. https://doi.org/10.1038/356231a0

Sverjensky, D. A., Shock, E. L., & Helgeson, H. C. (1997). Prediction of the thermodynamic properties of aqueous metal complexes to 1000°C and 5 kb. *Geochimica et Cosmochimica Acta*, *61*(7), 1359–1412. https://doi.org/10.1016/S0016-7037(97)00009-4

Szponar, N., Brazelton, W. J., Schrenk, M. O., Bower, D. M., Steele, A., & Morrill, P. L. (2013). Geochemistry of a continental site of serpentinization, the Tablelands Ophiolite, Gros Morne National Park: A Mars analogue. *Icarus*, *224*(2), 286–296. https://doi.org/10.1016/j.icarus.2012.07.004

Takai, K., Moyer, C. L., Miyazaki, M., Nogi, Y., Hirayama, H., Nealson, K. H., & Horikoshi, K. (2005). Marinobacter alkaliphilus sp. Nov., a novel alkaliphilic bacterium isolated from subseafloor alkaline serpentine mud from Ocean Drilling Program Site 1200 at South Chamorro Seamount, Mariana Forearc. *Extremophiles*, *9*(1), 17–27. https://doi.org/10.1007/s00792-004-0416-1

Tang, M., Chen, K., & Rudnick, R. L. (2016). Archean upper crust transition from mafic to felsic marks the onset of plate tectonics. *Science*, *351*(6271), 372–375. https://doi.org/10.1126/science.aad5513

Taran, Y. A., Fischer, T. P., Cienfuegos, E., & Morales, P. (2002). Geochemistry of hydrothermal fluids from an intraplate ocean island: Everman volcano, Socorro Island, Mexico. *Chemical Geology*, *188*(1), 51–63. https://doi.org/10.1016/S0009-2541(02)00061-X

Taran, Y. A., Varley, N. R., Inguaggiato, S., & Cienfuegos, E. (2010). Geochemistry of $H_2$- and $CH_4$-enriched hydrothermal fluids of Socorro Island, Revillagigedo Archipelago, Mexico. Evidence for serpentinization and abiogenic methane. *Geofluids*, *10*(4), 542–555. https://doi.org/10.1111/j.1468-8123.2010.00314.x

Taylor, H. P. (1974). The application of oxygen and hydrogen isotope studies to problems of hydrothermal alteration and ore deposition. *Economic Geology*, *69*(6), 843–883. https://doi.org/10.2113/gsecongeo.69.6.843

Taylor, R. M., Hansen, H. C. B., Stanger, G., & Koch, C. B. (1991). On the genesis and composition of natural pyroaurite. *Clay Minerals*, *26*(3), 297–309. https://doi.org/10.1180/claymin.1991.026.3.01

Taylor, S. R., & McLennan, S. M. (1985). *The continental crust: Its composition and evolution: an examination of the geochem. record preserved in sedimentary rocks*. Blackwell.

Templeton, A. S., & Ellison, E. T. (2020). Formation and loss of metastable brucite: Does Fe(II)-bearing brucite support microbial activity in serpentinizing ecosystems? *Philosophical Transactions of the Royal Society A: Mathematical, Physical and Engineering Sciences*, *378*(2165), 20180423. https://doi.org/10.1098/rsta.2018.0423

Thom, J. G. M., Dipple, G. M., Power, I. M., & Harrison, A. L. (2013). Chrysotile dissolution rates: Implications for carbon sequestration. *Applied Geochemistry*, *35*, 244–254. https://doi.org/10.1016/j.apgeochem.2013.04.016

Tiago, I., Chung, A. P., & Veríssimo, A. (2004). Bacterial diversity in a nonsaline alkaline environment: Heterotrophic aerobic populations. *Applied and Environmental Microbiology*, *70*(12), 7378–7387. https://doi.org/10.1128/AEM.70.12.7378-7387.2004

Tiago, I., & Veríssimo, A. (2013). Microbial and functional diversity of a subterrestrial high pH groundwater associated to serpentinization. *Environmental Microbiology*, *15*(6), 1687–1706. https://doi.org/10.1111/1462-2920.12034

Tijhuis, L., Loosdrecht, M. C. M. V., & Heijnen, J. J. (1993). A thermodynamically based correlation for maintenance gibbs energy requirements in aerobic and anaerobic chemotrophic growth. *Biotechnology and Bioengineering*, *42*(4), 509–519. https://doi.org/10.1002/bit.260420415

Trapp, J. M., & Millero, F. J. (2007). The oxidation of Iron(II) with oxygen in NaCl brines. *Journal of Solution Chemistry*, *36*(11), 1479–1493. https://doi.org/10.1007/s10953-007-9192-8

Tutolo, B. M., Luhmann, A. J., Tosca, N. J., & Seyfried, W. E. (2018). Serpentinization as a reactive transport process: The brucite silicification reaction. *Earth and Planetary Science Letters*, *484*, 385–395. https://doi.org/10.1016/j.epsl.2017.12.029

Tutolo, B. M., & Tosca, N. J. (2018). Experimental examination of the Mg-silicate-carbonate system at ambient temperature: Implications for alkaline chemical sedimentation and lacustrine carbonate formation. *Geochimica et Cosmochimica Acta*, *225*, 80–101. https://doi.org/10.1016/j.gca.2018.01.019

Tutolo, B. M., Evans, B. W., & Kuehner, S. M. (2019). Serpentine–Hisingerite solid solution in altered ferroan peridotite and olivine gabbro. *Minerals*, *9*(1), no. 47. https://doi.org/10.3390/min9010047

Twing, K. I., Brazelton, W. J., Kubo, M. D. Y., Hyer, A. J., Cardace, D., Hoehler, T. M., McCollom, T. M., & Schrenk, M. O. (2017). Serpentinization-influenced groundwater harbors extremely low diversity microbial communities adapted to high pH. *Frontiers in Microbiology*, *8*, no. 308. https://doi.org/10.3389/fmicb.2017.00308

Vacquand, C., Deville, E., Beaumont, V., Guyot, F., Sissmann, O., Pillot, D., Arcilla, C., & Prinzhofer, A. (2018). Reduced gas seepages in ophiolitic complexes: Evidences for multiple origins of the $H_2$-$CH_4$-$N_2$ gas mixtures. *Geochimica et Cosmochimica Acta*, *223*, 437–461. https://doi.org/10.1016/j.gca.2017.12.018

Vance, S., Harnmeijer, J., Kimura, J., Hussmann, H., deMartin, B., & Brown, J. M. (2007). Hydrothermal systems in small ocean planets. *Astrobiology*, *7*(6), 987–1005. https://doi.org/10.1089/ast.2007.0075

Velbel, M. A. (1993). Constancy of silicate-mineral weathering-rate ratios between natural and experimental weathering: Implications for hydrologic control of differences in absolute rates. *Chemical Geology*, *105*(1), 89–99. https://doi.org/10.1016/0009-2541(93)90120-8

Vidal, O., Lanari, P., Munoz, M., Bourdelle, F., & Andrade, V. de. (2016). Deciphering temperature, pressure and oxygen-activity conditions of chlorite formation. *Clay Minerals*, *51*(4), 615–633. https://doi.org/10.1180/claymin.2016.051.4.06

Wagman, D. D., Evans, W. H., Parker, V. B., Schumm, R. H., Halow, I., Bailey, S. M., Churney, K. L., & Nuttall, R. L. (1982). *The NBS tables of chemical thermodynamic properties: Selected values for inorganic and C1 and C2 organic substances in SI units*. American Chemical Soc.

Waite, J. H., Glein, C. R., Perryman, R. S., Teolis, B. D., Magee, B. A., Miller, G., Grimes, J., Perry, M. E., Miller, K. E., Bouquet, A., Lunine, J. I., Brockwell, T., & Bolton, S. J. (2017). Cassini finds molecular hydrogen in the Enceladus plume: Evidence for hydrothermal processes. *Science*, *356*(6334), 155–159. https://doi.org/10.1126/science.aai8703

Wang, D. T., Reeves, E. P., McDermott, J. M., Seewald, J. S., & Ono, S. (2018). Clumped isotopologue constraints on the origin of methane at seafloor hot springs. *Geochimica et Cosmochimica Acta*, *223*, 141–158. https://doi.org/10.1016/j.gca.2017.11.030

Warren, J. M. (2016). Global variations in abyssal peridotite compositions. *Lithos*, *248–251*, 193–219. https://doi.org/10.1016/j.lithos.2015.12.023

Weast, R. C., & Lide, D. R. (Eds.). (1989). *CRC handbook of chemistry and physics: A ready-reference book of chemical and physical data* (70. ed., 1989–1990). CRC Press.

Wetzel, L. R., & Shock, E. L. (2000). Distinguishing ultramafic-from basalt-hosted submarine hydrothermal systems by comparing calculated vent fluid compositions. *Journal of Geophysical Research: Solid Earth*, *105*(B4), 8319–8340. https://doi.org/10.1029/1999JB900382

Weyhenmeyer, C. E., Burns, S. J., Waber, H. N., Macumber, P. G., & Matter, A. (2002). Isotope study of moisture sources, recharge areas, and groundwater flow paths within the eastern Batinah coastal plain, Sultanate of Oman. *Water Resources Research*, *38*(10), no. 1184. https://doi.org/10.1029/2000WR000149

Wheat, C. G., Fryer, P., Fisher, A. T., Hulme, S., Jannasch, H., Mottl, M. J., & Becker, K. (2008). Borehole observations of fluid flow from South Chamorro Seamount, an active serpentinite mud volcano in the Mariana forearc. *Earth and Planetary Science Letters*, *267*(3), 401–409. https://doi.org/10.1016/j.epsl.2007.11.057

Wheat, C. G., Seewald, J. S., & Takai, K. (2020). Fluid transport and reaction processes within a serpentinite mud volcano: South Chamorro Seamount. *Geochimica et Cosmochimica Acta*, *269*, 413–428. https://doi.org/10.1016/j.gca.2019.10.037

White, A. F., & Brantley, S. L. (2003). The effect of time on the weathering of silicate minerals: Why do weathering rates differ in the laboratory and field? *Chemical Geology*, *202*(3), 479–506. https://doi.org/10.1016/j.chemgeo.2003.03.001

Whitman, W. B., Coleman, D. C., & Wiebe, W. J. (1998). Prokaryotes: The unseen majority. *Proceedings of the National Academy of Sciences*, *95*(12), 6578–6583. https://doi.org/10.1073/pnas.95.12.6578

Whitney, D. L., & Evans, B. W. (2010). Abbreviations for names of rock-forming minerals. *American Mineralogist*, *95*(1), 185–187. https://doi.org/10.2138/am.2010.3371

Wolery, T., & Jarek, R. (2003). *EQ3/6, Version 8.0, Software User's Manual* (No. 10813-UM-8.0-00; p. 376). US Department of Energy, Office of Civilian Radioactive Waste Management, Office of Repository Development.

Wolery, T. J., & Jove-Colon, C. F. (2004). *Qualification of thermodynamic data for geochemical modeling of mineral-water interactions in dilute systems* (ANL-WIS-GS-000003; p. 212). US Department of Energy, Office of Civilian Radioactive Waste Management, Office of Repository Development.

Worman, S. L., Pratson, L. F., Karson, J. A., & Klein, E. M. (2016). Global rate and distribution of $H_2$ gas produced by serpentinization within oceanic lithosphere. *Geophysical Research Letters*, *43*(12), 6435–6443. https://doi.org/10.1002/2016GL069066

Woycheese, K. M., Meyer-Dombard, D. R., Cardace, D., Argayosa, A. M., & Arcilla, C. A. (2015). Out of the dark: Transitional subsurface-to-surface microbial diversity in a terrestrial serpentinizing seep (Manleluag, Pangasinan, the Philippines). *Frontiers in Microbiology*, *6*, no. 44. https://doi.org/10.3389/fmicb.2015.00044

Yuce, G., Italiano, F., D'Alessandro, W., Yalcin, T. H., Yasin, D. U., Gulbay, A. H., Ozyurt, N. N., Rojay, B., Karabacak, V., Bellomo, S., Brusca, L., Yang, T., Fu, C. C., Lai, C. W., Ozacar, A., & Walia, V. (2014). Origin and interactions of fluids circulating over the Amik Basin (Hatay, Turkey) and relationships with the hydrologic, geologic and tectonic settings. *Chemical Geology*, *388*, 23–39. https://doi.org/10.1016/j.chemgeo.2014.09.006

Zarubin, D., & Nemkina, N. (1990). The solubility of amorphous silica in alkaline aqueous solutions at constant ionic strength. *Zh. Neorg. Khim*, *35*, 31–38.

Zgonnik, V., Beaumont, V., Larin, N., Pillot, D., & Deville, E. (2019). Diffused flow of molecular hydrogen through the Western Hajar mountains, Northern Oman. *Arabian Journal of Geosciences*, *12*(3), no. 71. https://doi.org/10.1007/s12517-019-4242-2

# APPENDIX A

# SUPPLEMENTARY FILES TO CHAPTER 2

Table A1

*Composition of Fluids Used in Reaction Path and Mixing Calculations*

| | Rainwater[1] | Shallow Groundwater[2] | Deep Subsurface Fluid A[3] | Deep Subsurface Fluid B[4] | Deep Subsurface Fluid C[5] | Deep Subsurface Fluid D[6] |
|---|---|---|---|---|---|---|
| pH | 5.6 | 8 | 12.3 | 11.7 | 11.1 | 10.6 |
| ΣNa (mmole/kg)[7] | 0.15 | 1 | 10 | 10 | 10 | 10 |
| ΣCa (mmole/kg) | 0.008 | 0.6 | 14.4 | 3.2 | 0.7 | 0.3 |
| ΣMg (µmole/kg) | 21 | 1700 | 0.03 | 0.2 | 2.6 | 20 |
| ΣCl (mmole/kg)[7] | 0.17 | 1 | 10 | 10 | 10 | 10 |
| ΣSi (µmole/kg) | 0.7 | 100 | 1.3 | 0.3 | 0.07 | 0.02 |
| DIC (µmole/kg) | 13 | 2070 | 8 | 10 | 20 | 50 |
| DO (mmole/kg)[8] | 0.3 | 0.3 | 0 | 0 | 0 | 0 |
| $H_{2(aq)}$ (mmole/kg)[9] | 0 | 0 | 0.75 | 0.75 | 0.75 | 0.75 |

[1] modified from Hao and others (2017)

[2] calculated for a fluid in equilibrium with chrysotile, calcite, magnesite, and the atmosphere at 25°C and 1 bar. pH given as 8 (see text).

[3] fluid in equilibrium with the Ctl-Brc-Di and calcite assemblage at 25°C and 1 bar.

[4] fluid in equilibrium with the Ctl-Brc-Cal assemblage, given 10 µmole/kg DIC, at 25°C and 1 bar.

[5] fluid in equilibrium with the Ctl-Brc-Cal assemblage, given 20 µmole/kg DIC, at 25°C and 1 bar.

[6] fluid in equilibrium with the Ctl-Brc-Cal assemblage, given 50 µmole/kg DIC, at 25°C and 1 bar.

[7] shallow and deep fluids were given ionic strengths equivalent to a 1 and 10 millimole/kg NaCl solution, respectively, following environmental observations (Paukert and others, 2012; 2019).

[8] dissolved $O_2$ (DO) value for rain and shallow groundwater in equilibrium with the atmosphere at 25°C and 1 bar.

[9] value for deep subsurface fluids in equilibrium with one bar of $H_{2(g)}$ at 25°C.

Table A2

*Summary of Experimental and Estimated Thermodynamic Data for End-member Fe-bearing Serpentinization-relevant Minerals Used in this Study*

| Mineral | Formula | $\Delta_f G^{\circ a,f}$ | $\Delta_f H^{\circ a,g}$ | $S^{\circ b,h}$ |
|---|---|---|---|---|
| Ferrous Hydroxide | $Fe^{+2}(OH)_2$ | -117730[i] | -137340 | 21.0[j] |
| Ferrotremolite | $Ca_2Fe^{+2}{}_5Si_8O_{22}(OH)_2$ | -2349100[m] | -2511300 | 163.5 |
| Greenalite | $Fe^{+2}{}_3Si_2O_5(OH)_4$ | -716530 | -787810 | 72.6 |
| Minnesotaite | $Fe^{+2}{}_3Si_4O_{10}(OH)_2$ | -1070060 | -1153380 | 83.5 |
| Mg-Cronstedtite | $(Mg_2Fe^{+3})(Fe^{+3}Si)O_5(OH)_4$ | -789000[n] | -865180 | 60.8[o] |
| Hisingerite | $Fe^{+3}{}_2Si_2O_5(OH)_4$ | -703430[n] | -777330 | 57.3[o] |

a. cal mol$^{-1}$. b. cal mol$^{-1}$ K$^{-1}$. c. cm$^3$ mol$^{-1}$. d. cal mol$^{-1}$ K$^{-2}$. e. cal K mol$^{-1}$. f. unless otherwise noted, data taken from Wolery and Jove-Colon (2004). g. calculated using the $\Delta_f G°$ and S° data in the table along with the entropy of the elements from Wagman and others (1982). h. unless otherwise noted, data taken from Helgeson and others (1978). i. Sverjensky and Molling (1992) using data from Baes and Mesmer (1976). j. Wagman and others (1982). k. Wolery and Jove-Colon (2004) using data from Weast and Lide (1989). l. McCollom and Bach (2009). m. Sverjensky (1985). n. Calculated using methods consistent with Wolery and Jove-Colon (2004). o. Calculated using methods consistent with Helgeson and others (1978) using reactions $(Mg_2Fe^{+3})(Fe^{+3}Si)O_5(OH)_{4(\text{Mg-Cronstedtite})} + Al_2O_3 \leftrightarrow (Mg_2Al)(AlSi)O_5(OH)_{4(\text{Amesite})} + Fe_2O_3$ and $Fe^{+3}{}_2Si_2O_5(OH)_{4(\text{Hisingerite})} + Al_2O_3 \leftrightarrow Al_2Si_2O_5(OH)_{4(\text{Kaolinite})} + Fe_2O_3$ to calculate properties for Mg-Cronstedtite and Hisingerite, respectively.

Table A2. (cont'd)

| | | | Maier-Kelley Coefficients | | |
|---|---|---|---|---|---|
| Mineral | $V^{\circ c,h}$ | $C_p^{\circ b,h}$ | $a^{b,h}$ | $b$ ´ $10^{3d,h}$ | $c$ ´ $10^{-5e,h}$ |
| Ferrous Hydroxide | 26[k] | 21.3[l] | 26.06[l] | 4.35[l] | -5.38[l] |
| Ferrotremolite | 283 | 169.2 | 197.93 | 58.95 | -41.17 |
| Greenalite | 115 | 74.1 | 81.65 | 32.60 | -15.39 |
| Minnesotaite | 148 | 88.5 | 88.31 | 42.61 | -11.15 |
| Mg-Cronstedtite | 108[o] | 71.8[o] | 77.03[o] | 40.52[o] | -15.40[o] |
| Hisingerite | 105[o] | 63.4[o] | 68.77[o] | 44.98[o] | -16.69[o] |

# APPENDIX B

# SUPPLEMENTARY FILES TO CHAPTER 3

## B.1. Computational Model

### *B.1.1. Model Setup*

Reactions that drive the transformation of rainwater to fluids that are reduced and hyperalkaline occur as it progressively reactswith ultramafic rocks, which can be tracked using reaction path calculations. These calculations simulate reactions of minerals with a fluid and determine the compositions of coexisting solid phases and fluid constituents attained at thermodynamic equilibrium at various extents of the overall reaction progress. Progress of the alteration process is related to an increase in the rock-to-water ratio, simulating a given mass of fluid reacting with more rock as it infiltrates deeper into the subsurface. Following Cipolli et al. (2003) and Paukert et al. (2012), the model starts as a system *open* to atmospheric exchange and then transitions into a system *closed* to input from the atmosphere, simulating fluid pathways infiltrating deeper into the aquifer. Simulations were run with a fluid-centered, flow-through physical system that tracks compositions as fluid reacts with rock. For the composition of the starting fluid, a global average rainwater composition compiled by Hao et al. (2017) from Berner and Berner (2012) was used. Reacting rocks have starting compositions typical of harzburgites common in the Oman ophiolite (Hanhoj et al., 2010) and are composed mostly of olivine (>60 mol%) with some orthopyroxene (< 40 mol%) and minor amounts of clinopyroxene (< 5 mol%). In the initial models, inputs from primary minerals are controlled by relative dissolution rates. Calculations were then performed where experimentally-derived dissolution rates of the primary minerals are used to assess timescales needed to reach various stages of the overall serpentinization progress.

Aside from reaction paths, dissolved concentration of solutes at a given pH in equilibrium with various serpentinization-relevant minerals (brucite, magnesite, calcite, serpentine, etc.) was calculated. Dissolved Mg concentrations in equilibrium with brucite at a given pH was determined. Predicted Mg concentrations constrained by the solubility of magnesite were also calculated. DIC levels in equilibrium with magnesite at given pH and calculated Mg values were determined using charge balance. Similar calculations were performed to determine the dissolved Ca and DIC concentrations of a fluid in equilibrium with calcite. Dissolved Si concentrations in equilibrium with serpentine (chrysotile) was determined using calculated Mg values in equilibrium with magnesite at pH <10 and brucite at pH >10.

The solubility-reaction path program EQ3/6 (Wolery and Jarek, 2003) with a customized thermodynamic database was used for these calculations. Thermodynamic data used in the calculations were calculated with the SUPCRT code (Johnson et al., 1992) using standard state thermodynamic data for aqueous species taken from Shock and Helgeson (1988), Shock et al. (1989, 1992, 1997), and Sverjensky et al. (1997), together with the revised Helgeson-Kirkham-Flowers equations of state (Shock et al., 1992). Data for minerals were mostly taken from Helgeson et al. (1978) and Wolery and Jove-Colon (2004) with the addition of estimated standard Gibbs energies of formation of Fe end-members of several serpentinization-relevant Mg- and Fe-bearing minerals. Data for these minerals were added, while maintaining internal thermodynamic consistency, to explore solid solution behavior during serpentinization. These data, including discussion of data sources, can be found in Leong and Shock (2020), which includes a wider range of model results that encompass the effects of variable temperatures (0-100°C), compositions of reacting ultramafic rocks, fluid salinity, and buffering capacities of serpentinization-relevant minerals.

### *B.1.2. Model Results: Stages of the Serpentinization Reaction Progress*

Results of calculations simulating the serpentinization of an ultramafic rock of the composition 85% olivine (Forsterite$_{90}$, $Mg_{1.8}Fe_{0.2}SiO_4$), 14% orthopyroxene (Enstatite$_{90}$, $Mg_{0.9}Fe_{0.1}SiO_3$), and 1% clinopyroxene (Diopside$_{95}$, $CaMg_{0.95}Fe_{0.05}Si_2O_6$) at ambient conditions (25°C, 1 bar) are shown in Figure B3. Results of simulations with other olivine-rich compositions yield similar trends as demonstrated by Leong and Shock (2020). Consequences of variable temperatures (0-100°C) and increasing pyroxene abundance on the compositions of the coexisting fluid and solid precipitates are also described in detail in the same study. The calculated increase in pH with reaction progress is shown in Figure B3a, and changes with increasing pH in the total concentrations of Ca, Mg, Si, Fe, and dissolved inorganic carbon (DIC), as well as the number of moles of secondary minerals produced or consumed, are depicted in Figures B3b and B3c, respectively. Calculated reaction paths are depicted in activity diagrams that show the stabilities of minerals relative to the activities of aqueous solutes in the $MgO\text{-}SiO_2\text{-}H_2O$ (Figure B3d) and $CaO\text{-}MgO\text{-}SiO_2\text{-}H_2O$ (Figure B3e) systems.

The predicted reaction path shown in Figure B3 can be divided into six general stages as indicated by the circled numbers that depict the starting points of these various stages. These stages are discussed in detail by Leong and Shock (2020) and summarized below where the phrases in italics encapsulate each stage.

(1) The *dissolution of primary minerals into rainwater* begins when rainwater reacts with ultramafic rocks that are formed in the Earth’s mantle. When transported to the surface through

tectonic events, ultramafic rocks are unstable and are readily altered in the presence of aqueous fluids. Rain is slightly acidic and contains protons derived from atmospheric $CO_{2(g)}$ via

$$\mathrm{CO_{2(g)} + H_2O \Leftrightarrow HCO_3{}^- + H^+} \tag{B1}$$

which drive the dissolution of primary minerals present in ultramafic rocks through hydrolysis reactions. Consumption of protons during mineral hydrolysis increases pH as illustrated in Figure B3a. Dissolution of minerals yields solutes to the fluid, driving an increase in the total Mg, Si, and Ca concentrations, as depicted in Figure B3b. The fluid pathway is open to atmospheric exchange and consequently, reaction B1 dictates that the DIC must increase with pH to maintain equilibrium with a constant atmospheric $fCO_{2(g)}$ of ~$10^{-3.5}$. The increase in DIC during this stage is depicted in Figure B3b. As shown in Figure B3c, no minerals except for an oxyhydroxide (goethite) precipitate at this stage. Also shown in the activity diagrams depicted in Figures B3d and B3e, the increase in pH and total Mg, Si, and Ca will drive the reaction path towards higher $a\mathrm{Mg}^{+2}/(a\mathrm{H}^+)^2$ and $a\mathrm{Ca}^{+2}/(a\mathrm{H}^+)^2$ (activity ratios) as well as higher $a\mathrm{SiO}_{2(aq)}$ (silica activity). This stage marks the transition from a slightly acidic and dilute rainwater to a circumneutral (pH 7-8) fluid enriched in $Mg^{+2}$ and $HCO_3^-$.

(2) The *onset of serpentinization* occurs as the solution is concentrated enough to precipitate serpentine, as represented by the mineral chrysotile. Quartz and talc can also be saturated at this stage, but the formation of these minerals was suppressed in the model to evaluate the maximum silica activity and total Si concentration attained when serpentine saturation is achieved, which occurs when the reaction path reaches the chrysotile saturation line as shown in Figure B3d. The precipitation of chrysotile from solutes, as depicted by the reaction

$$\mathrm{3Mg^{+2} + 2SiO_{2(aq)} + 5H_2O \rightarrow Mg_3Si_2O_5(OH)_{4(chrysotile)} + 6H^+}, \tag{B2}$$

consumes Si and causes a decrease in its concentration as depicted in Figure B3b. Precipitation of chrysotile also causes the reaction path depicted in Figure B3d to shift to lower silica activity along the chrysotile saturation line. Despite the consumption of Mg through reaction (B2), continuing dissolution of olivine-dominated rocks results in a surplus of Mg with respect to Si consumed during serpentinization as depicted by

$$2\mathrm{Mg_2SiO_{4(forsterite)}} + 2\mathrm{H^+} + \mathrm{H_2O} \rightarrow \mathrm{Mg_3Si_2O_5(OH)_{4(chrysotile)}} + \mathrm{Mg^{+2}}, \quad \text{(B3)}$$

leading to further increases in aqueous Mg at this stage. The pH continues to increase despite the release of protons during serpentine formation (reaction 2), as it is not enough to counter their consumption during the dissolution of primary minerals as exemplified by reaction (B3). Nevertheless, in addition to reaction (B1), the release of protons through precipitation reactions (e.g., reaction 2) can further drive dissolution and thus overall reaction progress.

(3) As fluids infiltrate deeper into the subsurface, a *transition from an open to a closed system* occurs. As shown in Figure B3a, a sharp increase in pH occurs without the atmosphere supplying protons via reaction (B1). The increase in pH, as well as the increasing concentrations of Mg and Ca, will result in the *precipitation of carbonates*. As shown in Figure B3c, the first carbonate to precipitate is dolomite followed by magnesite, the latter forming more abundantly than the former. As shown in Figure B3b, the precipitation of these Mg- and Ca-bearing carbonates drives a decrease in the DIC and the total Ca and Mg concentrations.

(4) *Brucite saturation* is attained once the pH is high enough (pH ~ 10). As shown in Figure B3d, brucite precipitation occurs at extremely low $a\mathrm{SiO_{2(aq)}}$ where the trend of decreasing $a\mathrm{SiO_{2(aq)}}$, observed since the onset of serpentinization at Stage 2, stops at the intersection of the brucite and chrysotile saturation lines. In Figure B3e, this corresponds to where the reaction path encounters the boundary between the chrysotile and brucite stability fields. From this point onward in overall reaction progress, the $a\mathrm{SiO_{2(aq)}}$ of the solution will be fixed by an equilibrium assemblage of chrysotile and brucite (Ctl-Brc) depicted by the reaction

$$3\mathrm{Mg(OH)_{2(brucite)}} + 2\mathrm{SiO_{2(aq)}} \Leftrightarrow \mathrm{Mg_3Si_2O_5(OH)_{4(chrysotile)}} + \mathrm{H_2O}. \quad \text{(B4)}$$

Despite the $a\mathrm{SiO}_{2(aq)}$ being fixed by reaction (B4), the speciation of Si allows for an increase in total dissolved Si, as depicted in Figure B3b, because the abundance of $\mathrm{HSiO_3^-}$, and consequently the total Si concentration, increases with increasing pH to maintain equilibrium with the reaction

$$\mathrm{SiO_{2(aq)} + H_2O \Leftrightarrow HSiO_3{}^- + H^+}. \quad \text{(B5)}$$

The precipitation of brucite causes an abrupt decrease in the total Mg concentration, as depicted in Figure B3b. Together with deceasing DIC, decrease in Mg causes magnesite and eventually, dolomite to stop precipitating as shown in Figure B3c. On the other hand, the total Ca concentration increases as more Ca is released into the fluid from the dissolution of clinopyroxene relative to its uptake through the precipitation of dolomite. This stage marks the transition from a fluid enriched in Mg and DIC to an increasingly alkaline and Ca-rich solution.

(5) In addition to becoming more alkaline, *fluids become more reduced* as $H_2$ is generated from the oxidation of ferrous iron from the primary minerals to ferric iron in secondary minerals coupled with the reduction of water to $H_2$ as depicted by the generalized reaction

$$\mathrm{2Fe(II)O_{(primary\ minerals)} + H_2O \rightarrow Fe(III)_2O_{3(secondary\ minerals)} + H_{2(aq)}}. \quad \text{(B6)}$$

At these reduced conditions, the main iron-hosting secondary mineral transitions from goethite to magnetite (Figure B3c). The results shown in Figure B3 are from a calculation without considering the incorporation of Fe into solid solutions of serpentine and brucite. If allowed, formation of magnetite is less favored, and most of the iron is incorporated into ferrous and ferric iron-bearing serpentine and ferrous iron-bearing brucite (see McCollom and Bach, 2009; Klein et al., 2009; 2013; 2014; Leong and Shock, 2020). Formation of methane is also favored at these reduced conditions. When not kinetically inhibited, the formation of methane will drive DIC to extremely low concentrations ($< 10^{-12}$ molal). If abiogenic methane formation is kinetically inhibited, as it is likely to be at low-temperature conditions (Shock, 1992; McCollom, 2016;

Wang et al., 2018) or in gas-poor systems (McCollom, 2016; Etiope and Whiticar, 2019), DIC can persist in solution at low but detectable concentrations (~10 μmolal) as depicted in Figure B3b. Increasing pH and Ca concentration will saturate calcite (Figure B3c). As the DIC concentration is minimal at this stage of the reaction progress, the amount of precipitating calcite will not be enough to counter the increasing Ca concentration brought about by the increasing amount of clinopyroxene dissolved. With increasing pH and total Ca concentration, the reaction path depicted in Figure B3e follows an increasing trajectory in $a\text{Ca}^{+2}/(a\text{H}^{+})^2$ along the boundary between the chrysotile and brucite stability fields until it reaches equilibrium with diopside.

(6) *Chrysotile-Brucite-Diopside (Ctl-Brc-Di) equilibrium* is attained when the reaction path depicted in Figure B3e reaches the point where the stability fields of chrysotile, brucite and diopside meet. So far, since the beginning of Stage 1, release of protons through precipitation reactions is not enough to counter its consumption through dissolution reactions, hence pH continues to increase. Throughout the overall reaction progress, releases of Mg and Si through the dissolution of primary minerals are mostly incorporated into precipitating serpentine, brucite, magnesite, and dolomite. On the other hand, especially during the latter stages of overall reaction progress, dissolved Ca will continue to accumulate in the fluid despite its incorporation into dolomite and calcite owing to the very low amount of DIC remaining in solution. The release of $\text{Ca}^{+2}$ into the solution from the dissolution of diopside is accommodated by the loss of $\text{H}^{+}$ (or depending on how the precipitation and dissolution reactions are written, release of $\text{OH}^{-}$) and causes the continuous increase in pH. The increasing pH trend stops when the fluid reaches equilibrium with diopside, as shown by point 6 in the activity diagram depicted in Figure B3e. At this point, diopside dissolution is no longer favorable. Moreover, the equilibrium assemblage of chrysotile, brucite and diopside (Ctl-Brc-Di), depicted by the reaction

$$\mathrm{CaMgSi_2O_{6(diopside)}} + 2\mathrm{Mg(OH)_{2(brucite)}} + 2\mathrm{H^+} \Leftrightarrow \mathrm{Ca^{+2}} + \mathrm{Mg_3Si_2O_5(OH)_{4(chrysotile)}} + \mathrm{H_2O}, \qquad \text{(B7)}$$

corresponds to an invariant point in the $CaO$-$MgO$-$SiO_2$-$H_2O$ system. Thus, not only the pH (Figure B3a) but also the Ca, Mg, and Si concentrations (Figure B3b) will remain unchanged despite continuing reaction progress, until diopside is completely reacted. As Ctl-Brc equilibrium (Stage 4, Figure B3d) ensures that the fluids stay undersaturated or out of equilibrium with forsterite (olivine) and enstatite (orthopyroxene) at low temperatures, fluids attaining equilibrium with diopside (clinopyroxene) are as close as possible to being in equilibrium with ultramafic rocks, and thus define the final stage, Stage 6, of overall serpentinization progress. Reaction (B7) also constrains the maximum pH allowed in serpentinizing environments (~12.2 at 25°C and 1 bar), explaining why extremely alkaline environments (pH >13) are rare in ultramafic environments (Leong & Shock, 2020).

Trends depicted in Figure B3 apply for reaction with olivine-rich lithologies. Greater contributions from orthopyroxene will generate fluids that first equilibrate with chrysotile and diopside before attaining brucite saturation. In the activity diagram depicted in Figure B3e, these reaction paths will track along the chrysotile-diopside boundary before reaching the Ctl-Brc-Di invariant point. Eventually, significant contributions from orthopyroxene (50-60 mole %) will yield fluids that end up at the chrysotile-tremolite-diopside (Ctl-Tr-Di) invariant point. Even greater (>60% mole %) orthopyroxene contribution will yield fluids in equilibrium with chrysotile-talc-tremolite (Ctl-Tlc-Tr). The latter two equilibrium assemblages imply higher $a\mathrm{SiO_{2(aq)}}$ and lower $a\mathrm{Ca^{+2}}/(a\mathrm{H^+})^2$ activity ratios compared to Ctl-Brc-Di equilibrium, as depicted in Figure

B3e, generating more Si-rich and less alkaline fluids. Dissolution of secondary minerals such as serpentine and brucite and relict clinopyroxene in partially serpentinized ultramafic rocks can also lead to Ctl-Brc-Di equilibrium, especially if brucite is still abundant. Lower amounts of reacting brucite can lead to reaction paths ending at the Ctl-Tr-Di or the Ctl-Tlc-Tr equilibrium points as in orthopyroxene-rich settings. Further details on the consequences of variable compositions of the reacting rocks on the compositions of fluids generated during low temperature and high temperature alteration of ultramafic rocks can be found in Leong and Shock (2020) and Klein et al. (2013), respectively.

### B.2. Differences in the Compositions of Ultramafic- and Gabbro-hosted Fluids

Most simulations of gabbro alteration are focused at high temperature and pressure conditions such as those occurring in submarine hydrothermal systems (McCollom and Shock, 1998; Palandri and Reed, 2004; Bach and Klein, 2009; Bach and others, 2013, Seyfried and others, 2015). Predictions of fluid compositions arising during interactions between meteoric water and gabbroic rocks in the continental subsurface are far more scarce. Gabbroic rocks comprise approximately a third of the surface exposures of the Samail ophiolite (Nicolas et al., 2000) and are also common in many other ophiolites. Gabbro-hosted hyperalkaline fluids are also documented in several studies (Neal and Stanger, 1985; Dewandel et al., 2005; Paukert et al., 2012; Chavagnac et al., 2013b; Cardace et al., 2013; Rempfert et al., 2017), and many of these springs occur near the gabbro-ultramafic contact. The influence of ultramafic rocks underlying the gabbroic rocks on the compositions of hyperalkaline fluids seeping out from gabbroic outcrops is largely unknown.

Reported compositions of gabbro-hosted fluids in the Samail ophiolite, together with those from this work, are plotted as orange symbols in Figure B4, where they can be compared with fluids documented in ultramafic environments (grey symbols). Compositions of most gabbro-hosted fluids overlap those hosted in ultramafic rocks. However, there are some notable differences that could be attributed to fluid-mineral reactions enabled when fluids encounter gabbroic rocks. Mineral solubility calculations were conducted to provide preliminary insights into how various minerals or mineral assemblages can account for these aqueous trends. Solubility calculations for 25°C and 1 bar were conducted using the same software package and thermodynamic data expounded upon in the method section of this paper. Results of calculations are plotted as red curves in Figure B4.

Gabbro- and ultramafic-hosted Type 1 fluids (circumneutral, pH 7-9) have overlapping total dissolved Si values as shown in Fig B1a. In contrast, some of the highest dissolved Si values measured in Type 2 fluids (hyperalkaline, pH >11) are from gabbro-hosted fluids. This could be attributed to the higher silica content of gabbros, which can lead to the precipitation of secondary minerals with higher silica contents than serpentine and brucite such as talc, quartz, chlorite, zeolites and clay minerals. As shown in Figure B4a, all fluids hosted in either gabbroic or ultramafic rocks are below amorphous silica saturation. Type 1 fluids hosted in both lithologies are typically above quartz saturation while Type 2 fluids are usually well below saturation with respect to quartz and the chrysotile-talc equilibrium assemblage. Type 2 fluids hosted in ultramafic rocks approach equilibrium with serpentine and brucite. In contrast, despite overlapping with fluids hosted in ultramafic rocks as shown in Figure B4a, the Si concentrations of gabbro-hosted fluids do not approach the low values dictated by chrysotile-brucite equilibrium. This trend is likely to be attributed to the geological setting of gabbro-hosted hyperalkaline springs, many of which occur near the gabbro-ultramafic lithological contact. As gabbros are stratigraphically above peridotites in the Samail ophiolite, it is likely that deep-seated fluids would have first reacted with ultramafic rocks before encountering gabbroic rocks on their way to discharge at the surface. Such a scenario is analogous to ultramafic to gabbro mass transfer processes at high temperatures that have been proposed to facilitate the formation of rodingites (Bach and Klein, 2009; Bach et al., 2013).

As shown in Figure B4b, there are no noticeable differences in the Mg concentrations of Type 1 fluids hosted in either ultramafic or gabbroic rocks. As in the case of ultramafic-hosted fluids, Mg concentrations of Type 1 gabbro-hosted fluids rarely fall below values dictated by magnesite solubility. On the other hand, there are some noticeable differences between the Mg concentrations of Type 2 hyperalkaline fluids in these two lithological environments. Some of the most Mg-depleted Type 2 fluids were sampled from gabbroic-hosted springs. Unlike most ultramafic-hosted samples, some gabbro-hosted samples have Mg values below those set by brucite solubility. These lower Mg concentrations could be attributed to the precipitation of relatively Si-rich Mg-silicate minerals (e.g., talc, saponite, chlorite) that commonly occur in altered mafic rocks. As an example, as depicted in Figure B4b, lower Mg concentrations can be attained if fluids are in equilibrium with chrysotile and talc. As with Si, more constraints can be provided on the Mg concentrations of fluids dictated by the solubility of aluminum-bearing silicates such as chlorite, zeolite and clay minerals that are commonly observed in gabbroic rocks altered at low temperatures (Bach et al., 2001).

Dissolved Ca concentrations of Type 2 fluids from both gabbro and ultramafic bodies have similar trends that follow the solubility of calcite as shown in Figures 3.5c and C4c. However, total calcium concentrations in Type 1 fluids are somewhat more enriched in gabbro-hosted fluids than ultramafic-hosted fluids. Type 1 fluids, as discussed in the main text of this work, are products of early stages of reaction progress dictated by the dissolution of protolith minerals. Gabbroic rocks are more enriched in Ca compared to ultramafic rocks due to the more abundant presence of Ca-plagioclase (anorthite) and Ca-clinopyroxene (diopside).

Like Ca, dissolved Na concentrations of Type 1 fluids hosted in gabbros are elevated compared to those hosted in ultramafic rocks as shown in Figure B4d. This could be attributed to the relatively elevated Na content of gabbroic rocks. However, similar observations can also be made for the dissolved Cl values of gabbro-hosted fluids plotted in Figure B4e, suggesting that leaching from salt minerals could be an alternative source for both Na and Cl. Figure B4f, however, shows no apparent differences between K trends of both gabbro- and ultramafic-hosted fluids, suggesting that leaching could be attributed only to halite (NaCl). In addition, leaching from other Na-bearing phases (*e.g.*, plagioclase and pyroxenes) can also occur concomitantly, as gabbro-hosted Type 1 fluids are typically more enriched in Na relative to Cl compared to Type 1 fluids hosted in ultramafic rocks as shown in Figure B4g.

As shown in Figure B4h, the total dissolved aluminum concentrations of Type 1 gabbro-hosted fluids overlap with those hosted in ultramafic rocks, but gabbro-hosted

Type 2 fluids have elevated total dissolved Al values, closely following those dictated by the solubility of gibbsite, as shown in Figure B4h. In contrast, all ultramafic-hosted Type 2 fluids remain highly undersaturated with respect to gibbsite, which is not surprising as ultramafic rocks are typically depleted in Al. Chavagnac and others (2013b) documented Al-bearing layered doubled hydroxides such as hydrotalcite and indigirite in gabbro-hosted hyperalkaline pools marked by elevated dissolved Al content.

Further insight into the underlying mineral controls on the compositions of gabbro-hosted fluids, in comparison to those hosted in ultramafic rocks, can be revealed through mineral activity diagrams. Activities of several aqueous species ($SiO_{2(aq)}$, $Ca^{+2}$, $H^+$) were evaluated from the measured values using the same thermodynamic database as all other calculations in this study and are plotted in an activity diagram for the $CaO$-$Al_2O_3$-$SiO_2$-$H_2O$ (phase boundaries as orange lines, balanced on $Al_2O_3$) and $CaO$-$MgO$-$SiO_2$-$H_2O$ system (black lines, balanced on MgO) systems shown in Figure B5. Calculated activities ($a\mathrm{Ca}^{+2}/(a\mathrm{H}^+)^2$, $a\mathrm{SiO}_2$) of gabbro- (orange symbols) and ultramafic-hosted (grey symbols, values similar to Figure 3.5f) fluids are overlain in the activity diagram. Gabbro-hosted hyperalkaline fluids typically have similar calcium to hydrogen activity ratios ($a\mathrm{Ca}^{+2}/(a\mathrm{H}^+)^2$) as those hosted in ultramafic bodies but are characterized by having somewhat higher silica activities ($a\mathrm{SiO}_2$). As shown in Figure B5, these gabbro-hosted fluids seem to be drawn to equilibrium with gibbsite, grossular (garnet), prehnite, and gismondine (zeolite), unlike ultramafic-hosted fluids that approach equilibrium with chrysotile and brucite resulting in lower $a\mathrm{SiO}_2$. Similarly, Type 1 fluids hosted in gabbroic rocks mostly have overlapping $a\mathrm{Ca}^{+2}/(a\mathrm{H}^+)^2$ with those hosted in ultramafic rocks but tend to have higher $a\mathrm{SiO}_2$. These gabbro-hosted fluids are within the stability field of scolecite and beidellite, which are minerals that belong to the zeolite and smectite groups, respectively. In addition to ultramafic rocks, the Oman Drilling Project (Kelemen et al., 2013) has recovered gabbroic rocks. Examination of low-temperature secondary phases from recovered cores would provide constraints on which minerals dictate the evolution of fluids during fluid-gabbro interactions. Thermodynamic simulations of low-temperature fluid-gabbro interactions and eventually testing these models with more comprehensive and in-depth investigations of gabbro-hosted fluids will bridge our current knowledge gap in this poorly explored fluid-rock system. Gabbros are the most common rocks that comprise the oceanic crust and are also common in ophiolites. Results of this future work can potentially inform future biogeochemical studies on the likelihood of these vast lithological systems to host habitable environments.

## B.3. Supplementary Tables

Table B1

*Saturation States of Various Relevant Minerals*

| Sample Number | Site | pH | T (°C) | Fo | En | Di | Brc | Ctl | Tlc | Am | Qz | Cal | Arg | Dol | Mgs | Anh |
|---|---|---|---|---|---|---|---|---|---|---|---|---|---|---|---|---|
| ***Fluids with pH between 7 to 9*** | | | | | | | | | | | | | | | | |
| 100112AI | Al Bana | 8.5 | 29 | -3.0 | -0.8 | -0.6 | -2.0 | 4.1 | 6.5 | -1.1 | 0.2 | 0.5 | 0.3 | 2.8 | 0.7 | -2.8 |
| 140110B | Dima | 8.4 | 23.5 | -3.9 | -1.2 | -1.3 | -2.5 | 3.0 | 5.5 | -1.0 | 0.3 | 0.5 | 0.4 | 2.8 | 0.7 | -2.9 |
| 090118P | Dima | 8.8 | 20.2 | -2.7 | -0.6 | -0.2 | -1.8 | 5.0 | 7.5 | -1.1 | 0.3 | 0.8 | 0.6 | 3.4 | 1.0 | -3.1 |
| 140114S | Falaij | 7.7 | 21 | -7.2 | -2.8 | -4.4 | -4.2 | -1.8 | 1.0 | -0.9 | 0.4 | -0.1 | -0.3 | 1.5 | -0.1 | -2.8 |
| 100107C | Masibt | 9.3 | 25.4 | -0.5 | 0.5 | 2.0 | -0.7 | 8.0 | 10.5 | -1.0 | 0.2 | 0.9 | 0.7 | 3.6 | 1.1 | -2.8 |
| 100107D | Masibt | 8.6 | 25.6 | -3.1 | -0.7 | 0.0 | -2.2 | 4.3 | 7.2 | -0.8 | 0.5 | 0.8 | 0.7 | 3.1 | 0.7 | -2.3 |
| 090120W | Masibt | 8.7 | 24.2 | -2.7 | -0.5 | 0.4 | -2.0 | 4.9 | 8.0 | -0.7 | 0.6 | 0.8 | 0.7 | 3.2 | 0.7 | -2.4 |
| 140111G | Qafifah | 8.9 | 22.6 | -1.8 | -0.1 | 0.7 | -1.5 | 6.3 | 9.1 | -0.9 | 0.4 | 0.9 | 0.7 | 3.8 | 1.2 | -3.1 |
| 120114O | Qafifah | 8.7 | 23 | -3.3 | -1.0 | -0.9 | -2.1 | 3.9 | 6.2 | -1.2 | 0.2 | 0.5 | 0.3 | 2.8 | 0.7 | -3.1 |
| 100109X | Qafifah | 8.9 | 23.3 | -1.7 | 0.0 | 0.9 | -1.4 | 6.4 | 9.3 | -0.9 | 0.4 | 1.0 | 0.8 | 3.9 | 1.3 | -3.0 |
| 090119S | Qafifah | 9.0 | 21.6 | -2.5 | -0.6 | -0.4 | -1.6 | 5.1 | 7.2 | -1.3 | 0.0 | 0.4 | 0.2 | 2.8 | 0.8 | -3.4 |
| 090119T | Qafifah | 8.6 | 24.8 | -3.2 | -0.8 | -0.7 | -2.1 | 4.1 | 6.8 | -0.9 | 0.4 | 0.3 | 0.2 | 2.7 | 0.7 | -3.1 |
| 140116B | Shumayt | 7.9 | 26.5 | -5.1 | -1.7 | -2.5 | -3.2 | 1.2 | 4.1 | -0.8 | 0.5 | 0.3 | 0.1 | 2.4 | 0.5 | -2.6 |
| 140116C | Shumayt | 8.7 | 27.3 | -1.9 | -0.2 | 0.6 | -1.5 | 5.8 | 8.5 | -0.9 | 0.4 | 1.0 | 0.9 | 3.9 | 1.3 | -2.6 |
| 120116Q | Shumayt | 7.7 | 25 | -6.2 | -2.3 | -3.6 | -3.7 | -0.4 | 2.6 | -0.8 | 0.5 | -0.1 | -0.2 | 1.8 | 0.3 | -2.6 |
| 100113AP | Shumayt | 7.9 | 27 | -5.1 | -1.7 | -2.5 | -3.2 | 1.1 | 4.0 | -0.8 | 0.4 | 0.3 | 0.1 | 2.4 | 0.5 | -2.5 |
| 090123E | Shumayt | 8.2 | 23.9 | -4.2 | -1.3 | -1.5 | -2.7 | 2.6 | 5.6 | -0.8 | 0.5 | 0.5 | 0.3 | 2.8 | 0.7 | -2.6 |
| 100114AR | Sudari | 8.8 | 21.5 | -3.5 | -1.2 | -1.2 | -2.1 | 3.5 | 5.4 | -1.4 | -0.1 | 0.7 | 0.5 | 3.1 | 0.7 | -2.8 |
| 090122B | Sudari | 8.8 | 17.1 | -3.9 | -1.3 | -1.9 | -2.3 | 3.2 | 5.4 | -1.3 | 0.1 | 0.0 | -0.1 | 2.4 | 0.7 | -3.4 |
| 100115AW | Uqaybah | 8.5 | 17.5 | -6.7 | -2.9 | -3.2 | -3.5 | -1.1 | 0.2 | -1.7 | -0.3 | n.c. | n.c. | n.c. | n.c. | -2.8 |
| ***Fluids with pH between 9 and 11*** | | | | | | | | | | | | | | | | |
| 140110D | Dima | 10.4 | 21.8 | 1.6 | 0.9 | 3.4 | 0.9 | 10.8 | 10.9 | -2.3 | -0.9 | 1.2 | 1.1 | 3.9 | 1.0 | -3.3 |
| 140112L | Dima | 9.8 | 21.3 | 0.0 | 0.5 | 2.0 | -0.2 | 8.7 | 10.0 | -1.6 | -0.3 | 1.1 | 1.0 | 4.0 | 1.3 | -3.3 |
| 090118N | Dima | 9.7 | 17.5 | -1.1 | -0.1 | 0.9 | -0.7 | 7.2 | 8.4 | -1.7 | -0.4 | 1.0 | 0.8 | 3.8 | 1.2 | -3.6 |
| 100107E | Masibt | 10.1 | 26.9 | 1.9 | 1.3 | 3.4 | 0.8 | 11.2 | 12.2 | -1.8 | -0.5 | 0.6 | 0.5 | 3.3 | 1.1 | -3.3 |
| 090120X | Masibt | 10.6 | 27.7 | 3.3 | 1.8 | 5.3 | 1.8 | 13.1 | 13.0 | -2.3 | -1.0 | 0.9 | 0.7 | 2.8 | 0.4 | -2.5 |
| 140111H | Qafifah | 10.2 | 20.2 | 1.4 | 1.1 | 3.1 | 0.6 | 10.8 | 11.7 | -1.9 | -0.5 | 1.1 | 1.0 | 4.2 | 1.4 | -3.7 |
| 140111I | Qafifah | 10.9 | 18.8 | 2.8 | 1.4 | 4.1 | 1.7 | 12.5 | 11.9 | -2.6 | -1.3 | 1.2 | 1.1 | 4.0 | 1.1 | -3.5 |
| 120114N | Qafifah | 9.8 | 21.8 | 0.0 | 0.5 | 2.1 | -0.2 | 8.7 | 10.2 | -1.6 | -0.3 | 1.1 | 1.0 | 4.1 | 1.3 | -3.5 |
| 100109T | Qafifah | 9.6 | 23.7 | 0.5 | 0.8 | 1.6 | -0.1 | 9.4 | 11.5 | -1.3 | 0.0 | 0.3 | 0.2 | 3.6 | 1.7 | -4.2 |
| 100109W | Qafifah | 10.3 | 20.8 | 1.5 | 1.0 | 3.1 | 0.7 | 10.8 | 11.4 | -2.0 | -0.7 | 1.2 | 1.1 | 4.4 | 1.5 | -3.6 |
| 090117J | Qafifah | 10.6 | 18.8 | 1.9 | 1.1 | 2.4 | 1.1 | 11.3 | 11.3 | -2.3 | -1.0 | 0.5 | 0.3 | 3.6 | 1.4 | -4.4 |
| 140116D | Shumayt | 9.1 | 27.1 | -0.6 | 0.4 | 1.9 | -0.8 | 7.7 | 10.2 | -1.0 | 0.2 | 1.3 | 1.2 | 4.4 | 1.5 | -2.6 |
| 120116R | Shumayt | 10.6 | 25.8 | 2.7 | 1.3 | 3.6 | 1.6 | 12.1 | 11.5 | -2.6 | -1.3 | 0.9 | 0.8 | 3.7 | 1.2 | -3.5 |
| 100113AN | Shumayt | 10.2 | 28.6 | 2.4 | 1.5 | 4.7 | 1.2 | 11.8 | 12.4 | -2.0 | -0.7 | 1.9 | 1.8 | 5.0 | 1.4 | -2.3 |
| 100113AO | Shumayt | 10.4 | 27.4 | 2.9 | 1.6 | 4.3 | 1.5 | 12.4 | 12.5 | -2.2 | -0.9 | 1.4 | 1.3 | 4.6 | 1.5 | -3.0 |
| 090123G | Shumayt | 10.6 | 27.6 | 3.6 | 1.9 | 5.1 | 1.9 | 13.5 | 13.6 | -2.2 | -0.9 | 1.2 | 1.1 | 4.1 | 1.2 | -2.8 |
| 090122A | Sudari | 10.9 | 17.4 | 2.3 | 0.9 | 3.4 | 1.7 | 11.6 | 10.0 | -3.2 | -1.8 | 1.1 | 1.0 | 3.6 | 0.8 | -3.0 |
| 090122C | Sudari | 10.8 | 18.5 | 0.9 | 0.0 | 2.5 | 1.1 | 9.3 | 7.2 | -3.4 | -2.0 | 1.3 | 1.2 | 3.2 | 0.2 | -2.6 |
| ***Hyperalkaline Spring Fluids (pH > 11)*** | | | | | | | | | | | | | | | | |
| 140115X | Al Bana | 11.4 | 29.5 | -3.0 | -2.8 | -0.3 | 0.0 | 2.0 | -3.7 | -5.1 | -3.9 | 0.4 | 0.3 | -1.7 | -3.8 | -4.2 |
| 140115Y | Al Bana | 11.6 | 24.5 | -2.2 | -2.5 | 0.1 | 0.5 | 3.5 | -2.4 | -5.2 | -3.9 | 0.9 | 0.8 | -0.2 | -2.8 | -4.0 |
| 140115Z | Al Bana | 11.3 | 32.2 | -3.3 | -3.1 | -0.7 | 0.0 | 1.4 | -4.9 | -5.3 | -4.1 | 0.5 | 0.3 | -1.8 | -3.8 | -4.4 |

| | | | | | | | | | | | | | | | | |
|---|---|---|---|---|---|---|---|---|---|---|---|---|---|---|---|---|
| 120118Y | Al Bana | 11.5 | 32.5 | -1.8 | -2.3 | 0.5 | 0.6 | 3.7 | -2.2 | -5.1 | -3.9 | 1.0 | 0.9 | -0.2 | -2.8 | -4.5 |
| 120118Z | Al Bana | 11.4 | 30.6 | -2.5 | -2.5 | 0.1 | 0.2 | 2.9 | -2.6 | -4.9 | -3.7 | 1.0 | 0.8 | -0.4 | -2.9 | -4.2 |
| 120129G | Al Bana | 11.0 | 37.3 | -2.7 | -2.5 | 0.0 | 0.0 | 2.4 | -2.5 | -4.6 | -3.4 | 0.6 | 0.5 | -1.0 | -3.2 | -4.7 |
| 120129H | Al Bana | 11.4 | 38.2 | -2.0 | -2.3 | 0.6 | 0.5 | 3.3 | -2.4 | -5.0 | -3.8 | 0.6 | 0.4 | -1.4 | -3.5 | -4.8 |
| 100111AA | Al Bana | 11.7 | 28.5 | -3.1 | -3.0 | -0.5 | 0.2 | 1.8 | -4.6 | -5.5 | -4.2 | 0.5 | 0.4 | -1.8 | -3.9 | -4.4 |
| 100111AB | Al Bana | 11.7 | 25.4 | -2.1 | -2.5 | 0.2 | 0.6 | 3.4 | -2.7 | -5.4 | -4.1 | 1.0 | 0.8 | -0.4 | -3.0 | -4.1 |
| 100111AC | Al Bana | 11.6 | 16.5 | 2.4 | 0.6 | 3.3 | 2.1 | 11.4 | 8.5 | -3.8 | -2.5 | 1.1 | 1.0 | 3.2 | 0.3 | -3.8 |
| 100111AD | Al Bana | 11.6 | 32.4 | -3.4 | -3.5 | -1.3 | 0.3 | 0.8 | -6.8 | -6.0 | -4.8 | 0.6 | 0.4 | -1.7 | -3.9 | -4.5 |
| 100111AE | Al Bana | 11.9 | 18.9 | -1.3 | -1.9 | 1.0 | 0.8 | 5.1 | -0.1 | -4.9 | -3.6 | 0.5 | 0.4 | -0.7 | -2.9 | -4.3 |
| 100111AF | Al Bana | 11.9 | 24.2 | -1.2 | -2.1 | 0.8 | 1.1 | 4.8 | -1.6 | -5.5 | -4.2 | 0.9 | 0.7 | -0.3 | -2.8 | -4.3 |
| 100112AG | Al Bana | 11.1 | 37.7 | -2.7 | -2.7 | -0.4 | 0.2 | 2.2 | -3.7 | -5.1 | -3.9 | 0.6 | 0.4 | -1.2 | -3.3 | -4.7 |
| 100112AH | Al Bana | 11.2 | 38.4 | -3.1 | -3.0 | -0.6 | 0.0 | 1.4 | -4.5 | -5.1 | -3.9 | 0.6 | 0.5 | -1.3 | -3.5 | -4.8 |
| 090116F | Al Hilayw | 11.8 | 26.3 | -1.7 | -2.1 | 0.8 | 0.7 | 4.2 | -1.5 | -5.1 | -3.8 | 0.9 | 0.7 | -0.5 | -3.0 | -3.5 |
| 090116G | Al Hilayw | 11.8 | 27.1 | -2.0 | -2.4 | 0.1 | 0.6 | 3.6 | -2.3 | -5.2 | -4.0 | 2.0 | 1.8 | 2.0 | -1.6 | -4.1 |
| 090116H | Al Hilayw | 11.5 | 24.5 | -1.6 | -1.6 | 1.2 | 0.2 | 4.9 | 1.4 | -4.0 | -2.7 | 1.1 | 0.9 | 0.7 | -2.0 | -4.1 |
| 090116I | Al Hilayw | 11.9 | 20.7 | -1.9 | -2.0 | 1.4 | 0.4 | 4.4 | -0.2 | -4.6 | -3.3 | 1.0 | 0.8 | -0.4 | -3.0 | -3.6 |
| 100121BB | Al Khoud | 10.9 | 39 | -5.0 | -3.2 | 0.0 | -1.6 | -0.7 | -4.0 | -3.8 | -2.6 | n.c. | n.c. | n.c. | n.c. | -1.9 |
| 140110C | Dima | 11.4 | 27 | -1.9 | -2.1 | 0.8 | 0.4 | 4.0 | -0.9 | -4.7 | -3.4 | 0.7 | 0.5 | -0.8 | -3.1 | -3.8 |
| 140112K | Dima | 11.4 | 26.9 | -1.5 | -1.9 | 0.9 | 0.6 | 4.6 | -0.3 | -4.7 | -3.5 | 0.5 | 0.4 | -0.9 | -3.0 | -3.6 |
| 140112M | Dima | 11.4 | 28.2 | -2.3 | -2.2 | 0.8 | 0.1 | 3.4 | -1.3 | -4.6 | -3.3 | 0.7 | 0.5 | -1.1 | -3.4 | -3.8 |
| 090118O | Dima | 11.5 | 30.3 | -0.6 | -1.3 | 1.9 | 0.9 | 5.9 | 1.4 | -4.5 | -3.2 | 0.9 | 0.8 | 0.1 | -2.4 | -4.2 |
| 140113O | Falaij | 11.4 | 28.4 | -2.0 | -2.2 | 0.7 | 0.4 | 3.8 | -1.4 | -4.9 | -3.6 | 0.7 | 0.6 | -0.8 | -3.1 | -4.2 |
| 140113P | Falaij | 11.5 | 25.9 | -2.2 | -2.4 | 0.2 | 0.5 | 3.4 | -2.3 | -5.2 | -3.9 | 0.6 | 0.5 | -0.9 | -3.2 | -4.0 |
| 140114R | Falaij | 11.6 | 21.1 | -2.2 | -2.3 | 0.4 | 0.4 | 3.8 | -1.7 | -5.0 | -3.7 | 0.6 | 0.4 | -0.9 | -3.2 | -3.6 |
| 140114T | Falaij | 11.4 | 27.2 | -1.9 | -2.3 | 0.3 | 0.6 | 3.8 | -1.9 | -5.1 | -3.8 | 0.6 | 0.4 | -0.8 | -3.0 | -3.7 |
| 140114U | Falaij | 11.4 | 21.7 | -0.1 | -0.9 | 1.8 | 1.1 | 7.2 | 3.1 | -4.3 | -3.0 | 1.1 | 0.9 | 1.4 | -1.3 | -2.8 |
| 140114V | Falaij | 11.4 | 24.4 | -1.1 | -1.7 | 0.8 | 0.9 | 5.3 | 0.1 | -4.9 | -3.6 | 1.3 | 1.1 | 1.2 | -1.8 | -3.7 |
| 120111A | Falaij | 11.6 | 22.3 | -1.2 | -1.6 | 1.6 | 0.6 | 5.5 | 1.1 | -4.5 | -3.2 | 0.8 | 0.7 | -0.1 | -2.6 | -3.9 |
| 120111B | Falaij | 11.4 | 29.4 | -1.8 | -2.0 | 0.9 | 0.4 | 4.1 | -0.7 | -4.7 | -3.4 | 0.9 | 0.7 | -0.3 | -2.8 | -3.7 |
| 120111C | Falaij | 11.3 | 31.9 | -1.6 | -1.8 | 1.3 | 0.5 | 4.4 | -0.2 | -4.5 | -3.3 | 0.8 | 0.6 | -0.6 | -3.0 | -3.8 |
| 120113I | Falaij | 11.4 | 30 | -1.3 | -1.9 | 0.9 | 0.8 | 4.7 | -0.6 | -4.9 | -3.6 | 1.1 | 0.9 | 0.3 | -2.3 | -4.0 |
| 120113J | Falaij | 11.6 | 25.8 | -2.2 | -2.3 | 0.7 | 0.3 | 3.5 | -1.6 | -4.8 | -3.6 | 0.9 | 0.8 | -0.6 | -3.2 | -4.2 |
| 120113K | Falaij | 11.4 | 30.9 | -1.7 | -1.7 | 1.9 | 0.2 | 4.4 | 0.6 | -4.1 | -2.9 | 1.0 | 0.9 | -0.5 | -3.1 | -3.9 |
| 120113L | Falaij | 11.3 | 28.4 | -1.6 | -1.5 | 1.6 | 0.2 | 4.8 | 1.5 | -3.9 | -2.7 | 0.9 | 0.8 | 0.0 | -2.5 | -4.3 |
| 100108J | Falaij | 11.7 | 23.9 | -1.6 | -2.2 | 0.4 | 0.9 | 4.3 | -1.9 | -5.4 | -4.1 | 0.7 | 0.5 | -0.7 | -3.0 | -4.1 |
| 100108K | Falaij | 11.7 | 24.7 | -1.6 | -2.3 | 0.4 | 0.9 | 4.2 | -2.1 | -5.4 | -4.2 | 0.8 | 0.6 | -0.5 | -2.9 | -4.2 |
| 100108L | Falaij | 11.6 | 29.2 | -2.6 | -2.9 | -0.5 | 0.5 | 2.4 | -4.4 | -5.7 | -4.4 | 0.8 | 0.6 | -0.9 | -3.3 | -4.2 |
| 100108M | Falaij | 11.7 | 26 | -2.1 | -2.2 | 1.0 | 0.4 | 3.7 | -1.5 | -4.9 | -3.6 | 0.8 | 0.7 | -1.0 | -3.5 | -3.8 |
| 100108N | Falaij | 11.6 | 27.6 | -2.7 | -3.1 | -1.1 | 0.6 | 2.1 | -5.3 | -6.0 | -4.7 | 0.5 | 0.4 | -1.3 | -3.4 | -4.1 |
| 100108O | Falaij | 11.8 | 22 | -2.3 | -2.7 | -0.3 | 0.7 | 3.2 | -3.6 | -5.7 | -4.4 | 0.8 | 0.6 | -0.7 | -3.1 | -4.1 |
| 100108P | Falaij | 11.5 | 23.3 | 0.3 | -0.8 | 1.7 | 1.4 | 7.6 | 3.2 | -4.5 | -3.2 | 0.5 | 0.3 | 0.4 | -1.7 | -3.8 |
| 100108Q | Falaij | 11.6 | 22.9 | -0.7 | -1.6 | 0.9 | 1.2 | 5.8 | 0.3 | -5.1 | -3.8 | 0.8 | 0.6 | 0.3 | -2.1 | -3.7 |
| 100108R | Falaij | 11.6 | 27.9 | -2.1 | -2.7 | -0.4 | 0.8 | 3.2 | -3.7 | -5.7 | -4.4 | 0.7 | 0.5 | -0.8 | -3.1 | -3.7 |
| 090115A | Falaij | 11.5 | 29.1 | 2.1 | 0.2 | 3.9 | 2.1 | 10.1 | 6.2 | -4.2 | -2.9 | 1.0 | 0.8 | 1.1 | -1.4 | -3.8 |
| 090115B | Falaij | 11.7 | 24.1 | -1.7 | -2.1 | 0.8 | 0.6 | 4.2 | -1.2 | -5.0 | -3.7 | 1.0 | 0.8 | -0.2 | -2.8 | -4.4 |
| 090115C | Falaij | 11.7 | 25.1 | 1.9 | -0.1 | 3.4 | 2.2 | 9.9 | 5.3 | -4.6 | -3.3 | 0.7 | 0.6 | 0.8 | -1.6 | -3.7 |
| 090115D | Falaij | 11.8 | 20.7 | -0.5 | -1.4 | 1.6 | 1.2 | 6.4 | 1.1 | -4.9 | -3.6 | 1.1 | 0.9 | 0.6 | -2.1 | -3.7 |
| 090115E | Falaij | 11.8 | 18 | -1.6 | -2.0 | 0.9 | 0.7 | 4.7 | -0.7 | -5.1 | -3.7 | 1.0 | 0.9 | 0.0 | -2.6 | -3.7 |
| 100107A | Masibt | 11.3 | 32.4 | -2.3 | -1.8 | 2.0 | -0.3 | 3.6 | 0.6 | -3.8 | -2.5 | 1.0 | 0.9 | -0.9 | -3.5 | -2.9 |
| 100107B | Masibt | 11.3 | 30.3 | 0.5 | -0.4 | 3.4 | 1.1 | 8.0 | 5.0 | -3.7 | -2.5 | 1.0 | 0.8 | 0.5 | -2.0 | -3.0 |
| 090120U | Masibt | 11.4 | 31.4 | 3.3 | 1.0 | 5.1 | 2.5 | 12.1 | 9.2 | -3.7 | -2.4 | 1.0 | 0.8 | 1.7 | -0.9 | -3.0 |
| 090120V | Masibt | 11.4 | 30.6 | 2.0 | 0.3 | 4.3 | 1.8 | 10.1 | 7.1 | -3.8 | -2.5 | 0.7 | 0.5 | 0.5 | -1.8 | -2.9 |
| 140111F | Qafifah | 11.6 | 23.8 | -0.3 | -1.1 | 2.3 | 1.1 | 6.7 | 2.4 | -4.4 | -3.1 | 0.5 | 0.4 | -0.5 | -2.7 | -3.8 |
| 120112E | Qafifah | 11.3 | 30.1 | -2.2 | -2.1 | 0.9 | 0.1 | 3.5 | -1.0 | -4.5 | -3.2 | 0.8 | 0.6 | -0.8 | -3.2 | -4.5 |

|  |  |  |  |  |  |  |  |  |  |  |  |  |  |  |  |  |
|---|---|---|---|---|---|---|---|---|---|---|---|---|---|---|---|---|
| 120112F | Qafifah | 11.4 | 27.4 | -1.5 | -1.8 | 1.1 | 0.6 | 4.7 | 0.0 | -4.6 | -3.4 | 1.0 | 0.8 | 0.0 | -2.5 | -4.2 |
| 120112H | Qafifah | 11.3 | 31.9 | -1.2 | -1.3 | 2.5 | 0.3 | 5.2 | 2.0 | -3.8 | -2.6 | 0.8 | 0.7 | -0.7 | -3.1 | -3.8 |
| 100109S | Qafifah | 11.8 | 22.4 | -2.3 | -2.4 | 0.6 | 0.4 | 3.5 | -1.9 | -5.0 | -3.7 | 0.9 | 0.8 | -0.6 | -3.2 | -4.4 |
| 100109U | Qafifah | 11.7 | 24.9 | -2.4 | -2.9 | -0.8 | 0.8 | 2.8 | -4.5 | -5.9 | -4.6 | 1.0 | 0.8 | -0.2 | -2.8 | -4.3 |
| 100109V | Qafifah | 11.2 | 23.7 | 3.1 | 1.2 | 4.1 | 2.2 | 12.3 | 10.4 | -3.3 | -2.0 | 1.3 | 1.2 | 3.7 | 0.7 | -3.4 |
| 090117K | Qafifah | 11.7 | 18.5 | 2.3 | 0.4 | 3.3 | 2.2 | 11.1 | 7.7 | -4.0 | -2.7 | 0.7 | 0.6 | 2.0 | -0.4 | -4.0 |
| 090117M | Qafifah | 11.7 | 22.6 | -0.2 | -1.3 | 1.6 | 1.3 | 6.6 | 1.4 | -4.9 | -3.6 | n.c. | n.c. | n.c. | n.c. | -4.4 |
| 090119Q | Qafifah | 11.7 | 23.2 | 2.5 | 0.4 | 4.3 | 2.3 | 11.1 | 7.3 | -4.2 | -2.9 | 1.0 | 0.9 | 1.6 | -1.1 | -3.7 |
| 090119R | Qafifah | 11.6 | 16.6 | 0.2 | -0.6 | 1.9 | 1.1 | 8.0 | 4.6 | -4.0 | -2.7 | 0.7 | 0.5 | 1.1 | -1.2 | -4.0 |
| 140117F | Shumayt | 11.5 | 26.2 | -1.6 | -2.0 | 0.7 | 0.7 | 4.4 | -1.0 | -5.0 | -3.7 | 0.4 | 0.3 | -1.1 | -3.2 | -4.3 |
| 140117G | Shumayt | 11.4 | 30.5 | -2.5 | -2.6 | -0.1 | 0.3 | 2.8 | -3.2 | -5.2 | -3.9 | 0.2 | 0.1 | -1.9 | -3.7 | -4.7 |
| 140117H | Shumayt | 11.5 | 29.6 | -2.1 | -2.4 | 0.2 | 0.6 | 3.4 | -2.6 | -5.2 | -4.0 | 0.4 | 0.3 | -1.5 | -3.5 | -4.6 |
| 140117I | Shumayt | 11.3 | 32.3 | -0.4 | -1.5 | 1.1 | 1.3 | 5.9 | 0.3 | -5.0 | -3.8 | 0.6 | 0.5 | -0.1 | -2.3 | -4.0 |
| 140117J | Shumayt | 11.3 | 31.6 | 1.8 | 0.3 | 3.9 | 1.7 | 9.8 | 7.1 | -3.6 | -2.4 | 0.6 | 0.5 | 0.7 | -1.5 | -3.1 |
| 140117K | Shumayt | 11.5 | 27.4 | -1.8 | -2.2 | 0.6 | 0.6 | 4.0 | -1.7 | -5.1 | -3.8 | 0.5 | 0.3 | -1.2 | -3.3 | -4.6 |
| 140117L | Shumayt | 11.6 | 27.3 | -1.8 | -2.3 | 0.5 | 0.7 | 4.0 | -2.0 | -5.2 | -4.0 | 0.2 | 0.0 | -1.8 | -3.6 | -4.6 |
| 120116P | Shumayt | 11.2 | 34.3 | -1.5 | -2.1 | 0.4 | 0.8 | 4.2 | -1.5 | -5.0 | -3.8 | 0.7 | 0.6 | -0.4 | -2.6 | -4.5 |
| 120116S | Shumayt | 11.4 | 29.5 | -0.9 | -1.7 | 0.9 | 1.0 | 5.3 | -0.2 | -5.0 | -3.7 | 0.8 | 0.7 | 0.2 | -2.3 | -4.2 |
| 120117T | Shumayt | 11.3 | 32.6 | -1.8 | -2.2 | 0.4 | 0.6 | 3.8 | -1.6 | -5.0 | -3.7 | 0.6 | 0.4 | -0.9 | -3.0 | -4.7 |
| 120117U | Shumayt | 11.3 | 32 | -2.3 | -2.5 | 0.0 | 0.4 | 3.0 | -2.8 | -5.1 | -3.9 | 0.5 | 0.4 | -1.2 | -3.3 | -4.6 |
| 120117V | Shumayt | 11.7 | 23.6 | -2.2 | -2.3 | 0.7 | 0.4 | 3.6 | -1.7 | -5.0 | -3.7 | 0.8 | 0.7 | -0.7 | -3.2 | -4.6 |
| 120117X | Shumayt | 11.3 | 32.8 | -2.6 | -2.6 | 0.0 | 0.1 | 2.5 | -2.9 | -4.9 | -3.7 | 0.1 | 0.0 | -2.2 | -3.9 | -4.7 |
| 100112AJ | Shumayt | 11.5 | 33.4 | -2.1 | -2.7 | -0.5 | 0.8 | 2.9 | -4.1 | -5.7 | -4.5 | 0.6 | 0.5 | -0.9 | -3.1 | -4.7 |
| 100112AK | Shumayt | 11.5 | 33.3 | -2.9 | -3.1 | -0.7 | 0.4 | 1.8 | -5.1 | -5.7 | -4.5 | 0.5 | 0.3 | -1.7 | -3.7 | -5.0 |
| 100112AL | Shumayt | 11.5 | 32.6 | -3.0 | -3.2 | -0.9 | 0.4 | 1.6 | -5.6 | -5.8 | -4.6 | 0.5 | 0.4 | -1.6 | -3.7 | -4.8 |
| 100112AM | Shumayt | 11.5 | 31.5 | -2.8 | -3.1 | -0.9 | 0.5 | 1.9 | -5.2 | -5.8 | -4.6 | 0.5 | 0.4 | -1.4 | -3.6 | -4.8 |
| 090123D | Shumayt | 11.5 | 34 | -1.3 | -2.0 | 0.6 | 1.0 | 4.4 | -1.6 | -5.2 | -4.0 | 0.8 | 0.7 | -0.2 | -2.7 | -4.5 |
| 090123F | Shumayt | 11.6 | 28.1 | -1.5 | -2.2 | 0.3 | 0.9 | 4.2 | -1.9 | -5.3 | -4.1 | 1.0 | 0.9 | 0.2 | -2.5 | -4.3 |
| 100114AS | Sudari | 11.3 | 18.2 | 2.3 | 0.6 | 3.0 | 2.0 | 11.2 | 8.5 | -3.7 | -2.3 | 1.0 | 0.9 | 3.2 | 0.5 | -3.4 |
| 100114AT | Sudari | 11.6 | 30.4 | -1.8 | -2.2 | 0.8 | 0.6 | 3.8 | -1.8 | -5.1 | -3.8 | 0.5 | 0.4 | -1.4 | -3.5 | -3.8 |
| 100114AU | Sudari | 11.6 | 20.08 | 2.6 | 0.5 | 3.2 | 2.4 | 11.4 | 7.7 | -4.2 | -2.8 | 0.3 | 0.2 | 1.4 | -0.6 | -3.5 |
| 090122Z | Sudari | 11.6 | 29.5 | -1.9 | -2.2 | 0.0 | 0.5 | 3.8 | -1.6 | -5.0 | -3.7 | 0.4 | 0.2 | -0.9 | -2.8 | -4.2 |
| 100115AV | Uqaybah | 11.6 | 21.4 | -1.9 | -2.6 | -0.5 | 0.9 | 3.8 | -3.2 | -5.8 | -4.5 | n.c. | n.c. | n.c. | n.c. | -3.0 |
| ***Well Fluids*** |  |  |  |  |  |  |  |  |  |  |  |  |  |  |  |  |
| 120119B | NSHQ-14 | 10.1 | 24 | -2.7 | -1.7 | -0.1 | -0.7 | 3.8 | 1.9 | -3.2 | -1.9 | 0.5 | 0.4 | 0.7 | -1.5 | -2.9 |
| 120119A | NSHQ-14 | 11.1 | 29.1 | -1.4 | -1.8 | 0.9 | 0.6 | 4.7 | 0.1 | -4.6 | -3.3 | 1.0 | 0.8 | 0.3 | -2.3 | -3.6 |
| 120119C | NSHQ-14 | 11.0 | 33.7 | -1.5 | -1.8 | 0.9 | 0.6 | 4.4 | -0.3 | -4.6 | -3.4 | 0.9 | 0.8 | 0.1 | -2.4 | -3.6 |
| 120123E | NSHQ-04 | 10.7 | 28.3 | -1.7 | -1.5 | 1.6 | 0.0 | 4.8 | 1.9 | -3.7 | -2.4 | 1.7 | 1.5 | 1.6 | -1.6 | -1.8 |
| 120126F | WDA-16 | 8.0 | 31.8 | -4.3 | -1.3 | -1.6 | -2.8 | 2.2 | 5.3 | -0.7 | 0.5 | -0.9 | -1.0 | 0.0 | -0.7 | -2.9 |
| 120127G | WDA-17 | 9.2 | 31 | -2.1 | -1.5 | -3.1 | -0.4 | 4.2 | 2.0 | -3.4 | -2.1 | 0.1 | 0.0 | 3.1 | 1.4 | -3.6 |
| 120130I | WDA-05 | 9.3 | 32.7 | -1.0 | -0.7 | -1.7 | 0.0 | 6.1 | 4.6 | -2.9 | -1.7 | 0.1 | 0.0 | 3.2 | 1.5 | -3.5 |
| 120130J | WDA-05 | 9.4 | 32.1 | -0.8 | -0.7 | -1.5 | 0.1 | 6.3 | 4.8 | -3.0 | -1.7 | 0.2 | 0.0 | 3.3 | 1.5 | -3.5 |
| 100119AX | SJA-04B | 7.2 | 33.8 | -7.4 | -2.9 | -4.4 | -4.3 | -2.6 | 0.2 | -0.8 | 0.4 | n.c. | n.c. | n.c. | n.c. | -2.4 |
| 100119AY | SJA-04A | 7.6 | 34 | -6.1 | -2.3 | -3.1 | -3.7 | -0.7 | 2.1 | -0.8 | 0.4 | n.c. | n.c. | n.c. | n.c. | -2.5 |
| 100120AZ | SJA-03 | 9.4 | 34.1 | -0.7 | -0.7 | -1.6 | 0.1 | 6.3 | 4.7 | -3.0 | -1.8 | n.c. | n.c. | n.c. | n.c. | -3.5 |

n.c. means not calculated due to lack in analytical data (*e.g.*, DIC for carbonate saturation)

Fo - forsterite; En - enstatite; Di - diopside; Brc - brucite; Ctl - chrysotile; Tlc - talc; Am - Amorphous Silica; Qz - quartz; Cal - calcite; Arg - aragonite; Dol - dolomite; Mgs - magnesite; Anh - anhydrite

Table B2

*Composition of Fluids Used in Mixing Calculations*

| | Surface Fluid (s)[1] | Deep Subsurface Fluid 1 ($d_1$)[2] | Deep Subsurface Fluid 2 ($d_2$)[3] | Deep Subsurface Fluid 3 ($d_3$)[4] |
|---|---|---|---|---|
| pH | 7.9 | 12.3 | 11.7 | 11.1 |
| Na (mmolal)[5] | 1.14 | 10 | 10 | 10 |
| Ca (mmolal) | 0.56 | 14.4 | 3.2 | 0.7 |
| Mg (µmolal) | 2810 | 0.03 | 0.2 | 2.6 |
| Cl (mmolal)[5] | 1.28 | 10 | 10 | 10 |
| Si (µmolal) | 303 | 1.3 | 0.3 | 0.1 |
| DIC (µmolal) | 5120 | 8 | 10 | 20 |

[1] composition taken from sample 140116B. Sample is closest to predicted compositions in equilibrium with secondary phases common in the shallow subsurface.

[2] fluid in equilibrium with the Ctl-Brc-Di and calcite assemblage at 25°C and 1 bar.
[3] fluid in equilibrium with the Ctl-Brc-Cal assemblage, given 10 µmole/kg DIC, at 25°C and 1 bar.

[4] fluid in equilibrium with the Ctl-Brc-Cal assemblage, given 20 µmole/kg DIC, at 25°C and 1 bar.

[5] Deep fluids were given Na and Cl concentrations of 10 mmolal as an average of the range of concentrations (3-20 mmolal) observed in environmental samples

## B.4. Supplementary Figures

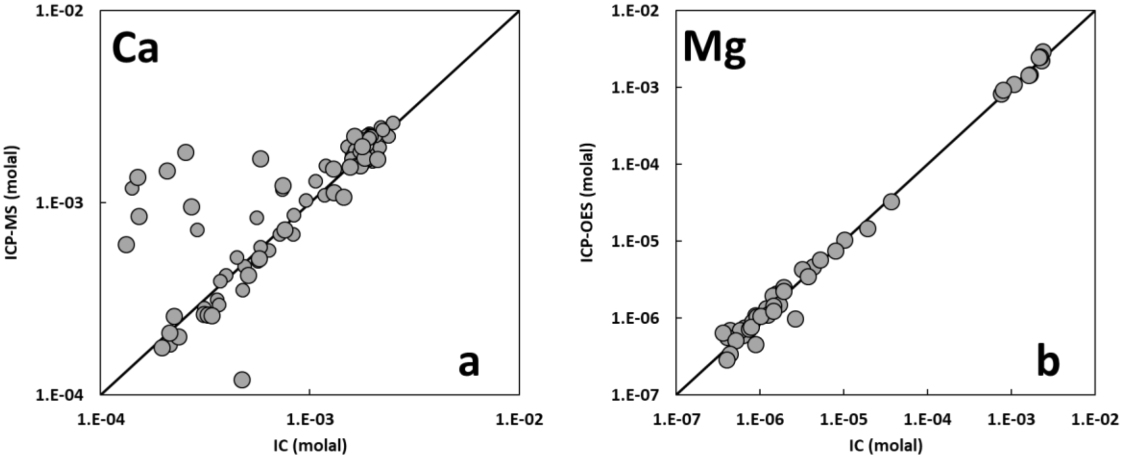

*Figure B1*. Comparison of dissolved Ca (a) and Mg (b) values determined using the ICP-MS and ICP-OES, respectively, with values determined using the IC.

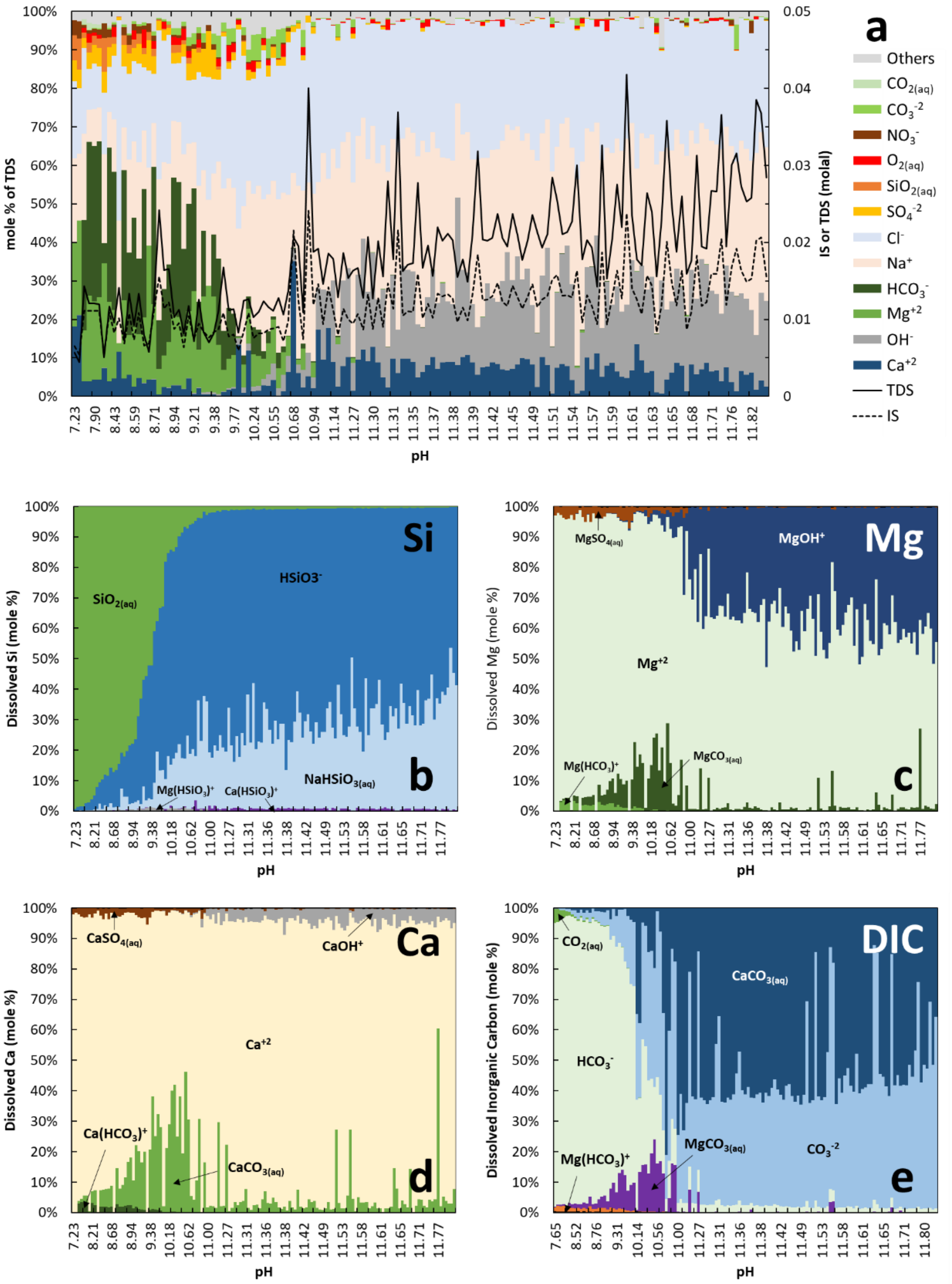

*Figure B2*. (a) Total dissolved solutes (TDS, solid black line) and ionic strength (IS, dashed black line) of sampled fluids (values at the right y-axis). Results of speciation calculation are depicted as a stacked bar chart where the color represents different aqueous species (in mole %, left y-axis). Also shown are the aqueous species that comprised total dissolved Si (b), Mg (c), Ca (d), and inorganic carbon (e).

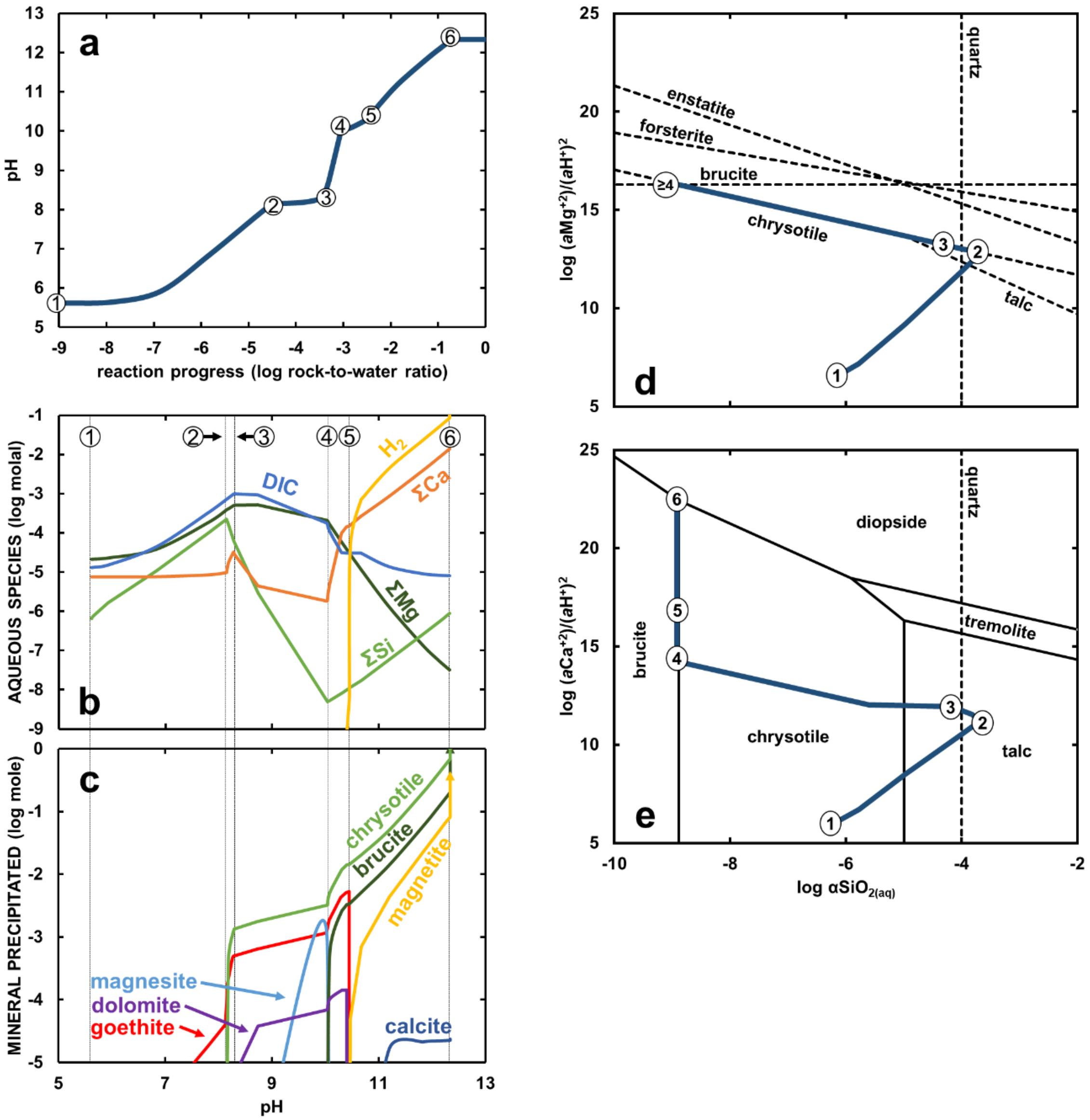

*Figure B3.* Reaction paths simulating serpentinization of an ultramafic rock with the composition 85% olivine-14% orthopyroxene-1% clinopyroxene. (a) depicts the increase in pH as serpentinization progresses, highlighting six stages discussed in the text. Progress of the serpentinization process is depicted in rock-to-water ratio (e.g., log value of -3 represents reaction of 1 g of reacted ultramafic rock in 1000 g water). (b) and (c) depict changes in the concentrations of aqueous species (in log molality) and amount of minerals precipitated (in log moles) with pH, respectively. Reaction paths are plotted on activity diagrams for the $MgO-SiO_2-H_2O$ (d) and $CaO-MgO-SiO_2-H_2O$ (e) systems. Dashed lines in (d) and (e) indicate saturation of indicated minerals, while solid lines in (e) represent boundaries for the stability fields of minerals. Dark blue curves show results of reaction path calculations. Numbers indicate the starting points of the six stages of serpentinization.

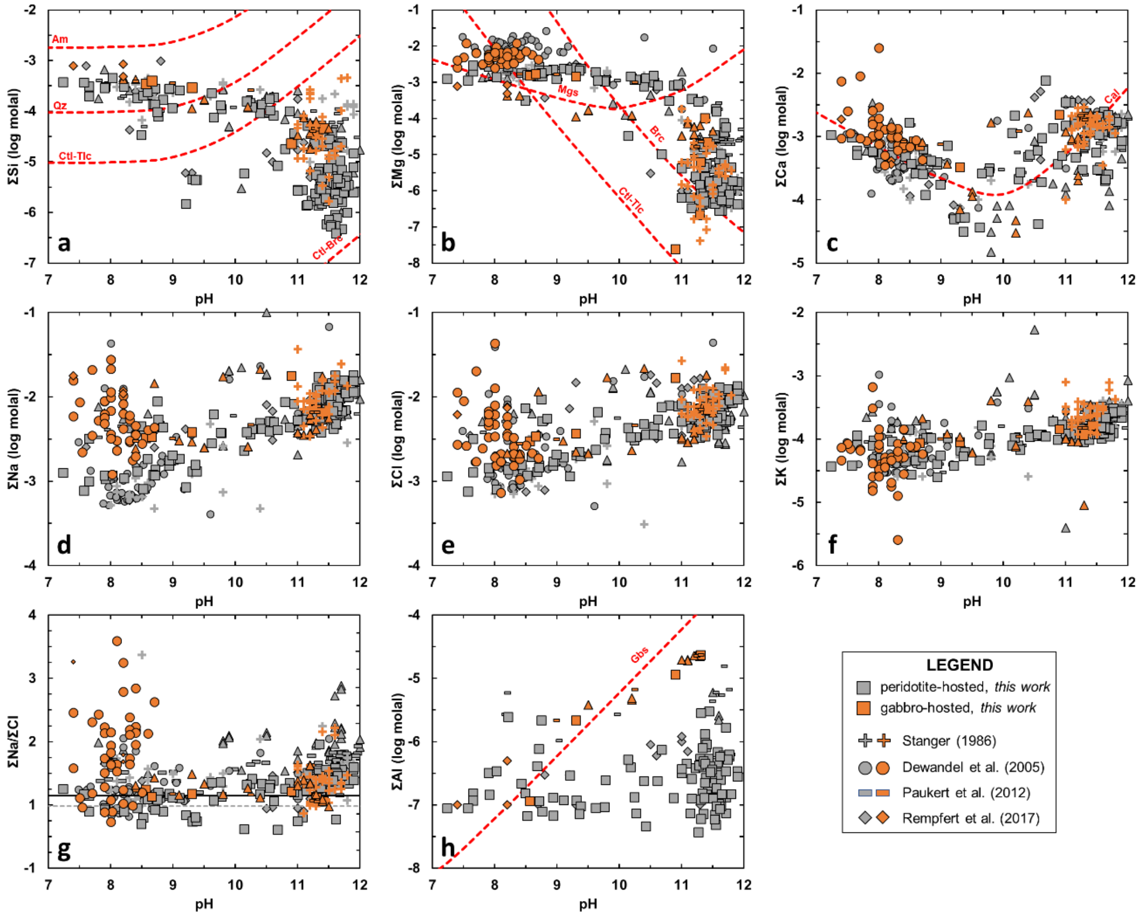

*Figure B4*. Comparison between ultramafic-hosted (grey symbols) and gabbroic-hosted (orange symbols) fluids in Oman. Symbol shapes and data sources are the same as in Figure 3. Trends in the total dissolved Si (a), Mg (b), Ca (c), Na (d), Cl (e), K (f), ratio between total dissolved Na and Cl (g), and total dissolved Al (h) with pH are shown. Dashed red lines and curves show solubility conditions for various minerals: Am – amorphous silica, Qz – quartz, Ctl – chrysotile, Tlc – talc, Brc – brucite, Mgs – magnesite, Cal – calcite, Gbs – gibbsite.

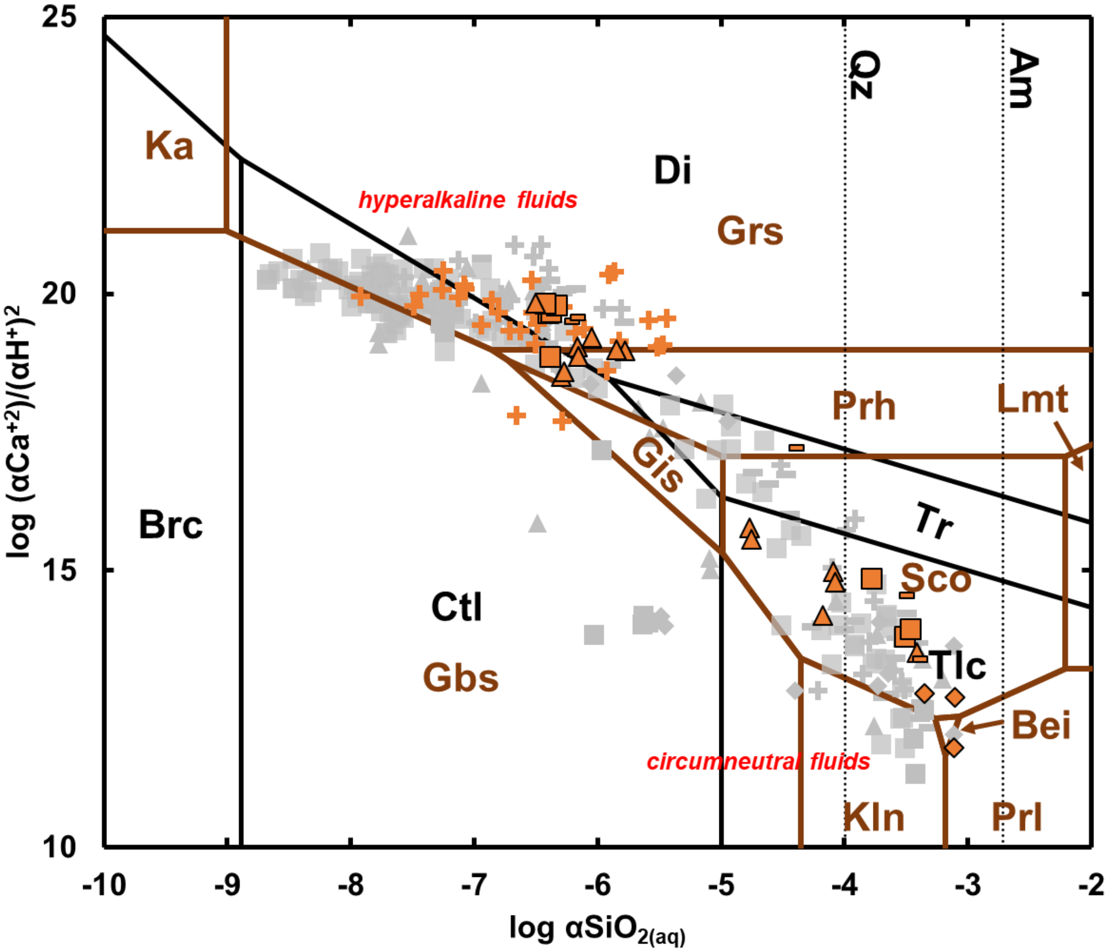

*Figure B5*. Log $a\mathrm{Ca}^{+2}/(\alpha\mathrm{H}^{+})^{2}$ vs $a\mathrm{SiO}_2$ of gabbro-hosted fluids (various symbols in orange) plotted on an activity diagram for the $CaO$-$Al_2O_3$-$SiO_2$-$H_2O$ system (phase boundaries as orange lines) at 25°C, 1 bar. Underlying it is an activity diagram for the $CaO$-$MgO$-$SiO_2$-$H_2O$ system (black lines) and plotted activities of ultramafic-hosted fluids (various symbols in grey), similar to those shown in Figure 3.5f. Symbols are the same as in Figure S1. Note that the lines represent stability boundaries between the indicated minerals: Brc – brucite; Ctl – chrysotile; Tlc – talc; Tr – tremolite; Di – diopside; Qz – quartz; Am – amorphous $SiO_2$, Gbs – gibbsite; Kln – kaolinite; Prl – pyrophyllite; Bei – beidellite; Sco – scolecite: Lmt – laumontite; Prh – prehnite; Grs – grossular; Ka – katoite. Thermodynamic properties of minerals are taken from Helgeson et al. (1978) and Wolery and Jove-Colon (2004).

# APPENDIX C

# SUPPLEMENTARY FILES TO CHAPTER 4

## C.1. Overview of the Compositions of Ultramafic- and Gabbro-hosted Fluids in the Oman Ophiolite

A subset of compositional data of fluids from the Oman ophiolite reported by the above companion studies (Canovas et al., 2017; Howells, in prep; Chapter 3 of this document) were used to quantify energy supplies via reactions shown in Table 4.1 as well as in estimating end-member fluids representative of the serpentinizing subsurface. These estimated compositions for end-member subsurface fluids were further used to quantify energy supplies in the serpentinizing subsurface. Compositional data of Oman samples are compiled in Table C1 and trends for major solutes are shown in Figure C1 which depicts trends in the dissolved concentrations of Si (Figure C1a), Mg (Figure C1b), Ca (Figure C1c), Na (Figure C1d), Cl (Figure C1e), and Al (Figure C1f) trends with pH. Most of samples were taken from ultramafic bodies while a few where hosted in gabbroic rocks. The overall trends in pH, temperature, and concentrations of major dissolved solutes measured from ultramafic- and gabbro-hosted fluids in the Oman ophiolite has been discussed by the above accompanying studies and are summarized below.

As shown in Figure C1 in Appendix C of this text, except for some minor differences (see below), trends in the concentration of dissolved solutes of fluids hosted in either ultramafic or gabbroic rocks are generally overlapping. The pH of fluids investigated by this work ranges from 7 to 11.7 and are within range of findings of numerous prior works concerning fluids from the Oman ophiolite (Neal and Stanger, 1985, Dewandel et al., 2005, Paukert et al., 2012; Chavagnac et al., 2013b; Rempfert et al., 2017; Giampouras et al., 2020) and other ultramafic bodies around the world (*e.g.*, Barnes et al., 1978 (USA); Schwarzenbach et al., 2013 (Italy); Szponar et al., 2013

(Canada); Cardace et al., 2015 (Philippines)). Neutral to slightly alkaline fluids (pH 7-9) occur as shallow groundwater and surface stream fluids while hyperalkaline fluids (pH >11) are observed in spring seeping from outcropping rocks and in wells tapping deep-seated groundwater. Dissolved concentrations of common rock-forming elements (Si, Mg, Ca, Na, Cl, and Al) vary with pH, as shown in Figure C1. Dissolved Si (Figure C1a) and Mg (Figure C1b) values are relatively higher in circumneutral fluids (>0.1 millimolal) and are very dilute in hyperalkaline fluids (<0.01 millimolal). In contrast, dissolved Ca (Figure C1c) is elevated in hyperalkaline fluids (> 1 millimolal). Circumneutral and hyperalkaline fluids are classified as *Type 1* $Mg^{+2}$-$HCO_3^-$ and *Type 2* $Ca^{+2}$-$OH^-$ fluids, respectively, after their most dominant dissolved components. Type 1 fluids are results of fluid interactions with shallow aquifer host rocks in a system open to atmospheric exchange that generate circumneutral to slightly basic (pH 7-9) fluids rich in $Mg^{+2}$ and $HCO_3^-$. Greater degrees of interactions between water and rock as fluids infiltrate deeper into the aquifer facilitate the transformation of meteoric and Type 1 fluids into reduced, hyperalkaline fluids that are enriched in $Ca^{+2}$ and $OH^-$. As the overall serpentinization process progresses, leaching from the rocks and loss of $H_2O$ due to hydration of the rock lead into an increase in the concentrations of Na and Cl with pH, as respectively shown in Figures C1d and C1e, respectively. In addition, as discussed in Chapter 3 of this document, fluids with intermediate pH values (9 to 11) that fall between the Type 1 and Type 2 end-member fluids are either a result of intermediate stages of the serpentinization process or mixing between the end-member fluids. These fluid types can be distinguished using coupled trends in pH and the total dissolved silicon concentration.

At the same pH, fluids at intermediate stages of serpentinization have considerably lower total dissolved silicon than fluids derived from mixing.

Trends in the overall compositions of gabbro-hosted fluids relative to those hosted in ultramafic rocks are discussed in detail in Appendix B and are summarized below. Compositions of circumneutral Type 1 fluids hosted in both lithologies have generally overlapping trends. Hyperalkaline Type 2 fluids hosted in both lithologies also overlapped but with some important differences. As an example, lowest dissolved Si concentration measured from gabbro-hosted fluids is ~10 µmolal while many ultramafic-hosted fluids can attain much lower dissolved Si values (<1 µmolal) approaching that dictated by the serpentine and brucite equilibrium (Figure C1b). In contrast and as a response to equilibrium with secondary phases with Si content larger, or Mg content lower, than serpentine and brucite, gabbro-hosted fluids can attain much lower Mg levels (~0.05 µmolal) than those hosted in ultramafic rocks (~0.5 µmolal), as shown in Figure C1a. Hyperalkaline fluids hosted in gabbros are much more enriched in dissolved Al relative to their ultramafic-hosted counterparts, as shown in Figure C1f. The above trends are consistent with the host rock's composition where gabbroic rocks are more enriched in Si and Al, and depleted in Mg relative to ultramafic rocks.

## C.2. Overview of Chemolithotrophic Strategies in Serpentinizing Environments

This work quantifies geochemical energy available to serpentinizing communities via 17 chemolithotrophic reactions compiled in Table 4.1. All of 17 studied reactions are detected or plausible in serpentinizing environments by a number of experimental and molecular studies (see Table 4.1). Physiological and accompanying genomic studies of isolates from serpentinizing environments present the most compelling evidence for a given metabolic strategy. In serpentinizing systems, much of physiological work has been focused on heterotrophs (*e.g.*, Tiago et al., 2004; Takai et al., 2005, Aissa et al., 2014; Cabria et al., 2014; Cohen et al., 2015) and less has been conducted on chemotrophic microorganisms. Chemoautotrophs from the genus *Serpentinomonas* capable of using $H_2$ and $O_2$ (hydrogen oxidation, reaction 4.1 in Table 4.1) as energy sources and utilizing calcite as its carbon sources where isolated and studied by Suzuki et al. (2014). Other strong evidences for the presence of a chemotrophic strategy are provided by experiments demonstrating enhanced rates of redox processes relative to abiotic controls as well as labeled isotope experiments that track assimilation and transformation of relevant compounds. Enrichment cultures targeting *Methanobacterium* from subsurface fluids from the Oman ophiolite were shown to cause large variations in the isotopic composition of generated methane in experiments conducted by Miller et al. (2018). Experiments were also used to detect the presence of microorganisms capable of aerobic oxidation of carbon monoxide (reaction 4.3 in Table 4.1) by Morrill et al. (2014) in Canada and Fones et al. (2019) in Oman, methanogenesis (reaction 4.8) by Brazelton et al. (2011) in Lost City, Kohl et al. (2016) in California, and Fones et al. (2019) in Oman, and the anaerobic oxidation of methane (reactions 4.10 – 4.12) by Brazelton et al. (2011) in Lost City. Expression of genes revealed by transcriptomic, proteonomic and biomarker analyses also provides compelling evidences for the presence of certain metabolic strategies. Lipid biomarker studies (Mottl et al., 2003; Bradley et al., 2009a; 2009b; Lincoln et al., 2013; Klein et al., 2015) support the presence of methanogens and anaerobic methanotrophs as well as ammonia oxidizers (reaction 4.5) and sulfate reducers (reaction 4.9) at several serpentinizing sites in the seafloor (*e.g.*, Lost City hydrothermal field in the Mid-Atlantic Ridge and South Chamorro Seamount in the Mariana Forearc, see Table 4.1). Metagenomic studies probing marker genes for a given metabolic process further support the presence of aerobic hydrogen oxidizers (*[Ni,Fe] and/or [Fe,Fe] hydrogenase*, Brazelton et al., 2011; 2012; 2013; 2017; Twing et al., 2017; Suzuki et al., 2017), carbon monoxide oxidizers (*carbon monoxide dehydrogenase* or *CODH*, Brazelton et al., 2012; Twing et al., 2017; Fones et al., 2019), methanogens or anaerobic methanotrophs (*mcrA* genes, Blank et al., 2009; Quéméneur et al., 2014; Postec et al., 2015; Brazelton et al., 2017; Crespo-Medina et al., 2009; Fones et al., 2019), and sulfate reducers (*dsrAB*, *dsrB*, *aprA* genes, Blank et al., 2009; Tiago and Veríssimo, 2013; Brazelton et al., 2017; Suzuki et al., 2017; Sabuda et al., 2020). In addition, marker genes for the aerobic oxidation of methane (*pmoABC*, Brazelton et al., 2017; Seyler et al., 2020) and sulfide (*sox*, *sqr*, *fccAB*, Brazelton and Baross, 2010; Tiago and Veríssimo, 2013; Sabuda et al., 2020), and the reduction of nitrate or nitrite (*narG* and/or *nirS*, Meyer-Dombard et al., 2015; Suzuki et al., 2017) and molecular nitrogen (*nifH*, Brazelton et al., 2011). Aerobic methanotrophy, aerobic oxidation of sulfide, nitrate reduction and nitrogen reduction/fixation are represented by reactions (4.2), (4.4), (4.13), and (4.14), respectively, in Table 4.1. Molecular data from 16s rRNA analysis of serpentinizing fluids and sediments provides additional, albeit at unknown uncertainties, inferences on the presence of certain microbial metabolic strategy. In addition to the above metabolism, numerous works involving 16s rRNA sequences suggest the presence microbes utilizing the aerobic oxidation of nitrite (reaction 4.6) and ferrous iron (reaction 4.7) as energy sources. In addition to the above metabolic processes, Canovas et al. (2017) suggests potentials for microbes availing the water-gas shift (reaction 4.15), anaerobic oxidation of ammonia or annamox (reaction 4.16), and carbon monoxide reduction (reaction 4.17) reactions as sources for energy, despite absence of molecular evidences from serpentinizing environments. All the above chemolithotrophic processes are summarized in Table 4.1, including a compilation of work supporting the presence of a given metabolic strategy. These evidences are classified accordingly based on a scheme (*Class I to V*, and *geochemical*) developed by Canovas et al. (2017) that accounts for the strength of a given evidence.

Calculations of energy supplies account for the full speciation of inorganic species and the reactions listed for a given chemolithotrophic process in Table 4.1 only serve as a representative example. For instance, at the hyperalkaline pH characteristic of serpentinizing fluids, the dominant dissolved inorganic carbon source are in the form of a neutral complex ($CaCO_{3(aq)}$) and the anion, $CO_3^{-2}$ (Leong and Shock, 2020, also see Figure C2a) and thus reaction (4.8) for methanogenesis would be best represented by these species instead of $CO_2$. Moreover, our calculations accounts for all dissolved components of a given redox-sensitive species to infer the maximum available energy, considering the lack of data especially at alkaline conditions on the available inorganic carbon species used specifically by microorganisms such as methanogens.

The 17 reactions studied in this work are not exhaustive of chemotrophic processes present in serpentinzing systems. Several chemolithotropic and chemoorganotrophic reactions such as acetogenesis (Suzuki et al., 2017; Twing et al., 2017; Seyler et al., 2020), fermentation or methanogenesis using organic compounds such as acetate and formate (Morrill et al., 2013; Kohl et al., 2016; Brazelton et al., 2017); sulfate reduction with formate (Lang et al., 2018), thiosulfate oxidation and disproportionation (Sabuda et al., 2020), and ferric iron reduction (Meyer-Dombard et al., 2018) are suggested to be present in serpentinizing environments but are otherwise not quantified in this work due to lack of data (*e.g.*, dissolved organic species, thiosulfate, ferric iron). Constraints on the above species would permit future quantification of available energy supplies through these reactions.

### C.3. Calculated Energy Supplies Available in Oman Ophiolite Fluids

Except for iron oxidation, which was not investigated, Canovas et al. (2017) showed that all other chemotrophic reactions listed in Table 4.1 are favored to proceed in all but a few of fluids they sampled from the Oman ophiolite. Using fluid compositional data from Canovas et al. (2017) as well as those reported in Chapter 3 of this work and by Howells (in prep) from the same study sites in Oman, this work offers further constraints on the maximum energy available to chemolithotrophs by quantifying energy per mass of a given fluid in addition to affinity values. Calculations for energy supplies available through iron oxidation is also conducted. Results of calculations of affinities ($A_r$) and energy yield ($E_r$) for the forward direction of studied reactions are compiled in Tables C3 and C4, respectively, in Appendix C of this work. $E_r$ for aerobic and anaerobic reactions are depicted in Figures C3 and C4, respectively.

As shown in Figures C3 and C4, most of study sites provide positive energy sources for all 17 chemotrophic reactions listed in Table 4.1. The forward reaction is only unfavorable for a few sites and negative energy supplies are not plotted. These were only observed for a few $CH_4$-rich, $H_2$-poor hyperalkaline sites (*e.g.*, sample 100110A, see Table C3) where methanogenesis is unfavorable. As discussed above, fluids investigated by this work exhibit variabilities of compositions ranging from that with circumneutral to hyperalkaline pH, as well as being hosted at different lithological settings (ultramafic *vs* gabbro-hosted). These variabilities in aqueous compositions result in variations in the available energy supplies for various reactions ranging from less than 1 μcalories to more than 1 calories per kilogram of fluid, as depicted in Figures C3 and C4. We first start discussions below on overall bionergetic trends observed from *ultramafic-hosted* fluids (grey symbols in Figures C3 and C4) which we have a more complete dataset. We then assess how energy supplies available in *gabbro-hosted* fluids (orange symbols) compare to fluids hosted in ultramafic rocks.

Trends for aerobic chemolithotrophic processes are depicted in Figure C3 which shows energy yield for the aerobic oxidation of dissolved hydrogen (Figure C3a), methane (Figure C3b), carbon monoxide (Figure C3c), sulfide (Figure C3d), ammonia (Figure C3e), nitrite (Figure C3f), and iron (Figure C3g). Except for the aerobic oxidation of nitrite and carbon monoxide, there is a general increase in the available energy for all other reactions as pH increases. These trends suggest that most of aerobic chemotrophic strategies listed in Table 4.1 would be favorable in serpentinization-generated fluids relative to those lower pH fluids that composed surficial runoffs and upper aquifers. However, note that the variation in energy supply also increases with increasing pH (*e.g.*, see Figures C3a, C3d, and C3e for hydrogen, sulfide and ammonia oxidation, respectively). These variabilities in energy supplies can be attributed to variations on the supply of limiting reactants at these conditions. The $A_r$ (calories/mole $e^-$ transferred) for a given reaction are not variable across the range of pH observed in this work, as shown in Table C3 and by previous work (Canovas et al., 2017). Consequently, total energy available per kg of fluid ($E_r$) will be dependent on the supply of limiting reactant (see equation 4.24). This trend is exemplified in Figure C3h which shows energy yield for hydrogen oxidation given the ratio dissolved $O_2$ and $H_2$ levels of investigated fluids. The ratios are normalized based on their stoichiometric coefficients in Table 4.1 for reaction (4.1) and thus values above and below zero represent $O_2$- and $H_2$-limited systems, respectively. Energy available for hydrogen oxidation in all fluids with $pH < 11$ (green symbols) are limited by $H_2$. Thus, energy supply trends positively as fluids become more $H_2$-rich towards the vertical dashed line in Figure C3h. Not all hyperalkaline ($pH > 11$, blue symbols in Figure C3h), despite results of serpentinization, are enriched in $H_2$. In the case for these fluids, $H_2$ is limiting and energy supply also trends positively as fluids become more $H_2$-rich. For hyperalkaline fluids enriched in $H_2$, as depicted by the blue symbols in the right side of the dashed vertical line in Figure C3h, energy supply is limited by $O_2$ levels and are increasing as fluids becomes more $O_2$-rich towards the dashed vertical line. As shown in Figures C3a and C3h, the highest energy supply available for aerobic hydrogen oxidizers is associated with hyperalkaline fluids. A number of hyperalkaline fluids, however, yields low energy via hydrogen oxidation and are even lower than those non-hyperalkaline fluids with similar $H_2/O_2$ ratio. Energy that can be available through the aerobic oxidation of dissolved methane, sulfide and ammonia exhibits similar trends as shown above for hydrogen oxidation where availability of the limiting reactant results in variabilities in the energy supply. Ultimately, predictions of available energy supply in the deep subsurface would entail detailed exploration on the availability of both electron donors and acceptors. This would require constraints on the extent of atmospheric $O_2$ infiltration into the subsurface as well as the variabilities in the dissolved $H_2$ levels of deep-seated serpentinizing fluids.

On the other hand, available energy from the oxidation of dissolved ferrous iron (Figure C3g) corresponds closely to trends in the dissolved ferrous iron concentration (Figure 4.2a), implying limitations on the energy supply by the availability of dissolved ferrous iron instead of dissolved $O_2$. The fast kinetics of ferrous iron oxidation observed at fluids with pH > 7 (Stumm and Lee, 1961; Trapp and Millero, 2007; St. Clair et al., 2019) would raise questions if energy supplies can be harvested by iron oxidizers at all, especially at the hyperalkaline conditions characteristic of serpentinizing environments. For example, St. Clair et al. (2019) observed limitations for iron oxidizing microorganisms at neutral to slightly alkaline fluids in the Alps. In serpentinization-generated fluids, the reduced nature of fluids can allow dissolved ferrous iron in the fluid to persist, despite the high pH, consistent with high levels of dissolved ferrous iron detected in the field at hyperalkaline Type 2 fluids (Canovas et al., 2017; Rempfert et al., 2017; Chapter 3 of this work). The persistence of dissolved ferrous iron permits opportunities for iron oxidizing microorganisms to take advantage of. The presence of putative iron oxidizers in serpentinizing and other hyperalkaline systems have been suggested by a number of 16s rRNA studies (Roadcap et al., 2006; Daae et al., 2013; Woycheese et al., 2015). Stronger evidence for the presence of iron oxidizers can be provided for by field and laboratory experiments that can probe how fast dissolved ferrous iron is oxidized by microbes present in serpentinizing fluids relative to abiotic controls. The serpentinizing subsurface stores a massive source of electron donors in the form of ferrous iron hosted in minerals like serpentine, brucite, and olivine that can potentially supply energy to various subsurface communities. Among the above minerals, brucite can readily mobilize electron donors due to its fast rates of dissolution relative to serpentine and olivine (Prokovsky and Schott, 2004) and could be a potential substrate for subsurface life (Templeton and Ellison, 2020).

Like most aerobic reactions, energy yielded via some anaerobic reactions also generally increases in magnitude as well as variation with increasing pH, as shown in Figure C4 for hydrogenotrophic methanogenesis (Figure C4a), sulfate reduction (Figure C4b), anaerobic oxidation of methane using sulfate (Figure C4c), nitrate (Figure C4d), and nitrite (Figure C4e) as electron acceptors. Energy yield through nitrate and nitrogen reduction seems to follow similar increasing but more variable trend as fluids becomes more alkaline, as shown in Figures C4f and C4g, respectively. Energy yield through the water-gas shift, annamox, and carbon monoxide reduction reactions does not show strong pH dependence, as depicted in Figures C4h, C4i, and C4j, respectively. As discussed above for the case of the aerobic oxidation of hydrogen, the large variation in the energy supply especially those calculated from hyperalkaline fluids can be attributed to the variabilities in the limiting supply of available electron donors and acceptors. Energy supply via methanogenesis given the ratio of the electron donor ($H_2$) and acceptor (DIC), corrected according to their stoichiometric coefficients depicted in reaction (4.8), is shown in Figure C4k. All non-hyperalkaline (pH <11, green symbols) and most hyperalkaline (pH >11, blue symbols) are $H_2$-limited. Energy varies by several order of magnitude ($10^6$ -$10^0$ calories/kg) but increases as fluids becomes more $H_2$-rich towards the vertical dashed line in Figure C4k. A few hyperalkaline fluids are DIC-limited, as shown in the right side of the vertical dashed line, and available energy generally increases as fluids becomes more DIC-rich towards the dashed line. Highest energy available for methanogens is generally available in hyperalkaline fluids relative those lower in pH. However, some hyperalkaline fluids yield low energy for methanogens that are even lower than non-hyperalkaline fluids with similar $H_2/O_2$ ratio. Although the latter has more potentials to support methanogens, Howells (in prep) have shown that no methanogens are present in these non-hyperalkaline fluids due to their high DO content that are toxic to these anaerobes.

There is less dataset on energy supplies quantified for analogous fluids hosted in gabbroic bodies, as shown by the few orange colored symbols in Figures C3 and C4. Despite gabbroic bodies comprising a significant component of continental ophiolites (*e.g.*, 31% the Oman ophiolite's surface, Nicolas et al., 2001), aqueous geochemical data warranted for estimation of geochemical energy supplies is lacking. Calculations of Canovas et al. (2017) and Cardace et al. (2017) include a few fluids hosted in gabbroic rocks. Both works, however, have discussed these fluids collectively with other ultramafic-hosted fluids and discussions on how gabbro-hosted differs in terms of energetic supplies is still warranted. In the discussions above, we showed that the compositions of gabbro-hosted fluids mostly overlap with their ultramafic-hosted counterparts. Many of these gabbro-hosted fluids are found close to the gabbro-ultramafic lithological boundaries and the overlapping compositions are likely results of the complex subsurface fluid pathways that allows interactions with both rocks at this lithological interface (see Appendix B). Nevertheless, pertinent differences in the concentrations of some redox-sensitive species from both geological settings could result in varying potentials for supporting different microbial strategies. For instance, while both types of fluids can attain hyperalkaline conditions, hyperalkaline gabbro-hosted fluids are typically poor in dissolved $H_2$ (Figure 4.1b) but can be enriched in dissolved

$CH_4$ (Figure 4.1d) and sulfide (Figure 4.2c). The methane-rich and sulfidic nature of gabbro-hosted fluids parallels those measured at submarine basalt-hosted hydrothermal vent fluids. Basaltic and gabbroic rocks are chemically similar and differs mainly on their mineralogical textures. Gabbros and basalts are both formed from the partial melting of ultramafic rocks that composed the Earth's mantle. Basalts are the eruptive component of the melt while the more crystalline gabbros are those that solidified at depth. However, despite similarities in the compositions of the host rocks, no low-temperature systems (<100 °C) hosted in basalts have been recorded to attain the hyperalkaline pH (>11) observed in gabbro-hosted systems in Oman. For instance, in the basaltic aquifer in Iceland, maximum pH measured by Arnorsson et al. (2002) is ~10.3 (at 20 °C). The hyperalkaline nature of fluids hosted in gabbroic rocks in ophiolites could be a nature of their proximity to ultramafic bodies but remains to be investigated further. Overall, despite their methane- and sulfide-rich nature, energy supplies for the aerobic oxidation of methane and sulfide in gabbro-hosted fluids, as respectively shown in Figures C3b and C3d (orange symbols), overlaps with most of those calculated for ultramafic-hosted fluids (grey symbols). Similar to that discussed above for ultramafic-hosted fluids, variations in energy supplies can be attributed to the variations in the amount of the limiting reactant, which can be dissolved $O_2$ in this case instead of dissolved methane or sulfide. Nevertheless, the maximum energy available to sulfide oxidizers is associated with a gabbro-hosted fluid, as shown in Figure C3d. The anaerobic oxidation of methane via the reduction of sulfate is also highly favorable in gabbro-hosted fluids relative to those occurring in ultramafic bodies, as shown in Figure C3c. In contrast, $H_2$ is depleted in gabbro-hosted fluids relative to most of those hosted in ultramafic rocks (see Figure 4.1b) and energy supplies available for hydrogenotrophs like hydrogen oxidizers (Figure C3a), methanogens (Figure C4a) and sulfate reducers (Figure C4b) in gabbro-hosted systems are lower than those calculated for most of fluids hosted in ultramafic rocks.

## C.4. Supplementary Tables

### Table C1

*Fluid and Gas Compositions of Samples Used in Bioenergetic Calculations*

| Sample Number | Lithology | pH | T<br>°C | Cond<br>µS/cm | DO<br>µmolal | Fe$^{+2}$<br>µmolal | S$^{-2}$<br>µmolal | DIC<br>millimolal | Cl$^{-}$<br>Millimolal | Br$^{-}$<br>µmolal |
|---|---|---|---|---|---|---|---|---|---|---|
| | | | | | ***non-hyperalkaline fluids (pH <11)*** | | | | | |
| 140110B | Ultramafic | 8.4 | 23.5 | 568 | 243.76 | 0.36 | 0.34 | 3.63 | 1.58 | 1.10 |
| 140114S | Ultramafic | 7.7 | 21 | 787 | 171.88 | 0.36 | b.d.l. | 4.39 | 3.19 | 1.80 |
| 100107C | Gabbro | 9.3 | 25.4 | 778 | 250.00 | n.m. | 6.89 | 1.93 | 3.71 | b.d.l. |
| 100107D | Gabbro | 8.6 | 25.6 | 809 | n.m. | n.m. | n.m. | 3.08 | 2.98 | b.d.l. |
| 140111G | Ultramafic | 8.9 | 22.6 | 586 | 221.88 | 0.36 | 0.09 | 4.11 | 1.53 | 1.04 |
| 100109X | Ultramafic | 8.9 | 23.3 | 664 | 196.88 | n.m. | 0.39 | 4.49 | 1.71 | b.d.l. |
| 140116B | Ultramafic | 7.9 | 26.5 | 760 | 125.01 | 0.90 | 0.25 | 5.13 | 1.28 | 0.82 |
| 140116C | Ultramafic | 8.7 | 27.3 | 777 | 228.13 | 0.36 | 0.63 | 4.75 | 1.54 | 0.93 |
| 120116Q | Ultramafic | 7.7 | 25 | 744 | 287.52 | n.m. | 0.33 | 5.22 | 1.28 | 0.24 |
| 100113AP | Ultramafic | 7.9 | 27 | 723 | 100.00 | n.m. | b.d.l. | 5.17 | 1.43 | b.d.l. |
| 100114AR | Ultramafic | 8.8 | 21.5 | 923 | 284.38 | n.m. | 0.27 | 3.04 | 5.19 | b.d.l. |
| 140110D | Ultramafic | 10.4 | 21.8 | 778 | 203.13 | 0.18 | 1.31 | 0.81 | 4.79 | 4.70 |
| 140112L | Ultramafic | 9.8 | 21.3 | 659 | 253.13 | 0.72 | 0.22 | 1.88 | 3.75 | 3.48 |
| 100107E | Ultramafic | 10.1 | 26.9 | 910 | n.m. | n.m. | n.m. | 0.68 | 4.86 | b.d.l. |
| 140111H | Ultramafic | 10.2 | 20.2 | 597 | 278.14 | 0.18 | 1.22 | 1.80 | 3.08 | 1.89 |
| 140111I | Ultramafic | 10.9 | 18.8 | 683 | 231.26 | b.d.l. | 2.03 | 0.85 | 3.69 | 2.36 |
| 120114N | Ultramafic | 9.8 | 21.8 | 667 | 462.53 | n.m. | 0.64 | 2.24 | 3.17 | 0.89 |
| 100109T | Ultramafic | 9.6 | 23.7 | 685 | 218.75 | n.m. | 0.54 | 3.56 | 2.38 | b.d.l. |
| 140116D | Ultramafic | 9.1 | 27.1 | 777 | 215.63 | 0.18 | 0.66 | 3.98 | 1.92 | 1.13 |
| 120116R | Ultramafic | 10.6 | 25.8 | 767 | 350.02 | n.m. | 0.97 | 0.76 | 3.51 | 0.83 |
| 100113AN | Ultramafic | 10.2 | 28.6 | 720 | 190.63 | n.m. | 1.36 | 1.66 | 3.32 | b.d.l. |
| 100113AO | Ultramafic | 10.4 | 27.4 | 734 | 168.75 | n.m. | 0.76 | 1.40 | 3.56 | b.d.l. |
| | | | | | ***Hyperalkaline Spring Fluids (pH > 11)*** | | | | | |
| 140115X | Ultramafic | 11.4 | 29.5 | 2949 | 43.80 | 13.30 | 6.97 | 0.03 | 11.40 | 5.36 |
| 140115Y | Ultramafic | 11.6 | 24.5 | 2778 | 140.63 | 20.10 | 3.59 | 0.11 | 11.80 | 5.49 |
| 140115Z | Ultramafic | 11.3 | 32.2 | 4050 | 34.40 | 12.40 | 6.25 | 0.03 | 12.60 | 9.19 |
| 120118Y | Ultramafic | 11.5 | 32.5 | 3343 | 35.40 | n.m. | 5.44 | 0.12 | 6.80 | 1.27 |
| 120118Z | Ultramafic | 11.4 | 30.6 | 2140 | 81.30 | n.m. | 7.56 | 0.12 | 9.85 | 1.44 |
| 120129G | Ultramafic | 11.0 | 37.3 | 1455 | n.m. | n.m. | n.m. | 0.05 | 5.11 | 1.04 |
| 100111AA | Ultramafic | 11.7 | 28.5 | 3400 | 59.38 | n.m. | 7.80 | 0.04 | 11.99 | b.d.l. |
| 100111AB | Ultramafic | 11.7 | 25.4 | 2770 | 187.50 | n.m. | 2.78 | 0.13 | 12.34 | b.d.l. |
| 100111AC | Ultramafic | 11.6 | 16.5 | 1873 | 271.88 | n.m. | 0.24 | 0.69 | 11.63 | 2.52 |
| 100111AD | Ultramafic | 11.6 | 32.4 | 3235 | 31.25 | n.m. | 5.41 | 0.05 | 13.05 | b.d.l. |
| 100111AE | Ultramafic | 11.9 | 18.9 | 2468 | 250.00 | n.m. | 0.24 | 0.07 | 13.44 | 5.49 |
| 100112AG | Ultramafic | 11.1 | 37.7 | 1421 | 9.75 | n.m. | 3.21 | 0.04 | 5.73 | b.d.l. |

| | | | | | | | | | | |
|---|---|---|---|---|---|---|---|---|---|---|
| 100112AH | Ultramafic | 11.2 | 38.4 | 1537 | 50.00 | n.m. | 3.48 | 0.05 | 5.77 | 1.31 |
| 140110C | Ultramafic | 11.4 | 27 | 2011 | 17.90 | 13.10 | 13.70 | 0.05 | 7.45 | 7.84 |
| 140112K | Ultramafic | 11.4 | 26.9 | 1870 | 8.63 | 12.20 | 16.70 | 0.04 | 7.16 | 7.83 |
| 140112M | Ultramafic | 11.4 | 28.2 | 2058 | 15.80 | 8.77 | 16.10 | 0.05 | 7.36 | 7.91 |
| 140113O | Ultramafic | 11.4 | 28.4 | 2329 | 59.40 | 10.60 | 5.84 | 0.06 | 7.92 | 5.94 |
| 140113P | Ultramafic | 11.5 | 25.9 | 2224 | 50.00 | 15.60 | 1.97 | 0.05 | 7.90 | 5.68 |
| 140114R | Ultramafic | 11.6 | 21.1 | 1844 | 34.40 | 11.30 | 1.87 | 0.04 | 7.10 | 4.55 |
| 140114T | Ultramafic | 11.4 | 27.2 | 2061 | 16.30 | 13.10 | 17.70 | 0.04 | 6.89 | 4.43 |
| 140114U | Ultramafic | 11.4 | 21.7 | 1479 | 218.76 | 0.18 | 3.41 | 0.17 | 4.72 | 4.58 |
| 140114V | Ultramafic | 11.4 | 24.4 | 1803 | 190.63 | 15.60 | 8.31 | 0.23 | 6.98 | 4.65 |
| 120111A | Ultramafic | 11.6 | 22.3 | 1737 | 462.53 | n.m. | 0.85 | 0.09 | 4.62 | 1.34 |
| 120111B | Ultramafic | 11.4 | 29.4 | 1912 | 368.77 | n.m. | 5.41 | 0.09 | 6.39 | 2.12 |
| 120111C | Ultramafic | 11.3 | 31.9 | 1889 | 93.80 | n.m. | 13.70 | 0.07 | 4.94 | 1.67 |
| 120113I | Ultramafic | 11.4 | 30 | 2276 | 68.80 | n.m. | 8.07 | 0.14 | 7.24 | 2.46 |
| 120113J | Ultramafic | 11.6 | 25.8 | 2343 | 275.02 | n.m. | 0.85 | 0.09 | 3.56 | 0.92 |
| 120113K | Ultramafic | 11.4 | 30.9 | 2364 | 356.27 | n.m. | 0.15 | 0.12 | 6.10 | 2.07 |
| 120113L | Ultramafic | 11.3 | 28.4 | 2297 | 743.80 | n.m. | b.d.l. | 0.16 | 10.32 | 4.14 |
| 100108J | Ultramafic | 11.7 | 23.9 | 2214 | 187.50 | n.m. | 5.65 | 0.05 | 8.58 | b.d.l. |
| 100108K | Ultramafic | 11.7 | 24.7 | 2266 | 171.88 | n.m. | 5.02 | 0.07 | 8.35 | b.d.l. |
| 100108L | Ultramafic | 11.6 | 29.2 | 2442 | 10.20 | n.m. | 5.96 | 0.07 | 8.44 | b.d.l. |
| 100107A | Gabbro | 11.3 | 32.4 | 1900 | 2.78 | n.m. | 117.47 | 0.11 | 7.25 | b.d.l. |
| 100107B | Gabbro | 11.3 | 30.3 | 1848 | 46.88 | n.m. | 83.30 | 0.11 | 7.31 | b.d.l. |
| 140111F | Ultramafic | 11.6 | 23.8 | 1470 | 8.59 | b.d.l. | 6.78 | 0.04 | 4.66 | 2.98 |
| 120112E | Ultramafic | 11.3 | 30.1 | 1762 | 150.01 | n.m. | 1.69 | 0.07 | 3.38 | 0.93 |
| 120112F | Ultramafic | 11.4 | 27.4 | 1781 | 37.80 | n.m. | 4.96 | 0.11 | 4.32 | 1.29 |
| 100109S | Ultramafic | 11.8 | 22.4 | 1685 | 81.25 | n.m. | 1.94 | 0.10 | 5.32 | b.d.l. |
| 100109U | Ultramafic | 11.7 | 24.9 | 1778 | 12.50 | n.m. | 6.56 | 0.12 | 5.06 | b.d.l. |
| 140117F | Ultramafic | 11.5 | 26.2 | 1868 | 25.00 | 12.00 | 4.72 | 0.03 | 5.35 | 3.12 |
| 140117G | Ultramafic | 11.4 | 30.5 | 2015 | 9.88 | 11.50 | 3.75 | 0.02 | 5.33 | 3.13 |
| 140117H | Ultramafic | 11.5 | 29.6 | 2067 | 21.90 | 13.10 | 5.47 | 0.03 | 5.77 | 3.70 |
| 140117I | Ultramafic | 11.3 | 32.3 | 2000 | 12.50 | 13.80 | 3.25 | 0.05 | 5.32 | 3.13 |
| 140117J | Ultramafic | 11.3 | 31.6 | 1387 | 31.30 | 6.98 | 2.31 | 0.07 | 4.71 | 2.82 |
| 140117K | Ultramafic | 11.5 | 27.4 | 1980 | 37.50 | 10.90 | 3.16 | 0.03 | 5.76 | 3.77 |
| 140117L | Ultramafic | 11.6 | 27.3 | 2087 | 21.90 | 8.95 | 3.59 | 0.02 | 5.81 | 4.17 |
| 120116P | Ultramafic | 11.2 | 34.3 | 1745 | 46.60 | n.m. | 2.81 | 0.06 | 4.49 | 1.06 |
| 120116S | Ultramafic | 11.4 | 29.5 | 1729 | 25.00 | n.m. | 3.84 | 0.08 | 4.58 | 0.65 |
| 120117T | Ultramafic | 11.3 | 32.6 | 1721 | 22.50 | n.m. | 2.87 | 0.04 | 3.28 | 0.49 |
| 120117U | Ultramafic | 11.3 | 32 | 1720 | 8.56 | n.m. | 3.51 | 0.04 | 5.15 | 1.41 |
| 120117V | Ultramafic | 11.7 | 23.6 | 1951 | 37.50 | n.m. | 2.18 | 0.08 | 5.40 | 1.52 |
| 120117X | Ultramafic | 11.3 | 32.8 | 1681 | 25.90 | n.m. | 2.18 | 0.01 | 5.10 | 1.51 |
| 100112AJ | Ultramafic | 11.5 | 33.4 | 1782 | n.m. | n.m. | 3.05 | 0.05 | 5.58 | 1.46 |
| 100112AM | Ultramafic | 11.5 | 31.5 | 1772 | 13.13 | n.m. | 3.17 | 0.04 | 5.51 | 2.74 |
| 100114AS | Ultramafic | 11.3 | 18.2 | 1013 | 256.25 | n.m. | 0.91 | 0.47 | 6.12 | b.d.l. |
| 100114AT | Ultramafic | 11.6 | 30.4 | 1893 | 106.25 | n.m. | 2.00 | 0.04 | 6.33 | b.d.l. |

| | | | | | | | | | | |
|---|---|---|---|---|---|---|---|---|---|---|
| 100114AU | Ultramafic | 11.6 | 20.08 | 1258 | 243.75 | n.m. | 1.00 | 0.07 | 6.24 | b.d.l. |

All data except dissolved $H_2$, $CH_4$, and CO values are reported in Chapter 3 of this work. $H_2$, $CH_4$, and CO values are taken from Canovas et al. (2017) and Howells (in prep).

Table C1. (cont'd.)

| **Sample Number** | **Lithology** | **pH** | **$SO_4^{-2}$**<br>µmolal | **$NO_3^-$**<br>µmolal | **$NO_2^-$**<br>µmolal | **$Na^+$**<br>millimolal | **$NH_4^+$**<br>µmolal | **$K^+$**<br>millimolal |
|---|---|---|---|---|---|---|---|---|
| | | | ***non-hyperalkaline fluids (pH <11)*** | | | | | |
| 140110B | Ultramafic | 8.4 | 346 | 63 | 0.30 | 1.31 | b.d.l. | 0.04 |
| 140114S | Ultramafic | 7.7 | 443 | 116 | 0.22 | 3.20 | 0.31 | 0.11 |
| 100107C | Gabbro | 9.3 | 734 | 211 | 4.26 | 3.81 | b.d.l. | 0.09 |
| 100107D | Gabbro | 8.6 | 822 | 323 | 348 | 3.24 | b.d.l. | 0.07 |
| 140111G | Ultramafic | 8.9 | 326 | 49 | 0.31 | 1.53 | 0.57 | 0.04 |
| 100109X | Ultramafic | 8.9 | 381 | 80 | 0.40 | 1.76 | b.d.l. | 0.03 |
| 140116B | Ultramafic | 7.9 | 696 | 170 | 0.45 | 1.06 | 0.23 | 0.10 |
| 140116C | Ultramafic | 8.7 | 680 | 160 | b.d.l. | 1.37 | 1.16 | 0.10 |
| 120116Q | Ultramafic | 7.7 | 646 | 99 | 0.14 | 1.00 | 0.53 | 0.08 |
| 100113AP | Ultramafic | 7.9 | 727 | 122 | 0.77 | 1.16 | b.d.l. | 0.08 |
| 100114AR | Ultramafic | 8.8 | 519 | 14 | b.d.l. | 5.43 | b.d.l. | 0.10 |
| 140110D | Ultramafic | 10.4 | 180 | 27 | b.d.l. | 4.92 | 6.61 | 0.14 |
| 140112L | Ultramafic | 9.8 | 243 | 37 | b.d.l. | 3.72 | 3.38 | 0.11 |
| 100107E | Ultramafic | 10.1 | 498 | 180 | b.d.l. | 4.89 | b.d.l. | 0.10 |
| 140111H | Ultramafic | 10.2 | 182 | 13 | 0.16 | 3.59 | 3.80 | 0.08 |
| 140111I | Ultramafic | 10.9 | 154 | 8 | 0.30 | 4.36 | 5.97 | 0.10 |
| 120114N | Ultramafic | 9.8 | 207 | 9 | 0.68 | 3.78 | 1.13 | 0.08 |
| 100109T | Ultramafic | 9.6 | 334 | 52 | b.d.l. | 2.83 | b.d.l. | 0.05 |
| 140116D | Ultramafic | 9.1 | 612 | 142 | 0.07 | 1.86 | 2.54 | 0.10 |
| 120116R | Ultramafic | 10.6 | 266 | 34 | 0.48 | 4.26 | 8.03 | 0.12 |
| 100113AN | Ultramafic | 10.2 | 399 | 45 | b.d.l. | 3.83 | b.d.l. | 0.11 |
| 100113AO | Ultramafic | 10.4 | 362 | 49 | b.d.l. | 4.18 | b.d.l. | 0.11 |
| | | | ***Hyperalkaline Spring Fluids (pH > 11)*** | | | | | |
| 140115X | Ultramafic | 11.4 | 4.75 | 0.35 | b.d.l. | 13.90 | 58.70 | 0.32 |
| 140115Y | Ultramafic | 11.6 | 9.99 | 1.61 | 1.83 | 14.30 | 50.50 | 0.33 |
| 140115Z | Ultramafic | 11.3 | 2.63 | 0.12 | b.d.l. | 17.10 | 87.60 | 0.33 |
| 120118Y | Ultramafic | 11.5 | 2.18 | 0.39 | 0.35 | 9.24 | 12.20 | 0.19 |
| 120118Z | Ultramafic | 11.4 | 6.37 | 0.63 | 0.63 | 12.11 | 19.40 | 0.27 |
| 120129G | Ultramafic | 11.0 | 1.32 | 0.62 | 0.44 | 5.19 | 6.25 | 0.15 |
| 100111AA | Ultramafic | 11.7 | 4.10 | b.d.l. | 2.01 | 15.12 | b.d.l. | 0.26 |
| 100111AB | Ultramafic | 11.7 | 9.54 | b.d.l. | b.d.l. | 15.68 | b.d.l. | 0.28 |
| 100111AC | Ultramafic | 11.6 | 123.13 | 1.95 | b.d.l. | 14.63 | b.d.l. | 0.29 |
| 100111AD | Ultramafic | 11.6 | 2.08 | b.d.l. | b.d.l. | 18.11 | b.d.l. | 0.27 |
| 100111AE | Ultramafic | 11.9 | 12.80 | 3.27 | b.d.l. | 18.28 | b.d.l. | 0.29 |
| 100112AG | Ultramafic | 11.1 | 1.13 | 4.28 | b.d.l. | 6.14 | b.d.l. | 0.15 |

|  |  |  |  |  |  |  |  |  |
|---|---|---|---|---|---|---|---|---|
| 100112AH | Ultramafic | 11.2 | 0.93 | b.d.l. | b.d.l. | 6.75 | b.d.l. | 0.14 |
| 140110C | Ultramafic | 11.4 | 10.80 | 0.47 | b.d.l. | 7.91 | 19.80 | 0.22 |
| 140112K | Ultramafic | 11.4 | 18.40 | 0.11 | 0.11 | 7.59 | 22.70 | 0.21 |
| 140112M | Ultramafic | 11.4 | 10.70 | 0.06 | b.d.l. | 7.89 | 21.10 | 0.22 |
| 140113O | Ultramafic | 11.4 | 3.84 | 0.18 | b.d.l. | 9.40 | 33.60 | 0.25 |
| 140113P | Ultramafic | 11.5 | 7.82 | 3.47 | 0.77 | 9.53 | 29.20 | 0.25 |
| 140114R | Ultramafic | 11.6 | 21.10 | 11.20 | 0.76 | 8.10 | 19.80 | 0.23 |
| 140114T | Ultramafic | 11.4 | 13.50 | 0.62 | 1.16 | 7.97 | 30.60 | 0.22 |
| 140114U | Ultramafic | 11.4 | 176.00 | 26.20 | 0.14 | 8.09 | 11.90 | 0.22 |
| 140114V | Ultramafic | 11.4 | 17.70 | 1.28 | 0.86 | 8.43 | 20.30 | 0.22 |
| 120111A | Ultramafic | 11.6 | 13.10 | 10.70 | 1.67 | 5.33 | 3.30 | 0.14 |
| 120111B | Ultramafic | 11.4 | 12.90 | 2.21 | 1.35 | 7.38 | 6.47 | 0.20 |
| 120111C | Ultramafic | 11.3 | 9.52 | 0.77 | 1.47 | 5.41 | 5.40 | 0.15 |
| 120113I | Ultramafic | 11.4 | 7.19 | 0.91 | 0.62 | 8.85 | 6.61 | 0.22 |
| 120113J | Ultramafic | 11.6 | 4.76 | 2.21 | 2.79 | 4.20 | 3.71 | 0.10 |
| 120113K | Ultramafic | 11.4 | 10.80 | 2.18 | 10.70 | 7.53 | 1.74 | 0.19 |
| 120113L | Ultramafic | 11.3 | 8.84 | 14.20 | 1.96 | 12.79 | 1.53 | 0.33 |
| 100108J | Ultramafic | 11.7 | 6.51 | b.d.l. | 0.14 | 10.37 | b.d.l. | 0.22 |
| 100108K | Ultramafic | 11.7 | 4.77 | b.d.l. | b.d.l. | 10.41 | b.d.l. | 0.22 |
| 100108L | Ultramafic | 11.6 | 5.05 | b.d.l. | b.d.l. | 10.61 | b.d.l. | 0.22 |
| 100107A | Gabbro | 11.3 | 69.90 | b.d.l. | b.d.l. | 7.18 | b.d.l. | 0.12 |
| 100107B | Gabbro | 11.3 | 63.70 | b.d.l. | b.d.l. | 7.16 | b.d.l. | 0.14 |
| 140111F | Ultramafic | 11.6 | 11.30 | 1.49 | b.d.l. | 5.86 | 15.50 | 0.14 |
| 120112E | Ultramafic | 11.3 | 1.87 | 0.19 | 0.45 | 4.20 | 1.64 | 0.10 |
| 120112F | Ultramafic | 11.4 | 4.14 | 0.31 | 0.28 | 5.45 | 3.09 | 0.13 |
| 100109S | Ultramafic | 11.8 | 3.71 | 3.60 | b.d.l. | 7.03 | b.d.l. | 0.13 |
| 100109U | Ultramafic | 11.7 | 4.57 | b.d.l. | b.d.l. | 6.90 | b.d.l. | 0.11 |
| 140117F | Ultramafic | 11.5 | 3.64 | 0.44 | 0.06 | 6.41 | 18.30 | 0.15 |
| 140117G | Ultramafic | 11.4 | 1.38 | 0.02 | b.d.l. | 6.27 | 19.50 | 0.15 |
| 140117H | Ultramafic | 11.5 | 1.58 | 0.11 | b.d.l. | 7.14 | 23.50 | 0.16 |
| 140117I | Ultramafic | 11.3 | 6.46 | 0.10 | b.d.l. | 6.28 | 19.40 | 0.15 |
| 140117J | Ultramafic | 11.3 | 111.00 | 0.08 | b.d.l. | 5.83 | 16.90 | 0.14 |
| 140117K | Ultramafic | 11.5 | 1.58 | 0.09 | b.d.l. | 7.16 | 21.30 | 0.16 |
| 140117L | Ultramafic | 11.6 | 1.60 | 0.10 | b.d.l. | 7.33 | 22.70 | 0.16 |
| 120116P | Ultramafic | 11.2 | 1.78 | 0.87 | 0.38 | 5.45 | 5.31 | 0.13 |
| 120116S | Ultramafic | 11.4 | 4.38 | 0.22 | 0.39 | 5.61 | 5.45 | 0.13 |
| 120117T | Ultramafic | 11.3 | 1.13 | 0.59 | 0.67 | 4.01 | 3.69 | 0.09 |
| 120117U | Ultramafic | 11.3 | 1.78 | 0.80 | 0.35 | 6.25 | 6.86 | 0.15 |
| 120117V | Ultramafic | 11.7 | 2.21 | 3.76 | 0.70 | 6.81 | 5.64 | 0.14 |
| 120117X | Ultramafic | 11.3 | 1.26 | 2.38 | 1.74 | 6.04 | 3.14 | 0.15 |
| 100112AJ | Ultramafic | 11.5 | 1.30 | b.d.l. | b.d.l. | 7.13 | b.d.l. | 0.12 |
| 100112AM | Ultramafic | 11.5 | 1.04 | b.d.l. | b.d.l. | 7.13 | b.d.l. | 0.12 |
| 100114AS | Ultramafic | 11.3 | 220.83 | 12.30 | b.d.l. | 7.42 | b.d.l. | 0.14 |
| 100114AT | Ultramafic | 11.6 | 12.10 | b.d.l. | b.d.l. | 8.40 | b.d.l. | 0.14 |

| | | | | | | | | |
|---|---|---|---|---|---|---|---|---|
| 100114AU | Ultramafic | 11.6 | 154.89 | 7.29 | b.d.l. | 7.80 | b.d.l. | 0.14 |

All data except dissolved $H_2$, $CH_4$, and CO values are reported in Chapter 3 of this work. $H_2$, $CH_4$, and CO values are taken from Canovas et al. (2017) and Howells (in prep).

Table C1. (cont'd.)

| **Sample Number** | **Lithology** | **pH** | **$Mg^{+2}$** µmolal | **$Ca^{+2}$** millimolal | **$Si^{+4}$** µmolal | **$Al^{+3}$** µmolal | **$H_2$** µmolal | **$CH_4$** µmolal | **CO** nanomolal |
|---|---|---|---|---|---|---|---|---|---|
| ***non-hyperalkaline fluids (pH <11)*** | | | | | | | | | |
| 140110B | Ultramafic | 8.4 | 1840 | 0.49 | 183 | 0.22 | 0.01 | 0.00 | 98 |
| 140114S | Ultramafic | 7.7 | 2010 | 0.60 | 200 | 0.15 | 0.02 | 0.02 | 113 |
| 100107C | Gabbro | 9.3 | 1445 | 0.33 | 289 | 2.19 | 0.03 | 2.10 | 246 |
| 100107D | Gabbro | 8.6 | 1522 | 0.84 | 347 | 0.12 | 0.02 | 0.08 | 155 |
| 140111G | Ultramafic | 8.9 | 2140 | 0.36 | 276 | 0.13 | 0.24 | 1.62 | 93 |
| 100109X | Ultramafic | 8.9 | 2290 | 0.40 | 283 | 0.07 | 0.06 | 1.05 | 161 |
| 140116B | Ultramafic | 7.9 | 2810 | 0.56 | 303 | 0.15 | 0.06 | 0.02 | 98 |
| 140116C | Ultramafic | 8.7 | 2680 | 0.63 | 279 | 0.12 | 2.18 | 0.92 | 114 |
| 120116Q | Ultramafic | 7.7 | 2908 | 0.51 | 309 | 0.12 | n.m. | n.m. | n.m. |
| 100113AP | Ultramafic | 7.9 | 2680 | 0.58 | 288 | 0.32 | 0.07 | 0.03 | 214 |
| 100114AR | Ultramafic | 8.8 | 1485 | 0.45 | 79 | 0.08 | 0.03 | 0.01 | 111 |
| 140110D | Ultramafic | 10.4 | 782 | 0.48 | 91 | 0.24 | 0.06 | 8.91 | 63 |
| 140112L | Ultramafic | 9.8 | 1150 | 0.31 | 111 | 0.25 | 0.01 | 1.32 | 71 |
| 100107E | Ultramafic | 10.1 | 885 | 0.14 | 214 | 6.67 | n.m. | n.m. | n.m. |
| 140111H | Ultramafic | 10.2 | 1170 | 0.21 | 145 | 0.13 | 1.10 | 8.00 | 186 |
| 140111I | Ultramafic | 10.9 | 807 | 0.37 | 100 | 0.13 | 2.07 | 7.75 | 97 |
| 120114N | Ultramafic | 9.8 | 1082 | 0.28 | 133 | 0.09 | n.m. | n.m. | n.m. |
| 100109T | Ultramafic | 9.6 | 1924 | 0.04 | 226 | 0.09 | 3.19 | 14.10 | 122 |
| 140116D | Ultramafic | 9.1 | 2430 | 0.72 | 260 | 0.12 | 12.50 | 0.14 | 231 |
| 120116R | Ultramafic | 10.6 | 807 | 0.19 | 83 | 0.24 | n.m. | n.m. | n.m. |
| 100113AN | Ultramafic | 10.2 | 1433 | 2.17 | 157 | 0.40 | 42.10 | 3.65 | 118 |
| 100113AO | Ultramafic | 10.4 | 1298 | 0.52 | 138 | 0.05 | 7.95 | 4.63 | 185 |
| ***Hyperalkaline Spring Fluids (pH > 11)*** | | | | | | | | | |
| 140115X | Ultramafic | 11.4 | 0.45 | 1.89 | 2.22 | 0.92 | 233.00 | 7.86 | 140 |
| 140115Y | Ultramafic | 11.6 | 1.26 | 1.79 | 2.16 | 0.30 | 20.80 | 3.25 | 80 |
| 140115Z | Ultramafic | 11.3 | 0.41 | 2.37 | 1.38 | 0.15 | 226.00 | 19.00 | 107 |
| 120118Y | Ultramafic | 11.5 | 1.02 | 1.88 | 2.36 | 0.41 | n.m. | n.m. | n.m. |
| 120118Z | Ultramafic | 11.4 | 0.70 | 1.50 | 2.96 | 0.49 | n.m. | n.m. | n.m. |
| 120129G | Ultramafic | 11.0 | 0.63 | 1.48 | 2.82 | 0.32 | n.m. | n.m. | n.m. |
| 100111AA | Ultramafic | 11.7 | 0.28 | 1.66 | 1.79 | 0.15 | 106.65 | 6.19 | 58 |
| 100111AB | Ultramafic | 11.7 | 0.79 | 1.61 | 2.45 | 0.52 | 7.26 | 1.46 | 130 |
| 100111AC | Ultramafic | 11.6 | 180.79 | 0.33 | 38.10 | 0.05 | 0.68 | 0.42 | 188 |
| 100111AD | Ultramafic | 11.6 | 0.28 | 2.18 | 0.55 | 0.10 | 104.31 | 11.00 | 101 |
| 100111AE | Ultramafic | 11.9 | 1.46 | 0.73 | 7.84 | 0.34 | 0.14 | 0.09 | 152 |
| 100112AG | Ultramafic | 11.1 | 0.65 | 1.73 | 1.37 | 0.07 | 273.40 | 37.70 | 65 |
| 100112AH | Ultramafic | 11.2 | 0.34 | 1.58 | 1.43 | 0.13 | 157.77 | 20.10 | 37 |
| 140110C | Ultramafic | 11.4 | 1.30 | 1.96 | 4.26 | 0.82 | 6.42 | 204.00 | 80 |
| 140112K | Ultramafic | 11.4 | 2.24 | 1.89 | 3.88 | 0.97 | 0.49 | 276.00 | 139 |
| 140112M | Ultramafic | 11.4 | 0.67 | 1.98 | 5.60 | 1.33 | 30.70 | 242.00 | 121 |
| 140113O | Ultramafic | 11.4 | 1.07 | 2.09 | 3.68 | 0.54 | 39.20 | 4.61 | 119 |
| 140113P | Ultramafic | 11.5 | 1.28 | 2.03 | 1.94 | 0.23 | 65.60 | 14.40 | 88 |
| 140114R | Ultramafic | 11.6 | 1.46 | 1.85 | 2.44 | 0.44 | 0.01 | 17.20 | 159 |
| 140114T | Ultramafic | 11.4 | 1.83 | 1.91 | 1.84 | 0.17 | 27.80 | 40.80 | 248 |
| 140114U | Ultramafic | 11.4 | 16.10 | 1.17 | 7.43 | 0.07 | 0.02 | 0.09 | 163 |
| 140114V | Ultramafic | 11.4 | 5.60 | 1.71 | 2.75 | 0.15 | 0.17 | 1.52 | 236 |
| 120111A | Ultramafic | 11.6 | 2.04 | 1.31 | 7.88 | 0.47 | n.m. | n.m. | n.m. |
| 120111B | Ultramafic | 11.4 | 1.32 | 1.71 | 4.46 | 0.40 | n.m. | n.m. | n.m. |

| | | | | | | | | | |
|---|---|---|---|---|---|---|---|---|---|
| 120111C | Ultramafic | 11.3 | 1.07 | 1.72 | 6.40 | 0.49 | n.m. | n.m. | n.m. |
| 120113I | Ultramafic | 11.4 | 2.42 | 1.71 | 3.29 | 0.23 | n.m. | n.m. | n.m. |
| 120113J | Ultramafic | 11.6 | 0.59 | 1.72 | 3.82 | 0.69 | n.m. | n.m. | n.m. |
| 120113K | Ultramafic | 11.4 | 0.45 | 1.60 | 20.40 | 3.04 | n.m. | n.m. | n.m. |
| 120113L | Ultramafic | 11.3 | 0.96 | 0.73 | 26.40 | 2.82 | n.m. | n.m. | n.m. |
| 100108J | Ultramafic | 11.7 | 1.97 | 1.89 | 1.73 | 0.13 | 1.61 | 0.81 | 275 |
| 100108K | Ultramafic | 11.7 | 1.78 | 1.87 | 1.60 | 0.07 | 11.00 | 2.95 | 266 |
| 100108L | Ultramafic | 11.6 | 0.70 | 1.94 | 0.89 | 0.09 | 159.36 | 16.20 | 93 |
| 100107A | Gabbro | 11.3 | 0.21 | 2.06 | 37.20 | 22.60 | 0.73 | 99.70 | 145 |
| 100107B | Gabbro | 11.3 | 6.31 | 1.91 | 39.30 | 23.30 | 0.13 | 38.80 | 268 |
| 140111F | Ultramafic | 11.6 | 3.82 | 1.69 | 10.50 | 0.25 | 263.00 | 158.00 | 93 |
| 120112E | Ultramafic | 11.3 | 0.68 | 1.74 | 5.56 | 0.54 | n.m. | n.m. | n.m. |
| 120112F | Ultramafic | 11.4 | 1.93 | 1.72 | 4.62 | 0.27 | n.m. | n.m. | n.m. |
| 100109S | Ultramafic | 11.8 | 0.54 | 1.59 | 3.77 | 0.63 | 22.70 | 51.90 | 141 |
| 100109U | Ultramafic | 11.7 | 1.23 | 1.51 | 0.47 | 0.35 | 111.20 | 131.62 | 78 |
| 140117F | Ultramafic | 11.5 | 1.94 | 1.85 | 2.65 | 0.25 | 265.00 | 13.30 | 168 |
| 140117G | Ultramafic | 11.4 | 0.79 | 1.90 | 1.50 | 0.13 | 2.75 | 9.29 | 44 |
| 140117H | Ultramafic | 11.5 | 1.04 | 2.08 | 1.66 | 0.13 | 225.00 | 12.70 | 181 |
| 140117I | Ultramafic | 11.3 | 8.09 | 1.86 | 1.96 | 0.12 | 227.00 | 13.60 | 159 |
| 140117J | Ultramafic | 11.3 | 19.50 | 0.83 | 48.90 | 0.06 | 218.00 | 13.30 | 187 |
| 140117K | Ultramafic | 11.5 | 1.48 | 2.08 | 2.26 | 0.23 | n.m. | n.m. | n.m. |
| 140117L | Ultramafic | 11.6 | 1.47 | 2.14 | 1.87 | 0.19 | n.m. | n.m. | n.m. |
| 120116P | Ultramafic | 11.2 | 2.49 | 1.67 | 1.70 | 0.38 | n.m. | n.m. | n.m. |
| 120116S | Ultramafic | 11.4 | 4.54 | 1.70 | 2.23 | 0.13 | n.m. | n.m. | n.m. |
| 120117T | Ultramafic | 11.3 | 1.48 | 1.65 | 2.08 | 0.43 | n.m. | n.m. | n.m. |
| 120117U | Ultramafic | 11.3 | 0.87 | 1.65 | 1.77 | 0.39 | n.m. | n.m. | n.m. |
| 120117V | Ultramafic | 11.7 | 0.68 | 1.75 | 3.63 | 0.61 | n.m. | n.m. | n.m. |
| 120117X | Ultramafic | 11.3 | 0.56 | 1.67 | 2.37 | 0.42 | n.m. | n.m. | n.m. |
| 100112AJ | Ultramafic | 11.5 | 1.33 | 1.90 | 0.59 | 0.33 | 321.27 | 26.20 | 66 |
| 100112AM | Ultramafic | 11.5 | 0.62 | 1.92 | 0.53 | 0.06 | 258.64 | 21.00 | 84 |
| 100114AS | Ultramafic | 11.3 | 291.09 | 0.30 | 22.70 | 0.04 | 0.03 | 1.31 | 88 |
| 100114AT | Ultramafic | 11.6 | 0.70 | 1.72 | 3.53 | 0.58 | 10.10 | 10.80 | 138 |
| 100114AU | Ultramafic | 11.6 | 156.80 | 0.29 | 16.10 | 0.10 | 0.20 | 1.01 | 131 |

All data except dissolved $H_2$, $CH_4$, and CO values are reported in Chapter 3 of this work. $H_2$, $CH_4$, and CO values are taken from Canovas et al. (2017) and Howells (in prep).

Table C2

*Calculated Eh, pe, and log f$O_2$ Values Using Dissolved $O_2$ and $H_2$ Concentrations of Investigated Fluids*

| **Sample Number** | **pH** | **T (°C)** | $O_2$ | | | $H_2$ | | |
|---|---|---|---|---|---|---|---|---|
| | | | Eh (V) | pe | log f$O_2$ | Eh (V) | pe | log f$O_2$ |
| ***Fluids with pH <11*** | | | | | | | | |
| 140110B | 8.4 | 23.5 | 0.7 | 12.3 | -0.7 | -0.3 | -5.9 | -73.5 |
| 140114S | 7.7 | 21 | 0.8 | 13.2 | -0.9 | -0.3 | -5.3 | -75.0 |
| 100107C | 9.3 | 25.4 | 0.7 | 11.3 | -0.7 | -0.4 | -7.1 | -74.1 |
| 100107D | 8.6 | 25.6 | n.c. | n.c. | n.c. | -0.4 | -6.3 | -73.9 |
| 140111G | 8.9 | 22.6 | 0.7 | 11.8 | -0.8 | -0.4 | -7.2 | -76.9 |
| 100109X | 8.9 | 23.3 | 0.7 | 11.8 | -0.8 | -0.4 | -6.9 | -75.5 |
| 140116B | 7.9 | 26.5 | 0.7 | 12.5 | -1.0 | -0.3 | -5.8 | -74.4 |
| 140116C | 8.7 | 27.3 | 0.7 | 11.7 | -0.7 | -0.4 | -7.4 | -77.3 |
| 120116Q | 7.7 | 25 | 0.8 | 13.0 | -0.7 | n.c. | n.c. | n.c. |
| 100113AP | 7.9 | 27 | 0.7 | 12.5 | -1.1 | -0.3 | -5.8 | -74.3 |
| 100114AR | 8.8 | 21.5 | 0.7 | 12.1 | -0.7 | -0.4 | -6.6 | -75.6 |
| 140110D | 10.4 | 21.8 | 0.6 | 10.4 | -0.8 | -0.5 | -8.4 | -75.9 |
| 140112L | 9.8 | 21.3 | 0.6 | 11.1 | -0.7 | -0.4 | -7.3 | -74.5 |
| 100107E | 10.1 | 26.9 | n.c. | n.c. | n.c. | -0.5 | -7.9 | -73.7 |
| 140111H | 10.2 | 20.2 | 0.6 | 10.7 | -0.7 | -0.5 | -8.9 | -79.1 |
| 140111I | 10.9 | 18.8 | 0.6 | 10.2 | -0.8 | -0.6 | -9.6 | -80.1 |
| 120114N | 9.8 | 21.8 | 0.7 | 11.1 | -0.5 | n.c. | n.c. | n.c. |
| 100109T | 9.6 | 23.7 | 0.7 | 11.1 | -0.8 | -0.5 | -8.4 | -78.8 |
| 140116D | 9.1 | 27.1 | 0.7 | 11.3 | -0.8 | -0.5 | -8.2 | -78.9 |
| 120116R | 10.6 | 25.8 | 0.6 | 10.0 | -0.6 | n.c. | n.c. | n.c. |
| 100113AN | 10.2 | 28.6 | 0.6 | 10.1 | -0.8 | -0.6 | -9.5 | -79.4 |
| 100113AO | 10.4 | 27.4 | 0.6 | 10.0 | -0.9 | -0.6 | -9.4 | -78.4 |
| ***Fluids with pH>11*** | | | | | | | | |
| 140115X | 11.4 | 29.5 | 0.5 | 8.7 | -1.4 | -0.7 | -11.1 | -80.6 |
| 140115Y | 11.6 | 24.5 | 0.5 | 9.0 | -1.0 | -0.6 | -10.8 | -80.2 |
| 140115Z | 11.3 | 32.2 | 0.5 | 8.6 | -1.5 | -0.7 | -11.0 | -79.7 |
| 120118Y | 11.5 | 32.5 | 0.5 | 8.4 | -1.5 | n.c. | n.c. | n.c. |
| 120118Z | 11.4 | 30.6 | 0.5 | 8.7 | -1.2 | n.c. | n.c. | n.c. |
| 120129G | 11.0 | 37.3 | n.c. | n.c. | n.c. | n.c. | n.c. | n.c. |
| 100111AA | 11.7 | 28.5 | 0.5 | 8.6 | -1.3 | -0.7 | -11.2 | -80.3 |
| 100111AB | 11.7 | 25.4 | 0.5 | 8.8 | -0.8 | -0.6 | -10.7 | -78.9 |
| 100111AC | 11.6 | 16.5 | 0.6 | 9.7 | -0.7 | -0.6 | -10.1 | -79.9 |
| 100111AD | 11.6 | 32.4 | 0.5 | 8.3 | -1.6 | -0.7 | -11.1 | -79.0 |
| 100111AE | 11.9 | 18.9 | 0.5 | 9.2 | -0.8 | -0.6 | -10.1 | -77.7 |
| 100112AG | 11.1 | 37.7 | 0.5 | 8.2 | -2.0 | -0.7 | -10.8 | -78.2 |
| 100112AH | 11.2 | 38.4 | 0.5 | 8.4 | -1.3 | -0.7 | -10.7 | -77.5 |

| | | | | | | | | |
|---|---|---|---|---|---|---|---|---|
| 140110C | 11.4 | 27 | 0.5 | 8.8 | -1.8 | -0.6 | -10.3 | -78.3 |
| 140112K | 11.4 | 26.9 | 0.5 | 8.7 | -2.2 | -0.6 | -9.8 | -76.1 |
| 140112M | 11.4 | 28.2 | 0.5 | 8.7 | -1.9 | -0.6 | -10.6 | -79.3 |
| 140113O | 11.4 | 28.4 | 0.5 | 8.8 | -1.3 | -0.6 | -10.7 | -79.4 |
| 140113P | 11.5 | 25.9 | 0.5 | 8.9 | -1.4 | -0.6 | -10.9 | -80.7 |
| 140114R | 11.6 | 21.1 | 0.5 | 9.1 | -1.6 | -0.5 | -9.2 | -74.8 |
| 140114T | 11.4 | 27.2 | 0.5 | 8.7 | -1.9 | -0.6 | -10.7 | -79.5 |
| 140114U | 11.4 | 21.7 | 0.6 | 9.5 | -0.8 | -0.5 | -9.1 | -74.9 |
| 140114V | 11.4 | 24.4 | 0.5 | 9.2 | -0.8 | -0.6 | -9.6 | -76.0 |
| 120111A | 11.6 | 22.3 | 0.5 | 9.3 | -0.5 | n.c. | n.c. | n.c. |
| 120111B | 11.4 | 29.4 | 0.5 | 9.0 | -0.5 | n.c. | n.c. | n.c. |
| 120111C | 11.3 | 31.9 | 0.5 | 8.7 | -1.1 | n.c. | n.c. | n.c. |
| 120113I | 11.4 | 30 | 0.5 | 8.7 | -1.2 | n.c. | n.c. | n.c. |
| 120113J | 11.6 | 25.8 | 0.5 | 9.0 | -0.7 | n.c. | n.c. | n.c. |
| 120113K | 11.4 | 30.9 | 0.5 | 8.8 | -0.5 | n.c. | n.c. | n.c. |
| 120113L | 11.3 | 28.4 | 0.5 | 9.2 | -0.2 | n.c. | n.c. | n.c. |
| 100108J | 11.7 | 23.9 | 0.5 | 8.9 | -0.8 | -0.6 | -10.4 | -78.1 |
| 100108K | 11.7 | 24.7 | 0.5 | 8.9 | -0.9 | -0.6 | -10.8 | -79.5 |
| 100108L | 11.6 | 29.2 | 0.5 | 8.4 | -2.1 | -0.7 | -11.2 | -80.4 |
| 100107A | 11.3 | 32.4 | 0.5 | 8.3 | -2.6 | -0.6 | -9.7 | -74.7 |
| 100107B | 11.3 | 30.3 | 0.5 | 8.7 | -1.4 | -0.6 | -9.4 | -73.9 |
| 140111F | 11.6 | 23.8 | 0.5 | 8.7 | -2.2 | -0.7 | -11.4 | -82.6 |
| 120112E | 11.3 | 30.1 | 0.5 | 8.9 | -0.9 | n.c. | n.c. | n.c. |
| 120112F | 11.4 | 27.4 | 0.5 | 8.8 | -1.5 | n.c. | n.c. | n.c. |
| 100109S | 11.8 | 22.4 | 0.5 | 8.9 | -1.2 | -0.6 | -11.0 | -80.9 |
| 100109U | 11.7 | 24.9 | 0.5 | 8.6 | -2.0 | -0.7 | -11.3 | -81.5 |
| 140117F | 11.5 | 26.2 | 0.5 | 8.8 | -1.7 | -0.7 | -11.2 | -81.8 |
| 140117G | 11.4 | 30.5 | 0.5 | 8.5 | -2.1 | -0.6 | -10.1 | -76.4 |
| 140117H | 11.5 | 29.6 | 0.5 | 8.5 | -1.7 | -0.7 | -11.2 | -80.6 |
| 140117I | 11.3 | 32.3 | 0.5 | 8.5 | -2.0 | -0.7 | -11.0 | -79.7 |
| 140117J | 11.3 | 31.6 | 0.5 | 8.6 | -1.6 | -0.7 | -11.0 | -79.9 |
| 140117K | 11.5 | 27.4 | 0.5 | 8.7 | -1.5 | n.c. | n.c. | n.c. |
| 140117L | 11.6 | 27.3 | 0.5 | 8.6 | -1.8 | n.c. | n.c. | n.c. |
| 120116P | 11.2 | 34.3 | 0.5 | 8.6 | -1.4 | n.c. | n.c. | n.c. |
| 120116S | 11.4 | 29.5 | 0.5 | 8.7 | -1.7 | n.c. | n.c. | n.c. |
| 120117T | 11.3 | 32.6 | 0.5 | 8.5 | -1.7 | n.c. | n.c. | n.c. |
| 120117U | 11.3 | 32 | 0.5 | 8.4 | -2.1 | n.c. | n.c. | n.c. |
| 120117V | 11.7 | 23.6 | 0.5 | 8.8 | -1.5 | n.c. | n.c. | n.c. |
| 120117X | 11.3 | 32.8 | 0.5 | 8.5 | -1.6 | n.c. | n.c. | n.c. |
| 100112AJ | 11.5 | 33.4 | n.c. | n.c. | n.c. | -0.7 | -11.2 | -79.6 |
| 100112AM | 11.5 | 31.5 | 0.5 | 8.3 | -1.9 | -0.7 | -11.2 | -80.1 |
| 100114AS | 11.3 | 18.2 | 0.6 | 9.8 | -0.8 | -0.5 | -9.1 | -76.6 |
| 100114AT | 11.6 | 30.4 | 0.5 | 8.5 | -1.0 | -0.6 | -10.6 | -77.6 |
| 100114AU | 11.6 | 20.08 | 0.5 | 9.4 | -0.8 | -0.6 | -9.8 | -77.6 |

n.c. - not calculated due to lack in compositional data

Table C3

*Calculated Affinities ($A_r$, kcal/mole $e^-$ transferred) via Chemolithotrophic Reactions Listed in Table 4.1.*

| Sample Number | pH | T (°C) | Hydrogen Oxidation | Aerobic Methane Oxidation | CO Oxidation | Sulfide Oxidation | Ammonia Oxidation | Nitrite Oxidation |
|---|---|---|---|---|---|---|---|---|
| ***Fluids with pH <11*** | | | | | | | | |
| 140110B | 8.4 | 23.5 | 24.7 | 23.8 | 29.9 | 23.3 | n.c. | 7.6 |
| 140114S | 7.7 | 21 | 24.9 | 23.7 | 29.3 | n.c. | 9.9 | 7.3 |
| 100107C | 9.3 | 25.4 | 25.0 | 24.5 | 31.0 | 23.6 | n.c. | 8.0 |
| 100107D | 8.6 | 25.6 | n.c. | n.c. | n.c. | n.c. | n.c. | n.c. |
| 140111G | 8.9 | 22.6 | 25.7 | 24.3 | 30.2 | 23.3 | 10.5 | 7.7 |
| 100109X | 8.9 | 23.3 | 25.3 | 24.3 | 30.3 | 23.4 | n.c. | 7.6 |
| 140116B | 7.9 | 26.5 | 25.2 | 23.7 | 29.3 | 23.0 | 9.9 | 7.3 |
| 140116C | 8.7 | 27.3 | 26.3 | 24.2 | 30.0 | 23.3 | 10.4 | n.c. |
| 120116Q | 7.7 | 25 | n.c. | n.c. | n.c. | 23.2 | 10.0 | 7.2 |
| 100113AP | 7.9 | 27 | 25.1 | 23.7 | 29.5 | n.c. | n.c. | 7.5 |
| 100114AR | 8.8 | 21.5 | 25.2 | 24.0 | 30.3 | 23.4 | n.c. | n.c. |
| 140110D | 10.4 | 21.8 | 25.3 | 24.9 | 31.9 | 23.8 | 11.0 | n.c. |
| 140112L | 9.8 | 21.3 | 24.8 | 24.5 | 31.0 | 23.6 | 10.8 | n.c. |
| 100107E | 10.1 | 26.9 | n.c. | n.c. | n.c. | n.c. | n.c. | n.c. |
| 140111H | 10.2 | 20.2 | 26.3 | 24.8 | 31.8 | 23.8 | 11.0 | 7.9 |
| 140111I | 10.9 | 18.8 | 26.5 | 25.0 | 32.5 | 23.9 | 11.2 | 8.2 |
| 120114N | 9.8 | 21.8 | n.c. | n.c. | n.c. | 23.7 | 11.0 | 8.5 |
| 100109T | 9.6 | 23.7 | 26.5 | 24.6 | 30.8 | 23.5 | n.c. | n.c. |
| 140116D | 9.1 | 27.1 | 26.8 | 24.1 | 30.6 | 23.4 | 10.5 | 6.9 |
| 120116R | 10.6 | 25.8 | n.c. | n.c. | n.c. | 23.8 | 11.1 | 7.9 |
| 100113AN | 10.2 | 28.6 | 27.1 | 24.7 | 31.7 | 23.6 | n.c. | n.c. |
| 100113AO | 10.4 | 27.4 | 26.6 | 24.8 | 32.1 | 23.6 | n.c. | n.c. |
| ***Fluids with pH>11*** | | | | | | | | |
| 140115X | 11.4 | 29.5 | 27.4 | 25.2 | 34.3 | 24.1 | 11.4 | n.c. |
| 140115Y | 11.6 | 24.5 | 27.0 | 25.3 | 34.1 | 24.2 | 11.5 | 9.1 |
| 140115Z | 11.3 | 32.2 | 27.3 | 25.2 | 34.2 | 24.1 | 11.5 | n.c. |
| 120118Y | 11.5 | 32.5 | n.c. | n.c. | n.c. | 24.1 | 11.3 | 8.8 |
| 120118Z | 11.4 | 30.6 | n.c. | n.c. | n.c. | 24.1 | 11.4 | 9.0 |
| 120129G | 11.0 | 37.3 | n.c. | n.c. | n.c. | n.c. | n.c. | n.c. |
| 100111AA | 11.7 | 28.5 | 27.2 | 25.3 | 34.3 | 24.2 | n.c. | n.c. |
| 100111AB | 11.7 | 25.4 | 26.7 | 25.3 | 34.5 | 24.3 | n.c. | n.c. |
| 100111AC | 11.6 | 16.5 | 26.2 | 25.1 | 33.6 | 24.0 | n.c. | n.c. |
| 100111AD | 11.6 | 32.4 | 27.1 | 25.3 | 34.4 | 24.1 | n.c. | n.c. |
| 100111AE | 11.9 | 18.9 | 25.7 | 25.2 | 34.8 | 24.2 | n.c. | n.c. |

| | | | | | | | | |
|---|---|---|---|---|---|---|---|---|
| 100112AG | 11.1 | 37.7 | 27.1 | 25.0 | 33.5 | 23.8 | n.c. | n.c. |
| 100112AH | 11.2 | 38.4 | 27.1 | 25.2 | 33.5 | 24.1 | n.c. | n.c. |
| 140110C | 11.4 | 27 | 26.2 | 25.3 | 33.8 | 24.0 | 11.2 | n.c. |
| 140112K | 11.4 | 26.9 | 25.4 | 25.2 | 34.0 | 23.8 | 11.2 | 8.6 |
| 140112M | 11.4 | 28.2 | 26.7 | 25.3 | 33.9 | 23.9 | 11.3 | n.c. |
| 140113O | 11.4 | 28.4 | 26.9 | 25.2 | 34.2 | 24.1 | 11.5 | n.c. |
| 140113P | 11.5 | 25.9 | 27.1 | 25.3 | 34.2 | 24.0 | 11.2 | 8.5 |
| 140114R | 11.6 | 21.1 | 24.6 | 25.3 | 34.4 | 23.9 | 11.1 | 8.1 |
| 140114T | 11.4 | 27.2 | 26.7 | 25.2 | 34.3 | 23.9 | 11.2 | 8.9 |
| 140114U | 11.4 | 21.7 | 25.0 | 25.0 | 33.9 | 24.0 | 11.2 | 7.6 |
| 140114V | 11.4 | 24.4 | 25.6 | 25.2 | 34.0 | 24.2 | 11.5 | 9.0 |
| 120111A | 11.6 | 22.3 | n.c. | n.c. | n.c. | 24.3 | 11.3 | 8.7 |
| 120111B | 11.4 | 29.4 | n.c. | n.c. | n.c. | 24.3 | 11.4 | 9.0 |
| 120111C | 11.3 | 31.9 | n.c. | n.c. | n.c. | 24.2 | 11.3 | 9.2 |
| 120113I | 11.4 | 30 | n.c. | n.c. | n.c. | 24.1 | 11.3 | 8.8 |
| 120113J | 11.6 | 25.8 | n.c. | n.c. | n.c. | 24.2 | 11.4 | 9.2 |
| 120113K | 11.4 | 30.9 | n.c. | n.c. | n.c. | 24.0 | 11.4 | 9.7 |
| 120113L | 11.3 | 28.4 | n.c. | n.c. | n.c. | n.c. | 11.3 | 8.7 |
| 100108J | 11.7 | 23.9 | 26.3 | 25.3 | 34.9 | 24.3 | n.c. | n.c. |
| 100108K | 11.7 | 24.7 | 26.8 | 25.4 | 34.8 | 24.3 | n.c. | n.c. |
| 100108L | 11.6 | 29.2 | 27.1 | 25.1 | 34.0 | 23.9 | n.c. | n.c. |
| 100107A | 11.3 | 32.4 | 25.2 | 24.9 | 33.4 | 23.6 | n.c. | n.c. |
| 100107B | 11.3 | 30.3 | 25.1 | 25.2 | 34.0 | 24.1 | n.c. | n.c. |
| 140111F | 11.6 | 23.8 | 27.3 | 25.3 | 34.1 | 23.8 | 11.0 | n.c. |
| 120112E | 11.3 | 30.1 | n.c. | n.c. | n.c. | 24.2 | 11.4 | 9.3 |
| 120112F | 11.4 | 27.4 | n.c. | n.c. | n.c. | 24.1 | 11.2 | 8.8 |
| 100109S | 11.8 | 22.4 | 26.9 | 25.5 | 34.4 | 24.2 | n.c. | n.c. |
| 100109U | 11.7 | 24.9 | 27.1 | 25.2 | 33.9 | 24.0 | n.c. | n.c. |
| 140117F | 11.5 | 26.2 | 27.4 | 25.2 | 34.4 | 24.0 | 11.3 | 8.2 |
| 140117G | 11.4 | 30.5 | 25.8 | 25.1 | 33.9 | 23.9 | 11.4 | n.c. |
| 140117H | 11.5 | 29.6 | 27.3 | 25.2 | 34.5 | 24.1 | 11.4 | n.c. |
| 140117I | 11.3 | 32.3 | 27.2 | 25.0 | 34.0 | 23.8 | 11.2 | n.c. |
| 140117J | 11.3 | 31.6 | 27.3 | 25.1 | 33.9 | 23.7 | 11.4 | n.c. |
| 140117K | 11.5 | 27.4 | n.c. | n.c. | n.c. | 24.1 | 11.4 | n.c. |
| 140117L | 11.6 | 27.3 | n.c. | n.c. | n.c. | 24.1 | 11.4 | n.c. |
| 120116P | 11.2 | 34.3 | n.c. | n.c. | n.c. | 24.0 | 11.2 | 8.6 |
| 120116S | 11.4 | 29.5 | n.c. | n.c. | n.c. | 23.9 | 11.2 | 8.9 |
| 120117T | 11.3 | 32.6 | n.c. | n.c. | n.c. | 24.0 | 11.1 | 8.8 |
| 120117U | 11.3 | 32 | n.c. | n.c. | n.c. | 23.8 | 10.9 | 8.3 |
| 120117V | 11.7 | 23.6 | n.c. | n.c. | n.c. | 24.1 | 11.1 | 8.4 |
| 120117X | 11.3 | 32.8 | n.c. | n.c. | n.c. | 24.0 | 11.0 | 8.7 |
| 100112AJ | 11.5 | 33.4 | n.c. | n.c. | n.c. | n.c. | n.c. | n.c. |
| 100112AM | 11.5 | 31.5 | 27.2 | 25.2 | 34.1 | 24.0 | n.c. | n.c. |
| 100114AS | 11.3 | 18.2 | 25.3 | 25.1 | 33.1 | 23.9 | n.c. | n.c. |
| 100114AT | 11.6 | 30.4 | 26.6 | 25.4 | 34.7 | 24.1 | n.c. | n.c. |
| 100114AU | 11.6 | 20.08 | 25.8 | 25.3 | 34.2 | 24.0 | n.c. | n.c. |

n.c. - not calculated due to lack in compositional data

Table C3 (cont’d.)

| **Sample Number** | **pH** | **T (°C)** | **Methanogenesis** | **Sulfate Reduction** | **Anaerobic Methane Oxidation (sulfate)** | **Anaerobic Methane Oxidation (nitrate)** | **Anaerobic Methane Oxidation (nitrite)** |
|---|---|---|---|---|---|---|---|
| | | | ***Fluids with pH <11*** | | | | |
| 140110B | 8.4 | 23.5 | 0.9 | 1.4 | 0.5 | 21.0 | 14.5 |
| 140114S | 7.7 | 21 | 1.2 | n.c. | n.c. | 21.2 | 14.7 |
| 100107C | 9.3 | 25.4 | 0.6 | 1.4 | 0.8 | 21.5 | 14.9 |
| 100107D | 8.6 | 25.6 | 1.0 | n.c. | n.c. | 21.4 | 15.4 |
| 140111G | 8.9 | 22.6 | 1.4 | 2.4 | 1.0 | 21.3 | 14.7 |
| 100109X | 8.9 | 23.3 | 1.1 | 1.9 | 0.9 | 21.4 | 14.7 |
| 140116B | 7.9 | 26.5 | 1.5 | 2.1 | 0.6 | 21.2 | 14.6 |
| 140116C | 8.7 | 27.3 | 2.1 | 3.0 | 0.9 | 21.4 | n.c. |
| 120116Q | 7.7 | 25 | n.c. | n.c. | n.c. | n.c. | n.c. |
| 100113AP | 7.9 | 27 | 1.5 | n.c. | n.c. | 21.2 | 14.7 |
| 100114AR | 8.8 | 21.5 | 1.2 | 1.9 | 0.6 | 20.9 | n.c. |
| 140110D | 10.4 | 21.8 | 0.5 | 1.5 | 1.1 | 21.4 | n.c. |
| 140112L | 9.8 | 21.3 | 0.3 | 1.3 | 1.0 | 21.3 | n.c. |
| 100107E | 10.1 | 26.9 | 0.3 | n.c. | n.c. | 21.6 | n.c. |
| 140111H | 10.2 | 20.2 | 1.5 | 2.5 | 1.0 | 21.3 | 14.6 |
| 140111I | 10.9 | 18.8 | 1.4 | 2.5 | 1.1 | 21.3 | 14.6 |
| 120114N | 9.8 | 21.8 | n.c. | n.c. | n.c. | n.c. | n.c. |
| 100109T | 9.6 | 23.7 | 1.9 | 2.9 | 1.1 | 21.5 | n.c. |
| 140116D | 9.1 | 27.1 | 2.7 | 3.4 | 0.7 | 21.2 | 14.3 |
| 120116R | 10.6 | 25.8 | n.c. | n.c. | n.c. | n.c. | n.c. |
| 100113AN | 10.2 | 28.6 | 2.4 | 3.5 | 1.1 | 21.4 | n.c. |
| 100113AO | 10.4 | 27.4 | 1.9 | 3.0 | 1.1 | 21.4 | n.c. |
| | | | ***Fluids with pH>11*** | | | | |
| 140115X | 11.4 | 29.5 | 2.2 | 3.3 | 1.2 | 21.2 | n.c. |
| 140115Y | 11.6 | 24.5 | 1.7 | 2.7 | 1.1 | 21.3 | 14.8 |
| 140115Z | 11.3 | 32.2 | 2.1 | 3.3 | 1.2 | 21.1 | n.c. |
| 120118Y | 11.5 | 32.5 | n.c. | n.c. | n.c. | n.c. | n.c. |
| 120118Z | 11.4 | 30.6 | n.c. | n.c. | n.c. | n.c. | n.c. |
| 120129G | 11.0 | 37.3 | n.c. | n.c. | n.c. | n.c. | n.c. |
| 100111AA | 11.7 | 28.5 | 1.9 | 3.0 | 1.1 | n.c. | 14.8 |
| 100111AB | 11.7 | 25.4 | 1.3 | 2.4 | 1.1 | n.c. | n.c. |
| 100111AC | 11.6 | 16.5 | 1.2 | 2.3 | 1.1 | 21.0 | n.c. |
| 100111AD | 11.6 | 32.4 | 1.8 | 3.0 | 1.2 | n.c. | n.c. |
| 100111AE | 11.9 | 18.9 | 0.5 | 1.5 | 1.1 | 21.1 | n.c. |
| 100112AG | 11.1 | 37.7 | 2.1 | 3.3 | 1.2 | 21.5 | n.c. |
| 100112AH | 11.2 | 38.4 | 1.9 | 3.1 | 1.1 | n.c. | n.c. |
| 140110C | 11.4 | 27 | 0.9 | 2.3 | 1.4 | 21.5 | n.c. |
| 140112K | 11.4 | 26.9 | 0.1 | 1.6 | 1.4 | 21.3 | 14.7 |

| | | | | | | | |
|---|---|---|---|---|---|---|---|
| 140112M | 11.4 | 28.2 | 1.4 | 2.7 | 1.4 | 21.2 | n.c. |
| 140113O | 11.4 | 28.4 | 1.7 | 2.8 | 1.1 | 21.0 | n.c. |
| 140113P | 11.5 | 25.9 | 1.8 | 3.1 | 1.3 | 21.5 | 14.8 |
| 140114R | 11.6 | 21.1 | -0.7 | 0.7 | 1.4 | 21.7 | 14.8 |
| 140114T | 11.4 | 27.2 | 1.5 | 2.7 | 1.3 | 21.4 | 14.9 |
| 140114U | 11.4 | 21.7 | 0.0 | 1.0 | 0.9 | 21.3 | 14.3 |
| 140114V | 11.4 | 24.4 | 0.4 | 1.3 | 0.9 | 21.1 | 14.6 |
| 120111A | 11.6 | 22.3 | n.c. | n.c. | n.c. | n.c. | n.c. |
| 120111B | 11.4 | 29.4 | n.c. | n.c. | n.c. | n.c. | n.c. |
| 120111C | 11.3 | 31.9 | n.c. | n.c. | n.c. | n.c. | n.c. |
| 120113I | 11.4 | 30 | n.c. | n.c. | n.c. | n.c. | n.c. |
| 120113J | 11.6 | 25.8 | n.c. | n.c. | n.c. | n.c. | n.c. |
| 120113K | 11.4 | 30.9 | n.c. | n.c. | n.c. | n.c. | n.c. |
| 120113L | 11.3 | 28.4 | n.c. | n.c. | n.c. | n.c. | n.c. |
| 100108J | 11.7 | 23.9 | 0.9 | 1.9 | 1.0 | n.c. | 14.4 |
| 100108K | 11.7 | 24.7 | 1.4 | 2.4 | 1.1 | n.c. | n.c. |
| 100108L | 11.6 | 29.2 | 2.0 | 3.2 | 1.2 | n.c. | n.c. |
| 100107A | 11.3 | 32.4 | 0.3 | 1.5 | 1.2 | n.c. | n.c. |
| 100107B | 11.3 | 30.3 | -0.1 | 1.1 | 1.2 | n.c. | n.c. |
| 140111F | 11.6 | 23.8 | 2.0 | 3.5 | 1.4 | 21.6 | n.c. |
| 120112E | 11.3 | 30.1 | n.c. | n.c. | n.c. | n.c. | n.c. |
| 120112F | 11.4 | 27.4 | n.c. | n.c. | n.c. | n.c. | n.c. |
| 100109S | 11.8 | 22.4 | 1.5 | 2.7 | 1.3 | 21.6 | n.c. |
| 100109U | 11.7 | 24.9 | 1.8 | 3.1 | 1.3 | n.c. | n.c. |
| 140117F | 11.5 | 26.2 | 2.2 | 3.4 | 1.2 | 21.3 | 14.5 |
| 140117G | 11.4 | 30.5 | 0.8 | 1.9 | 1.2 | 20.9 | n.c. |
| 140117H | 11.5 | 29.6 | 2.1 | 3.2 | 1.2 | 21.1 | n.c. |
| 140117I | 11.3 | 32.3 | 2.1 | 3.4 | 1.3 | 21.0 | n.c. |
| 140117J | 11.3 | 31.6 | 2.2 | 3.6 | 1.4 | 20.9 | n.c. |
| 140117K | 11.5 | 27.4 | n.c. | n.c. | n.c. | n.c. | n.c. |
| 140117L | 11.6 | 27.3 | n.c. | n.c. | n.c. | n.c. | n.c. |
| 120116P | 11.2 | 34.3 | n.c. | n.c. | n.c. | n.c. | n.c. |
| 120116S | 11.4 | 29.5 | n.c. | n.c. | n.c. | n.c. | n.c. |
| 120117T | 11.3 | 32.6 | n.c. | n.c. | n.c. | n.c. | n.c. |
| 120117U | 11.3 | 32 | n.c. | n.c. | n.c. | n.c. | n.c. |
| 120117V | 11.7 | 23.6 | n.c. | n.c. | n.c. | n.c. | n.c. |
| 120117X | 11.3 | 32.8 | n.c. | n.c. | n.c. | n.c. | n.c. |
| 100112AJ | 11.5 | 33.4 | 2.1 | 3.3 | 1.2 | n.c. | n.c. |
| 100112AM | 11.5 | 31.5 | 2.1 | 3.3 | 1.2 | n.c. | n.c. |
| 100114AS | 11.3 | 18.2 | 0.2 | 1.3 | 1.1 | 21.3 | n.c. |
| 100114AT | 11.6 | 30.4 | 1.1 | 2.5 | 1.4 | n.c. | n.c. |
| 100114AU | 11.6 | 20.08 | 0.5 | 1.8 | 1.3 | 21.4 | n.c. |

n.c. - not calculated due to lack in compositional data

Table C3. (cont’d)

| Sample Number | pH | T (°C) | Nitrate Reduction | Nitrogen Reduction | Water-Gas Shift | Annamox | CO Reduction |
|---|---|---|---|---|---|---|---|
| *Fluids with pH <11* | | | | | | | |
| 140110B | 8.4 | 23.5 | n.c. | n.c. | 5.2 | n.c. | 2.9 |
| 140114S | 7.7 | 21 | 15.0 | 2.7 | 4.4 | 23.0 | 3.1 |
| 100107C | 9.3 | 25.4 | n.c. | n.c. | 5.9 | n.c. | 2.8 |
| 100107D | 8.6 | 25.6 | n.c. | n.c. | 5.2 | n.c. | 3.0 |
| 140111G | 8.9 | 22.6 | 15.3 | 2.8 | 4.5 | 23.1 | 3.4 |
| 100109X | 8.9 | 23.3 | n.c. | n.c. | 5.0 | n.c. | 3.1 |
| 140116B | 7.9 | 26.5 | 15.3 | 2.9 | 4.1 | 23.0 | 3.4 |
| 140116C | 8.7 | 27.3 | 15.9 | 3.3 | 3.7 | n.c. | 4.0 |
| 120116Q | 7.7 | 25 | n.c. | n.c. | n.c. | 22.9 | n.c. |
| 100113AP | 7.9 | 27 | n.c. | n.c. | 4.4 | n.c. | 3.4 |
| 100114AR | 8.8 | 21.5 | n.c. | n.c. | 5.0 | n.c. | 3.3 |
| 140110D | 10.4 | 21.8 | 14.3 | 1.7 | 6.5 | n.c. | 2.8 |
| 140112L | 9.8 | 21.3 | 14.0 | 1.3 | 6.2 | n.c. | 2.5 |
| 100107E | 10.1 | 26.9 | n.c. | n.c. | 6.9 | n.c. | 2.7 |
| 140111H | 10.2 | 20.2 | 15.2 | 2.7 | 5.5 | 23.0 | 3.8 |
| 140111I | 10.9 | 18.8 | 15.3 | 2.8 | 6.1 | 23.0 | 4.0 |
| 120114N | 9.8 | 21.8 | n.c. | n.c. | n.c. | 23.2 | n.c. |
| 100109T | 9.6 | 23.7 | n.c. | n.c. | 4.4 | n.c. | 3.9 |
| 140116D | 9.1 | 27.1 | 16.3 | 3.6 | 3.8 | 23.0 | 4.8 |
| 120116R | 10.6 | 25.8 | n.c. | n.c. | n.c. | 23.1 | n.c. |
| 100113AN | 10.2 | 28.6 | n.c. | n.c. | 4.6 | n.c. | 4.8 |
| 100113AO | 10.4 | 27.4 | n.c. | n.c. | 5.4 | n.c. | 4.3 |
| *Fluids with pH>11* | | | | | | | |
| 140115X | 11.4 | 29.5 | 16.0 | 3.6 | 6.9 | n.c. | 5.2 |
| 140115Y | 11.6 | 24.5 | 15.4 | 3.0 | 7.2 | 23.3 | 4.6 |
| 140115Z | 11.3 | 32.2 | 15.8 | 3.5 | 6.9 | n.c. | 5.0 |
| 120118Y | 11.5 | 32.5 | n.c. | n.c. | n.c. | 22.5 | n.c. |
| 120118Z | 11.4 | 30.6 | n.c. | n.c. | n.c. | 22.8 | n.c. |
| 120129G | 11.0 | 37.3 | n.c. | n.c. | n.c. | 22.5 | n.c. |
| 100111AA | 11.7 | 28.5 | n.c. | n.c. | 7.1 | n.c. | 4.9 |
| 100111AB | 11.7 | 25.4 | n.c. | n.c. | 7.8 | n.c. | 4.4 |
| 100111AC | 11.6 | 16.5 | n.c. | n.c. | 7.4 | n.c. | 4.0 |
| 100111AD | 11.6 | 32.4 | n.c. | n.c. | 7.3 | n.c. | 4.8 |
| 100111AE | 11.9 | 18.9 | n.c. | n.c. | 9.0 | n.c. | 3.7 |
| 100112AG | 11.1 | 37.7 | n.c. | n.c. | 6.4 | n.c. | 4.9 |
| 100112AH | 11.2 | 38.4 | n.c. | n.c. | 6.4 | n.c. | 4.7 |
| 140110C | 11.4 | 27 | 15.0 | 2.8 | 7.6 | n.c. | 3.8 |
| 140112K | 11.4 | 26.9 | 14.2 | 2.0 | 8.6 | 22.6 | 3.0 |
| 140112M | 11.4 | 28.2 | 15.3 | 3.2 | 7.3 | n.c. | 4.3 |
| 140113O | 11.4 | 28.4 | 15.4 | 3.2 | 7.3 | n.c. | 4.7 |
| 140113P | 11.5 | 25.9 | 15.9 | 3.4 | 7.1 | 23.0 | 4.8 |
| 140114R | 11.6 | 21.1 | 13.5 | 1.0 | 9.7 | 23.1 | 2.4 |
| 140114T | 11.4 | 27.2 | 15.5 | 3.1 | 7.6 | 23.1 | 4.5 |
| 140114U | 11.4 | 21.7 | 13.8 | 1.2 | 8.9 | 22.7 | 3.0 |
| 140114V | 11.4 | 24.4 | 14.1 | 1.7 | 8.4 | 23.1 | 3.4 |

| | | | | | | | |
|---|---|---|---|---|---|---|---|
| 120111A | 11.6 | 22.3 | n.c. | n.c. | n.c. | 22.8 | n.c. |
| 120111B | 11.4 | 29.4 | n.c. | n.c. | n.c. | 22.8 | n.c. |
| 120111C | 11.3 | 31.9 | n.c. | n.c. | n.c. | 22.7 | n.c. |
| 120113I | 11.4 | 30 | n.c. | n.c. | n.c. | 22.6 | n.c. |
| 120113J | 11.6 | 25.8 | n.c. | n.c. | n.c. | 22.9 | n.c. |
| 120113K | 11.4 | 30.9 | n.c. | n.c. | n.c. | 22.9 | n.c. |
| 120113L | 11.3 | 28.4 | n.c. | n.c. | n.c. | 22.6 | n.c. |
| 100108J | 11.7 | 23.9 | n.c. | n.c. | 8.7 | n.c. | 4.1 |
| 100108K | 11.7 | 24.7 | n.c. | n.c. | 8.0 | n.c. | 4.5 |
| 100108L | 11.6 | 29.2 | n.c. | n.c. | 6.9 | n.c. | 5.0 |
| 100107A | 11.3 | 32.4 | n.c. | n.c. | 8.2 | n.c. | 3.2 |
| 100107B | 11.3 | 30.3 | n.c. | n.c. | 8.9 | n.c. | 2.8 |
| 140111F | 11.6 | 23.8 | 16.3 | 4.0 | 6.8 | n.c. | 5.0 |
| 120112E | 11.3 | 30.1 | n.c. | n.c. | n.c. | 22.3 | n.c. |
| 120112F | 11.4 | 27.4 | n.c. | n.c. | n.c. | 22.4 | n.c. |
| 100109S | 11.8 | 22.4 | n.c. | n.c. | 7.5 | n.c. | 4.4 |
| 100109U | 11.7 | 24.9 | n.c. | n.c. | 6.8 | n.c. | 4.7 |
| 140117F | 11.5 | 26.2 | 16.2 | 3.9 | 7.0 | 22.4 | 5.3 |
| 140117G | 11.4 | 30.5 | 14.5 | 2.5 | 8.1 | n.c. | 3.7 |
| 140117H | 11.5 | 29.6 | 15.9 | 3.8 | 7.2 | n.c. | 5.2 |
| 140117I | 11.3 | 32.3 | 15.9 | 3.8 | 6.8 | n.c. | 5.1 |
| 140117J | 11.3 | 31.6 | 15.9 | 3.9 | 6.6 | n.c. | 5.1 |
| 140117K | 11.5 | 27.4 | n.c. | n.c. | n.c. | n.c. | n.c. |
| 140117L | 11.6 | 27.3 | n.c. | n.c. | n.c. | n.c. | n.c. |
| 120116P | 11.2 | 34.3 | n.c. | n.c. | n.c. | 22.4 | n.c. |
| 120116S | 11.4 | 29.5 | n.c. | n.c. | n.c. | 22.5 | n.c. |
| 120117T | 11.3 | 32.6 | n.c. | n.c. | n.c. | 22.5 | n.c. |
| 120117U | 11.3 | 32 | n.c. | n.c. | n.c. | 22.5 | n.c. |
| 120117V | 11.7 | 23.6 | n.c. | n.c. | n.c. | 22.7 | n.c. |
| 120117X | 11.3 | 32.8 | n.c. | n.c. | n.c. | 22.7 | n.c. |
| 100112AJ | 11.5 | 33.4 | n.c. | n.c. | 6.7 | n.c. | 5.0 |
| 100112AM | 11.5 | 31.5 | n.c. | n.c. | 6.9 | n.c. | 5.1 |
| 100114AS | 11.3 | 18.2 | n.c. | n.c. | 7.9 | n.c. | 2.9 |
| 100114AT | 11.6 | 30.4 | n.c. | n.c. | 8.1 | n.c. | 4.2 |
| 100114AU | 11.6 | 20.08 | n.c. | n.c. | 8.4 | n.c. | 3.5 |

n.c. - not calculated due to lack in compositional data

Table C4

*Calculated Energy Yield (Er, log calories/kg fluid) via Chemolithotrophic Reactions Listed in Table 4.1.*

| **Sample Number** | **pH** | **T (°C)** | **Hydrogen Oxidation** | **Aerobic Methane Oxidation** | **Carbon Monoxide Oxidation** | **Sulfide Oxidation** | **Ammonia Oxidation** | **Nitrite Oxidation** |
|---|---|---|---|---|---|---|---|---|
| ***Fluids with pH <11*** | | | | | | | | |
| 140110B | 8.4 | 23.5 | -3.5 | -3.1 | -2.2 | -1.2 | n.c. | -2.3 |
| 140114S | 7.7 | 21 | -3.1 | -2.5 | -2.2 | n.c. | -1.6 | -2.5 |
| 100107C | 9.3 | 25.4 | -2.9 | -0.4 | -1.8 | 0.1 | n.c. | -1.2 |
| 100107D | 8.6 | 25.6 | n.c. | n.c. | n.c. | n.c. | n.c. | n.c. |
| 140111G | 8.9 | 22.6 | -1.9 | -0.5 | -2.3 | -1.8 | -1.3 | -2.3 |
| 100109X | 8.9 | 23.3 | -2.5 | -0.7 | -2.0 | -1.1 | n.c. | -2.2 |
| 140116B | 7.9 | 26.5 | -2.5 | -2.5 | -2.2 | -1.3 | -1.7 | -2.2 |
| 140116C | 8.7 | 27.3 | -0.9 | -0.7 | -2.2 | -0.9 | -1.0 | n.c. |
| 120116Q | 7.7 | 25 | n.c. | n.c. | n.c. | -1.2 | -1.4 | -2.7 |
| 100113AP | 7.9 | 27 | -2.5 | -2.3 | -1.9 | n.c. | n.c. | -1.9 |
| 100114AR | 8.8 | 21.5 | -2.8 | -2.6 | -2.2 | -1.3 | n.c. | n.c. |
| 140110D | 10.4 | 21.8 | -2.5 | 0.2 | -2.4 | -0.6 | -0.2 | n.c. |
| 140112L | 9.8 | 21.3 | -3.3 | -0.6 | -2.4 | -1.4 | -0.5 | n.c. |
| 100107E | 10.1 | 26.9 | n.c. | n.c. | n.c. | n.c. | n.c. | n.c. |
| 140111H | 10.2 | 20.2 | -1.2 | 0.2 | -1.9 | -0.6 | -0.5 | -2.6 |
| 140111I | 10.9 | 18.8 | -1.0 | 0.2 | -2.2 | -0.4 | -0.3 | -2.3 |
| 120114N | 9.8 | 21.8 | n.c. | n.c. | n.c. | -0.9 | -1.0 | -1.9 |
| 100109T | 9.6 | 23.7 | -0.8 | 0.4 | -2.1 | -1.0 | n.c. | n.c. |
| 140116D | 9.1 | 27.1 | -0.2 | -1.6 | -1.8 | -0.9 | -0.7 | -3.0 |
| 120116R | 10.6 | 25.8 | n.c. | n.c. | n.c. | -0.7 | -0.1 | -2.1 |
| 100113AN | 10.2 | 28.6 | 0.4 | -0.1 | -2.1 | -0.6 | n.c. | n.c. |
| 100113AO | 10.4 | 27.4 | -0.4 | 0.0 | -1.9 | -0.8 | n.c. | n.c. |
| ***Fluids with pH>11*** | | | | | | | | |
| 140115X | 11.4 | 29.5 | 0.7 | 0.2 | -2.0 | 0.1 | 0.3 | n.c. |
| 140115Y | 11.6 | 24.5 | 0.0 | -0.2 | -2.3 | -0.2 | 0.7 | -1.5 |
| 140115Z | 11.3 | 32.2 | 0.6 | 0.5 | -2.1 | 0.1 | 0.2 | n.c. |
| 120118Y | 11.5 | 32.5 | n.c. | n.c. | n.c. | 0.0 | 0.0 | -2.2 |
| 120118Z | 11.4 | 30.6 | n.c. | n.c. | n.c. | 0.2 | 0.2 | -2.0 |
| 120129G | 11.0 | 37.3 | n.c. | n.c. | n.c. | n.c. | n.c. | n.c. |
| 100111AA | 11.7 | 28.5 | 0.8 | 0.1 | -2.4 | 0.2 | n.c. | n.c. |
| 100111AB | 11.7 | 25.4 | -0.4 | -0.5 | -2.0 | -0.3 | n.c. | n.c. |
| 100111AC | 11.6 | 16.5 | -1.4 | -1.1 | -1.9 | -1.3 | n.c. | n.c. |
| 100111AD | 11.6 | 32.4 | 0.5 | 0.3 | -2.2 | 0.0 | n.c. | n.c. |
| 100111AE | 11.9 | 18.9 | -2.1 | -1.7 | -2.0 | -1.3 | n.c. | n.c. |
| 100112AG | 11.1 | 37.7 | 0.0 | 0.0 | -2.4 | -0.2 | n.c. | n.c. |

| | | | | | | | | |
|---|---|---|---|---|---|---|---|---|
| 100112AH | 11.2 | 38.4 | 0.7 | 0.6 | -2.6 | -0.2 | n.c. | n.c. |
| 140110C | 11.4 | 27 | -0.5 | 0.3 | -2.3 | 0.2 | -0.1 | n.c. |
| 140112K | 11.4 | 26.9 | -1.6 | -0.1 | -2.0 | -0.1 | -0.4 | -2.7 |
| 140112M | 11.4 | 28.2 | 0.2 | 0.2 | -2.1 | 0.2 | -0.1 | n.c. |
| 140113O | 11.4 | 28.4 | 0.3 | 0.0 | -2.1 | 0.1 | 0.4 | n.c. |
| 140113P | 11.5 | 25.9 | 0.6 | 0.5 | -2.2 | -0.4 | 0.4 | -1.9 |
| 140114R | 11.6 | 21.1 | -3.2 | 0.5 | -2.0 | -0.4 | 0.2 | -1.9 |
| 140114T | 11.4 | 27.2 | 0.2 | 0.2 | -1.8 | 0.2 | -0.1 | -1.7 |
| 140114U | 11.4 | 21.7 | -3.1 | -1.7 | -2.0 | -0.2 | 0.0 | -2.7 |
| 140114V | 11.4 | 24.4 | -2.1 | -0.5 | -1.8 | 0.2 | 0.3 | -1.8 |
| 120111A | 11.6 | 22.3 | n.c. | n.c. | n.c. | -0.8 | -0.5 | -1.5 |
| 120111B | 11.4 | 29.4 | n.c. | n.c. | n.c. | 0.0 | -0.2 | -1.6 |
| 120111C | 11.3 | 31.9 | n.c. | n.c. | n.c. | 0.4 | -0.3 | -1.6 |
| 120113I | 11.4 | 30 | n.c. | n.c. | n.c. | 0.2 | -0.2 | -2.0 |
| 120113J | 11.6 | 25.8 | n.c. | n.c. | n.c. | -0.8 | -0.5 | -1.3 |
| 120113K | 11.4 | 30.9 | n.c. | n.c. | n.c. | -1.5 | -0.8 | -0.7 |
| 120113L | 11.3 | 28.4 | n.c. | n.c. | n.c. | n.c. | -0.9 | -1.5 |
| 100108J | 11.7 | 23.9 | -1.1 | -0.8 | -1.7 | 0.0 | n.c. | n.c. |
| 100108K | 11.7 | 24.7 | -0.2 | -0.2 | -1.7 | 0.0 | n.c. | n.c. |
| 100108L | 11.6 | 29.2 | 0.0 | 0.0 | -2.2 | 0.0 | n.c. | n.c. |
| 100107A | 11.3 | 32.4 | -1.4 | -0.6 | -2.0 | -0.6 | n.c. | n.c. |
| 100107B | 11.3 | 30.3 | -2.2 | 0.7 | -1.7 | 0.7 | n.c. | n.c. |
| 140111F | 11.6 | 23.8 | 0.0 | -0.1 | -2.2 | -0.1 | -0.4 | n.c. |
| 120112E | 11.3 | 30.1 | n.c. | n.c. | n.c. | -0.5 | -0.8 | -2.1 |
| 120112F | 11.4 | 27.4 | n.c. | n.c. | n.c. | 0.0 | -0.6 | -2.3 |
| 100109S | 11.8 | 22.4 | 0.1 | 0.9 | -2.0 | -0.4 | n.c. | n.c. |
| 100109U | 11.7 | 24.9 | 0.1 | 0.1 | -2.3 | 0.1 | n.c. | n.c. |
| 140117F | 11.5 | 26.2 | 0.4 | 0.4 | -1.9 | 0.0 | 0.1 | -3.0 |
| 140117G | 11.4 | 30.5 | -0.8 | 0.0 | -2.5 | -0.1 | -0.3 | n.c. |
| 140117H | 11.5 | 29.6 | 0.4 | 0.3 | -1.9 | 0.0 | 0.0 | n.c. |
| 140117I | 11.3 | 32.3 | 0.1 | 0.1 | -2.0 | -0.2 | -0.3 | n.c. |
| 140117J | 11.3 | 31.6 | 0.5 | 0.4 | -1.9 | -0.4 | 0.2 | n.c. |
| 140117K | 11.5 | 27.4 | n.c. | n.c. | n.c. | -0.2 | 0.2 | n.c. |
| 140117L | 11.6 | 27.3 | n.c. | n.c. | n.c. | -0.2 | 0.0 | n.c. |
| 120116P | 11.2 | 34.3 | n.c. | n.c. | n.c. | -0.3 | -0.3 | -2.2 |
| 120116S | 11.4 | 29.5 | n.c. | n.c. | n.c. | -0.1 | -0.3 | -2.2 |
| 120117T | 11.3 | 32.6 | n.c. | n.c. | n.c. | -0.3 | -0.5 | -1.9 |
| 120117U | 11.3 | 32 | n.c. | n.c. | n.c. | -0.2 | -0.4 | -2.2 |
| 120117V | 11.7 | 23.6 | n.c. | n.c. | n.c. | -0.4 | -0.3 | -1.9 |
| 120117X | 11.3 | 32.8 | n.c. | n.c. | n.c. | -0.4 | -0.6 | -1.5 |
| 100112AJ | 11.5 | 33.4 | n.c. | n.c. | n.c. | n.c. | n.c. | n.c. |
| 100112AM | 11.5 | 31.5 | 0.2 | 0.1 | -2.2 | -0.2 | n.c. | n.c. |
| 100114AS | 11.3 | 18.2 | -2.8 | -0.6 | -2.2 | -0.8 | n.c. | n.c. |
| 100114AT | 11.6 | 30.4 | -0.3 | 0.3 | -2.0 | -0.4 | n.c. | n.c. |
| 100114AU | 11.6 | 20.08 | -2.0 | -0.7 | -2.0 | -0.7 | n.c. | n.c. |

n.c. - not calculated due to lack in compositional data

Table C4 (cont'd.)

| Sample Number | pH | T (°C) | Methanogenesis | Sulfate Reduction | Anaerobic Methane Oxidation (sulfate) | Anaerobic Methane Oxidation (nitrate) | Anaerobic Methane Oxidation (nitrite) |
|---|---|---|---|---|---|---|---|
| | | | ***Fluids with pH <11*** | | | | |
| 140110B | 8.4 | 23.5 | -4.9 | -4.7 | -4.8 | -3.2 | -3.1 |
| 140114S | 7.7 | 21 | -4.4 | n.c. | n.c. | -2.5 | -2.5 |
| 100107C | 9.3 | 25.4 | -4.5 | -4.1 | -1.9 | -0.4 | -0.5 |
| 100107D | 8.6 | 25.6 | -4.3 | n.c. | n.c. | -1.8 | -1.8 |
| 140111G | 8.9 | 22.6 | -3.2 | -2.9 | -1.9 | -0.6 | -1.6 |
| 100109X | 8.9 | 23.3 | -3.9 | -3.6 | -2.1 | -0.7 | -1.5 |
| 140116B | 7.9 | 26.5 | -3.7 | -3.6 | -4.1 | -2.6 | -2.5 |
| 140116C | 8.7 | 27.3 | -2.0 | -1.9 | -2.2 | -0.8 | n.c. |
| 120116Q | 7.7 | 25 | n.c. | n.c. | n.c. | n.c. | n.c. |
| 100113AP | 7.9 | 27 | -3.7 | n.c. | n.c. | -2.3 | -2.3 |
| 100114AR | 8.8 | 21.5 | -4.1 | -3.9 | -4.2 | -2.7 | n.c. |
| 140110D | 10.4 | 21.8 | -4.3 | -3.8 | -1.1 | 0.2 | n.c. |
| 140112L | 9.8 | 21.3 | -5.3 | -4.6 | -2.0 | -0.6 | n.c. |
| 100107E | 10.1 | 26.9 | -4.7 | n.c. | n.c. | -0.1 | n.c. |
| 140111H | 10.2 | 20.2 | -2.5 | -2.3 | -1.2 | 0.1 | -1.9 |
| 140111I | 10.9 | 18.8 | -2.2 | -2.0 | -1.2 | 0.0 | -1.7 |
| 120114N | 9.8 | 21.8 | n.c. | n.c. | n.c. | n.c. | n.c. |
| 100109T | 9.6 | 23.7 | -1.9 | -1.7 | -0.9 | 0.4 | n.c. |
| 140116D | 9.1 | 27.1 | -1.2 | -1.1 | -3.1 | -1.6 | -2.3 |
| 120116R | 10.6 | 25.8 | n.c. | n.c. | n.c. | n.c. | n.c. |
| 100113AN | 10.2 | 28.6 | -0.7 | -0.5 | -1.5 | -0.2 | n.c. |
| 100113AO | 10.4 | 27.4 | -1.5 | -1.3 | -1.4 | -0.1 | n.c. |
| | | | ***Fluids with pH>11*** | | | | |
| 140115X | 11.4 | 29.5 | -0.3 | -1.0 | -1.4 | -1.4 | n.c. |
| 140115Y | 11.6 | 24.5 | -1.2 | -0.9 | -1.5 | -0.8 | -0.9 |
| 140115Z | 11.3 | 32.2 | -0.3 | -1.2 | -1.7 | -1.9 | n.c. |
| 120118Y | 11.5 | 32.5 | n.c. | n.c. | n.c. | n.c. | n.c. |
| 120118Z | 11.4 | 30.6 | n.c. | n.c. | n.c. | n.c. | n.c. |
| 120129G | 11.0 | 37.3 | n.c. | n.c. | n.c. | n.c. | n.c. |
| 100111AA | 11.7 | 28.5 | -0.4 | -1.0 | -1.5 | n.c. | -0.8 |
| 100111AB | 11.7 | 25.4 | -1.7 | -1.5 | -1.9 | n.c. | n.c. |
| 100111AC | 11.6 | 16.5 | -2.8 | -2.5 | -2.4 | -1.2 | n.c. |
| 100111AD | 11.6 | 32.4 | -0.4 | -1.4 | -1.8 | n.c. | n.c. |
| 100111AE | 11.9 | 18.9 | -3.9 | -3.4 | -3.1 | -1.8 | n.c. |
| 100112AG | 11.1 | 37.7 | -0.1 | -1.6 | -2.0 | -0.3 | n.c. |
| 100112AH | 11.2 | 38.4 | -0.2 | -1.7 | -2.1 | n.c. | n.c. |
| 140110C | 11.4 | 27 | -1.9 | -1.5 | -1.0 | -1.3 | n.c. |
| 140112K | 11.4 | 26.9 | -3.9 | -2.8 | -0.7 | -1.9 | -2.1 |

|  |  |  |  |  |  |  |  |
|---|---|---|---|---|---|---|---|
| 140112M | 11.4 | 28.2 | -1.1 | -0.8 | -1.0 | -2.2 | n.c. |
| 140113O | 11.4 | 28.4 | -0.9 | -1.1 | -1.5 | -1.7 | n.c. |
| 140113P | 11.5 | 25.9 | -0.6 | -0.8 | -1.1 | -0.4 | -1.2 |
| 140114R | 11.6 | 21.1 | n.c. | -4.8 | -0.7 | 0.1 | -1.3 |
| 140114T | 11.4 | 27.2 | -1.1 | -0.8 | -0.9 | -1.2 | -1.1 |
| 140114U | 11.4 | 21.7 | -6.4 | -4.5 | -3.2 | -1.8 | -2.0 |
| 140114V | 11.4 | 24.4 | -3.9 | -3.3 | -1.9 | -0.9 | -1.2 |
| 120111A | 11.6 | 22.3 | n.c. | n.c. | n.c. | n.c. | n.c. |
| 120111B | 11.4 | 29.4 | n.c. | n.c. | n.c. | n.c. | n.c. |
| 120111C | 11.3 | 31.9 | n.c. | n.c. | n.c. | n.c. | n.c. |
| 120113I | 11.4 | 30 | n.c. | n.c. | n.c. | n.c. | n.c. |
| 120113J | 11.6 | 25.8 | n.c. | n.c. | n.c. | n.c. | n.c. |
| 120113K | 11.4 | 30.9 | n.c. | n.c. | n.c. | n.c. | n.c. |
| 120113L | 11.3 | 28.4 | n.c. | n.c. | n.c. | n.c. | n.c. |
| 100108J | 11.7 | 23.9 | -2.5 | -2.2 | -2.2 | n.c. | -2.0 |
| 100108K | 11.7 | 24.7 | -1.5 | -1.3 | -1.6 | n.c. | n.c. |
| 100108L | 11.6 | 29.2 | -0.2 | -0.9 | -1.4 | n.c. | n.c. |
| 100107A | 11.3 | 32.4 | -3.4 | -2.6 | -0.2 | n.c. | n.c. |
| 100107B | 11.3 | 30.3 | n.c. | -3.5 | -0.4 | n.c. | n.c. |
| 140111F | 11.6 | 23.8 | -0.2 | -0.6 | -0.9 | -0.8 | n.c. |
| 120112E | 11.3 | 30.1 | n.c. | n.c. | n.c. | n.c. | n.c. |
| 120112F | 11.4 | 27.4 | n.c. | n.c. | n.c. | n.c. | n.c. |
| 100109S | 11.8 | 22.4 | -1.2 | -1.1 | -1.5 | -0.4 | n.c. |
| 100109U | 11.7 | 24.9 | -0.4 | -1.0 | -1.4 | n.c. | n.c. |
| 140117F | 11.5 | 26.2 | -0.3 | -1.1 | -1.5 | -1.3 | -2.4 |
| 140117G | 11.4 | 30.5 | -2.4 | -2.0 | -1.9 | -2.8 | n.c. |
| 140117H | 11.5 | 29.6 | -0.3 | -1.4 | -1.9 | -1.9 | n.c. |
| 140117I | 11.3 | 32.3 | -0.1 | -0.8 | -1.2 | -2.0 | n.c. |
| 140117J | 11.3 | 31.6 | 0.0 | 0.2 | -0.8 | -2.1 | n.c. |
| 140117K | 11.5 | 27.4 | n.c. | n.c. | n.c. | n.c. | n.c. |
| 140117L | 11.6 | 27.3 | n.c. | n.c. | n.c. | n.c. | n.c. |
| 120116P | 11.2 | 34.3 | n.c. | n.c. | n.c. | n.c. | n.c. |
| 120116S | 11.4 | 29.5 | n.c. | n.c. | n.c. | n.c. | n.c. |
| 120117T | 11.3 | 32.6 | n.c. | n.c. | n.c. | n.c. | n.c. |
| 120117U | 11.3 | 32 | n.c. | n.c. | n.c. | n.c. | n.c. |
| 120117V | 11.7 | 23.6 | n.c. | n.c. | n.c. | n.c. | n.c. |
| 120117X | 11.3 | 32.8 | n.c. | n.c. | n.c. | n.c. | n.c. |
| 100112AJ | 11.5 | 33.4 | -0.1 | -1.5 | -1.9 | n.c. | n.c. |
| 100112AM | 11.5 | 31.5 | -0.2 | -1.6 | -2.1 | n.c. | n.c. |
| 100114AS | 11.3 | 18.2 | -5.0 | -4.1 | -1.9 | -0.7 | n.c. |
| 100114AT | 11.6 | 30.4 | -1.6 | -1.3 | -0.9 | n.c. | n.c. |
| 100114AU | 11.6 | 20.08 | -3.7 | -3.2 | -2.0 | -0.8 | n.c. |

n.c. - not calculated due to lack in compositional data

Table C4. (cont'd)

| Sample Number | pH | T (°C) | Nitrate Reduction | Nitrogen Reduction | Water-Gas Shift | Annamox | CO Reduction |
|---|---|---|---|---|---|---|---|
| ***Fluids with pH <11*** | | | | | | | |
| 140110B | 8.4 | 23.5 | n.c. | n.c. | -3.0 | n.c. | -4.4 |
| 140114S | 7.7 | 21 | -3.3 | -4.1 | -3.0 | -1.8 | -4.0 |
| 100107C | 9.3 | 25.4 | n.c. | n.c. | -2.5 | n.c. | -3.8 |
| 100107D | 8.6 | 25.6 | n.c. | n.c. | -2.8 | n.c. | -3.8 |
| 140111G | 8.9 | 22.6 | -2.1 | -2.9 | -3.1 | -1.7 | -2.8 |
| 100109X | 8.9 | 23.3 | n.c. | n.c. | -2.8 | n.c. | -3.4 |
| 140116B | 7.9 | 26.5 | -2.7 | -3.4 | -3.1 | -1.8 | -3.4 |
| 140116C | 8.7 | 27.3 | -1.2 | -1.8 | -3.1 | n.c. | -2.6 |
| 120116Q | 7.7 | 25 | n.c. | n.c. | n.c. | -2.0 | n.c. |
| 100113AP | 7.9 | 27 | n.c. | n.c. | -2.7 | n.c. | -3.3 |
| 100114AR | 8.8 | 21.5 | n.c. | n.c. | -3.0 | n.c. | -3.6 |
| 140110D | 10.4 | 21.8 | -2.8 | -3.7 | -3.1 | n.c. | -3.5 |
| 140112L | 9.8 | 21.3 | -3.6 | -4.6 | -3.1 | n.c. | -4.4 |
| 100107E | 10.1 | 26.9 | n.c. | n.c. | -2.6 | n.c. | -3.8 |
| 140111H | 10.2 | 20.2 | -1.5 | -2.2 | -2.7 | -2.0 | -2.4 |
| 140111I | 10.9 | 18.8 | -1.2 | -1.9 | -2.9 | -1.7 | -2.6 |
| 120114N | 9.8 | 21.8 | n.c. | n.c. | n.c. | -1.3 | n.c. |
| 100109T | 9.6 | 23.7 | n.c. | n.c. | -3.0 | n.c. | -2.5 |
| 140116D | 9.1 | 27.1 | -0.4 | -1.0 | -2.8 | -2.3 | -2.2 |
| 120116R | 10.6 | 25.8 | n.c. | n.c. | n.c. | -1.5 | n.c. |
| 100113AN | 10.2 | 28.6 | n.c. | n.c. | -3.0 | n.c. | -2.5 |
| 100113AO | 10.4 | 27.4 | n.c. | n.c. | -2.7 | n.c. | -2.3 |
| ***Fluids with pH>11*** | | | | | | | |
| 140115X | 11.4 | 29.5 | -1.4 | 0.2 | -2.7 | n.c. | -2.4 |
| 140115Y | 11.6 | 24.5 | -0.7 | -0.9 | -2.9 | -0.9 | -2.7 |
| 140115Z | 11.3 | 32.2 | -1.8 | 0.2 | -2.8 | n.c. | -2.5 |
| 120118Y | 11.5 | 32.5 | n.c. | n.c. | n.c. | -1.6 | n.c. |
| 120118Z | 11.4 | 30.6 | n.c. | n.c. | n.c. | -1.4 | n.c. |
| 120129G | 11.0 | 37.3 | n.c. | n.c. | n.c. | -1.5 | n.c. |
| 100111AA | 11.7 | 28.5 | n.c. | n.c. | -3.1 | n.c. | -2.8 |
| 100111AB | 11.7 | 25.4 | n.c. | n.c. | -2.7 | n.c. | -2.5 |
| 100111AC | 11.6 | 16.5 | n.c. | n.c. | -2.6 | n.c. | -2.3 |
| 100111AD | 11.6 | 32.4 | n.c. | n.c. | -2.8 | n.c. | -2.5 |
| 100111AE | 11.9 | 18.9 | n.c. | n.c. | -2.6 | n.c. | -3.0 |
| 100112AG | 11.1 | 37.7 | n.c. | n.c. | -3.1 | n.c. | -2.7 |
| 100112AH | 11.2 | 38.4 | n.c. | n.c. | -3.3 | n.c. | -3.0 |
| 140110C | 11.4 | 27 | -1.3 | -1.4 | -2.9 | n.c. | -2.7 |
| 140112K | 11.4 | 26.9 | -1.9 | -2.7 | -2.6 | -2.1 | -2.6 |
| 140112M | 11.4 | 28.2 | -2.1 | -0.7 | -2.8 | n.c. | -2.5 |
| 140113O | 11.4 | 28.4 | -1.6 | -0.6 | -2.8 | n.c. | -2.5 |
| 140113P | 11.5 | 25.9 | -0.4 | -0.3 | -2.9 | -1.3 | -2.6 |
| 140114R | 11.6 | 21.1 | -3.5 | -4.6 | -2.5 | -1.3 | -4.2 |
| 140114T | 11.4 | 27.2 | -1.1 | -0.8 | -2.4 | -1.1 | -2.2 |
| 140114U | 11.4 | 21.7 | -3.3 | -4.4 | -2.5 | -2.0 | -4.0 |
| 140114V | 11.4 | 24.4 | -2.3 | -3.2 | -2.4 | -1.2 | -2.9 |

|  |  |  |  |  |  |  |  |
|---|---|---|---|---|---|---|---|
| 120111A | 11.6 | 22.3 | n.c. | n.c. | n.c. | -0.9 | n.c. |
| 120111B | 11.4 | 29.4 | n.c. | n.c. | n.c. | -1.0 | n.c. |
| 120111C | 11.3 | 31.9 | n.c. | n.c. | n.c. | -1.0 | n.c. |
| 120113I | 11.4 | 30 | n.c. | n.c. | n.c. | -1.4 | n.c. |
| 120113J | 11.6 | 25.8 | n.c. | n.c. | n.c. | -0.7 | n.c. |
| 120113K | 11.4 | 30.9 | n.c. | n.c. | n.c. | -0.9 | n.c. |
| 120113L | 11.3 | 28.4 | n.c. | n.c. | n.c. | -1.0 | n.c. |
| 100108J | 11.7 | 23.9 | n.c. | n.c. | -2.3 | n.c. | -2.2 |
| 100108K | 11.7 | 24.7 | n.c. | n.c. | -2.4 | n.c. | -2.1 |
| 100108L | 11.6 | 29.2 | n.c. | n.c. | -2.9 | n.c. | -2.6 |
| 100107A | 11.3 | 32.4 | n.c. | n.c. | -2.6 | n.c. | -2.6 |
| 100107B | 11.3 | 30.3 | n.c. | n.c. | -2.3 | n.c. | -3.1 |
| 140111F | 11.6 | 23.8 | -0.7 | 0.3 | -2.9 | n.c. | -2.6 |
| 120112E | 11.3 | 30.1 | n.c. | n.c. | n.c. | -1.5 | n.c. |
| 120112F | 11.4 | 27.4 | n.c. | n.c. | n.c. | -1.7 | n.c. |
| 100109S | 11.8 | 22.4 | n.c. | n.c. | -2.7 | n.c. | -2.4 |
| 100109U | 11.7 | 24.9 | n.c. | n.c. | -3.0 | n.c. | -2.7 |
| 140117F | 11.5 | 26.2 | -1.2 | 0.3 | -2.6 | -2.4 | -2.3 |
| 140117G | 11.4 | 30.5 | -2.7 | -1.9 | -3.1 | n.c. | -3.0 |
| 140117H | 11.5 | 29.6 | -1.9 | 0.2 | -2.6 | n.c. | -2.3 |
| 140117I | 11.3 | 32.3 | -1.9 | 0.2 | -2.7 | n.c. | -2.3 |
| 140117J | 11.3 | 31.6 | -2.0 | 0.2 | -2.6 | n.c. | -2.2 |
| 140117K | 11.5 | 27.4 | n.c. | n.c. | n.c. | n.c. | n.c. |
| 140117L | 11.6 | 27.3 | n.c. | n.c. | n.c. | n.c. | n.c. |
| 120116P | 11.2 | 34.3 | n.c. | n.c. | n.c. | -1.6 | n.c. |
| 120116S | 11.4 | 29.5 | n.c. | n.c. | n.c. | -1.6 | n.c. |
| 120117T | 11.3 | 32.6 | n.c. | n.c. | n.c. | -1.3 | n.c. |
| 120117U | 11.3 | 32 | n.c. | n.c. | n.c. | -1.6 | n.c. |
| 120117V | 11.7 | 23.6 | n.c. | n.c. | n.c. | -1.3 | n.c. |
| 120117X | 11.3 | 32.8 | n.c. | n.c. | n.c. | -0.9 | n.c. |
| 100112AJ | 11.5 | 33.4 | n.c. | n.c. | -3.1 | n.c. | -2.7 |
| 100112AM | 11.5 | 31.5 | n.c. | n.c. | -2.9 | n.c. | -2.6 |
| 100114AS | 11.3 | 18.2 | n.c. | n.c. | -2.9 | n.c. | -3.8 |
| 100114AT | 11.6 | 30.4 | n.c. | n.c. | -2.7 | n.c. | -2.5 |
| 100114AU | 11.6 | 20.08 | n.c. | n.c. | -2.7 | n.c. | -2.9 |

n.c. - not calculated due to lack in compositional data

Table S5

*Composition of End-member Subsurface Fluids Used in Mixing Calculations*

| Fluid | pH[a] | Ca[a] | Mg[a] | Si[a] | Na[b] | Cl[b] | $O_2$[c] | DIC[a] | $SO_4^{-2}$[c] |
|---|---|---|---|---|---|---|---|---|---|
| Shallow | 8 | 0.6 | 1.7 | 0.1 | 1 | 1 | 0.3 | 2.1 | 1 |
| Deep | 12.3 | 14.4 | 0 | 0.001 | 10 | 10 | 0 | 0.01 | 0 |

all concentrations are in millimolal

[a] Shallow end-member composition is calculated for a fluid in equilibrium with chrysotile, calcite, magnesite, and the atmosphere at 25°C and 1 bar with pH given as 8. Deep end-member composition is calculated in equilibrium with the chryositle, brucite, diopside, and calcite assemblages.

[b] shallow and deep fluids were given ionic strengths equivalent to a 1 and 10 millimole/kg NaCl solution, respectively, following environmental observations (Paukert and others, 2012; 2019).

[c] Concentration for shallow end-member is in saturation with atmospheric levels. Concentrations for deep-seated fluids assumed to be zero.

[d] Concentrations for shallow end-member fluid given average compositions observed in surface circumneutral fluids. Concentrations for deep-seated fluids assumed to be zero.

[e] Concentration for shallow end-member fluid in saturation with atmospheric levels. Deep-seated end-member concentration taken from average of environmental samples.

[f] Concentrations for both shallow and deep end-member fluids assumed to be in saturation with atmospheric levels.

[g] Concentration for shallow end-member fluid is assumed to be zero, in equilibrium with atmospheric conditions. Concentration for deep end-member fluid calculated at saturation with an atmosphere with 1 bar $H_2$ at 25°C.

[h] Concentration for shallow end-member fluid is assumed to be zero, in equilibrium with amospheric conditions. Concentration for deep end-member fluid calculated aussmed at either 1 picomolal and 1 millimolal.

[i] Concentration for shallow end-member fluid is assumed to be zero, in equilibrium with atmospheric conditions. Concentration for deep end-member fluid follows observation from fluid samples in equilibrium with the ferrous-hydroxide and magnetite mineral assemblage.

[j] Concentration for shallow end-member fluid is assumed to be zero, in equilibrium with atmospheric conditions. Concentration for deep end-member fluid follows observation from fluid samples in equilibrium with pyrrothite.

[j] Concentration for shallow end-member fluid is assumed to be zero, in equilibrium with atmospheric conditions. Concentration for deep end-member fluid follows observation from fluid samples in equilibrium with pyrrothite.

[k] Concentration for shallow end-member fluid is assumed to be zero, in equilibrium with atmospheric conditions. Concentration for deep end-member fluid follows observation from the most saline fluid samples.

Table C5. (cont'd.)

| Fluid | pH[a] | $NO_3^-$[c] | $NO_2^-$[d] | CO[e] | $N_2$[f] | $H_2$[g] | $CH_4$[h] | $Fe^{+2}$[i] | $H_2S$[j] | $NH_3$[k] |
|---|---|---|---|---|---|---|---|---|---|---|
| Shallow | 8 | 0.5 | 0.001 | 0 | 0.5 | 0 | 0 | 0 | 0 | 0 |
| Deep | 12.3 | 0 | 0 | 0.0003 | 0.5 | 0.75 | 0 or 1 | 0.1 | 0.07 | 0.1 |

## C.5. Supplementary Figures

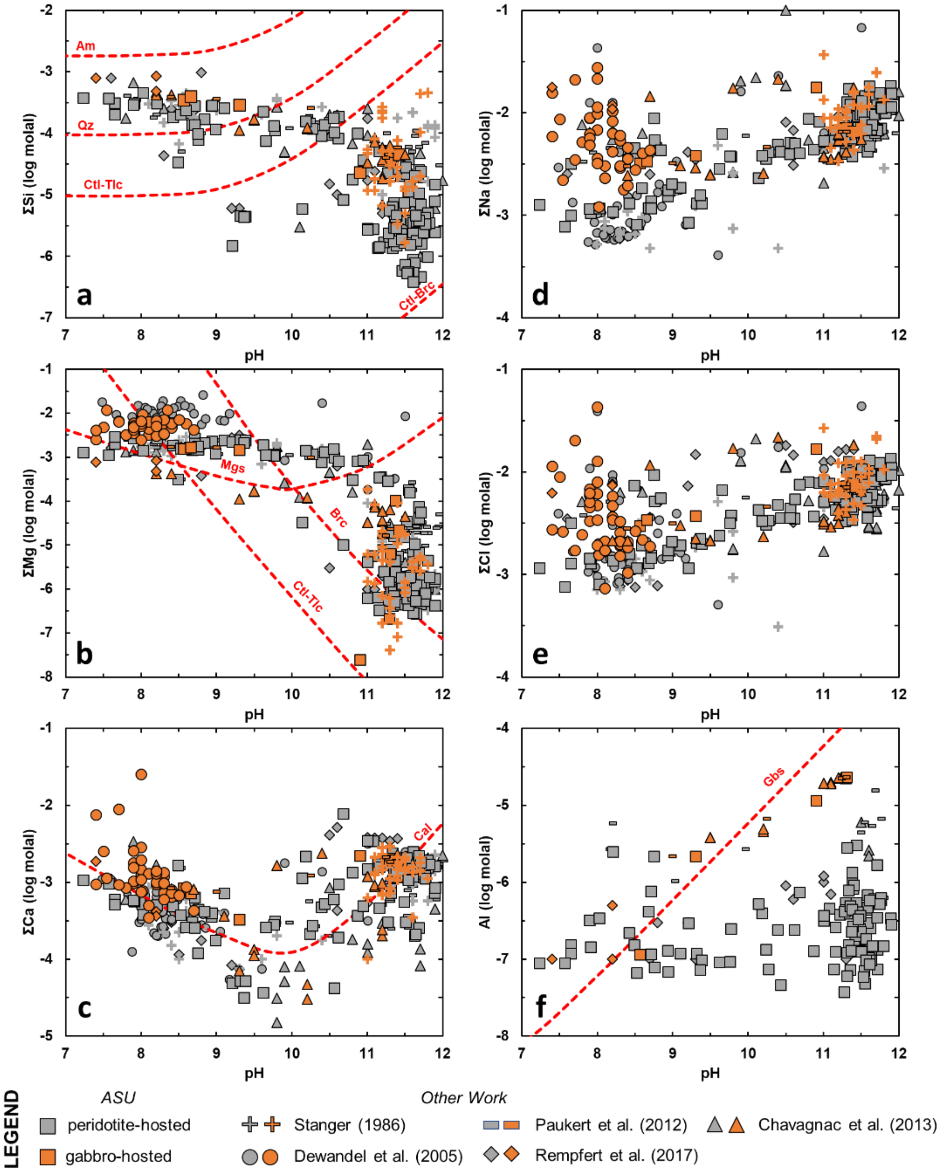

*Figure C1*. Comparison between ultramafic-hosted (grey symbols) and gabbroic-hosted (orange symbols) fluids in Oman. Total dissolved Si (a), Mg (b), Ca (c), Na (d), Cl (e), and Al (f). Dashed red lines and curves show solubility conditions for various minerals Am – amorphous silica, Qz – quartz, Ctl – chrysotile, Tlc – talc, Brc – brucite, Mgs – magnesite, Cal – calcite, Gbs – gibbsite.

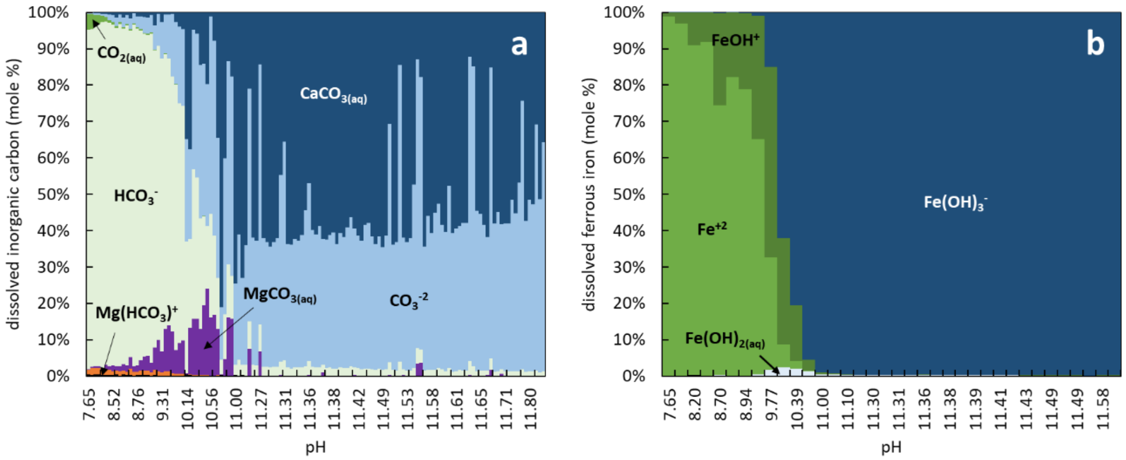

*Figure C2*. Speciation of dissolved inorganic carbon (a) and ferrous iron (b) in investigated fluids.

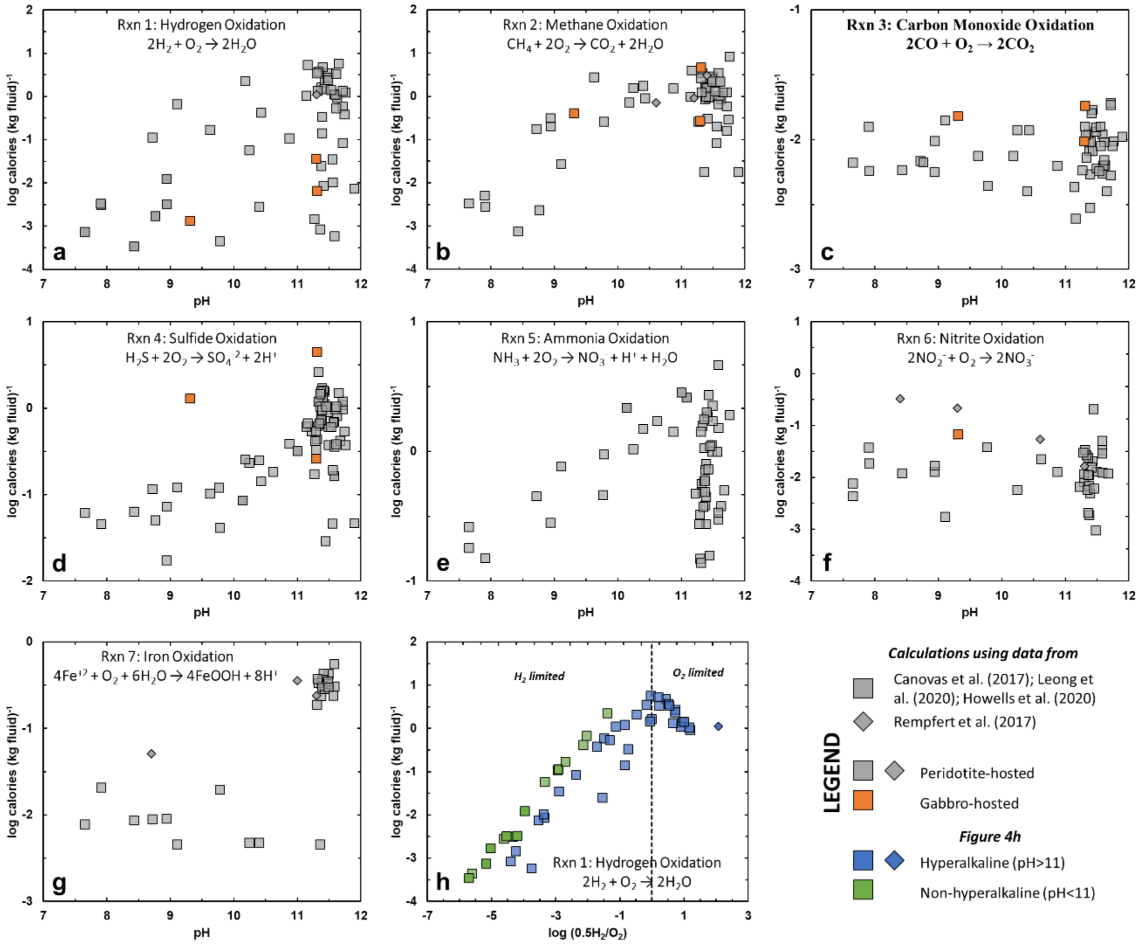

*Figure C3*. Calculated energy yield (log calories/kg fluid) via the aerobic oxidation of hydrogen (a), methane (b), carbon monoxide (c), sulfide (d), ammonia (e), nitrite (f), and iron (g). Square symbols depict energy yields from fluids sampled by accompanying works of this study while diamond symbols denote those obtained from wells by Rempfert et al. (2017). Symbols colored in grey and orange depict ultramafic- and gabbro-hosted fluids, respectively. (h) Energy yield for the aerobic oxidation of hydrogen as a function of the ratio of the electron donor ($H_2$) and acceptor ($O_2$), corrected by their stoichiometric coefficients. Vertical dashed line depicts boundary between an $H_2$ or $O_2$-limited systems. Blue and green symbols depict hyperalkaline (pH >11) and non-hyperalkaline (pH <11) samples, respectively.

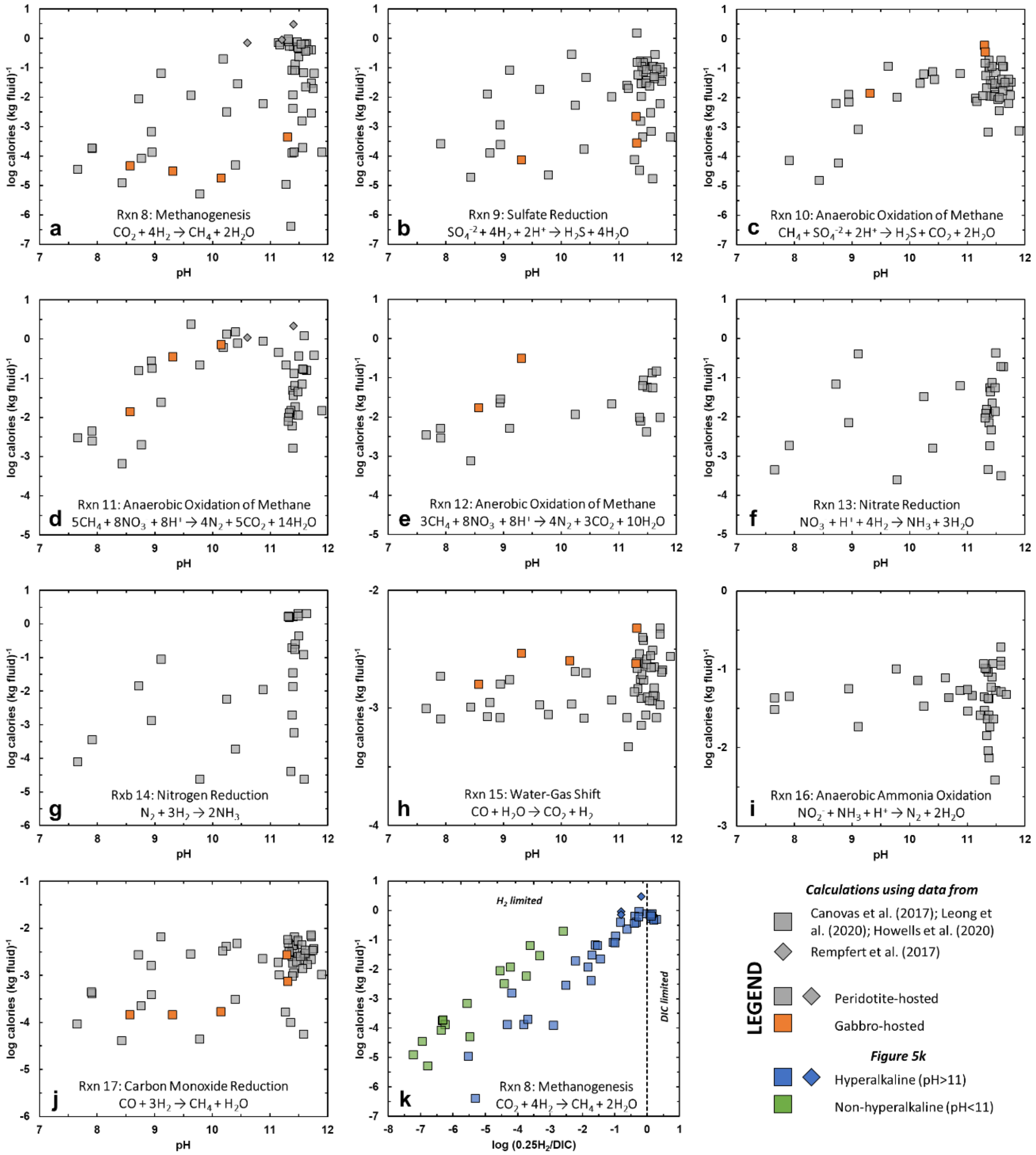

*Figure C4*. Calculated energy yield (log calories/kg fluid) via anaerobic reactions: autotrophic methanogenesis (a), sulfate reduction (b), anaerobic oxidation of methane with sulfate (c), nitrate (d), and nitrite (e) as electron acceptors, nitrate reduction (f), $N_2$ reduction or fixation (g), water-gas shift reaction (h), anaerobic ammonia oxidation or annamox (i), and carbon monoxide reduction (j). (k) Energy yield through methanogenesis as a function of the ratio of the electron donor ($H_2$) and acceptor (DIC), corrected by their stoichiometric coefficients. Vertical dashed line depicts boundary between an $H_2$ or DIC-limited systems. Symbols similar to those shown in Figure C3.

# APPENDIX D

# SUPPLEMENTARY FILES TO CHAPTER 5

## D.1. $H_2$ generation potentials of various Fe-bearing igneous rocks

The amounts of $H_2$ predicted to form during the low-temperature alteration (25 °C) of various Fe-bearing igneous rocks are summarized in Figures 5.1a and 5.1b. As shown in Figure D1a, the FeO contents of rocks used in the simulations, except for the most enriched basalts (MgO content < 10 wt. %), are closely similar (8-10 wt. %). Despite having similar amounts of starting materials (ferrous iron) that can potentially be oxidized and yield $H_2$ from the coupled reduction of $H_2O$, the potentials to generate $H_2$ during alteration of these rocks vary. Instead of the FeO content of the rock, the potential to produce $H_2$ is tied to the overall bulk composition of the rock which in turn dictates how Fe is distributed and speciated in the secondary assemblages during rock alteration. Generally, alteration of MgO-rich rocks (>35 wt. % MgO), except for those that are the most enriched in MgO (>45 wt. % MgO), results in the highest potential to generate $H_2$ (Figures 5.1a and 5.1b). MgO-rich rocks tend to be depleted in $SiO_2$, CaO, $Al_2O_3$, $Na_2O$ and $K_2O$. Hence, as shown in Figures D1b to D1f, the potentials to generate $H_2$ during rock alteration tend to decrease, depicted by the transition to cooler colors in Figure D1, as the reacting rock becomes more enriched in these chemical components.

Overall, the potentials to generate $H_2$ closely trend with the amounts of serpentine that form in the models, as shown in Figure 5.1c. Precipitation of brucite, chlorite, talc, and clay minerals can sequester large proportions of ferrous iron into their crystal structures unoxidized and inhibit $H_2$ production through reaction (5.2). In contrast, serpentine minerals typically exclude ferrous iron into their crystal structure and accommodate ferric iron instead. Several studies have shown $Fe^{+3}/\Sigma Fe$ in serpentine can attain values above 0.5, with some observations indicating values up to 1 (Andreani et al., 2013; Mayhew and Ellison, 2020). The mechanism explaining why serpentine excludes ferrous iron from its crystal structure relative to other minerals such as chlorite is unknown. While the volumes of the octahedral sites, where ferrous iron can substitute with Mg, in serpentine and chlorite are similar (*i.e.*, similar average divalent cation-oxygen, $M^{+2}$-O, bond length), octahedral sites in serpentine are much more irregular (*i.e.*, $M^{+2}$-O bond lengths are less uniform) than those of chlorites (Mellini et al., 1982; Mellini and Zanazzi, 1987; Smyth et al., 1997). Possibly the distorted octahedral sites in serpentine inhibit incorporation of ferrous iron into the mineral.

As shown in Figures 5.1a and 5.1b, the potential to generate $H_2$ during alteration increases as the MgO content of the rock decreases from 50 to 40 wt. % where serpentine is increasingly favored to form at the expense of brucite. In contrast, potentials to form $H_2$ decrease as the MgO content of the reacting rock decreases from 40 to 20 wt. % as serpentine becomes less favored relative to chlorite. Moreover, as the $SiO_2$ contents of rocks typically increase with decreasing MgO content (see Figure D1b), the composition of the precipitating Fe-bearing serpentine trends toward the more Si-rich Fe(II)-endmember (greenalite, $Fe(II)_3Si_2O_5(OH)_4$) instead of the Fe(III)-endmember (cronstedtite, $(Fe(II)_2Fe(III))(Fe(III)Si)O_5(OH)_4$), resulting in less $H_2$ formation (Leong and Shock, 2020). Serpentine is not favored to form during the alteration of rocks with MgO content of less than 20 wt. %, resulting in minimal potentials to generate $H_2$ during the alteration of these rocks (left side of Figures 5.1a and 5.1b). This range in rock composition encompasses all basaltic and some picritic rocks where the dominant Fe-bearing secondary assemblages are chlorite, talc, and clay minerals (Figure 5.1c). Other minerals (gray symbols in Figure 5.1c) that precipitated in alteration simulations of basaltic and picritic rocks are predominantly zeolites, prehnite, secondary plagioclase, and tremolitic amphibole.

Aside from serpentine, another Fe(III)-bearing silicate mineral that can form during low-temperature alteration is garnet (see Figure 5.1c), specifically, those that are andraditic ($Ca_3Fe(III)_2Si_3O_{12}$) in composition. The precipitation of andraditic garnet and its hydrated equivalents (hydrogarnets) have been invoked as another source for $H_2$ during serpentinization of peridotitic bodies (Plümper et al., 2014). Results of calculations shown in Figures 5.1a-5.1c show that komatiitic rocks have similar or greater potentials to precipitate garnets that can supply additional $H_2$ during alteration. The rock that yielded the most $H_2$ in the simulations (see Figure 5.1a), as well as the most garnet precipitated in the model (see Figure 5.1c), is a komatiite that is enriched in CaO (see sample with high CaO content and MgO content between 30-35 wt. % in Figure D1c).

Note that the calculations described above simulate low-temperature alteration processes in continental aquifers. $H_2$ concentrations measured from basalt-hosted submarine vent fluids (which can attain values >1 mmolal) and their ultramafic analogs (>10 mmolal) are less divergent than their low-temperature continental counterparts. Higher temperature water-rock reactions (>300 °C) occurring in geothermal aquifers and submarine hydrothermal systems can lead to the formation of other mineral assemblages. At higher temperatures, epidote which is a Fe(III)-bearing Ca hydrous silicate mineral, is favored to form during hydrothermal alteration of basalts and results in the formation of $H_2$ (*e.g.*, Seyfried et al., 1991). In addition, further simulations that consider incorporation of ferric iron into chlorite, which has been observed in natural samples (Dyar et al., 1992; Munoz et al., 2006; Vidal et al., 2006), albeit at lesser extents than those measured in serpentine (*e.g.*, Andreani et al., 2013; Mayhew and Ellison, 2020), can refine estimates on $H_2$ production during basalt and picritic rock alteration where chlorite formation can be significant.

### D.2. Estimating the $H_2$ generation potentials of komatiitic rocks

The $H_2$ generation potentials of komatiitic rocks ($x_K$) are quantified at various extents of the rock alteration progress, given the compositions of the reacting rocks and fluids. Results of calculations are shown in Figure D2. The curves in Figure D2 depict predicted amounts of $H_2$ generated at various extents of alteration for a given volume of komatiite of varying composition, indicated by the 34 curves of similar color. In these simulations, each komatiite is reacted with fluids with varying DO compositions that are in equilibrium with an atmosphere composed of $10^{-5}$, $10^{-4}$, $10^{-3}$, $10^{-2}$ and $10^{-0.7}$ bars $O_2$ as represented by the various colors in Figure D2. Results of simulations involving a starting fluid in equilibrium with $10^{-5}$ and $10^{-4}$ bars $O_2$ atmosphere are close to those calculated for a fluid in equilibrium with $10^{-3}$ bars $O_2$ and are thus not shown. As depicted in Figure D2, the $H_2$ generation potentials of various starting komatiites reacted with different starting fluids at different stages of overall reaction progress (water-to-rock ratio) are variable. That variability maximizes in high water-to-rock ratio conditions (left side of Figure D2) where komatiites can generate large amounts of $H_2$ if they react with fluids with small starting amounts of $O_2$ (grey curves in Figure D2). In contrast, negligible amounts of $H_2$, below the range shown in the figure, are generated if the reacting fluid is enriched in $O_2$ (red curves in Figure D2) at high water-to-rock conditions. The latter simulation depicts scenarios more familiar to modern Earth settings where an $O_2$-rich atmosphere results in the oxidation of ferrous iron in surficial or near-surficial rocks to ferric phases (*e.g.*, goethite, hematite) via reaction (5.1), in a process known as oxidative weathering. It is only when fluids infiltrate into the deeper aquifer where fluids react with more and more rocks, *i.e.* becoming more of a rock-dominated system (right side of Figure D2), that dissolved $O_2$ is exhausted and $H_2$ can accumulate through the oxidation of ferrous iron with water via reaction (5.2). Perhaps this explains why in modern active serpentinizing environments, $H_2$-rich and hyperalkaline fluids can only be found in deep wells or in outcropping spring seeps that are sourced from the deep aquifer.

In contrast to modern Earth conditions, if the starting fluid is devoid in dissolved oxygen (grey curves in Figure D2) $H_2O$ can become the main oxidant and the alteration process can generate $H_2$ early in the reaction progress (at high water-to-rock ratios). It is thus likely that in the Archean, when the atmosphere was mostly devoid of $O_2$, oxidative weathering can still occur but unlike how it occurs in modern settings. In the Archean, surficial weathering can generate $H_2$ via reaction (5.2) when ferrous iron in komatiites is oxidized to ferric iron that can be incorporated into the serpentine structure, which is known to host both ferrous and ferric iron (O'Hanley and Dyar, 1998; Andreani et al., 2013). It is likely that oxidative weathering of surficial komatiites during the Archean is a source for $H_2$ independent of the $H_2$ generated in deeper aquifers at rock-dominated conditions (low water-to-rock ratios). However, at water-dominated conditions, the compositions of the starting reacting fluids would have greater influence on the precipitating phases, as shown by studies on mineral precipitates in surficial and shallow subsurficial environments characterized by fluid recharge and high water-to-rock conditions (*e.g.*, Bach et al., 2001).

Reacting fluids representative of Archean environments are highly unconstrained. Our simplistic approach of assuming reacting fluids with dilute concentrations does not fully capture the minerals likely to form at fluid-dominated conditions. However, as the process progresses towards rock-dominated conditions, the compositions of the rocks increasingly dictate the resulting fluid and volatile compositions as shown in the right side of Figure D2 where the $H_2$-generation potentials for most komatiites converge with decreasing water-to-rock ratio, despite differences in the compositions of the reacting fluids. Thus, quantifications of $H_2$ flux in this work are focused on conditions occurring in deeper settings that are characterized by water-to-rock ratios lower than 100, as shown by the blue field in Figure D2, where the starting fluid is less likely to influence the output mineral, fluid, and volatile compositions. While this work is focused on mineral alteration reactions occurring in rock-dominated systems in deeper aquifers, oxidative weathering of surficial rocks during the Archean can supply additional $H_2$. Work incorporating constraints on surficial fluid compositions and weathering environments (*e.g.*, Hao et al., 2016; 2019) can refine future models by quantifying those $H_2$ sources that are independent from the alteration processes occurring at deeper systems and ultimately derive a full flux model comprising both surficial and deep crustal systems.

As depicted in Figure D2, results of models of komatiite serpentinization at water-rock ratio <100 show that the amount of $H_2$ generated via komatiite serpentinization is variable. Most of these variations can be attributed to the variabilities the water-to-rock ratio and to the composition of the komatiite. In general, most komatiites have decreasing potentials to generate $H_2$ with decreasing water-to-rock ratios. For these komatiites, minerals that host ferrous iron such as chlorite and the $Fe^{+2}$-bearing serpentine endmember (greenalite) are favored over those that host ferric iron (*e.g.*, $Fe^{+3}$-bearing serpentine endmember or cronstedtite) as the conditions become more and more rock dominated. In contrast, the $H_2$ generation potentials of some komatiites, particularly those yielding the greatest amounts of $H_2$, are not particularly sensitive to the water-to-rock ratios and variations are mostly a result of the composition of the reacting rock. At the minimum water-to-rock ratio modelled in our simulations (0.2), the $H_2$ generation potentials of most of the 34 komatiites investigated in this work vary from $10^9$ – $10^{12}$ moles $H_2$ per $km^3$ of rock. We terminated our calculations at water-to-rock ratio = 0.2 as lower values result in simulations with no water left due to the extensive hydration process.

## D.3. Supplementary Tables

Table D1

*Composition of Various Fe-bearing Igneous Rocks Used as Inputs in Rock Alteration Simulations.*

| No. | Rock Type | Bulk Rock Composition* | | | | | | | Sample Name** |
|---|---|---|---|---|---|---|---|---|---|
| | | MgO | $SiO_2$ | FeO | CaO | $Na_2O$ | $Al_2O_3$ | $K_2O$ | |
| 1 | komatiite | 38.0 | 44.3 | 10.4 | 2.8 | 0.3 | 4.2 | 0.04 | SD6/290 |
| 2 | komatiite | 36.9 | 47.4 | 9.7 | 2.2 | 0.3 | 3.4 | 0.01 | 176/724 |
| 3 | komatiite | 35.7 | 45.6 | 11.1 | 3.7 | 0.4 | 3.5 | 0.01 | 176/725 |
| 4 | komatiite | 33.8 | 46.8 | 10.3 | 3.3 | 0.0 | 5.7 | 0.01 | 179/757 |
| 5 | komatiite | 33.4 | 47.4 | 8.9 | 4.9 | 0.2 | 5.3 | 0.01 | 422/86 |
| 6 | komatiite | 32.8 | 46.2 | 11.2 | 5.4 | 0.4 | 3.7 | 0.17 | 49J |
| 7 | komatiite | 32.4 | 45.6 | 9.8 | 5.8 | 0.5 | 5.9 | 0.06 | SD4/193 |
| 8 | komatiite | 32.0 | 46.1 | 10.1 | 5.7 | 0.3 | 5.7 | 0.01 | 331/347 |
| 9 | komatiite | 31.6 | 45.0 | 8.5 | 11.6 | 0.3 | 3.0 | 0.01 | 176/723 |
| 10 | komatiite | 31.2 | 46.7 | 9.5 | 6.0 | 0.2 | 6.4 | 0.01 | 422/84 |
| 11 | komatiite | 30.1 | 46.6 | 10.7 | 6.0 | 0.3 | 6.1 | 0.17 | 331/434 |
| 12 | komatiite | 29.9 | 47.3 | 11.0 | 5.3 | 0.2 | 6.1 | 0.25 | 331/488 |
| 13 | komatiite | 29.7 | 48.2 | 10.0 | 5.8 | 0.1 | 6.3 | 0.01 | 179/756 |
| 14 | komatiite | 29.6 | 46.3 | 10.9 | 6.2 | 0.6 | 6.4 | 0.03 | 331/144/42 |
| 15 | komatiite | 29.5 | 49.3 | 8.0 | 6.7 | 0.3 | 6.1 | 0.01 | 422/96 |
| 16 | komatiite | 28.6 | 47.5 | 10.9 | 5.9 | 0.2 | 6.4 | 0.46 | 331/487 |
| 17 | komatiite | 28.5 | 48.7 | 11.1 | 6.9 | 0.6 | 4.1 | 0.12 | 331/497 |
| 18 | komatiite | 28.2 | 47.5 | 10.8 | 6.4 | 0.8 | 6.3 | 0.00 | B-R1 |
| 19 | komatiite | 28.1 | 45.4 | 10.4 | 8.7 | 0.4 | 7.0 | 0.01 | SD6/400 |
| 20 | komatiite | 28.0 | 47.5 | 10.8 | 6.4 | 0.8 | 6.4 | 0.00 | B-R2 |
| 21 | komatiite | 27.9 | 50.8 | 9.1 | 8.3 | 0.1 | 3.8 | 0.00 | B-B5 |
| 22 | komatiite | 27.3 | 47.7 | 12.6 | 7.5 | 0.3 | 4.5 | 0.01 | 331/777a |
| 23 | komatiite | 27.2 | 49.1 | 10.7 | 7.6 | 0.7 | 4.7 | 0.04 | 331/779 |
| 24 | komatiite | 27.1 | 48.2 | 12.3 | 7.4 | 0.3 | 4.6 | 0.02 | 331/783 |
| 25 | komatiite | 26.8 | 49.4 | 11.0 | 7.5 | 0.7 | 4.5 | 0.04 | 331/81 |
| 26 | komatiite | 26.0 | 46.7 | 11.2 | 7.9 | 0.8 | 7.5 | 0.03 | SD5/354.5 |
| 27 | komatiite | 24.7 | 50.3 | 9.5 | 8.4 | 0.2 | 7.0 | 0.02 | 179/755 |
| 28 | komatiite | 23.8 | 54.8 | 9.8 | 5.3 | 0.7 | 5.6 | 0.10 | B-H2 |
| 29 | komatiite | 23.9 | 46.6 | 11.1 | 8.9 | 0.8 | 8.5 | 0.15 | 422/95 |
| 30 | komatiite | 23.8 | 49.4 | 10.8 | 7.4 | 0.3 | 8.3 | 0.02 | 179/751 |
| 31 | komatiite | 23.7 | 48.2 | 10.9 | 7.7 | 1.1 | 8.2 | 0.12 | 331/948 |
| 32 | komatiite | 23.1 | 46.5 | 11.1 | 9.5 | 0.4 | 9.3 | 0.03 | 422/94 |

| | | | | | | | | | |
|---|---|---|---|---|---|---|---|---|---|
| 33 | komatiite | 22.5 | 46.4 | 12.0 | 9.1 | 0.7 | 9.2 | 0.06 | 422/91 |
| 34 | komatiite | 19.3 | 49.6 | 11.3 | 9.0 | 1.3 | 9.4 | 0.04 | 331/531 |
| 35 | picrite | 9.1 | 49.7 | 10.2 | 13.0 | 1.7 | 16.3 | 0.06 | BI/DI/20 |
| 36 | picrite | 10.1 | 49.8 | 10.9 | 12.7 | 1.6 | 14.9 | 0.09 | BI/CS/32 |
| 37 | picrite | 10.9 | 49.6 | 10.1 | 12.7 | 1.7 | 14.9 | 0.05 | DUR1 |
| 38 | picrite | 12.2 | 49.3 | 10.2 | 11.6 | 1.7 | 14.8 | 0.12 | BI/CS/8 |
| 39 | picrite | 13.2 | 49.2 | 10.1 | 12.1 | 1.4 | 14.0 | 0.05 | BI/DI/13 |
| 40 | picrite | 14.2 | 47.7 | 10.8 | 12.0 | 1.4 | 13.8 | 0.04 | BI/CS/13 |
| 41 | picrite | 15.1 | 48.7 | 10.3 | 10.1 | 1.4 | 14.4 | 0.09 | BI/PI/18 |
| 42 | picrite | 16.1 | 48.2 | 10.5 | 10.7 | 1.3 | 13.1 | 0.04 | BI/CS/12 |
| 43 | picrite | 17.4 | 48.2 | 10.2 | 10.4 | 1.4 | 12.4 | 0.04 | BI/CS/11 |
| 44 | picrite | 18.3 | 47.7 | 10.6 | 10.1 | 1.4 | 11.9 | 0.02 | BI/PI/29 |
| 45 | picrite | 19.1 | 47.5 | 10.1 | 10.2 | 1.3 | 11.7 | 0.02 | BI/PI/28 |
| 46 | picrite | 20.2 | 47.2 | 10.5 | 9.6 | 1.3 | 11.2 | 0.05 | BI/CS/19 |
| 47 | picrite | 21.1 | 47.2 | 11.4 | 8.3 | 1.3 | 10.5 | 0.14 | BI/PI/19 |
| 48 | picrite | 22.1 | 45.7 | 11.6 | 9.1 | 1.2 | 10.2 | 0.08 | BI/PI/20 |
| 49 | picrite | 23.1 | 45.9 | 11.3 | 8.4 | 1.2 | 10.0 | 0.05 | BI/CS/27 |
| 50 | picrite | 24.0 | 46.1 | 10.8 | 8.4 | 1.1 | 9.6 | 0.04 | BI/DI/25 |
| 51 | picrite | 25.3 | 45.9 | 10.6 | 7.7 | 0.9 | 9.5 | 0.02 | BI/PI/21 |
| 52 | picrite | 26.3 | 45.6 | 11.0 | 7.1 | 0.9 | 9.1 | 0.03 | BI/DI/22 |
| 53 | picrite | 27.2 | 45.4 | 10.5 | 7.2 | 0.9 | 8.7 | 0.02 | BI/PI/16 |
| 54 | picrite | 28.5 | 45.4 | 9.7 | 7.4 | 0.8 | 8.1 | 0.03 | BI/CS/6 |
| 55 | picrite | 29.5 | 45.1 | 10.5 | 6.0 | 0.3 | 8.5 | 0.02 | BI/CS/17 |
| 56 | picrite | 9.8 | 49.8 | 10.8 | 12.8 | 1.8 | 14.9 | 0.10 | BI/PI/22 |
| 57 | picrite | 10.7 | 49.5 | 10.0 | 13.1 | 1.4 | 15.2 | 0.05 | BI/CS/28 |
| 58 | picrite | 11.5 | 49.4 | 10.0 | 12.3 | 1.5 | 15.3 | 0.07 | BI/CS/1 |
| 59 | picrite | 12.7 | 49.3 | 10.1 | 11.1 | 1.5 | 15.2 | 0.13 | BI/CS/25 |
| 60 | picrite | 13.8 | 47.9 | 10.2 | 11.6 | 1.5 | 14.9 | 0.05 | BI/CS/24 |
| 61 | picrite | 14.8 | 47.9 | 10.4 | 11.2 | 1.4 | 14.3 | 0.04 | BI/CS/14 |
| 62 | picrite | 15.7 | 49.5 | 10.9 | 8.9 | 1.1 | 13.6 | 0.16 | BI/CS/18 |
| 63 | picrite | 17.8 | 47.9 | 10.4 | 10.4 | 1.4 | 12.1 | 0.05 | BI/CS/23 |
| 64 | picrite | 18.7 | 47.7 | 10.0 | 10.3 | 1.2 | 12.0 | 0.03 | BI/CS/16 |
| 65 | picrite | 20.6 | 47.0 | 10.4 | 9.7 | 1.2 | 11.0 | 0.03 | BI/PI/33 |
| 66 | picrite | 21.7 | 46.5 | 10.8 | 9.0 | 1.0 | 11.0 | 0.02 | BI/CS/15 |
| 67 | picrite | 22.5 | 46.9 | 9.9 | 9.0 | 1.1 | 10.6 | 0.03 | BI/CS/21 |
| 68 | picrite | 23.5 | 46.6 | 10.5 | 8.0 | 0.9 | 10.5 | 0.03 | BI/PI/42 |
| 69 | picrite | 24.6 | 46.2 | 11.0 | 8.0 | 1.1 | 9.1 | 0.03 | BI/DI/21 |
| 70 | picrite | 25.8 | 45.9 | 10.7 | 7.6 | 0.8 | 9.2 | 0.03 | BI/CS/10 |
| 71 | picrite | 27.9 | 45.3 | 10.3 | 7.2 | 0.8 | 8.6 | 0.02 | BI/CS/3 |
| 72 | picrite | 29.1 | 45.0 | 10.6 | 6.6 | 0.5 | 8.1 | 0.05 | BI/CS/20 |

| | | | | | | | | | |
|---|---|---|---|---|---|---|---|---|---|
| 73 | picrite | 20.3 | 46.3 | 11.0 | 10.4 | 1.2 | 10.7 | 0.04 | BI/CS/22 |
| 74 | picrite | 20.8 | 47.2 | 10.4 | 9.2 | 1.1 | 11.2 | 0.03 | BI/CS/5 |
| 75 | picrite | 21.4 | 46.1 | 11.6 | 9.0 | 1.3 | 10.3 | 0.28 | BI/DI/26 |
| 76 | picrite | 21.9 | 46.5 | 10.5 | 9.0 | 1.2 | 10.9 | 0.02 | BI/CS/4 |
| 77 | picrite | 22.2 | 46.0 | 10.8 | 9.1 | 1.2 | 10.6 | 0.02 | DUR6 |
| 78 | picrite | 22.8 | 46.5 | 9.8 | 9.3 | 1.0 | 10.6 | 0.03 | BI/CS/26 |
| 79 | picrite | 23.4 | 46.3 | 10.6 | 8.5 | 0.9 | 10.3 | 0.03 | DUR7 |
| 80 | picrite | 23.8 | 46.5 | 10.4 | 8.0 | 0.6 | 10.6 | 0.09 | PAD6 |
| 81 | picrite | 24.2 | 46.3 | 10.8 | 7.6 | 1.0 | 10.0 | 0.04 | BI/PI/30 |
| 82 | picrite | 24.8 | 46.2 | 10.6 | 7.8 | 0.7 | 9.8 | 0.04 | DUR3 |
| 83 | picrite | 25.0 | 45.7 | 12.2 | 7.4 | 1.2 | 8.4 | 0.17 | AP05 |
| 84 | picrite | 25.7 | 46.0 | 10.4 | 7.9 | 1.0 | 9.0 | 0.03 | BI/DI/14 |
| 85 | picrite | 11.1 | 49.3 | 10.0 | 12.9 | 1.5 | 15.1 | 0.05 | PAD5 |
| 86 | picrite | 9.5 | 49.7 | 9.4 | 13.6 | 1.7 | 16.1 | 0.03 | BI/DI/27 |
| 87 | picrite | 9.8 | 50.3 | 10.1 | 13.1 | 1.4 | 15.2 | 0.07 | BI/CS/30 |
| 88 | picrite | 10.9 | 49.4 | 10.8 | 12.2 | 1.5 | 15.2 | 0.07 | PAD7 |
| 89 | picrite | 11.2 | 49.6 | 10.8 | 12.1 | 1.7 | 14.4 | 0.07 | PAD8 |
| 90 | picrite | 12.4 | 49.0 | 10.5 | 12.1 | 1.4 | 14.5 | 0.12 | 400492 |
| 91 | picrite | 12.9 | 49.0 | 10.0 | 11.5 | 1.5 | 15.0 | 0.07 | 332771 |
| 92 | picrite | 13.5 | 48.6 | 10.2 | 11.4 | 1.9 | 14.2 | 0.12 | BI/CS/7 |
| 93 | picrite | 14.0 | 48.6 | 10.9 | 11.8 | 1.0 | 13.6 | 0.09 | PAD2 |
| 94 | picrite | 14.4 | 48.7 | 10.2 | 11.2 | 1.2 | 14.3 | 0.05 | PAD4 |
| 95 | picrite | 15.3 | 49.7 | 10.3 | 9.1 | 0.8 | 14.7 | 0.11 | 354754 |
| 96 | picrite | 15.9 | 48.2 | 10.8 | 10.7 | 1.3 | 13.1 | 0.05 | 400444 |
| 97 | picrite | 16.5 | 48.6 | 10.0 | 10.7 | 1.4 | 12.7 | 0.04 | 340740 |
| 98 | picrite | 16.9 | 48.0 | 10.2 | 10.4 | 1.1 | 13.1 | 0.42 | 410152 |
| 99 | picrite | 17.6 | 47.9 | 10.4 | 10.3 | 1.2 | 12.5 | 0.03 | BI/DI/29 |
| 100 | picrite | 20.3 | 46.4 | 10.9 | 10.3 | 1.2 | 10.9 | 0.04 | 400452 |
| 101 | picrite | 20.3 | 47.8 | 9.6 | 9.7 | 0.9 | 11.6 | 0.05 | BI/PI/34 |
| 102 | picrite | 21.0 | 46.3 | 11.4 | 9.1 | 1.2 | 10.9 | 0.17 | BI/DI/28 |
| 103 | picrite | 21.2 | 45.8 | 11.1 | 10.1 | 1.3 | 10.5 | 0.06 | 400230 |
| 104 | picrite | 21.8 | 46.3 | 10.8 | 9.5 | 1.2 | 10.4 | 0.05 | 264217 |
| 105 | picrite | 21.9 | 46.6 | 10.7 | 8.7 | 1.2 | 10.9 | 0.02 | AP04 |
| 106 | picrite | 22.9 | 46.4 | 10.7 | 8.7 | 1.0 | 10.4 | 0.02 | DUR5 |
| 107 | picrite | 22.9 | 45.9 | 11.2 | 8.8 | 1.0 | 10.1 | 0.07 | BI/PI/31 |
| 108 | picrite | 23.1 | 46.5 | 10.4 | 8.5 | 1.0 | 10.4 | 0.02 | 400457 |
| 109 | picrite | 23.4 | 46.6 | 10.7 | 8.3 | 0.9 | 10.0 | 0.02 | DUR8 |
| 110 | picrite | 23.6 | 45.7 | 10.8 | 8.3 | 1.0 | 10.3 | 0.24 | BI/PI/44 |
| 111 | picrite | 23.5 | 46.5 | 10.6 | 8.4 | 1.0 | 10.0 | 0.03 | BI/DI/18 |
| 112 | picrite | 23.9 | 46.5 | 10.9 | 8.0 | 0.9 | 9.8 | 0.02 | BI/PI/27 |

| | | | | | | | | |
|---|---|---|---|---|---|---|---|---|
| 113 | picrite | 24.4 | 46.1 | 11.1 | 7.5 | 1.0 | 9.8 | 0.07 | BI/PI/32 |
| 114 | picrite | 24.7 | 46.1 | 10.7 | 7.8 | 0.9 | 9.8 | 0.03 | 138345 |
| 115 | picrite | 24.7 | 46.0 | 10.7 | 7.9 | 0.8 | 9.8 | 0.02 | BI/DI/19 |
| 116 | picrite | 25.5 | 44.8 | 11.1 | 8.3 | 1.2 | 9.1 | 0.04 | BI/PI/35 |
| 117 | picrite | 15.8 | 48.6 | 10.3 | 10.0 | 1.2 | 13.9 | 0.11 | BI/DI/17 |
| 118 | picrite | 26.4 | 45.9 | 10.5 | 7.7 | 0.9 | 8.6 | 0.02 | AP03 |
| 119 | picrite | 26.4 | 45.6 | 10.6 | 7.4 | 0.9 | 9.1 | 0.04 | BI/CS/29 |
| 120 | picrite | 16.4 | 50.9 | 10.7 | 7.6 | 0.6 | 13.6 | 0.10 | BI/DI/23 |
| 121 | picrite | 16.8 | 47.7 | 10.4 | 10.7 | 1.0 | 13.3 | 0.09 | BI/DI/15 |
| 122 | picrite | 17.7 | 48.0 | 9.9 | 10.5 | 1.4 | 12.5 | 0.02 | BI/DI/24 |
| 123 | picrite | 18.8 | 48.0 | 10.1 | 9.9 | 1.3 | 11.9 | 0.04 | BI/PI/23 |
| 124 | picrite | 18.9 | 48.0 | 10.3 | 9.4 | 1.1 | 12.2 | 0.15 | BI/PI/43 |
| 125 | picrite | 26.8 | 45.5 | 10.0 | 7.5 | 0.7 | 9.5 | 0.04 | 332901 |
| 126 | picrite | 27.3 | 44.7 | 11.4 | 7.4 | 0.7 | 8.4 | 0.14 | BI/PI/26 |
| 127 | picrite | 27.9 | 45.4 | 10.7 | 6.9 | 0.7 | 8.5 | 0.02 | 362077 |
| 128 | picrite | 28.0 | 45.4 | 10.6 | 6.8 | 0.5 | 8.7 | 0.07 | AP07 |
| 129 | picrite | 28.8 | 45.5 | 10.6 | 6.1 | 0.3 | 8.6 | 0.02 | BI/DI/16 |
| 130 | picrite | 11.5 | 49.6 | 10.7 | 12.3 | 1.3 | 14.5 | 0.06 | BI/PI/24 |
| 131 | picrite | 12.4 | 49.4 | 10.2 | 11.3 | 1.7 | 14.9 | 0.15 | PAD3 |
| 132 | picrite | 12.6 | 48.4 | 10.9 | 12.2 | 1.4 | 14.5 | 0.02 | BI/PI/38 |
| 133 | picrite | 13.9 | 49.3 | 10.4 | 10.7 | 1.5 | 14.1 | 0.15 | BI/PI/37 |
| 134 | picrite | 14.2 | 48.7 | 10.3 | 11.0 | 1.4 | 14.4 | 0.09 | BI/PI/36 |
| 135 | picrite | 14.3 | 49.0 | 10.2 | 10.7 | 1.3 | 14.5 | 0.08 | 400485 |
| 136 | picrite | 15.2 | 48.0 | 10.4 | 11.0 | 1.4 | 13.9 | 0.05 | AP01 |
| 137 | picrite | 15.2 | 48.3 | 11.0 | 10.9 | 1.6 | 13.0 | 0.03 | BI/PI/25 |
| 138 | picrite | 15.3 | 48.8 | 10.3 | 10.1 | 1.4 | 14.1 | 0.11 | BI/PI/41 |
| 139 | picrite | 15.3 | 48.1 | 8.0 | 11.6 | 1.1 | 15.8 | 0.05 | PAD9 |
| 140 | picrite | 15.3 | 47.7 | 10.7 | 10.6 | 1.4 | 14.2 | 0.05 | BI/PI/39 |
| 141 | picrite | 15.8 | 51.0 | 10.6 | 7.7 | 0.9 | 13.9 | 0.12 | BI/CS/31 |
| 142 | picrite | 15.8 | 48.3 | 10.4 | 10.4 | 1.5 | 13.5 | 0.12 | BI/PI/40 |
| 143 | basalt | 3.1 | 59.1 | 13.2 | 7.3 | 2.8 | 13.8 | 0.67 | WASTUNE-7-053-001XGL |
| 144 | basalt | 3.6 | 55.4 | 8.1 | 7.0 | 5.7 | 17.6 | 2.68 | TULCUR1-002-010GL |
| 145 | basalt | 4.1 | 55.9 | 13.6 | 8.4 | 3.2 | 14.6 | 0.23 | KLM0417-R034GL |
| 146 | basalt | 4.7 | 51.9 | 19.3 | 9.5 | 2.7 | 11.9 | 0.18 | DST0041-001-174GL |
| 147 | basalt | 5.2 | 51.7 | 18.0 | 9.9 | 2.7 | 12.2 | 0.18 | DST0041-001-121GL |
| 148 | basalt | 5.6 | 52.5 | 15.0 | 10.8 | 2.6 | 13.3 | 0.19 | SON0012-130-A2GL |
| 149 | basalt | 6.1 | 51.9 | 14.9 | 11.0 | 2.6 | 13.2 | 0.22 | LYN1971-019-024GL |
| 150 | basalt | 6.6 | 53.0 | 12.1 | 10.6 | 3.2 | 14.2 | 0.16 | WASTSDY-006-VG1466GL |
| 151 | basalt | 7.1 | 51.7 | 12.7 | 11.4 | 2.6 | 14.3 | 0.15 | OCNGR68-010-VG104GL |
| 152 | basalt | 7.6 | 50.7 | 11.4 | 12.5 | 2.8 | 14.8 | 0.16 | WFL2005-874-GS11-4GL |

| | | | | | | | | | |
|---|---|---|---|---|---|---|---|---|---|
| 153 | basalt | 8.1 | 51.7 | 8.1 | 11.9 | 3.2 | 16.6 | 0.38 | MELWEST-10-083-025GL |
| 154 | basalt | 8.6 | 51.1 | 9.6 | 12.3 | 2.7 | 15.5 | 0.11 | AII0125-24-R066GL |
| 155 | basalt | 9.1 | 51.4 | 9.2 | 12.8 | 1.8 | 15.6 | 0.17 | GIL0103-033-007GL |
| 156 | basalt | 9.6 | 50.1 | 8.8 | 13.0 | 2.0 | 16.4 | 0.14 | ALV0526-001-B-VG3397GL |
| 157 | basalt | 10.1 | 50.5 | 8.6 | 12.8 | 2.1 | 15.8 | 0.09 | ALV0534-002-001CGL |
| 158 | basalt | 10.6 | 50.4 | 8.6 | 12.9 | 2.2 | 15.3 | 0.07 | ALV0530-003-001GL |
| 159 | basalt | 11.3 | 48.4 | 9.1 | 12.4 | 2.2 | 16.5 | 0.10 | ALV0519-004-001GL |
| 160 | basalt | 11.9 | 47.5 | 11.1 | 12.2 | 1.9 | 15.4 | 0.06 | ENV7025-004-062GGL |
| 161 | basalt | 5.4 | 52.9 | 14.8 | 9.6 | 3.4 | 13.5 | 0.38 | DSC1983-R002-001GL |
| 162 | basalt | 5.9 | 52.6 | 13.8 | 10.6 | 3.1 | 13.7 | 0.12 | END0113-012-001GL |
| 163 | basalt | 6.4 | 52.0 | 13.4 | 10.6 | 3.4 | 14.0 | 0.20 | MELPROT-9-052-054GL |
| 164 | basalt | 6.9 | 52.3 | 11.1 | 11.4 | 3.3 | 14.8 | 0.12 | GIL0104-001-003GL |
| 165 | basalt | 7.4 | 51.9 | 10.5 | 10.8 | 3.3 | 15.9 | 0.12 | TRI0138-006-SG07GL |
| 166 | basalt | 7.9 | 51.2 | 10.4 | 12.3 | 3.0 | 15.0 | 0.16 | NHOCHEP-036-005GL |
| 167 | basalt | 8.4 | 52.0 | 9.0 | 12.0 | 3.0 | 15.6 | 0.16 | MELWEST-10-084-029-02GL |
| 168 | basalt | 8.9 | 52.1 | 9.7 | 11.3 | 2.6 | 15.1 | 0.31 | CHRRI88-010-104GL |
| 169 | basalt | 9.4 | 50.8 | 8.2 | 12.3 | 2.7 | 16.6 | 0.04 | KAK83NP-2-004-008AGL |
| 170 | basalt | 9.9 | 50.6 | 8.3 | 13.0 | 2.1 | 16.2 | 0.04 | AII0112-24-005-003GL |
| 171 | basalt | 10.4 | 48.5 | 8.6 | 12.5 | 2.5 | 17.5 | 0.02 | EWI0004-082-003GL |
| 172 | basalt | 10.8 | 49.0 | 9.2 | 12.0 | 2.2 | 16.6 | 0.08 | ALV0518-002-002GL |
| 173 | basalt | 11.7 | 48.9 | 8.7 | 12.2 | 2.4 | 16.1 | 0.10 | ALV0525-005-002GL |
| 174 | peridotite | 46.6 | 42.9 | 9.5 | 0.1 | 0.1 | 0.8 | 0.02 | Prot 31D-38 |
| 175 | peridotite | 46.3 | 44.9 | 8.1 | 0.0 | 0.0 | 0.7 | 0.00 | Prot 34D-1 |
| 176 | peridotite | 46.2 | 45.8 | 7.1 | 0.1 | 0.0 | 0.9 | 0.00 | ANTP 125D-9 |
| 177 | peridotite | 46.0 | 44.0 | 8.6 | 0.3 | 0.0 | 1.0 | 0.00 | ANTP 87D-7 |
| 178 | peridotite | 45.9 | 44.4 | 9.0 | 0.0 | 0.0 | 0.6 | 0.00 | Prot 16D-YN1 |
| 179 | peridotite | 45.9 | 44.4 | 8.1 | 0.4 | 0.0 | 1.2 | 0.00 | ANTP 84D-10 |
| 180 | peridotite | 45.7 | 44.8 | 8.6 | 0.0 | 0.0 | 1.0 | 0.00 | IO11-76-59-51 |
| 181 | peridotite | 45.4 | 44.9 | 7.4 | 0.8 | 0.0 | 1.4 | 0.01 | WW3 12D-1-9 |
| 182 | peridotite | 45.4 | 44.5 | 9.1 | 0.1 | 0.0 | 0.9 | 0.00 | INMD8 15D-7 |
| 183 | peridotite | 45.4 | 45.2 | 8.4 | 0.0 | 0.0 | 1.0 | 0.00 | IO11-76-59-54 |
| 184 | peridotite | 45.3 | 46.0 | 6.5 | 1.5 | 0.0 | 0.7 | 0.05 | CIRCE 82D-2 |
| 185 | peridotite | 45.3 | 45.0 | 8.8 | 0.0 | 0.0 | 0.8 | 0.03 | ANTP 135D-9 |
| 186 | peridotite | 45.1 | 44.5 | 8.5 | 0.6 | 0.0 | 1.3 | 0.10 | CIRCE 97D-6 |
| 187 | peridotite | 45.0 | 46.7 | 7.2 | 0.0 | 0.0 | 0.9 | 0.04 | ANTP 135D-10 |
| 188 | peridotite | 45.0 | 44.3 | 8.5 | 0.6 | 0.1 | 1.4 | 0.01 | AII 93.5 2D-HD1 |
| 189 | peridotite | 44.9 | 45.0 | 9.4 | 0.0 | 0.0 | 0.6 | 0.08 | CIRCE 82D-4 |
| 190 | peridotite | 44.8 | 44.9 | 8.0 | 0.5 | 0.1 | 1.7 | 0.01 | WW3 12D-1-63 |
| 191 | peridotite | 44.8 | 44.9 | 9.0 | 0.0 | 0.2 | 1.0 | 0.03 | Prot 5-40-89 |
| 192 | peridotite | 44.7 | 44.9 | 7.5 | 1.2 | 0.1 | 1.7 | 0.01 | ANTP 125D-11 |

| | | | | | | | | | |
|---|---|---|---|---|---|---|---|---|---|
| 193 | peridotite | 44.6 | 45.9 | 8.0 | 0.0 | 0.1 | 1.3 | 0.01 | Prot 5-39-6 |
| 194 | peridotite | 44.6 | 44.7 | 8.9 | 0.3 | 0.0 | 1.3 | 0.04 | INMD8 15D-5 |
| 195 | peridotite | 44.5 | 44.2 | 8.4 | 1.0 | 0.0 | 1.9 | 0.00 | ANTP 87D-3 |
| 196 | peridotite | 44.4 | 45.2 | 8.1 | 0.8 | 0.0 | 1.4 | 0.01 | WW3 12D-1-47 |
| 197 | peridotite | 44.3 | 44.6 | 8.7 | 0.3 | 0.1 | 2.0 | 0.00 | Prot 15D-35 |
| 198 | peridotite | 44.1 | 42.5 | 9.7 | 3.2 | 0.0 | 0.3 | 0.08 | CIRCE 93D-J |
| 199 | peridotite | 44.1 | 46.3 | 8.0 | 0.0 | 0.0 | 1.5 | 0.01 | AII107-40-23 |
| 200 | peridotite | 44.1 | 45.4 | 8.7 | 0.1 | 0.0 | 1.8 | 0.02 | RLF ANTP 114D-1 |
| 201 | peridotite | 44.1 | 45.3 | 8.6 | 0.9 | 0.0 | 1.1 | 0.01 | WW3 12D-1-11 |
| 202 | peridotite | 44.0 | 45.7 | 8.7 | 0.5 | 0.0 | 1.1 | 0.02 | Prot 13D-46 |
| 203 | peridotite | 44.1 | 45.3 | 8.3 | 0.4 | 0.0 | 1.9 | 0.00 | IO11-76-59-24 |
| 204 | peridotite | 44.0 | 45.2 | 8.2 | 1.2 | 0.0 | 1.3 | 0.00 | ANTP 126D-5 |
| 205 | peridotite | 44.0 | 46.2 | 8.4 | 0.1 | 0.0 | 1.3 | 0.01 | Prot 5-30--4 |
| 206 | peridotite | 43.9 | 45.6 | 8.2 | 1.2 | 0.1 | 1.0 | 0.02 | Prot 24D-35 |
| 207 | peridotite | 43.9 | 45.2 | 7.9 | 0.0 | 0.2 | 2.8 | 0.02 | Prot 5-29-24 |
| 208 | peridotite | 43.8 | 44.7 | 8.3 | 1.0 | 0.1 | 1.9 | 0.04 | Prot 10D-6 |
| 209 | peridotite | 43.6 | 44.1 | 10.3 | 1.3 | 0.0 | 0.7 | 0.04 | CIRCE 93D-G |
| 210 | peridotite | 43.6 | 45.2 | 7.7 | 1.1 | 0.1 | 2.4 | 0.01 | WW3 12D-1-62 |
| 211 | peridotite | 43.5 | 44.8 | 8.1 | 1.9 | 0.1 | 1.6 | 0.02 | Prot 38D-1 |
| 212 | peridotite | 43.5 | 46.2 | 8.7 | 0.4 | 0.1 | 1.1 | 0.05 | AII93-5-2D-HD7 |
| 213 | peridotite | 43.5 | 46.3 | 8.1 | 0.2 | 0.1 | 1.8 | 0.02 | RC27-9-34-37 |
| 214 | peridotite | 43.4 | 46.0 | 8.6 | 0.3 | 0.2 | 1.4 | 0.07 | Prot 39D-13 |
| 215 | peridotite | 43.3 | 46.8 | 8.1 | 0.1 | 0.1 | 1.6 | 0.03 | Vulcan 5-41-23 |
| 216 | peridotite | 43.1 | 46.5 | 8.3 | 0.5 | 0.1 | 1.5 | 0.04 | RLF INMD 12D-1 |
| 217 | peridotite | 43.1 | 44.9 | 8.1 | 1.5 | 0.0 | 2.3 | 0.01 | WW3 12D-1-8 |
| 218 | peridotite | 43.1 | 45.1 | 8.1 | 1.9 | 0.0 | 1.9 | 0.00 | Prot 5-38-1 |
| 219 | peridotite | 43.0 | 47.0 | 8.1 | 0.7 | 0.2 | 1.0 | 0.01 | Prot 40D-54 |
| 220 | peridotite | 43.0 | 46.7 | 8.7 | 0.2 | 0.1 | 1.4 | 0.01 | RC27-9-35-49 |
| 221 | peridotite | 42.9 | 44.5 | 7.9 | 2.1 | 0.1 | 2.4 | 0.00 | Prot 5-19--9 |
| 222 | peridotite | 42.9 | 45.1 | 8.3 | 1.1 | 0.3 | 2.2 | 0.03 | WW3 12D-1-64 |
| 223 | peridotite | 42.9 | 45.1 | 8.0 | 1.6 | 0.1 | 2.3 | 0.00 | WW3 12D-1-30 |
| 224 | peridotite | 42.7 | 46.1 | 8.2 | 0.8 | 0.1 | 2.2 | 0.00 | Prot 13D-43 |
| 225 | peridotite | 42.5 | 45.5 | 8.1 | 1.6 | 0.0 | 2.2 | 0.00 | WW3 12D-1-66 |
| 226 | peridotite | 42.5 | 46.0 | 8.0 | 0.7 | 0.3 | 2.6 | 0.01 | Vulcan 5-41-96 |
| 227 | peridotite | 42.4 | 48.2 | 6.7 | 0.5 | 0.2 | 2.0 | 0.02 | Vulcan 5-34-61 |
| 228 | peridotite | 42.4 | 45.2 | 8.9 | 1.6 | 0.2 | 1.8 | 0.01 | Vulcan 5-35-15 |
| 229 | peridotite | 42.3 | 45.9 | 7.9 | 2.8 | 0.1 | 1.0 | 0.06 | Prot 21D-3 |
| 230 | peridotite | 42.3 | 46.9 | 8.0 | 0.3 | 0.1 | 2.3 | 0.04 | Vulcan 5-41-26 |
| 231 | peridotite | 42.3 | 46.2 | 9.0 | 1.2 | 0.1 | 1.2 | 0.03 | AII107-40-8 |
| 232 | peridotite | 42.2 | 45.1 | 9.2 | 1.2 | 0.1 | 2.2 | 0.03 | AII 93.5 3D-HD7 |

| | | | | | | | | | |
|---|---|---|---|---|---|---|---|---|---|
| 233 | peridotite | 42.1 | 47.3 | 8.4 | 0.5 | 0.0 | 1.6 | 0.00 | RC27-9-35-80 |
| 234 | peridotite | 42.1 | 47.1 | 8.1 | 1.3 | 0.1 | 1.3 | 0.01 | Prot 24D-6 |
| 235 | peridotite | 42.0 | 47.0 | 8.1 | 0.5 | 0.0 | 2.3 | 0.01 | IO11-76-56-18 |
| 236 | peridotite | 41.9 | 46.9 | 7.3 | 1.9 | 0.1 | 1.9 | 0.01 | WW3 13D-4-1 |
| 237 | peridotite | 41.9 | 46.6 | 8.5 | 1.1 | 0.1 | 1.7 | 0.00 | RC27-9-34-43 |
| 238 | peridotite | 41.8 | 45.5 | 7.1 | 2.4 | 0.2 | 3.1 | 0.02 | Prot 5-19--1 |
| 239 | peridotite | 41.7 | 44.6 | 12.2 | 0.1 | 0.1 | 1.3 | 0.01 | Vulcan 5-35-3 |
| 240 | peridotite | 41.7 | 46.1 | 9.1 | 0.9 | 0.1 | 2.0 | 0.01 | Vulcan 5-41-97 |
| 241 | peridotite | 41.7 | 45.6 | 8.4 | 2.3 | 0.0 | 1.9 | 0.00 | Vulcan 5-41-28 |
| 242 | peridotite | 41.7 | 46.2 | 9.3 | 0.9 | 0.1 | 1.9 | 0.01 | Vulcan 5-37-3 |
| 243 | peridotite | 41.7 | 46.7 | 8.8 | 1.3 | 0.1 | 1.4 | 0.06 | Prot 5-29-31 |
| 244 | peridotite | 41.5 | 45.9 | 8.6 | 1.9 | 0.1 | 1.9 | 0.02 | Vulcan 5-41-55 |
| 245 | peridotite | 41.5 | 47.2 | 8.5 | 0.8 | 0.1 | 1.8 | 0.02 | RC27-9-44-1 |
| 246 | peridotite | 41.4 | 47.0 | 8.3 | 0.9 | 0.1 | 2.2 | 0.03 | RC27-9-35-63 |
| 247 | peridotite | 41.3 | 47.1 | 8.6 | 0.4 | 0.1 | 2.4 | 0.03 | IO11-76-56--1 |
| 248 | peridotite | 41.2 | 45.2 | 9.1 | 2.0 | 0.2 | 2.2 | 0.02 | RC27-9-6--8 |
| 249 | peridotite | 41.2 | 46.2 | 8.7 | 1.4 | 0.1 | 2.4 | 0.02 | IO11-76-58--3 |
| 250 | peridotite | 41.1 | 46.6 | 7.3 | 3.0 | 0.1 | 1.9 | 0.00 | WW3 13D-4-3 |
| 251 | peridotite | 41.1 | 45.5 | 8.5 | 2.1 | 0.2 | 2.7 | 0.01 | Vulcan 5-41-52 |
| 252 | peridotite | 41.1 | 47.1 | 8.9 | 0.3 | 0.2 | 2.4 | 0.04 | RC27-9-30-42 |
| 253 | peridotite | 41.1 | 46.1 | 9.4 | 1.0 | 0.1 | 2.3 | 0.01 | AII93-5-3-HD7 |
| 254 | peridotite | 41.0 | 46.3 | 8.0 | 0.7 | 0.1 | 4.0 | 0.01 | Vulcan 5-41-25 |
| 255 | peridotite | 40.9 | 45.5 | 8.8 | 2.6 | 0.2 | 2.1 | 0.02 | Vulcan 5-41-29 |
| 256 | peridotite | 40.9 | 46.6 | 9.1 | 1.5 | 0.2 | 1.6 | 0.05 | Vulcan 5-35-30 |
| 257 | peridotite | 40.9 | 47.2 | 8.8 | 1.0 | 0.1 | 2.0 | 0.01 | Vulcan 5-41-14 |
| 258 | peridotite | 40.8 | 46.4 | 9.6 | 1.0 | 0.2 | 2.1 | 0.02 | RC27-9-34-33 |
| 259 | peridotite | 40.8 | 47.3 | 7.3 | 2.2 | 0.3 | 2.1 | 0.02 | Vulcan 5-35-20 |
| 260 | peridotite | 40.7 | 47.0 | 9.0 | 1.2 | 0.2 | 2.0 | 0.02 | RC27-9-34-66 |
| 261 | peridotite | 40.7 | 47.5 | 7.3 | 2.4 | 0.1 | 2.0 | 0.00 | WW3 13D-5-1 |
| 262 | peridotite | 40.6 | 46.7 | 8.6 | 1.5 | 0.3 | 2.3 | 0.04 | Prot 15D-20 |
| 263 | peridotite | 40.6 | 47.4 | 7.9 | 2.1 | 0.1 | 1.8 | 0.06 | WW3 13D-5-2 |
| 264 | peridotite | 40.5 | 47.4 | 8.5 | 1.3 | 0.2 | 2.0 | 0.05 | Vulcan 5-35-25 |
| 265 | peridotite | 40.4 | 46.1 | 7.4 | 3.1 | 0.0 | 2.9 | 0.01 | CIRCE 97D-W |
| 266 | peridotite | 40.4 | 47.7 | 8.9 | 1.3 | 0.1 | 1.6 | 0.03 | AII107-40-6 |
| 267 | peridotite | 40.4 | 46.4 | 9.9 | 1.7 | 0.2 | 1.4 | 0.02 | AII107-40-27 |
| 268 | peridotite | 40.5 | 44.1 | 11.4 | 1.8 | 0.1 | 2.1 | 0.05 | ANTP 134D-1 |
| 269 | peridotite | 40.3 | 46.3 | 8.6 | 2.2 | 0.1 | 2.4 | 0.01 | IO11-76-58-34 |
| 270 | peridotite | 40.2 | 47.5 | 8.2 | 1.9 | 0.1 | 2.0 | 0.01 | Vulcan 5-35-37 |
| 271 | peridotite | 40.2 | 45.6 | 9.2 | 2.2 | 0.2 | 2.6 | 0.03 | RC27-9-18-37 |
| 272 | peridotite | 40.1 | 48.2 | 7.9 | 1.4 | 0.1 | 2.2 | 0.06 | IO11-76-59-49 |

| | | | | | | | | | |
|---|---|---|---|---|---|---|---|---|---|
| 273 | peridotite | 40.1 | 45.7 | 10.0 | 1.1 | 0.4 | 2.6 | 0.09 | IO11-76-56-23 |
| 274 | peridotite | 40.1 | 46.8 | 8.8 | 2.0 | 0.1 | 2.1 | 0.07 | RLF ANTP 117D-3 |
| 275 | peridotite | 39.8 | 46.0 | 8.7 | 2.6 | 0.2 | 2.6 | 0.02 | RC27-9-18-33 |
| 276 | peridotite | 39.6 | 47.1 | 8.8 | 1.3 | 0.2 | 2.9 | 0.04 | Vulcan 5-37-5 |
| 277 | peridotite | 39.6 | 46.7 | 8.8 | 1.9 | 0.3 | 2.8 | 0.05 | RC27-9-18-45 |
| 278 | peridotite | 39.5 | 46.4 | 9.1 | 2.1 | 0.2 | 2.7 | 0.01 | Vulcan 5-41-13 |
| 279 | peridotite | 39.4 | 46.7 | 9.3 | 1.6 | 0.4 | 2.4 | 0.05 | IO11-76-56-26 |
| 280 | peridotite | 39.4 | 46.9 | 9.0 | 1.6 | 0.2 | 2.8 | 0.05 | IO11-76-56-30 |
| 281 | peridotite | 39.3 | 45.1 | 9.5 | 3.1 | 0.2 | 2.8 | 0.03 | Vulcan 5-41-30 |
| 282 | peridotite | 39.3 | 45.3 | 10.2 | 2.1 | 0.2 | 2.7 | 0.03 | WW3 13D-6-1 |
| 283 | peridotite | 39.2 | 45.5 | 8.8 | 3.4 | 0.4 | 2.6 | 0.05 | RC27-9-6--3 |
| 284 | peridotite | 39.1 | 47.5 | 9.0 | 2.0 | 0.2 | 2.1 | 0.05 | Vulcan 5-35-40 |
| 285 | peridotite | 39.1 | 46.9 | 8.6 | 1.8 | 0.1 | 3.5 | 0.01 | Vulcan 5-41-15 |
| 286 | peridotite | 39.0 | 48.8 | 8.3 | 1.6 | 0.3 | 2.0 | 0.05 | Vulcan 5-35-2 |
| 287 | peridotite | 38.7 | 47.2 | 8.0 | 2.5 | 0.5 | 3.1 | 0.02 | AII107-60-40 |
| 288 | peridotite | 38.5 | 46.8 | 8.3 | 2.6 | 0.3 | 3.3 | 0.17 | RC27-9-25-141 |
| 289 | peridotite | 38.5 | 47.1 | 8.6 | 2.6 | 0.3 | 2.8 | 0.04 | Vulcan 5-35-19 |
| 290 | peridotite | 38.4 | 46.7 | 9.2 | 2.1 | 0.3 | 3.2 | 0.03 | RC27-9-18-31 |
| 291 | peridotite | 38.4 | 47.3 | 8.8 | 2.5 | 0.2 | 2.8 | 0.01 | RC27-9-30-44 |
| 292 | peridotite | 38.3 | 46.3 | 8.0 | 4.0 | 0.1 | 3.2 | 0.02 | RC27-9-30-28 |
| 293 | peridotite | 38.0 | 48.5 | 8.9 | 1.9 | 0.4 | 2.2 | 0.04 | AAII107-60-59 |
| 294 | peridotite | 37.9 | 46.8 | 8.7 | 3.2 | 0.2 | 3.2 | 0.03 | RC27-9-25-138 |
| 295 | peridotite | 37.8 | 47.5 | 8.6 | 3.2 | 0.2 | 2.7 | 0.03 | Prot 5-15-90 |
| 296 | peridotite | 37.5 | 48.3 | 9.0 | 1.7 | 0.2 | 3.2 | 0.03 | AII93-5-9-HD1 |
| 297 | peridotite | 37.0 | 48.4 | 9.2 | 2.3 | 0.2 | 2.8 | 0.08 | IO11-76-56--6 |
| 298 | peridotite | 36.4 | 49.0 | 8.6 | 2.5 | 0.3 | 3.2 | 0.04 | RC27-9-30-31 |
| 299 | peridotite | 45.1 | 44.6 | 8.0 | 1.1 | 0.1 | 1.0 | 0.00 | OM94-52h |
| 300 | peridotite | 46.2 | 44.1 | 8.0 | 0.9 | 0.1 | 0.7 | 0.01 | OM94-53 |
| 301 | peridotite | 46.9 | 42.6 | 8.7 | 0.9 | 0.1 | 0.8 | 0.00 | OM94-54 |
| 302 | peridotite | 46.6 | 44.5 | 7.6 | 0.5 | 0.1 | 0.8 | 0.01 | OM94-61 |
| 303 | peridotite | 45.0 | 44.5 | 8.1 | 1.3 | 0.1 | 1.1 | 0.00 | OM94-67 |
| 304 | peridotite | 44.5 | 45.1 | 7.9 | 1.4 | 0.1 | 1.0 | 0.00 | OM94-74h |
| 305 | peridotite | 44.8 | 44.5 | 8.3 | 1.2 | 0.1 | 1.0 | 0.00 | OM94-79 |
| 306 | peridotite | 46.1 | 43.7 | 8.7 | 0.8 | 0.1 | 0.6 | 0.00 | OM94-81 |
| 307 | peridotite | 45.0 | 44.9 | 8.4 | 0.8 | 0.1 | 0.8 | 0.00 | OM94-98 |
| 308 | peridotite | 46.0 | 44.2 | 8.2 | 0.9 | 0.1 | 0.7 | 0.00 | OM94-100 |
| 309 | peridotite | 44.6 | 45.1 | 8.4 | 1.1 | 0.1 | 0.7 | 0.00 | OM94-101 |
| 310 | peridotite | 44.3 | 45.2 | 8.5 | 1.0 | 0.1 | 0.8 | 0.00 | OM94-1031 |
| 311 | peridotite | 43.9 | 45.9 | 8.1 | 1.0 | 0.1 | 0.9 | 0.00 | OM94-104 |
| 312 | peridotite | 43.4 | 45.7 | 7.5 | 2.5 | 0.1 | 0.9 | 0.00 | OM94-106 |

|  |  |  |  |  |  |  |  |  |  |
|---|---|---|---|---|---|---|---|---|---|
| 313 | peridotite | 45.1 | 43.1 | 9.1 | 1.1 | 0.1 | 1.5 | 0.00 | OM94-1141 |
| 314 | peridotite | 46.4 | 43.7 | 8.5 | 0.7 | 0.1 | 0.5 | 0.00 | OM94-1151 |
| 315 | peridotite | 48.8 | 40.3 | 9.4 | 0.1 | 0.2 | 1.2 | 0.00 | OM94-52d1 |
| 316 | peridotite | 49.8 | 40.9 | 8.7 | 0.3 | 0.1 | 0.3 | 0.00 | OM94-55 |
| 317 | peridotite | 49.6 | 40.9 | 9.0 | 0.2 | 0.1 | 0.2 | 0.00 | OM94-57 |
| 318 | peridotite | 50.5 | 41.0 | 8.0 | 0.2 | 0.1 | 0.2 | 0.00 | OM94-69 |
| 319 | peridotite | 49.2 | 40.8 | 9.3 | 0.2 | 0.1 | 0.3 | 0.00 | OM94-74d |
| 320 | peridotite | 49.4 | 40.7 | 9.3 | 0.2 | 0.1 | 0.4 | 0.00 | OM94-78 |
| 321 | peridotite | 49.3 | 40.9 | 9.3 | 0.1 | 0.1 | 0.2 | 0.00 | OM94-80 |
| 322 | peridotite | 48.8 | 40.5 | 10.3 | 0.1 | 0.1 | 0.2 | 0.00 | OM94-99 |
| 323 | peridotite | 46.7 | 42.3 | 10.1 | 0.6 | 0.1 | 0.3 | 0.00 | OM94-1101 |
| 324 | peridotite | 48.5 | 40.4 | 10.2 | 0.2 | 0.1 | 0.5 | 0.00 | OM94-1111 |
| 325 | peridotite | 46.2 | 40.8 | 10.0 | 0.8 | 0.1 | 2.1 | 0.00 | OM94-1121 |

*Composition of reacting rocks in alteration simulations includes only the major oxides MgO, $SiO_2$, CaO, $Na_2O$, $K_2O$, $Al_2O3$ and FeO, calculated to anhydrous basis.

**Unique sample name from the literature source: (1-34) Sossi et al. (2016); (35-142) Starkey et al. (2009); (143-173) Gale et al. (2013); (174-298) Niu (2004); (299-325) Hanghoj et al. (2010).

Table D2

*Range and Percentile in the $H_2$ Generation Potential and Flux Predicted During Low-temperature Alteration of Various Fe-bearing Igneous Rock Types.*

| Rock Type | $H_2$ Generation Potential (log mole $H_2$ (km$^3$ rock)$^{-1}$) | | | | | |
|---|---|---|---|---|---|---|
| | Range | | Percentile | | | |
| | min | max | 5th | 25th | 75th | 95th |
| peridotite | 10.1 | 11.9 | 10.3 | 11.0 | 11.6 | 11.7 |
| komatiite | 3.8 | 12.1 | 7.0 | 10.1 | 11.0 | 11.5 |
| picrite | 3.8 | 11.4 | 4.3 | 6.1 | 10.0 | 11.1 |
| basalt | 4.3 | 9.0 | 4.7 | 5.6 | 7.5 | 7.9 |

*Calculated assuming alteration rates of 0.3 mm yr$^{-1}$.

**Calculated assuming alteration rates of 1 mm yr$^{-1}$.

Table S2. (cont'd)

| Rock Type | $H_2$ Flux (log mole $H_2$ km$^{-2}$ yr$^{-1}$)* | | | | | |
|---|---|---|---|---|---|---|
| | Range | | Percentile | | | |
| | min | max | 5th | 25th | 75th | 95th |
| peridotite | 3.6 | 5.3 | 3.7 | 4.5 | 5.1 | 5.2 |
| komatiite | -2.7 | 5.6 | 0.4 | 3.6 | 4.4 | 5.1 |
| picrite | -2.7 | 4.8 | -2.3 | -0.4 | 3.5 | 4.6 |
| basalt | -2.2 | 2.5 | -1.8 | -0.9 | 0.9 | 1.4 |

Table S2. (cont'd)

| Rock Type | $H_2$ Flux (log mole $H_2$ km$^{-2}$ yr$^{-1}$)** | | | | | |
|---|---|---|---|---|---|---|
| | Range | | Percentile | | | |
| | min | max | 5th | 25th | 75th | 95th |
| peridotite | 4.1 | 5.9 | 4.3 | 5.0 | 5.6 | 5.7 |
| komatiite | -2.2 | 6.1 | 1.0 | 4.1 | 5.0 | 5.5 |
| picrite | -2.2 | 5.4 | -1.7 | 0.1 | 4.0 | 5.1 |
| basalt | -1.7 | 3.0 | -1.3 | -0.4 | 1.5 | 1.9 |

## D.4. Supplementary Figures

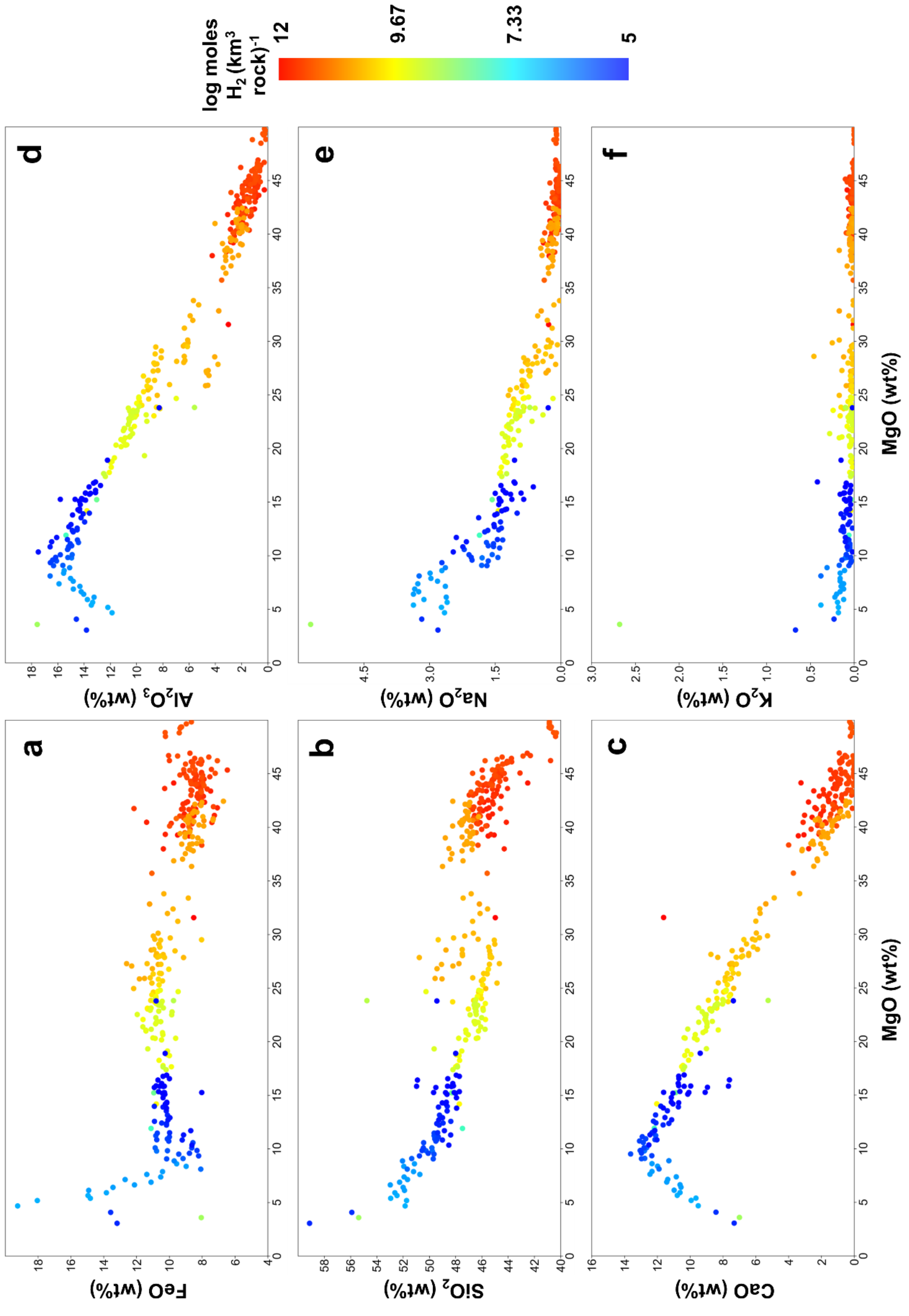

*Figure D1.* (prev. page) Influences of the major element compositions of rocks on calculated amounts of $H_2$ generated during hydrous alteration. The FeO (a), $SiO_2$ (b), CaO (c), $Al_2O_3$ (d), $Na_2O$ (e), and $K_2O$ (f) contents of compositions used in the simulations are plotted against their MgO content, while symbol color represents amount of $H_2$ produced (log mole $H_2$ ($km^3$ rock)$^{-1}$).

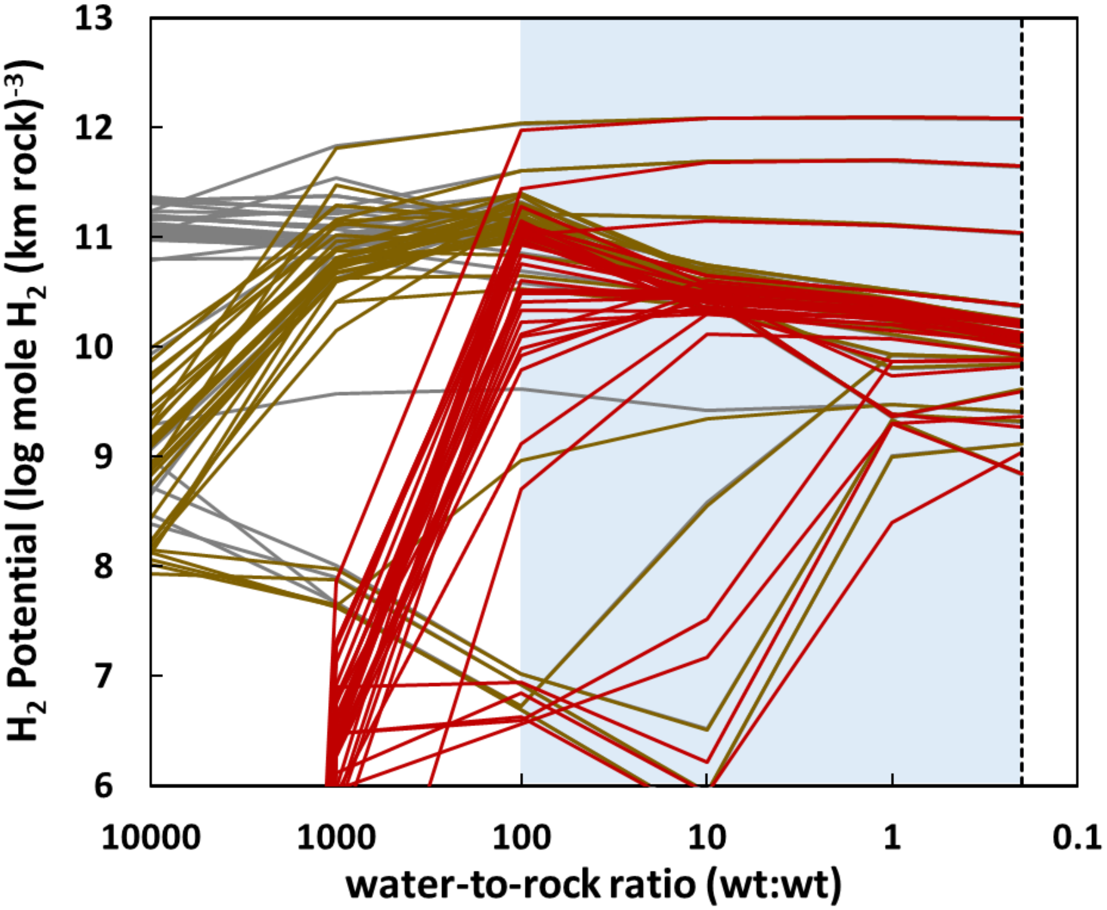

*Figure D2*. Calculated $H_2$ generated during hydrous alteration of komatiites at various degrees of water-to-rock ratios (x-axis). Left and right sides of the figure depict initial (high water-to-rock ratio or water-dominated systems) and advanced (low water-to-rock ratio or rock dominated systems) stages in the rock alteration progress, respectively. Colors depict results of simulations using various fluids with different starting dissolved $O_2$ in equilibrium with atmospheres with $10^{-0.7}$ (modern levels, red curves), $10^{-2}$ (brown curves), and $10^{-3}$ (grey curves) bars of $O_{2(g)}$. There are 34 curves of each color representing the reacting komatiites of variable compositions. Vertical dashed line indicates the lowest water-to-rock ratio (0.2) simulated. Blue field indicates conditions where water-to-rock ratio is <100, which are used in calculations of $H_2$ flux and global production rate.